University of Nevada, Reno

METALLOGENESIS OF THE PEÑASQUITO POLYMETALLIC DEPOSIT: A CONTRIBUTION TO THE UNDERSTANDING OF THE MAGMATIC ORE SYSTEM

A dissertation submitted in partial fulfillment of the requirements for
the degree of Doctor of Philosophy in Geology

By

Macario Rocha-Rocha

Dr. Tommy B. Thompson, Dissertation Advisor

May, 2016

THE GRADUATE SCHOOL

We recommend that the dissertation
prepared under our supervision by

MACARIO ROCHA-ROCHA

Entitled

METALLOGENESIS OF THE PEÑASQUITO POLYMETALLIC DEPOSIT: A CONTRIBUTION TO THE UNDERSTANDING OF THE MAGMATIC ORE SYSTEM

be accepted in partial fulfillment of the
requirements for the degree of

DOCTOR OF PHILOSOPHY

Tommy B. Thompson, Ph.D., Advisor

Peter G. Vikre, Ph. D., Committee Member

Thom Seal, Ph. D., Committee Member

John McCormack, Ph. D., Committee Member

Victor R. Vasquez, Ph.D., Graduate School Representative

David W. Zeh, Ph. D., Dean, Graduate School

May, 2016

ABSTRACT

In the study area, the Peñasquito ore deposit, there are some polymetallic ore bodies with singular physical, chemical, and mineralogical features, such as diatreme breccias, stockwork zones, skarn system, and a porphyry complex. The geotectonic characteristics suggest that the ore bodies are associated with a buried Late Eocene plutonic complex and that three sets of faults, which converge in Peñasquito played an important role during the formation of the ore deposit. The mineralization is hosted mainly in the diatreme breccia system, Caracol Formation, skarn system, and, to a lesser degree, the plutonic complex. The ore occurs as disseminations, veinlets, faults, veins, mantos, and irregular bodies. The mineralogy consists of base metal sulfides, sulfosalts, oxides, gold, electrum, bismuthinite, and accessory minerals, such as carbonates, calc-silicates, fluorite, and quartz. The hydrothermal alteration included a potassic core mainly developed from a plutonic complex of orthoclase, quartz, and plagioclase, which is surrounded by an aureole of calc-silicates and marble as well as an external phyllic halo and local peripheral zones of propylitic alteration which are overprinted by a late stage of carbonate.

The geochemical statistical analysis of the ore bodies typically exhibits a strong relationship between metallic elements (Au, Ag, Zn, Pb, Cu, Fe, Co, Mo, Cd, Hg) and semi-metallic elements (As, Sb, Bi, V), suggesting the presence of sulfosalt minerals. The metal content of these ore bodies is up to 536 ppm Au, up to 8,280 ppm Ag, up to 496,000 ppm Pb, up to 393,000 ppm Zn, up to 293,000 ppm Cu, and up to 4,880 ppm

Mo. The major geochemical elements in the plutonic products exhibit the following ranges: 54.1 to 80.2 % SiO_2, 0.4 to 18 % TiO_2, 10.5 to 17.6 % Al_2O_3, 0.2 to 2 % Fe_2O_3, 0.5 to 6.7 % FeO, 0.01 to 1.2 MnO, 0.4 to 4 % MgO, 0.4 to 22.2 % CaO, 0.1 to 4.7 % Na_2O, and 1.7 to 12.2 % K_2O, and 0.9 to 0.77 P_2O_5, reflecting both magmatic compositions and hydrothermal overprinting. The REE pattern indicated enrichment in LREE and depletion in HREE that are in agreement with the chemical signature of the upper crust. The bulk of the plutonic rocks exhibit intermediate compositions and the chemical classification ranges from sub-alkaline to alkaline to; however, magmas are calc-alkaline in source. Though the bulk of porphyries may chemically classify as quartz-monzonite and quartz-monzodiorite, some are classified as, granodiorite and others as quartz microdiorite. The trace elements and major oxides corroborated magmatic evolution-fractionation. The major oxides, trace elements, and REE suggested that magmas were generated in the upper crust during a continental epeirogenic uplift and expansive tectonic setting. However, the source could also be related to subduction, indicating possible crustal contamination. This ore deposit is located on the western border of a high magnetic anomaly and two diatreme breccias exhibit a low gravity and resistivity anomaly.

Microthermometric studies of fluid inclusions revealed homogenization tempera-tures (Th) in a range from 177°C to 600°C. The melting temperatures (Tm) observed in unsaturated fluid inclusions varied between -7.5°C and -21°C, which corresponds to 11.1 and 23.05 equivalent weight percent NaCl, but saturated fluid inclusions range between 30 to 58.32 equivalent weight percent NaCl, and 20 to 23 equivalent weight percent KCl.

The most common eutectic temperature (Te) was approximately -21°C, suggesting a predominance of sodium-chloride brine with moderate potassic-chloride brine. The C isotope analysis ($\delta^{13}C$ $_{VPDB}$), in calcite and rhodochrosite from veins related to these ore bodies, showed a range of -6.9 to -1.6 ‰; whereas, results of oxygen isotopes ($\delta^{18}O$ $_{VPDB}$) showed a range from -17.8 to -11.6 ‰. The range obtained for the standard $\delta^{18}O$ $_{VSMOW}$ was from 12.5 to 19 ‰. These results indicate a limestone source for oxygen and suggest a thermal influence on the isotopic fractionation or depletion. The results of the S isotope analysis ($\delta^{34}S$ $_{VCDT}$) varied from -2.1 to 3.2 ‰; for example, analyses of chalco-pyrite ranged from -2.1to 0.2 ‰ $\delta^{34}S$ $_{VCDT}$, the galena results ranged between -1.1 and -0.1 ‰ $\delta^{34}S_{VCDT}$, those of pyrite were between 0.3 and 2.8 ‰ $\delta^{34}S$ $_{VCDT}$, the sphalerite showed a range from -0.5 to 2.3 ‰ $\delta^{34}S$ $_{VCDT}$, and a sample of arsenopyrite was 0.8 ‰ $\delta^{34}S$ $_{VCDT}$. These results indicate that the sulfur source was related to the igneous system and linked to a gold-copper-type porphyry system. In addition, several isotopic mineral pairs, Sp-Gn, Sp-Py, and Py-Apy, from the main ore stage suggested temperatures from 264° and 561°C that are in agreement with the homogenization temperatures of fluid inclusions.

The U-Pb-Th geochronological data on zircons from the buried porphyries and diatreme breccia system indicate a magmatic pulse throughout ~46 to ~41 Ma and another magmatic stage at ~33.97 Ma (Valencia, 2010). The Re-Os molybdenite ages range from 35.72 ± 0.18 to 34.97 ± 0.17 Ma, indicating coeval mineralization in the Pe-ñasquito ore deposit. Hydrothermal orthoclase and biotite, ^{40}Ar-^{30}Ar geochronological

data are Early Oligocene about ~33.49 (i.e. biotite ages ranged between 33.95 ± 0.085 and 33.87 ± 0.065, and K-feldspar ages ranged from 32.82 ± 0.12 to 33.32 ± 0.16), suggesting that the bulk of the potassic alteration came slightly after crystallization of the second magmatic pulse, and these ages may be considered as the main mineralization age of the Peñasquito ore deposit. These ages suggest that the Mesozoic marine sedimentary sequence was intruded by several magmatic pulses that prepared and altered the sedimentary sequence providing metal ions which formed ore bodies after the Laramide orogeny thrust.

ACKNOWLEDGMENTS

which have been key factors in my personal and professional development. Furthermore, this work is also dedicated to the memory of M.Sc. Arlen Navarro-Moctezuma and M.Sc. Victor Vargas-Gutiérrez who provided support for this doctoral project.

Finally, the author is appreciative of those who contributed to this project and are not mentioned above. Without all of the excellent work and support, I would not have been able to complete this professional project. THANK YOU!

TABLE OF CONTENTS

LIST OF FIGURES

LIST OF TABLES

CHAPTER I INTRODUCTION AND REGIONAL SETTING

General Statement

Peñasquito is Mexico's largest gold, silver, lead, and zinc producing mine, located at the west central border of the Sierra Madre Oriental (SMOr). The country rock consists of a Mesozoic marine sequence intruded by Tertiary magmas. The ore deposit is comprised of two contiguous deposits (i.e. Peñasco Breccia and Azul Breccia), stockwork zones, a skarn system, and a porphyry complex with economic values of gold, silver, lead, zinc, and copper. Since late 2006, the ore deposit has been owned by Goldcorp. The Peñasco diatreme is being mined as an open pit, and production consists of enriched sulfide ore, which is treated by conventional flotation, and oxidized ore, which is subjected to a heap leaching procedure. As of December 31, 2015, the production totals are 860,300 oz Au, 25,926,500 oz Ag, 173,900 klb (thousand pounds) Pb, and 388,800 klb Zn, whereas, the total proven and probable reserves are: 10.17 Moz Au, 581.96 Moz Ag, 3,701 Mlbs Pb, and 8,886 Mlbs Zn.

The Peñasquito area is in the Mexican Belt of Folds and Faults (geological province), which is dominated by a Mesozoic sedimentary marine sequence intruded by a Tertiary stock complex, which developed endoskarn, exoskarn, skarnoid, hornfels, marble, and diatremes. The Peñasquito ore deposit is located on the western border of a wide mag-netic anomaly, and both diatremes exhibit a low-gravity anomaly. The diatreme breccias extend more than 1,000 m in depth, are of an inverted conical shape, and consist of five main types of heterolithic-monolithic breccias that are cut by felsic tuffisite and interme-

diate composition dikes. The stockwork zones were developed near the diatreme breccia systems within the Caracol Formation and are made of veinlets that are filled by primary sulfides, sulfosalts, and local calcite and quartz. A skarn system (including mantos) has been found between 700 and 1,300 m below the surface, but is open at depth, and includes massive primary sulfides, local sulfosalts and local secondary oxides. Mantos were predominantly developed in the Indidura and Cuesta de Cura formations with thicknesses exceeding 20 m. The skarn system, however, was developed in the Indidura, Cuesta de Cura, La Peña, Cupido, and La Caja formations, and is intercalated with marble sheets of irregular shape. The bulk of the quartz-feldspar porphyry stocks are below 1,000 m in depth, include disseminated sulfides, and contain veinlets of chalcopyrite, molybdenite, and local zinc and lead sulfides.

The economic mineralogy includes primary sulfides, sulfosalts, oxides, and local carbonates; all have a close relationship with physical controls (e.g., structural, stratigraphic, and karst features) and are related to a specific hydrothermal alteration system. The mineralization has been found as: (1) disseminated and/or filling veinlets in the quartz-feldspar porphyry; (2) massive in mantos and spread in the skarn system, and (3) disseminated and filling veins and veinlets throughout the stockwork zones and the diatreme breccia system. The hydrothermal alteration is formed by specific mineralogical assemblages, suggesting a zonation of halos configured around a potassic alteration core, enveloped by calc-silicates halo, marble and recrystallization, all of which were overprinted by a phyllic assemblage, and a distal propylitic alteration. In general, the paragenetic sequence was developed in several stages: (1) initially, primary sulfides were deposited

with the potassic and calc-silicate altered rocks; (2) a precipitation of sulfosalts and gold followed; (3) carbonates of manganese, zinc, and lead were developed mainly in shallow levels; and finally, (4) weathering effects developed limonite minerals.

The soil geochemistry has confirmed wide anomalies (Au-Ag-Pb-Zn-Cu-Ar-Sb) in the Peñasquito area. The geochemical statistics from drill cores have demonstrated that gold is associated with silver, bismuth, cadmium, copper, lead, antimony, and zinc; whereas, silver is strongly associated with lead, antimony, cadmium, zinc, and copper. In addition, a spatial distribution of economic chemical elements through the bedrock is evident, and the vertical zonation includes Au-Ag on top, Zn-Pb in the middle, and Cu-Mo at the base of whole hydrothermal system. The geochemical trace elements, major oxides, and REE's from the plutonic complex have indicated that the bulk of the plutonic rocks exhibited an intermediate composition. The chemical influence ranged from alkaline to sub-alkaline, and these magmas were generated in the upper crust. The Peñasquito ore deposit is located on the western borderer of a magnetic anomaly, and the diatreme breccias exhibit a gravity low anomaly. The fluid inclusions have demonstrated that the ore fluid temperatures ranged from 177° to 600°C. The results of the S isotope analysis ($\delta^{34}S_{VCDT}$) ranged from -2.1 to 3.2 ‰, suggesting that the sulfur source was related to the igneous system and linked to a porphyry copper-type magmatism. According to radiometric data, the ore bodies were formed during the Eocene about 35 to 33 Ma.

This research summarizes the exploration history of the project, describes the regional geologic setting, stratigraphy, structural and local lithology, geophysics and geo-

chemical signatures, hydrothermal alteration and mineralization features, documents the lifecycle of the hydrothermal system and genesis of the source, and discusses the geologic evolution of the mineralization within a regional tectonomagmatic framework. This document is based on more than two years of work by the author, during the dissertation program, and includes 1:1,000-scale pit mapping as well as 1:100-scale logging of 160,000 m of preexisting drill cores, 28 samples analyzed for major oxides, 270 petrographic-petrologic analyses, 38 microthermometric analyses, 38 isotopic analyses, three Re-Os molybdenite dates, four ^{40}Ar-^{39}Ar hydrothermal orthoclase and biotite dates, 30 SEM analyses, and the statistical geochemistry of millions of data. Previous published studies related to the survey area, including regional geologic and regional geophysical surveys as well as extensive unpublished in-house data (Goldcorp), provide the basis for this synthesis, such as local geophysics survey, soil geochemistry, porphyry dating, and technical reports.

Localization and Accessibility

The Peñasquito area is situated in the western half of the Concepción del Oro district (i.e. in north-central Mexico) which corresponds to the northeast border of the state of Zacatecas, Mexico, and about 228 km N23°E from the city of Zacatecas. Also, the area is situated N86°W from the town of Mazapil, Zacatecas. The geographical coordinates of the central Peñasquito area are: 24° 38' 56.1' north latitude, and 101° 40' 19.1'' west longitude (Fig. 1.1).
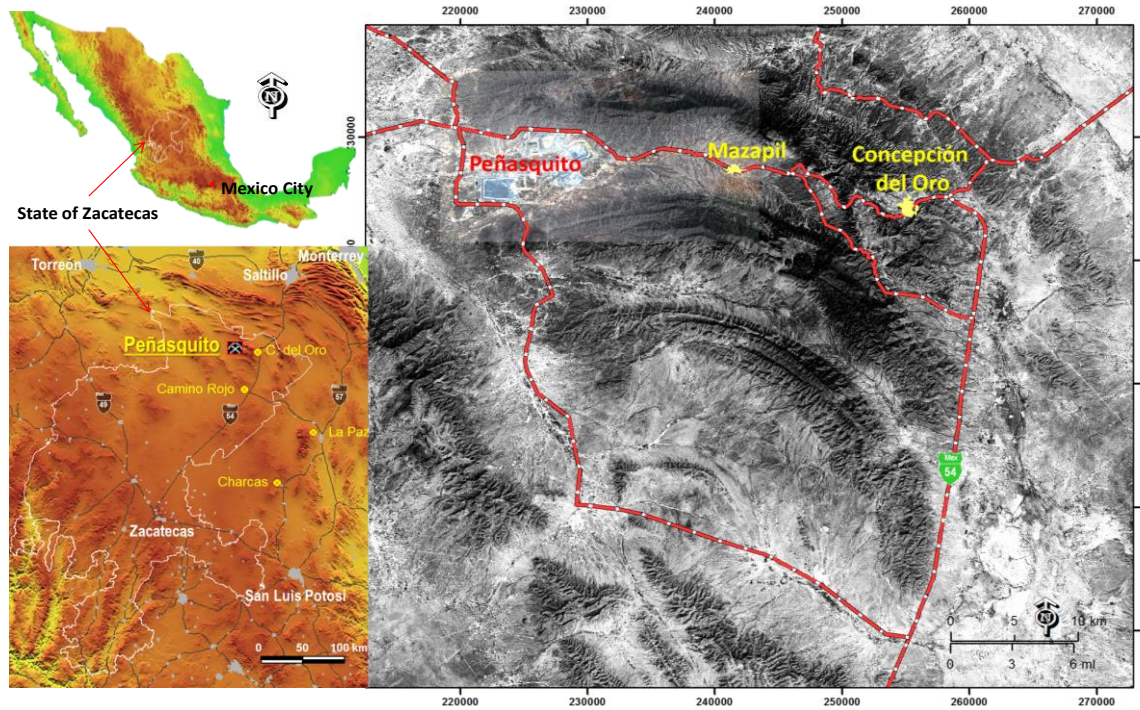
Fig. 1.1. Maps showing Mexico, state of Zacatecas, and the Peñasquito mine area (Images, roads, and highway were modified from MGS and INEGI database).

The area is accessible by two main paved roads (i.e. 45 and 71 km in length) northwest of national highway 54 with respective intersections approximately 6 and 38 kilometers south of Concepción del Oro. In addition, an airport is operating on site with connections to international airports in the cities of Hermosillo, Zacatecas, Saltillo, and Monterrey (Fig. 1.1).

Orography

The Peñasquito area is located in the western part of the Mazapil valley which is an elongated topographic basin with east-west orientation and a westward opening. The valley is 30 km in length by 5 km in width and is bordered to the north by Sierra La Caja-Concepción del Oro and to the south by Sierra Santa Rosa, which converge at the eastern

part of the valley. The topography of valley gradually decreases westward. The morphology of the valley is generally flat with some small rolling hills that are part of the landscape. The altitude of the valley ranges between 1,650 and 2,400 meters above sea level; however the predominant elevation of the Peñasquito area is 1,950 meters above sea level (INEGI, 2012). A stream runs throughout the valley (i.e. with direction from east to west), with small perennial springs in the eastern part. Also, an elongated topographic dome known as Cerro Gordo is present in the central-south part of the valley that is 2,500 meters in length, 800 meters in width, and up to 2,202 meters above sea level (Fig. 1.2).
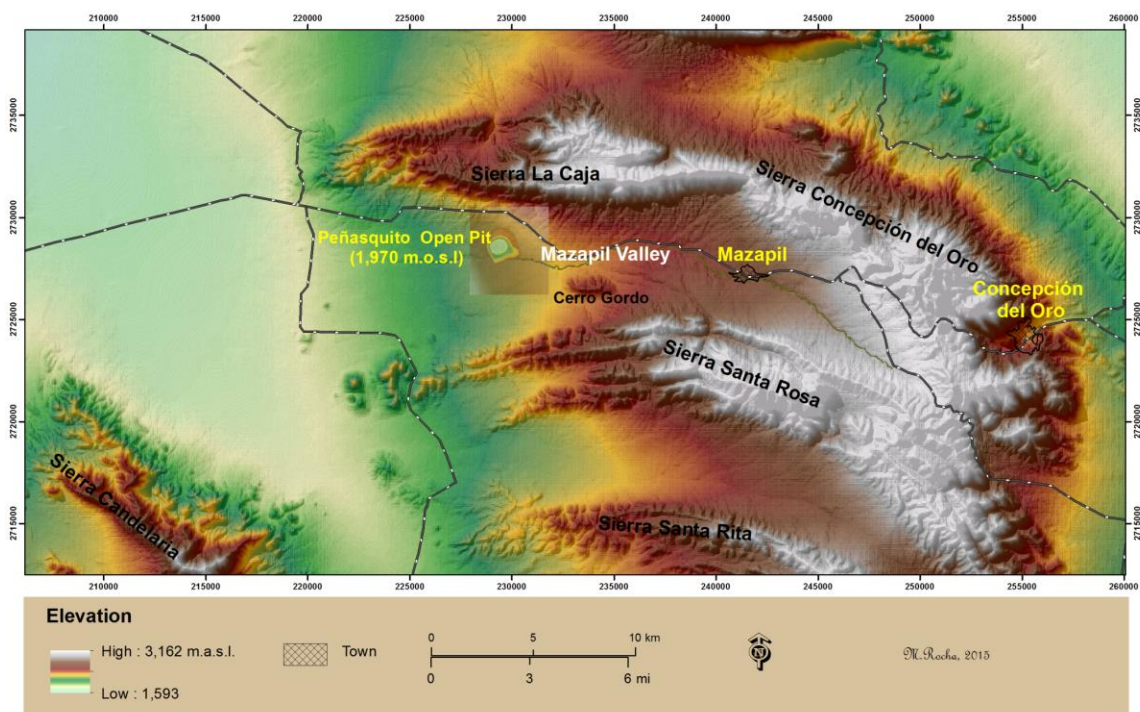
Fig. 1.2. Orography at Peñasquito area showing the mine and other localities mentioned above.

Climate

The region is dominated by a dry climate and a semi-desert environment. The climate is generally dry with seasonal precipitation principally in the summer. The temperature ranges between 20 and 30 degrees Celsius in the summer; however, in the winter, the temperature ranges between zero and 15 degrees Celsius (INEGI, 2012). The valleys are mostly covered by indigenous vegetation, such as creosote bush, cactus, and coarse grasses. The sierras are dominated by conifers, native palms, and wild agave (i.e. agavoideae bub-family).

Local Physiography

The Peñasquito property is characterized by features due to facilities developed during the mining operation. These include a semi-circular open pit 1.7 km in diameter and approximately 500 m in depth, spaces for tailings disposal, mine waste disposal (i.e. tailings dam), and mining-related infrastructure (i.e. processing plants, roads, workshops, and offices), as well as, artificial mounds (i.e. waste rock storage facilities) that protrude up to 200 m in height from the original physiography (Fig. 1.3). In addition, the accommodation infrastructure consists of a 2,000-bed camp with full dining, laundry, sport areas, and recreational facilities that are operational year-round. Noteworthy that the mining operation caused the interruption and deviation of the original stream (Arroyo Grande) to the southern portion; however, west of Peñasco open pit, the stream is not affected and maintains its natural pathway (Fig. 1.3).
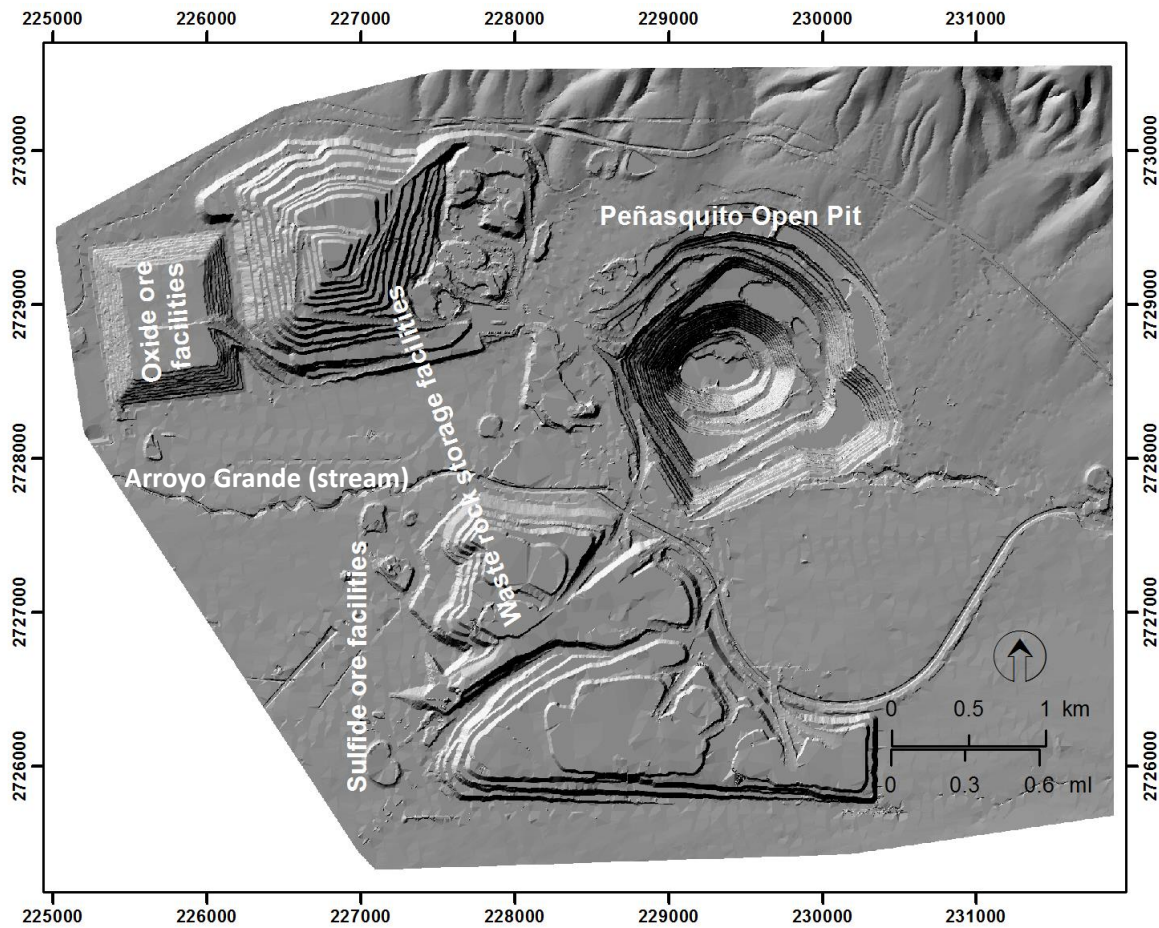
Fig. 1.3. 3D perspective of the Peñasquito area showing current mine-related features.

Purpose and Scope

The chief research aim is to document the physical-chemical conditions, and geological characteristics of this important, but little known, polymetallic ore deposit, and develop a model for its genesis. For this purpose, the research was focused on several ore bodies (i.e. the diatreme systems, stockwork zones, the skarn system, and the porphyry complex) using different inquiry techniques to establish the source and the relative timing of the ore deposit. As a result, the lithology and structural features from the diatreme systems and their surroundings have been examined and mapped in detail. The dikes

cutting the diatremes and the plutonic complex emplaced throughout the marine sedimentary sequence have been classified based on petrographic and geochemical data. The hydrothermal alteration, paragenesis, and geochemical zonation have been characterized and projected, resulting in an economic vectorization for the complete system. Some temperatures of formation for hydrothermal minerals and the source of sulfur and hydrothermal water were estimated based on stable isotope results (i.e. sulfur, carbon, and oxygen); furthermore, microthermometric data for primary fluid inclusions in the ore and gangue minerals (sphalerite, quartz, garnet, and fluorite) were obtained. Finally, the age of the hydrothermal system has been indicated based on results of radiogenic isotopes from hydrothermal products (i.e. biotite, K-feldspar, and molybdenite).

Historical Exploration

The region in which the Peñasquito polymetallic ore deposit is located has had a strong mining tradition that goes at least back to the early 16th century. It is believed that natives would have exploited some minerals around Concepción del Oro before the Spanish conquest, and they showed some ore bodies to Francisco de Urdiñola (Rogers et al., 1956; Mapes-Vázquez et al., 1964). The documented mining history began after the Spanish conquest in 1548, when Spanish conquistadors, commanded by Francisco de Urdiñola and Francisco de Ibarra, established one of the first mining haciendas in northern Mexico about 11.8 km N86°E from Peñasquito (i.e. Real de Minas de Mazapil). In this site, the Spanish auriferous-argentiferous production was monitored, which was exploited from chimneys and replacement deposits (San Eligio and Albarran mines) in the Sierra La

Caja-Concepción del Oro range (Rogers et al., 1956; Mapes-Vázquez et al., 1964; Bakewell, 1971).

The earliest direct recorded mine working in the Peñasquito area consist of artisanal exploratory work and a shallow shaft (MC Mexico, 2001; SGM, 2004). However, during the last twenty-four years, the aggressive exploration campaigns in Peñasquito have discovered and evaluated a large ore deposit, which was carried out by six companies: Kennecott S.A de C.V (Kennecott), Western Copper Holdings Limited (Western Copper), Western Silver Corporation (Western Silver), Mauricio Hochschild & Cia Ltda. (Hochschild), Glamis Gold Corporation (Glamis), and Goldcorp Inc (Goldcorp) (Belanger et al., 2010). The first five companies focused on three principal areas (i.e. Peñasco and Azul breccias, Chile Colorado stockwork), and conducted prospecting or geological reconnaissance, geochemical and geophysical surveys (gravity, controlled source audio frequency magnetotelluric "CSAMT", reconnaissance induced polarization "RIP", induced polarization "IP", radiometric and magnetic airborne) as well as drilling campaigns (i.e. rotary air blast "RAB", reverse circulation "RC", and core drilling).

The original outcrop of the Peñasco Breccia curiously protruded from the flat morphology in the Mazapil valley (i.e. 200 m^2 and up to 3 m in height). It is believed that under Spanish domain some artisanal explorations; such as shallow shafts were developed in order to explore the unknown area (Goldcorp, 2011). During the 1970s, Peñoles, a Mexican Company, funded a shaft (i.e. more than 60 m in depth) through Peñasco Breccia, and crosscut to the old Spanish workings. In addition, Peñoles completed two core holes

(i.e. 100 m in depth) but the results are unknown (MC Mexico, 2001; SGM, 2004; Gold-corp, 2014, verbal communication Gongora-Flemate, 2014).
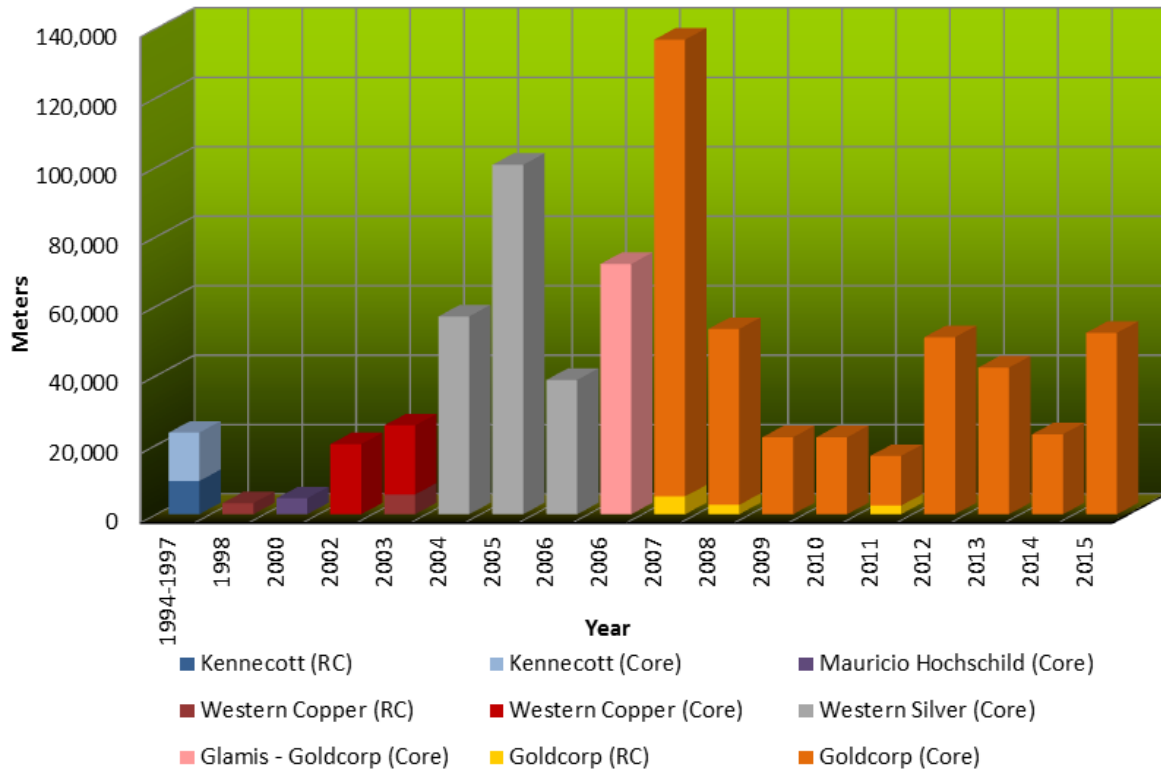
Fig. 1.4. Histogram showing the historical drilling at the Peñasquito area.

In 1994, Kennecott Canada Explorations Inc., through its Mexican subsidiary initiated a comprehensive exploration program, resulting in the recognition of some ore bodies and comprehension of the economic potential of the Peñasquito ore deposit. Between 1994 and 1997, Kennecott completed soil geochemistry, airborne and ground based geo-physical surveys (i.e. CSAMT: 45 linear km, RIP, IP: linear 33 km, radiometrics, magnetics, and ground magnetics), as well as drilling campaigns (MC Mexico, 2001). These explora-tion programs provided an understanding of ore deposits and well-defined targets (Belanger et al., 2014). For instance, the Peñasco and Azul Breccias were suggested due

the convergence of a low gravity anomaly and the broad geochemical anomalies of Au-Ag-Zn-Pb-Cu, while an IP survey indicated concentrations of sulfides adjacent to the Azul Breccia (i.e. Chile Colorado stockwork). The drilling programs were focused around the Peñasco outcrop; thus, 250 shallow RAB holes were completed (9,314 meters), and 72 RC holes (13,935 meters), the deepest extending to 997 m in depth (Fig. 1.4; Table 1.1). The results were the confirmation of mineralization consisting of silver-lead-zinc-gold-copper in the Peñasco and Azul Breccias, as well as the Chile Colorado zone (Goldcorp, 2014).

Table. 1.1. Summary of drill holes through December 2015 (Peñasquito Goldcorp records).

Year	Project Operator	RC		Core		Total	
		Number Holes	Meters	Number Holes	Meters	Number Holes	Meters
1994-1997	Kennecott	250	9,560	72	13,935	72	23,495
1998	Western Copper			9	3,185	9	3,185
2000	Mauricio Hochschild			14	4,601	14	4,601
2002	Western Copper			46	20,198	46	20,198
2003	Western Copper	57	5,699	46	19,897	103	25,596
2004	Western Silver			120	56,988	120	56,988
2005	Western Silver			169	100,626	169	100,626
2006	Western Silver			69	38,681	69	38,681
2006	Glamis–Goldcorp			123	72,071	123	72,071
2007	Goldcorp	24	5,146	194	131,535	218	136,681
2008	Goldcorp	10	2,702	58	50,643	68	53,345
2009	Goldcorp			47	22,182	47	22,182
2010	Goldcorp			37	22,175	37	22,175
2011	Goldcorp	59	2495.1	22	14,299	81	16,794
2012	Goldcorp			85	50,985	85	50,985
2013	Goldcorp			72	42,245	72	42,245
2014	Goldcorp			16	23,058	16	23,058
2015	Goldcorp			112	52,250	112	52,250
Totals						1,461	765,155

Note: RC (Reverse circulation)

In early 1998, Western Copper, a Canadian company, acquired 100% of the Peñasquito Project from Kennecott (MC Mexico, 2001, Goldcorp, 2014). Western Copper resumed drilling as well as geochemical and geophysical surveys (MC Mexico, 2001). For example, nine core holes (3,185 meters) were completed and 13.4 lineal kilometers of

geophysical survey (i.e. CSAMT) were carried out on the Peñasquito mining property with a focus on the Chile Colorado and Azul Breccia (Belanger et al., 2014). However, in August of 2000, Western Copper optioned the property to Hochschild, a Peruvian company. During late 2000, Hochschild completed 14 core drill holes (4,601 meters drill program) with 11 drill holes in the Chile Colorado zone (MC Mexico, 2001). The drilling reached down to 452 m in depth, and one result was the limitation of the ore body known as Chile Colorado, suggesting an influence up to 400 by 400 meters and contained in stockwork veinlets with Au-Ag-Pb-Zn-Cu mineralization (MC Mexico, 2001).

In late 2001, the property was returned to Western Copper. In 2002, this company resumed drilling and 46 core drill holes were completed (20,198 meters). In 2003, 57 RC (5,699 meters) and 46 more core drill holes (19,897 meters) were completed (see Fig. 1.4). Western Copper underwent a name change in 2004 and became Western Silver (Belanger et al., 2014). The exploration focused on the Peñasquito area with specific targets. In 2004, Western Silver carried out CSAMT and IP surveys with more coverage than the pre-existing geophysics surveys and continued drilling. The geophysical data provided an identification of the underlying lithology as well as new targets of interest. Between 2004 and April 2006, Western Silver drilled a total of 358 core drill holes (196,295 meters) throughout the entire Peñasquito property with some extending 476 meters below the surface. According to Belanger et al. (2014) in 2004, a pre-feasibility study was completed; a year later a feasibility study was undertaken, and later updated in 2006.

During the first semester of 2006, Glamis acquired Western Silver and in November 2006, Glamis was merged with Goldcorp. Glamis-Goldcorp drilled 123 core drill holes (72,071 meters).

Goldcorp continued aggressive drilling through the end of 2007; however, the drilling activity has decreased during the course of the last six years. Between 2007 and December 2015, Goldcorp completed a total of 93 RC (10,343 meters) and 736 core drill holes (419,715 meters) throughout the Peñasquito property with some drilling reaching more than 2,000 m in depth (see Fig. 1.4). The targets were the condemnation of mining facility areas (i.e. evaluation of bedrock under the alluvial cover up to 450 m below the current surface) and deep anomalies such as the skarn system and the porphyry complex. The results have provided a thorough understanding of the Peñasquito ore deposit as well as the delimitation of ore bodies within the skarn system. Furthermore, Goldcorp updated the feasibility study before mining began in July 2007. Throughout 2010 and 2011, a HELITEM time domain EM helicopter survey, a high-sensitivity aeromagnetic survey, and airborne gravity surveys were completed that included the Peñasquito area.

In summary, between 1994 and 2015, a total of 1,461 drill holes were completed in Peñasquito area (see Table 1.1). This corresponds to a total of 765,155 meters, focused on the exploration and delimitation of targets such as the Peñasco and Azul Breccias, the Chile Colorado stockwork, the skarn system, and the porphyry complex.

Metallurgical Process

The Peñasquito mine is currently owned by Goldcorp and is operated by Minera Pe-
ñasquito S.A. de C.V., which is a subsidiary of Goldcorp. In 2007, construction of the mine
and related facilities began. By year-end 2010, the process plant elements were com-
pleted (i.e. metallurgical plants, main roads, pre-strip of the Peñasco deposit, etc.); at that
time, the operation began production that has increased through 2014 (Belanger et al.,
2010, 2014).

Table 1.2. Summary of statistical data of metallurgical processes (modified from Belanger et al.,
2010, 2014 and Goldcorp, 2015,2016).

Plant Product Statistics – Oxide						
Year	2010	2011	2012	2013	2014	2015
Ore processed (dmt)	10,540,200	11,126,000	5,954,500	10,471,500	3,053,000	3,038,400
Au Produced (oz)	78,400	55,800	42,700	62,300	36,600	27,600
Ag Produced (oz)	3,006,200	1,891,000	1,420,300	1,684,100	931,600	642,200

Plant Product Statistics – Sulfide						
Year	2010	2011	2012	2013	2014	2015
Ore processed (dmt)	20,637,600	30,999,200	36,406,900	38,762,400	39,913,100	39,079,400
Pb Concentrate (dmt)	79,800	132,500	144,900	155,100	154,200	159,300
Zn Concentrate (dmt)	143,700	258,300	298,400	267,300	328,000	375,100
Au Grade (g/t)	0.27	0.37	0.50	0.45	0.65	1.00
Au Rec (%)	48	61	69	66	70	72
Au Produced (oz)	89,800	198,300	368,600	341,500	531,200	832,700
Ag Grade (g/t)	27.57	26.20	27.41	23.95	26.78	28.25
Ag Rec (%)	58	74	77	77	79	80
Ag Produced (oz)	10,946,400	17,154,500	22,284,500	20,763,300	24,875,500	25,284,300
Pb Grade (wt%)	0.38	0.34	0.28	0.27	0.25	0.30
Pb Rec (%)	60	70	74	73	74	71
Pb Produced (klb)	97,400	154,700	153,700	159,100	152,300	173,900
Zn Grade (wt%)	0.63	0.64	0.62	0.53	0.56	0.68
Zn Rec (%)	65	76	77	73	80	79
Zn Produced (klb)	154,500	286,400	324,200	279,300	329,700	388,800

Note: dmt (dry metric tonnes, oz (ounces), klb (thousand pounds).

The Peñasco diatreme breccia is being mined as an open pit and its products are processed by two separate metallurgical facilities (i.e. an oxide ore facility and a plant to process sulfide ore). It is noteworthy that all production has been processed at Peñasquito facilities; therefore, there is a leach facility with the capacity to process a nominal 25,000 metric tonnes per day (t/d) of oxide ore as well as a sulfide plant with the capacity to process a nominal 130,000 t/d of sulfide ore in two metallurgical lines. Since early 2008, the oxide ore has been processed through a heap leach (i.e. Merrill-Crowe facility). Meanwhile, since the third quarter of 2009, the sulfide plant began operating and the first lead and zinc concentrates were produced in October 2009, whereas the first sales were recorded in November 2009 (Belanger et al., 2010).

Heap Leaching Procedure

In the Peñasquito facilities, a leach pad of oxidized ore is used to recover precious metals. This leaching operation has multiple levels with a total pad capacity of 87,688,000 tonnes, and at the base an underlying impervious coating (polyethylene membrane) is completely containing all of the leach solution (Rivera-Zamora, 2014). The placement of the heap leach pad began in February 2008 and was completed two months later with the first gold pour on May 10, 2008 (Belanger et al., 2014; Rivera-Zamora, 2014). The leach pad occupies 90 hectares and was designed with a total of 15 levels of 10 m in height (see Fig. 1.3). The oxidized blasted ore (ROM) is gradually placed on the leach pad and distributed on the levels (Fig. 1.3, 1.5).

At the end of the second quarter 2014, a total of 72,000,000 dry metric tonnes of oxidized ore have been placed on the leach pad (i.e. this represents 86% of its total storage capacity). The plant has a capacity to process about 18,250,000 tons per year (i.e. oxidized ore that has been extracted directly from the mine). The coarse and oxidized ore ideally contains 0.18 g/t gold and 23.3 g/t silver (Rivera-Zamora, 2014). In the period from 2010 to 2014, a total of 275,800 oz Au and 8,933,200 oz Ag have been produced from the oxide facility (Belanger et al., 2014, and Goldcorp, 2015) and the cumulative recovery has reached up to 56 percent for gold and up to 24 percent for silver. Annual production has reached up to 82,000 ounces of gold and 3, 418,000 ounces of silver (Rivera-Zamora, 2014).
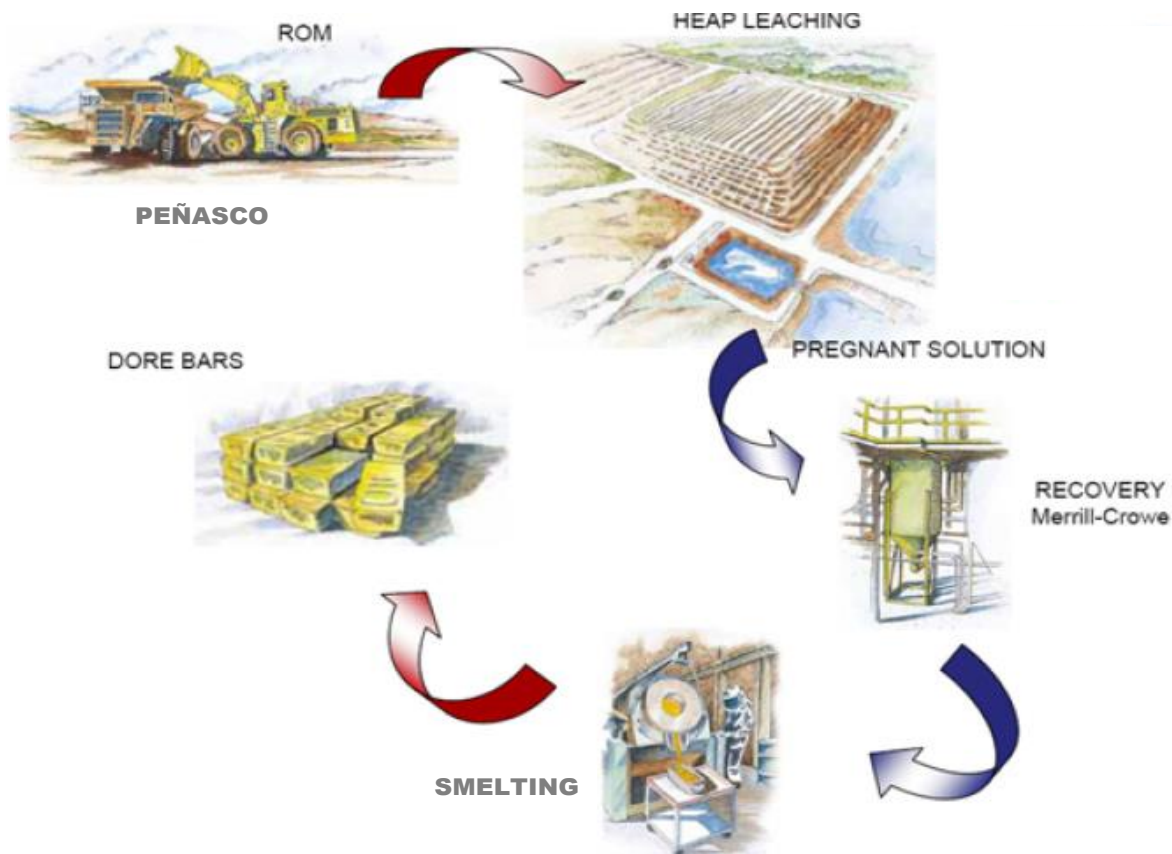
Fig. 1.5. Oxide flowsheet (modified from Belanger et al., 2014)

According to Rivera-Zamora (2014) gold and silver are recovered from the leach pad levels through the distribution of a solution of dilute sodium cyanide on the surface of the oxidized ore heap. As the solution percolates down through the oxidized ore, the cyanide leach solution is enriched in gold and silver. The enriched solution (auriferous and argentiferous) flows by gravity from the dump or platform to the pool of metal rich solution. Gold and silver are then extracted from the rich solution using the Merrill-Crowe process in order to get doré bars.

The Merrill-Crowe process involves a chemical reaction with zinc dust in order to precipitate the gold and silver (i.e. $2Au(CN)^{2-} + Zn = 2Au + Zn(CN)_4^{-2}$ and $2Ag(CN)^{2-} + Zn = 2Ag + Zn(CN)_4^{-2}$) (Rivera-Zamora, 2014). The procedure includes several stages in the recovery plant: (1) the enriched solution is passed through pressure clarifying filters where horizontal blades are used to remove suspended solids; (2) the solution is passed through a deaerator in order to remove dissolved oxygen (i.e. deoxygenation); (3) zinc powder is added to the solution to precipitate the enriched gold and silver; and lastly, (4) the solution of gold and silver is filtered to produce a cake of precipitate and a clean, sterile solution (i.e. without gold and silver) that is returned to the water system. The nominal flow of enriched solution to the recovery plant is 1,364 m^3/hr (Fig. 1.5). Meanwhile, the cake of precipitate is refined through a procedure that includes two stages: (1) the cake must be dried in an oven in order to remove any mercury; and (2) finally, the smelting process includes precipitation and distillation in order to produce doré bars with a purity up to 99.4 %, which includes up to 96% Ag and up to 3% Au (Rivera-Zamora, 2014).

Sulfide Procedure

In 2010, the sulfide plant (Fig. 1.6) began full operations with two main metallurgic lines, producing lead and zinc concentrates. Production of the zinc line was initiated on September 19, 2009, and the lead line initiated operation on June 8, 2010 (Belanger et al., 2014). The plant has gradually increased its production; for instance, in 2013, approximately 104,000 metric tonnes of sulfide ore were processed each day (i.e. functioning at 80% of its total capacity). The ore must have a sulfurization index greater than 60% (Romero, 2014). In the period from 2010 to 2014, the average grade of ore has been about 0.45 g/t Au, 26.38 g/t Ag, 3000 ppm Pb, and 6000 ppm Zn; meanwhile, the average recovery has been about 62.80% Au, 73% Ag, 70.2% Pb, 74.20% Zn. In this way a total of 1,529,400 oz Au, 96,024,200 oz Ag, 717,200 klb Pb, and 1,374,100 klb Zn have been produced from the sulfide facilities (Belanger et al., 2014).

The sulfide recovery consists of a several stage procedure that has required stages in order to achieve the concentrates. Initially, the sulfide ore (ROM) from the mine is delivered to a primary crusher dump with a crushing capacity of 5,300 metric tonnes per day. The crushed material (up to 3 inches in diameter) is then fed into a secondary grinding which reduces the particle size to a range of 125-145 microns in diameter. The fine material is passed through a lead circuit that has 15 primary cells in tanks up to 250 cubic meters, and forms a lead concentrate. Subsequently, the material is then integrated into the zinc circuit, which includes 18 cells and results in a zinc concentrate. Finally, the

waste material undergoes a thickening process and is deposited behind a tailings dam (Fig. 1.6).
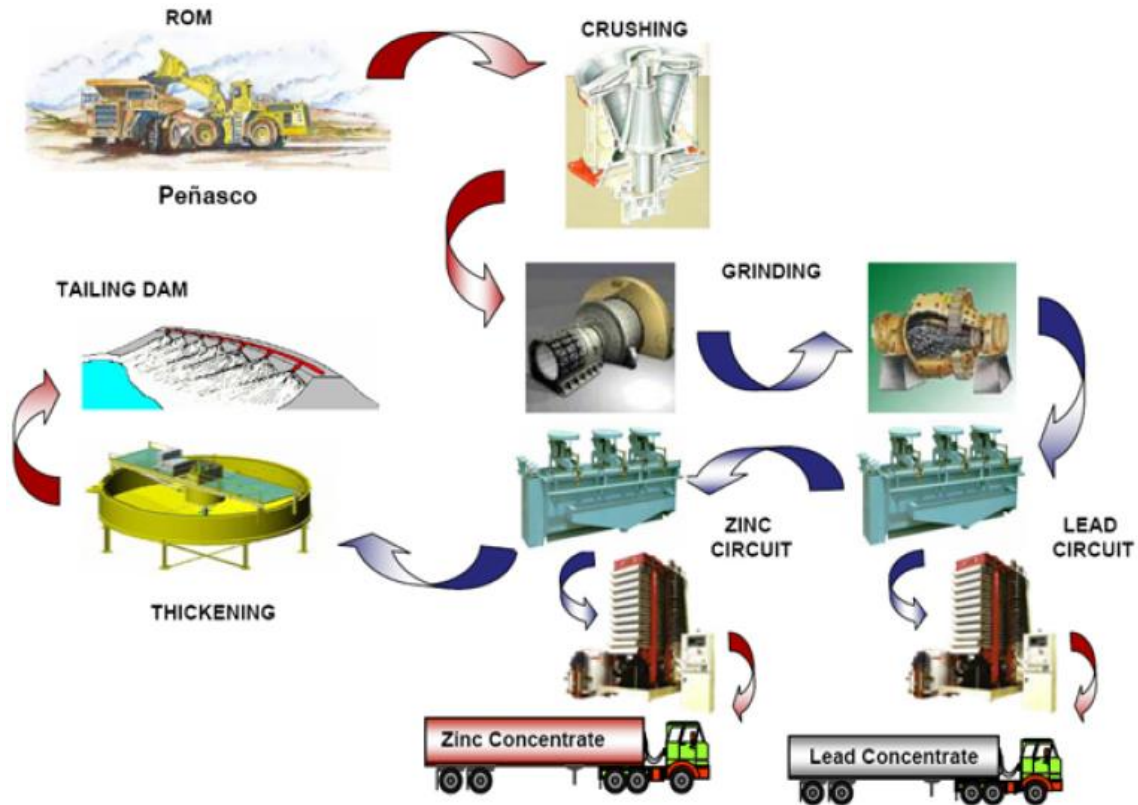
Fig. 1.6. Sulfide flowsheet (modified from Belanger et al., 2014)

Total Production and Reserves

The total metals production has increased gradually from the beginning of mining operations. The polymetallic production has mainly been from the Peñasco diatreme. The mined ore includes primary sulfides and sulfosalts found in vein/veinlets and disseminated through the breccias as well as oxides in the country rock. From 2010 to 2015, the total production was estimated to be 2,665,500 oz Au, 130,883,900 oz Ag, 891,100 lb lead, and 1,762,900 lb Zn (Fig. 1.7).

Total Au Produced (Oz)

Total Ag Produced (Oz)

Total Pb Produced (klb)

Total Zn Produced (klb)
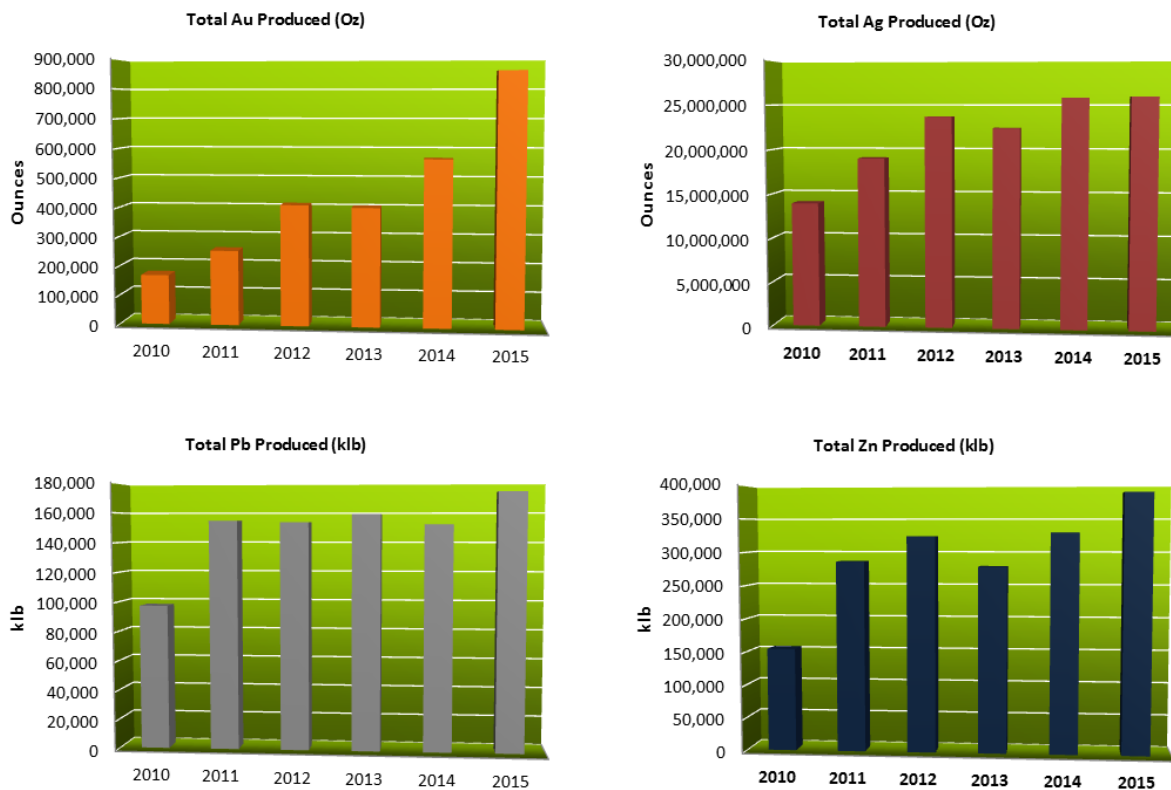
Fig. 1.7. Histograms showing the polymetallic historical production from Peñasquito mine. Note: Klb (Thousand pounds), oz (ounces).

In 2015, the total removed material from the Peñasco open pit was estimated to be 194,041,300 tonnes (Goldcorp, 2016). This mined material included: 1) sulfide ore (39,079,400 tonnes); 2) oxide ore (3,038,400 tonnes), and 3) waste (151,923,500 tonnes). Mining operations are conducted year-round.

The proven and probable reserves increased from 2007, peaking in 2010 (i.e. 18.57 Moz Au, 1,068.7 Moz Ag, 7,275 Mlbs Pb, and 17,575 Mlbs Zn), and have gradually de-creased in 2013 (Fig. 1.8). From 2014 to 2015, the proven and probable reserves increased slightly (Fig. 1.8 and Table 1.3.) due to the addition of newly explored targets including the skarn system, which could further increase the ore reserves in the future.

Gold Ore/Mineral Reserves

	2007	2008	2009	2010	2011	2012	2013	2014	2015
Heap Leach	0.65	0.8	0.4	0.4	0.53	0.52	1.00	0.85	0.30
Mill	12.4	16.63	17.42	18.17	16.01	15.17	10.62	9.70	9.87

Silver Ore/Mineral Reserves

	2007	2008	2009	2010	2011	2012	2013	2014	2015
Heap Leach	64.40	72.10	34.50	36.55	43.12	42.28	76.88	81.52	15.41
Mill	799.50	973.60	1,035.	1,068.	917.10	899.52	528.23	529.65	566.55

Lend Ore/Mineral Reserves

	2007	2008	2009	2010	2011	2012	2013	2014	2015
Mill	5,876.	7,070.	7,211.	7,275.	6,165.	5,814.	3,695.	3,757.	3,701.

Zinc Ore/Mineral Reserves

	2007	2008	2009	2010	2011	2012	2013	2014	2015
Mill	12,806	15,364	15,930	17,575	14,767	13,961	8,973.	9,081.	8,886.

Fig. 1.8. Histograms showing proven and probable reserves in the Peñasquito ore deposit.

Table 1.3. Summary of reserves in Peñasquito (Data from Goldcorp 2013, 2015, 2016; Belanger et al., 2010, 2014).

Year			2007		2008		2009		2010		2011		2012		2013		2014		2015	
Destination process			Heap Leach	Mill	Heap Leach	Mill	Heap Leach	Mill	Heap Leach	Mill	Heap Leach	Mill	Heap Leach	Mill	Heap Leach	Mill	Heap Leach	Mill	Heap Leach	Mill
Gold	PROVEN	Tonnage (Mt)	42.20	426.80	57.80	561.21	72.50	580.58	18.69	719.99	33.32	626.47	32.34	577.90	41.97	335.03	43.78	336.26	16.32	398.28
		Grade (g /t)	0.21	0.57	0.20	0.63	0.17	0.62	0.23	0.51	0.15	0.54	0.15	0.55	0.42	0.71	0.35	0.64	0.45	0.58
		Contained (Moz)	0.28	7.85	0.36	11.39	0.40	11.47	0.14	11.88	0.16	10.93	0.16	10.27	0.56	7.67	0.49	6.92	0.24	7.48
	PROBABLE	Tonnage (Mt)	68.30	380.30	124.65	447.73	_	564.19	49.11	701.42	92.10	517.19	87.41	484.71	41.49	194.94	45.96	210.72	5.46	188.40
		Grade (g /t)	0.17	0.37	0.11	0.36	_	0.33	0.27	0.28	0.13	0.31	0.13	0.31	0.33	0.47	0.24	0.41	0.37	0.39
		Contained (Moz)	0.37	4.55	0.43	5.25	_	5.93	0.26	6.29	0.37	5.08	0.36	4.90	0.44	2.95	0.35	2.77	0.07	2.39
	PROVEN & PROBABLE	Tonnage (Mt)	110.50	807.10	182.45	1,008.94	72.50	1,144.76	67.80	1,421.41	125.42	1,143.65	119.75	1,062.61	83.46	529.97	89.74	546.98	21.78	586.68
		Grade (g /t)	0.18	0.48	0.14	0.51	0.17	0.47	0.18	0.40	0.13	0.44	0.13	0.44	0.37	0.62	0.29	0.55	0.43	0.52
		Contained (Moz)	0.65	12.40	0.80	16.63	0.40	17.42	0.40	18.17	0.53	16.01	0.52	15.17	1.00	10.62	0.85	9.70	0.30	9.87
Silver	PROVEN	Tonnage (Mt)	42.20	426.80	57.80	561.21	72.50	580.58	18.69	719.99	33.32	626.47	32.34	577.90	41.97	335.03	43.78	336.26	16.32	398.28
		Grade (g/t)	20.90	34.00	18.40	33.90	14.80	23.00	20.10	27.00	14.39	28.89	14.58	29.37	32.66	34.67	31.67	33.31	22.71	32.63
		Contained (Moz)	28.30	455.90	34.30	611.50	34.50	618.02	12.07	625.69	15.41	581.92	15.16	575.76	44.07	373.42	44.58	360.11	11.92	417.86
	PROBABLE	Tonnage (Mt)	68.30	380.30	124.65	447.73	_	564.19	49.11	701.42	92.10	517.19	87.41	484.71	41.49	194.94	45.96	210.72	5.46	188.40
		Grade (g/t)	16.40	27.20	9.40	25.20	_	23.00	15.50	19.60	9.36	20.16	9.65	20.78	24.60	24.70	25.00	25.03	19.89	24.55
		Contained (Moz)	36.10	332.60	32.80	362.10	_	417.58	24.48	443.03	27.71	335.18	27.12	323.76	32.81	154.81	36.94	169.54	3.49	148.69
	PROVEN & PROBABLE	Tonnage (Mt)	110.50	807.10	182.45	1,008.94	72.50	1,144.76	67.80	1,421.41	125.42	1,143.65	119.75	1,062.61	83.46	529.97	89.74	546.98	21.78	586.68
		Grade (g/t)	18.10	30.80	12.30	30.00	14.80	28.10	16.80	23.40	10.69	24.94	10.98	25.45	28.65	31.00	28.25	30.12	22.00	30.04
		Contained (Moz)	64.40	799.50	72.10	973.60	34.50	1,035.60	36.55	1,068.72	43.12	917.10	42.28	899.52	76.88	528.23	81.52	529.65	15.41	566.55
Lead	PROVEN	Tonnage (Mt)		426.80		561.21		580.58		719.99		626.47		577.90		335.03		336.26		398.28
		Grade (%)		36.00		0.26		0.35		0.27		0.29		29.00		0.35		0.35		0.32
		Contained (Mlbs)		3,432.00		4,437.00		4,450.00		4,303.00		3,955.00		3,702.99		2,621.00		2,578.00		2,774.00
	PROBABLE	Tonnage (Mt)		380.30		447.73		564.19		701.42		517.19		484.71		194.94		210.72		188.40
		Grade (%)		0.29		0.27		0.22		0.19		0.19		0.20		0.25		0.25		0.22
		Contained (Mlbs)		2,444.00		2,633.00		2,761.00		2,972.00		2,211.00		2,111.00		1,074.00		1,179.00		927.00
	PROVEN & PROBABLE	Tonnage (Mt)		807.10		1,008.94		1,144.76		1,421.41		1,143.65		1,062.61		529.97		546.98		586.68
		Grade (%)		0.33		0.32		0.29		0.25		0.24		0.25		0.32		0.31		0.29
		Contained (Mlbs)		5,876.00		7,070.00		7,211.00		7,275.00		6,165.00		5,814.00		3,695.00		3,757.00		3,701.00
Zinc	PROVEN	Tonnage (Mt)		426.80		561.21		580.58		719.99		626.47		577.90		335.03		336.26		398.28
		Grade (%)		0.78		0.77		0.75		0.65		0.69		0.70		0.85		0.84		0.78
		Contained (Mlbs)		7,365.00		9,587.00		9,647.00		10,376.00		9,526.00		8,928.54		6,308.00		6,232.00		6,812.00
	PROBABLE	Tonnage (Mt)		380.30		447.73		564.19		701.42		517.19		484.71		194.94		210.72		188.40
		Grade (%)		0.65		0.59		0.50		0.47		0.46		0.47		0.62		0.61		0.50
		Contained (Mlbs)		5,442.00		5,776.00		6,281.00		7,198.00		5,241.00		5,032.00		2,665.00		2,847.00		2,074.00
	PROVEN & PROBABLE	Tonnage (Mt)		807.10		1,008.94		1,144.76		1,421.41		1,143.65		1,062.61		529.97		546.98		586.68
		Grade (%)		0.72		0.69		0.63		0.57		0.59		0.60		0.77		0.75		0.69
		Contained (Mlbs)		12,806.00		15,364.00		15,930.00		17,575.00		14,767.00		13,961.00		8,973.00		9,081.00		8,886.00

Note: Mt (metric tonnes), g/t (gram per ton), Moz (Millions of ounces), MLbs (millions of pounds), % (percent).

Previous Research in the Area

The Peñasquito region has been the focus of diverse investigations; thus, there is a geological heritage, including reports and publications with different approaches. However, most publications refer to features of regional geology and stratigraphy, tectonic, geophysical anomalies as well as partial descriptions of some metasomatic ore deposits found in the region. Goldcorp has in its collection, partial reports documenting some characteristics of the Peñasquito ore deposit.

One of the early surveys, conducted by Burckhardt (1906), defined the regional stratigraphy and included a regional geological map between the mountain ranges known as La Caja, Concepción del Oro, and Santa Rosa (including Mazapil Valley) as well as further emphasized the potential of phosphorite deposits in the La Caja Formation. Meanwhile, Imlay (1936) conducted work involving a regional stratigraphic description of sedimentary units, and named lithologic formations from the Jurassic and Cretaceous. Mapes-Vázquez et al. (1964) and Buseck (1966) documented physicochemical features, geology, structural control, and dating of metasomatic replacement deposits at Concepción del Oro. Mitre (1989) produced a structural interpretation of the region, and suggested that there are two major structural controls as well as deep structural lineaments, such as the San Tiburcio mega-fault, that affected regional tectonic evolution. During the last few decades, the Mexican Geology Survey (1996, 2000, 2003, 2008) updated the regional geological mapping and carried out airborne magnetics, highlighting a broad

anomaly and its spatial relationship with major polymetallic deposits in the region (including the Peñasquito area).

Since the discovery of the Peñasquito ore deposit, researchers have documented some of the deposit's characteristics including stratigraphy, geochemistry and geophysics signatures, some mineralogical analysis, and dating of magmatic events. Kennecott (1997) conducted a soil geochemistry survey at Peñasquito and the results suggested broad anomalies of Au-Ag-Pb-Zn-Cu around the Peñasco and Azul diatremes. Meanwhile, Goldcorp funded Valencia (2010) to research the dating of magmatic zircons from regional plutons, including Peñasquito, and results suggested Eocene ages for the magmatism in the Peñasquito area. Moreover, Goldcorp has, in its collection, some optical microscopy studies conducted by various authors. Hernandez-Perez et al. (1997, 2008) presented the results of the geophysical signature at Peñasquito based on a geophysical survey funded by SGM. In addition to this research, multiple Goldcorp annual reports as well as deposit summaries have contributed to the knowledge of the historical background, paragenesis, and geological settings at Peñasquito.

CHAPTER II GEOLOGICAL SETTING

Paleogeography and Magmatic Evolution

The Peñasquito region is linked to the tectonic evolution of the Gulf of Mexico, which includes northern and northeastern Mexico. This region is depicted by a Mesozoic divergent margin base formed through the drifting and extension of Pangea followed by the breakup, the spread of the sea-floor, migration of tectonic plates (Dickinson and Coney, 1980; Pindell and Dewey, 1982; Pindell and Barrett, 1990; Goldhammer, 1999), sedimentation, and emplacement of magmatic arcs. In general, the Peñasquito region is part of the Mexican geosyncline that was partially confined to the north by the Coahuila block or platform, to the east by the San Carlos Island, to the southeast by the Valle-San Luis Potosi platform, and to the west by a magmatic arc (Fig. 2.1). All of these were uplifted terranes and influenced by the sedimentation as well as the contribution of sediments for the Mexican geosyncline. The geotectonic part of this continent portion was developed through several stages. Initially, the motion of blocks was caused by strike-slip faulting that affected the Paleozoic basement, as well as, magmatic arcs generated by oblique subduction from the Paleo-Pacific margin (Goldhammer, 1999; Ocampo-Díaz, 2011). Consequently, the extensional tension generated accommodation spaces on Paleozoic basement (i.e. pull-apart basins and grabens) and then sedimentation began (Goldhammer, 1999). Afterward, a northeast thrusting of the sedimentary sequence was due to the Laramide Orogeny and the subsequent contraction that generated parallel anticlines and synclines. Consequently, plutonic arcs were emplaced through weakness zones and related to the subduction of the Farallon plate from the Pacific margin. Finally, a continental

clastic cover was deposited in the basins due to erosion, and a mafic intraplate volcanic episode developed in the area with alluvial deposition continuing in valleys or basins.
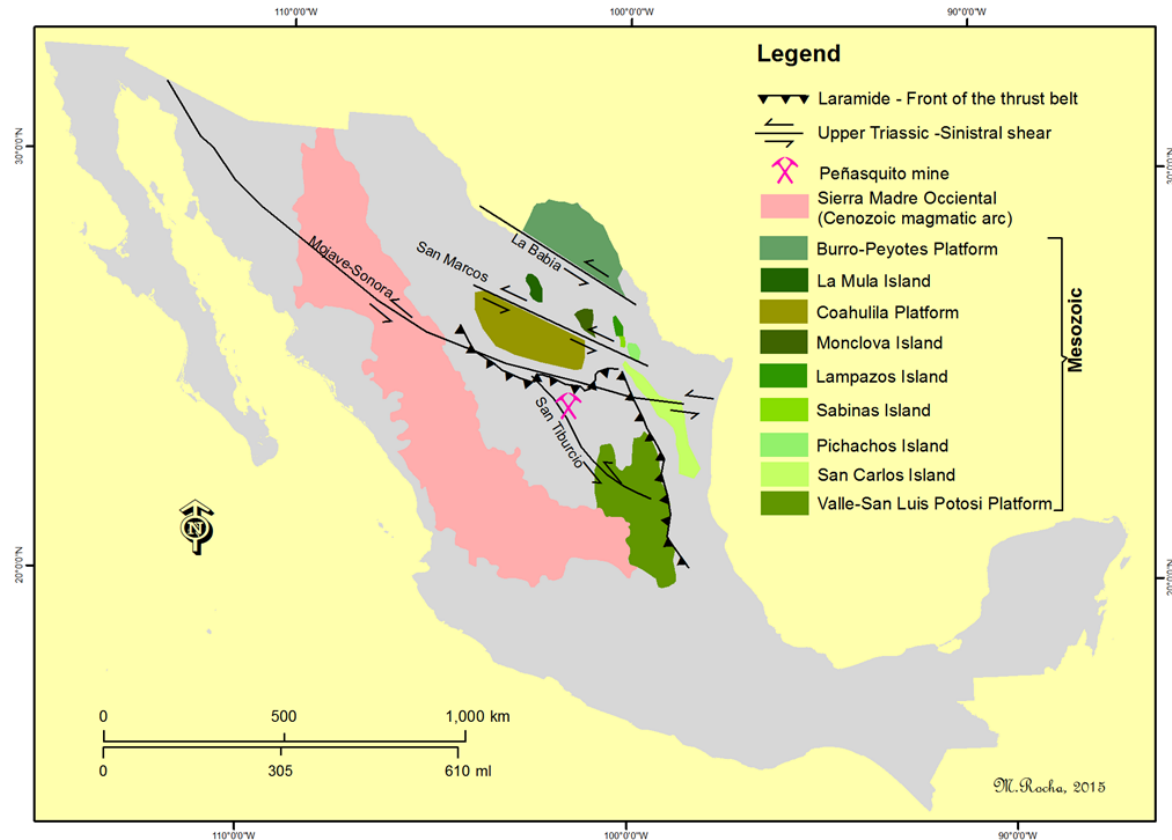
Fig. 2.1. Map showing Mesozoic and Cenozoic paleotectonic features of northeastern Mexico.

During the Late Paleozoic, northern and northeastern Mexico was formed by the suture of the North American, South American, and Yucatan plates, and this basement played an important role in the Mesozoic stratigraphy (Pindell and Dewey, 1982; Goldhammer, 1999). Subsequently, during the Permian to Triassic periods, an igneous belt (granite-granodiorite) was emplaced through the Paleozoic sequence related to the roots of an island arc developed on the continental suture, and this belt is documented in the northern and eastern Sierra Madre Oriental (Pindell and Dewey, 1982; Goldhammer, 1999).

During the Late Triassic to Middle Jurassic, Pangea was rifting and segmenting, causing basement highs and lows (Fig. 2.2B) (Goldhammer, 1999) which were commonly bounded by left-lateral faults cutting across through the strike of the Permian-Triassic intrusive belt (Fig. 2.2B). In addition, the movement combinations of strike-slip faults with normal faults generated pull-apart basins and grabens, which controlled the distribution of lithological facies as well as successive sedimentation and igneous activity (Goldhammer, 1999; Ocampo-Díaz, 2011). The consequence of this separation was the deposition of a sequence of red beds that ranged up to 1,000 meters in thickness (Fig. 2.3). Furthermore, evaporitic deposits were developed at shallow

Fig. 2.2. Schematic tectonic model for the evolution of the northeastern Mexico and the Gulf of Mexico (GOM). The schematic cross sections traverse approximately northwest-southeast (from left to right) across Mexico (modified from Goldhammer et al., 1999)

levels as well as hydrothermal veins and dikes of andesitic and rhyolitic compositions.

The separation of Yucatan block was caused by rifting and left-lateral movements with northwest-southeast strike (e.g. the Mojave-Sonora megashear) (Anderson and Schmidt, 1983; Pindell, 1985). The left lateral movement in northern Mexico was derived from the oblique subduction of the Kula-Farallon plate beneath the Yaqui and South American plates, which caused calc-alkaline volcanism located in the northwest and northeast part of Mexico from Late Triassic through Late Jurassic (Pindell and Dewey, 1982).
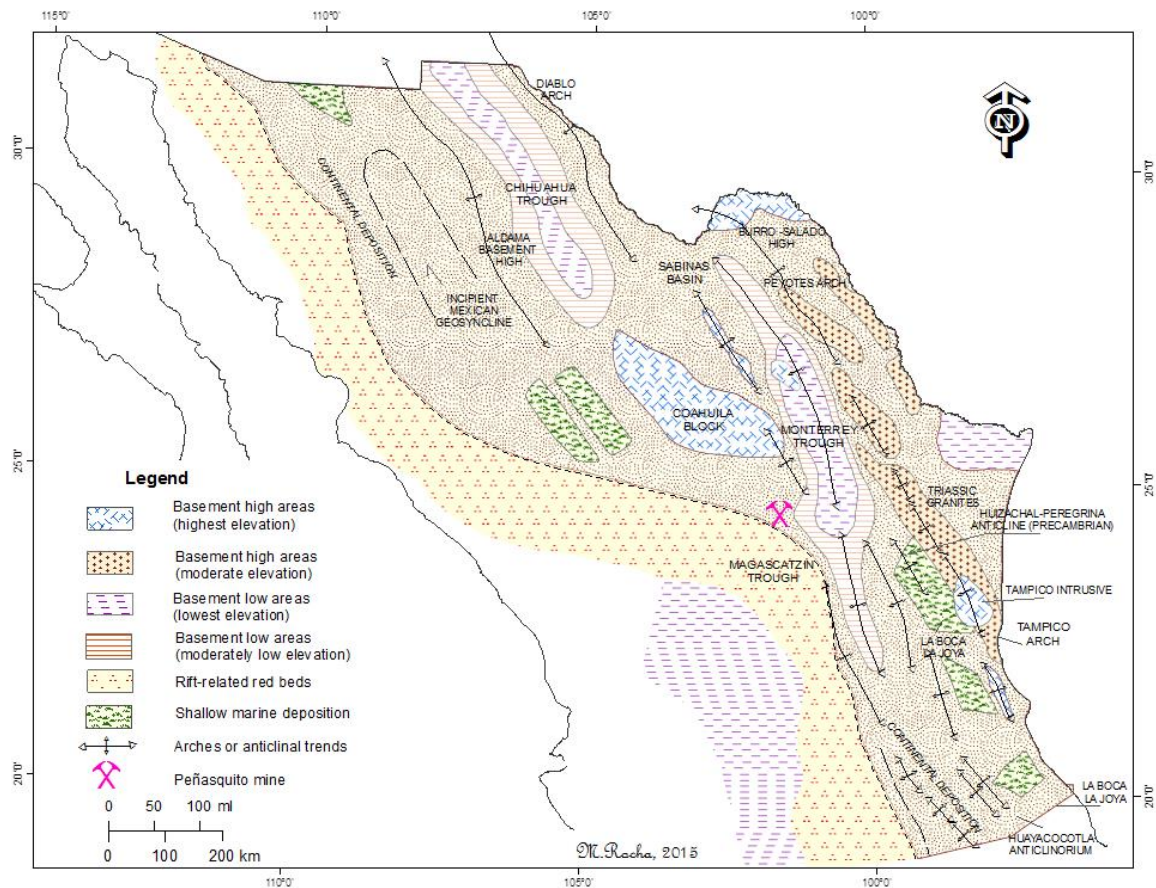
Fig. 2.3. Map showing Late Triassic to Middle Jurassic paleogeography of northern and northeastern Mexico (modified from Goldhammer et al., 1999)

In the Late Jurassic, the sea-floor began to spread within the Gulf of Mexico and the Yucatan block migrated to the south (Fig.2.2C). In addition, the fault movement ceased and the region was covered by carbonate and evaporitic sediments during the Oxfordian, which masked the megashear (Pindell, 1985; Goldhammer, 1999). In the Kimmeridgian, sedimentation was characterized by carbonate, argillaceous, and clastic-marine sediments (Fig. 2.4) (Goldhammer, 1999).
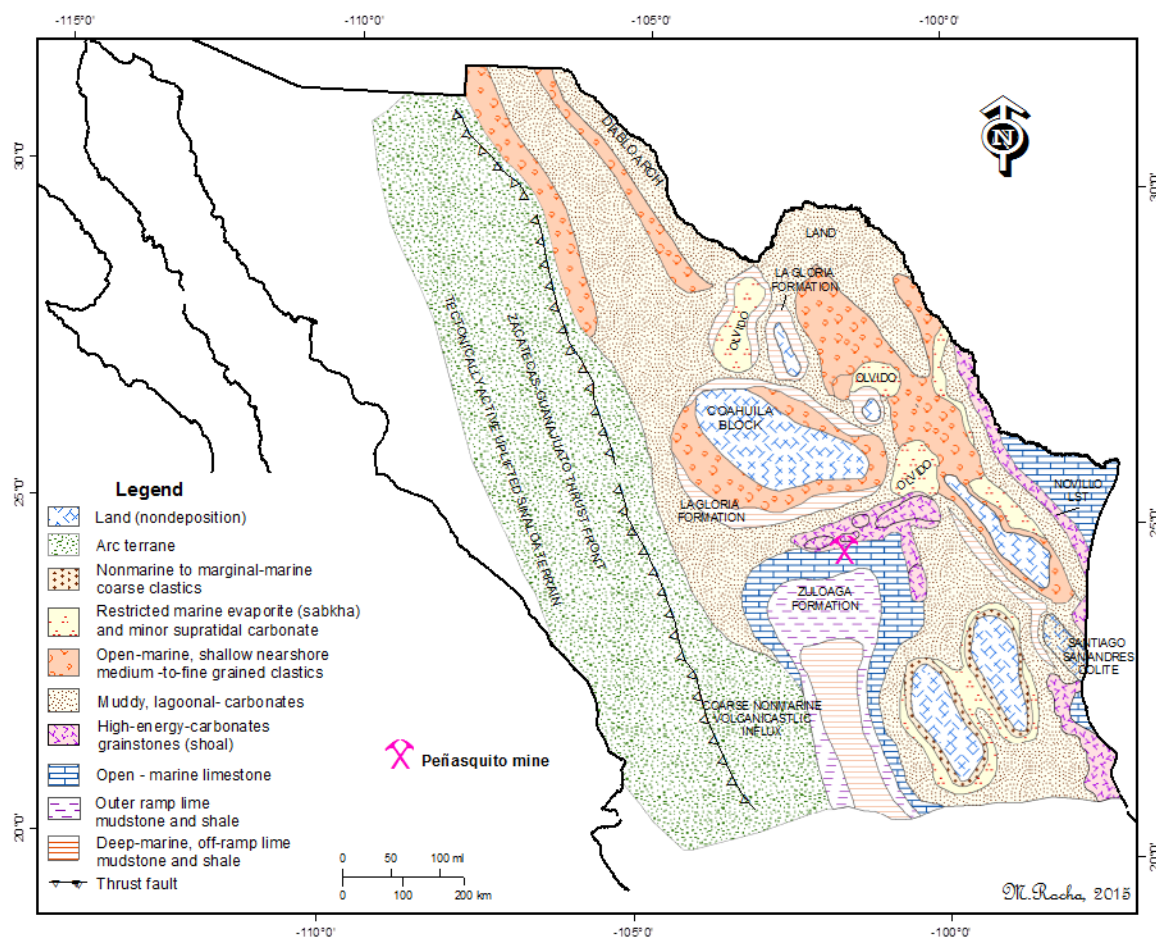
Fig. 2.4. Map showing Late Jurassic paleogeography of northern and northeastern Mexico (modified from Goldhammer et al., 1999).

During the Cretaceous, in northern and northeastern Mexico, a passive margin prevailed, and carbonate sediments accumulated at different facies as well as a system of

siliciclastic sedimentation (Fig. 2.5) (Goldhammer, 1999), which resulted from the disinte-

gration of lithological units due to the effects of the Laramide Orogeny (Fig. 2.2E). In addi-

tion, during the Late Cretaceous and Early Tertiary, the Orogeny caused uplift, folding, and

deformation in Mesozoic units as well as a volcanic arc in the western Pacific margin and

the thrusting of the Mesozoic sequence to the northeast. The Coahuila and San Carlos

blocks caused the deflection of the Sierra Madre Oriental in an east-west strike between

Torreon and Monterrey.
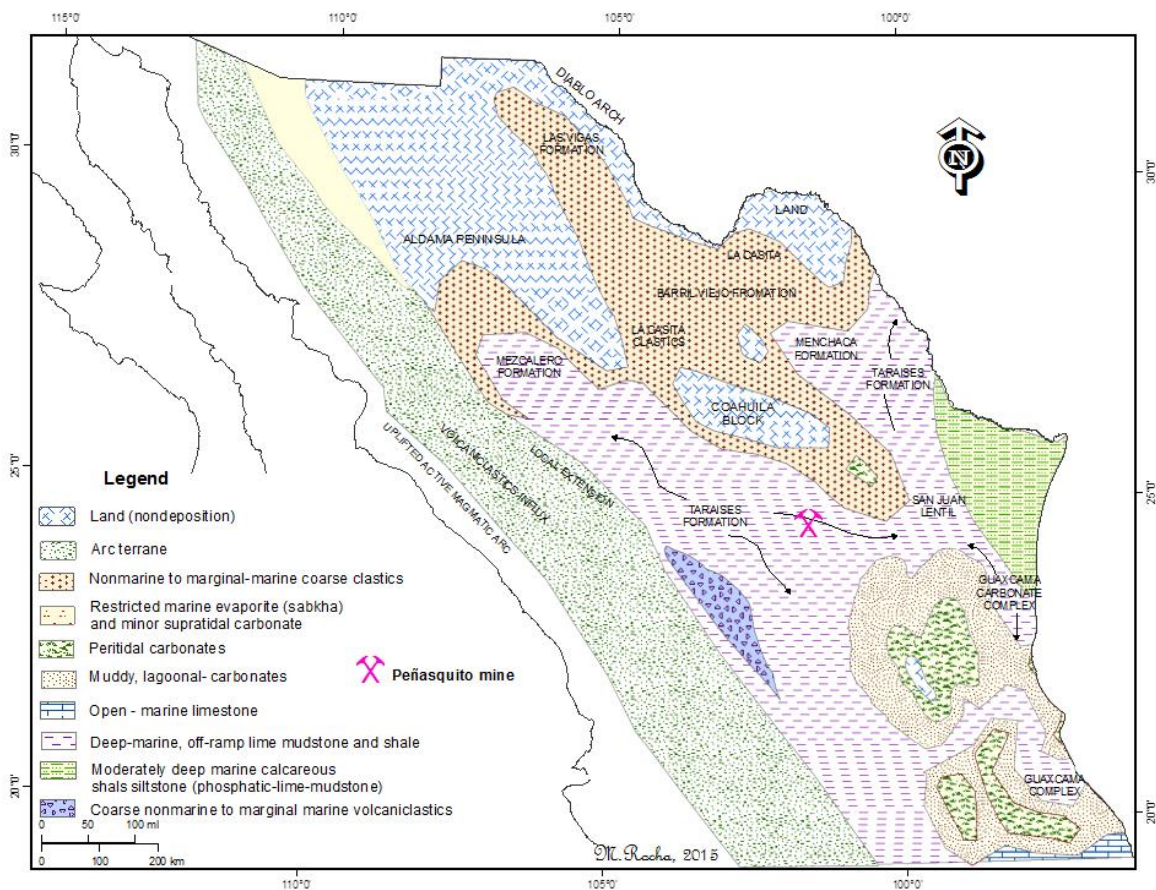
Fig. 2.5. Map showing Early Cretaceous paleogeography of northern and northeastern Mexico (modified from Goldhammer et al., 1999).

During the Tertiary, a low angle subduction prevailed from the Pacific margin and caused the migration of the magmatic arc and emplacement of stocks in the eastern part of Mexico (Fig. 2.3F). Subsequently, the subduction regime changed to a high angle causing the regression of the magmatic arc to the central and western parts of Mexico (Damon et al., 1981). In the Quaternary, in the central and northern part of Mexico, an intra-plate mafic volcanic system was developed, which was limited to small volcanic fields or outcrops.

Regional Geology

The Peñasquito area is in the geological province known as the Mexican Belt of Folds and Faults (Ortega-Gutierrez, 1992), which presents successions of synclines and anticlines with east to west orientation and north-northeast vergence (Fig. 2.6). The province is bordered by the Coahuila Platform to the north, the Gulf of Mexico miogeosyncline to the east, the Valles-San Luis Potosí Platform, the Zacatecana to the south, and the Mexican ignimbrite belt to the west. The current landscape is dominated by a Mesozoic sedimentary marine sequence which was folded and faulted during the Cenozoic (i.e. the Laramide deformation); Tertiary plutonic stocks crop out along some fold axes and local volcanic rocks are found in valleys with alluvial cover from the Quaternary.

The Peñasquito region is in the tectonostratigraphic terrane known as Sierra Madre (Fig. 2.7) (Campa and Coney, 1983). The basement of the Sierra Madre is part of the Oaxaquia microcontinent. The term "Oaxaquia" was coined for rocks with ages of ca. 1 Ga that occur in the northeastern, central-eastern, and southern parts of Mexico. This

microcontinent is made up of a crystalline rock mass and surrounded by ubiquitous Mesozoic and Cenozoic rocks (Ortega-Gutiérrez, 1995; Keppie, 2010).
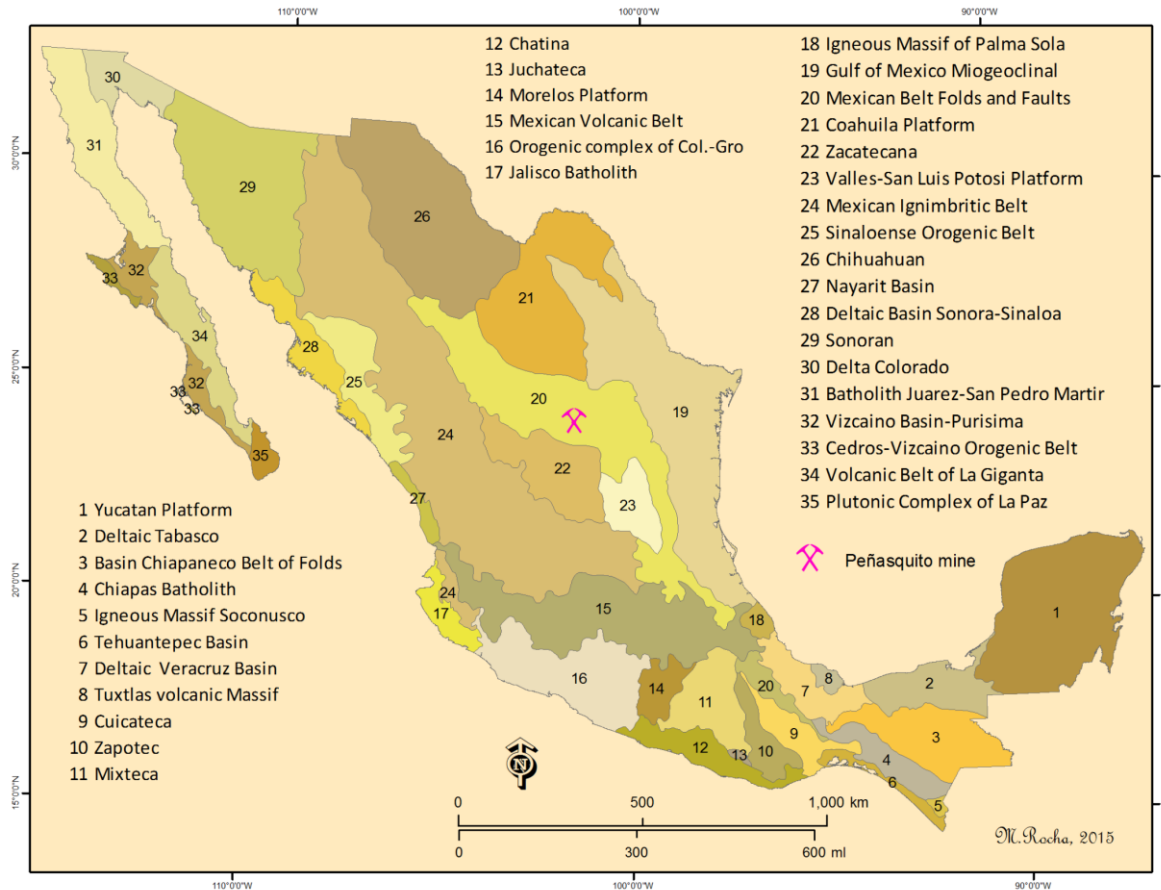
Fig. 2.6. Map showing Geological provinces of Mexico (Modified from Ortega et al., 1992).

The microplate includes a dual character, such as metamorphic rocks of a low to medium grade, like meta-anorthosite, ortho-gneiss, and charnockite that are juxtaposed with pelitic-schist, and lenses of serpentinite, meta-gabbro, meta-basalt, and meta-chert, which were deposited from the Neoproterozoic to Silurian and possibly to Devonian (Ruiz et al., 1988; Ortega-Gutiérrez et al., 1995; Keppie et al., 2010; Barboza-Gudiño et al., 2011; Hildebrand, 2013). The above lithology is unconformably overlain by the Late Paleozoic sedimentary sequence which is made up of conglomeratic successions, carbonate rocks

with abundant brachiopods and echinoderms as well as Silurian to Early Permian rhyolitic

tuff, shale, and sandstone (Carrillo-Bravo, 1961; Gursky et al., 1989; Stewart et al., 1999).
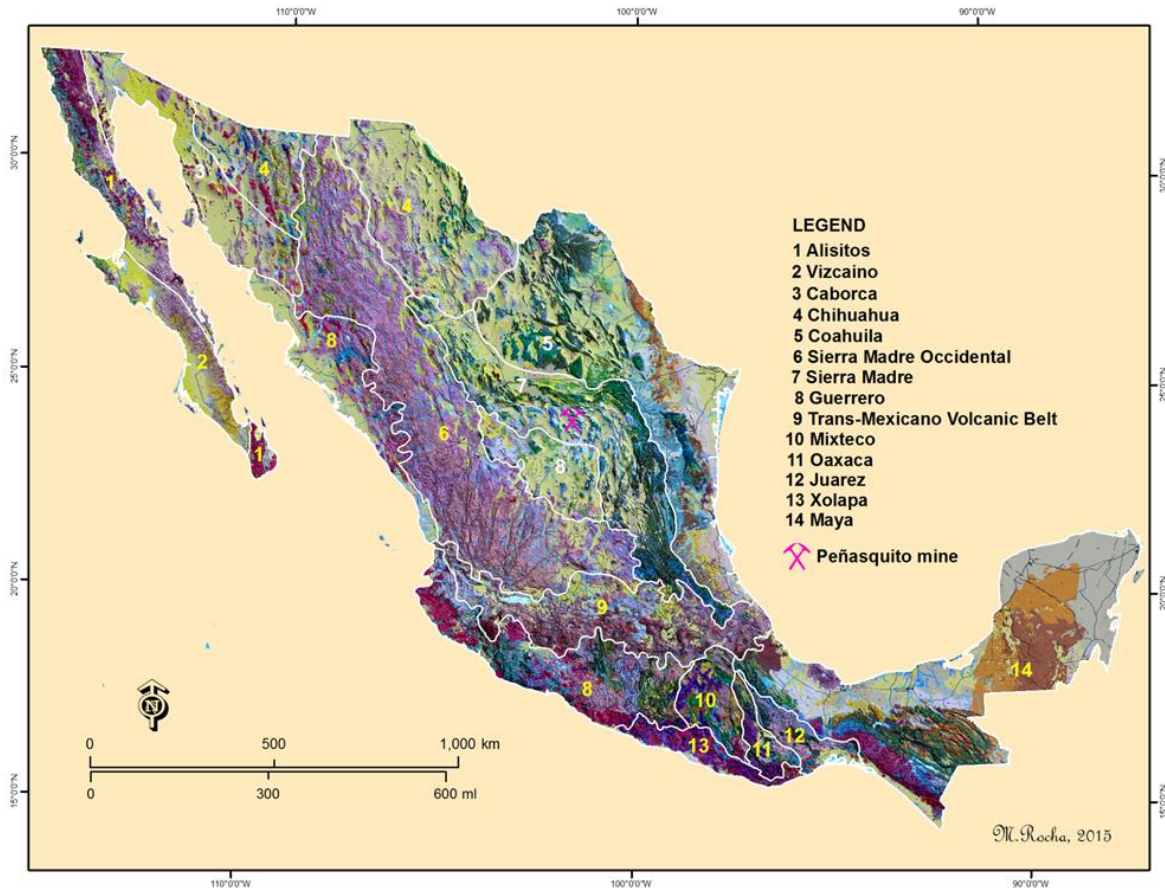
Fig. 2.7. Map showing tectonostratigraphic terrane of Mexico (modified from Campa and Coney, 1983). Also shown is the regional geology (from SGM, 2006).

During the Permian-Triassic and Triassic-Middle Jurassic, volcanic arcs (granite-gran-

odiorite) were emplaced through the Sierra Madre basement (Pindell and Dewey, 1982;

Jones et al., 1995; Dickinson and Lawton, 2001; Centeno-García, 2005; Barboza-Gudiño et

al., 2008; Rubio-Cisneros and Lawton, 2011) and crop out in northeastern Mexico about

254 km and 110° from Peñasquito.

During the Early-Middle Jurassic, volcanic and volcaniclastic sequences, made up of intermediate to felsic volcanic rocks, were deposited and related to continental arcs developed in the southwestern portion of the North American craton (Grajales-Nishimura et al., 1992; Jones et al., 1995; Bartolini et al., 2003; Barboza-Gudiño et al., 1999, 2008; Rubio-Cisneros and Lawton, 2011). In the Peñasquito region, the above lithology is represented by the Taray and Nazas formations, which crop out in an elongated belt with northwest to southeast orientation and are located at the western (i.e. 45 and 32 km) and southwestern (i.e. 19 km and 227°) part of Peñasquito.

As mentioned above, in this region, a transtensional regime prevailed during the Late Jurassic-Early Cretaceous. This tectonic evolution was linked to an oblique subduction in the paleo-Pacific margin. The geological effects included rifting and drifting in the Gulf of Mexico, the generation of strike-slip basin rate on the southern edge of the North American craton and the smaller displacement of blocks of petrochemical assemblages (Tardy et al., 1989; Bassett and Busby, 2005; Haenggi and Muehlberger, 2005; Ocampo-Díaz, 2011). A second rifting event was developed during the deposition of marine sediments. A tectonic regime combined transcurrent strike-slip movement with oblique extension, which was associated to oceanic spreading ridges and transformed faults. Therefore, the resulting sedimentation was developed in different facies, which resulted in carbonates, siliciclastic deposits, and evaporites. In the Peñasquito region, the Late Jurassic and the Early Cretaceous rock sequences formed the outcrop in cores of anticlines. The Late Cretaceous was characterized by siliciclastic sedimentation (Goldhammer, 1999). This regimen of sedimentation was influenced by transgression and flysch-type deposits (De

Cserna, 1956). In the Peñasquito region, the Late Cretaceous formations include the Cara-col and Parras formations that partially crop out in valleys or synclines.

The Tertiary is primarily represented by stocks that were emplaced through the Mesozoic sequence. The stocks emplacement was a result of a low angle subduction from the Pacific margin. The stocks developed aureoles of contact metamorphism and meta-somatism. These plutons that are cropping out in anticlines provided the polymetallic mineralization. The Quaternary is characterized by alluvial cover and mafic volcanic rocks that are exposed in basins and locally in ranges.

Stratigraphy

The stratigraphic sequence has formally been described by authors who have con-ducted mapping and lithological research in central and northeastern Mexico (e.g. Imlay, 1953; Rogers et al., 1956). Furthermore, recent studies have provided important details about stratigraphic and paleontological features, and chronology (e.g. Montañez-Castro et al., 2000, 2003; Ocejo-Paredes et al., 2003; Barboza-Gudiño et al., 2004, 2008, 2010; Va-lencia, 2010; Pinzon-Sotelo, 2012). Therefore, the stratigraphic units are briefly described in order to give a general idea of regional and local stratigraphy (Fig. 2.8). In addition, field observations were completed on cross sections at anticlines of La Caja-Concepción del Oro as well as observations during the logging of cores from the Peñasquito drilling. The re-gional geological map is the compilation of geological cartography to 1:50,000 scale, which is based on geological cartography data from the Mexican Geological Survey (i.e. Servicio Geológico Mexicano) including modifications made during fieldwork.

In this region, Triassic, Jurassic, and Cretaceous sediments are predominantly exposed in anticlines that were deposited on a metamorphic basement from the Paleozoic in the Mexican Geosyncline. The Triassic lithological sequence was deformed during the Late Jurassic-Tertiary; Jurassic and Cretaceous lithological sequences were folded and influenced by thrust faults and longitudinal faults during Late Jurassic and Early Eocene. Subsequently, in the anticlines of La Caja-Concepción del Oro, Santa Rosa, and Santa Rita, the folds were modified due to the intrusion of magmatic stocks with felsic to intermediate composition, which caused metasomatism and contact metamorphism (Fig. 2.9.). During the Late Tertiary, basins were developed due to arching of the upward lithological sequence, whose orientation is oblique to the direction of the fold's axes. Through time, these valleys were filled with alluvial cover due to uplift and subsequent erosion. In addition, mafic volcanism is present and is representative of the last magmatic event developed during Late Miocene.

Triassic

The Triassic outcrops are aligned in a belt with northwest-southeast orientation and localized in the San Rafael and San Julian ranges (about 40 km east from Peñasquito). This sequence is overlain by Early Jurassic lithological units. This Triassic lithological sequence is known as the Taray Formation and is the oldest lithological unit in the Peñasquito region (Fig. 2.8). This sequence is made up of fine-grained clastic marine deposits intercalated with volcanic marine products that were deformed by compressive tectonic events during the Early Mesozoic.
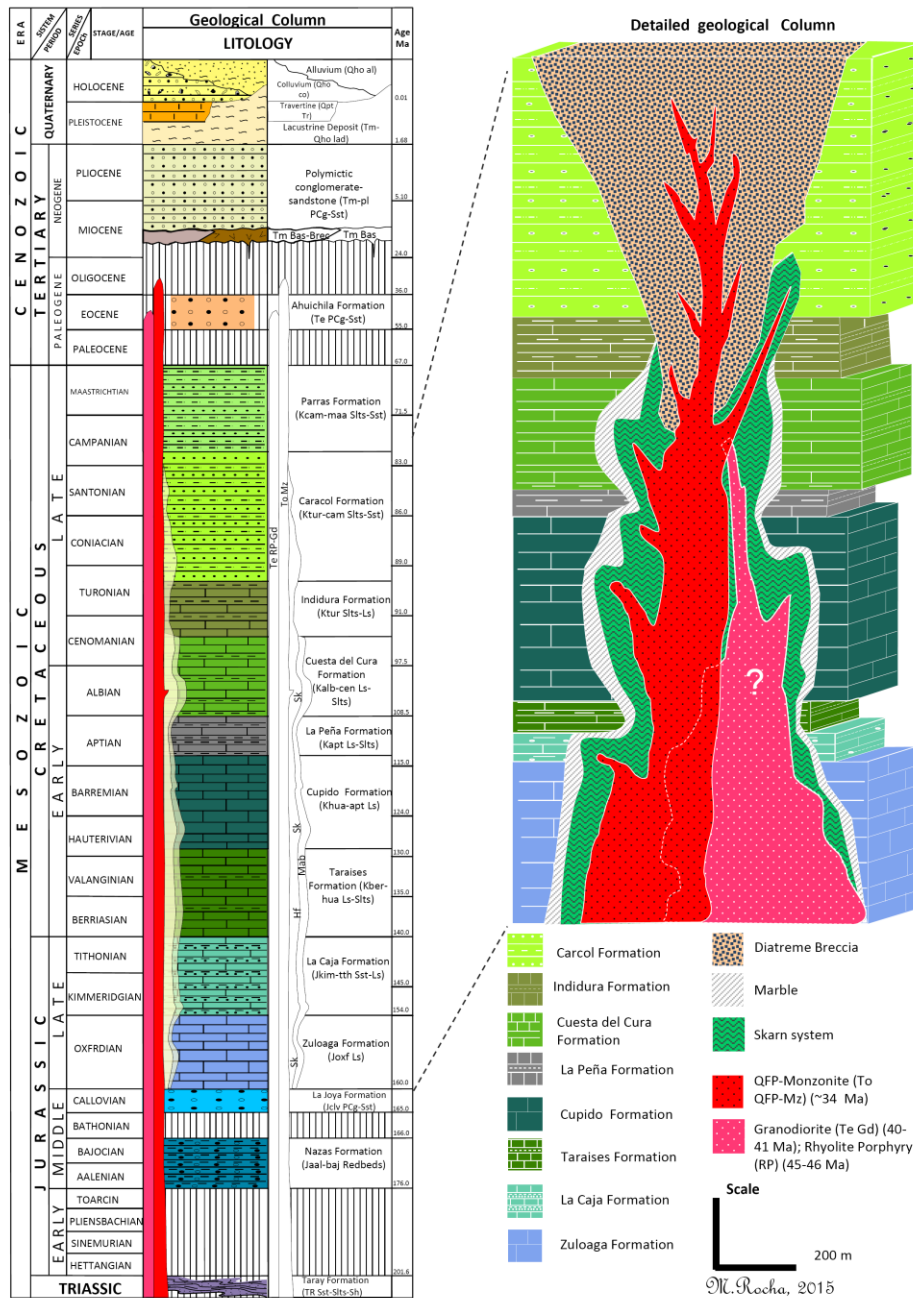
Fig. 2.8. Geological column for the Peñasquito region. Also showing the detailed lithological column for the Peñasquito area (Right side).

Taray Formation (TR Sst-Sslt-Sh)

This lithological unit was formally named the Taray Formation by Cordoba (1964) and is exposed along the Taray creek in the Sierra de Teyra range in northern Zacatecas (about 40 km east from Peñasquito). Silva-Romo et al. (2000) conducted research on Tri-

assic units in the Mesa Central, including the Taray Formation in the San Rafael ridge (about 55 km east from Peñasquito), and described a turbiditic marine sequence, quartz graywacke, and local intercalated greenstones that suggested protolithic-like pillow lavas. This sequence, which is present in the San Rafael ridge, is 4,500 m in thickness. Specifically, the Taray Formation includes several lithofacies made of sandstone beds up to 60 cm thick (Bouma sequence) intercalated with low grade phyllite, siltstone, and shale, which exhibit textures such as flow clasts, rip up clasts, graded bedding, and some worm tracks. Toward the top, the lithological unit includes conglomerate with clasts of schist, sandstone, shale, chert, milky quartz, and two different granites, rounded pebbles, and cobbles supported by a sand and mud matrix (Silva-Romo et al., 2000). According to Silva-Romo et al. (2000), this lithological unit was deformed together with a continental unit made up of conglomerate and lavas during the beginning of the Late Jurassic transgression. A Triassic age has been suggested for the Taray Formation because of its similar lithology and stratigraphic position with the Triassic rocks that are present in the Mesa Central from Central Mexico and is considered part of an alluvial fan (Barboza-Gudiño, 2008, 2010; Silva-Romo et al., 2000).

Jurassic

Jurassic sediments include four lithological formations that have been deposited in different geological facies and a singular constitution (i.e. Nazas Formation, La Joya Formation, Zuloaga Formation, and La Caja Formation). The Early Jurassic outcrops are located at the San Julian and Candelaria (El Toro) anticlines and consist of a lithological sequence made up of volcanic, volcanoclastic, and clastic sediments. The Late Jurassic litho-

logical units crop out in the cores of anticlines and are made up of marine sediments of chemical, organic, and clastic origin (Fig. 2.9).
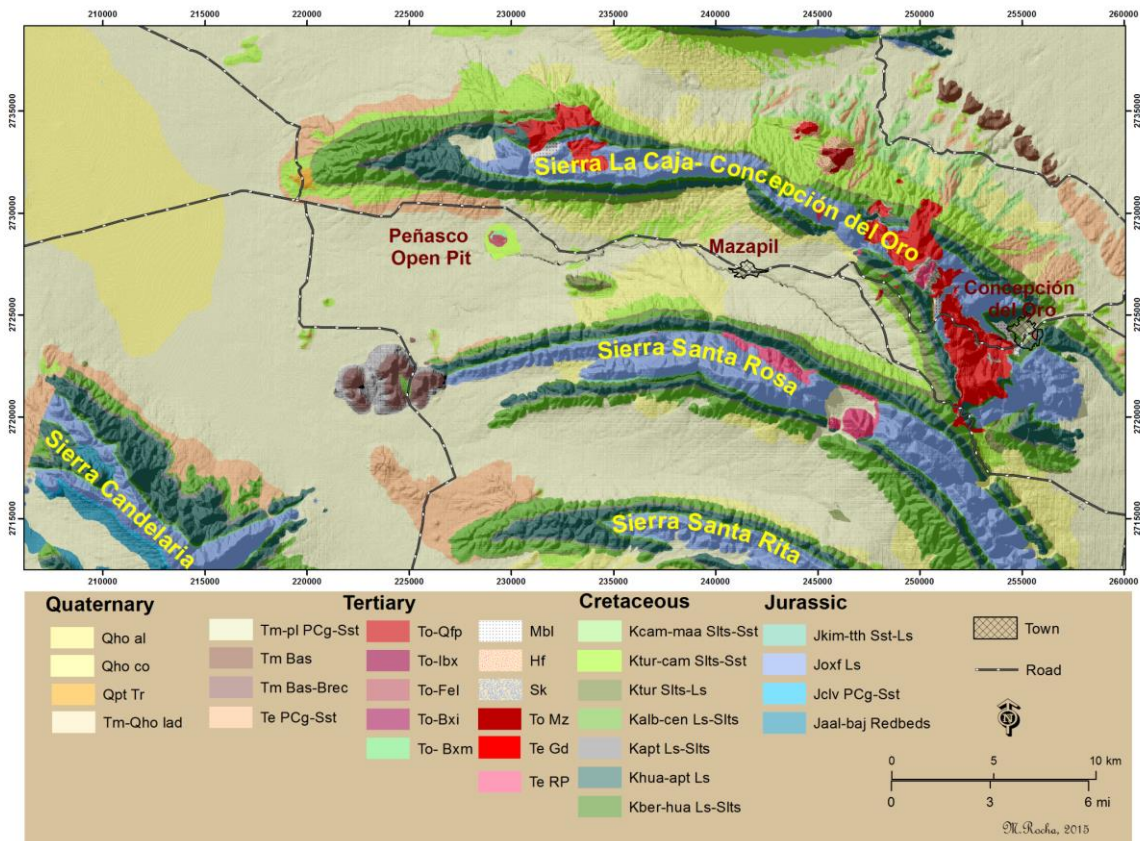
Fig. 2.9. Map showing lithology of Peñasquito Region (modified from SGM, 2013). Also shown is the Peñasco open pit lithology.

Nazas Formation (Jaal-baj Redbeds)

This lithological unit near San Pedro de Gallo, Durango, about 281 km and 291° from Peñasquito, was defined by Pantoja-Alor (1972), who described a lithological sequence made up of a volcanic and volcaniclastic succession including basaltic andesite, rhyolites, and redbeds and reported Pb-α age 230 ± 20 Ma from a rhyolitic flow. In the Peñasquito region, the Nazas Formation crops out in the San Julian-Candelaria anticlines (about 32 km east and 24 km and 215° from Peñasquito) and unconformably overlies the Taray For-

mation and unconformably underlies deposits of the La Joya Formation (Barboza-Gudiño et al., 1999; Ocejo-Paredes et al., 2003). The Nazas Formation is made up of volcanic and volcaniclastic sequences including andesite, basalt, basalt-andesite, rhyolite, and redbeds (Barboza-Gudiño et al., 1999, 2004, 2010). The Nazas Formation has both ductile and brittle deformation phases, and a total structural thickness up to 500 m has been estimated (Silva-Romo, 2000). Geochronology research has been conducted from detrital zircon in the Sierra de Catorce range, San Luis Potosi (about 130 km and 140° from Peñasquito) and results have determined the age of the Nazas Formation as Early-Middle Jurassic (i.e. 174.7 ± 1.3 Ma) (Barboza-Gudiño et al., 2004). Results of whole-rock geochemistry reveal that felsic rocks of the Nazas Formation are of calc-alkaline character, and patterns of trace elements suggest an environment of continental arc andean-type deposition (Barboza-Gudiño et al., 2008). The Nazas Formation has been interpreted as a product of a remnant volcanic arc from the Late Triassic-Early Jurassic and related to the active continental margin of western North America based on its constitution and nature of volcanic products (Jones et al., 1995; Barboza-Gudiño et al., 1999, 2004).

La Joya Formation (JClv PCg-Sdt)

This lithological unit was formally named by Míxon et al. (1959) in the Huizachal valley, Tamaulipas, and described as a conglomerate intercolated between redbeds of Huizachal Formation and Zuloaga Limestone. Outcrops are located on the southwest flank of anticlines of the San Julian (32 km east from Peñasquito) and Candelaria (24 km at 215° from Peñasquito) where the base of the lithological unit is made up of consolidated and polymictic conglomerates with gradation. These conglomerates consist of subangular-sub-

rounded fragments of igneous and metamorphic rocks cemented by calcium carbonates, sand and silt; furthermore, white quartz veinlets are also present. At the top of the formation, there is abundant medium-fine grained sandstone that is made up of quartz, feldspar, and opaque minerals, cemented by silica, calcium carbonate, and hematite, and local siltstone horizons are present (Ocejo-Paredes et al., 2003).

The lithological unit exhibits various colors such as red, orange, and brown and the estimated thickness is up to 30 m (Ocejo-Paredes et al., 2003). La Joya Formation overlies by an angular and erosional unconformity the Nazas Formation (Mixon et al., 1959; Ocejo-Paredes et al., 2003) and unconformably underlies deposits of the Zuloaga Formation. The age of the lithological sequence is 164 ± 3 Ma (Callovian), which is based on the chronological analysis of detrital zircons (Rubio-Cisneros et al., 2011). This lithological unit was deposited in submarine channels and proximal alluvial facies as fanglomerates and conglomerates (Ocejo-Paredes et al., 2003). The composition of La Joya Formation suggests the belated development of a rift-type basin as well as the exposing of basement rocks (Salvador, 1987; Rubio-Cisneros and Lawton, 2011), and the upper units mark the beginning of the marine transgression from the Early Jurassic (Goldhammer, 1999).

Zuloaga Formation (Joxf Ls)

This lithological unit was initially studied by Burckhardt (1906a, 1906b, 1930), who named it "Limestone with Nerinea" (cited in De Cserna, 1956). Later, the unit was described by Imlay (1938) in the Sierra de Sombreretillo (about 25 km north of Peñasquito), who named this unit Zuloaga Limestone. The Zuloaga Formation is dense, light

to dark gray in color, fine-grained, occurs in layers with thicknesses ranging from 0.9 to 3 m (Imlay, 1938), and locally interbedded with calcareous siltstone. Also, this lithological unit locally exhibits large stylolites, locally microcrystalline dolomite (Rogers et al., 1957), small nodules of light gray chert, local horizons of Nerinea Sp., and concentrations of coral fragments (Barboza-Gudiño et al., 2004). The thickness is variable and ranges between 275 and 700 m; however, it thins toward the eastern Sierra Madre Oriental (Imlay, 1938; Rogers et al., 1956; Barboza-Gudiño et al., 2004). In the Peñasquito region, the Zuloaga Formation is locally unconformably underlain by the Nazas Formation and La Joya Formation (Ocejo-Paredes, 2003; Barboza-Gudiño et al., 2004), and transitionally overlain by La Caja Formation.

The fossil content reported for this unit is characterized by bivalves, gastropods, corals, Nerinea Sp., brachiopods, echinoid fragments of the terebratulid type, and local benthic foraminifera (Rogers et al., 1956; Barboza-Gudiño et al., 2004). Imlay (1953) mentions that the top of this unit was deposited during the Oxfordian due to the faunal content (ammonites) and suggests a bathyal type environment near shore. In the Peñasquito region, the Zuloaga Formation forms cores in anticlines (e.g. La Caja-Concepción del Oro, Santa Rosa and Santa Rita). In addition, the Zuloaga Formation hosts economic mineralization, such as metasomatic bodies with disseminated polymetallic mineralization (i.e. La Caja-Concepción del Oro anticline). The polymetallic chimneys (up to hundreds of meters in depth) are located in a semi-vertical contact between Zuloaga and La Caja formations. Drilling at Peñasquito has intercepted the Zuloaga Formation at a depth ranging from 1,775 m (188 m.a.s.l.) to 2,006 m (-6 m.a.s.l.) below the surface. Some core drill holes

have shown that the Zuloaga Formation presents evidence of calc-silicate alteration and incipient polymetallic mineralization, and it is believed that this lithological unit may be a potential receptor of economic mineralization at depth.

La Caja Formation (Jkim-tth Sst-Ls)

This lithological unit was formally described in the Sierra La Caja (Burckhardt, 1930; cited in Imlay, 1938). Later, the lithological unit was studied by Rogers et al. (1956) with an economic focus on the phosphate content. The lithological unit consists of thin to medium layers, gray in color, made up of an alternation of calcareous siltstone, phosphoric limestone, argillaceous limestone, and chert and exhibits a wackestone texture. This unit occurs as thin parallel bands on the flanks of anticline cores. La Caja Formation ranges in age from Kimmeridgian to Tithonian based on the presence of ammonites (Imlay, 1953). At La Caja and Concepción del Oro anticlines, the reported thickness is between 40 and 150 m (Rogers et al., 1957). This lithological unit overlies the Zuloaga Formation and underlies the Taraises Formation. The environment of this deposition is in the intraneritic zone of shallow water and intensive agitation (Rogers et al., 1957). In the Concepción del Oro anticline, the unit exhibits development of hornfels, skarn, and skarnoid. Drilling at Peñasquito has intercepted the unit from about 1,713 m (250 m.a.s.l.) to ~2,006 m (-6 m.a.s.l.) in depth below the surface and the average thickness has been calculated at ~72 m. Drill cores have shown exoskarn in La Caja Formation with primary sulfides and a concentration of fluorite up to 30 m in thickness.

Cretaceous

The Early Cretaceous includes four sedimentary formations (i.e. Taraises, Cupido, La Peña, and Cuesta del Cura), while the Late Cretaceous consists of three sedimentary formations (i.e. Indidura, Caracol, and Parras). In general, sediments from the Early Cretaceous are overlying the Late Jurassic sequence; however, at La Caja anticline (Fig. 2.9), some thrust faults have been documented (Fig. 2.13). The Early Cretaceous includes sediments deposited in mixed environments during the Neocomian, such as extra-littoral and intra-littoral environments. During the Aptian, an invasion of fine clastics was developed. The Albian to Early Cenomanian was characterized by the absence of terrigenous sediment with development of reefs. On the other hand, rocks from the Late Cretaceous are made of clastic succession with an increase in grain size toward the top due to a transgression that developed sedimentary flysch-type deposits.

Taraises Formation (Kber-hua Ls-Slts)

This lithological unit was formally described by Imlay (1936) at the Taraises Canyon on the west side of the Sierra de Parras, Coahuila (about 101 km and 320° from Peñasquito). This unit is comprised of two members: (1) the lower member being a dark gray limestone with medium layers and a thickness up to 74 m, and (2) the upper member being a limestone made up of interleaving layers of sandstone with fine-grained, light gray, thin layers that are interbedded with calcareous siltstone, and a thickness up to 68 m (Imlay, 1936; De Cserna, 1956). In La Caja anticline, the lower member contains fossils that indicate a Berriasian-Valanginian age (Imlay, 1938). Furthermore, Barboza-Gudiño et al.

(2004) have suggested an age of Berriasian-Valanginian due to the presence of calpionellid planktonic microfossils.

In the Peñasquito region, the Taraises Formation forms a narrow band around the Late Jurassic lithological units, which are exposed along axes of anticlines. According to regional cartography, the thickness has been estimated at 80 to 100 m (Montañez-Castro et al., 2003; Ocejo-Paredes et al., 2003). Barboza-Gudiño et al. (2004) suggested that the Taraises Formation was deposited in a pelagic environment on the border of a basin. At the Concepción del Oro anticline (about 21 km and 98° from Peñasquito), this formation exhibits development of hornfels at its base and presents a ductile deformation phase. Drilling at Peñasquito has intercepted this unit from ~1,645 m (380 m.a.s.l.) to ~1,926 m (76 m.a.s.l.) below the surface with an average thickness calculated to be ~77 m. In addition, drill cores have shown a development of hornfels in the Taraises Formation as well as disseminated primary sulfides.

Cupido Formation (Khua-apt Ls)

Cupido Limestone has been described on the north wall of the Mimbre canyon and southern part of the Sierra de Parras, Coahuila (about 66 km north from Peñasquito). This unit overlies the Taraises Formation, underlies La Peña Formation (Imlay, 1937) and crops out on the flanks of the anticlines of La Caja-Concepción del Oro, Santa Rosa, and Santa Rita ranges. In general, the Cupido Formation consists of dark gray limestone in medium to thick layers with conchoidal fracture, chert nodules and lenses, and thick stylolites. At La Caja-Concepción del Oro anticline, the lithological unit contains abundant pyrite con-

cretions, gray nodules and lenses of chert as well as macrocrystalline limestone horizons (Imlay, 1937; Rogers et al., 1957). Rogers et al. (1956) further reported interbedded limestone, shale and calcareous siltstone in this formation. Imlay (1937) suggested a Hauterivian-Barremian age based on the fossil content of adjacent formations. Also, PEMEX (1988) and Pantoja (1963) have suggested a Barremian-Aptian age based on its faunal content and stratigraphic position. In the region of Concepción del Oro, a thickness up to 300 m has been reported (Rogers et al., 1957). The depositional environment that has been suggested consists of three main facies: lagoon, reef, and pre-reef (PEMEX, 1988b). In the southern portion of the Concepción del Oro anticline (about 20 km and S82°E from Peñasquito), the Cupido Formation has abundant veinlets and fractures filled by calcite and local primary sulfides (forming a stockwork), which suggest a fragile deformation phase. Drilling at Peñasquito has intercepted this unit from ~1,176 m (786 m.a.s.l.) to ~1,836 m (163 m.a.s.l.) below the current surface, and an average thickness of ~464 m has been estimated. In addition, drill cores have shown a development of skarn and marble in the Cupido Formation as well as disseminated primary sulfides.

La Peña Formation (Kapt Ls-Slts)

La Peña Formation was originally described on the western flank of the Sierra de Parras, Coahuila, (about 100 km northeast from Peñasquito) by Imlay (1936), who differentiated a lower member made of a calcareous composition and an upper member made of a calcareous-argillaceous composition. In the Peñasquito region, this lithological unit crops out as narrow bands on the flanks of the anticlines and consists of two members: (1) the base is mainly limestone, dark-brown to gray in color, medium to thin layers,

and also includes clay, calcareous siltstone, black chert nodules and small pyrite concretions, and (2) the upper member is limestone and argillaceous limestone of yellowish to light-gray color, which occurs in thin layers, as well as, thin gypsum horizons. Southeast of Concepción del Oro, the thickness has been estimated up to 105 m (Padilla and Sánchez, 1982). In the Peñasquito region, this lithological unit locally overlies the Cupido Limestone and underlies the Cuesta del Cura Formation. La Peña Formation is rich in macro and micro fauna such as ammonites of Dufrenoyia Sp. (De Cserna, 1956); therefore, an Aptian age has been suggested for this formation (Imlay, 1936). The depositional environment of the lithological unit has been generally suggested as a deep-sea bathyal to epibathyal zone; however, lateral variations suggest a shallower pericontinental environment and more detrital continental influence (González-Sánchez et al., 2007; Lopez-Doncel et al., 2007). Drilling at Peñasquito has intercepted this unit from ~1,128 m (825 m.a.s.l.) to ~1,376 m (623 m.a.s.l.) below the current surface, and ~60 m in average thickness has been estimated. In addition, drill cores have shown zones with skarnoid and marble in La Peña Formation.

Cuesta del Cura Formation (Kalb-cen Ls-Slts)

This lithological unit was initially described at the western part of the Sierra de Parras (about 100 km northeast from Peñasquito) by Imlay (1936) as a lithological unit made of a succession of limestone with intercalation of clays and chert bands. In the Peñasquito region, the Cuesta del Cura Formation consists of dark gray to black limestone in medium-thin layers with undulating stratification, siltstone horizons (Rogers et al., 1957), and abundant lenses and nodules of black chert. In La Caja anticline, this formation has been

estimated to be up to 270 m in thickness (Rogers et al., 1956). In the Peñasquito region, this lithological unit crops out as parallel bands on the flanks of anticlines, and in the Mazapil Valley, the unit forms the core of the Cerro Gordo dome. The Cuesta del Cura limestone overlies La Peña Formation and is overlain by the Indidura Formation. The age of this formation is based on its fossil content and stratigraphic position, and an Albian-Cenomanian age has been suggested for this lithological unit (Barboza-Gudiño et al., 2004). Imlay (1936) suggested that the depositional environment was deep water; mean-while, Barboza-Gudiño et al. (2004) suggested a deep neritic deposit type depositional environment, with good oxygenation and a constant cyclic input of terrigenous sediments. In Peñasquito, the lithological unit was intercepted at a depth from ~836 m (1,126 m.a.s.l.) to ~1,306 (693 m.a.s.l.) below the surface, and an average thickness of ~280 m has been estimated. Drill cores have shown zones with skarn and marble in the Cuesta del Cura Formation, which also hosts disseminated mineralization and massive sulfide mantos. The base of the Peñasco breccia diatreme is located in this formation.

Indidura Formation (Ktur Slts-Ls)

The lithological unit was formally named the Hendidura Formation and described by Kelly (1936) as a laminated sequence made up of siltstone and limestone, which crop out in the southern portion of the Sierra de Santa Ana, southeast of Delicias, Coahuila (about 120 km northeast from Peñasquito). Over time, this lithological unit was renamed the In-didura Formation. In Concepción del Oro, the Indidura Formation has been described as a lithological unit composed of two members: (1) the lower member is made up of argilla-ceous limestone and calcareous siltstone which occurs in thin layers, with medium to thick

layers of laminar limestone, and (2) the upper member contains very dark gray fissile shale (Rogers et al., 1956). The Indidura Formation has a very limited outcrop area due to erosion and alluvial cover. The distribution is restricted to narrow and elongated outcrops located in the lower parts of the flanks of the anticlines (La Caja and Santa Rosa). Drilling at Peñasquito has intercepted this unit from ~716 m (1,246 m.a.s.l.) to ~1,036 m (963 m.a.s.l.) below the current surface, and an average thickness of ~150 m has been estimated.

In the Peñasquito region, the lithological unit consists of calcareous siltstone with a thin interlayer of laminated fine limestone, dark gray to black in color with some horizons of sandstone and sandy siltstone. At the base, the lithological unit has argillaceous limestone with a wackestone texture, grayish color, thin to medium layers, and interbedded siltstone. At the middle and top parts, the limestone exhibits wackestone to grainstone texture. In addition, the siltstone is interbedded with calcareous material and local sandstone horizons. Inoceramus labiatus (i.e. Pelecypods), characteristic of the Turonian age (Soto-Araiza et al., 2012), are present in some layers. At La Caja anticline and north of Peñasquito, the lithological unit exhibits limestone of a light gray to beige color that becomes pinkish in color due to weathering effects. The texture is wackestone with layers that range between 0.10 and 0.15 m in thickness, that alternate with siltstones of ocher to beige color, whose layers range from 0.05 to 0.15 m thick. The lithological unit presents locally interbedded fine-grained sandstone with brown gray tones due to weathering effects, and layers ranging from 0.10 to 0.15 m in thickness. The lithological characteristics

suggest a deposition environment of shallow water with terrigenous contribution, either near the coast or sublittoral.

The Indidura Formation overlies the Cuesta del Cura Formation (Kace Cz-Lu), while its top portion is concordantly and transitionally overlain by the Caracol Formation (K ktur-com Ar-Lu); however, in some areas, the lithological unit is unconformably overlain by alluvial or colluvial cover. The age of this formation is based on its stratigraphic position and the microfauna content and is suggested to be from the Cenomanian-Turonian (Kelly, 1936; Barboza-Gudiño et al., 2004; Soto-Araiza et al., 2012). In Peñasquito, drill cores have revealed hornfels, skarn, and skarnoid in this formation, all of which exhibited disseminated polymetallic mineralization as well as mantos composed of massive sulfide. The lower portions of the Peñasco and Azul diatreme breccias are located in this formation.

Caracol Formation (Ktur-cam Slts-Sst)

The lithological unit was originally described in Caracol Creek, located in the eastern part of the Sierra de Parras, Coahuila (about 100 km northeast from Peñasquito) and formally named the Caracol Formation by Imlay (1936), who described a rhythmic sequence of devitrified tuff, siltstone, and minor amounts of limestone. On the south flank of La Caja-Concepción del Oro anticline 20 km and 101° from Peñasquito (i.e. locality known as Novillos), the Caracol Formation has been systematically studied by Pinzon-Sotelo (2012), who suggested a thickness of 1,000 to 1,400 meters and determined two members. The lower member is made of a rhythmic alternation of siltstone and sandstone and contains parallel and cross lamination, suggesting a shallow depositional environment. The upper

member is comprised of an alternation of sandstone, siltstone, and local conglomerate. The textural features include amalgamated sandstone strata, parallel and cross lamination, staggered ripples, synsedimentary folds, and floated clasts, suggesting a deep sedimentary environment. This lithological unit becomes dark-gray and light brown in color due to weathering effects.

In the Peñasco pit, the Caracol Formation is made up of alternating sandstone and siltstone which occur as sub-flat layers with a dark gray color on fresh fractures and a yellow ocher color due to weathering effects. The sandstone is made up of poorly sorted grains, gray in color with medium to coarse-grains and includes rounded grains of feldspar, quartz, and clays which are supported by a fine matrix. The sandstone crops out in layers ranging up to 80 cm in thickness. The siltstone exhibits fine-grained, dark gray and yellow-ocher color due to weathering effects in layers varying from 0.03 to 0.10 m in thickness. This formation was altered by sericite and pyrite, which were overprinted by carbonate. Drilling at Peñasquito has intercepted this lithological unit from 36 (1,963 m.a.s.l.) to ~856 m (1,142 m.a.s.l.) below the current surface and an average thickness of ~786 m has been estimated.

In the Peñasquito region, the Caracol Formation crops out in synclines. The lithological unit conformably overlies the Indidura Formation and underlies, by concordant and transitional contact, the Parras Formation and/or is covered by conglomerate and alluvial cover. Pinzon-Sotelo (2012) has suggested an age range between Turonian-Campanian based on its stratigraphic position and the content of microfauna (i.e. Inoceramus labiatus and ammonites of the genus Texanites Sp.). In Peñasquito, the lithological unit hosts the

bulk of the diatreme breccia system as well as stockwork, vein, and mantos, which were filled partially by sulfide, oxides and carbonates. Drill cores have revealed that the Caracol Formation was locally transformed to hornfels with disseminated sulfides and affected by hydrothermal fluids, which caused moderate potassic alteration, pervasive and weak phyllic alteration, and local propylitic alteration, overprinted by carbonates.

Parras Formation (Kcam Slts-Sst)

This lithological unit was originally described by Imlay (1936) in eastern Parras, Coahuila (about 120 km northwest of Peñasquito) and reported as a sequence made of calcareous and carbonaceous siltstone, dark gray in color with fissile and nodular structure, and alternating with fine-grained calcareous sandstone. Rogers et al. (1956) detailed the Parras Formation at Bonanza Valley, Zacatecas (about 18 km 102° from Peñasquito) and reported a lithological sequence made up of an alternation of limestone, black siltstone, and sandstone. Meanwhile, Pinzon-Sotelo (2012) described a lithological sequence consisting of siltstone of a black color that weathers to a greenish gray, with locally interbedded fine to medium grained sandstone, which shows abundant fracturing and calcite veins up to 7 cm in thickness.

In the Bonanza Valley, the thickness reported by Rogers et al. (1956) is 1,300 m, while, Pinzon-Sotelo (2012) suggested a thickness up to 1,400 m based on a section between localities known as Novillos and Cerro Pachona (about 18 km 102° from Peñasquito). This lithological unit overlies, by concordant and transitional contact, the Caracol Formation and underlies, by angular unconformably, the Tertiary conglomerate de-

posits (Pinzon-Sotelo, 2012; Montañez-Castro et al., 2003). The suggested age is Campanian-Maastrichtian based on its faunal content (Tardy, 1972; PEMEX, 1988) and stratigraphic position (Montañez-Castro et al., 2000, 2003).

Tertiary

Ahuichila Formation (Te PCg-Sst)

The clastic Ahuichila sequence was formally described and named by Rogers et al. (1961) at the Ahuichila Valley, Zacatecas (about 108 km and 298° from Peñasquito) as a conglomerate made of limestone fragments, arkose, siltstone, freshwater limestone, tuffs, pyroclastic material, and rhyolite, which overlie by angular unconformity, marine Mesozoic units. This lithological unit crops out on the lower limbs of anticlines and edges of the valley. North-northwest of Peñasquito, the Ahuichila Formation is made up of a conglomerate that includes sub-angular to sub-rounded fragments with a variable diameter of 2-20 cm that include limestone, siltstone, sandstone, chert, and volcanic material, which are cemented by calcite, sandstone, clay, carbonate, and locally silica. Montañez-Castro et al. (2003) suggest a thickness up to 30 m, however in the Peñasco open pit, a conglomerate with characteristics similar to the ones mentioned above is present with a thickness up to 5 meters. De Cserna (1956) suggests that the Ahuichila Formation is a continental molasse deposit type, which accumulated after the folding of the Sierra Madre Oriental. This unit overlies, by angular and erosional contact, a sequence from the Late Cretaceous and uncomfortably underlies clastic deposits (alluvial cover) from the Miocene-Pliocene. The

Eocene age is suggested for this unit based on its stratigraphic position (Montañez-Castro et al., 2003).

Polymictic conglomerate-sandstone (Tm-pl PCg-Sst)

This clastic sedimentary lithological unit was deposited in the valleys and topographic depressions along anticlines. The lithological unit is made up of poorly consolidated polymictic conglomerate that includes sub-angular and sub-rounded fragments of limestone, sandstone, siltstone, local igneous rocks, chert, and other clastic materials, which are moderately cemented by calcium carbonate and clays. This clastic unit is intercalated sand and gravel horizons. The thicknesses may vary; for instance, at Peñasquito, this clastic cover is 40 m in average thickness, but increases in thickness to the west. It is worth mentioning that this clastic unit locally forms small hillocks up to 50 m in height. This continental unit is the result of mechanical disruption and erosion of pre-existing rocks. The clastic unit unconformably overlies a marine Mesozoic sequence and underlies alluvial materials. The Miocene to Pliocene age is suggested for this clastic unit is based on its stratigraphic position.

Intrusive rocks

In the Peñasquito region, the Tertiary intrusive rocks crop out along anticlinal axes of La Caja-Concepción del Oro and Santa Rosa ranges (Fig. 2.9). The stocks emplaced in the Mesozoic sedimentary sequence developed aureoles of metasomatism and contact metamorphism, which are responsible for providing polymetallic mineralization. Several authors have identified three main types of intrusive rocks of felsic to intermediate composi-

tion (i.e. granodiorite, monzonite, and rhyolite porphyry). In Peñasquito, drilling has inter-cepted varieties of intrusive rocks emplaced through the Mesozoic sedimentary sequence and some ones through the diatreme breccia system (see Chapters III and IV). According to radiometric dating, this plutonic complex was emplaced and crystallized during the Eocene (Ohmoto et al., 1966; Buseck, 1962; Mújica-Mondragón et al., 1983; Valencia 2010), though radiometric dating of hydrothermal products (i.e. biotite and K-feldspar) indicated phases of recrystallization and cooling from Late Eocene and Oligocene (Fig. 2.10).

Rhyolite porphyry (Te RP)

The rhyolite porphyry outcrops are located in the anticlines of La Caja-Concepción del Oro and Santa Rosa ranges and cover an area of more than 657 ha, forming elongated and eroded stocks with smooth and abrupt morphologies. In general, the rocks are mainly made up of phenocrysts of K-feldspar, quartz, and plagioclase which are floating in an aphanitic matrix. These stocks were emplaced through the Mesozoic lithological sequence and are locally cut by the granodiorite (Montañez-Castro et al., 2003). Montañez-Castro et al. (2000) reported results of a petrographic analysis from the stock located in the Sierra de Santa Rosa and indicated that the rock was made up of phenocrysts of sodium plagio-clase, orthoclase, quartz, biotite, zircon and opaque minerals floating in a quartz-feldspar matrix with strong sericitization, chloritization, and silicification. The suggested classifica-tion is a hypabyssal rock with felsic composition and porphyritic texture (Montañez-Castro et al., 2000, 2003). According to Valencia (2010), the crystallization age for plutonic products (i.e. rhyolite porphyry and tuff) from Santa Rosa is ~45 Ma. It is worth

mentioning that Valencia (2010) reported a radiometric age of ~46 Ma for zircons from a plutonic fragment (i.e. felsite) from the Azul Breccia.

Granodiorite (Te Gd)

Granodiorite outcrops are located along the axes of La Caja-Concepción del Oro anticlines and occupy a large area, of more than 2,584 ha. These stocks occur in elongated exposures with eroded and abrupt morphologies. Granodiorite was emplaced through the Mesozoic lithological sequence and developed aureoles of contact metamorphism and metasomatism that caused folds as well as halos of skarn, hornfels, and marble. Montañez-Castro et al. (2000) reported results of a petrographic analysis from two stocks suggesting a granodiorite-monzonite classification. At Terminal Providence (about 21 km and 72° from Peñasquito) the stock is made up of sodium plagioclase, quartz, apatite, opaque minerals, sericite, clays, hematite, limonite, chlorite, biotite, and calcite with a porphyritic texture, and feldspathic matrix with seritization and chloritization (Montañez-Castro et al., 2000, 2003). At Noche Buena (about 6 km and 25° from Peñasquito), the stock is made of plagioclase, quartz, orthoclase, opaque minerals, augite, hypersthene, diopside, apatite, chlorite, biotite, sericite, clays, hematite, and limonite and exhibits an equigranular texture (Montañez-Castro et al., 2000, 2003).

According to radiometric dating, this plutonic complex crystallized during the Late Eocene (~40 Ma) (Ohmoto et al., 1966; Buseck, 1962; Mújica-Mondragón et al., 1983; Valencia, 2010). In Peñasquito, Valencia (2010) reported a crystallization age of ~41 Ma for a fragment of porphyry from diatreme breccia system, indicating the heterogeneity of intru-

sive fragments in diatreme breccias, and suggesting the presence of granodiorite in the Mazapil syncline, which could be found at some hundred meters beneath the current surface.
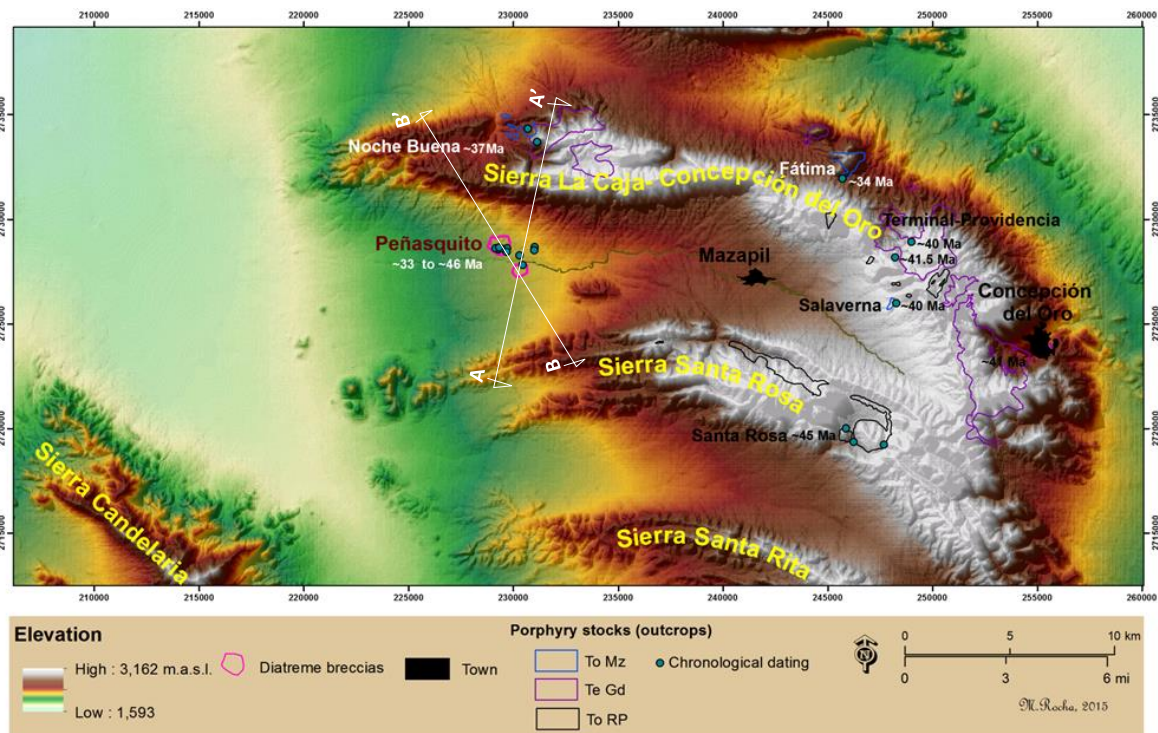
Fig. 2.10. Map showing radiogenic ages for intrusive rock from the Peñasquito Region (data from Ohmoto et al., 1966; Buseck, 1962; Mújica-Mondragón et al., 1983; Valencia, 2010). Also shown are current outcrops of Tertiary plutons and localities mentioned above. Cross sections A-A' and B-B' are shown in Fig. 2.11.

Monzonite (To Mz)

The monzonite outcrops are located along the north and south flanks of La Caja anticline (about 5, 16, and 19 km north, northeast, and east of Peñasquito).These stocks have a semi-elliptical shape and were emplaced in the Early Cretaceous sedimentary lithological sequence. This intrusion caused contact metamorphism and metasomatism, and the stock exhibits phyllic alteration, oxidation and argillization. According to Ocejo-

Paredes et al. (2003), the intrusive rock exhibits a light-gray color and porphyritic texture and is made up of 5% quartz, 25% plagioclase (oligoclase-andesine), 5% potassium feldspar, hornblende, muscovite, local fine-grained biotite, silica, clays, and microcrystalline groundmass.
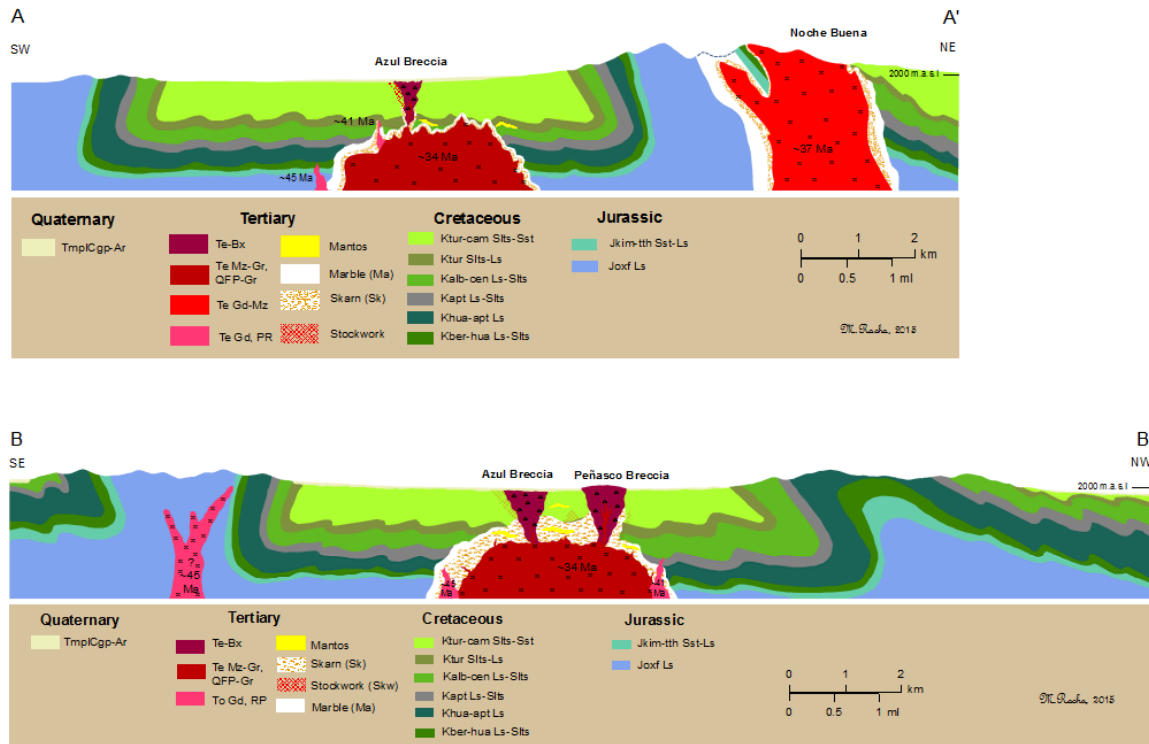
Fig. 2.11. Schematic cross sections showing magmatic event at the Peñasquito region. A-A' schematic cross section is cutting up throughout the Azul Breccia and Noche Buena, 13° in orientation, and looking to the northwest. B-B' schematic cross section is cutting up throughout Azul and Peñasco Breccias, 350° in orientation, and looking to the southwest. See Fig. 2.10 for cross section locations.

At Noche Buena, the monzonite contains economic auriferous mineralization that is related to limonite minerals due to supergene effects. In Salaverna, the monzonite developed metasomatic aureoles of a grandite skarn with polymetallic mineralization. In Peñasquito, the polymetallic mineralization is chiefly related with the monzonite, quartz-monzonite, and quartz-monzodiorite pulses (Fig. 2.11). Valencia (2010) reported Late Eo-

cene crystallization ages (~34 Ma) for porphyry complex from Peñasquito, and minerals of potassic alteration are ~33 Ma (i.e. biotite and orthoclase). Detailed petrology of the Peñasquito system is presented in chapter III.

Age for the plutonic system

The plutonic systems between Peñasquito and Concepción del Oro have been dated by various authors with the resulting ages ranging from Eocene to Oligocene (Ohmoto et al., 1966; Buseck, 1966; Mújica-Mondragón et al., 1983; Valencia, 2010) (Table 2.1). Specifically, Ohmoto et al. (1966) reported that in a sample from the Terminal Providence-Concepción del Oro stock, the K-Ar age of biotite from the granodiorite stocks was ~40 Ma. Meanwhile, Buseck (1962, 1966) reported ~40 Ma of biotite from the granodiorite of Concepción del Oro. Mújica-Mondragón et al., (1983) reported ~41 Ma for the Concepción del Oro stock (Table 2.1).

In addition, Valencia (2010) conducted a chronology survey on zircons from samples of granodiorite, quartz-monzonite, and rhyolite porphyry corresponding to the stocks localized in Peñasquito, Noche Buena, Santa Rosa, and Salaverna as well as diatreme products from Peñasquito using the U-Pb-Th method (Table 2.1). The U-Pb age for rhyolite porphyry from Santa Rosa was ~ 45 Ma (Valencia, 2010). In Peñasquito, the plutonic complex and magmatic products range in U-Pb-Th ages from 33.7 ± 0.5 to 46.0 ± 0.02 Ma that are considered crystallization ages (Valencia, 2010), indicating more than one magmatic pulse within the Mazapil syncline through the Mesozoic sedimentary sequence. The Salaverna stock contains zircons with consistent U-Pb-Th ages from 39.6 ± 0.6 to 41.5 ± 0.6

Ma, although, this pluton also contains zircons with U-Pb-Th age of 33.6 ± 0.4 (Valencia, 2010). Stocks of Noche Buena presented consistent U-Pb-Th ages from 36.6 ± 0.1 to 37 ± 0.6 Ma for the granodiorite, and from 36.3 ± 0.6 to 36.8 ± 0.5 Ma for quartz-monzonite porphyry, suggesting differentiated magmas (Valencia, 2010).

Table 2.1. Historical summary showing radiometric dating of the magmatism in the Peñasquito region. Note: Datum-Nat 27.

Sample	Coor-X	Coor-Y	Elevation (m.o.s.l)	Age (Ma)	Error (±)	Dated mineral	Method	Zone	Locality	Rock	Author
WC335-332	229674	2728623	1682	41.9	0.6	Zrn	U-Pb-Th		Azul	Tuffisite	Valencia, 2010
GP557-08-1140	229261	2728565	949	34.4	0.4	Zrn	U-Pb-Th		Peñasquito	QFP	Valencia, 2010
282-1	229669	2728464		34.1	0.7	Zrn	U-Pb-Th		Peñasquito	QFP	Valencia, 2010
GP595-1391	229669	2728464		33.7	0.4	Zrn	U-Pb-Th	Peñasquito	Peñasquito	QFP	Valencia, 2010
WC300-511	229418	2728601	1513	34.1	0.6	Zrn	U-Pb-Th		Peñasquito	QFP	Valencia, 2010
GP568-670	229669	2728464		33.7	0.5	Zrn	U-Pb-Th		Peñasquito	QFP	Valencia, 2010
342-1	229669	2728464		46.0	0.02	Zrn	U-Pb-Th		Azul	Tuffisite	Valencia, 2010
342-1	229669	2728464		33.4	0.4	Zrn	U-Pb-Th		Azul	Green dike	Valencia, 2010
WC360-525	229126	2728619	1494	34.4	0.01	Zrn	U-Pb-Th		Peñasquito	QFP	Valencia, 2010
NBD-13	230680	2734349		36.3	0.6	Zrn	U-Pb-Th		Noche Buena	QFP	Valencia, 2010
NBD-12	230680	2734349		36.8	0.6	Zrn	U-Pb-Th		Noche Buena	QFP	Valencia, 2010
NBD-11	230680	2734349		36.6	0.5	Zrn	U-Pb-Th		Noche Buena	QFP	Valencia, 2010
NBD-10	230680	2734349		37.1	0.5	Zrn	U-Pb-Th		Noche Buena	QFP	Valencia, 2010
NBD-9	230680	2734349		36.7	0.5	Zrn	U-Pb-Th		Noche Buena	QFP	Valencia, 2010
NBD-8	231116	2733714		37.0	0.6	Zrn	U-Pb-Th	Noche Buena	Noche Buena	Gd	Valencia, 2010
NBD-7	231116	2733714		36.6	0.01	Zrn	U-Pb-Th		Noche Buena	Gd	Valencia, 2010
NBD-6	230680	2734349		36.8	0.5	Zrn	U-Pb-Th		Noche Buena	QFP	Valencia, 2010
NBD-5	230680	2734349		36.5	0.7	Zrn	U-Pb-Th		Noche Buena	QFP	Valencia, 2010
NBD-4	230680	2734349		36.6	0.5	Zrn	U-Pb-Th		Noche Buena	QFP	Valencia, 2010
NBD-2	230680	2734349		37.0	0.02	Zrn	U-Pb-Th		Noche Buena	QFP	Valencia, 2010
NBD-1	230680	2734349		36.9	0.5	Zrn	U-Pb-Th		Noche Buena	QFP	Valencia, 2010
Sample-6	-	-	-	39.7	0.6	Zrn	U-Pb-Th		Gloria Estela	Gd	Valencia, 2010
Sample-5	245678	2731956	-	33.6	0.4	Zrn	U-Pb-Th		Fortuna	Mz	Valencia, 2010
Sample-4	248980	2728936	-	40.3	0.6	Zrn	U-Pb-Th		Fátima	Gd	Valencia, 2010
Sample-3	248190	2728179	-	41.5	0.6	Zrn	U-Pb-Th	Salaverna	Rucio Mina	Gd	Valencia, 2010
Sample-2	248253	2726001	-	39.6	0.6	Zrn	U-Pb-Th		Salaverna	Gr-Mz	Valencia, 2010
Sample-1	248253	2726001	-	40.4	0.6	Zrn	U-Pb-Th		Santiago Mina	Gd	Valencia, 2010
1ab-2ab-3	-	-	-	39.3	2	Bi	K-Ar		Terminal Providence - Concepción del Oro	Gd	Ohmoto et al., 1966
4ab	-	-	-	34.2	2	Ms	K-Ar		Terminal-Providence	Gd	Ohmoto et al., 1966
6b				34.3	3	Ab	K-Ar		-	Ore	Ohmoto et al., 1966
6b-7				38.0	3	Ad	K-Ar		-	Ore	Ohmoto et al., 1966
-	-	-	-	40.0	1.2	Bi	K-Ar	Concepción del Oro	-	Gd	Buseck, 1962
-	-	-	-	38.0	1.2	Ad	K-Ar		-	Gd	Buseck, 1962
-	-	-	-	41.0	3	-	K-Ar		-	Gd	Mújica-Mondragón et al., 1983
SR-3	245859	2720017		44.7	0.5	Zrn	U-Pb-Th		Santa Rosa	Tuff	Valencia, 2010
SR-2	246209	2719375		45.2	0.8	Zrn	U-Pb-Th	Santa Rosa	Santa Rosa	RP	Valencia, 2010
SR-1	247668	2719243		45.3	0.5	Zrn	U-Pb-Th		Santa Rosa	RP	Valencia, 2010

Metamorphic rocks

The plutons have developed metamorphism and metasomatism through the Meso-zoic sedimentary sequence. At La Caja-Concepción del Oro anticline, skarn zones are exposed around the granodiorite, and the mapped outcrops cover more than 256 ha. Skarn was developed in the Zuloaga, La Caja, Taraises and Cuesta del Cura formations. The outcrops occur as narrow and elongated bands, and endoskarn and exoskarn zones consist of garnets (andradite and grossularite), epidote, chlorite, and local pyroxene minerals. The skarn system hosts disseminated polymetallic mineralization as well as irregular bodies filled by massive sulfides and oxides. In Peñasquito, the drilling has intercepted skarn in the Zuloaga, La Caja, Cupido, and Cuesta del Cura formations, but the bulk of the skarn has been found in La Caja, Cupido, and Cuesta del Cura formations. This skarn exhibits disseminated sulfides and oxides and economic values of gold, copper, lead, zinc, and silver. Massive sulfide mantos have also been found in the skarn system. The skarn may be interleaved with marble, hornfels, and local skarnoid.

The recognized hornfels outcrops in La Caja-Concepción del Oro anticline cover more than 287 hectares and form aureoles around the monzonite and granodiorite stocks. This hornfels has been developed in the Taraises and Caracol formations. In Peñasquito, the drilling has intersected hornfels in the Taraises, La Peña, Indidura, and Caracol formations, but the bulk of hornfels was developed in the Caracol Formation. The hornfels is made of calc-silicates (wollastonite, and local garnets and amphibole), disseminated sulfides, quartz and sulfide veinlets, which are usually overprinted by phyllic hydrothermal

alteration and retrograde hydrothermal alteration (chlorite, epidote). The hornfels is gradually converted to skarnoid; however it depends on the composition of the protolith.

In addition, marble is localized in La Caja-Concepción del Oro anticline, and mapped outcrops cover a total area of more than 141 ha. The marble was developed on margins of the skarn and within the Zuloaga and Cupido formations. The drilling at Peñasquito has intercepted marble concentrations in the Zuloga, Cupido, La Peña, and Cuesta del Cura formations where it exhibits a white to light gray color, is coarse-grained, and contains local disseminated sulfides.

Quaternary

Basalt (Tm Bas)

Extrusive mafic igneous rocks are present in two areas. These rocks protrude from the valleys as small hills and plateaus. In general, the rocks are from a volcanic flow, and a fissural origin has been suggested (Aranda-Gómez et al., 2005). The rock exhibits a varied color (light gray, black and brown) and varied texture (phaneritic and aphanitic). The volcanic outcrop located in the town known as Las Mesas (about 7 km and 219° from Peñasquito) was described by Ocejo-Paredes et al. (2003) and reported as dark gray basalt, with aphanitic texture surrounded by pyroclastic flows of basalt and basaltic breccia with porphyritic texture. These authors suggest a thickness up to 100 m in an outcrop that is about 1,000 ha, which unconformably overlies the Cuesta del Cura and Ahuichila formations. According to Ocejo-Paredes et al. (2003), this rock includes 50-75% calcic plagio-

clase, 5-25% olivine, 5% augite-hypersthene, 5% glass, 5% calcite, opaque minerals (hematite-magnetite), clays, chlorite, and a microcrystalline matrix of plagioclase and pyroxene.

At the Providence Terminal (about 24 km and 70° from Peñasquito) some volcanic rock is present, forming discontinuous outcrops in small hills. Montañez-Castro et al. (2000, 2003) reported a petrographic analysis from a volcanic rock that exhibits varied color (dark gray, black, and brown), aphanitic texture with calcite-filled vesicles, amygdules, glassy matrix, and levels of pyroclastic breccia. In a thin section, the sample consists of plagioclase microlites (50-75% labradorite), 5-25% glass, < 5% olivine, <5% apatite and < 5% opaque minerals, suggesting a basalt or andesitic-basalt (Montañez-Castro et al., 2000).

Luhr et al. (1995) conducted chronological and geochemical research at Los Encinos volcanic field (about 130 km and 151° from Peñasquito) where the rocks exhibit features similar to the ones described above. The K-Ar ages obtained ranged from 10.6 to 13.6 Ma and the classification suggested nepheline hawaiites (Luhr et al., 1995; Aranda-Gómez et al., 2005). Therefore, mafic rocks from the Peñasquito region may be interpreted as magmatism that developed during the Middle Miocene, emplaced through an intraplate, and related to an area of crustal weakness due to fractionated liquids derived from basanite magmas.

Lacustrine Deposits (Tm-Qho Si-Cly)

Lacustrine deposits consist of alluvial materials that include silt, clay, and salts. These materials were deposited in closed lagoons, which allowed the evaporation of wa-

ter and consequent salt precipitation. These deposits are present at the northeast portion

of the Concepción del Oro ridge (about 35 km from Peñasquito). The deposit may be more

than 20 m in thickness. According to Montañez-Castro et al. (2003), these continental de-

posits consist of fine and coarse-grained silt and clay that are poorly consolidated, graded

with conglomeratic lenses and salt layers (i.e. sodium and magnesium chloride). A Mio-

cene to Holocene age suggested for this clastic and chemical unit is based on its strati-

graphic position.

Travertine (Qpt Tr)

The travertine deposit is located at the western end of La Caja anticline (10 km and

284° from Peñasquito) and is related to a fault and thermal spring. This travertine consists

of fine grained $CaCO_3$ and locally silica, limonite minerals, and clays (Ocejo-Paredes et al.,

2003). The travertine is brownish and whitish in color with a porous and banded texture.

The travertine crops out over a surface area of about 640,000 m^2 with a thickness of about

12 m (Ocejo-Paredes et al., 2003). The related fault feeder exhibits a NW-SE orientation

and cuts the Cuesta del Cura Formation. A Pleistocene to Holocene age suggested for this

chemical unit is based on its stratigraphic position.

Colluvium (Qpt-ho Gv-PCg)

The colluvium is made of gravels, rounded pebbles, and cobbles that are poorly ce-

mented by clays and calcareous material and form morphologies such as irregular fans.

These materials are present on the lower parts of the mountains, mainly at the mouths of

streams. The main components are gravel and big rock fragments, which exhibit sub-an-

gular to rounded forms and include fragments of limestone, igneous rocks, and chert that are poorly cemented by carbonates (caliche) and clays. These deposits are overlying litho-logical units from the Mesozoic and Tertiary units and are a result of erosion of preexisting rocks. The suggested age for this unit is Pleistocene-Holocene based on its stratigraphic position and relationship with adjacent lithological units.

Alluvium (Qho Al)

The alluvium deposits are alluvial transported materials which include clay, silt, gravel, and cobbles. The alluvial deposits are located towards the western portion of the Peñasquito area and the eastern portion of Concepción del Oro. In general, these deposits consist of silt, clay, gravel, and conglomeratic lenses that are poorly consolidated and graded. The thickness ranges, however, in the western portion of the Peñasquito facilities; drilling revealed about 450 meters of polymictic conglomerate and alluvial cover. In general, these deposits unconformably overly polymictic conglomerate deposits from the Miocene-Pliocene and unconformably overlie rocks from the Mesozoic to Tertiary. The age suggested for these sedimentary deposits is Holocene (Montañez-Castro et al., 2003).

Tectonic and Structural features

In the northern and northeastern parts of Mexico, the structural geology is domi-nated by compressive deformation, a low grade of extensional faulting, as well as, local deformation and faulting which was developed in the Mesozoic sequence. The defor-mation was caused by a compressive stress during the Laramide Orogeny followed by ex-tension during the Early Tertiary, which prepared areas of weakness for Middle-Late Ter-

tiary magmatic body emplacement. During the Late Cretaceous, the thrusting of the Laramide Orogeny began from the paleo-Pacific margin with a northeast direction and mainly affected the Mesozoic sequence. However, the high blocks (i.e. Block of Coahuila, Islands of San Carlos, and other ones) counteracted the Laramide thrust. This effect caused the deflection of the Sierra Madre Oriental between Torreon and Monterrey in an east to west direction (Fig. 2.12). The extensional faulting is represented by parallel basins. Magmatic bodies were emplaced along anticlines and local syncline axes and the intersections of deep faults in the form of stocks and dikes, causing local deformation (i.e. Cerro Gordo and Santa Rosa). For example, the Peñasquito diatreme system and igneous masses are located along a syncline axis; this suggests there is potential for other ore systems along synclines.

In the region of Peñasquito, the sedimentary sequence from the Mesozoic presents a series of arcuate folds that form elongated anticlines and flat synclines as well as faulting due to effects of Laramide Orogeny with local intrusion of stocks. The Peñasquito-Concepción del Oro block is made up of parallel anticlines and synclines that are striking in an east to west orientation (Fig. 2.13). The structural block is bounded on the east by normal faults, while, to the west, it is bounded by a structural lineament known as San Tiburcio shear (Mitre-Salazar, 1989). Based on the current morphology, the arrangement of structural blocks and geological features, the San Tiburcio fault may be interpreted as a strike-slip-fault with left lateral movement (pre-Laramide), which played an important role in the regional structural geology (Fig. 2.13).
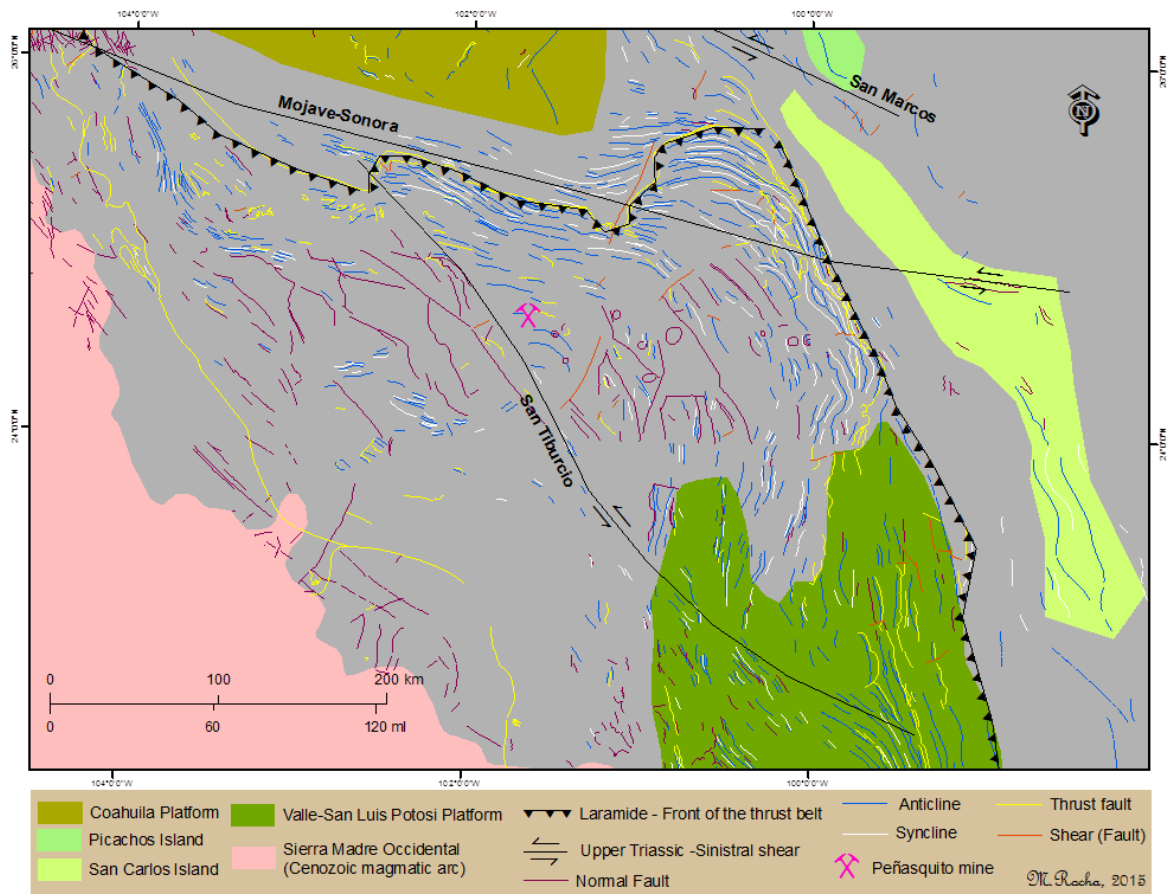
Fig. 2.12. Map showing major structures from northeastern Mexico that included Triassic movements (Black), Cretaceous (blue-white-yellow-orange) and Tertiary (brown) (data taken and modified from SGM database, 2013). Also shown are Mesozoic paleo-elements and the Tertiary volcanic influence.

The anticlines of La Caja-Concepción del Oro, Santa Rosa, and Santa Rita ranges present a marked flexure to the west and were affected by transverse faults with lateral displacement (Montañez-Castro et al., 2003). The La Caja-Concepción del Oro anticline was affected by thrust faults that exhibit a northeast vergence. In the eastern part of Peñasquito, an anticline known as Candelaria (El Toro) is present with a northwest-southeast strike. All anticlines were affected by transverse-normal faults with lateral displacement and striking northeast-southwest (Fig. 2.13) (Ocejo-Paredes et al., 2003; Montañez-Castro et al., 2003).
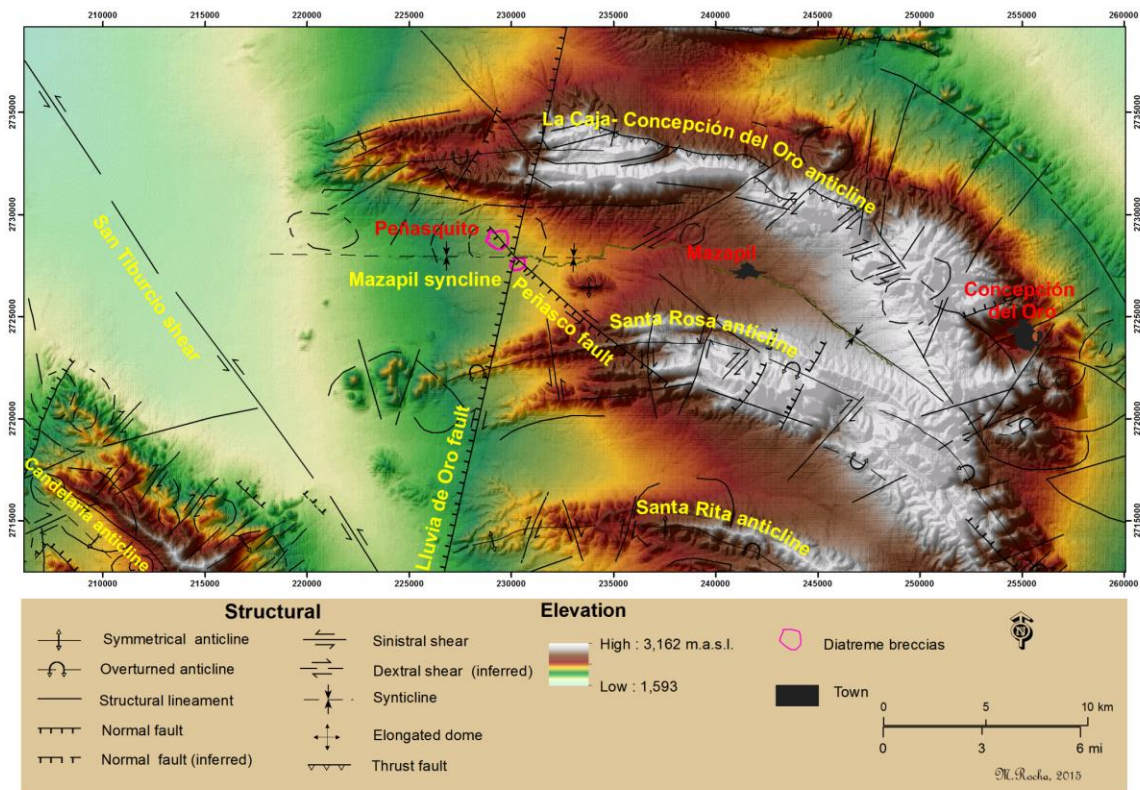
Fig. 2.13. Map showing major structures of the Peñasquito Region. Also shown are the elevation and the diatreme breccia system at Peñasquito. Note: The dashed circular lines are fractures or faults detected on satellite images.

Structural Features at Peñasquito

At Peñasquito, three main structural systems converge suggesting a stress regime, and semi-circular structures (Fig. 2.13) have also been identified indicating a deformation caused by buried plutons. The area is located on the axis of a flat syncline, which has been affected by systems of transverse faults (i.e. the Peñasco and Lluvia de Oro set of faults) as well as faults parallel to the syncline axis (Fig. 2.14). The first set of structures is striking N70°W and corresponds to normal faults with right lateral components. The second system extends N40-50°W throughout the Peñasco Breccia, consists of normal faults, and some exhibit lateral movements. These fault systems create an oval geometric arrange-

ment resulting in the Peñasco Breccia. The third structural system is striking north-north-east with regional extent and includes normal faults; however, some exhibit lateral displacement. In addition, some curved structures that are forming three semicircular rings around the Peñasquito ore deposit have been identified (Fig. 2.15).
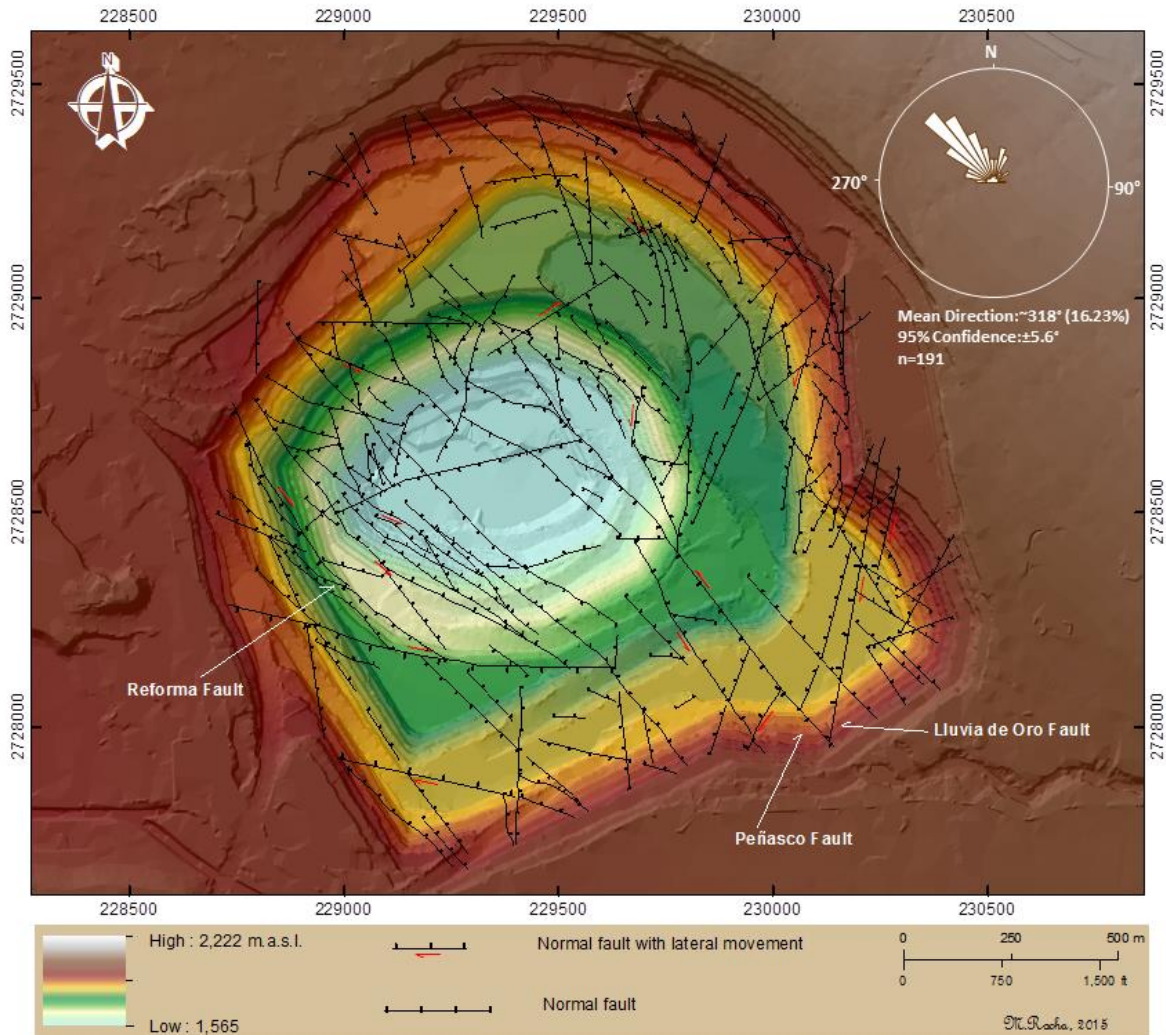
Fig. 2.14. Map showing the structural features in the Peñasco open pit. The insert is showing statistical significance of data (Map by author and Exploration staff of Goldcorp Peñasquito, 2014).

The first structural system was developed along the axis of the syncline. These structures form a small graben, which caused the development of a stream within the Caracol Formation. The structural set is cut by a system of faults with a north-northeast trend

forming a geometric grid and the intersection angle is ~80°. Furthermore, the structural

system is cut by a second fault system that forms a 40° geometric grid. It is noteworthy

that sulfides, oxides, and carbonates partially fill the intersections of these structures.
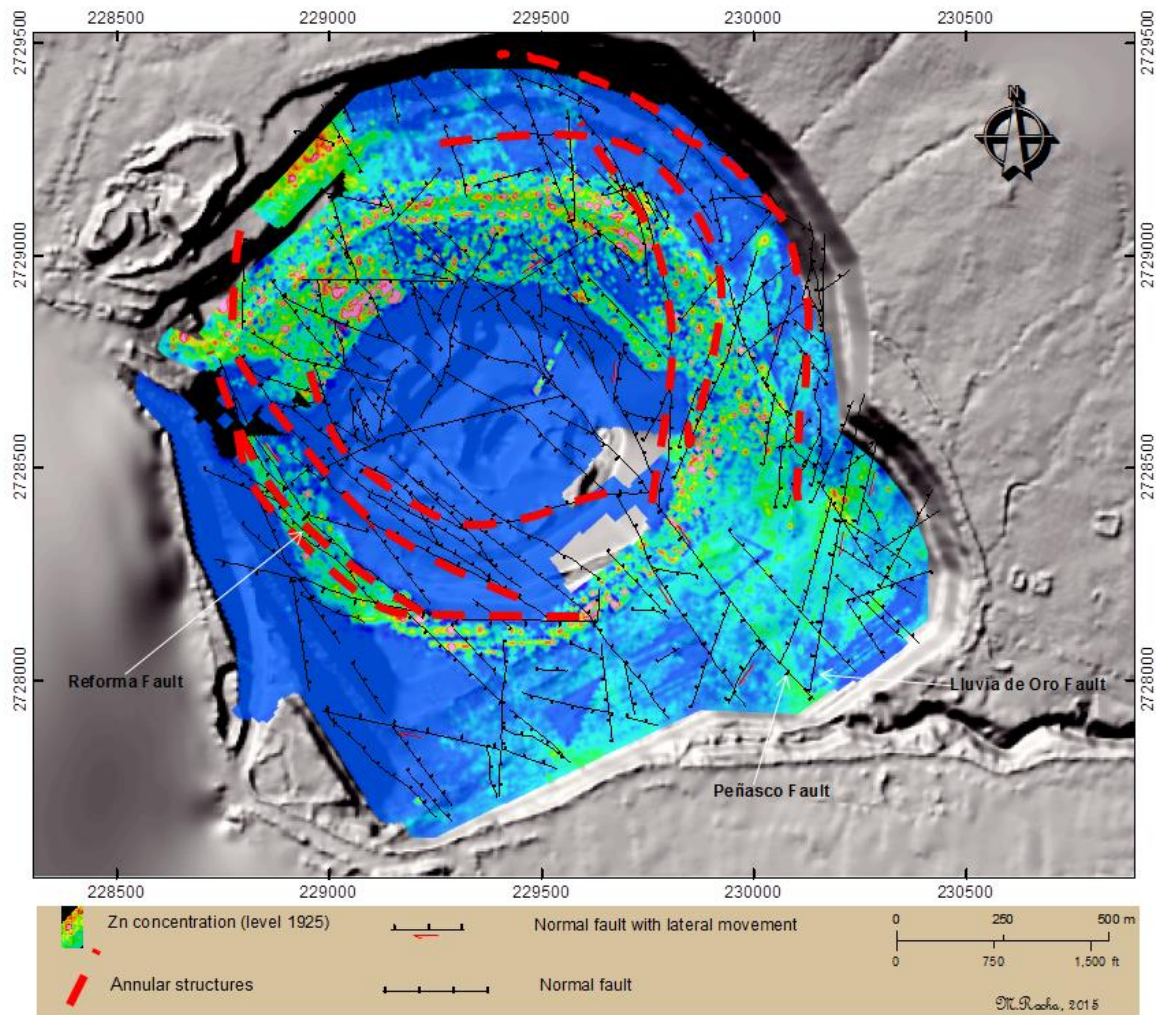
Fig. 2.15. Structural map and blast hole geochemical distribution for zinc in the Peñasco open
pit (the geochemistry data were taken from Goldcorp database). Also shown is the
annular orientation of some structures illustrated by dashed red lines.

The Peñasco and Reforma structural sets strike through the Peñasco Breccia and

correspond to a set of normal faults and local sinistral lateral components. Locally, this

system exhibits reverse faults that caused local deformation within the Caracol Formation.

In addition, this system exhibits parallel and flexural structures that form an elongated oval (NW-SE orientation) around the Peñasco Breccia diatreme (Fig. 2.15). This structural set played an important role during the development of the diatreme breccia system, and structures were good ore fluid feeders. Therefore, these structures present good relationships with economic mineralization (Au-Ag-Pb-Zn-Cu). At depth, this structural set increases the concentration of sulfides, oxides, and carbonates (i.e. below 1,850 m.a.s.l).

The third structural set presents a north-northeast trend and has been regionally identified, suggesting a deep structure of pre-magmatic age. These structures are common in the area situated between the Peñasco and Azul Breccias. In the intersection with the second structural set, these structures form a geometric grid and the interception angle is 45-55° (Fig. 2.14, 15). The system is partially filled by secondary oxides of iron and locally exhibits good correlation with mineralization (Au-Ag-Pb-Zn-Cu). The Lluvia de Oro fault (Fig. 2.14, 15) is representative of this structural set and consists of a normal fault with a dextral lateral component that is partially filled by limonite minerals, local platy calcite, and clays. This fault has been identified for more than 35 km in length between Sierra Zuloaga and Sierra Santa Rita (i.e. 20 km to northeast and 16 km to southwest from Peñasquito, respectively). In the southern portion of the Peñasco pit, the Lluvia de Oro Fault exhibits a displacement to the southeast caused by the Peñasco Fault.

Finally, structural lineaments suggest that parallel semi-circular faults developed around the Peñasquito ore deposit. The alluvial cover masks this structural evidence; however, it is believed that this structural geometry could have been caused by the system of buried plutons in the syncline or by concentric collapse associated with diatreme

development that caused local deformation. These structures may be seen on satellite images and are most clearly noticeable on the northern part of Peñasquito. Within the influence of this semi-circular ring (western portion), the original morphology of the stream (i.e. pre-mining) had noticeable changes of pathway (northwest-southeast orienta-tion), indicating a structural control related to the Peñasco structural set (Fig. 2.16).
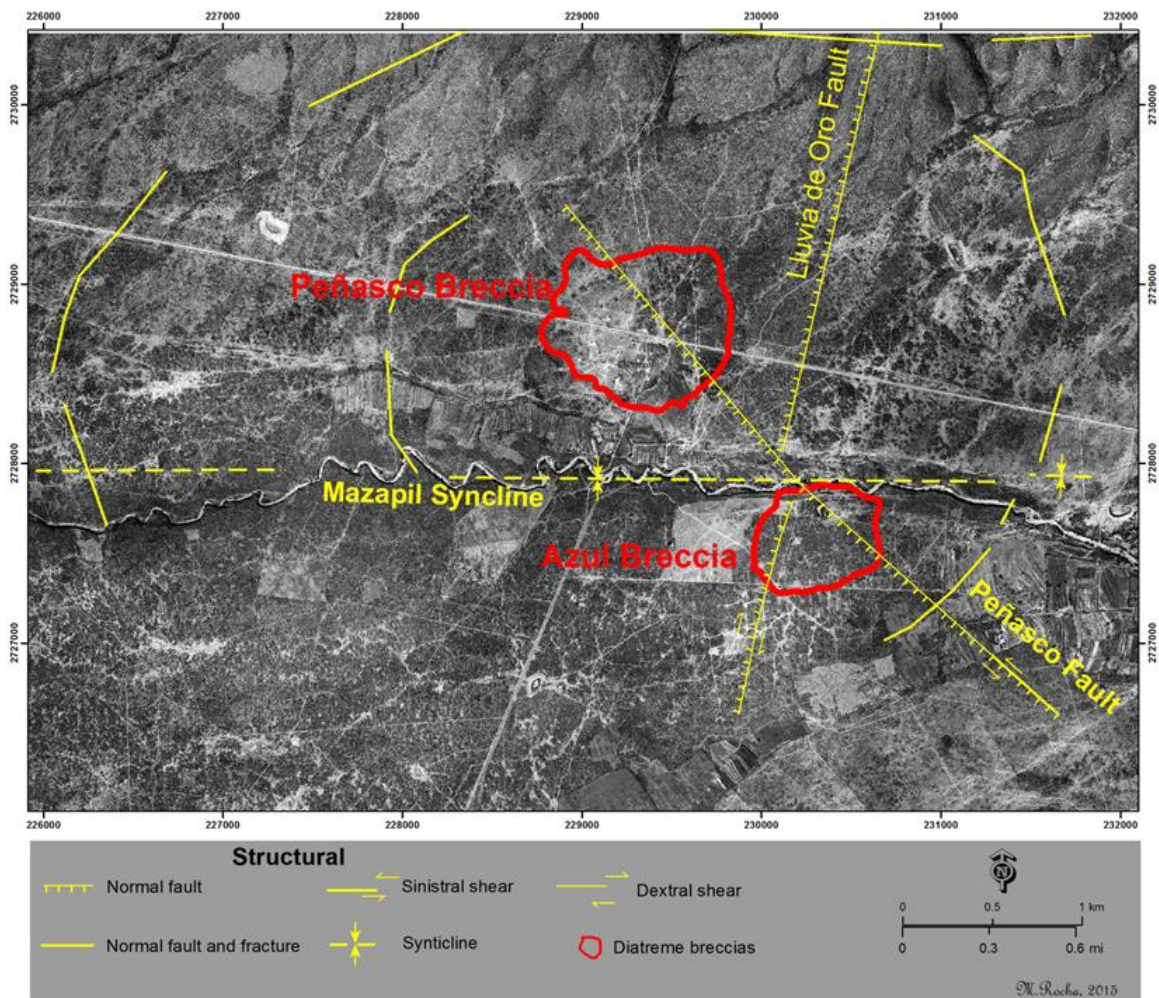
Fig. 2.16. Map showing original morphology of Peñasquito area. Also shown are major faults, diatreme breccias, and annular structures.

CHAPTER III PETROLOGY AND GEOCHEMISTRY OF THE MAGMATIC SYSTEM

Introduction

In the following chapter, petrological and petrographic descriptions, as well as geochemical interpretation (i.e. data of major, trace, and rare earth elements) are presented for each of the porphyries and diatreme breccias found in the Peñasquito area. Several field seasons of mapping and logging resulted in the reconnaissance of the plutonic complex and the relationship to the lithological column and ore bodies at Peñasquito. The specimen selection consisted of representative samples from the plutonic complex, which is emplaced through the Mesozoic sedimentary marine sequence, and the lithological products of the diatreme breccia system. The chemical analyses were completed by ALS Chemex. The geochemical interpretation was completed using specialized software in order to give a petrogenetic classification and magmatic evolution. Petrological and petrographic results are also presented.

Sampling and Methodology of Petrographic Analyses

Samples, which were handpicked from drillcores (Fig. 3.1) and the Peñasco open pit, are distributed throughout the explored area, where the geological context is well known due to detailed logging during fieldwork. The petrography focused on representative specimens from different zones and depths. The sampling included specimens from the porphyry complex (i.e. stocks and dikes) and dikes from the diatreme breccia system. The samples were prepared at the facilities of the University of Nevada, Reno, where samples were cut with a water-based slab saw. In addition, samples were stained with sodium

cobaltinitrite to corroborate the potassic alteration. The thin and polished sections were completed by the Spectrum Petrographics Laboratory. The petrography was completed by using a traditional optical microscope (i.e. Olympus BX53, and BX52) with reflected and optional transmitted light to identify and quantify the minerals. The petrographic modal classification is based on the QAP diagram that was completed and recommended by the IUGS Subcommission (Streckeisen, 1974, 1978), using unaltered samples or with weak potassic alteration. The petrography and staining of samples were performed in the Mackay School laboratories at the University of Nevada, Reno.
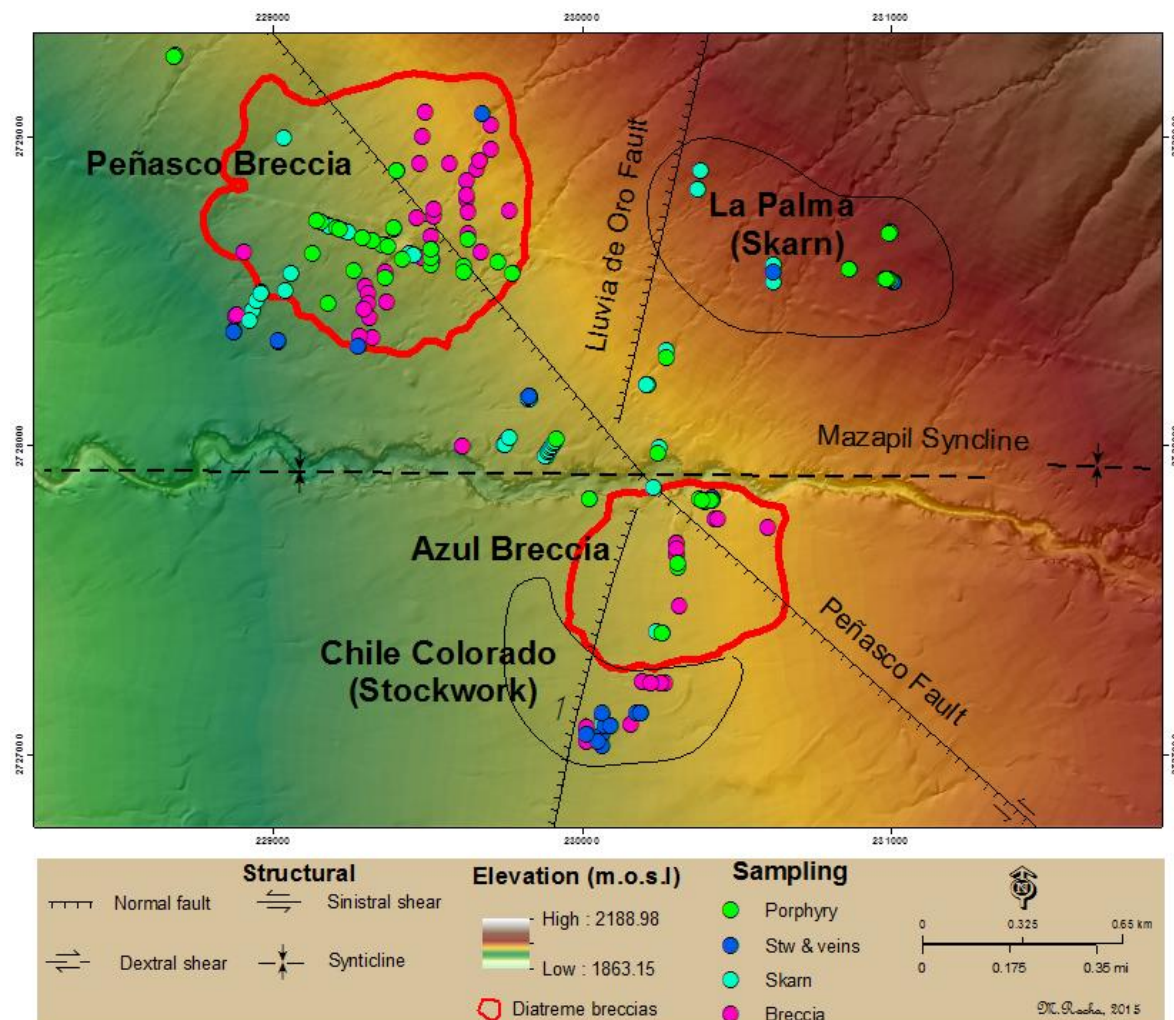
Fig. 3.1. Map showing distribution of sampling from porphyry complex. Samples are from ~80 to 1,901 m.a.s.l. and projected to surface.

Internal Structure of the Plutonic Complex

In the Mazapil syncline, the sedimentary marine sequence from Jurassic and Cretaceous, as well as the diatreme breccia system were intruded by a plutonic complex. The exploration in the Peñasquito area has demonstrated that the plutonic complex occurs as stocks, dikes, and presumably sills, which are considered the source of the polymetallic mineralization and hydrothermal alteration. The stocks and dikes are irregular in shape and exhibit textural and mineralogical differentiation. This plutonic complex has been intercepted by the exploratory drilling and the mining work between ~4 to ~1,886 m at depth (i.e. ~1,966 and ~85 m.a.s.l.) but the bulk of the plutonic complex was developed beneath ~900 m at depth (i.e. ~1,070 m.a.s.l.) and in two main zones (i.e. the zone of Peñasco and Azul breccias and La Palma zone) (Fig. 3.1).

The plutonic complex caused hydrothermal alteration halos through the igneous bodies, marine sedimentary sequence, and the diatreme breccia system. The exploratory drilling has demonstrated that this plutonic complex has an extensive potassic alteration halo (i.e. altered cupola in the top) developed in stock, dikes, the diatreme breccia system and locally in the skarn system. The plutonic complex is surrounded by an extensive calc-silicate aureole followed by a marble shell developed in the Jurassic and Cretaceous sedimentary marine sequence due to the chemical interaction with stocks and dikes (Fig. 3.2). In addition, hydrothermal fluids from the plutonic complex developed huge phyllic and carbonate aureoles, which overprinted the potassic alteration and the skarn system, and propylitization is locally developed in dikes that intruded the diatreme breccia system and the Caracol Formation (i.e. dikes intercepted above 1,500 m.a.s.l.) (Fig. 3.2).
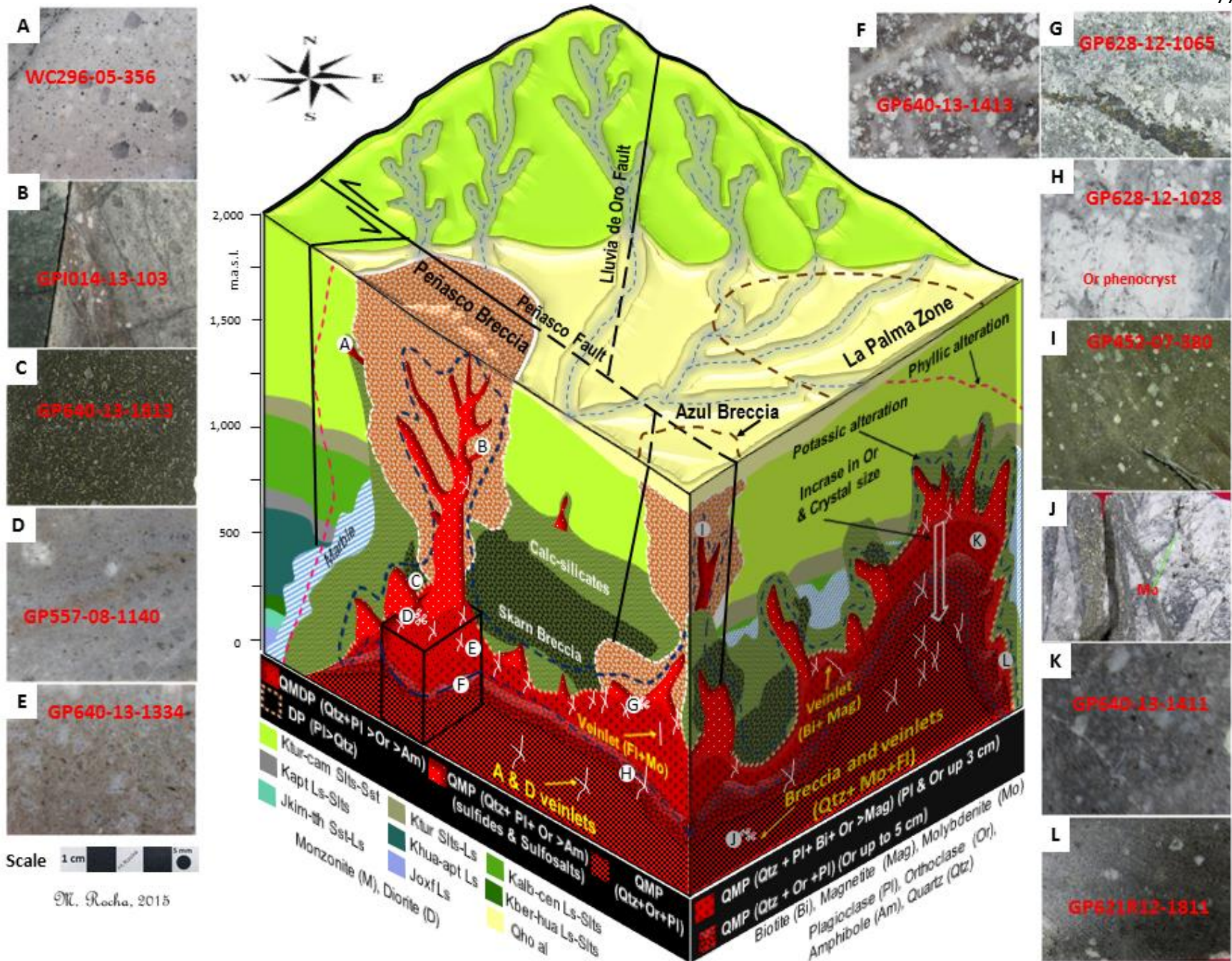
Fig. 3.2. 3D block showing the internal structure for the plutonic complex in the Peñasquito ore deposit. A-L. Photographs showing porphyry types cut by the exploratory drilling.

Petrographic results have demonstrated that this plutonic complex does not have a textural-mineralogical uniform character but usually exhibits a porphyritic texture and is rich in phenocrysts and quartz eyes. The major forming minerals of the plutonic complex are varied including plagioclase, orthoclase, quartz, biotite, and ampibole, documenting textural and mineralogical differentiation. The plagioclase is predominant at the top of the stock cupola and margins (i.e. as plagioclase microlites and/or plagioclase phenocrysts) (Fig. 3.2C, E); while, the biotite occurs as phenocrysts and veinlets, forming concentrations beneath the stock cupola (Fig. 3.2K), followed by concentrations of orthoclase phenocrysts and quartz (Fig. 3.2H, F). Intrusive breccias have been locally intercepted by drills in the cupola and adjacent to the diatreme breccias (Fig. 3.2D). Pyroxene and amphibole are locally present at the top of cupola and have spatial relation with calc-silicate shell (Fig. 3.2 B, L). Most plutonic rocks exhibit zircon and sphene in the groundmass. Dikes and stocks exhibit sulfides, sulfosalts, and oxides at the top (Fig. 3.2G, A), but the molybdenite occurs locally as veinlets in the stock cupola and as disseminations beneath the cupola (Fig. 3.2J).

Although hydrothermal fluids may have changed the original composition of each intrusive rock, the bulk of the plutonic complex could be considered as quartz-feldspar porphyry (QFP). This QFP is not homogeneous in mineralogy and texture (Fig. 3.3), suggesting magmatic differentiation, and several magmatic pulses have been identified and are considered the main source of the diatreme breccia system. The color of the igneous mass is varied including light-gray, local dark-gray, light-pink, and green olive (Fig. 3.3). In addition, drill-cores intersected igneous rocks with high silica content (Fig. 3.3M-

O), as well as fractured porphyry, and intermediate intrusive rock (Fig. 3.3J). In total, six types of intrusive rocks and intrusive breccias can be distinguished in the plutonic complex of Peñasquito, most them were altered causing changes in their original composition, but the mineralogical composition suggests porphyry plutons as quartz-monzonite, quartz-monzodiorite, and quartz diorite (Fig. 3.4). All petrography and mineralogy data are reported in Appendix B.
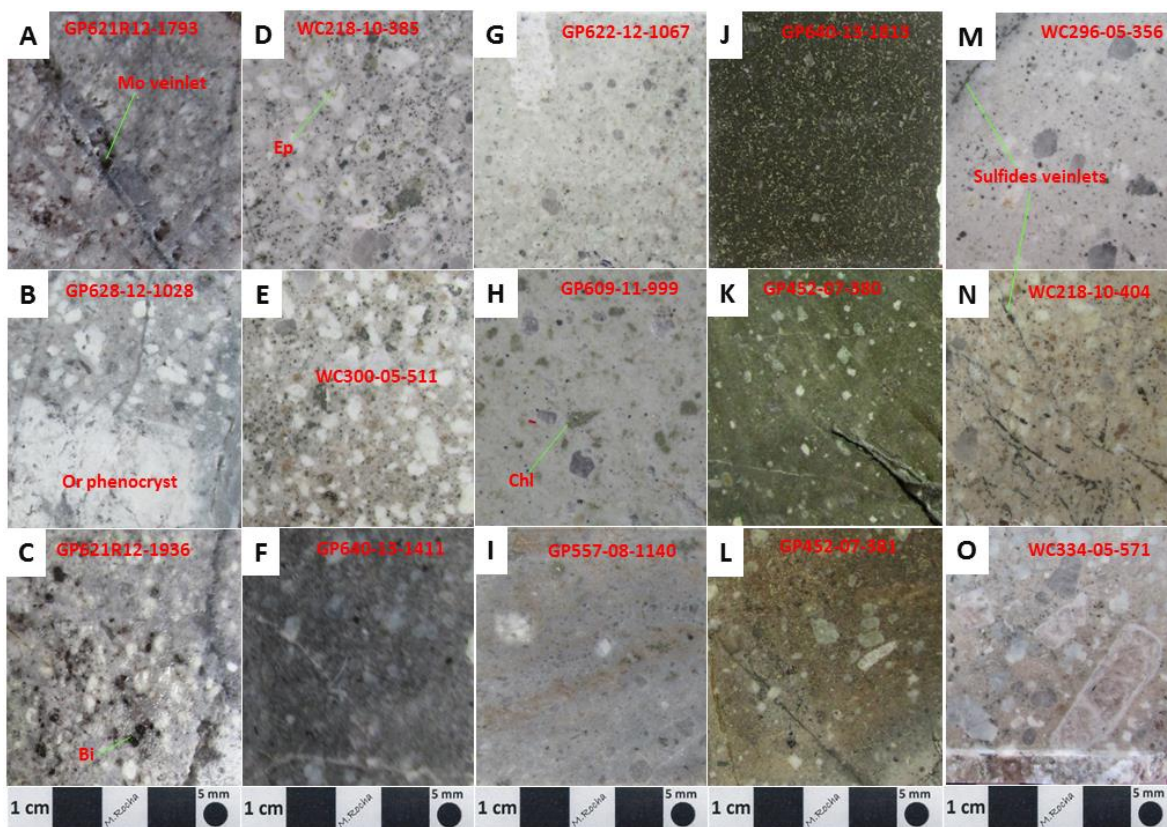
Fig. 3.3. Hand samples displaying porphyries from the Peñasquito area. A.B.C. Hand samples showing quartz monzonite found beneath the cupola of the plutonic complex. D.E. Hand samples showing mineralized quartz-monzonite from dikes in Peñasco Breccia. F. Biotitized quartz monzonite from stock and beneath the cupola of the plutonic complex. G.H.I. Hand samples showing intrusive breccias of quartz monzodiorite found in adjacent zones to the bottom of diatreme breccia system that are cut by quartz-monzonite (presumably IBx). J. Hand samples showing quartz-microdiorite found in the cupola of the plutonic complex. K.L. Hand samples showing chloritized quartz monzodiorite porphyries found in top of the plutonic complex as chloritized dikes. M.N.O. Hand samples showing dikes of silicified and mineralized quartz monzonite porphyries found in top of the plutonic complex. Ep (epidote), Mo (molybdenite) Bi (biotite), Chl (chlorite).

Petrological Features

The geochronological data and observations during fieldwork provide a basis to re-construct the magmatism in the Mazapil syncline. Zircon U-Pb dating yields crystallization ages from Paleogene for this plutonic complex (Valencia, 2010), confirming the close relationship to stocks from La Caja-Concepción del Oro and Santa Rosa. Specifically, U-Pb zircon ages from the plutonic rocks reveal three main episodes of magmatic activity, suggesting crystallization during Middle Eocene, Late Eocene, and Early Oligocene (See Table 2.1 and Fig. 2.11), but only the last two plutonic episodes are documented in this investigation, due to limited exploratory drilling that has not intercepted Middle Eocene rocks . Field observations corroborate high concentration of plagio-

Fig. 3.4. QAP modal classification of plutonic rocks from the Peñasquito area (based on Streckeisen, 1976). Note: dashed red line represents the field for plutonic rocks in the Mazapil syncline.

clase in the plutonic cupola and borders, forming quartz-diorite and quartz-monzo-diorite that were cut by quartz-monzonite dikes, which represent late magmatic event in this area (Figs. 3.2, 4). Furthermore, geochemistry results have demonstrated that the bulk of plutonic complex presents a fractionated crystallization and a signature between diorite and monzonite, suggesting a diapirism-crystallization-type plutonic complex, as well as a

last episode of diking. Therefore, early magmatic episodes in the Mazapil Valley could have intruded as dikes in the Mesozoic sedimentary marine sequence during Middle Eocene, followed by a large magmatic episode as stock and dike (i.e. quartz diorite, quartz-monzodiorite, and quartz monzonite) during Late Eocene, which caused a large halo of calc-silicates, deposition of mineralization, brecciation in the plutonic cupola, formation of the diatreme system, ending with diking in the diatreme breccia system and Caracol Formation (i.e. quartz-monzodiorite and quartz-monzonite) and crystallization at depth (i.e. quartz-monzonite) during Early Oligocene, causing potassic alteration, remobilization and deposition of mineralization, and formation of a large phyllic and carbonates aureoles (Figs. 2.11, 3.2).

Quartz Microdiorite (QMD)

The type of intrusive is an intermediate rock that was intercepted in core at 1,870 m depth (~100 m.a.s.l.) beneath the base of Peñasco Breccia and border of the plutonic complex. This intrusive rock occurs as dikes and sills in the Caja Formation with a high content of plagioclase, which is thus representing an early crystallization phase of the main stock that was presumably emplaced during Late Eocene. This plutonic rock exhibits microcrystalline and local medium-grained (<3 mm) groundmass, and dark green color. The groundmass exhibits pilotaxitic texture. This rock consists of aphanitic plagioclase (microlites) and quartz as major rock forming minerals (microcrystals up to 70%) as well as alteration minerals. The crystals of plagioclase (~65%), and local quartz eyes are locally altered by aphanitic orthoclase, quartz-sericite-pyrite, and carbonate. The quartz crystals

locally exhibit resorption texture. The aphanitic groundmass consists of plagioclase, hydro-

thermal orthoclase, and local quartz.
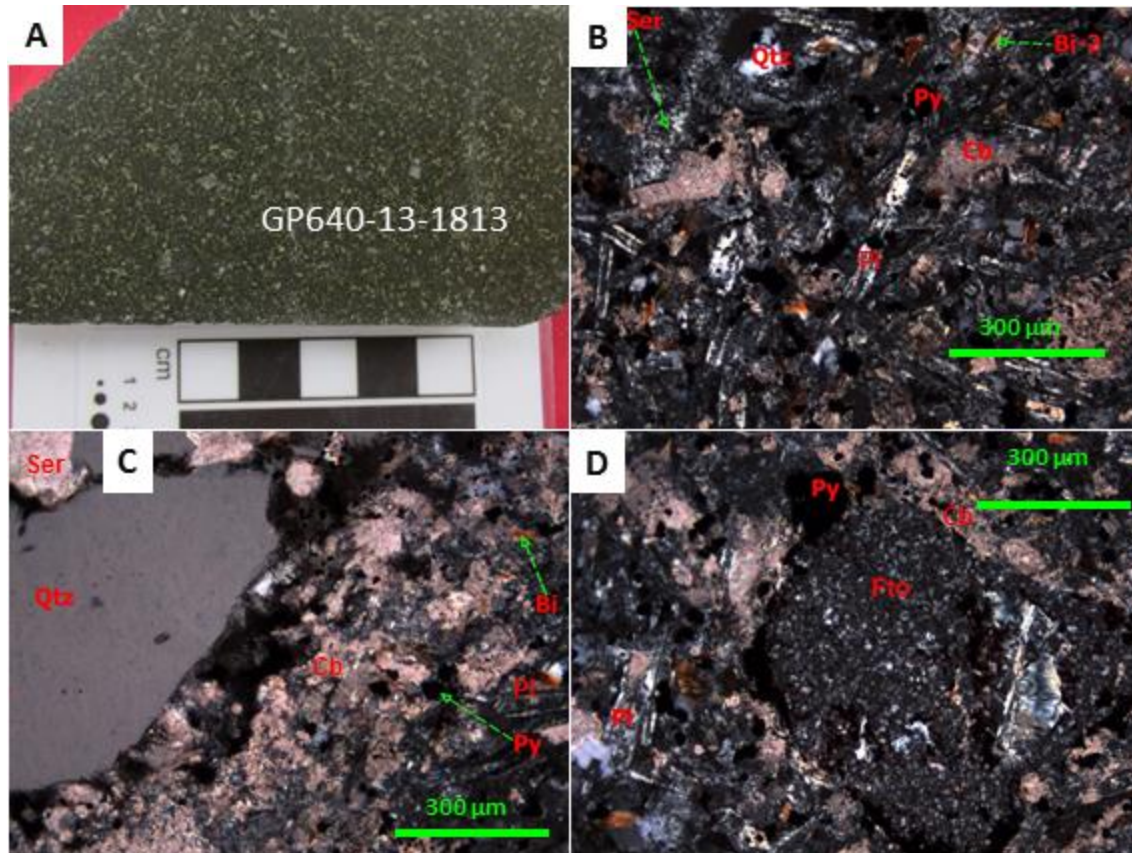
Fig. 3.5. Hand samples and photomicrographs displaying porphyry of quartz microdiorite. A. Hand samples. B. Plagioclase groundmass (Pl) replaced by sericite (Ser), quartz (Qtz), biotite (Bi-2), pyrite (Py), and carbonate (Cab). C. Quartz phenocryst rimmed by sericite and carbonate. D. Altered plagioclase phenocryst (Fto) floating in the plagioclase groundmass.

This intermediate dike exhibits a weak to moderate potassic alteration (i.e. ortho-

clase and biotite), moderate phyllic overprint alteration (quartz>sericite>>pyrite), both of

which were locally overprinted by carbonate (up to 7%). The K-feldspar is present in the

groundmass and locally overprinted by sericite. The secondary biotite (5%) is spread in the

groundmass and among plagioclase microlites. The sericite (3%) is microcrystalline, anhe-

dral, and spread throughout the groundmass. The pyrite (up to 5%) exhibits an anhedral

shape and is fine-grained (Fig. 3.5). Petrographic classification suggests the rock is quartz micro-diorite (Fig. 3.4), and chemical data of trace elements suggest a similar signature as diorite (See Figs. 3.22, 23).

Quartz Monzodiorite Porphyry (QMDP)

This type of intrusive rock is a differentiated quartz-feldspar porphyry with high content of plagioclase, found in the cupola of the plutonic complex (Fig. 3.2 B, I). These plutonic rocks have been discontinuously intercepted by drilling at ~278 and 1,798 m at depth (1,692 and 172 m.a.s.l) and occur as stock and dikes through the Mesozoic sedimentary marine sequence, as well as local dikes through the Peñasco Breccia. These intrusive rocks exhibit a porphyritic texture, light-gray and light-brown color, and moderate to pervasive hydrothermal alteration. These porphyries consist of quartz eyes, phenocrysts, local opaque minerals (i.e. pyrite, sphalerite, chalcopyrite, sulfosalts), which are floating in a microcrystalline groundmass. Phenocrysts present include plagioclase (up to 45%) and orthoclase (up to 20 %), resorbed quartz eyes (up to 5%), and local biotite, as major rock forming minerals; alteration minerals, such as, aphanitic hydrothermal orthoclase (up to 20%), sericite (up to 15%), amorphous quartz (~5%), pyrite (up to 10%), carbonate (up to 10%) and local chlorite, amphibole, epidote and magnetite have overprinted the original rock.

These intrusive rocks exhibit a moderate to pervasive potassic alteration (orthoclase>biotite>>apatite), weak phyllic alteration (sericite> quartz >pyrite), as well as chlorite, epidote and amphibole spread in the groundmass, and all of which are locally

overprinted by chlorite and carbonate. The aphanitic hydrothermal orthoclase is present in the groundmass and locally overprinted by sericite (Fig. 3.6). The sericite is microcrystalline, anhedral in shape, and spread throughout the groundmass. The base of both diatreme breccias are connected to these porphyry types (Fig. 3.2), and these rocks were locally cut by late quartz-monzonite porphyry (Fig. 3.7C).
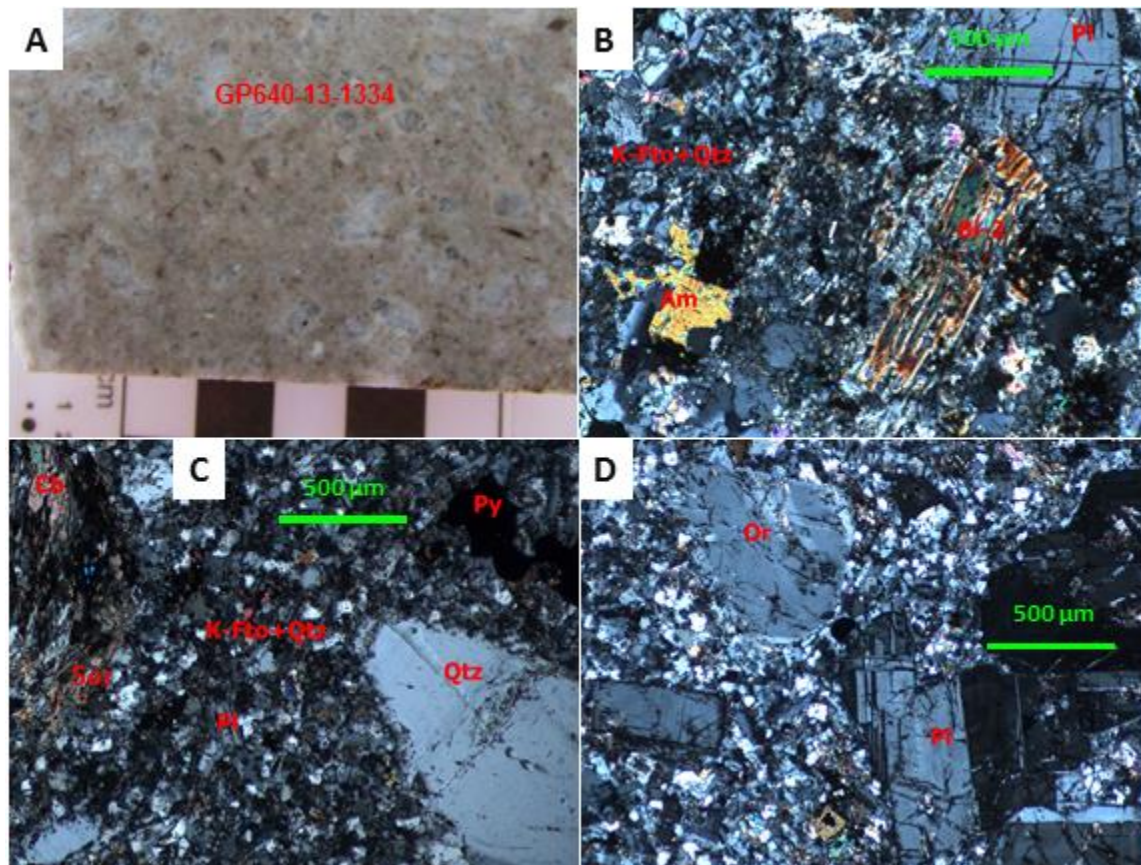
Fig. 3.6. Hand sample and photomicrographs displaying porphyries classified as quartz-monzodiorite. A. Hand sample. B. Plagioclase phenocryst (Pl) and biotite (Bi-2) floating in groundmass of orthoclase (K-Fto), quartz (Qtz) and amphibole (Am). C. Quartz eye floating in groundmass of orthoclase and quartz replaced by sericite (Ser), pyrite (Py) and carbonate (Cb). D. Orthoclase (Or) and plagioclase phenocrysts floating in groundmass of plagioclase and quartz.

The content of plagioclase and quartz, suggests quartz-monzodiorite porphyry with a mineralogical and textural transition between fields of quartz-monzonite porphyry and

granodiorite (Fig. 3.4); also, trace element data suggest a signature between fields of monzonite, diorite, and granodiorite (See Figs. 3.22, 23). The high content of plagioclase and occurrence suggest an early crystallization of the main stock that was presumably emplaced during Late Eocene.
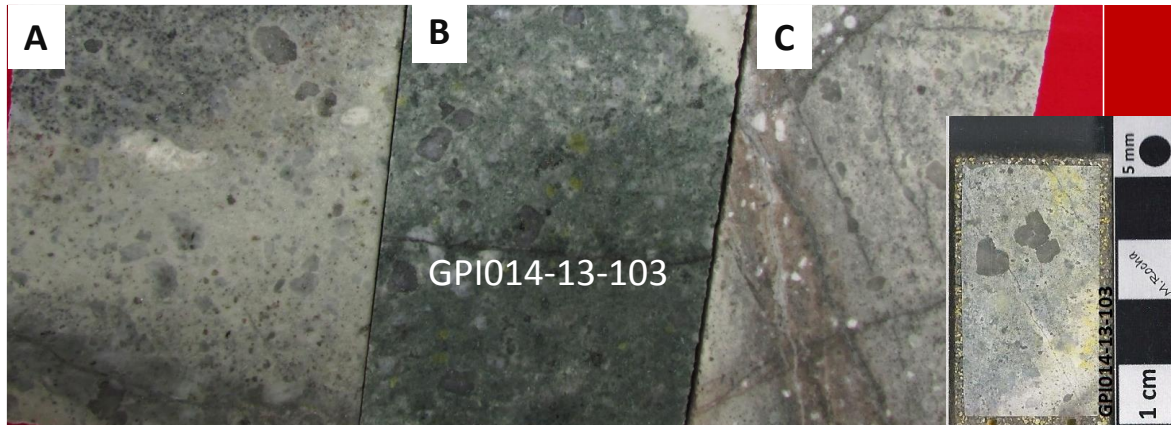
Fig. 3.7. Hand samples displaying specimens of the quartz-monzodiorite cut by quartz-monzodiorite. A-B. Hand samples showing textural features of quartz-monzodiorite porphyry. C. Hand sample and billet are showing staining of K-feldspar with sodium cobaltinitrite in yellow color (Note that quartz monzonite porphyry is cut by QFP- pink color).

Chloritized Quartz Monzodiorite Porphyry

This type of intrusive rock consists of quartz-feldspar porphyry found in the top of the plutonic complex as green dikes that crystalized during the Late Eocene (Valencia, 2010). This porphyry has been intercepted by drill core to 322 m at depth (~1,648 m.a.s.l.) in the Azul Breccia and the Caracol Formation. The porphyry exhibits porphyritic texture (phenocrysts <5 mm), microcrystalline groundmass, varied color (green, light-brown and light-gray), and has been affected by hydrothermal alteration (Fig. 3.8). The dike may be interpreted as late magmatic pulses from the quartz monzodiorite cupola, and pervasive propylitic alteration developed during Late Eocene.
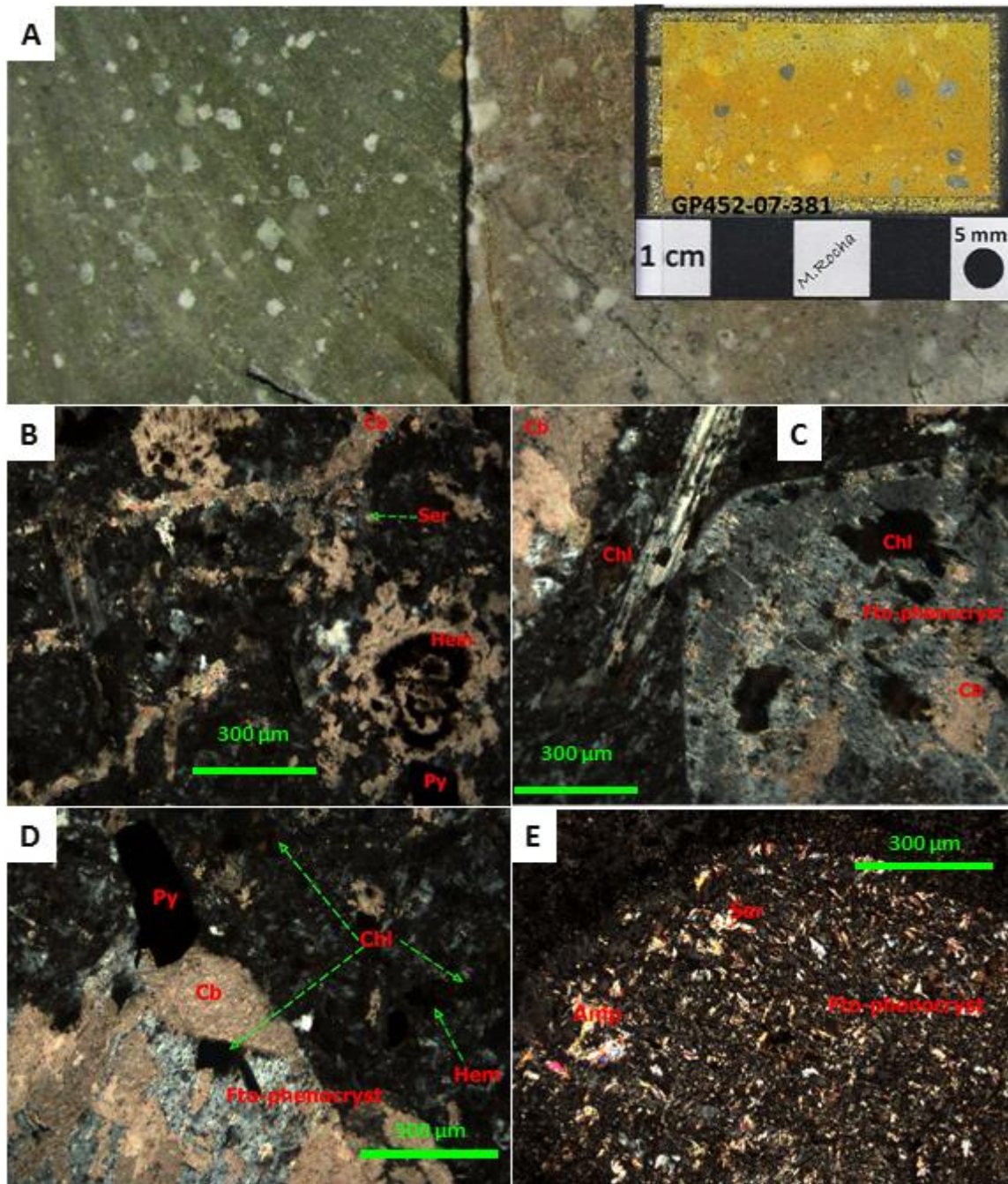
Fig. 3.8. Hand samples and photomicrographs displaying specimen of chloritized quartz-feld-spar porphyry. A. Hand samples and billets are showing staining of K-feldspar with sodium cobaltinitrite in yellow color; also, note the transitional color of samples (green to brown). B-D. Orthoclase groundmass replaced by sericite, quartz, chlorite (Chl), pyrite (Py), hematite (Hem), and carbonate (Cb). C-E. Plagioclase phenocrysts (Fto) replaced by sericite (Ser), amphibole (Amp), and carbonate. Note: at the stained billet (A) the plagioclase phenocrysts exhibit a margin that has been K-feldspathized, but the interior of the phenocrysts is plagioclase-sericite.

This intrusive rock consists of plagioclase phenocrysts (up to 10%), plagioclase microlites (up to 25%), orthoclase phenocrysts (up to 5%), quartz eyes (up to 2%), as well as opaque minerals including pyrite (up to 3%), which are floating in an aphanitic groundmass that includes aphanitic orthoclase (up to >20%), chlorite (up to 15%), carbonate (up to 5%), amorphous quartz (up to 2%), sericite (up to 5%), as well as local biotite and amphibole (Fig. 3.8). The phenocrysts of plagioclase are partially replaced by K-feldspar, quartz-sericite-pyrite, chlorite, and overprinted by carbonates. The porphyry exhibits local veinlets filled by carbonate.

This intrusive rock exhibits a pervasive potassic alteration (orthoclase), a weak phyllic alteration (quartz>sericite>pyrite), a moderate to pervasive propylitic alteration (chlorite-calcite-pyrite), and all of which were locally overprinted by carbonate. The sericite is microcrystalline and anhedral. The fine-grained pyrite exhibits an anhedral shape. Hydrothermal alteration caused mineralogical and chemical changes to the original composition; thus, petrographic classification may be misleading but the content of plagioclase and quartz, suggests quartz-monzodiorite porphyry; also, chemical results of trace elements suggest a similar signature to the diorite field (See Figs. 3.22, 23).

Biotitized Quartz Monzonite Porphyry

This type of porphyry includes altered quartz-feldspar porphyry with high biotite concentration that has been intercepted discontinuously by drilling at ~349 to ~1,500 m depth (~1,621 to ~470 m.a.s.l., respectively). These porphyries have been found as massive bodies beneath the stock cupola, indicating magmatic differentiation (Fig. 3.2K),

and as local dikes through the diatreme breccias, suggesting magmatism from Late Eocene (i.e. an intermediate-final phase of crystallization in the main stock). This porphyry exhibits hydrothermal alteration, grayish color, porphyritic texture, aphanitic groundmass (including orthoclase, quartz, and local plagioclase), and phenocrysts (up to 3 cm). These intrusive rocks consist of phenocrysts of plagioclase (up to 25%), orthoclase (up to 15%), quartz eyes (up to 5%), biotite (15%), as well as opaque minerals as pyrite (up to 5%), which are floating in aphanitic groundmass that includes aphanitic hydrothermal ortho-clase (~15%), aphanitic quartz (up to 10%), carbonate (up to 10%), and sericite (up to 10%), as well as local zircon, apatite, and amphibole(Fig. 3.9). The quartz eyes exhibit no-ticeable resorption, and phenocrysts of plagioclase and orthoclase are partially replaced by quartz-sericite-pyrite and carbonates (i.e. aphanitic calcite), and some borders of plagioclase phenocrysts are partially replaced by K-feldspar.

These plutonic rocks exhibit moderate to pervasive potassic alteration (ortho-clase>biotite>>apatite), pervasive phyllic alteration (i.e. quartz>pyrite>sericite), as well as amphibole in the groundmass, and all of which are locally overprinted by aphanitic car-bonate. The biotite and aphanitic orthoclase spread throughout the groundmass that is locally overprinted by microcrystalline sericite. The sericite is microcrystalline, anhedral, and spread throughout the groundmass and phenocrysts. Molybdenite-fluorite veinlets are locally present throughout groundmass of these porphyries (see Fig. 8.5). The content of plagioclase and quartz, suggests quartz-monzonite porphyry with a mineralogical and textural transition to the field of quartz-monzodiorite porphyry (Fig. 3. 9); also, trace

element data suggest a signature between the fields of monzonite and diorite (See Figs. 3.22, 23).
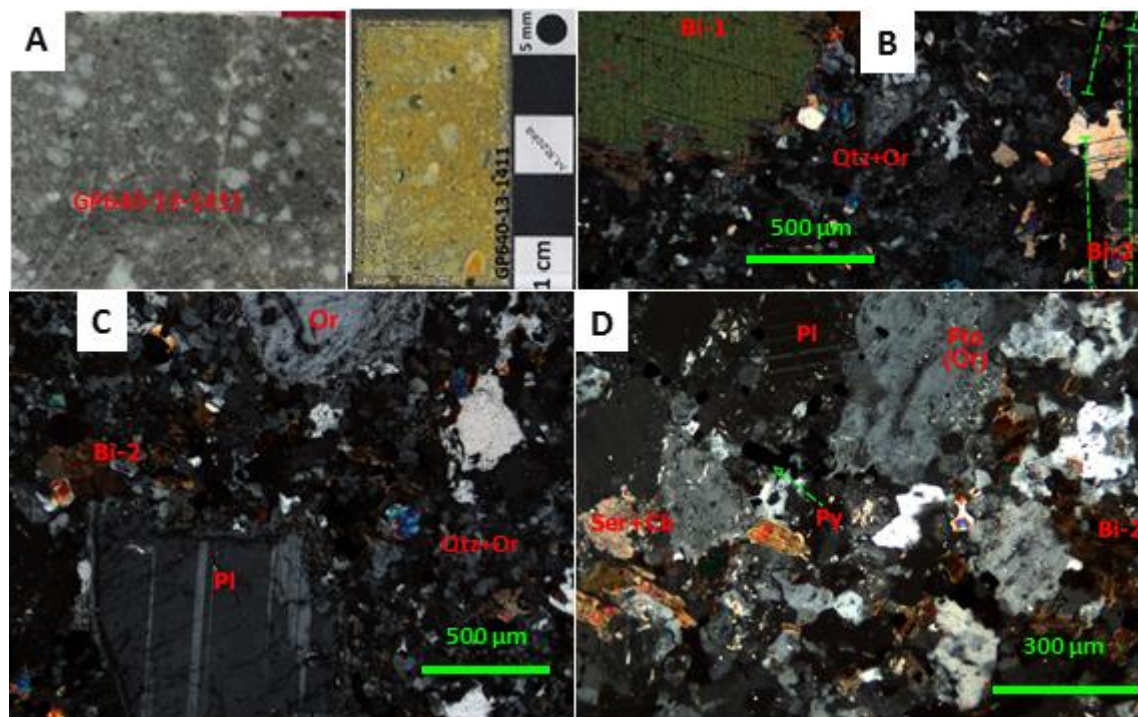
Fig. 3.9. Hand sample and photomicrographs displaying specimen of biotitized quartz-feldspar porphyry. A. Hand sample and billet are showing staining of K-feldspar with sodium cobaltinitrite in yellow color. B. Primary biotite (B1) floating in groundmass of quartz-orthoclase that is cut by secondary biotite veinlet (Bi-2). C-D. Plagioclase (Pl) and or-thoclase (Or) phenocrysts are floating in groundmass, which is overprinted by sec-ondary biotite (Bi-2). Note sericite, carbonate, and pyrite through the groundmass.

Quartz Monzonite Porphyry with large phenocrysts and molybdenite

This type of plutonic rock consists of differentiated quartz-feldspar porphyry (Fig. 3.3A-C) that exhibits weak potassic alteration, pervasive to moderate phyllic alteration, local concentration of molybdenite (Fig. 3.10A), and large phenocrysts. These porphyries have been intersected beneath the stock cupola and biotitized quartz monzonite porphyry (i.e. biotite zone) between ~1,786 and ~1,920 m at depth (from 184 to 50 m.a.s.l.) (Fig. 3.2).
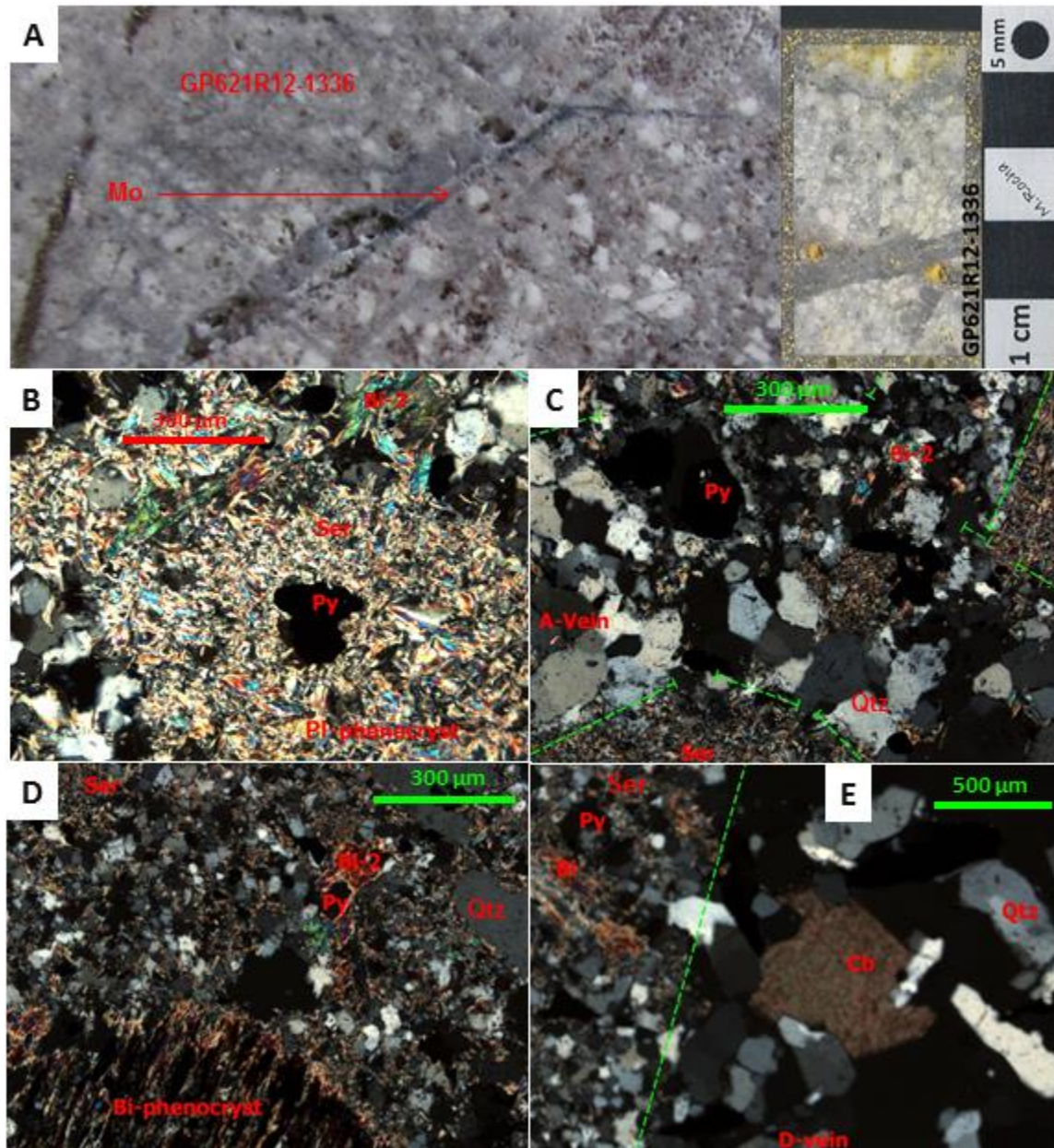
Fig. 3.10. Hand sample and photomicrographs (plane-polarized light) displaying quartz-feldspar porphyries with molybdenite. A. Hand samples showing molybdenite veinlet and billet is showing staining of K-feldspar with sodium cobaltinitrite in yellow color. B. Plagioclase phenocryst (Fto) replaced by biotite, pyrite, and sericite. C. "A" veinlet filled by quartz cut by "D" veinlet filed by quartz-pyrite-sericite and local hydrothermal alteration. D. Biotite replaced by sericite, resorbed quartz, and biotite; sericite and pyrite are spread in groundmass. F. "D" vein filled by quartz replaced by carbonate and sericite and hydro-hydrothermal biotite in groundmass

These intrusive rocks are rich in phenocrysts including plagioclase and orthoclase up to five centimeters in length (Fig. 3.2H) but these gradually decrease in size at depth. Resorbed quartz eyes and local biotite are also present as phenocrysts; the total content of phenocrysts ranges from 20 to 50 modal%. Analyzed samples exhibit propylitic texture and local pegmatitic texture, veinlets, fine-grained to coarse-grained, and molybdenum mineralization as veinlets and local dissemination in intrusive breccias (Fig. 3.2J). These porphyries exhibit "A" veinlets (quartz) that are locally cut by "D" veinlets (quartz-sericite-pyrite). The potassic alteration consists of fine orthoclase, local biotite, and apatite, which are overprinted by quartz>sericite>pyrite and aphanitic carbonate (Fig. 3.10E).

The collective features of this intrusive igneous system indicate an extended time of crystallization, suggesting that the final phase of crystallization within the main stock occurred during the Late Eocene. The content of plagioclase and quartz suggests porphyritic quartz monzonite, and chemical results of trace elements suggest a signature as fields of monzonite to diorite (See Figs. 3.22, 23).

Quartz Monzonite Porphyry with polymetallic mineralization

This type of porphyry includes mineralized quartz monzonite that has been intercepted discontinuously by drilling at ~4 and 1,630 m depth (between 1,966 and 341 m.a.s.l., respectively). These porphyries occur as stock and dikes through the Mesozoic sedimentary marine sequence and diatreme breccia system, suggesting ones of the last magmatic pulsations pulses during the Late Eocene and Early Oligocene (Fig. 3.3D, E). The dikes exhibit disseminated polymetallic mineralization, hydrothermal alteration, light-gray

and grayish-green in color, porphyritic texture, aphanitic groundmass, and phenocrysts

(up to 3 cm).
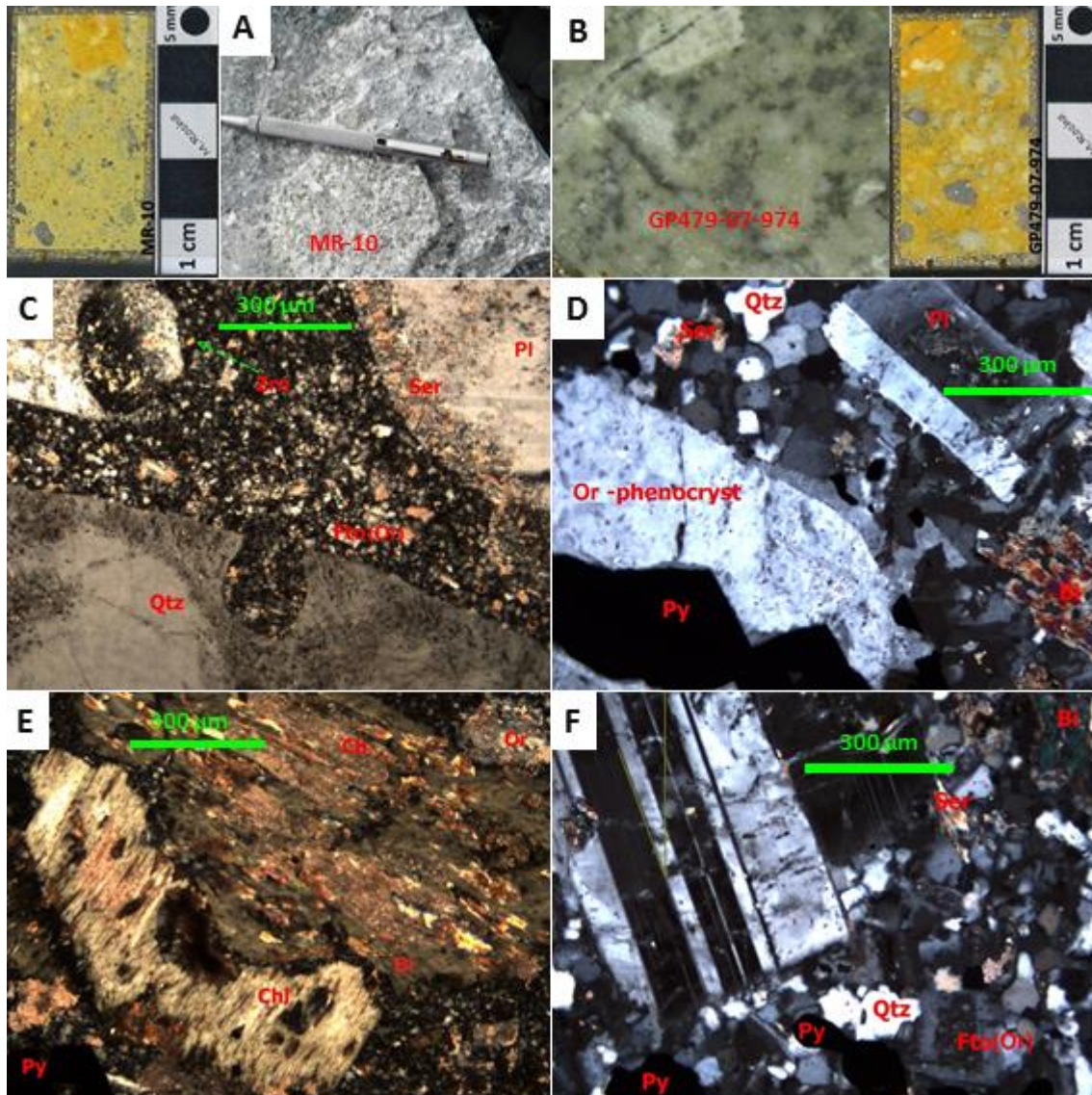
Fig. 3.11. Hand samples and photomicrographs (plane-polarized light) displaying specimens of altered quartz-monzonite porphyry (QMP) from the diatreme breccia system. A., B. Hand samples and billets is showing staining of K-feldspar with sodium cobaltinitrite in yellow color. C. Quartz eye and plagioclase (Pl) replaced by sericite and overprinted by carbonate and floating in microcrystalline groundmass. D) Phenocrysts of orthoclase (Or), and plagioclase floating in the groundmass that is partially replaced by sericite and biotite (Bi). E. Biotite phenocryst replaced by sericite and carbonate that is floating in a microcrystalline groundmass. F. Plagioclase phenocryst (Fto) floating in the groundmass of quartz, aphanitic orthoclase and local plagioclase, which is replaced by sericite, biotite, and carbonate.

These intrusive rocks consist of phenocrysts of orthoclase and plagioclase (Ab_{60} - An_{40}), quartz eyes, biotite, as well as opaque minerals as pyrite (up to 7%), sphalerite, sulfosalts, hematite, magnetite, and chalcopyrite, which are floating in aphanitic groundmass that includes aphanitic hydrothermal orthoclase (>15 %), aphanitic quartz (up to 30%), carbonate, sericite, local zircon and sphene; as well as local epidote, chlorite, and wollastonite are locally present due to spatial relationship with the skarn system and/or limestone. The quartz eyes exhibit noticeable resorption, and phenocrysts of plagioclase and orthoclase are partially replaced by quartz-sericite-pyrite, local chlorite, and carbonates (i.e. aphanitic calcite) (Fig. 3.11).

These plutonic rocks exhibit pervasive to moderate potassic alteration (orthoclase>biotite>magnetite>>apatite), moderate phyllic alteration (i.e. disseminations and D veinlets filled by quartz>pyrite>sericite), and silicification, as well as chlorite, epidote and amphibole in the groundmass, and all of which are locally overprinted by chlorite and aphanitic carbonate (Fig. 3.12).

The best examples of silicified and mineralized intrusive porphyries have been discontinuously intercepted between 247 and 1,017 m at depth (from ~1,723 to 953 m.a.s.l., respectively) (e.g. Fig. 3.M-N). These are cutting through the Mesozoic sedimentary marine sequence and the breccia diatreme system. These plutonic rocks exhibit porphyritic texture (coarse-grained 3 cm in length), aphanitic groundmass, light-gray and greenish colors, , and local disseminated sulfides (Fig. 3.3D, E, M,N).
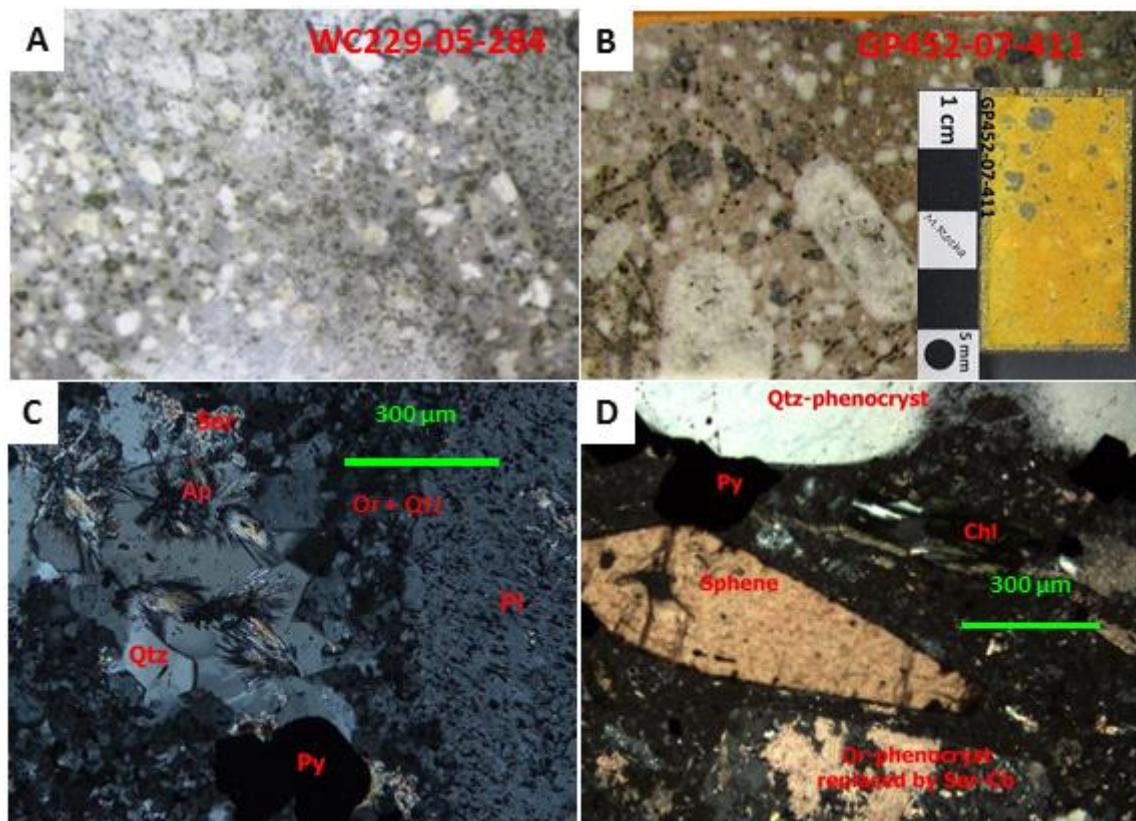
Fig. 3.12. Hand samples and photomicrographs (plane-polarized light) displaying specimens of quartz-feldspar porphyries. A., B. Hand samples and billet show staining of K-feldspar with sodium cobaltinitrite in yellow color. C. Plagioclase phenocryst (Pl) (replaced by sericite) floating in the groundmass that includes quartz, pyrite, sericite, and apatite. D. Quartz eye with resorption texture that is floating in a fine groundmass replaced by quartz, pyrite, and carbonate. E. Plagioclase phenocryst replaced by carbonate that is floating in fine groundmass of orthoclase (K-fto), quartz, and carbonate. F. Quartz eye, sphene and orthoclase (replaced by sericite and carbonate) floating in a fine groundmass altered by sericite, chlorite and carbonate

The content of plagioclase and quartz, suggests quartz monzonite and textural transition regarding to the field of quartz monzodiorite, while chemical results of trace elements suggest a signature to field between monzonite and diorite.

Petrological Features and Internal structure of the Diatreme Breccia System

The diatreme breccia system was emplaced through the Mesozoic sedimentary marine sequence, and different types of breccias form the internal structure, which are cut by dikes of quartz-feldspar porphyry (Fig. 3.13). The breccias usually consist of heterolithic fragments and broken minerals, which are poorly sorted, exhibit irregular shape, and are supported by rock flour. The diatreme pipes consist of heterolithic mixed breccia (Bxm), heterolithic breccia (Bxi) supported by a milled igneous matrix, monolithic breccia (IBx) supported by milled igneous matrix, heterolithic breccia (Bxs) mostly composed of sedimentary fragments and matrix, tuffisite dikes (i.e. fine breccia), and local crackle breccia.
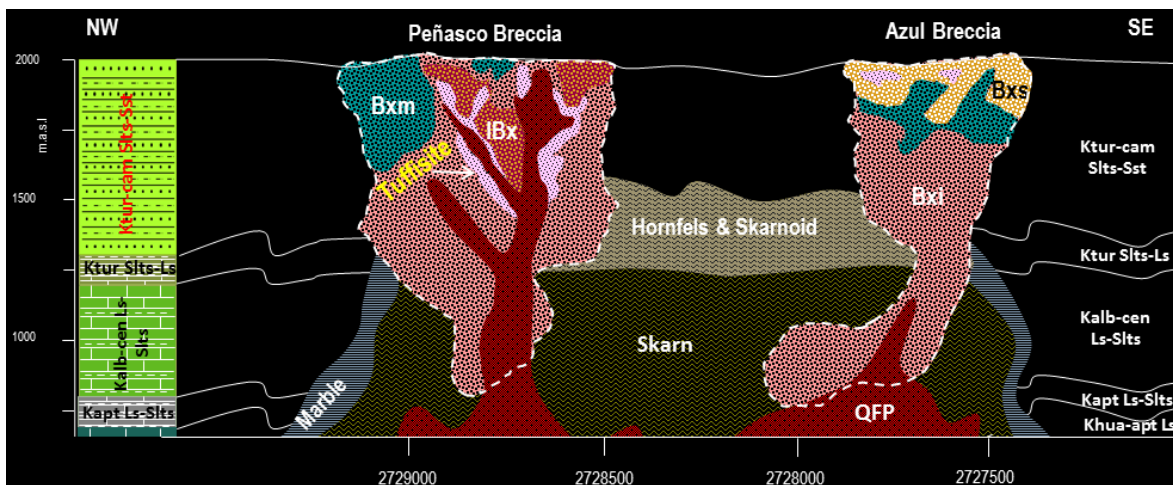
Fig. 3.13. Schematic cross section showing mineralized bodies at the Peñasquito polymetallic ore deposit. The cross section is oriented 340° with view to the northeast. The lithology column is displayed on left side. The Chile Colorado stockwork is displayed on the right side and adjacent to the Azul Breccia. Note: Quartz-feldspar porphyry (QFP), intrusive breccia (IBx), heterolithic breccia with intrusive matrix (Bxi), heterolithic breccia with mixed matrix (Bxm), Sedimentary breccia (BxS), Cupido Formation (Khua-apt-Ls) La Peña Formation (Kapt Ls-Slts), Cuesta del Cura Formation (Kalb-cen Ls-Slts), Indidura Formation (Ktur Slts-Ls), Caracol Formation (Ktur-cam Slts-Sst).

Tuffisite Breccia

In the Peñasco open pit, tuffisite occurs as irregular dikes cutting the heterolithic breccias and is cut by quartz-monzonite dikes. The tuffisite is a heterolithic breccia of fine-grained and locally microcrystalline minerals, which include broken crystals of orthoclase (up to 15%), quartz (7%), and local zircon and plagioclase, as well as sericite (up to 7%), opaque minerals (i.e. pyrite, sphalerite, galena, and chalcopyrite), sulfosalts, and carbonate (up to 15%), and other igneous fragments.
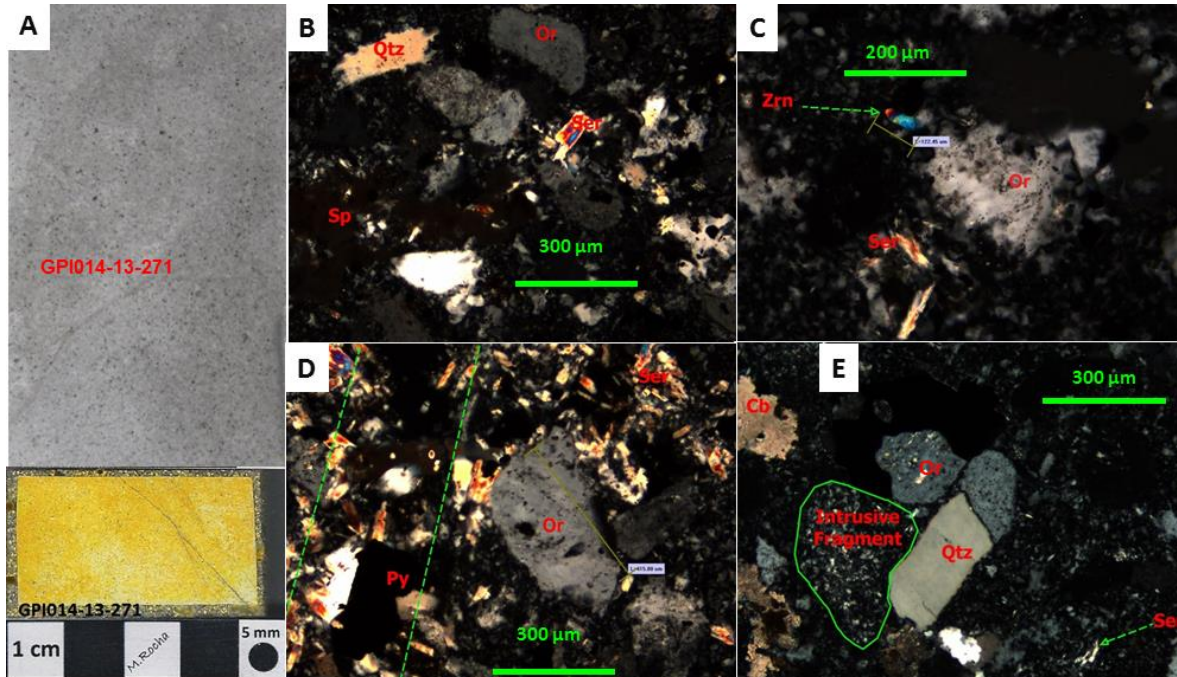
Fig. 3.14. Hand sample and photomicrographs (plane-polarized light) displaying tuffisite. A. Hand samples and billet showing staining of K-feldspar with sodium cobaltinitrite in yellow color. B. Milled quartz (qtz), feldspar and sphalerite (Sp) are hosted in a fine matrix. C. Zircon (Zrn) and hydrothermal orthoclase in fine matrix. D. Veinlet of quartz-sericite cutting the matrix, as well as broken feldspar hosted in the matrix. E. Milled feldspar and quartz, and intrusive fragments cemented by fine matrix.

The broken phenocrysts (plagioclase, orthoclase, and quartz) exhibit a sub-rounded shape and are floating in the fine and brecciated matrix that consists of fine hydrothermal

orthoclase and minor quartz. The microcrystalline orthoclase is part of the fine breccia matrix (as cement) and is locally overprinted by sericite-pyrite. The sericite is microcrystalline, anhedral in shape, spread in the breccia matrix and local in broken feldspar phenocrysts. The pyrite exhibits an anhedral shape, is fine-grained, and disseminated in the breccia matrix. The sphalerite, galena, chalcopyrite and sulfosalts are disseminated throughout the tuffisitic matrix. In addition, the tuffisite exhibits veinlets filled by quartz-sericite-pyrite that cut through the matrix, suggesting the tuffisitic dikes are the plumbing source of the phyllic alteration.

The tuffisite dikes exhibit pervasive to moderate potassic alteration (K-feldspar) and a weak phyllic alteration (Ser >Py >>Qtz), and both alterations are locally overprinted by carbonates (Fig. 3.14).

Intrusive Monolithic breccia (IBx)

The monolithic breccia (IBx) is composed of intrusive fragments encased in a milled matrix with hydrothermal alteration and disseminated mineralization. This type of breccia includes quartz (35%), orthoclase (25%), sericite (up to 10%), pyrite (up to 10%), carbonate (7%), and local montmorillonite.

The monolithic breccia exhibits broken phenocrysts of feldspar and quartz. The feldspar fragments exhibit a sub-rounded shape, are coarse-grained, hosted in the breccia matrix, and locally altered by sericite and local carbonate. Some of the quartz eyes are anhedral and sub-rounded in shape and hosted in the milled matrix, while others are fine-grained and present in the breccia matrix. The breccia matrix consists of fine-grained

hydrothermal orthoclase with lesser amounts of quartz. Sphalerite (up to 3%) is associated with sulfosalts (up to 2%) that are disseminated throughout the breccia matrix. This breccia includes local parallel veinlets of quartz and sericite (Fig. 3.15.A).
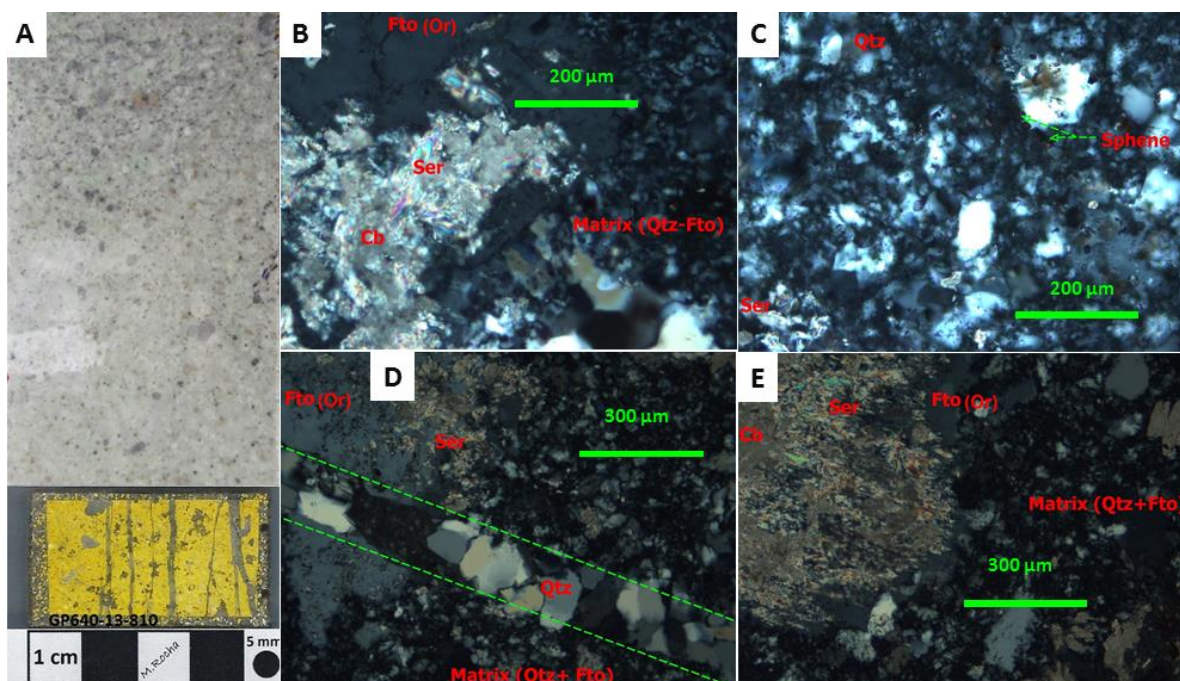
Fig. 3.15. Hand sample and photomicrographs (plane-polarized light) displaying monolithic breccia (IBx). A. Hand samples and billet showing staining of K-feldspar with sodium cobaltinitrite in yellow color. B. Broken orthoclase (Or) is hosted in a fine ingenuous matrix and altered by sericite and carbonate. C. Fine matrix and disseminated sphalerite. D. veinlet of quartz is cutting sericitized feldspar phenocryst and the fine igneous matrix. E. Feldspar phenocryst altered by sericite and carbonate is hosted in quartz-feldspar matrix.

This type of breccia exhibits pervasive to moderate potassic alteration (orthoclase), moderate phyllic alteration (sericite>pyrite>>quartz), and both alterations are locally overprinted by carbonate and montmorillonite. The sericite is microcrystalline, anhedral, present in the breccia matrix, and is locally overprinted by carbonate and montmorillonite (up to 3%). Euhedral pyrite is disseminated through the breccia matrix (Fig. 3.15).

Heterolithic Breccia (BxI)

The heterolithic breccia (BxI) is composed of angular and sub-rounded fragments (i.e. intrusive>sedimentary rocks), broken phenocrysts, and disseminated sulfides (7%), that are hosted in an igneous matrix of rock flour. The breccia includes broken phenocrysts (i.e. 10% feldspar, 7% quartz, and up to 5% biotite) and intrusive and sedimentary fragments (10 %) that are cemented by a fine intrusive breccia matrix and locally altered by orthoclase (10%), sericite (7%), pyrite (5%), and carbonate (5%). The breccia matrix is fine-grained and composed of quartz, hydrothermal orthoclase, and opaque minerals. The quartz fragments locally exhibit resorption texture and the feldspar fragments are locally altered to sericite and carbonates.

The heterolithic breccia exhibits pervasive to moderate potassic alteration (orthoclase), and moderate to weak phyllic alteration (quartz >sericite> pyrite), which are locally overprinted by carbonate. Aphanitic orthoclase floods the breccia matrix and is overprinted locally by sericite-pyrite. The sericite is fine grained, anhedral and is disseminated in the matrix and locally in feldspar fragments. The secondary pyrite is disseminated in the matrix, exhibits anhedral shapes and is fine-grained. The potassic and phyllic alterations are locally overprinted by carbonate (Fig. 3.16).

Heterolithic Breccia (BxM)

The heterolithic breccia (BxM) is composed of angular and sub-rounded fragments (i.e. sedimentary>intrusive rocks>>skarn), local broken phenocrysts, and disseminated sulfides (7%) that are contained in a mixed matrix of the rock flour (i.e. igneous and sedi-

mentary products). This breccia includes broken phenocrysts of feldspar (up to 5%), quartz eyes (up to 10%), intrusive and sedimentary fragments, and local skarn fragments that are cemented by a mixed breccia matrix and locally altered by orthoclase (up to 10%), sericite (up to 15%), pyrite (up to 7%), and carbonate (up to 10%). The fragments and broken crystals exhibit sub-rounded and sub-euhedral shapes, are coarse-grained and hosted in a fine and mixed breccia matrix. The lithic fragments are mainly sandstone, siltstone, intrusive porphyry, and local limestone and skarn. The breccia matrix is fine-grained and composed of milled sediments, quartz, local orthoclase, and opaque minerals including pyrite and sphalerite (up to 3%), and local marcasite, chalcopyrite, and hematite.
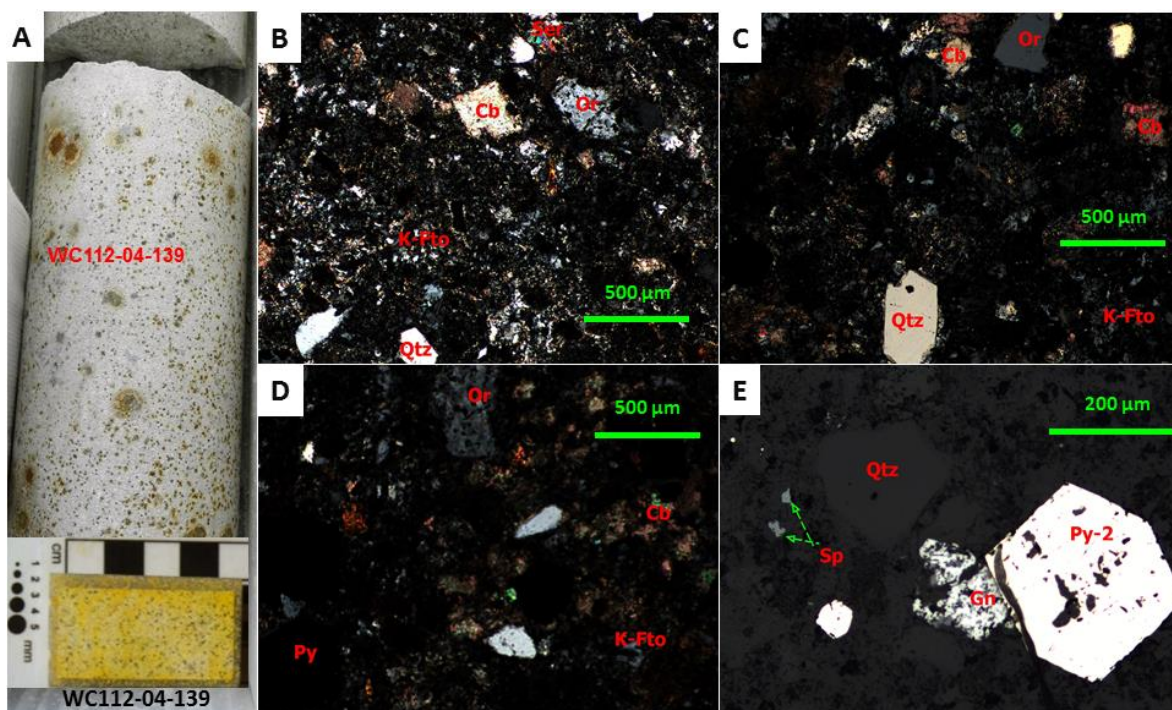
Fig. 3.16. Hand sample and photomicrographs (plane-polarized light) displaying heterolithic breccia (Bxl). A. Hand samples and billet showing staining of K-feldspar with sodium cobaltinitrite in yellow color. B. Broken quartz (Qtz) and feldspar (Or) are hosted in a fine matrix. C. D. quartz and broken feldspar in fine matrix altered by sericite and carbonate. E. Primary sulfides (pyrite, sphalerite and galena are hosted in the fine matrix).

This heterolithic breccia (BxM) exhibits a weak to moderate potassic alteration (fine orthoclase), and moderate phyllic alteration (quartz>sericite>pyrite), which are over-printed by carbonate. The fine orthoclase floods the mixed breccia matrix and is over-printed locally by sericite-pyrite-quartz and carbonate. The sericite is fine grained, anhe-dral and is disseminated in the matrix and locally in feldspar fragments. The pyrite is dis-seminated in the matrix, exhibited anhedral shapes and related to marcasite. The potassic and phyllic alterations are overprinted by carbonate (Fig. 3.17).
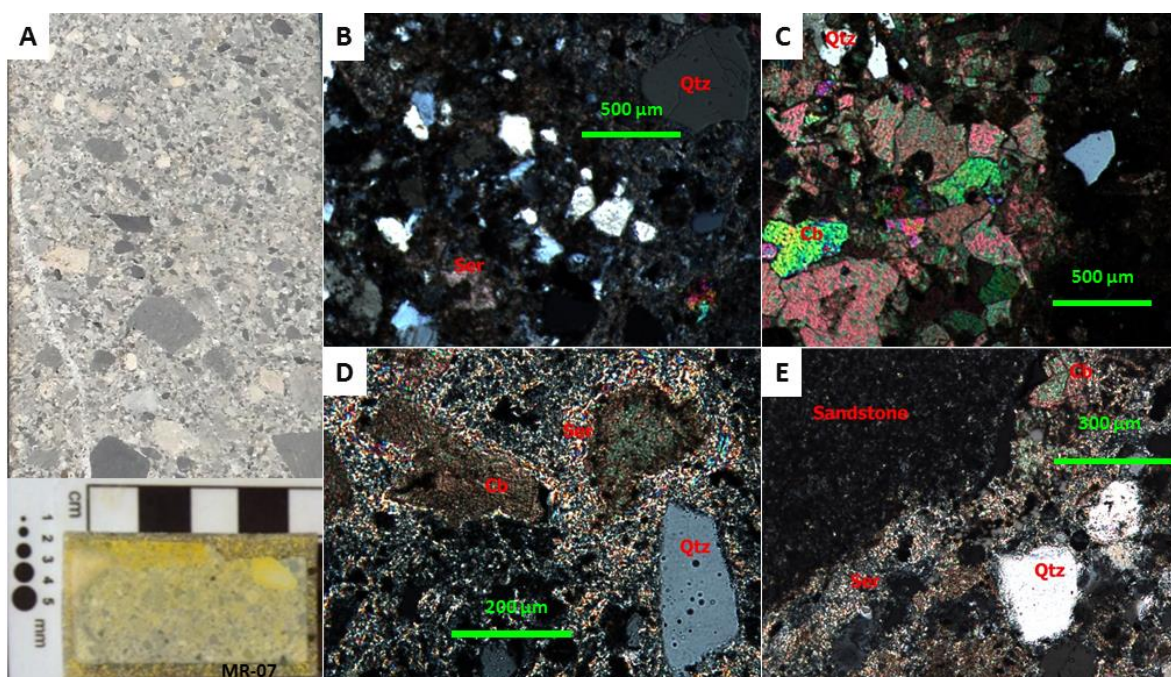
Fig. 3.17. Hand sample and photomicrographs (plane-polarized light) displaying poorly sorted heterolithic breccia (BxM). A. Hand sample and billet showing staining of K-feldspar with sodium cobaltinitrite in yellow color. B. Broken quartz (Qtz) is hosted in a fine-mixed matrix. C. Carbonate veinlet. D. Broken quartz is hosted in a fine-mixed matrix that is altered by sericite and carbonate. E. Sandstone and quartz fragments are hosted in the fine-mixed matrix that is altered by sericite and carbonate.

Sedimentary Breccia (BxS)

The sedimentary breccia (BxS) is composed of angular and sub-rounded fragments (i.e. sedimentary rocks), local disseminated sulfides that are hosted in a matrix of the rock flour (i.e. mainly sedimentary products). The lithic fragments are mainly sandstone, silt-stone, and local limestone that are poorly-sorted. The breccia matrix is fine-grained and composed of milled sediments, pyrite, and hematite. The heterolithic fragments exhibit a moderate phyllic alteration (sericite> pyrite >>quartz), which is overprinted by carbonate (Fig. 3.18).

Fig. 3.18. Hand sample displaying a poorly sorted sedimentary heterolithic breccia (BxS).

Internal Structure of the Peñasco Breccia

The Peñasco Breccia was emplaced through the Cuesta del Cura, Indidura, and Cara-col formations (Fig. 3.13). Different types of breccias form the internal structure, which are cut by tuffisitic dikes (i.e. fine and well sorted breccia) and dikes of quartz-feldspar porphyry. The northern portion of the Peñasco Breccia is composed of a mixed breccia (Bxm) that extends down to 1,600 m.a.s.l. In the open pit this mixed breccia occupies 31% of the Peñasco Breccia and appears in other sections in lesser amounts (Fig. 3.19). The southern and western portions of the Peñasco Breccia are mostly occupied by a breccia (Bxi) composed of heterolithic fragments, including clasts of igneous and sedimentary rocks that are supported by a milled igneous matrix. This breccia extends to the base of the diatreme, and in the Peñasco open pit, occupies 36% of the area of the diatreme brec-cia. A monolithic breccia (IBx) composed of igneous rock fragments and supported by a matrix composed of milled igneous breccia is present. This breccia occupies a longitudinal outcrop (NW-SE) in the center of the Peñasco Breccia and cuts across the heterolithic breccia (Bxm). In the Peñasco open pit, this breccia is cut by tuffisitic and quartz-feldspar dikes. The BxI occupies 22% of the area in the Peñasco Breccia and ranges from 1,870 (m.a.s.l) to 1,400 (m.a.s.l) at depth. Tuffisite composed of fine fragments, broken pheno-crysts and igneous rock flour is also present in the Peñasco Breccia. At the center of the Peñasco Breccia, the tuffisite occurs in dikes that cut through the BxI and Ibx breccias and, in the Peñasco open pit, this breccia occupies 4% of the Peñasco Breccia. Furthermore, dikes of quartz-feldspar porphyry are cutting through all of the above-described breccias,

and in the Peñasco open pit, these dikes occupy an area of up to 6% of the diatreme brec-

cia, and apparently are associated with normal faults.
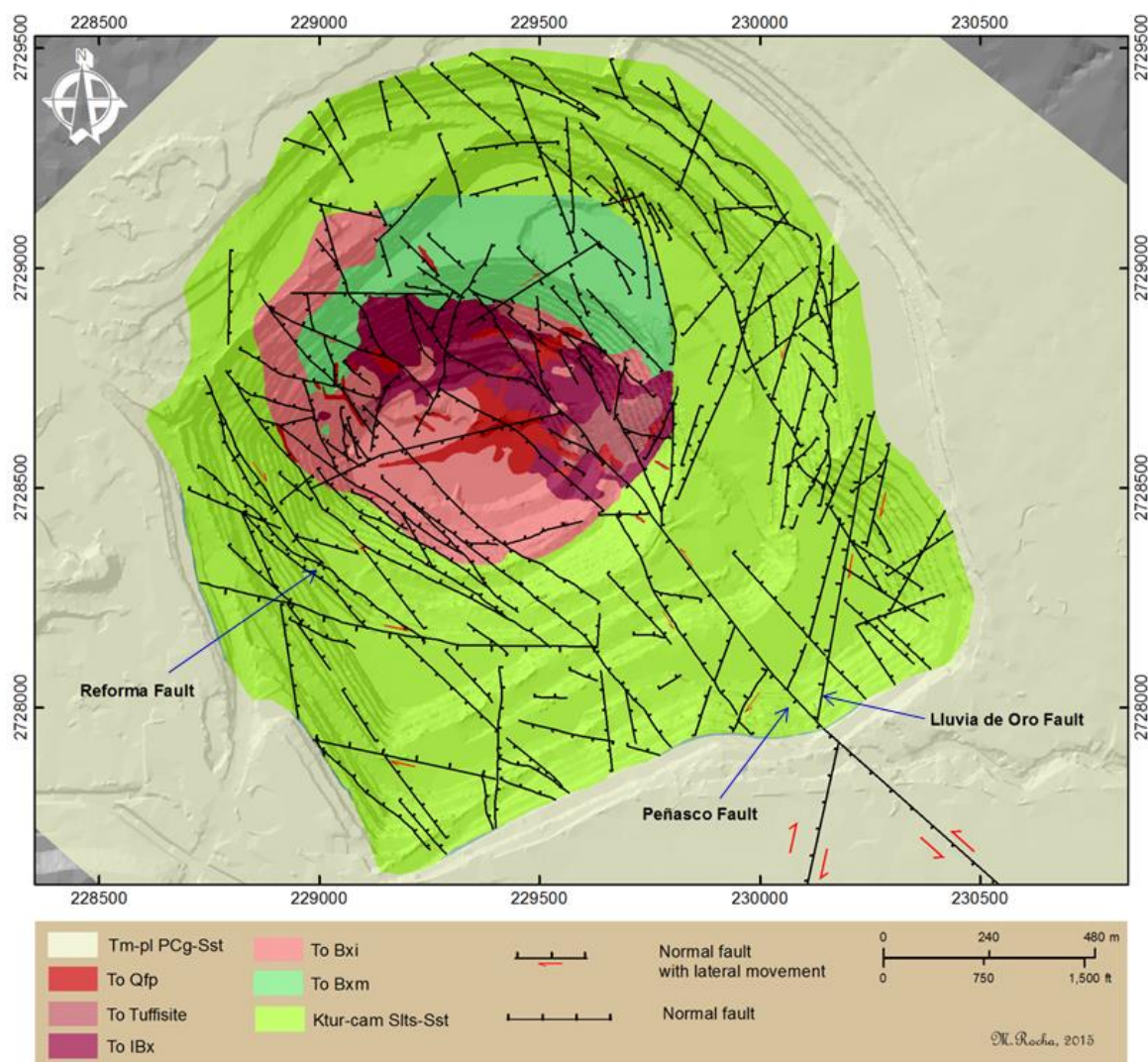
Fig. 3.19. Map showing local lithology and structural fabric in the Peñasco open pit. (Map by Author and Exploration staff of Goldcorp Peñasquito, 2014). Also shown is the offset of Lluvia de Oro fault by Peñasco fault. Note: polymictic conglomerate and sandstone (PCg-Sst), Quartz-feldspar porphyry (Qfp), tuffisite (Fel), intrusive breccia (IBx), heterolithic breccia with intrusive matrix (Bxi), heterolithic breccia with mixed matrix (Bxm), Caracol Formation intercalation of layers of siltstone and sandstone (Slts-Sst), Tertiary (T), Miocene (m), Pleistocene (p), K (Cretaceous), Turonian (tur), and Campanian (cam).
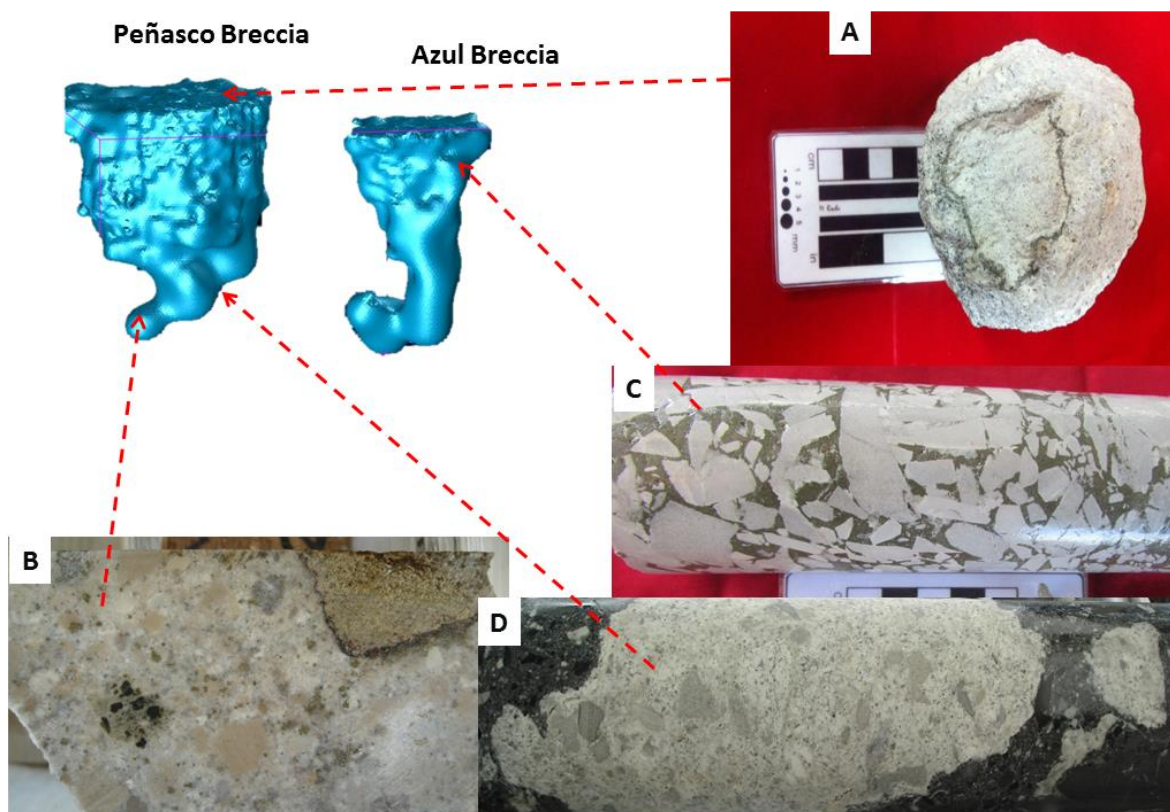
Fig. 3.20. Photographs of representative samples recovered from the diatreme breccias system with singular composition. A. Accretionary lapilli. B. Heterolithic breccia showing skarn and sedimentary fragments hosted in mixed matrix breccia. C. Monolithic breccia cemented by sulfides. D. Heterolithic breccia showing sedimentary fragments and juvenile igneous fragments with wispy texture.

Crackle breccia has been intercepted by drilling and is located on the borders of the diatreme breccia. In addition, a monolithic breccia composed of rotated sedimentary fragments and cemented by sulfides is locally present between the Peñasco Breccia and the host rock (Caracol Formation) (Fig. 3.20 C). At the base of the Peñasco Breccia, core drilling has locally intersected heterolithic breccia composed of skarn and intrusive clasts supported by a breccia matrix composed of milled rock that exhibits a gray color (Fig. 3.20B). In addition, juvenile porphyry clasts, with a wispy texture, have been intercepted at depth in the heterolithic breccia (Bxm), suggesting they formed at the root of the Peñasco diatreme (Fig. 3.20D). In the Peñasco open pit (i.e. the 1,760 bank) accretionary

lapilli have been found (Fig. 3.20A), composed of a core of rock flour enveloped by a thin concentric layer of fine sulfides and milled matrix breccia, which is similar to the mono-lithic breccia (Ibx) Their presence suggests fluidization processes were active along various pathways in the breccia leading to suspended fragments with electrochemical formation of the lapilli.

Internal Structure of the Azul Breccia

The Azul Breccia was emplaced through Cuesta del Cura, Indidura, and Caracol for-mation (Fig. 3.13). Different types of breccias formed the internal structure, which are cut by tuffisite and dikes of quartz-feldspar porphyry. At the top, this diatreme breccia in-cludes tuffisite dikes and a heterolithic breccia (Bxs) composed of sedimentary rock clasts that are supported by milled sedimentary material, extending down to ~1,750 m.a.s.l. In the upper level, the Azul Breccia includes a mixed breccia (Bxm) composed of clasts of sedimentary and intrusive rocks that are supported by milled sedimentary and igneous material, extending down to 1,600 m.a.s.l.

At the central and bottom parts of the Azul Breccia, the breccia is mostly composed of heterolithic fragments, including clasts of intrusive and sedimentary rocks that are sup-ported by a milled igneous matrix material (Bxi). The breccia ranges from 1,750 (m.a.s.l.) to 750 (m.a.s.l.) at depth (Fig. 3.13). According to Goldcorp logging database, a crackle breccia has been locally intercepted by drilling and is located on the borders of the di-atreme breccia.

Sampling and methodology of Geochemistry and Petrogenesis

This section presents a petrochemical interpretation and petrogenetic classification of magmatic products from Peñasquito. Chemical results of twenty-six samples from the plutonic complex as well as ten samples from intrusive products that generated the diatreme breccias were selected, analyzed, and plotted on petrogenetic classification diagrams. The objective is to characterize, classify, and define the petrogenesis of the plutonic system and intrusive products that have been found in Peñasquito. The results include major oxides, trace elements, and REE.

The database includes 36 samples; however, samples WC218-385, WC218-404, WC296-322, WC296-343, and WC36-661 were from data reported by Valencia (2010) and were used to support the petrogenesis of the plutonic complex found in the Mazapil syncline.

During the selection for geochemistry analysis, samples were selected to minimize, where possible, alteration effects. Since the plutons are adjacent to, and commonly weakly mineralized or related to strongly mineralized areas, some samples have hydrothermal alteration. Therefore, the samples were cut with a water-base slab saw to recover unaltered samples; however, some specimens exhibit noticeable potassic alteration that can affect chemical results.

The chemical analyses were performed at ALS Chemex (USA) by combining a number of methods: (1) a whole rock analytical package (ME-ICP06), plus a carbon and sulfur combustion furnace (ME-IR08 analytical package) in order to quantify the major

elements; (2) trace and REE elements reported from three digestions with either an ICP-AES or ICP-MS finish; 3) a lithium borate fusion for the resistive elements (ME-MS81 analytical package); 4) a four acid digestion for the base metals (ME-4ACD81 analytical package); and 5) an aqua regia digestion for the volatile gold-related trace elements (i.e. As, Bi, Sb, Hg, Se,Te) (ME-MS42 analytical package)(http://www.alsglobal.com, 2014).

The results are divided in to seven groups of samples (Table 3.1) with similar petro-logical features and differentiated by symbols (i.e. diamonds and triangle) with a singular color and shape. Group 1 includes four samples of quartz monzodiorite porphyry, two samples of biotitized quartz monzonite porphyry, two samples of quartz monzodiorite porphyry, and one samples of silicified quartz monzonite porphyry. The Group 2 consists of six samples of quartz monzonite porphyry with molybdenite. The Group 3 is formed by two samples classified as quartz-monzodiorite (GPI14-13-102 and GP609-11-999), two samples of intrusive breccia (GP622-12-1067, and GP554-08-1140) found in adjacent zones to the bottom of diatreme breccia system and related to the quartz monzodiorite contact zone. The Group 4 includes five samples classified as mineralized quartz-monzonite and mineralized quartz-monzodiorite. The Group 5 includes one sample classified as chloritized quartz monzodiorite porphyry. The Group 6 includes one sample classified as quartz microdiorite. The Group 7 consists of eight heterolithic breccias and two tuffisite, which were selected from the Peñasco open pit and some core drill between 170 and 970 m at depth (~1,800 to ~1,000 m.a.s.l., respectively); these form the bulk compositions of the diatreme pipes (Peñasco and Azul Breccias) but with included magmatic products.

The chemical results were normalized to an anhydrous base and total iron (Fe_2O_3) in order to plot samples on different diagrams. Specifically, rock-types were plotted on a diagram of total alkali versus silica (Le Bas et al., 1986; Le Bas, 1989, 2000), and CIPW norms were calculated on an anhydrous 100% adjusted basis and use a Fe_2O_3/FeO ratio as suggested by Middlemost (1989). The results were obtained using the SINCLAS computer program (Verma et al., 2002) and these diagrams were constructed using the MINPET 2.02 computer program.

Diagrams, both binary and ternary (i.e. the petrochemical discriminations), were used for scientific support and provided a reliable result for the petrogenesis of igneous rocks; furthermore, the spider diagrams were used in order to interpreted the magma source. Explicitly, Harker (1909) used binary diagrams where any major oxide may be plotted against silica (SiO_2). These diagrams reveal the evolution of magmas and the classification of rocks. The chemical classification of igneous rocks at Peñasquito is based on binary TAS diagrams where the total alkali content ($Na_2O + K_2O$) is plotted against silica (SiO_2) and the limits used were suggested by Le Maitre et al. (1989); Irvine and Baragar (1971) proposed a limit for alkaline and sub-alkaline rocks. In addition, several variation and/or discrimination diagrams were plotted using results of trace elements and major oxides (Table 3.1). The chemical analysis of trace elements is used to infer the possible tectonomagmatic origin and petrogenetic evolution of the rocks. The trace elements are not part of the stoichiometry of mineral phases present within the system and do not significantly affect the chemical and physical properties of a system; thus, trace elements have singular chemical properties and may record geological processes.

Table 3.1 Representative Major Oxides for rocks of the Peñasquito magmatic complex.

Sample	Group	SiO$_2$	TiO$_2$	Al$_2$O$_3$	Fe$_2$O$_3$	FeO	MnO	MgO	CaO	Na$_2$O	K$_2$O	P$_2$O$_5$	Total
WC300-05-511	1	65.97	0.62	14.78	1.37	2.73	0.10	1.64	3.57	2.56	6.43	0.25	98
MR-12	1	66.18	0.65	15.48	1.13	2.26	0.09	1.40	4.88	3.08	4.63	0.22	100
WC218-385	1	66.21	0.63	15.87	1.10	2.75	0.06	1.76	3.81	3.46	4.06	0.29	99
GP640-13-1334	1	67.06	0.62	14.77	0.92	1.85	0.02	1.35	5.16	3.25	4.74	0.27	97
GP640-13-1410	1	67.25	0.56	14.62	1.25	3.13	0.02	1.44	4.19	3.53	3.78	0.23	98
GP615-12-1172	1	69.71	0.54	14.14	1.16	2.91	0.04	1.38	3.13	3.39	3.39	0.21	100
WC360-06-526	1	67.13	0.62	15.39	0.74	1.85	0.05	1.83	4.89	3.43	3.82	0.25	100
WC224-05-730	1	68.23	0.49	14.89	0.96	1.93	0.08	1.44	2.96	2.11	6.73	0.19	99
GP622-12-1059	1	68.62	0.65	15.75	0.64	1.61	0.11	1.11	6.74	0.28	4.24	0.25	100
GP621R-1792-5	2	76.71	0.63	12.39	1.12	2.23	0.01	0.81	0.64	0.24	5.04	0.19	101
GP621R-1794-2	2	71.35	0.63	14.24	0.41	0.82	0.08	1.13	1.77	0.42	8.94	0.21	100
GP621R-1794-8	2	80.28	0.53	10.55	0.99	1.97	0.02	0.54	0.93	0.18	3.83	0.21	101
GP621R-1798-4	2	77.88	0.48	10.80	0.48	0.96	0.03	1.34	1.26	0.28	6.34	0.15	100
GP621R-1786-7	2	54.10	0.64	14.39	0.99	3.30	0.17	1.52	22.30	0.14	2.19	0.27	94
GP621R-1800-3	2	75.53	0.47	11.93	0.29	0.57	0.05	0.84	2.57	0.36	7.23	0.18	101
GP622-12-1067	3	70.39	0.44	14.83	0.76	1.89	0.21	1.01	4.47	0.19	5.66	0.16	100
GP557-08-1140	3	70.52	0.47	14.65	0.30	0.75	0.03	0.90	6.67	3.83	1.70	0.18	96
GPI14-13-102	3	61.45	0.95	16.08	1.19	2.38	0.10	2.58	6.13	4.57	4.23	0.34	101
GP609-11-999	3	70.94	0.43	14.46	0.95	1.90	0.14	1.07	3.59	1.40	4.94	0.18	101
WC334-05-571	4	66.01	0.68	15.55	1.00	2.01	0.05	1.44	3.82	3.53	5.67	0.24	98
WC296-05-356	4	62.40	0.97	16.48	1.38	2.77	0.06	2.51	3.91	3.81	5.37	0.34	100
WC296-343	4	67.20	0.65	16.37	0.60	1.19	0.11	0.93	3.16	2.41	7.08	0.32	100
WC218-404	4	66.64	0.77	17.60	0.52	1.30	0.12	0.40	6.42	0.18	5.69	0.36	98
WC296-322	4	64.82	0.72	16.66	1.39	3.46	0.15	0.81	5.67	0.15	5.82	0.36	99
GP452-07-381	5	59.53	1.15	15.27	1.73	3.45	0.23	2.19	4.84	0.21	10.82	0.60	94
GP640-13-1813	6	56.75	1.87	16.92	2.02	6.75	0.10	4.77	5.58	0.79	3.67	0.77	98
WC335-05-332	7	68.86	0.50	14.99	0.55	1.11	0.01	1.03	0.41	0.26	12.20	0.09	101
GP640-13-825	7	69.16	0.42	13.36	0.85	1.69	0.05	0.82	1.91	0.29	11.28	0.17	100
GP652-13-501	7	68.83	0.42	14.09	1.14	2.29	0.07	0.80	1.23	0.19	10.77	0.16	101
WC36-661	7	66.00	0.53	14.26	0.53	1.05	1.26	0.95	3.34	0.28	11.57	0.24	99
1-1865	7	68.95	0.44	14.58	0.98	2.44	0.31	1.23	6.08	0.28	4.54	0.16	99
2-1865	7	73.67	0.57	13.47	1.61	3.23	0.08	1.35	1.77	0.11	3.92	0.23	102
3-1865	7	67.43	0.52	15.22	0.98	2.44	0.13	1.33	5.57	0.81	5.40	0.18	99
3-1865A	7	64.97	0.63	14.76	1.28	3.21	0.30	1.14	8.59	0.12	4.85	0.15	98
6-1865	7	66.06	0.50	14.51	1.00	2.51	0.21	1.50	8.19	1.09	4.24	0.19	98
7-1865	7	66.83	0.53	15.04	0.82	2.04	0.26	0.88	7.41	0.14	5.87	0.19	100

▽ Group 1	◆ Group 2	◆ Group 3	◆ Group 4	◆ Group 5	◀ Group 6	▲ Group 7
QMP& QMDP	QMP (Molybdenite)	QMDP & Breccias	QMP&QMDP	QMDP (Chloritized)	QMcrD	Breccias

All data of trace elements are reported in Appendix B.

Harker Diagrams

In general, the samples range in the content of major elements. Some samples exhibit important variations of Al_2O, Na_2O, K_2O, CaO, TiO_2, and MgO (Fig. 3.21). Specifically, samples from Groups 1, 3, 4, 5, and 6 are characterized by intermediate to high Al_2O contents. Samples from Groups 1, 3, and 4 are characterized by intermediate to high Na_2O contents; however, Group 1 exhibited an ascendant linear trend (Na_2O and CaO, FeO) that may be interpreted as possible evolution in the magma source. Low Na_2O, CaO, and MnO contents characterized Group 2; however, this Group also had intermediate to high Si_2O contents.

Group 2 is characterized by the clustering of two populations around K_2O contents; for example, most samples from Group 2 are characterized by elevated K_2O contents these samples come from depth. Group 6 is characterized by high K_2O contents, but this sample exhibited an elevated amount of orthoclase phenocrysts and pervasive potassic alteration. Other samples were characterized by low CaO contents and intermediate to high Si_2O contents. Groups 1, 2, 3, 4, and 5, exhibit a gradual decrease in Al_2O with increasing Si_2O and contents ranged from 11 to 18 % and from 58 to 75 %, respectively. The sample of Group 6 is characterized by high TiO_2, FeO, and MgO contents, suggesting a possible association with a primitive mantle source. Groups 1, 3, and 4 exhibit an ascendant linear trend in Fe_2O_3 that may be interpreted as possible evolution in the magma source.
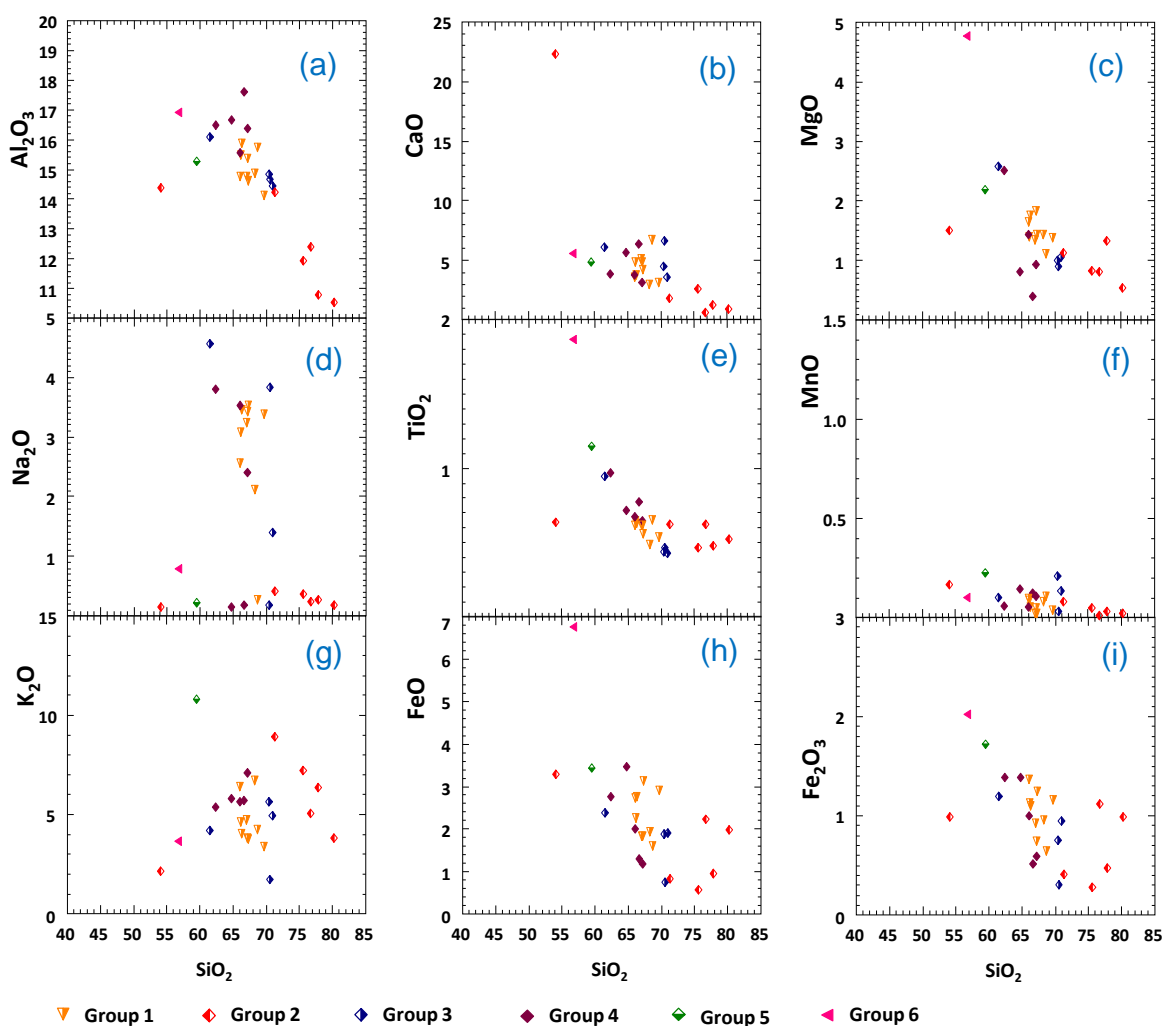
Fig. 3.21. Harker variation diagram exhibiting the major element compositions. Note: the different scale for the oxide elements.

Diagrams of Chemical Classification

Two types of diagrams were used to classify the rocks according to the chemical components of alkalis and silica. The samples exhibit variation in the alkalis (Na_2O+K_2O) weight percent and silica (SiO_2) weight percent contents (Fig. 3.22). The bulk of the specimens exhibit a felsic composition; however, five specimens exhibit an intermediate composition. The majority of the specimens exhibit a sub-alkaline influence, but eight

samples plot in the alkaline field. The chemical classification suggests that the bulk of the specimens are quartz-monzonite and granodiorite rocks.
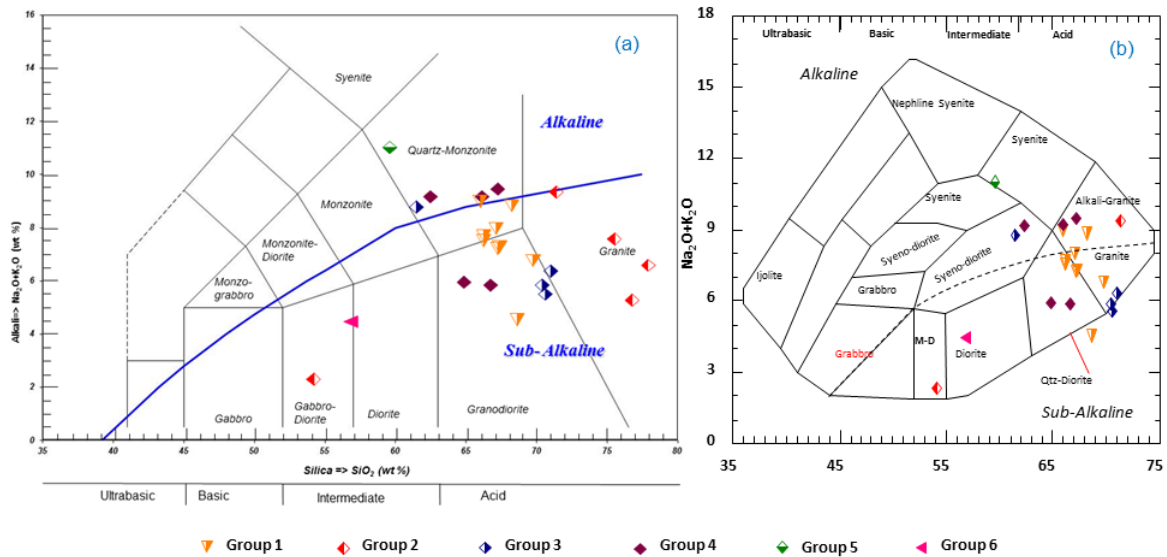
Fig. 3.22. TAS diagrams (a) limits suggested by Le Maitre et al. (1989) and limits of alkaline and sub-alkaline rocks suggested by Irvine and Baragar (1971), (b) limits suggested by Cox et al. (1979).

Group 1 is characterized by alkaline contents from 4.5 to 9.2. Group 2 is characterized by very wide alkaline contents from 2 to 9.6. Group 3 is also characterized by wide alkaline contents of 5.5 to 9. Group 4 is characterized by two compact groups with alkaline contents of ~6 and ~7. Group 5 is characterized by an alkaline content of ~11. Group 6 is characterized by a low alkaline content of ~4.5. Group 7 is characterized by two restricted groups with alkaline contents of 4 and 12.6. Groups 1 and 2 are classified as sub-alkaline rocks and characterized by a widely evolved magmatic trend (gabbro-diorite-granodiorite-granite); however, Group 1 exhibits a wide chemical dispersion that could be caused by the hydrothermal alteration overprints.

Group 3 is characterized by a wide chemical dispersion that included three speci-
mens in the sub-alkaline field and one in the alkaline field and characterized by a widely
evolved magmatic trend (i.e. quartz-monzonite, granodiorite, and granite), although the
dispersion is almost certainly caused by hydrothermal alteration overprints. Group 4 is
characterized by two compacted populations situated between alkaline and sub-alkaline
fields and may be classified as granodiorite to quartz-monzonite. The samples from Group
5 are characterized by an alkaline influence and situated in the quartz-monzonite field.
The sample from Group 6 is characterized as sub-alkaline and situated in the gabbro-dio-
rite field. Group 7 is characterized by two groups situated in the alkaline and sub-alkaline
fields (Fig. 3.22).

In addition, several trace diagrams were used in order to corroborate the classifica-
tion of rocks. The binary plot of Zr/TiO_2 vs. SiO_2 corroborated a widely evolved magmatic
trend of Groups 2, 4, and 7 (Fig. 3.23a), which were also exhibited on the TAS diagrams;
however, the SiO_2 may be increased by potassic alteration. The binary plot of TiO_2 vs. Zr
showed that the bulk of specimens had a similar composition; however, it also confirmed
a magmatic evolution for Groups 3 and 4. The samples from Groups 5 and 6 were less
differentiated compared to other groups and may be classified as andesite porphyry (Figs.
3.23a, 3.23b). The binary diagrams (Nb/Y vs. Zr/TiO_2) demonstrated that groups were
situated in three fields and corroborated the classification of the TAS diagrams (Fig. 3.23b,
3.23d). In general, plots of trace diagrams demonstrated that most samples were igneous
rock of intermediate composition, principally monzonite and granodiorite (Fig. 3.23).
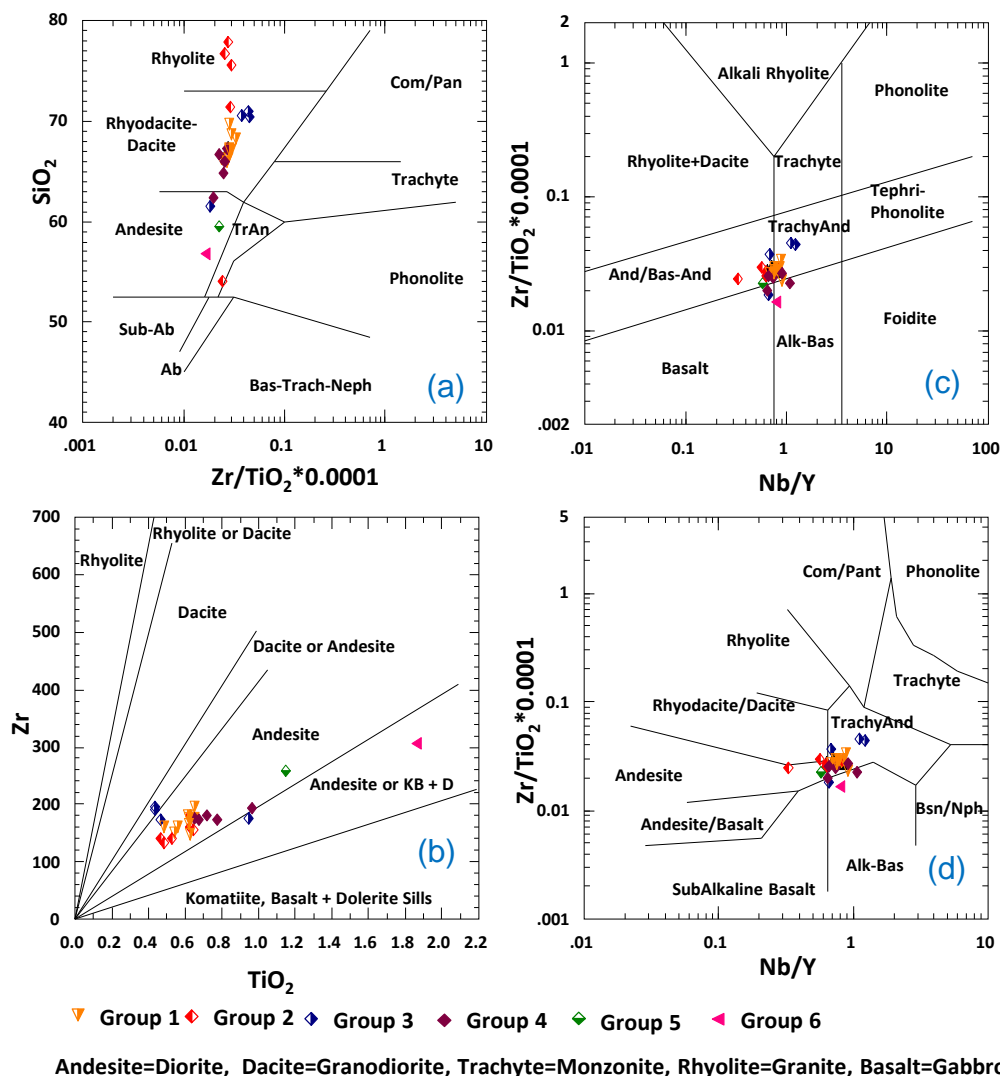
Fig. 3.23. Classification diagrams with silica, major elements, and trace elements. a) Zr/TiO$_2$*0.0001-SiO$_2$ (Winchester and Floyd 1979) (c) Zr/TiO$_2$ -NB/Y plot (Pearson, 1996), d) Zr/TiO$_2$ *0.0001-NB/Y plot (Winchester and Floyd 1979).

Discrimination Diagrams

Several discrimination diagrams were completed in order to interpret a possible tectonic setting of precursor magmas. These included major and trace elements, which are represented on ternary and binary diagrams. The ternary diagram of alkali (Na_2O+K_2O) vs. $MgO-FeO_t$ (Irvine and Baragar, 1971) displays that all specimens plot in the calc-alkaline field (Fig. 3.24a).
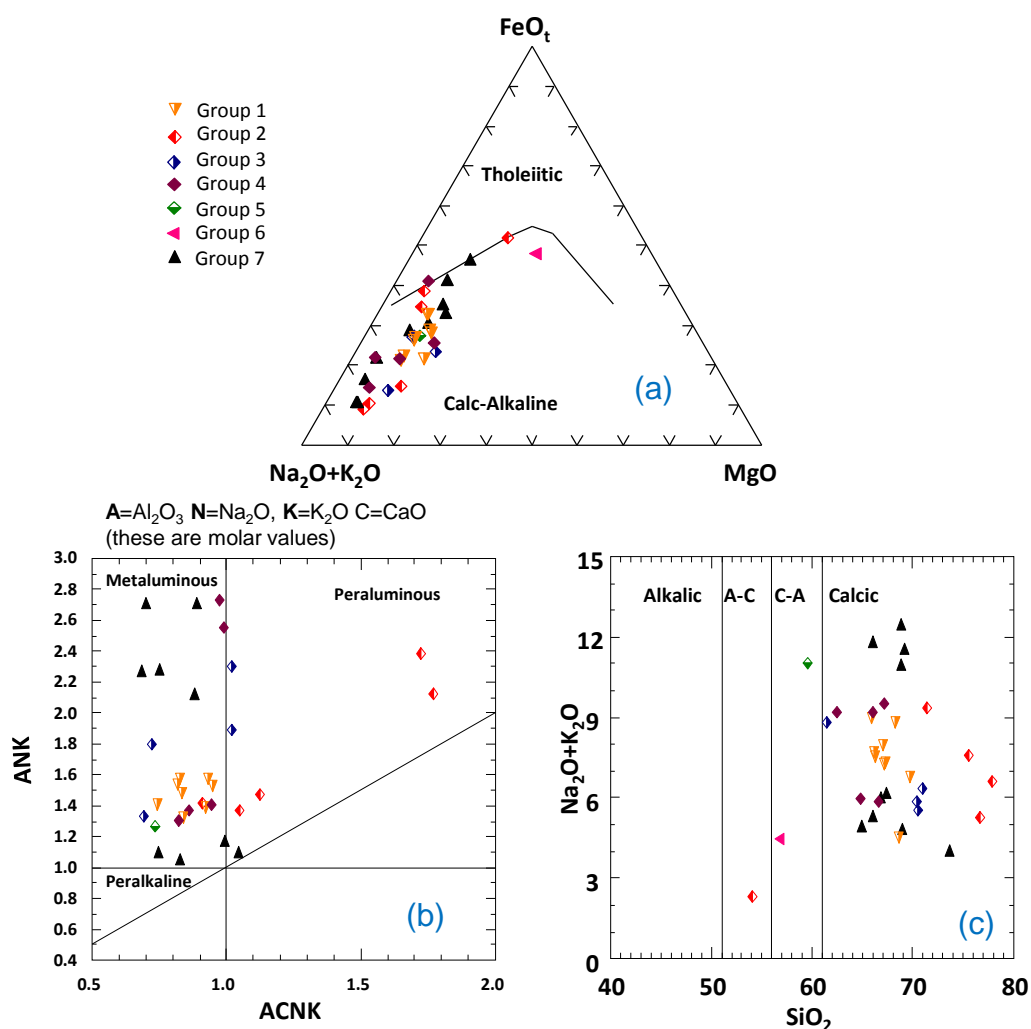
Fig. 3.24. Ternary and binary diagrams with combinations of major oxides (fields suggested by Irvine and Baragar, 1971; Maniar and Picolli, 1989; Peacock, 1931).

The calc-alkaline rocks are relatively rich in both calcium and alkali metals; therefore, it may suggest that these magmas were generated in the continental crust.

The binary plot of ANK vs. ACNK (Maniar and Picolli, 1989) shows three fields (metaluminous, peraluminous, and peralkaline). ANK and ACNK are molar values that correspond to A=Al_2O_3 C=CaO, N=Na_2O, K=K_2O.Group 1 plots in the metaluminous field as a compact group. The samples from Groups 2, 3 and 7 exhibit two populations and fall in the metaluminous and peraluminous fields (Fig. 3.24b). Group 4 exhibits two populations that are situated in the metaluminous field but the separation could be caused by the hydrothermal alteration overprints (Fig. 3.24b). Metaluminous rocks have lower aluminum oxide concentration; in contrast, peraluminous rocks have a molar proportion of aluminum oxide higher than the combination of sodium oxide, potassium oxide and calcium oxide. Therefore, some peraluminous samples from Groups 2 and 3 may include minerals, such as biotite, sericite, and garnet. In contrast, metaluminous minerals include pyroxene, hornblende, and biotite and may be generated by the partial melting of an igneous protolith. The alkali versus silica diagram (Fig. 3.24c) shows four fields (alkali, alkali-calcic, calcic-alkali, and calcic) (Peacock, 1931). This diagram demonstrated that the bulk of samples plot in the calcic field. The samples from Groups 5 and 6 are situated in the calcic-alkali field. A sample from Group 2 is situated in the alkali-calcic field and Group 1 exhibits a linear trend (Fig. 3.24c).
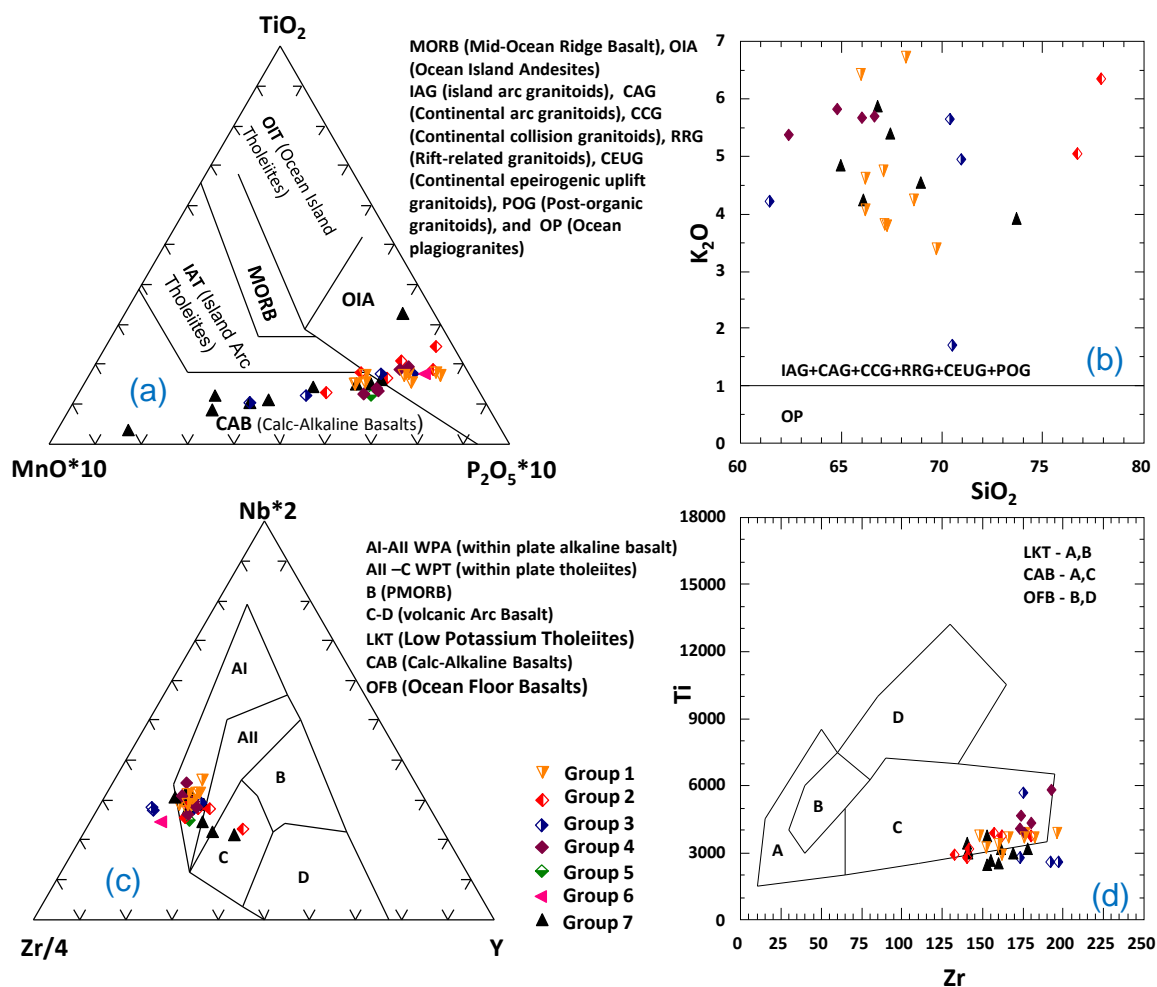
Fig. 3.25. Ternary and binary diagrams showing the tectonic settings (Field suggested by Mullen, 1983; Maniar and Piccolli, 1989; Meschede, 1986; Pearce and Cann, 1973).

The ternary plot of MnO*10-P_2O_5*10-TiO_2 (Mullen, 1983) shows that specimens exhibit a similar chemical composition to magmas from CAB and OIA. As can be seen (Fig. 3.25a), Groups 1, 2, 3, 4, and 7 are situated in the CAB and OIA fields and exhibit a linear trend. Group 6 is positioned in the OIA field and Group 5 is found in the CAB field, however, the P_2O_5 may be increased by potassic alteration (i.e. apatite content). Furthermore, the binary plot of SiO_2 vs. K_2O (Maniar and Piccolli, 1989) reveals that the bulk of samples from Groups 1, 2, 3, 4, and 7 are high in silica (>60%) and situated in the field

of IAG-CAG-CCG-RRG-CEUG-POG, suggesting a continental environment. It is believed that these igneous rocks were generated during a continental epeirogenic uplift (Fig. 3.25b).

In addition, the ternary plot of Zr/4-Y-Nb*2 (Meschede, 1986) shows that the bulk of samples exhibit a chemical composition similar to alkaline basalts generated within the plate (Fig. 3.25c). The binary plot of Zr vs. Ti (Pearce and Cann, 1973) suggests that the bulk of specimens have a similar chemical composition to calc-alkaline basalts (Fig. 3.25d).
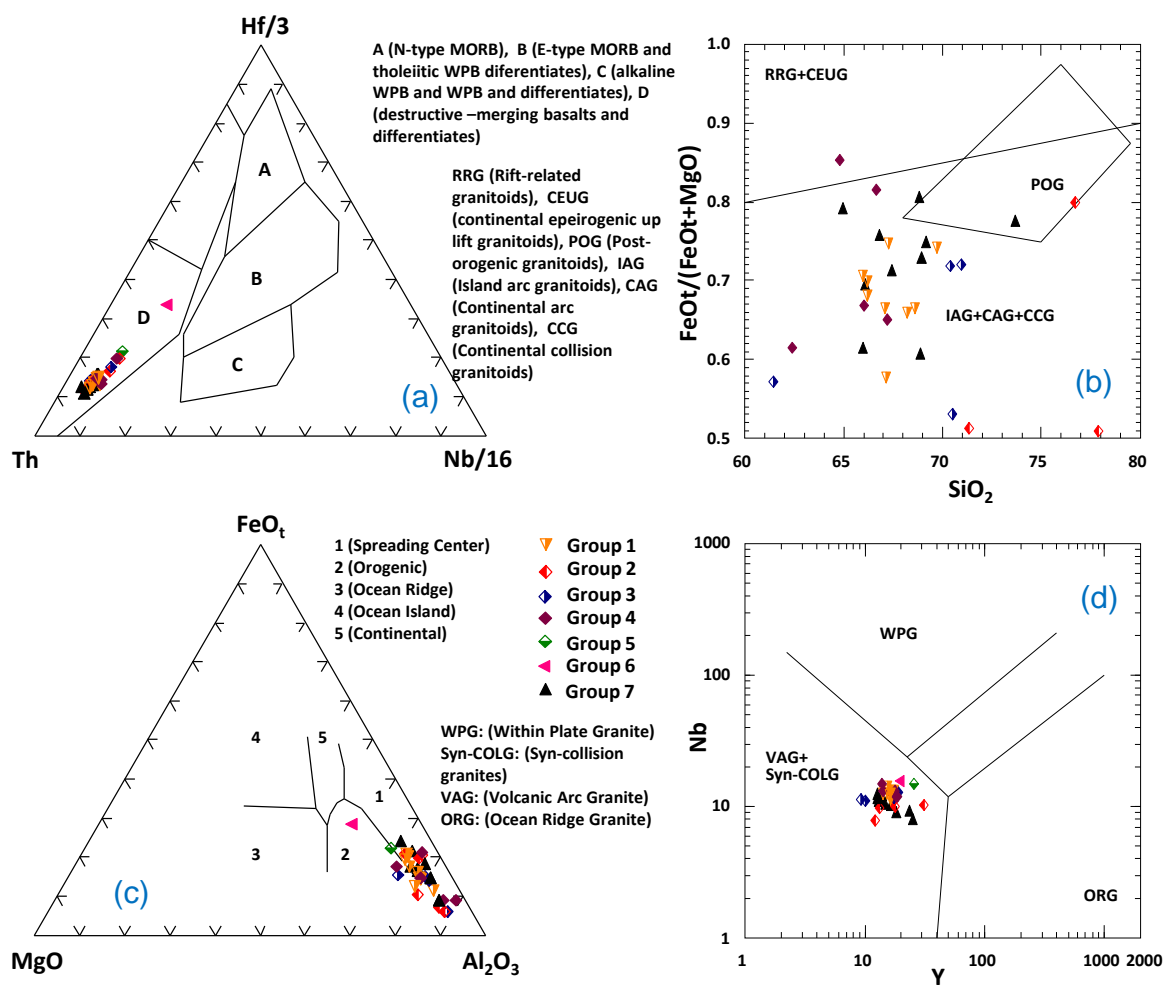
Fig. 3.26. Ternary and binary diagrams display samples in specific tectonic settings (Fields suggested by Wood, 1980; Maniar and Picolli, 1989; Pearce et al., 1977; Pearce et al., 1984).

The ternary plot of Th- Nb/16- Hf/3 (Wood, 1980) demonstrated that the bulk of samples exhibit a chemical composition similar to differentiated magmas formed in a destructive margin environment (Fig. 3.26a). The binary plot of SiO_2 vs. $FeO_t/(FeO_t+MgO)$ (Maniar and Picolli, 1989) indicates that the bulk of specimens were situated in the IAG-CAG-CCG (island arc granitoids, continental arc granitoids, and continental collision granitoids) fields, and it is believed that plutons from Peñasquito are related to continental arc granitoids or continental collision granitoids (Fig. 3.26b).

The ternary plot of $MgO/Al_2O_3/FeO_t$ (Pearce et al., 1977) shows that the specimens exhibit a linear trend, suggesting that these magmas may be related to a spreading center and/or an orogenic event (Fig. 3.26c). The binary discrimination plot of Y vs. Nb (Pearce et al., 1984) demonstrates that the bulk of specimens are related to syn-collisional granites and volcanic arc granites, suggesting that Peñasquito plutons may be related to I-type granites that were generated in the crust (Fig. 3.26d).

In the binary plot of SiO_2 vs. Ba/La, samples from Groups 1, 4 and 7 exhibit a linear trend in trace elements, suggesting that these specimens may be related to subduction (Fig. 3.27 a). The diagram SiO_2 vs. La/Yb exhibited a linear trend of samples from Group 7, which may suggest evolved magmas (Fig. 3.27b). The diagram SiO_2 vs. Cr/V shows three populations and Groups 1 and 7 exhibit a linear trend, suggesting that these samples may be related to primitive and evolved magmas (Fig. 3.27c). The plot of SiO_2 vs. Sm/Yb exhibits a linear trend of samples from Group 3, suggesting evolved magmas. In addition, the bulk of samples formed a population but the tectonic environment is unclear with respect to MORB (Fig. 3.27d).
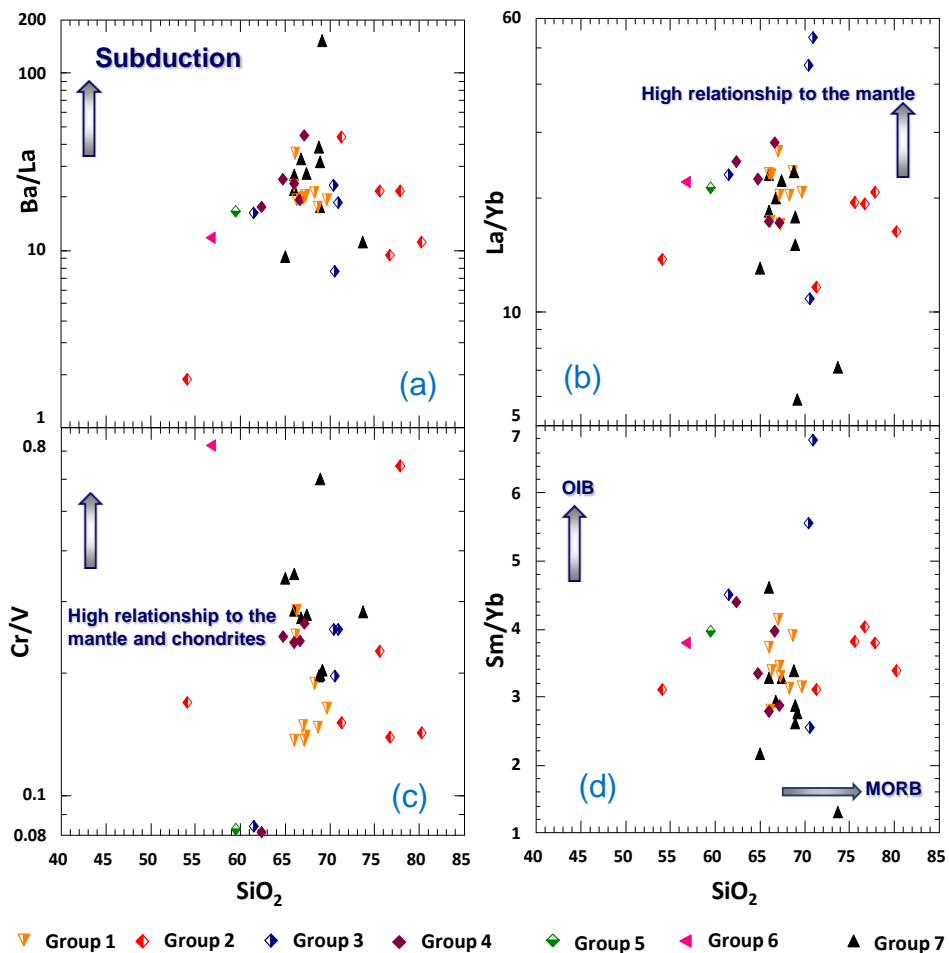
Fig. 3.27. Binary diagrams of trace elements vs silica showing the magmatic affinity (Fields taken from Martínez-Esparza, 2008).

The binary plot of Nb vs. Ba/Nd showed that most specimens are situated in the sub-alkaline rock field and exhibit an increasing linear trend in Ba/Nb, suggesting a relationship to a magmatic source from a subduction event (Fig. 3.28a). The plot of Ba/Nd vs. TiO_2/K_2O exhibits three populations and a sample from Group 2 is situated in the field of ocean island basalts (Fig. 3.28b). The plot of Nb vs. Nb/Zr exhibited a compact group, but Groups 5 and 6 exhibit similar chemical features, and all groups do not definite a tectonic setting (Fig. 3.28c). The plot of Sm vs. La/Sm exhibits an increasing linear trend in La/Sm related to a partial melting event (Fig. 3.28d). The plot of Y vs. Sr/Y illustrates that the bulk of

samples plot d in the calc-alkaline field and samples from Groups 2 and 7 exhibited a descending linear trend that is similar to a slab melting event (Fig. 3.28e). The plot of Ba/Nb vs. Gd/Yb exhibits a wide dispersion, and samples from Group 7 plot along an increasing linear trend in Ba/Nb, suggesting a correlation to granites related to partial melting of the depleted mantle (Fig. 3.28f).
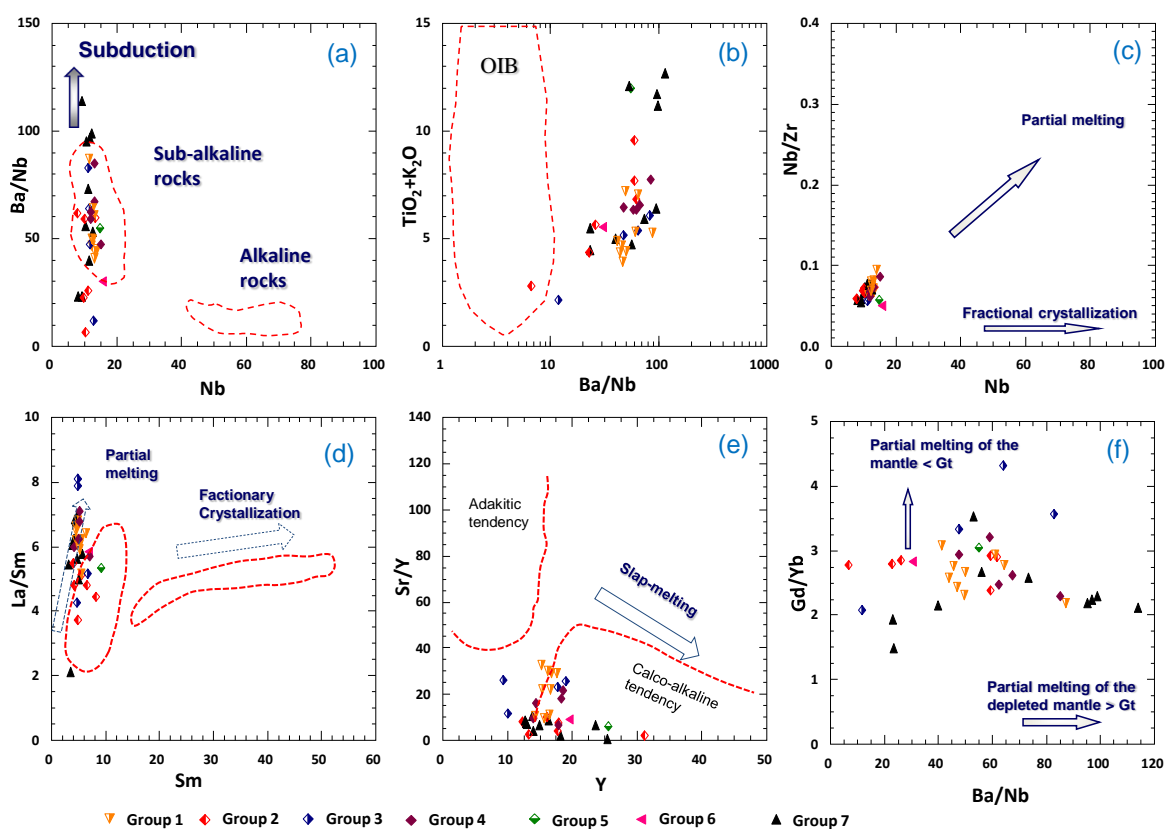
Fig. 3.28. Discrimination diagrams showing trace element composition and tectonic trend (Fields taken from Martínez-Esparza, 2008).

REE elements or spider diagrams

REE diagrams include Light Rare Earth Elements (LREE) and Heavy Rare Earth Elements (HREE) and are completed in order to obtain the signature of each group of samples and determine their geological affinity. Samples were plotted and compared with signature standards, such as upper crust, lower crust, and chondrite. The REE diagrams normalized to the upper crust (Fig. 3.29a) exhibit sub-horizontal and homogeneous patterns in LREE, minor depletion in HREE, and slight positive Eu anomalies. Group 1 is used as a comparative signature on every diagram (Fig. 3.29). Groups 1 and 4 are characterized by sub-horizontal and homogeneous patterns in LREE, minor depletion in HREE, and slightly positive Eu anomalies, suggesting affinity to the continental upper crust composition. Group 2 is characterized by sub-horizontal and homogeneous patterns in LREE and a slight decreasing trend in HREE, suggesting affinity to the continental upper crust composition. Most samples from the Group 3 are characterized by sub-horizontal and homogeneous patterns in LREE, depletion partition in HREE, and slightly positive Eu anomalies; however, one sample exhibited a slight depletion in LREE. Groups 5 and 6 are characterized by sub-horizontal and homogeneous patterns in LREE, moderate depletion in HREE, and slightly negative Eu anomalies. Most samples from Group 7 are characterized by sub-horizontal and homogeneous patterns in LREE, minor partition in HREE, and distinctly negative Eu anomalies (Fig. 3.29b,c); however, one sample exhibited clear depletion in LREE and marked depletion in La (i.e., sample GP640-13-825).
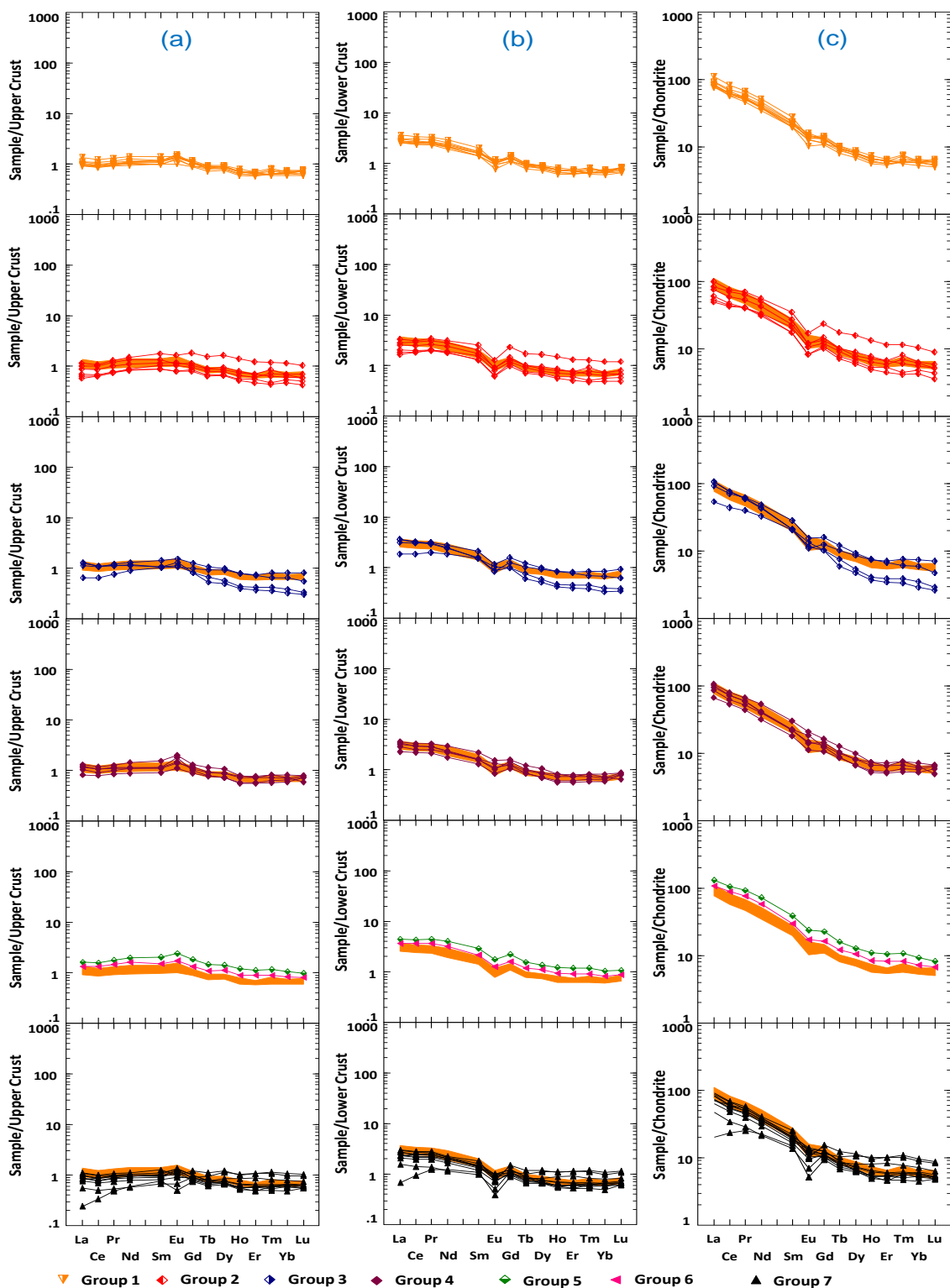
Fig. 3.29. Cordierite-normalized spider diagrams showing REE compositions and chemical patterns. Note that Group 1 REE spider plot is reproduced on each figure as a solid comparison line. a) normalized to the upper crust, b) normalized to the lower crust, c) normalized to chondrite.

REE diagrams normalized to the lower crust (Fig. 3.29b) reveal that the Peñasquito samples were characterized by a decreasing trend between LREE and HREE (Fig. 3.29b). Specifically, the bulk of the specimens exhibited a homogeneous pattern of LREE, marked depletion in HREE, and moderate to pronounced negative Eu anomalies, suggesting a lack of correlation with the lower crust. In addition, Group 3 is characterized by a decreasing and moderate partition in HREE; therefore suggesting a differentiated magma. Moreover, Group 7 is also characterized by a decreasing trend and depletion in LREE.

Finally, the REE diagrams normalized to chondrite make known that groups were characterized by a pronounced decreasing trend between LREE and HREE (Fig. 3.29c). In general, the samples exhibit homogeneous patterns of LREE, marked depletion in HREE, and moderate to pronounced negative Eu anomalies, suggesting a lack of correlation with the chondrite, or mantle. In addition, Groups 2, 3, and 7 are characterized by a decreasing and moderate partition in HREE, therefore suggesting a differentiated magma. Moreover, Group 7 is also characterized by a decreasing trend and partition in LREE.

CHAPTER IV ECONOMIC GEOLOGY

Synopsis of the Peñasquito Ore Deposit

The Peñasquito ore deposit is in the Mazapil syncline, confined to the Cretaceous and Jurassic sedimentary sequence, and related to a Tertiary plutonic complex. The ore deposit includes two diatreme breccias hosted mainly in the Late Cretaceous sedimentary marine sequence and related to the plutonic complex. The diatreme breccias are aligned in a northwest-southeast direction and are known as the Peñasco and Azul Breccias, respectively. Also, stockwork zones are found surrounding the diatreme breccia system and within the Late Cretaceous sedimentary marine sequence. In addition, a skarn system was developed in the Cretaceous and Late Jurassic sedimentary marine sequences, which include mantos and disseminated mineralization. Although the calc-silicate aureole was developed throughout the Mesozoic sedimentary marine sequence, the bulk of mineralized skarn has been intercepted between 700 and 1,300 meters below the surface and is related to the plutonic complex. The plutonic complex may represent an economic potential due to the fact that drilling has intercepted zones with potassic hydrothermal alteration with veinlet and disseminated mineralization. In general, the ore deposit includes primary sulfides, sulfosalts, oxides, and carbonates with economic values of gold, silver, lead, zinc, and copper.

At Peñasquito, the ore system lies under an alluvial cover up to ~50 m in thickness. Before 2007, an outcrop of the Peñasco Breccia protruded from the valley fill and occu-

pied only a few hundred square meters (Fig. 4.1). Also, the Caracol Formation locally crops

out along streams in the Mazapil valley.

Fig. 4.1. Image showing the original outcrop of Peñasco Breccia (Photography captured in 2005 and courtesy of Acacio E.).

The Peñasquito ore deposit is hosted in the Mesozoic sedimentary marine sequence, and controlled by three major structural patterns that intersected at both diatreme breccias (see Fig. 3.14 in Chapter III). In the Peñasco open pit, the diatreme breccia is hosted in the Caracol Formation (Fig. 4.2), which exhibits phyllic and local potassic alteration and ~90 meters of weathering effects. The Peñasquito ore deposits include several economic ore bodies that have been explored up to ~2,000 meters in depth.

The Diatreme Breccia Systems

The diatreme breccias are aligned over 2.5 km and 320°, spaced out from one another (740 m), and occupy a total area of 350 hectares at their upper levels. The dia-

treme breccias are located on flanks of the Mazapil syncline that is represented by the trace of the Arroyo Grande stream. The Peñasco Breccia had an irregular outcrop that occupied 49 m^2 and protruded up to 3 m above the alluvial cover (Fig. 4.1). The Azul Breccia is covered by ~40 m of alluvial cover (Fig. 4.2).
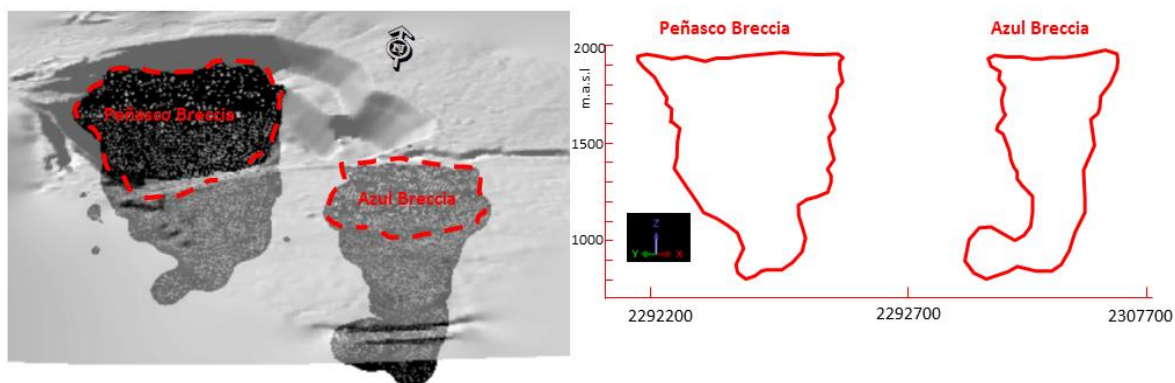
Fig. 4.2. Real model geometry of Peñasco and Azul Breccias.

Morphology and Dimensions of the Peñasco Breccia

The Peñasco Breccia exhibits a conical shape which tapers downward. This diatreme breccia occupies 72.1 ha (i.e. 1,940 m.a.s.l.), however the area of the cross section gradually decreases (up to 75%) with depth. At the top, the diatreme breccia has a rounded shape with a 1 km diameter in an east-west section and an 886 m diameter in a north-south section (i.e. 1,940 m.a.s.l.). The northern contact of the Peñasco Breccia is inclined inward at 20° from vertical, while the southern contact dips inward at 12° from vertical (Fig. 4.2). At the base (i.e. 900 m.a.s.l.), this diatreme breccia becomes sub-horizontal to the west and connected to the quartz-feldspar porphyry (Figs. 4.2, 3).

The Peñasco diatreme ore body exhibits disseminations, veinlets, faults, and fractures with polymetallic economic values. The mineralogy consists of primary sulfides (py-

rite, sphalerite, and galena), sulfosalts, precious native elements (gold-silver-electrum) (Fig. 4.4), carbonates (rhodochrosite and calcite), and secondary oxides (i.e. limonite group and copper carbonates).
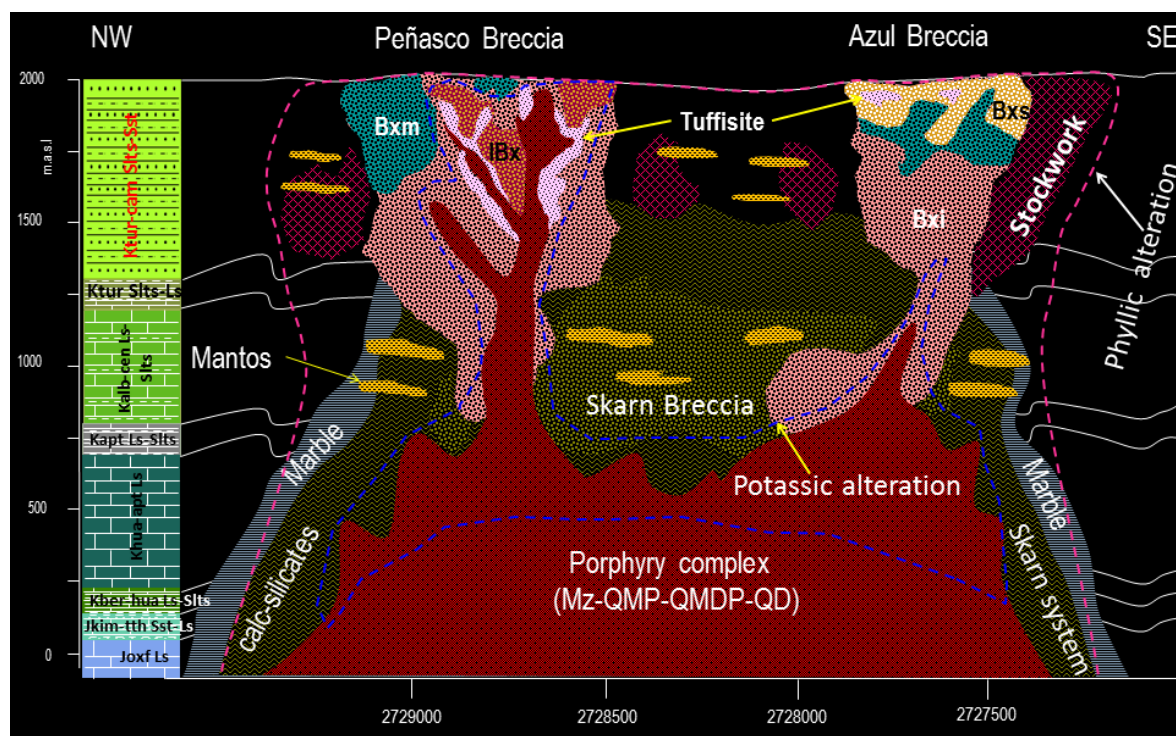
Fig. 4.3 Schematic cross section showing mineralized bodies at the Peñasquito polymetallic ore deposit. The cross section is oriented 340° with view to the northeast. The lithology column is displayed on left side. The Chile Colorado stockwork is displayed on the right side and adjacent to the Azul Breccia. Bxm (Heterolithic Mixed Breccia), Ibx (Intrusive Breccia), BxI (Heterolithic breccia supported by flour igneous rock), Bxs (Sedimentary breccia), Stw (Stockwork), Mz (Monzonite), QMP (Quartz monzonite porphyry) QMDP (Quartz monzodiorite porphyry) QD (Quartz diorite).

The geochemical analyses have demonstrated that the Peñasco diatreme ore body includes economic gold, zinc, silver, and lead. The hydrothermal alteration consists of a potassic halo (K-feldspar and local biotite and apatite) related to dikes of quartz-feldspar porphyry, tuffisite, IBX, and BxI, which are overprinted by phyllic alteration (sericite-pyrite-quartz), and subsequently overprinted by carbonate. In the Peñasco diatreme, veins,

faults, and fractures exhibit supergene enrichment (below 1,850 m.a.s.l.) including limonite minerals and copper carbonates. The Peñasco breccias yielded good chemical values, such as Au (up 43 ppm), Ag (up to 2,300 ppm), lead (up to 223,000 ppm), and zinc (up to 245,000 ppm).

Morphology and Dimensions of the Azul Breccia

The Azul Breccia exhibits a conical shape, which tapers downward and its upper surface is located ~50 m below the current surface beneath alluvial cover. This diatreme breccia occupies 33.74 ha (i.e. calculated area at 1,940 m.a.s.l.); however, the area of the cross section gradually decreases (up to 55%) with depth. At the top, the breccia has a sub-rounded shape with a 715 m km diameter in an east-west section and 592 m diameter in a north-south section (i.e. 1,940 m.a.s.l.). The northern contact of the Azul Breccia is inclined inward at 15° from vertical, while the southern contact dips inward at 20° from
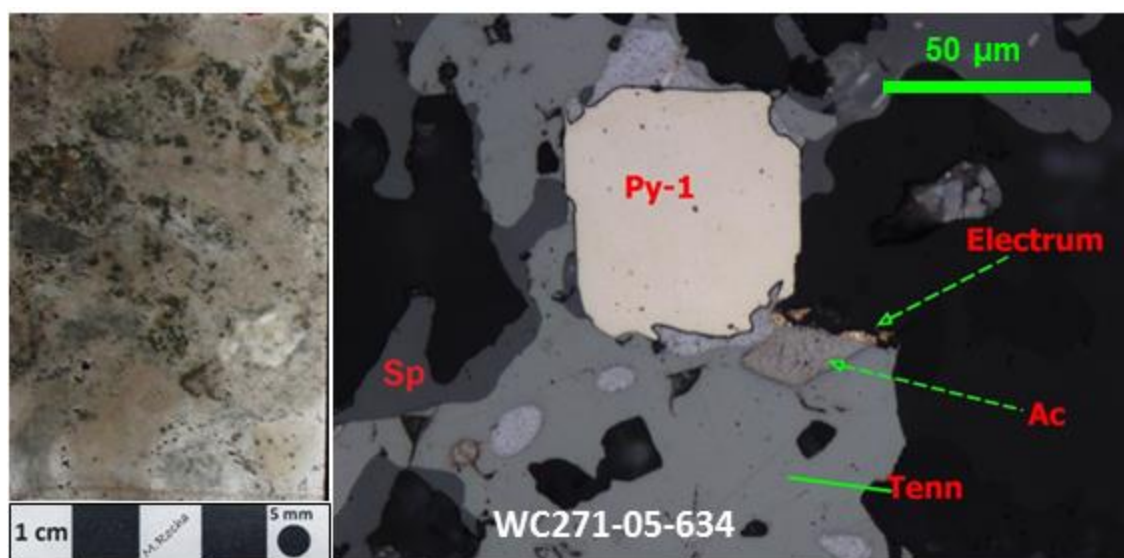
Fig. 4.4. Hand sample and photomicrography (reflected light) displaying mineralization in the Peñasco Breccia. Note: Py (pyrite), Tenn (tennantite), Ac (acanthite), Galena (Ga), and Sp (sphalerite).

vertical. At the base (i.e. between 797 and 1,056 m.a.s.l.), the breccia becomes sub-horizontal to the north (about 300 meters in longitude) and connected to the quartz-feldspar porphyry (Figs. 4.2, 3).
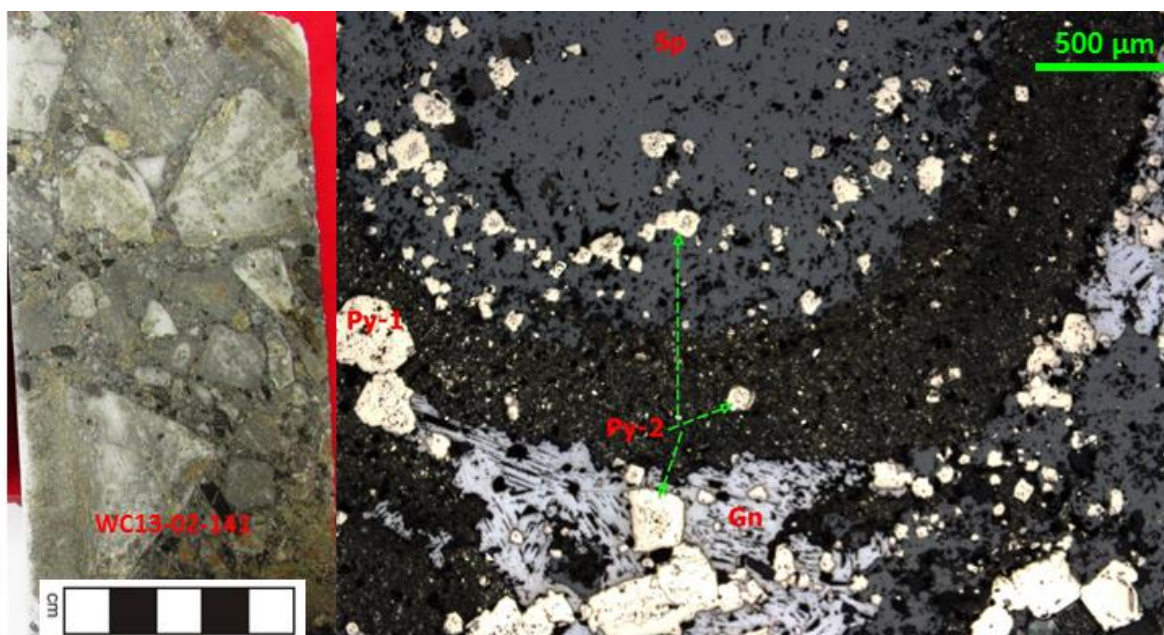
Fig. 4.5. Hand sample (billet) and photomicrography (reflected light) displaying mineralization in the Azul Breccia. Note: Py (pyrite), Gn (Galena), and Sp (sphalerite).

The Azul diatreme ore body exhibits disseminations, veinlets, faults, and fractures with polymetallic economic value. The mineralogy includes primary sulfides (pyrite, sphalerite, galena, and local molybdenite), sulfosalts, carbonates (rhodochrosite and calcite), and secondary oxides (i.e. limonite group and copper carbonates) (Fig. 4.5). The geochemical analyses have demonstrated that this ore body includes economic gold, zinc, silver, and lead. This ore body is usually affected by potassic and phyllic alteration from moderate to pervasive intensity that is related to dikes of quartz-monzonite porphyry, and both alterations are overprinted by carbonate. The Azul Breccia yielded good chemical

values, such as Au (up 11.9 ppm), Ag (up to 989 ppm), lead (up to 136,000 ppm), and zinc (up to 307,000 ppm).

Stockwork and Veins

In the Peñasquito ore deposit, drill programs have intersected stockwork zones and veins. The stockwork zones are usually hosted in the Caracol Formation, adjacent to the diatreme breccia system; however, veins with economic values are present in the skarn system (Fig. 4.3). The stockwork is composed of mineralized fractures, faults, and veinlets with diverse lengths and thicknesses. The mineralogy includes primary sulfides, sulfosalts, and subordinate carbonates, but secondary oxides are also locally present due to supergene effects. The stockwork and veins usually have high metallic grades, such as gold, silver, zinc, lead, with lesser amounts of copper. These ore bodies are usually affected by phyllic alteration from moderate to pervasive intensity; local chlorite and fine calcite are also present in the host rock (Fig. 4.6C).

In Peñasquito, the best representative stockwork is the Chile Colorado mineralized zone. In the 1990s, this ore body was first indicated by a geophysical survey as results exhibited a low resistivity anomaly in a crescent shape on the southern and western parts of the Azul diatreme, suggesting an elongated ore body near the surface with a NW-SE orientation and a possible extent of about 32 ha. Subsequent drilling helped to corroborate and outline this irregular body that developed in the Caracol Formation. The Chile Colorado stockwork is adjacent to the Azul Breccia and its vertical extent is more than 400 meters with a horizontal dimension of ~200 meters; however, between 1,950 and 1,700 m.a.s.l.,

the horizontal extent is more than 300 meters (Fig. 4.3). The Chile Colorado stockwork

exhibits good chemical values, such as Au (0.5-1 ppm), Ag (up to 8,280 ppm), lead (up to

496,000 ppm), and zinc (9,173-39,300 ppm).
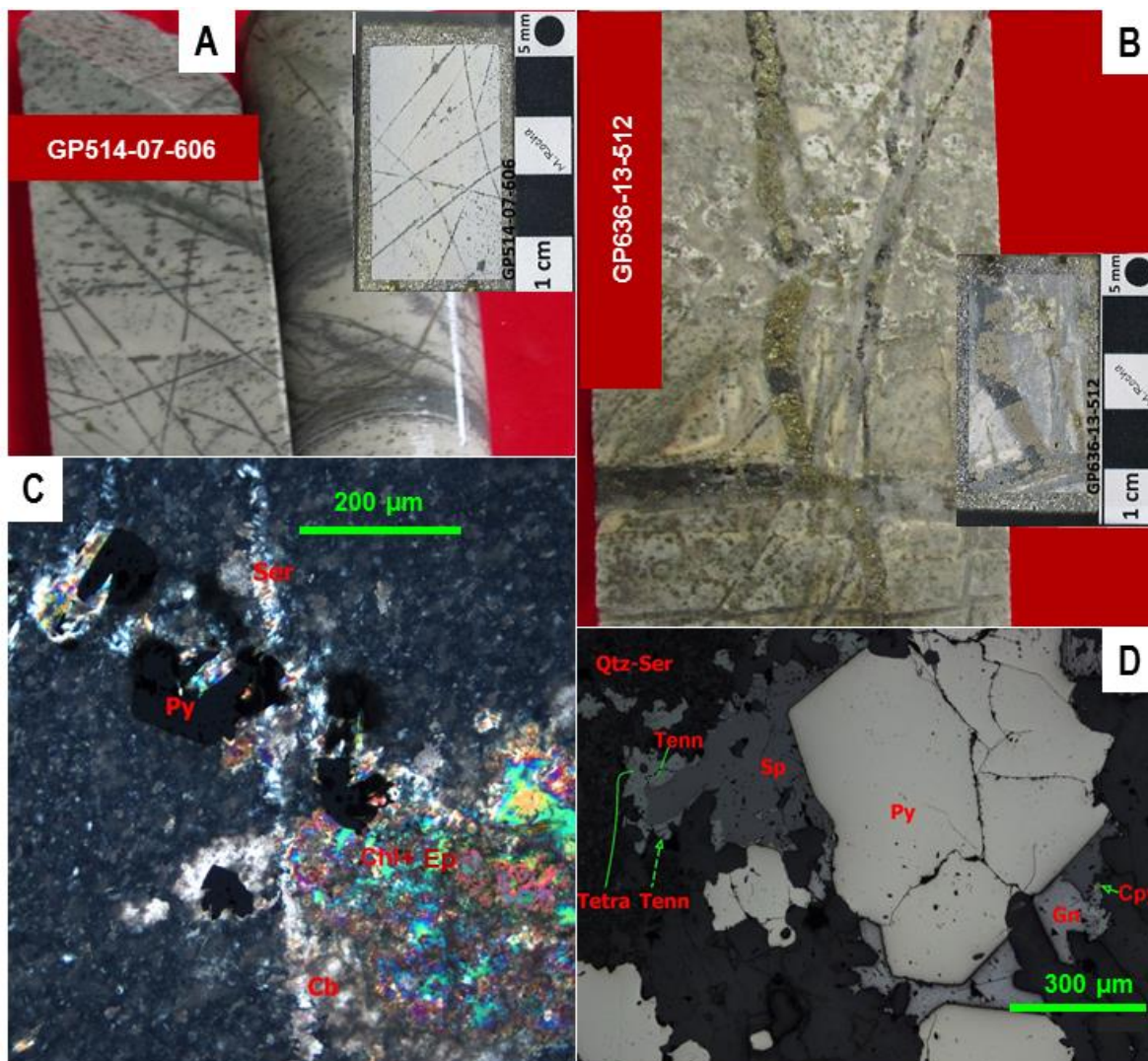
Fig. 4.6. Hand samples (billets) and photomicrographs (plane-polarized & reflected light) displaying stockwork specimens. A. Hand sample and billet showing multiple veinlets hosted in hornfels. B. Hand sample and billet showing multiple veins of pyrite and sulfosalts that are hosted in the Caracol Formation. C. Veinlets of sericite-pyrite throughout the hornfels and overprinted by chlorite, epidote, and carbonate. D. Sulfides (Py, Ga, Sp, and Cpy) and sulfosalt in veinlets.

The bulk of mineralized veins and faults have been documented between and/or in the vicinity of both diatreme masses. The ore body type is locally associated with hydro-thermal breccias and has a vertical range of about 600 meters. In the Peñasco open pit, the veins, faults, and fractures are mineralized beneath 1,850 m.a.s.l. The mineralization includes primary sulfides (pyrite, sphalerite, and galena), local sulfosalts, carbonates (rho-dochrosite and calcite), and secondary oxides (i.e. limonite group and copper carbonates) (Fig. 4.6C). The geochemical analyses have demonstrated that veins and faults include economic gold and lesser zinc, silver, and lead mineralization.

Skarn System

In the Peñasquito area, a skarn system was developed through the Jurassic and Cretaceous sedimentary marine sequence with a distinct mineral zonation. The chemical interaction of fluids from magma and each protolith developed distinct mineral zones. This metasomatism developed endoskarn, exoskarn, skarnoid, and hornfels, which are intercalated with a marble shell (Fig. 4.3). The skarn system hosts economic mineralization (Au-Cu-Zn-Pb-Ag), mainly including calc-silicates, sulfides, primary oxides with fewer sul-fosalts, and precious native elements with local secondary oxides, in association with fluorite, carbonates, and quartz.

The exploration drilling documented the extent of the skarn system up to a depth of 2,000 meters in the Peñasquito area. The vertical range of the skarn system is about 1,300 meters; however, the bulk of the mineralized skarn system is developed between 1,300 and 700 meters above sea level (Fig. 4.7). The hornfels shell was developed from 1,750 to

1,300 and ~700 meters above sea level (i.e. in the Caracol and La Peña formations) (Fig. 4.3).
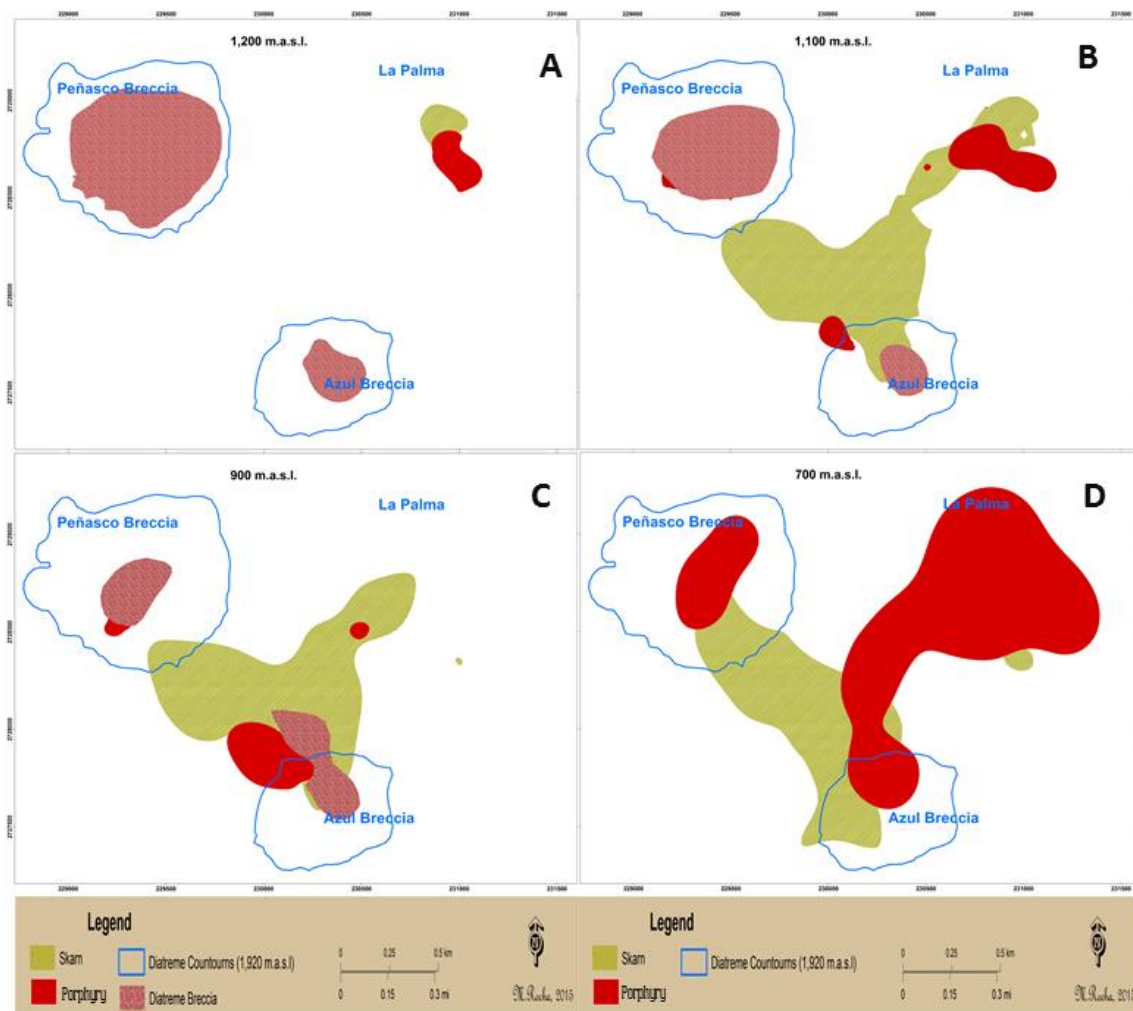
Fig. 4.7. Maps showing the influence of skarn system, diatreme breccias, and porphyry complex in the Mazapil syncline. A. Map showing skarn, diatreme breccia, and porphyry at 1,200 m.a.s.l. B. Map showing skarn, diatreme breccia, and porphyry at 1,100 m.a.s.l. C. Map showing skarn, diatreme breccia, and porphyry at 900 m.a.s.l. D. Map showing skarn, diatreme breccia, and porphyry at 700 m.a.s.l. Note: boundaries of diatreme breccias at 1,920 m.a.s.l. is used on all maps as special location (blue lines) in order to have a geographical reference. La Palma not discussed.

The skarn system developed before the diatreme system as some skarn fragments are in the breccia. The skarn system was mainly developed in the Cuesta del Cura For-

mation (between 700 and 1,200 m.a.s.l.), with a large extention and irregular shape, forming a major area at 1,100 m.a.s.l. (~70 ha) that is developed between both breccia diatremes, as well as, between the Azul breccia and the Palma zone (Figs. 4.3, 7).

The endoskarn shell has been found for several meters along the borders of the porphyry complex and calcareous rocks. The endoskarn consists of phenocrysts of plagioclase, orthoclase, as well as local pyroxene, magnetite, and wollastonite. The endoskarn halo contains local sulfides,

Fig. 4.8. Hand sample and photomicrographs (plane-polarized light) displaying endoskarn. A. Hand sample and billet showing dark endoskarn. B. Zoned Orthoclase (Fto) phenocryst floating in a microcrystalline groundmass altered by epidote, carbonate, and sericite. C. Plagioclase (Pl) phenocrysts floating in a microcrystalline groundmass altered by epidote (Ep) and carbonate (Cb).

retrograde minerals including epidote and chlorite, as well as sericite and carbonate (Fig. 4.8). In the Palma zone, the endoskarn is developed between the quartz-feldspar porphyry and concentrations of magnetite and/or mineralized andradite (i.e. Py- Sp-Ga-Mar, Mag-Hem, Tetra, Tenn, Cpy-Cpr-Cv) (Fig. 4.9).

The exoskarn host of the bulk of the primary economic mineralization is composed of garnet (andradite and grossularite), pyroxene, wollastonite, primary sulfides and oxides (magnetite) and lesser amounts of sulfosalts, gold, chlorite, epidote, aphanitic orthoclase, sericite-quartz, carbonate, and secondary oxides (hematite and limonite minerals).
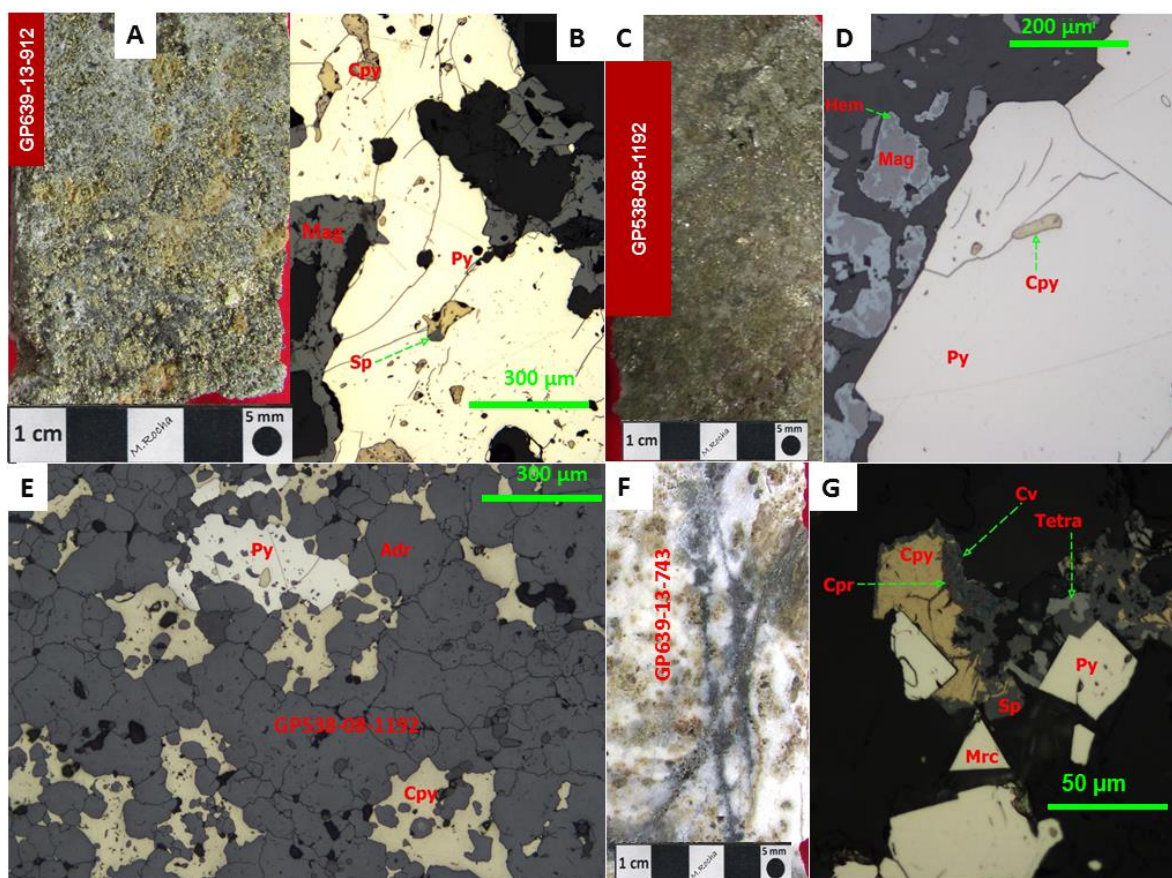
Fig. 4.9. Hand sample and photomicrographs (reflected light) are displaying a magnetite skarn specimen and mineralized andradite. A. Hand sample showing magnetite and primary sulfides, hosted in groundmass of andradite. B. Photomicrograph showing magnetite (Mag), pyrite (Py), chalcopyrite (Cpy), and sphalerite (Sp). C. Hand sample showing primary sulfides and magnetite. D. Photomicrograph showing magnetite, hematite (Hem), pyrite, and chalcopyrite. E. Photomicrograph showing pyrite and chalcopyrite in andradite. F. Hand sample showing andradite skarn cut off by veinlets filled by supergene minerals. G. Photomicrograph showing pyrite, chalcopyrite, marcasite (Mrc), cuprite (Cpr), covellite (Cv), and tetrahedrite (Tetra).

The ore minerals occur as disseminations, massive mantos, and local fracture fillings of primary sulfides with lesser amounts of sulfosalts, and primary and secondary oxides (Fig. 4.10).
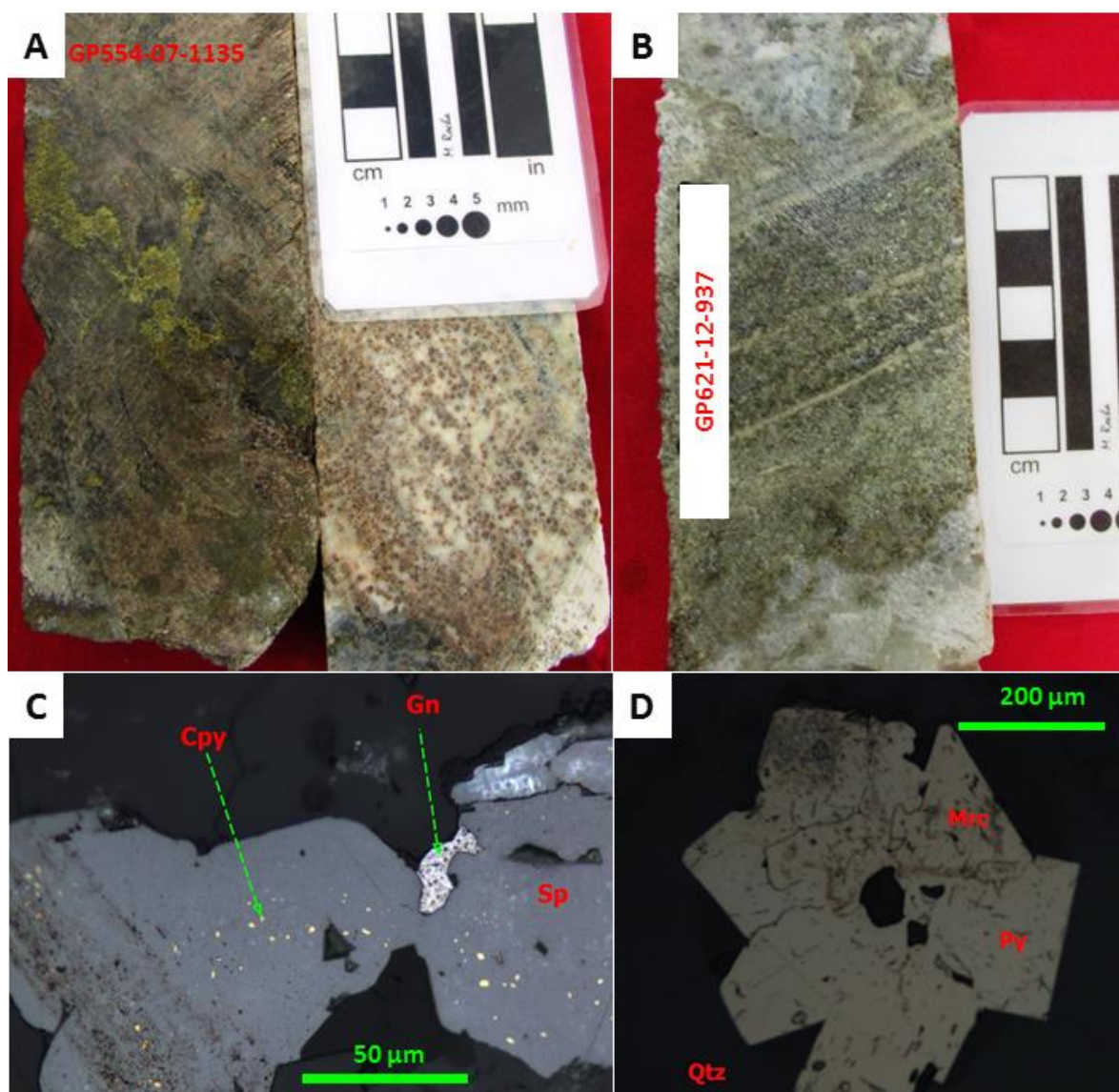
Fig. 4.10. Hand samples and photomicrographs (reflected light) are displaying a skarn of andradite and grossularite. A. Hand sample showing andradite skarn specimen and disseminated chalcopyrite. B. Hand sample showing a grossular skarn. C. Photomicrograph showing sphalerite (Sp), galena (Gn), chalcopyrite (Cpy) hosted in an andradite skarn. D. Photomicrograph showing aggregate of pyrite (Py) and marcasite (Mrc) hosted in a epithermal quartz vein.
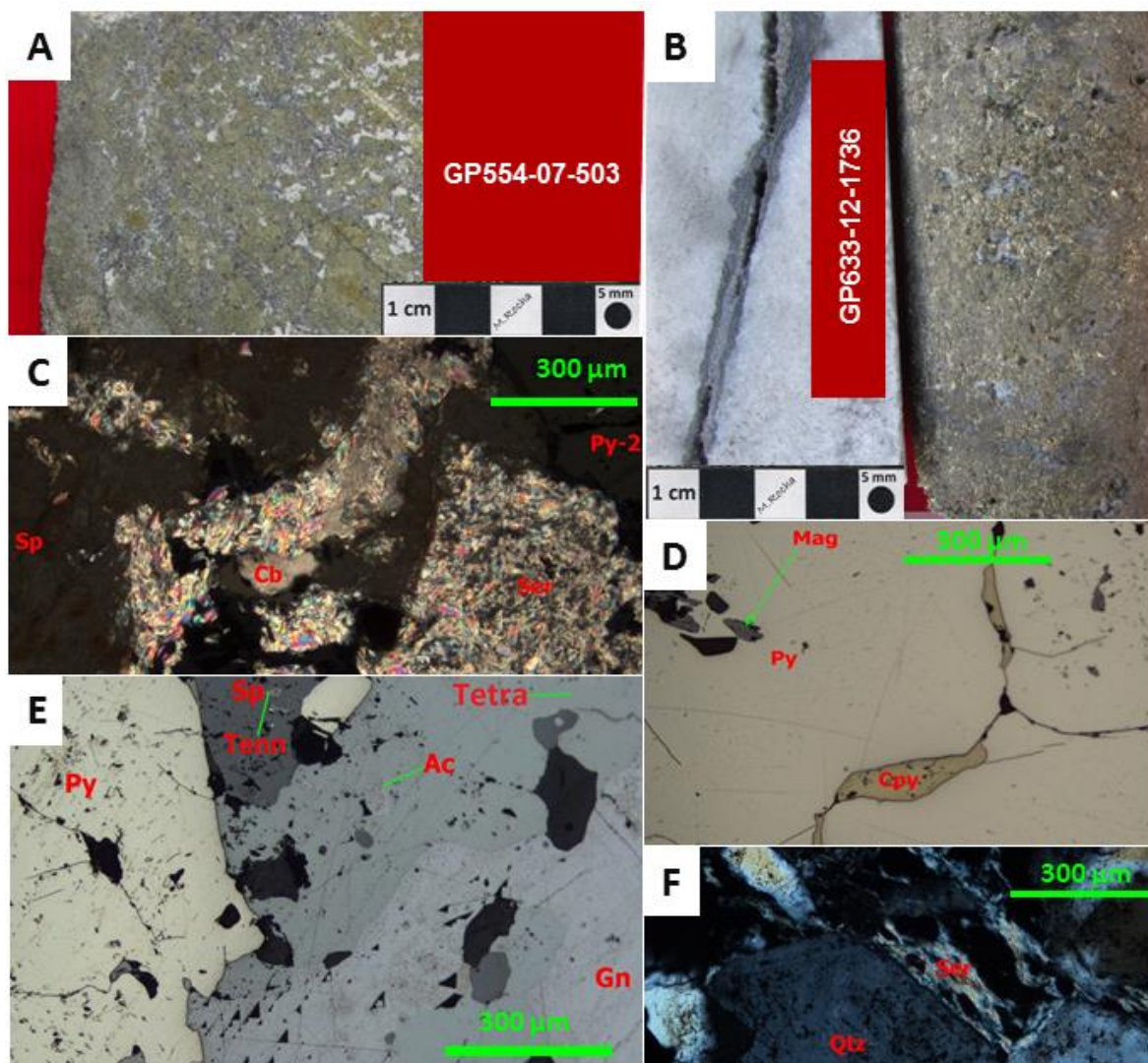
Fig. 4.11. Hand samples and photomicrographs (plane-polarized and reflected light) are displaying mantos specimens. A. B. Hand samples showing massive sulfides. C. Photomicrograph showing sericite and carbonate in mantos. D. Pyrite (Py), chalcopyrite (Cpy), and magnetite (Mag). E) Primary sulfides (Py,Sp,Ga) and sulfosalts (Tetra,Tenn,Ac). F. Quartz and sericite as fine groundmass in mantos.

The massive mineralization in exoskarn consists of elongated mantos. These are principally found in the Cuesta del Cura Formation; however, in the Peñasco open pit, mantos are hosted in the Caracol Formation, which are up to 30 cm in thickness and exhibit tens of meters in length. Mantos in the Cuesta del Cura Formation are composed of

massive sulfides and local oxides (Fig. 4.11) with thicknesses up to 20 meters. The bulk of the exoskarn was developed in the Cuesta del Cura and Indidura formations.
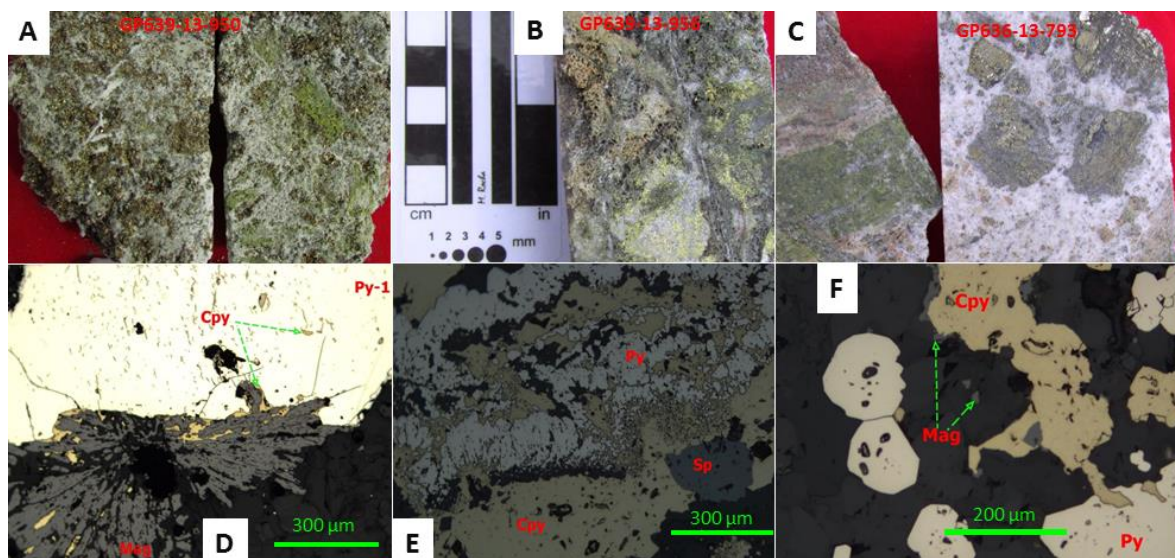
Fig. 4.12. Hand samples and photomicrographs (reflected light) displaying skarn breccias. A-B-C. Hand samples showing breccias from skarn system. D-E-F. Photomicrographs showing pyrite (Py), and magnetite (Mag), sphalerite (Sp), and chalcopyrite (Cpy). The platy habit of magnetite in D suggests that early iron oxide was specularite that was later reduced to magnetite.

A mineralized breccia has been identified in the skarn system. The skarn breccia is composed of fragments of skarn, sulfides, marble, primary sulfides, carbonates, secondary oxides, with local epidote and chlorite (Fig. 4.12). The bulk of the breccia is present between both diatremes and the Palma zone with a vertical range of about 250 meters (i.e. between 1,100 and 850 m.a.s.l.). The breccia exhibits zones with intense oxidation and is cemented by calcite, suggesting a late-stage hydrothermal event.

A skarnoid was developed and gradually changed to hornfels between the Indidura and Caracol formations (Fig. 4.3). The skarnoid included wollastonite, tremolite, calc-silicates (fine-grained), primary sulfides, local sulfosalts, gold, epidote, chlorite, sericite-

quartz, carbonate, and secondary oxides. The hornfels shell was developed in the Caracol

Formation between 1,750 and 1,300 meters above sea level. The hornfels development is

primarily in the vicinity of the diatreme system. The metallic mineralization is present in

small crystalline disseminations and veinlet fillings (Fig. 4.13). The hornfels exhibit locally

oxidation of primary sulfides.
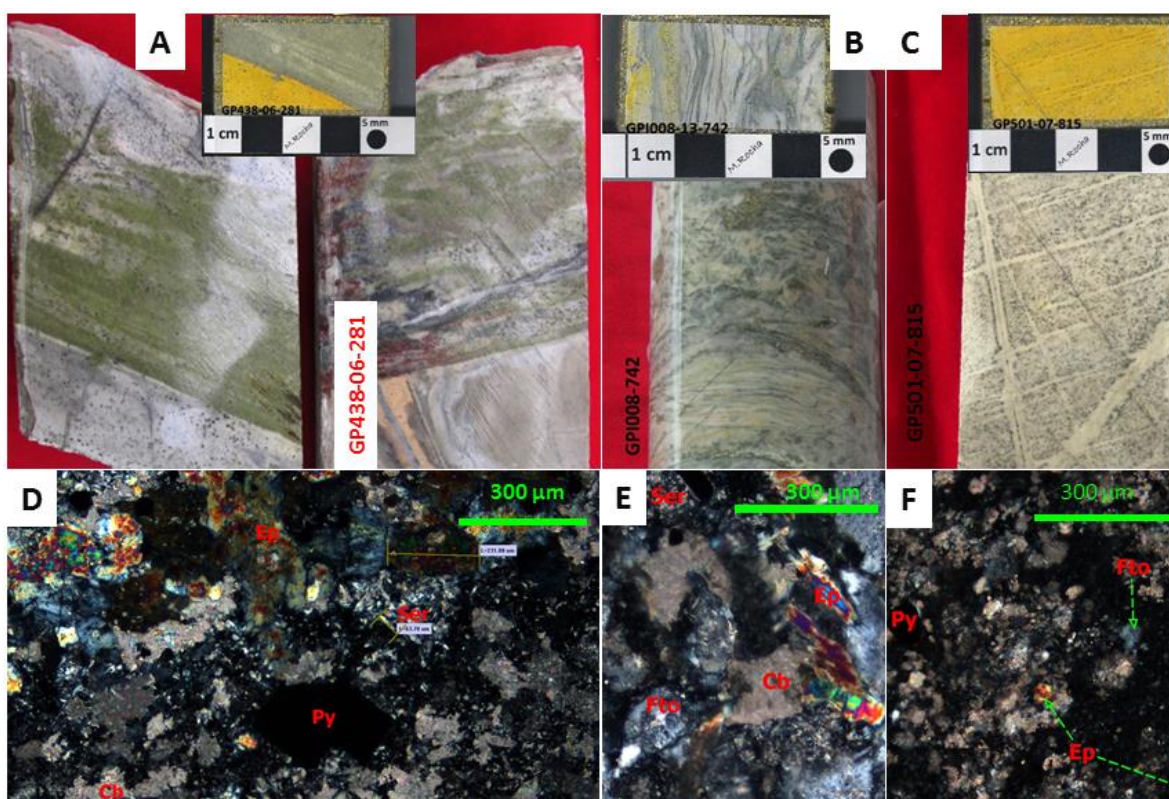
Fig. 4.13. Hand samples and photomicrographs (plane-polarized light) are displaying hornfels specimens. A.B.C. Hand samples and billets showing staining of K-feldspar with sodium cobaltinitrite in yellow color of hornfels specimens with disseminated mineralization and local oxidation. D. Photomicrograph showing sericite (Ser), epidote (Ep), and carbonate (Cb). E. Groundmass replaced by orthoclase (Fto), sericite, epidote, and carbonate. F. Groundmass replaced by orthoclase (Fto), sericite (Ep) carbonate (Ep), and pyrite (Py).

The skarnoid-skarn ore bodies are present between 1,300 and 700 meters above sea

level. The skarn system is locally affected by potassic and retrograde alteration, whereas

phyllic alteration is present throughout the skarnoid and hornfels shells (Figs. 4.13 A,B,C).

The skarn system hosts economic concentrations of copper, gold, silver, zinc, lead, and subordinate molybdenum.

Plutonic complex Mineral Deposits

The bulk of the plutonic complex is situated below 700 m.a.s.l. but dikes have been intercepted up ~1,966 m.a.s.l. and the potassic shell includes zones with primary economic Au-Cu and local Mo mineralization. This polymetallic mineralization is developed in quartz-monzonite and quartz-monzodiorite porphyries, and the molybdenite is locally concentrated in quartz-monzonite, which were altered at the top to an orthoclase-quartz-hydrothermal biotite-magnetite-apatite assemblage. These porphyries are composed of orthoclase and plagioclase phenocrysts, quartz eyes, biotite, and local magnetite, which are floating in a fine groundmass, composed of quartz, K-feldspar (aphanitic orthoclase) cut by veinlets of quartz, biotite, quartz-sericite-pyrite and fluorite-molybdenite. The best-mineralized potassic zones have been found beneath and in the vicinity of the Azul Breccia; however, in the eastern portion of the breccia system (i.e. Palma zone) drill cores have exposed a large hydrothermal potassic zone with lesser amounts of sulfides, suggesting an exploration target.

The mineralization occurs as disseminations and fracture fillings with primary sulfides and lesser amounts of sulfosalts and primary oxides. Specifically, the potassic shell includes primary pyrite, molybdenite, sphalerite, galena, chalcopyrite, and local sulfosalts. The potassic shell is overprinted by a late phyllic alteration (i.e. quartz-sericite-pyrite) with local carbonate overprinting on both alteration types (Fig. 4.14).

The drill core (GP621R12) has intercepted an altered monzonite with molybdenite
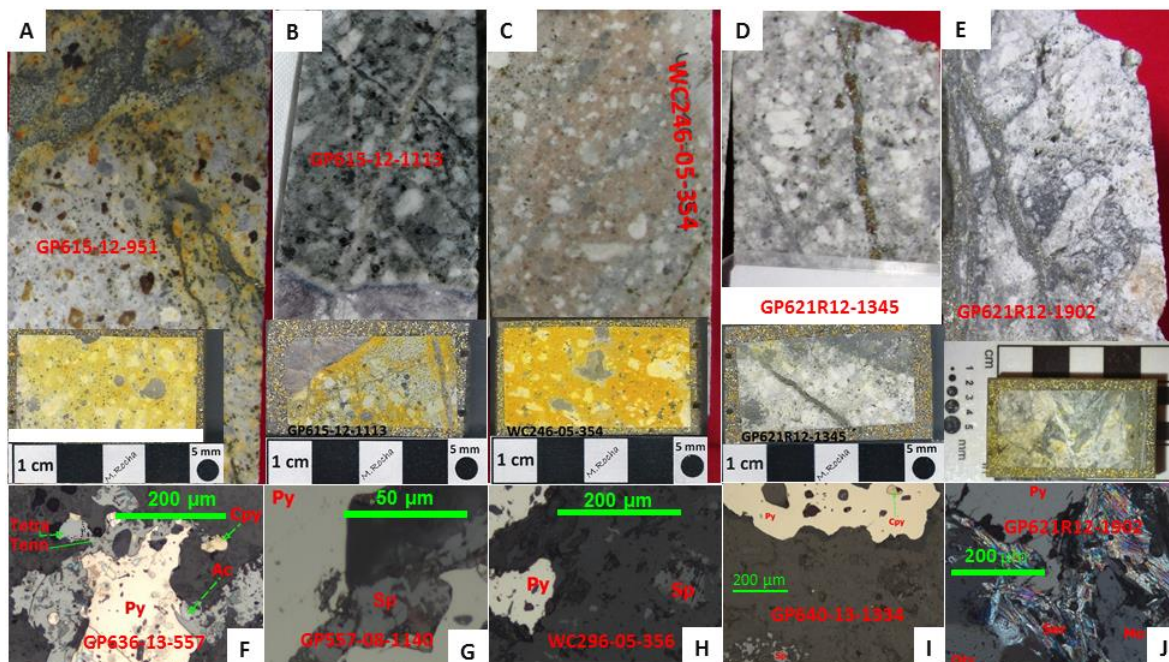
Fig. 4.14. Hand samples and billets showing mineralized porphyry types, as well as photomicro-graphs (reflected and plane-polarized light) displaying mineralization in the porphyry complex. The billets are showing the staining of K-feldspar with sodium cobaltinitrite in yellow color. A. Quartz-monzonite porphyry hosting disseminated sulfides and pervasive potassic alteration (K-feldspar). B. Quartz-monzonite of biotite is hosting veinlets of molybdenite-fluorite and pyrite-quartz with pervasive potassic alteration (orthoclase and biotite). C. Quartz-monzodiorite is hosting disseminated sulfides with pervasive potassic alteration (K-feldspar). D. Monzonite is hosting veinlets of pyrite-sphalerite. E. Monolithic breccia with fragments of monzonite porphyry cemented by molybdenite and pyrite. F. Photomicro-graphs showing pyrite (Py) chalcopyrite and sulfosalts (Tetra,Tenn, Ac). G-H-I. Photomicro-graphs showing pyrite, sphalerite (Sp), and chalcopyrite. J. Photomicrographs showing py-rite and molybdenite (Mo), sericite (Ser), and quartz (Qtz).

mineralization. This mineralization occurs as disseminations, veinlets fillings, and, locally, in brecciated porphyry. The molybdenite mineralization has been located between ~1,786 to 1,800 m at depth (from 184 to 170 m.a.s.l.).

Hydrothermal Alteration and the Relationship with Mineralization

In the Peñasquito ore deposit, the hydrothermal alteration exhibits a large spatial distribution through the plutonic complex, Mesozoic sedimentary marine sequence, and

diatreme breccia system. In general, the hydrothermal influence developed a mineralogical zonation, forming parallel shells (Fig. 4.3). The hydrothermal alteration ranges from weak, weak-moderate, and moderate-pervasive grades.

The early fluids formed a potassic alteration composed of orthoclase-quartz and hydrothermal biotite-magnetite-apatite assemblage. This hydrothermal alteration was developed on the cupola of the plutonic complex, in the diatreme breccias, and to a lesser extent in the plutonic complex, and late adularia has locally been found in the skarn system (Fig. 4.15).
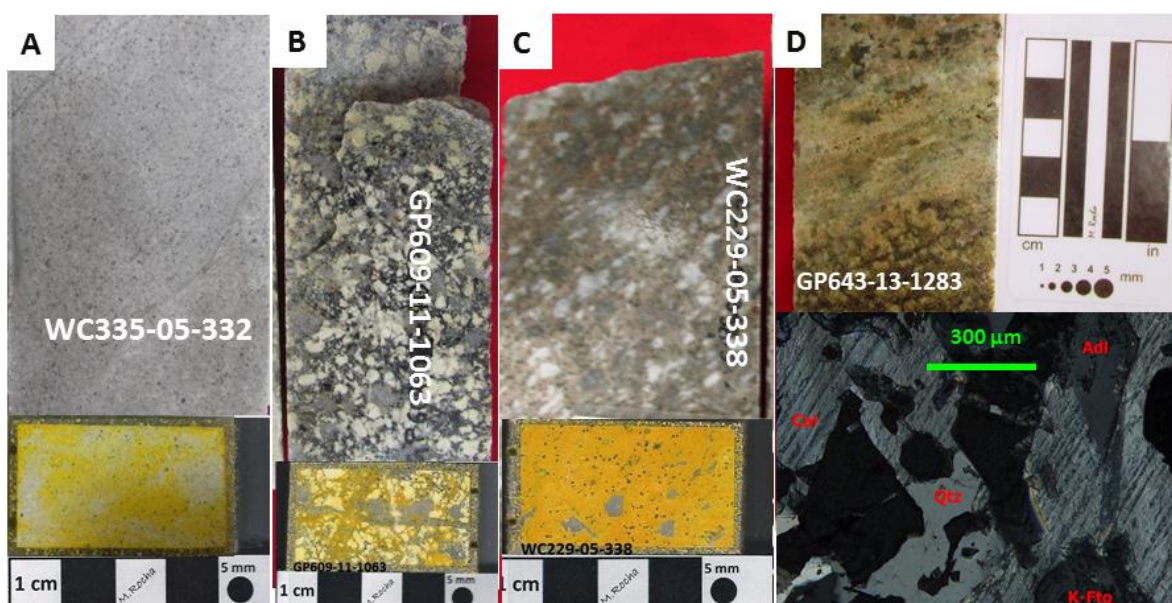
Fig. 4.15. Hand samples and billets showing potassic alteration. The billets are showing the staining of K-feldspar with sodium cobaltinitrite in yellow color. A. Tuffisite showing moderate potassic alteration. B. Quartz feldspar porphyry showing local potassic alteration. C. Deformed quartz feldspar porphyry showing pervasive potassic alteration. D. Skarn of andradite showing adularia (Adl), hydrothermal orthoclase (Fto), and quartz (Qtz). Note: adularia exhibits double prismatic shape, while orthoclase exhibits an irregular shape in D.

The second hydrothermal alteration was caused by interaction between early magma and the calcareous sequence, causing an irregular shell of calc-silicates. This meta-

somatic system was developed through the Jurassic and Cretaceous sedimentary marine sequence and exhibited a mineralogical zonation, forming shells of endoskarn, exoskarn, skarnoid, and hornfels, which are locally intercalated with marble. The skarn system demonstrates a garnet zonation, which includes andradite concentration developed adjacent to the plutonic complex, while the grossular garnet is developed in distal zones from the plutonic complex. The interaction of magmatic fluids and calcareous rock caused a chemical interchange and developed calc-silicates, amphiboles, pyroxenes, recrystallization, and a diffusion of minerals through the marine sequence.
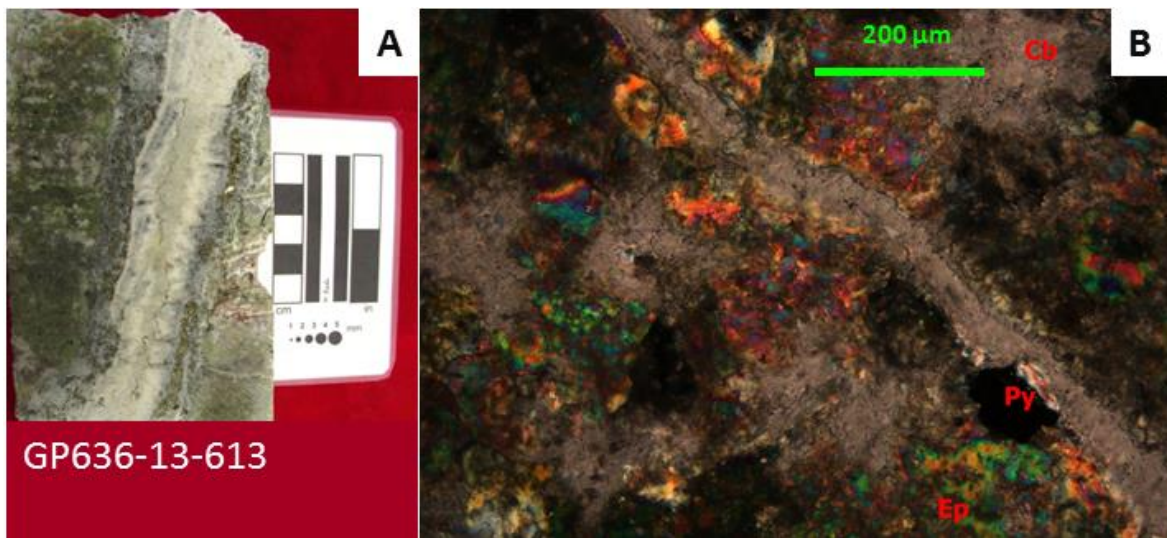
Fig. 4.16. Hand samples and photomicrographs (plane-polarized light) are displaying calc-silicates alteration. A. Skarn of andradite overprinted by epidote and cut by calcite-pyrite vein. B. Photomicrograph displaying epidote (Ep), pyrite (Py) and sericite, and late carbonate.

In addition, a mobilization of retrograde fluids followed, and it is believed that this event could have mobilized metallic ions, increasing the metallic content in some zones. This event was developed through the skarn system and is represented by an epidote-chlorite assemblage (Fig. 4.16).

The third hydrothermal event consisted of a quartz-sericite-pyrite assemblage that developed through the plutonic complex, skarn system, and diatreme breccias. This phyllic alteration formed over a large area and the grade of alteration (i.e. pervasive, moderate, and weak) was controlled by the permeability of the rock package; fractures also played an important role during this stage. Pervasive phyllic alteration is developed through the diatreme breccias. This hydrothermal event presumably is post-mineral (Fig. 4.17).
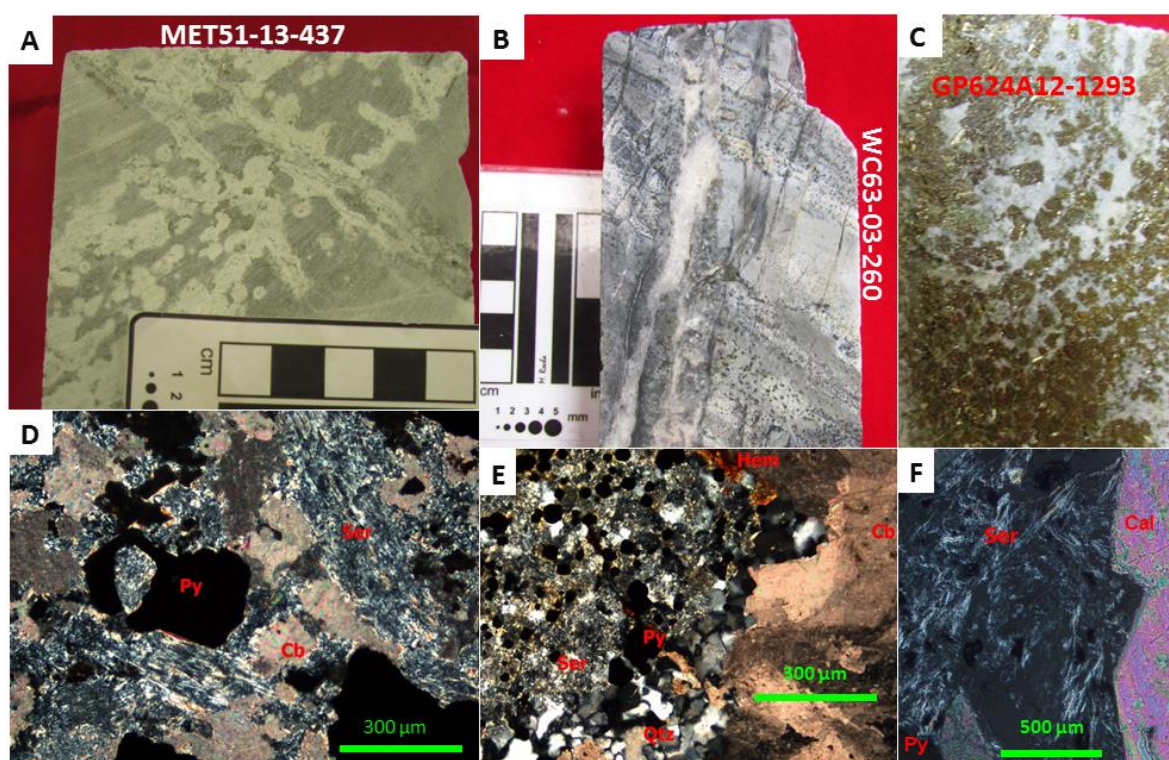
Fig. 4.17. Hand samples and photomicrographs (plane-polarized light) are displaying phyllic altera-
tion. A. B. Siltstone showing pervasive and moderate phyllic alteration in white color. C.
Mineralized skarn sample showing sulfides. D.E. Photomicrographs displaying minerals of
phyllic alteration (sericite-pyrite-quartz) that are overprinted by late carbonate and local
hematite. F. Photomicrograph showing late phyllic alteration minerals (Sericite-pyrite) and
overprinted by calcite.

Some distal zones from the porphyry and the diatreme breccia system exhibit a chlorite-calcite-pyrite assemblage, suggesting propylitic alteration. It is believed that the fluids responsible for this assemblage traveled through narrow fractures in the Caracol

Formation. The hydrothermal alterations mentioned above are usually overprinted by carbonate (i.e. calcite>>dolomite). The carbonate is fine-grained and found in different amounts within any assemblage of hydrothermal alteration and/or metal mineralization (Figs. 4.16, 17).

Weathering effects are present in the shallow levels. These effects developed secondary oxides throughout the Caracol Formation and the diatreme breccias (Fig. 4.18, and Fig. 5.4.). This event caused some metal mobilization and release of precious metals as well as the formation of some clays due to the supergene fluid acidity.
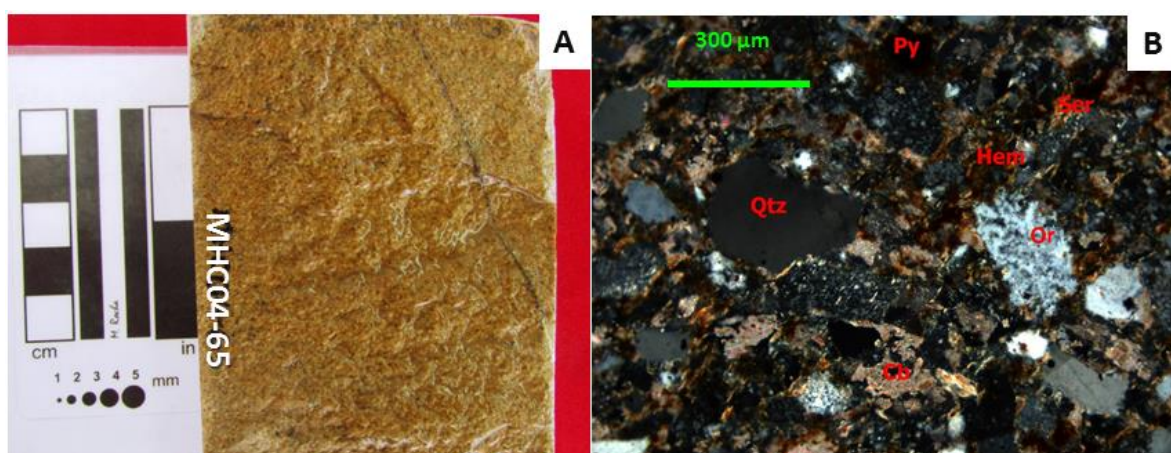
Fig. 4.18. Hand samples and photomicrographs (plane-polarized light) displaying phyllic alteration. A. Siltstone is showing oxidation in light brown color. B. Photomicrograph displaying groundmass of quartz (Qtz) and orthoclase (Or) replaced by oxidized pyrite (Py) and sericite (Ser) partially replaced by hematite (Hem) and all overprinted by carbonate (Cb).

CHAPTER V

MINERALOGY ZONING, GEOCHEMICAL SIGNATURES, AND GEOCHEMICAL HALOS

Mineragraphy

This section presents the results of mineragraphy, mineralogical field observations, and the location of analyzed samples as well as the relationship between mineralization and hydrothermal alteration. In Peñasquito, several hydrothermal stages occurred and developed mineral assemblages that are concentrated in different ore bodies. The zonation has been recognized throughout a depth of 2,000 meters in the explored Mesozoic marine sequence. The main ore bodies include the diatreme breccia system, stockwork and veins, the skarn system, and mineralized potassic zones in the porphyry complex. Therefore, a mineralogical study was conducted in order to understand the paragenetic succession as distinguished by ore microscopy. The mineralogy consists of primary sulfides and oxides, sulfosalts, secondary oxides, gold, electrum, bismuthinite, and subordinate minerals, such as rhodochrosite, rhodonite, calcite, fluorite, and quartz. The associated hydrothermal alteration includes orthoclase-biotite-apatite, calc- silicates, sericite-pyrite-quartz, magnetite-epidote-chlorite-calcite, and carbonates.

Sampling and Methodology of Mineragraphy Analyses

Samples were handpicked from drill cores distributed throughout the explored area where the geological context was well known due to detailed logging during field work. The mineragraphy focused on specimens with complicated epigenetic mineralogy from

different ore bodies and depths. The mineragraphy was investigated by conventional and scanning electronic microscopes. The sampling included specimens from the porphyry complex, the skarn system, stockwork, veins, and the diatreme breccia system. The specimens were situated between 1,901 to 100 m in elevation (m.a.s.l.) and distributed through the Peñasquito ore bodies and porphyry complex. In total, 223 samples were analyzed, including 57 samples from the porphyry complex, 85 specimens from the skarn system, 59 specimens from the diatreme breccia system, and 22 samples from the stockwork system and veins (Fig. 5.1).
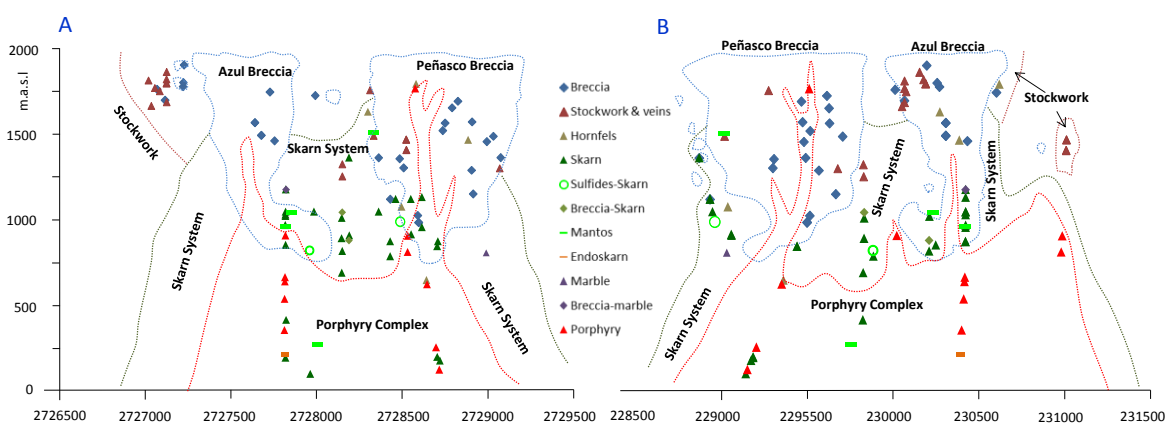
Fig. 5.1. Sample distribution for mineragraphy analysis (data projected). Also shown are the geologic cross sections of the Peñasquito ore deposit. A. Cross section looking to the west. B. Cross section looking to the north.

The mineragraphic analyses were completed on polished thin sections and represented the bulk of economic mineralogy. The polished thin sections were initially prepared at a thickness of 30 microns on a glass slide completed by Spectrum Petrographics Inc. Laboratory. Subsequently, the mineragraphy and petrography was completed with a traditional optical microscope (i.e. Olympus BX53 and BX52) with reflected and optional transmitted light, where the minerals were identified and quantified. The mineragraphy

was performed in the ore petrography laboratory at the University of Nevada, Reno campus. Additionally, selected samples were completed by a SEM (Scanning Electron Microscope) technique after the mineragraphy analysis. The SEM analyses were performed in the Chihuahua Experimental Laboratory at the Mexican Geological Survey. Specifically, the SEM (i.e. JXA-8230 with 5 WDS spectrometer and Jeol brand) analyses consisted of several steps: (1) a selection of specific sites were completed on samples by traditional microscopy technique; (2) the sample was covered by carbon in an empty evaporator; (3) the sample was placed in the holder of the SEM microscope; (4) the sample was scanned by an EDS analyzer in order to identify, map, and quantify elements in the sample; and (5) the quantified mineral species were verified, using contents and/or grades by a stoichiometric substitution or a chemical balancing in order to determine the identity of the scanned mineral.

Mineralogical Metal Distribution

The metallic epigenetic concentrations in Peñasquito are composed primarily of sulfides and sulfosalts with lesser amounts of carbonates and silicates as well as metallic supergene concentrations of oxides present at shallow levels. The mineralogy demonstrates a zonation through the hydrothermal system, although the diatreme breccia system presented a mineralogical mixture, which occurs mostly as disseminations and fracture fillings, as well as massive sulfides in mantos. Primary mineralization is associated with shells of calc-silicates and potassic alteration at depth. Secondary mineralization occurs as disseminations and fracture fillings of oxides, local sulfides and sulfosalts, and subordinate carbonates.
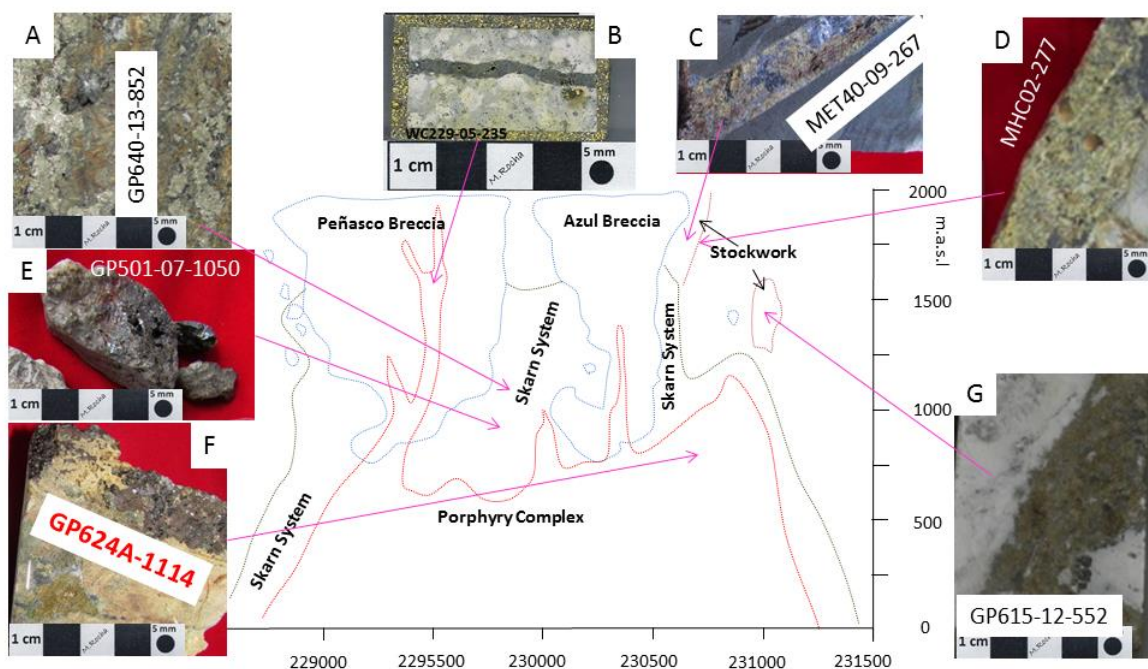
Fig. 5.2. Zones of the Peñasquito ore deposit showing the sphalerite type. The cross section is looking to the north. A. Drill core sample showing brown sphalerite from mantos within the skarn system. B. Billet showing vein filled by dark brown sphalerite that is cutting a porphyry dike. C-D-G. Drill core samples showing blond sphalerite from the stockwork. E-F. Hand samples showing dark brown sphalerite from the skarn system.

The primary sulfides found in Peñasquito include pyrite, sphalerite, galena, chalcopyrite, molybdenite, and subordinate amounts of bornite, covellite, arsenopyrite, pyrrhotite, tennantite, tetrahedrite, and marcasite. Two stages of pyrite have been identified throughout the whole hydrothermal system; however, the stage 1 pyrite is correlated with the main mineralization stage, while the stage 2 pyrite is related to phyllic alteration, which included sericite with lesser amounts of quartz and local marcasite. Sphalerite and galena occur together throughout the diatreme breccias, stockwork and veins, and the skarn system with lesser amounts in the porphyry complex and massive concentrations in the skarn system. The sphalerite usually exhibits a range in color from blond (at shallow

levels) to light brown (at middle levels) and then to dark brown (at deeper levels) (Fig. 5.2).
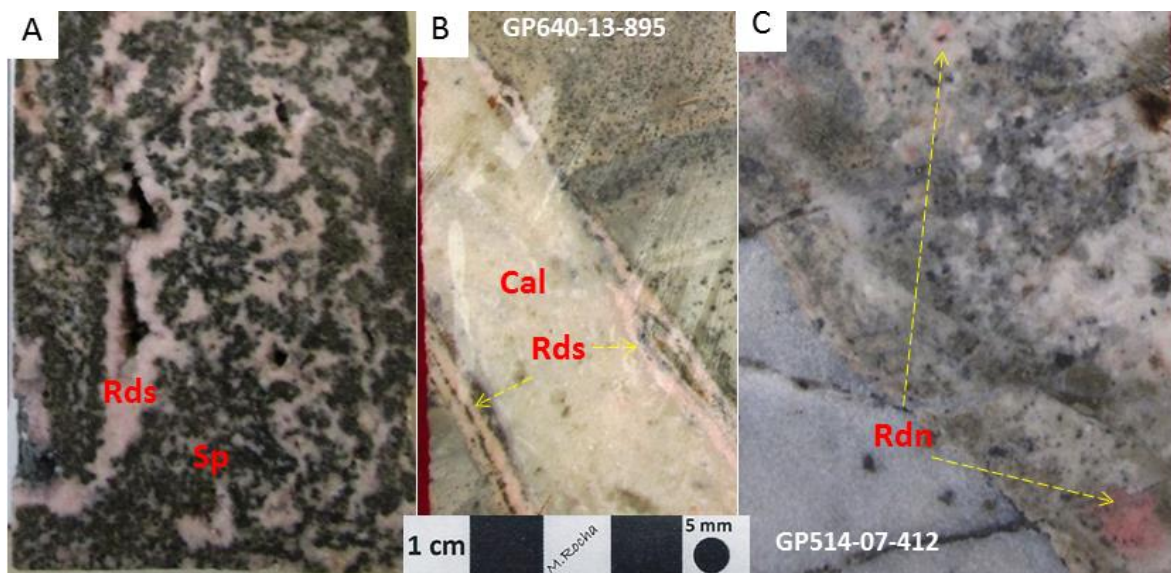
Fig. 5.3. Specimens showing rhodochrosite and rhodonite from Peñasco ore deposit. A. Rhodochrosite (Rds) appears to be open space filling around sphalerite (Sp) from western Peñasco Breccias at 1,860 m.a.s.l. B. Calcite (Cal) and rhodochrosite vein cutting through the hornfels. C. Rhodonite (Rdn) disseminated in the skarn system.

The chalcopyrite occurs in lesser amounts in the diatreme breccias, stockwork, and veins, but increases with depth in the skarn system and porphyry complex. The molybdenite occurs in lesser amounts in diatreme breccias, stockwork, and veins and in greater amounts in the porphyry complex and locally in the skarn system. Arsenopyrite and pyrrhotite are found in the skarn systems. The bornite and covellite occur in decreasing amounts in the diatreme breccias, stockwork, and veins and in even lesser amounts in the skarn system.

The most common sulfosalts are tetrahedrite, tennantite, and acanthite, which occur as irregular aggregates in the diatreme breccias, stockwork, and veins with a decreasing amount in the skarn system and an even lesser amount in the porphyry complex. The

gold, silver, and electrum are usually associated with epigenetic sulfosalts. Rhodochrosite appears to be open space filling in sphalerite and galena in the diatreme breccias, stockwork zones, and veins, indicating a late mineralized stage (Fig. 5.3A). In addition, rhodonite is locally present in the skarn system (Fig. 5.3C).
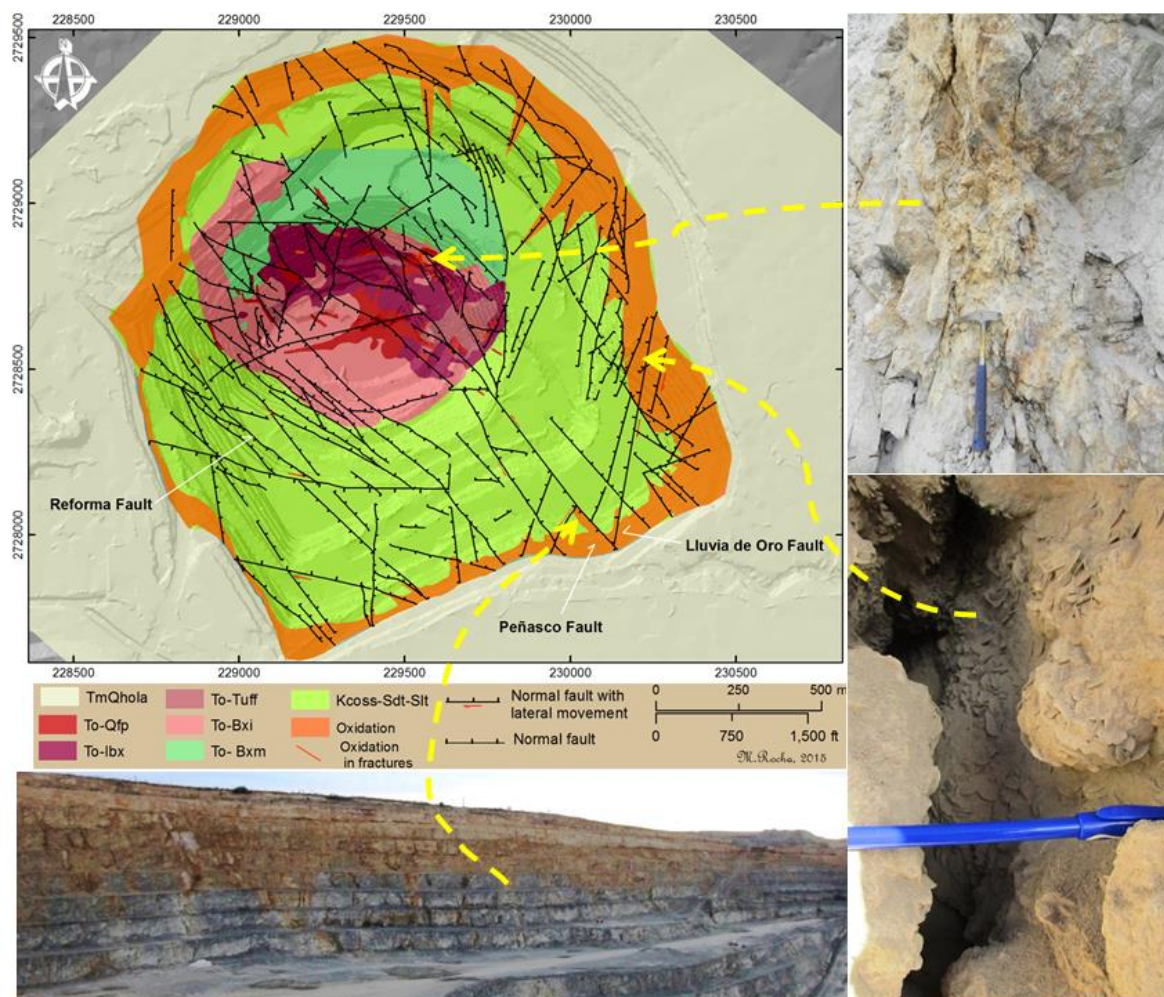
Fig. 5.4. Map showing the oxidation influence. The photographs showing limonite minerals in Peñasco open pit. The map by the author and Exploration staff of Peñasquito (2014).

The leached and primary oxides present in some ore bodies include limonite minerals and magnetite. The primary sulfides and sulfosalts have been affected by the leaching process resulting in secondary oxides, such as hematite, goethite, and jarosite. In general,

these secondary oxides form an extensive semi-flat area at shallow levels in the Caracol

Formation and the diatreme breccia system (Fig. 5.4).
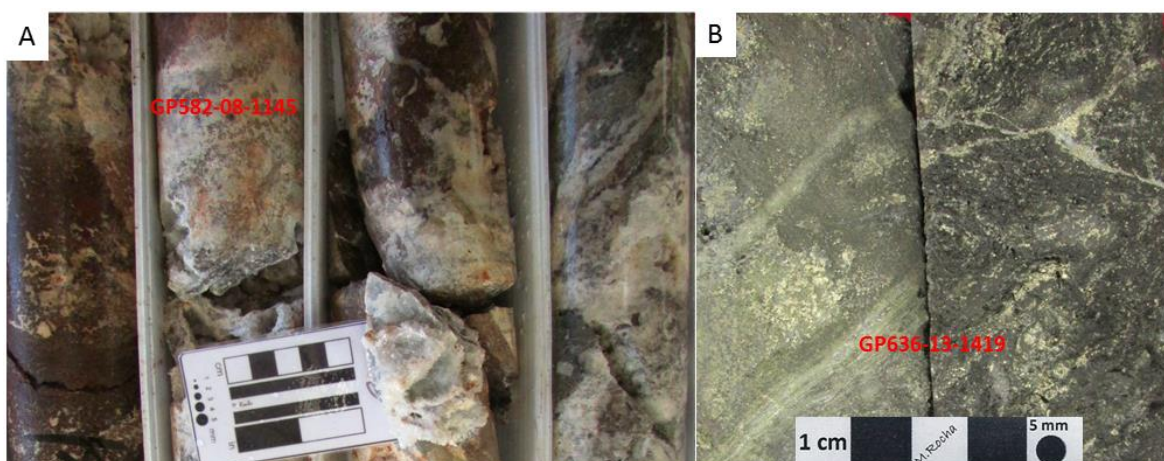
Fig. 5.5. Photographs showing representative specimens of secondary and primary oxides drill
cores. A. Secondary hematite hosted in the skarn system. B. Massive magnetite hosted in
the skarn system.

In the Peñasco open pit, the bulk of the leaching is up to 90 meters in thickness (i.e.

1,970 and 1,881 m.a.s.l.) and strongly developed along fractures and faults, forming

downward peaks with a saw-tooth shape. Peñasco Breccia exhibits exotic limonites that

are developed along faults and fractures for more than 300 meters in depth (Fig. 5.4). This

shallow oxidation is composed of jarosite and lesser amounts of goethite and hematite,

and some faults and fractures exhibit carbonates and silicates of copper. Moreover, the

oxidation that has been found up to 935 m deep (i.e. 1,035 m.a.s.l.) is developed in the

skarn system (Fig. 5.5A), suggesting post-mineral deep and open fractures. This oxidation

is developed in the mantos and skarn breccia, which mainly includes hematite as well as

lesser goethite and subordinate carbonates. Primary magnetite occurs locally in massive

concentrations in the endoskarn (Fig. 5.5B) and as disseminations in mineralized shells of

exoskarn and porphyry.

Paragenesis for the Porphyry Complex

The primary economic mineralization (Au-Cu-Zn-Mo) in the porphyry complex occurs as disseminations and fracture fillings, which includes primary sulfides with lesser amounts of sulfosalts, and primary and secondary oxides. The bulk of the economic mineralization is developed in a potassic alteration shell, and the molybdenite is hosted in quartz monzonite porphyry. The paragenesis includes five types of products: (1) igneous (2) an early potassic alteration, (3) primary sulfides and oxides, fluorite, sulfosalts, and oxides, (4) two late hydrothermal alteration assemblages, and (5) supergene minerals (Table 5.1).

Table. 5.1. Paragenetic sequence for the porphyry complex.

| Mineral | Hypogene | | | | Supergene |
	Igneous	Alteration	Mineralization	Late Alteration	
Plagioclase	--------			-----	
Quartz	---	-------			
Zircon	-				
Sphene	-				
Biotite	--	-----			
Orthoclase	---		--------		
Apatite		--			
Magnetite			--		
Pyrite			----	----	
Fluorite			--		
Molybdenite			--		
Sphalerite			----		
Galena			---		
Chalcopyrite			---		
Tennantite			--		
Tetrahedrite			--		
Acanthite			--		
Wollastonite				-	
Chlorite				--	
Epidote				--	
Sericite				------	
Calcite				-----	
Hematite					------
Jarosite					---
Goethite					---

The mineralized zones are developed in monzonite, quartz-monzonite, and quartz-monzodiorite porphyries, which exhibit potassic and phyllic assemblages. These porphyries consist of orthoclase and plagioclase phenocrysts, quartz eyes, biotite, local magnetite, which are floating in a fine groundmass of quartz, orthoclase, apatite, quartz-sericite-pyrite, and carbonate. The monzonite and quartz-monzonite are cut by veinlets of quartz, quartz-sericite, biotite, and fluorite-molybdenite.
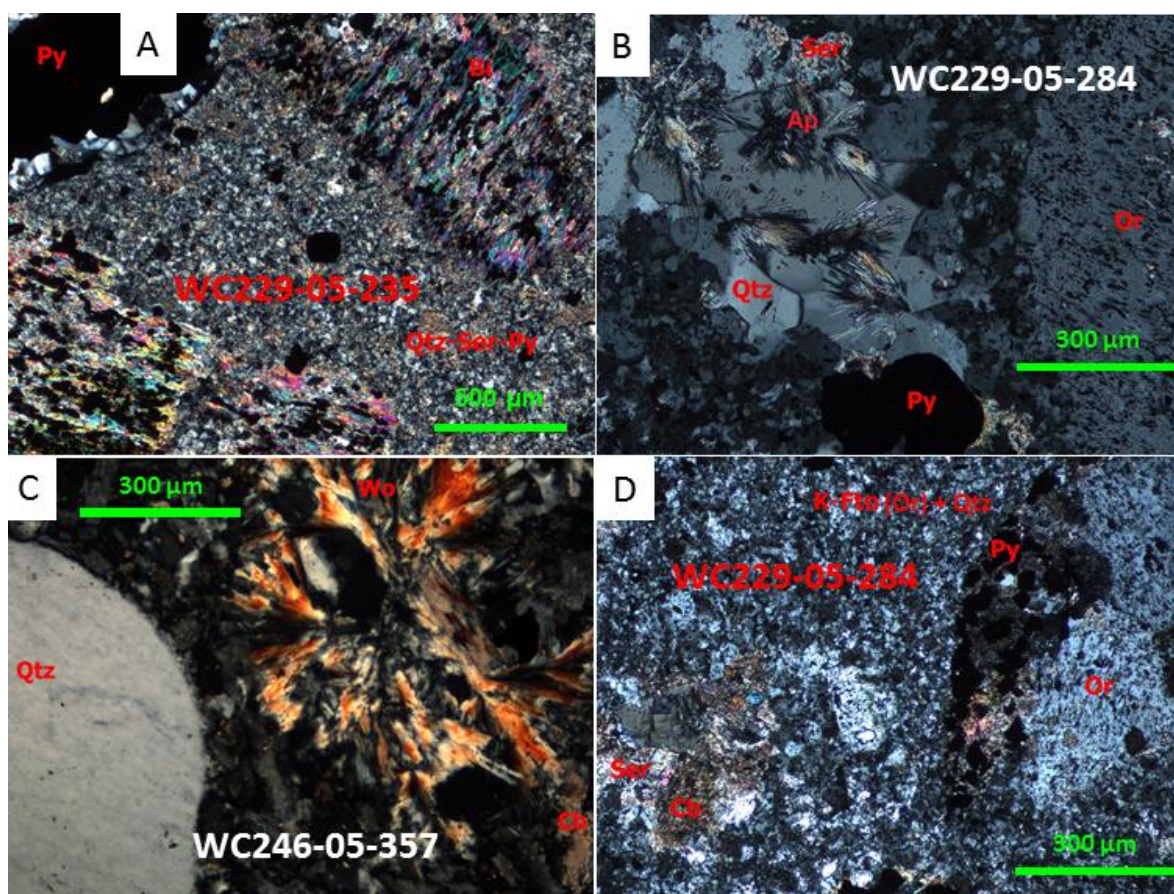
Fig. 5.6. Photomicrographs (plane-polarized light) showing alteration minerals from the productive porphyry complex. A. Biotite (Bi) phenocrysts floating in groundmass and replaced by pyrite (Py), sericite (Ser), and quartz (Qtz). B. Groundmass replaced by apatite (Ap) and orthoclase (Or) overprinted by quartz-sericite-pyrite. C. Wollastonite (Wo) has replaced groundmass of quartz-orthoclase, and overprinted by carbonate. D. Groundmass altered by orthoclase (Fto) overprinted by quartz-sericite-pyrite and carbonate (Cb).

The potassic alteration consists of quartz, orthoclase, hydrothermal biotite, and apatite developed in the groundmass (Fig. 5.6). Wollastonite and magnetite are locally present in the groundmass, suggesting a close relationship with the skarn system and limestone. Magnetite is replaced by pyrite and chalcopyrite (Fig. 5.7A).
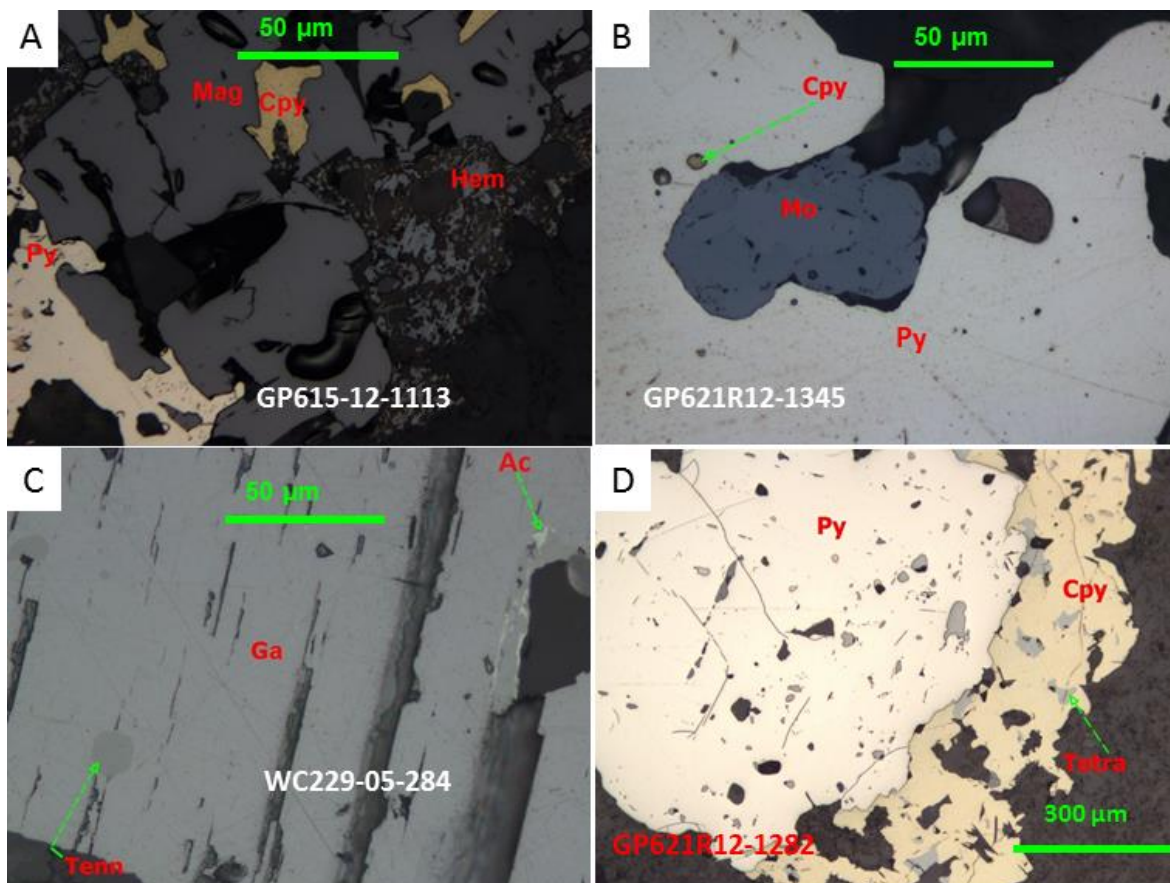
Fig. 5.7. Photomicrographs (reflected light) showing primary sulfides, oxides, and sulfosalts. A. Magnetite (Mag) replaced by pyrite (Py) and chalcopyrite (Cpy), and hematite (Hem). B. Pyrite replaced by molybdenite (Mo) and chalcopyrite. C. Galena replaced by tennantite (Tenn) and acanthite (Ac). D. Pyrite replaced by chalcopyrite and tetrahedrite (Tetra).

The primary sulfides include primary pyrite, molybdenite, sphalerite, galena, and chalcopyrite. Stage 1 pyrite (up to ~5%) exhibits a sub-euhedral shape, is coarse-grained (up to 3 mm in size), and replaced by sphalerite, galena, local sulfosalts, chalcopyrite,

quartz-sericite, and carbonate. Sphalerite is replaced by sulfosalts, chalcopyrite (as veinlets and inclusions), and carbonate. Galena is fine-grained, replaced by sulfosalts, and associated with sphalerite (Fig. 5.7C).

The common sulfosalts include tetrahedrite, tennantite, and acanthite, which exhibit anhedral shapes, range in size between coarse-grained and medium-grained, and are re-placed by chalcopyrite, quartz-sericite, and carbonate. Tennantite is usually encapsulated by tetrahedrite, and the acanthite replaced tetrahedrite. Primary sulfides and sulfosalts locally exhibit brecciation and are cemented by carbonates. The fluorite occurs in veinlets and is associated with molybdenite. The sericite, stage 2 pyrite, and quartz are present in the groundmass with intensity ranges between pervasive and weak. Stage 2 pyrite is euhedral in shape and fine-grained. The feldspar phenocrysts are locally altered to sericite and cut by carbonate veinlets. The carbonate is present in the groundmass and replaces phyllic and potassic alteration, suggesting a late hydrothermal event. The supergene minerals include hematite, goethite, and jarosite which are developed around chalcopyrite and magnetite (Fig. 5.7A). All petrography and mineralogy data are reported in Appendix B.

Paragenesis for the Skarn System

The primary Au-Cu-Pb-Zn-Ag mineralization in the skarn system occurs as dissemina-tions, massive replacement mantos, and in local fracture fillings of primary sulfides with lesser amounts of sulfosalts and primary and secondary oxides. This metasomatic system exhibits a mineralogical zonation of endoskarn, exoskarn, skarnoid, and hornfels shells, as

well as, breccias present in the skarn systems with fragments of skarn, sulfides, and marble cemented by carbonates, sulfides, and local epidote, suggesting a relationship with diatreme breccias, and fluidization and collapse processes. These ore bodies exhibit metallic grades of Au (up to 344 ppm), Ag (up to 7,168 ppm), Zn (up to 39.3%), Pb (49.6%), Cu (8.48%), Mo (0.48%) and are developed adjacent to and beneath the diatreme breccias.

Table 5.2. Paragenetic sequence for the skarn system.

Mineral	Hypogene			Supergene
	Alteration	Mineralization	Late Alteration	
Biotite	--			
Orthoclase	---			
Garnet	-------			
Pyroxene	-----			
Amphibole	-----			
Wollastonite	---			
Magnetite		----		
Pyrite		----	-------	
Sphalerite		------		
Galena		----		
Pyrrhotite		-		
Arsenopyrite		-		
Fluorite		-		
Chalcopyrite		----		
Tennantite		---		
Tetrahedrite		---		
Acanthite		--		
Enargite		-		
Hessite		-		
Freibergite		-		
Gold		-		
Silver		-		
Electrum		-		
Bismuth		-		
Bismuthinite		-		
Adularia			-	
Epidote			--------	
Chlorite			----	
Marcasite			----	
Quartz			-------	
Sericite			-------	
Rhodonite			-	
Rhodochrosite			--	
Calcite			------	
Dolomite			--	
Bornite				---
Chalcocite				--
Covellite				--
Cuprite				--
Digenite				--
Hematite		--		---

The ore bodies are locally affected by potassic alteration; other zones exhibit pervasive retrograde and phyllic alterations that are present throughout the skarnoid and hornfels shells. The bulk of the metallic economic mineralization in the skarn system has been

intercepted between 1,250 and 750 meters above sea level. The mineralogical succession

includes several stages: (1) metasomatism minerals, (2) primary sulfides, sulfosalts, and

precious native elements, (3) local brecciation stage, (4) three stages of hydrothermal

alteration assemblages, and (5) supergene minerals (Table 5.2).
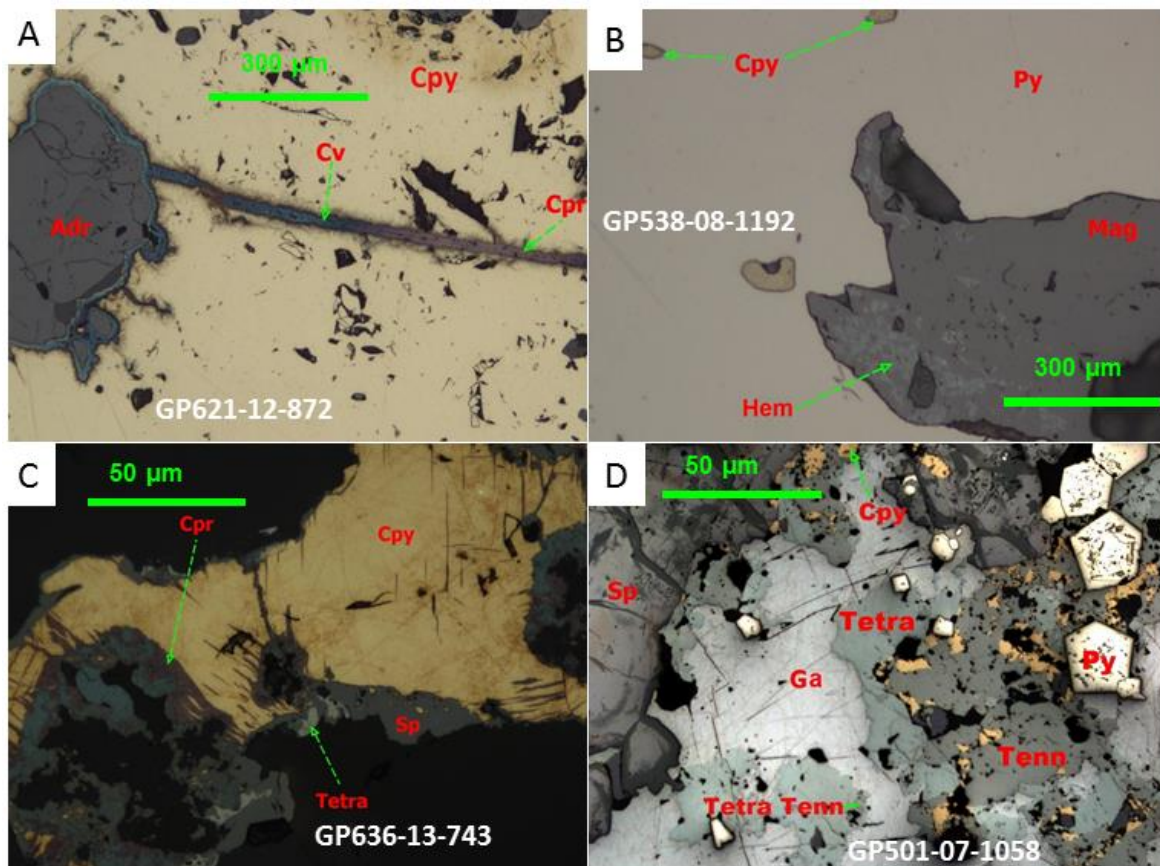
Fig. 5.8. Photomicrographs (reflected light) showing primary sulfides, sulfosalts, and supergene minerals from the skarn system. A. Chalcopyrite (Cpy) in andradite (Adr) skarn replaced by covellite (Cv) and cuprite (Cpr). B. Magnetite (Mag) replaced by hematite (Hem) and pyrite, and pyrite (Py) replaced by chalcopyrite. C. Chalcopyrite replaced by cuprite and sphalerite that is replaced by tetrahedrite (Tetra). D. Pyrite 1 (Py) replaced by galena (Ga), sphalerite (Sp), tetrahedrite (Tetra), Tennantite (Tenn), and Chalcopyrite; galena and sphalerite replaced by chalcopyrite, tetrahedrite, and tennantite.

The direct interaction between magmas and calcareous rocks developed zoned

shells made up of phenocrysts (i.e. pyroxenes, amphiboles, and plagioclase), primary sul-

fides and oxides, sulfosalts, local retrograde minerals, K-feldspar (orthoclase and local

adularia), sericite-quartz, and carbonates. It is believed that this zonation was influenced by the components of each protolith and the hydrothermal fluids from the porphyry complex.

Chemical formula	ms%	mol%	Sigma	Net	K rat
S	15.46	37.14	0.16	7559329	0.0000000
Fe	1.35	1.86	0.61	257806	0.0000000
Cu	5.01	6.07	1.16	602635	0.0000000
Ag	67.35	48.08	0.49	198520840	0.0000001
Sb	10.83	6.85	0.93	1940671	0.0000000
Total	100.00	100.00			

Chemical formula	ms%	mol%	Sigma	Net	K rat
Ag	18.06	28.70	0.35	4342663	0.0000000
Au	81.94	71.30	0.33	225892700	.0000001
Total	100.00	100.00			
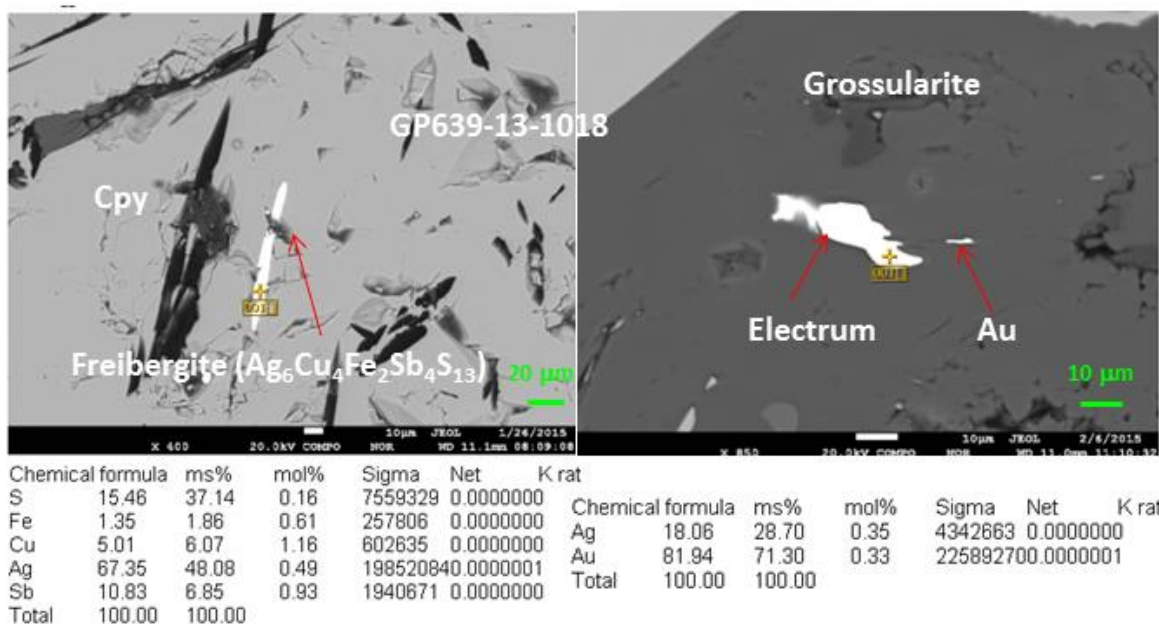
Fig. 5.9. Photomicrographs (Scanning Electron Microscope JXA-8230 9s) showing freibergite, electrum, and gold in vugs and veinlets within chalcopyrite and garnet.

In the first mineral zone, an endoskarn shell was developed within the borders of the porphyry complex; it ranges up to five meters in width. The phenocrysts, such as plagioclase (Ab_{62}-An_{38}), biotite, orthoclase, and pyroxene, exhibit a chaotic texture and subhedral shapes, were partially replaced by primary sulfides, primary oxides, sulfosalts, epidote, chlorite, and local sericite-quartz. Stage 1 pyrite (up to 7%) is coarse-grained and disseminated, exhibits an anhedral shape, and is replaced by magnetite and chalcopyrite (Fig. 5.8B), sphalerite, galena, and sulfosalts (Fig.5.8D). The magnetite (up to 10%) exhibits an anhedral shape, ranges in size between fine-grain and medium-grain, and is replaced by chalcopyrite and hematite (Fig. 5.8B).

The chalcopyrite (up to 3%) exhibits an anhedral shape and is replaced by stage 2 pyrite, bornite, digenite, cuprite, chalcocite, and covellite (Fig. 5.8A-C). The tennantite is usually encapsulated by tetrahedrite (Fig. 5.8D).The tetrahedrite, tennantite, and acanthite exhibit anhedral shapes, and are replaced by enargite, hessite, freibergite, gold, silver, electrum, bismuth, and bismuthinite (Figs. 5.9, 10, 11).

Chemical formula	ms%	mol%	Sigma
S	19.40	56.56	0.13	1602394
Ag	17.63	15.28	0.45	640228
Bi	62.97	28.16	0.58	2644971
Total	100.00	100.00		

Chemical formula	ms%	mol%	Sigma
Fe	2.05	5.73	0.65	359826
Ag	2.36	3.41	0.65	517443
Te	41.03	50.14	1.00	6935375
Bi	54.56	40.72	0.82	1176231
Total	100.00	100.00		
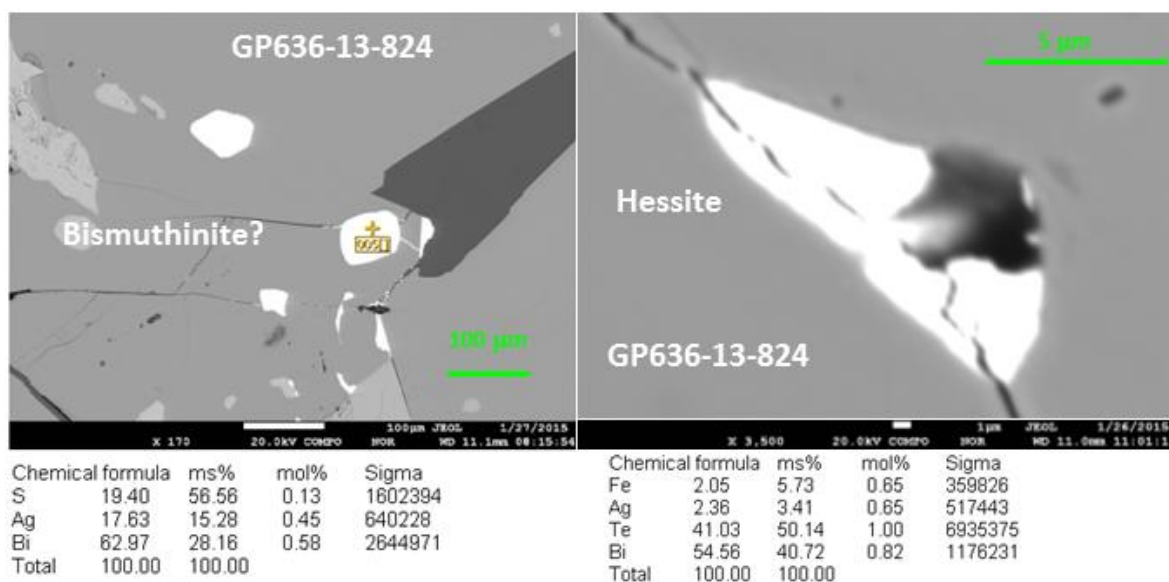
Fig. 5.10. Photomicrographs (Scanning Electron Microscope JXA-8230 9s) showing bismuthinite and hessite in vugs within chalcopyrite and pyrite.

The retrograde alteration consists of chlorite and epidote that exhibit anhedral shapes and are present in the groundmass. The phyllic alteration consists of sericite, stage 2 pyrite and minor quartz. Stage 2 pyrite (up to 3%) is fine-grained, occurs in veinlets and in the groundmass, is euhedral-subhedral, and related to sericite and quartz. Carbonate is present in the groundmass, exhibits an irregular shape, is fine-grained, and replaced by sericite and groundmass, indicating a late alteration stage.

GP628-12-1065

Pyrite

20 μm

Tennantite (03)

04

Enargite (01)   02

(05)

03

Chemical formula	ms%	mol%	Sigma
S	29.66	48.62	0.16	15646088
Fe	10.61	9.99	0.52	2645391
Cu	32.33	26.75	1.06	4752005
As*	10.42	7.31	11.97	160450
Sb	16.98	7.33	0.71	4514155
Total	100.00	100.00		

04

	ms%	mol%		Sigma
C	0.00	3.42	0.00	11211
S	0.00	38.60	0.00	469070
Fe	0.00	1.62	0.00	10835
Cu	0.00	38.90	0.00	169933
As	0.00	8.82	0.00	18643
Sb	0.00	3.50	0.00	65083
Pb	0.00	5.14	0.00	200306
Total	0.00	100.00		

05

	ms%	mol%		Sigma
C	0.00	6.57	0.00	21460
S	0.00	38.65	0.00	468444
Fe	0.00	22.38	0.00	147221
Cu	0.00	24.30	0.00	105211
Sb	0.00	1.30	0.00	24072
Pb	0.00	6.80	0.00	264141
Total	0.00	100.00		

01

Chemical formula	ms%	mol%	Sigma
S	27.17	45.35	0.15	17094138
Fe	1.02	0.98	0.44	339451
Cu	30.16	25.40	0.88	6014146
As	36.26	25.90	10.22	732086
Sb	5.38	2.37	0.62	1816387
Total	100.00	100.00		

02

Chemical formula	ms%	mol%	Sigma
S	25.99	45.44	0.15	14297383
Fe	2.78	2.79	0.46	748778
Cu	32.73	28.88	0.93	5269611
As*	17.93	13.42	10.57	300147
Sb	20.58	9.47	0.63	5902527
Total	100.00	100.00		

Fig. 5.11. Photomicrographs (Scanning Electron Microscope JXA-8230 9s) showing enargite and tennantite in vugs within pyrite.

In the second zone, an exoskarn of garnet (grandite) exhibits metallic mineralization that occurs as disseminations, fracture fillings, and massive mantos. The metallic mineralization includes primary sulfides, oxides, sulfosalts, bismuthinite, gold, and super-gene minerals, as well as retrograde minerals (epidote and chlorite), orthoclase, local adularia, sericite-quartz, and carbonate. The andradite is euhedral in shape, coarse-grained, developed near the porphyry with gradual zones outward to grossularite (i.e. distal to the porphyry), and partially replaced by magnetite, primary sulfides, retrograde minerals, orthoclase and local adularia, sericite-quartz, and carbonate. Two stages of magnetite are present and exhibit anhedral shapes and are replaced by sphalerite, galena, chalcopyrite, pyrrhotite, and sulfosalts. Stage 1 pyrite is anhedral in shape, medium-grained, replaced by galena, sphalerite, chalcopyrite, magnetite, pyrrhotite, and sulfosalts (Fig. 5.12A). The sphalerite is dark brown in color, exhibits euhedral shape, ranges in size between fine-grain and coarse-grain, is related to galena, and replaced by chalcopyrite, sulfosalts, and

local gold (Fig. 5.12C). Galena is fine-grained, associated with sphalerite, and replaced by sulfosalts and stage 2 pyrite. Chalcopyrite exhibits an anhedral shape, is replaced by pyrite and galena, and developed into sphalerite as inclusions and also onto the cleavage (Fig. 5.12D). The tetrahedrite and tennantite are fine-grained, anhedral in shape, and replaced sphalerite and pyrite (Fig. 5.12B).The retrograde alteration is made of chlorite and epidote that exhibit anhedral shapes and are present in the groundmass. The potassic alteration, which consists of adularia and orthoclase, is locally present throughout the bedding in the exoskarn zones. The phyllic alteration consists of sericite, pyrite and minor quartz. This pyrite (up to 3%) is fine-grained, found in veinlets and the groundmass, euhedral in shape, and associated with sericite and quartz. The exoskarn locally exhibits massive concentrations of fine-grained fluorite that are purple in color and intercalated with andradite.

Mantos were developed in the exoskarn and local marble shell, which include massive primary sulfides (Py, Sp, Ga, Po, Mrc), sulfosalts (tetrahedrite, tennantite and acanthite), local secondary oxides (hematite), supergene minerals (covellite and bornite), local fine-grained orthoclase and sericite-quartz.

In addition, breccia zones are present in the exoskarn shell, and three main breccias types are identified: (1) a breccia made of skarn and chalcopyrite, cemented by a breccia matrix (skarn micro-fragments) and calcite, developed at depth and near the porphyry complex; (2) a breccia made up of skarn fragments and lesser disseminated sulfides and sulfosalts, cemented by calcite and limonite, developed between both diatremes breccias; and (3) a breccia made up of marble fragments, cemented by a breccia matrix that in-

cludes micro-fragments of skarn, sulfides, and calcite, and developed between exoskarn and marble shells (Fig. 5.13).
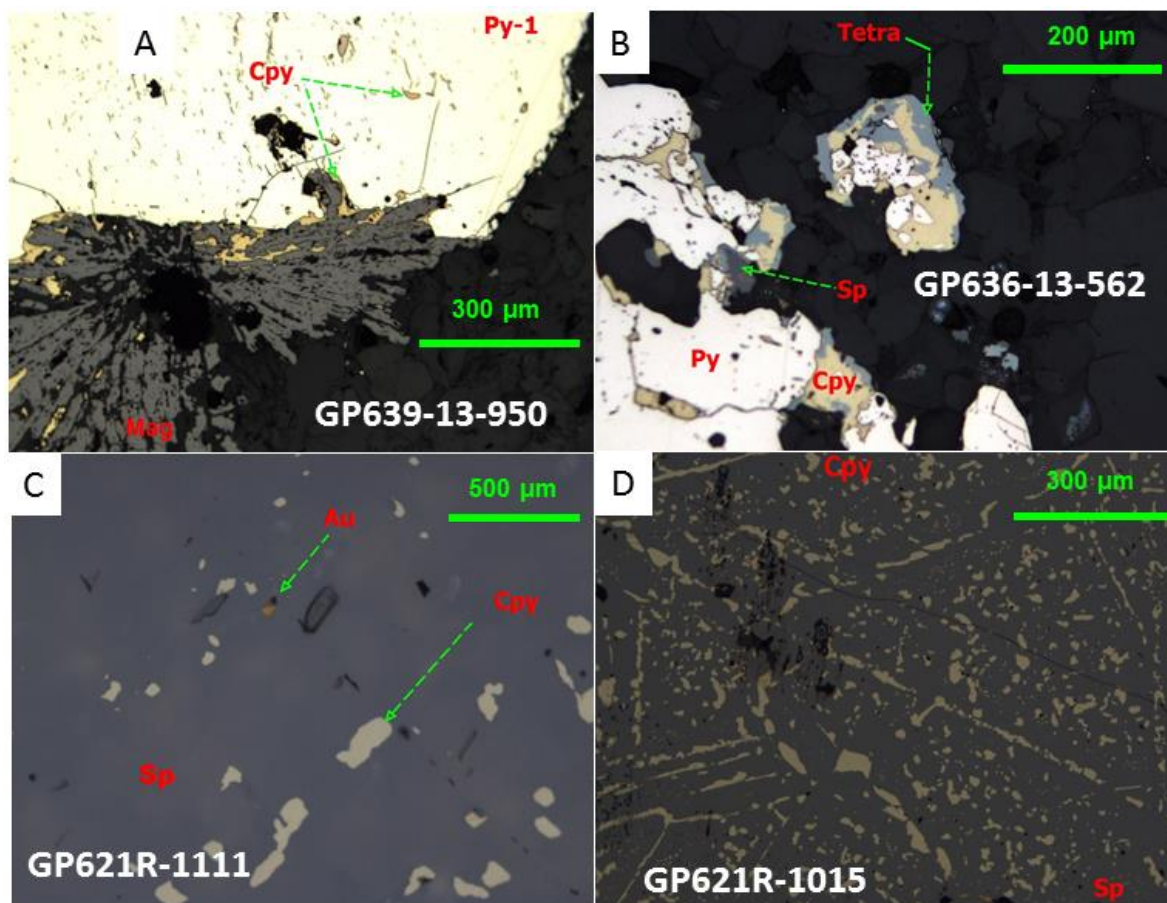
Fig. 5.12. Photomicrographs (reflected light) showing primary sulfides and oxides, sulfosalts, and free gold the skarn system. A. Prismatic Magnetite (Mag) pseudomorphs of specularite partially replaced by pyrite (Py) and subsequent chalcopyrite (Cpy) replaced both. B. Pyrite (Py) replaced by chalcopyrite and sphalerite (Sp), and all replaced by tetrahedrite (Tetra). C. Gold and chalcopyrite are hosted in sphalerite. D. "Disease" texture of sphalerite replaced by chalcopyrite.

In the third zone, a skarnoid consists of wollastonite, tremolite, calc-silicates (fine-grained), primary sulfides (Py, Zn, Ga, Mrc), local sulfosalts, gold, retrograde minerals (epidote and chlorite), sericite-quartz, carbonate, and supergene minerals. The bulk of the skarnoid was developed between the Indidura and Caracol formations, and this halo grades outward into hornfels (Fig. 5.13). Metallic mineralization is present as small

disseminated grains and veinlets. All petrography and mineralogy data are reported in Appendix B.
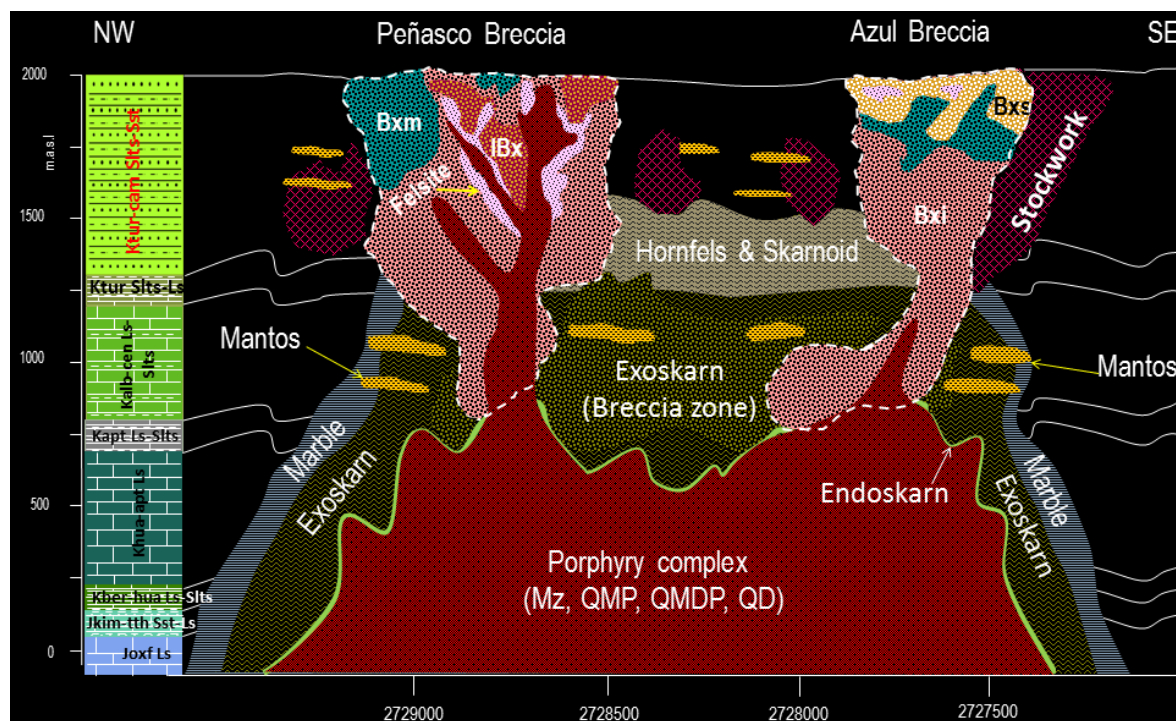
Fig. 5.13. Schematic cross section showing zonation of the skarn system and mineralized bodies in the Peñasquito polymetallic ore deposit. The cross section is oriented at 340° and looking to the northeast. The lithology column is displayed on left side.

Paragenesis for the Stockwork Zones and Veins

The stockwork zones and veins consist of crossing fractures, faults, and veinlets that are filled by primary sulfides, sulfosalts, and subordinate carbonates; however, local oxides are also present. These ore bodies exhibit good metallic grades of Au (up to 5 ppm), Ag (up to 1,325 ppm), Zn (up to 16.8%), Pb (22.3%), and Cu (0.5%) and are developed adjacent to diatreme breccias hosted in the Caracol Formation. The veinlets and veins found in these ore bodies exhibit a range of thicknesses from millimeters to meters, and are associated with hydrothermal breccias. The ore bodies are usually affected by phyllic alteration

that ranges from moderate to pervasive intensity, and chlorite is also present as an altera-

tion product. The paragenesis includes three types of products: (1) primary sulfides, sul-

fosalts, and precious native minerals; (2) three stages of hydrothermal alteration assem-

blages; and (3) weathering minerals (Table 5.3). All petrography and mineralogy data are

reported in Appendix B.

Table 5.3. Paragenetic sequence for the stockwork and veins.

Mineral	Hypogene — Alteration-Mineralization-Alteration			Supergene
Orthoclase	------			
Pyrite		-------	----	
Sphalerite		----------		
Galena		------		
Chalcopyrite		---		
Tennantite		---		
Tetrahedrite		---		
Acanthite		--		
Gold		-		
Silver		-		
Tellurobismuthite		-		
Fluorite		-		
Quartz			------	
Sericite			------	
Chlorite			---	
Calcite			----	
Rhodochrosite			---	
Chalcocite				---
Covellite				--
Hematite				------
Jarosite				----
Goethite				----

The early mineralization mainly includes primary sulfides (e.g. Py, Sp, Ga, Cpy) and

sulfosalts (e.g. tetrahedrite, tennantite, and acanthite). Primary pyrite (more than 15%)

exhibits sub-euhedral and anhedral shapes, ranges from coarse-grained to medium-

grained, and is replaced partially by galena, sphalerite, chalcopyrite, and sulfosalts. The

sphalerite (up to ~30%) usually exhibits euhedral shape, ranges in size from coarse-grained

to medium-grained, associated with galena, and is replaced by sulfosalts, chalcopyrite,

and stage 2 pyrite. Galena (up to ~5%) exhibits euhedral shapes, ranges in size from
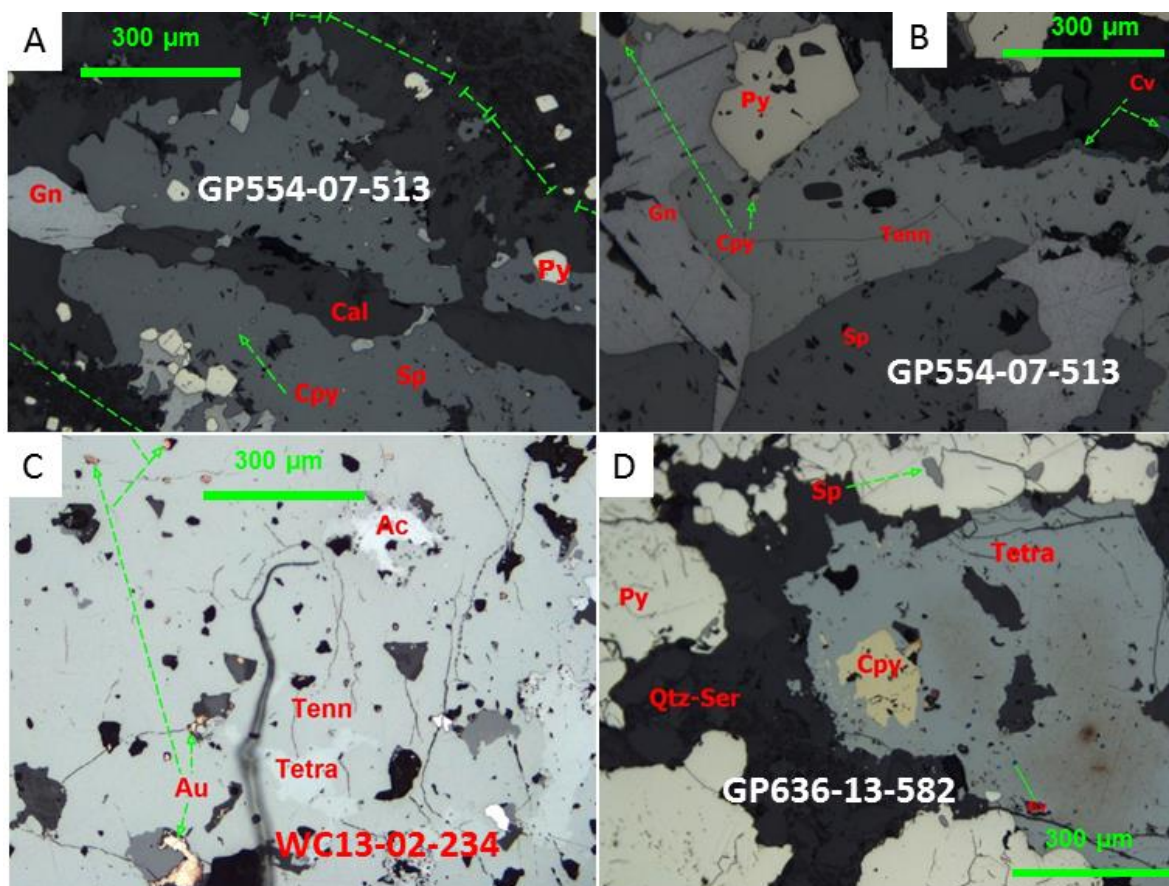
Fig. 5.14. Photomicrographs (reflected light) showing primary sulfides, sulfosalts, gold, and supergene minerals from the stockwork system. A. Vein of sulfides and late calcite; pyrite is overgrown by galena that cuts-replaces sphalerite. B. Pyrite replaced by galena, sphalerite and tennantite (Tenn) replaced by covellite (Cv). C. Gold in vugs within tennantite with vug fill and veinlet acanthite replacing tennantite. Note tetrahedrite veining/replacing tennantite. D. Pyrite cut by quartz-sericite veinlets and Tetrahedrite replaces chalcopyrite.

coarse-grain to medium-grain, and is partially replaced by sulfosalts, chalcopyrite, and stage 2 pyrite. Chalcopyrite (less than 2%) exhibits an anhedral shape, is fine-grained, and is replaced by primary pyrite, sphalerite, and sulfosalts. The most common sulfosalts (up to 7%) consist of tetrahedrite, tennantite, and acanthite, which exhibit anhedral shapes, range from medium-grained to fine-grained, and are replaced by chalcopyrite, covellite, hematite, and local pyrite-quartz-sericite with local gold and silver also present. Gold is

related to the sulfosalts and is fine-grained (up to 20 μm in size) (Fig. 5.14). The fluorite is fine-grained, purple in color, and cuts sulfides and sulfosalts.

The late mineralization includes rhodochrosite and calcite developed on sphalerite grain borders with anhedral shape. The supergene minerals are hematite, jarosite, goethite and covellite which were derived from sulfosalts and/or pyrite that freed the gold, silver, and tellurobismuthite that exhibit an irregular shape (Fig. 5.15).
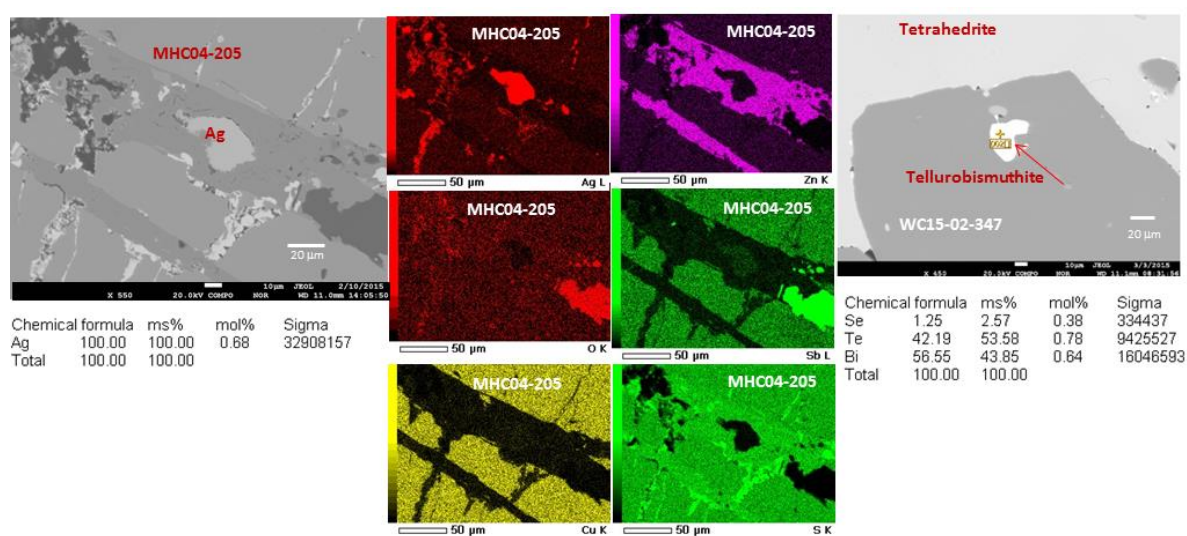
Fig. 5.15. Photomicrographs (Scanning Electron Microscope JXA-8230 9s) showing native silver in vugs and veinlets within tetrahedrite and sphalerite veinlets. Also shown are tellurobismuthite within sphalerite and tetrahedrite.

The stockwork and veins exhibit a local moderate chloritization as well as a moderate to pervasive phyllic alteration, which is overprinted by carbonates. The chlorite is fine-grained, locally present in veinlets and veins in the Caracol Formation, and locally associated with calcite, suggesting propylitic alteration. The phyllic alteration is made up of sericite-pyrite-quartz with local marcasite that was developed through the Caracol Formation, affecting the vein and veinlets. Stage 2 pyrite and marcasite exhibit anhedral

shapes, are fine-grained, and are associated with sericite and quartz. The carbonates over-print both hydrothermal alterations (i.e. propylitic and phyllic), are fine-grained, and pre-sent throughout the stockwork zones.

Paragenesis for the Diatreme Breccia System

The diatreme breccia system contains economic Au-Ag-Pb-Zn mineralization in-cluded as primary sulfides, sulfosalts, oxides, and local native minerals that occur as fillings and disseminations. The paragenesis includes four types of products: (1) igneous products, sub-rounded fragments, broken phenocrysts, and rock flour of the breccia matrix; (2) primary sulfides, sulfosalts, and precious native minerals; (3) three stages of hydrothermal alteration assemblages; and (4) weathering products (Table 5.4).

In general, the breccias are mainly made up of heterolithic and local monolithic frag-ments, exhibit sub-rounded and sub-angular shapes, vary in size, and are held by a breccia matrix that includes broken phenocrysts, such as quartz, plagioclase, and orthoclase as well as local zircon, sphene, biotite, epidote, and fluorite (Fig. 5.16). Early mineralization occurred in small disseminated grains and filled veinlets and both mineral occurrences mainly included primary sulfides (e.g. Py, Sp, Ga, Cpy) and sulfosalts (e.g. tetrahedrite, tennantite, and acanthite). Some fragments exhibit veinlets that predated breccia development, but veinlets cut breccia fragments and matrix. The stage 1 pyrite (up to 10%) exhibits a sub-euhedral and anhedral shape, ranging in size from coarse-grain to medium-grain, and is replaced partially by galena, sphalerite, chalcopyrite, and sulfosalts. Sphalerite (up to 10%) usually exhibits a wispy texture and euhedral shape, ranging in size

Table 5.4. Paragenetic sequence for the diatreme breccia system.

Mineral	Igneous	Brecciation	Hypogene — Alteration-Mineralization-Alteration			Supergene
Plagioclase	----					
Zircon	-					
Sphene	-					
Biotite		-				
Orthoclase		--	----			
Quartz		---			----	
Epidote		-				
Rock fragments		----------				
Fluorite		-				
Molybdenite		-				
Pyrite 1A		---				
Pyrite 1B			----			
Sphalerite		-		---		
Galena		-		---		
Chalcopyrite		-		--		
Tennantite				--		
Tetrahedrite				--		
Bournonite				-		
Acanthite				-		
Altaite				-		
Hessite				-		
Sylvanite				-		
Silver				-		
Gold				-		
Electrum				-		
Bismuth				-		
Tellurobismuthite				-		
Pyrite 2					---	
Marcasite					-	
Sericite					-----	
Rhodochrosite					--	
Calcite					----	
Dolomite					-	
Bornite						---
Covellite						--
Digenite						---
Chlorargyrite						-
Hematite						---
Jarosite						--
Goethite						--

from medium-grain to fine-grain, and is replaced by galena, sulfosalts, and chalcopyrite.

Galena (up to 4%) exhibits euhedral shapes, ranges in size from medium-grain to fine-grain, and is replaced by sulfosalts, chalcopyrite, and pyrite 2. Chalcopyrite (up to 2%) exhibits a fine-grained anhedral shape, and is replaced by covellite, bornite, digenite, and

hematite. The pyrite, sphalerite, galena and molybdenite are locally present as small grains in the breccia matrix, and exhibit an anhedral shape.
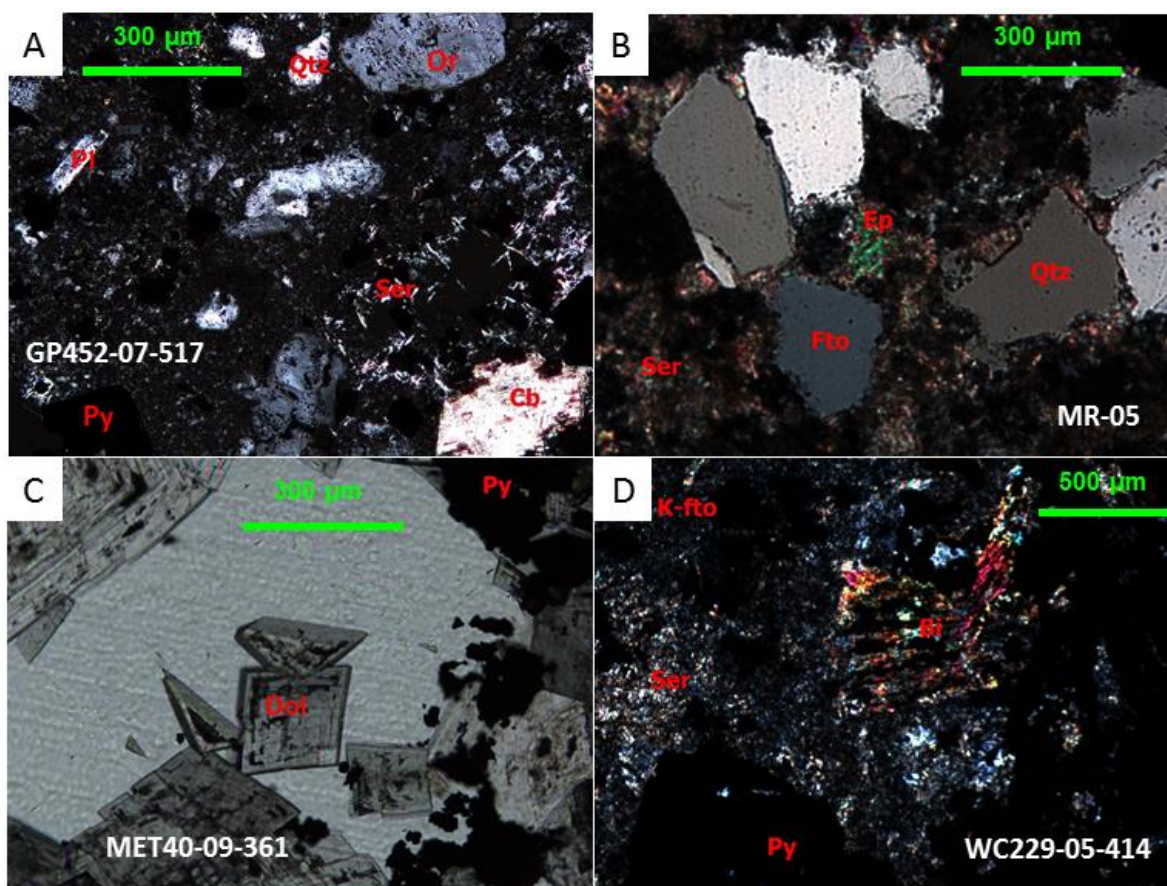
Fig. 5.16. Photomicrographs (plane-polarized light) showing broken crystals and alteration minerals from the diatreme breccia system. A.B. Broken quartz (Qtz), orthoclase (Fto), and epidote floating in fine-matrix altered by sericite (Ser) and carbonate (Cb). C. Pyrite (Py) coated by zoned dolomite (Dol). D. Broken biotite (Bi) phenocryst floating in fine-matrix altered by orthoclase (K-Fto), sericite (Ser) and pyrite (Py).

The bulk of the sulfosalts (up to 7%) consist of tetrahedrite, tennantite, acanthite, and local bournonite, all of which exhibit anhedral shapes, range from fine-grained to medium-grained, and are replaced by altaite, hessite, sylvanite, tellurobismuthite, gold, silver, electrum, bismuthinite, and local pyrite-quartz-sericite (Fig. 5.17, 18,19). Gold (i.e. up to 20 μm in size), silver, electrum, altaite, hessite, tellurobismuthite and bismuthinite (i.e.

up to 200 μm in size) exhibit irregular shapes, are microcrystalline, and usually associated

with tetrahedrite and acanthite. The native silver exhibits supergene effects and is

replaced by chlorargyrite (Figs. 5.18, 19). All petrography and mineralogy data are

reported in Appendix B**.**
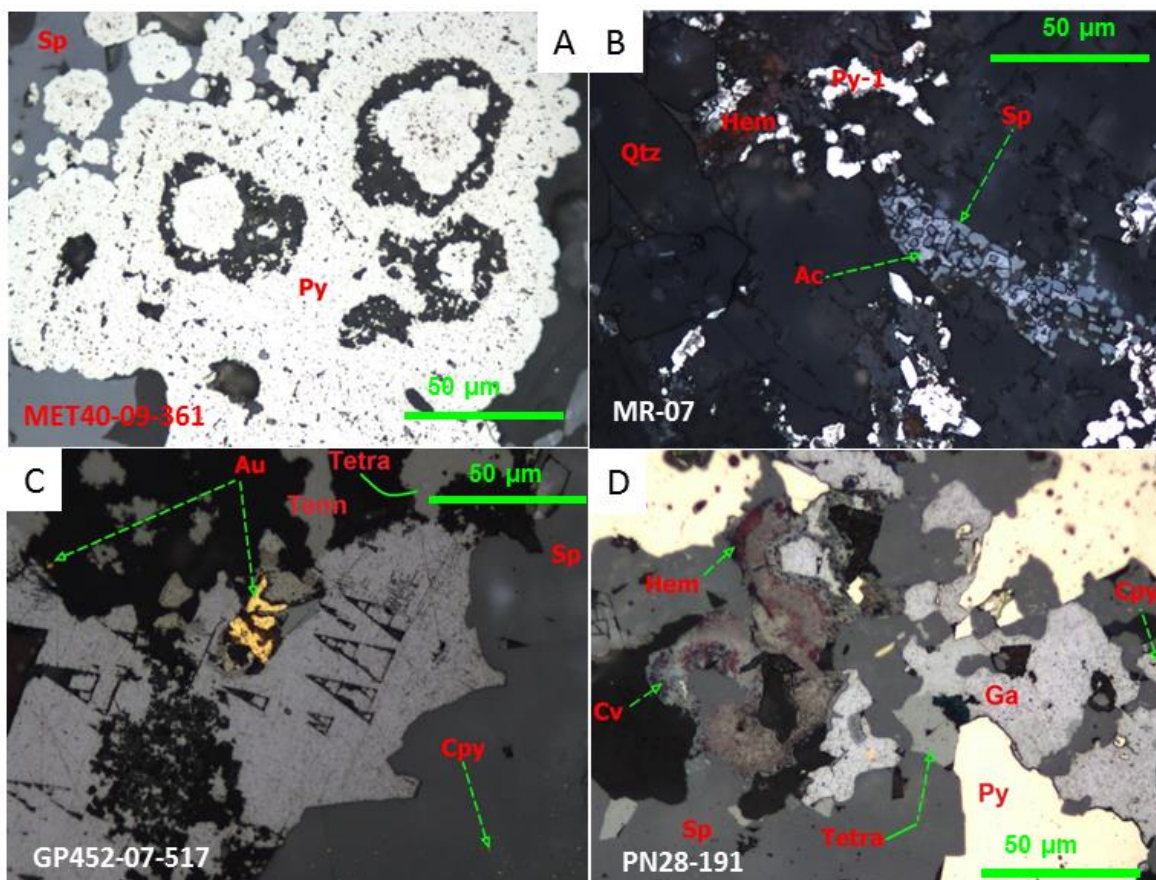
Fig. 5.17. Photomicrographs (reflected light) showing primary sulfides, sulfosalts, gold, and supergene minerals from the diatreme breccia system. A. Framboidal pyrite 1 (Py) replaced by sphalerite (Sp). B. Pyrite replaced by hematite (Hem) and sphalerite replaced by acanthite (Ac) floating in fine-matrix. C. Sphalerite replaced by galena (Ga), chalcopyrite, and sulfosalts (Tetra, Tenn) that exhibit native gold (Au). D. Pyrite replaced by sphalerite, galena, and tetrahedrite that are replaced by covellite (Cv) and hematite (Hem).

The late mineralization includes rhodochrosite associated with calcite and local

dolomite. Rhodochrosite and calcite exhibit anhedral shapes, are developed on sphalerite

and galena borders as thin, parallel bands, and are filling some fractures and veins, up to

20 cm in width, at shallow levels. The supergene minerals are more common at shallow

levels, consist of hematite, jarosite, goethite bornite, digenite, and covellite, which are

sub-products of the sulfosalts and/or pyrite that freed the gold, silver, and electrum (Figs.

5.18, 19).
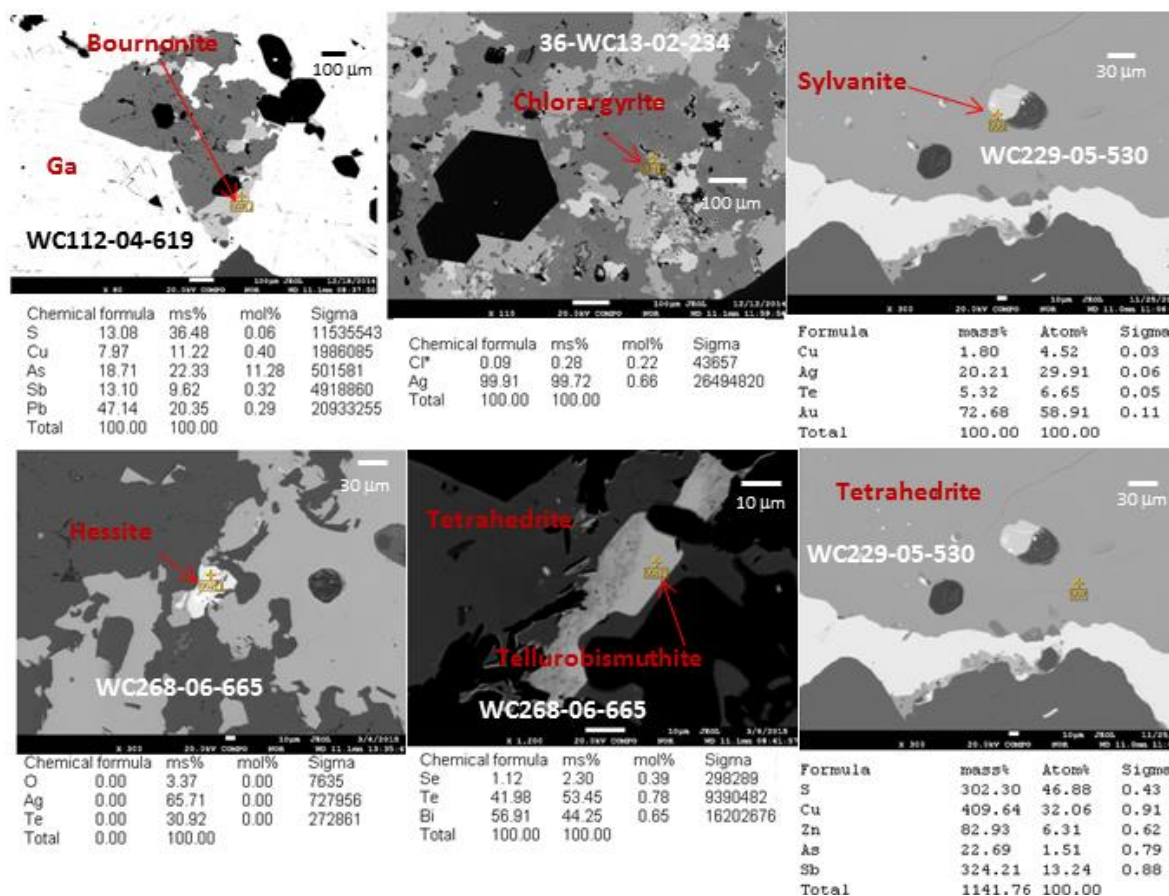
Fig. 5.18. Photomicrographs (Scanning Electron Microscope JXA-8230 9s) showing fine sulfosalts
from the diatreme breccia system.

The diatreme breccias locally exhibit moderate potassic as well as moderate to

pervasive phyllic alterations, which are overprinted by carbonate (i.e. calcite and local

dolomite). The potassic alteration consists of microcrystalline K-feldspar (orthoclase) that

is present in the breccia matrix and igneous fragments. The phyllic alteration consists of sericite-pyrite-quartz and local marcasite, developed throughout the diatreme breccias, affecting sulfides, sulfosalts, and orthoclase fragments (local pervasive sericite). The stage 2 pyrite and marcasite exhibit a fine-grained anhedral shape, and are related to sericite and quartz. The carbonate overprints both alterations stages, exhibits fine-grained texture, and is locally present in the breccia matrix.
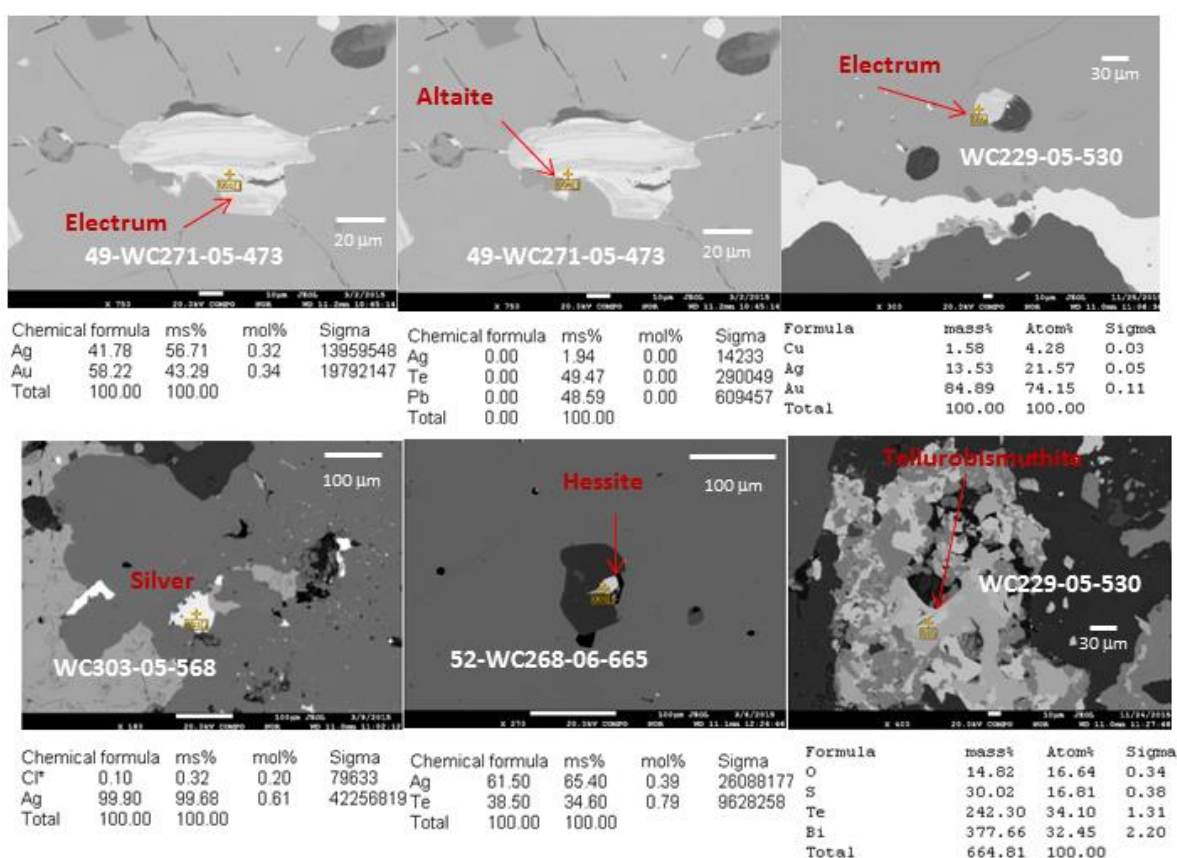
Fig. 5.19. Photomicrographs (Scanning Electron Microscope JXA-8230 9s) showing fine sulfosalts, electrum, and native silver from the diatreme breccia system.

Geochemistry

This section presents the results of geochemical statistical analyses, such as soil and drill cores geochemistry, which have been obtained from the Peñasquito ore deposit during exploration programs. The soil samples were collected systematically from the surface. The sampling of drill holes are 2 m sample intervals. The objective is to document the soil geochemical signature and document chemical distributions in the Peñasquito ore deposit.

In 1998, Kennecott funded a soil geochemical survey in the Peñasquito area that was conducted by Barringer GeoSystems. A total of 450 soil samples from the surface were collected along parallel lines with north-south orientation and a separation between 200 and 75 meters. These samples were submitted to a laboratory for 32 element ICP-MS analysis. Furthermore, thousands of samples from drilling campaigns, drill cuttings and core samples, spanning from 1995 to 2013, are kept at the Peñasquito facilities. A systematic sampling was submitted to several laboratories (e.g. ALS Minerals) for a 37 element ICP analysis that included ICP-MS and ICP-AES methods. These samples were from bedrock and ore, corresponding to more than 600,000 meters of drilling, extending down to 2,000 meters deep.

Methodology of Statistical Chemical Analysis

During this statistical chemical analysis, the drilling samples were separated by zones and occurrence, including ore bodies and hydrothermal alterations. The sample sets were standardized in order to obtain similar element values (i.e. ppb for the soil

geochemistry and ppm for the drill geochemistry) and for each element without value, the limit of detection, suggested by ALS Mineral (2014), was used. Microsoft Excel 2010, ArcGis and Geochemistry for ArcGis were used during the statistic correlations. The generation of correlation matrices included several stages: (1) a file was generated for each database (i.e. soil, diatreme breccias, skarn and porphyry systems, and alteration halos) in order to visualize and validate each sample suite in geographic space (Locations.csv) and develop the geochemical statistics (Assay.csv); (2) the data base was updated in Geochemistry for ArcGis software, thus, the Locations.csv and Assay.csv files were exported in order to develop each correlation matrix; and (3) the statistical analysis was completed by the above software, resulting in a graphic chart, indicating association among elements. The correlations were based on a linear trend between elements suggested by Pearson (1972); for that reason, both positive and negative associations must be considered as important associations (Table 5.5).

Table 5.5. Summary of correlative meaning.

Value	Meaning
-1	Negative and perfect correlation
-0.9 to -0.99	Negative and very strong correlation
-0.7 to -0.89	Negative and strong correlation
-0.4 to -0.69	Negative and moderate correlation
-0.2 to -0.39	Negative and weak correlation
-0.01 to -0.19	Negative and very weak correlation
0	Null correlation
0.01 to 0.19	Positive and very weak correlation
0.2 to 0.39	Positive and weak correlation
0.4 to 0.69	Positive and moderate correlation
0.7 to 0.89	Positive and strong correlation
0.9 to 0.99	Positive and very strong correlation
1	Positive and perfect correlation

Correlation Matrix for the Soil Geochemistry

The correlation matrix for the soil geochemistry (Table 5.6) revealed that gold is most moderately correlated with silver (0.58), cobalt (0.54), chromium (0.57), copper (0.59), gallium (0.51), lead 208 (0.46), palladium (0.51), platinum (0.61), antimony (0.53),

titanium (0.49), vanadium (0.55), tungsten (0.58), and zinc (0.55). Silver is most strongly correlated with lead 204 (0.84), lead 206 (0.82), lead 207 (0.83), lead 208 (0.81), antimony (0.68), and zinc (0.73). Lead is most strongly correlated with bismuth (0.71), zinc (0.78), cadmium (0.67), and antimony (0.68). In addition, zinc most strongly correlates with tungsten (0.66), antimony (0.66), and copper (0.78). Chromium is most strongly correlated with titanium (0.82), vanadium (0.65), and cobalt (0.68). Cadmium is most strongly correlated with bismuth (0.69). Arsenic is most strongly correlated with antimony (0.84). Barium is most strongly correlated with gallium (0.64). Vanadium is most strongly correlated with cobalt (0.65), and titanium (0.71). Gallium is most strongly correlated with manganese (0.72). Palladium is most strongly correlated with platinum (0.70). Molybdenum is most strongly correlated with uranium (0.73). Antimony is most strongly correlated with tungsten (0.67). Tin is most strongly correlated with titanium (0.73).

These correlations may suggest the presence of sulfosalts, primary sulfides, and some high temperature minerals, indicating a magmatic influence. Precious metals may also be associated with sulfosalts.

Table 5.6. Correlation matrix for the soil geochemistry.

	Ag	Al	As	Au	Ba	Bi	Ca	Cd	Co	Cr	Cu	Ga	K	Mg	Mn	Mo	Na	Ni	Pb_204	Pb_206	Pb_207	Pb_208	Pd	Pt	Sb	Sn	Sr	Th	Ti	U	V	W
Al	0.18																															
As	0.41	-0.07																														
Au	0.58	0.04	0.45																													
Ba	0.24	0.28	0.47	0.26																												
Bi	0.51	-0.19	0.33	0.27	-0.03																											
Ca	-0.02	-0.13	0.30	0.26	0.33	-0.27																										
Cd	0.47	-0.04	0.28	0.18	0.17	0.69	-0.22																									
Co	0.20	0.07	0.45	0.54	0.31	0.04	0.25	-0.08																								
Cr	0.29	0.29	0.30	0.47	0.17	0.05	0.12	-0.21	0.68																							
Cu	0.63	0.10	0.54	0.59	0.27	0.49	-0.02	0.34	0.58	0.50																						
Ga	0.34	0.39	0.51	0.51	0.64	-0.14	0.32	-0.03	0.57	0.62	0.41																					
K	0.06	0.34	-0.16	0.04	0.35	0.04	-0.09	0.03	0.14	0.23	0.15	0.18																				
Mg	-0.13	0.41	-0.22	-0.06	-0.02	-0.23	0.01	-0.22	0.11	0.19	-0.07	0.11	0.19																			
Mn	0.55	0.38	0.49	0.43	0.60	0.06	0.19	0.17	0.39	0.43	0.39	0.72	0.29	-0.06																		
Mo	-0.14	-0.21	0.45	0.25	0.17	-0.18	0.54	-0.23	0.60	0.29	0.25	0.25	-0.17	0.05	-0.09																	
Na	0.07	0.49	-0.06	0.25	0.20	-0.46	0.22	-0.45	0.34	0.53	0.12	0.46	0.14	0.43	0.25	0.16																
Ni	0.08	0.03	0.39	0.30	0.31	-0.06	0.29	-0.08	0.64	0.45	0.41	0.40	0.08	0.04	0.20	0.62	0.24															
Pb_204	0.84	0.14	0.33	0.45	0.20	0.70	-0.27	0.67	0.12	0.13	0.58	0.18	0.16	-0.21	0.53	-0.35	-0.18	-0.03														
Pb_206	0.82	0.13	0.33	0.44	0.18	0.70	-0.29	0.66	0.12	0.13	0.58	0.16	0.14	-0.20	0.49	-0.33	-0.20	-0.03	0.98													
Pb_207	0.83	0.14	0.33	0.45	0.19	0.71	-0.28	0.67	0.12	0.13	0.58	0.17	0.15	-0.20	0.51	-0.34	-0.18	-0.03	1.00	0.98												
Pb_208	0.81	0.15	0.33	0.46	0.19	0.65	-0.23	0.63	0.13	0.14	0.57	0.20	0.12	-0.17	0.50	-0.31	-0.14	-0.02	0.95	0.93	0.95											
Pd	0.18	0.08	0.37	0.51	0.15	-0.08	0.45	-0.19	0.56	0.56	0.32	0.42	0.01	0.10	0.24	0.54	0.50	0.40	-0.03	-0.04	-0.04	0.02										
Pt	0.24	0.04	0.43	0.61	0.35	-0.02	0.55	-0.10	0.59	0.55	0.37	0.56	0.01	0.08	0.41	0.46	0.42	0.40	0.05	0.04	0.05	0.07	0.70									
Sb	0.68	-0.04	0.84	0.53	0.36	0.52	0.16	0.46	0.28	0.24	0.58	0.39	-0.12	-0.30	0.54	0.19	-0.10	0.20	0.65	0.63	0.64	0.62	0.34	0.35								
Sn	0.34	0.14	0.43	0.39	0.07	0.26	0.12	-0.03	0.36	0.62	0.38	0.39	-0.07	0.12	0.28	0.26	0.29	0.20	0.20	0.20	0.21	0.22	0.56	0.49	0.48							
Sr	-0.27	-0.26	0.02	0.04	0.23	-0.08	0.49	-0.03	0.24	-0.12	0.00	0.01	0.08	0.10	-0.29	0.49	-0.08	0.28	-0.34	-0.33	-0.33	-0.32	0.03	0.14	-0.20	-0.25						
Th	0.27	0.15	0.14	0.29	0.22	0.08	0.14	0.00	0.32	0.37	0.24	0.32	0.31	0.01	0.42	0.07	0.21	0.16	0.24	0.23	0.21	0.30	0.36	0.23	0.30	-0.16						
Ti	0.40	0.25	0.40	0.49	0.15	0.14	0.10	-0.13	0.51	0.82	0.45	0.58	0.05	0.07	0.51	0.13	0.50	0.24	0.23	0.22	0.23	0.25	0.60	0.56	0.43	0.73	-0.34	0.34				
U	-0.06	-0.08	0.34	0.21	0.17	-0.09	0.26	-0.13	0.47	0.25	0.29	0.23	-0.12	0.04	-0.10	0.73	0.13	0.48	-0.20	-0.17	-0.19	-0.11	0.40	0.24	0.16	0.21	0.36	0.02	0.14			
V	0.42	0.22	0.58	0.55	0.28	0.10	0.17	0.04	0.75	0.65	0.59	0.59	-0.10	0.06	0.54	0.41	0.41	0.49	0.31	0.31	0.32	0.36	0.62	0.54	0.53	0.51	-0.11	0.25	0.71	0.44		
W	0.62	0.09	0.51	0.58	0.31	0.33	0.00	0.30	0.37	0.33	0.55	0.40	0.01	-0.25	0.60	0.00	0.13	0.16	0.60	0.59	0.60	0.60	0.37	0.35	0.67	0.33	-0.26	0.25	0.50	0.08	0.61	
Zn	0.73	0.23	0.57	0.55	0.39	0.47	-0.13	0.53	0.48	0.36	0.78	0.49	0.19	-0.14	0.63	0.04	0.02	0.34	0.78	0.77	0.78	0.76	0.17	0.25	0.66	0.24	-0.15	0.24	0.33	0.13	0.59	0.66

Color Coding
(signficance 0.950)
- very strong
- strong
- moderate
- weak
- very weak
- null

Summary of geochemistry associations for the soil														
Very strong	Strong			Moderate										
Ag-Pb_204	Ag-Pb_206	Cd-Pb_204	Pb_204-Sb	Ag-Au	As-Mn	Au-Pt	Bi-Zn	Co-Ni	Cu-Pb_204	Ga-V	Mn-Zn	Pb_208-W	Ti-W
Ag-Pb_207	Ag-Pb_208	Cd-Pb_206	Pb_204-Zn	Ag-Bi	As-V	Au-Sb	Ca-Mo	Co-Ti	Cu-Pb_206	Ga-Zn	Na-Pd	Pd-Sn	V-W
As-Sb	Ag-Sb	Cd-Pb_207	Pb_206-Zn	Ag-Cd	As-W	Au-Ti	Ca-Pt	Co-U	Cu-Pb_207	Mn-Pb_204	Na-Ti	Pd-Ti	V-Zn
Pb_204-Pb_204	Ag-Zn	Co-Cr	Pb_208-Zn	Ag-Cu	As-Zn	Au-V	Ca-Sr	Co-Zn	Cu-Pb_208	Mn-Pb_206	Ni-U	Pd-V	
Pb_204-Pb_207	Ba-Ga	Co-V	Pd-Pt	Ag-Mn	Au-Co	Au-W	Cd-Pb_208	Cr-Cu	Cu-Sb	Mn-Pb_207	Ni-V	Pt-Sn	
Pb_204-Pb_208	Bi-Cd	Cr-Ti	Sb-W	Ag-W	Au-Cr	Au-Zn	Cd-Sb	Cr-Ga	Cu-V	Mn-Pb_208	Pb_204-W	Pt-Ti	
Pb_206-Pb_207	Bi-Pb_204	Cr-V	Sb-Zn	Ag-Na	Au-Cu	Ba-Mn	Cd-Zn	Cr-Na	Cu-W	Mn-Sb	Pb_206-Sb	Pt-V	
Pb_206-Pb_208	Bi-Pb_206	Cu-Zn	Sn-Ti	As-Ba	Au-Ga	Bi-Cu	Co-Cu	Cr-Pd	Ga-Na	Mn-Ti	Pb_206-W	Sb-Sn	
Pb_207-Pb_208	Bi-Pb_207	Ga-Mn	Ti-V	As-Cu	Au-Pb_208	Bi-Na	Co-Ga	Cr-Pt	Ga-Pt	Mn-V	Pb_207-W	Sb-V	
	Bi-Pb_208	Mo-U	W-Zn	As-Ga	Au-Pd	Bi-Sb	Co-Mo	Cr-Sn	Ga-Ti	Mn-W	Pb_208-Sb	Sn-V	

Correlation Matrix for the Recrystallization Halo

The correlation matrix for the recrystallization halo (i.e. including recrystallized limestone and/or marble formation effects) (Table 5.7) revealed that gold is most moderately correlated with silver (0.58), cadmium (0.53), copper (0.49), gallium (0.51), lead (0.57), antimony (0.56), and zinc (0.53). Silver is most strongly correlated with lead (0.85), antimony (0.78), zinc (83), cadmium (0.81), and copper (0.71). Lead is most strongly correlated with arsenic (0.65), zinc (0.76), cadmium (0.76), and antimony (0.68). Zinc is most strongly correlated with cadmium (0.94), antimony (0.73), copper (0.78), bismuth (0.67), and manganese (0.65). Aluminum is most strongly correlated with titanium (0.83) and phosphorus (0.64). Copper is most strongly correlated with cadmium (0.69), manganese (0.67), antimony (0.66), and iron (0.67). Nickel is most strongly correlated with vanadium (0.70) and titanium (0.62), phosphorus (0.63), cobalt (0.67), and chromium (0.63). Calcium is most strongly correlated strontium (0.72). Phosphorus is most strongly correlated with titanium (0.69). Iron is most strongly correlated with sulfur (0.73). Chromium is most strongly correlated with vanadium (0.63). Cadmium is most strongly correlated with antimony (0.67), bismuth (0.62). Arsenic is most strongly correlated with antimony (0.67). These correlations may suggest the presence of sulfosalts with fewer primary sulfides, and some high temperature minerals, suggesting magmatic fluids.

	Ag	Al	As	Au	B	Ba	Be	Bi	Ca	Cd	Co	Cr	Cu	Fe	Ga	Hg	K	La	Mg	Mn	Mo	Na	Ni	P	Pb	S	Sb	Sc	Sr	Th	Ti	Tl	U	V	W	Zn
Ag																																				
Al	0.09																																			
As	0.59	0.16																																		
Au	0.58	0.06	0.51																																	
B	0.15	0.36	0.33	0.13																																
Ba	0.11	0.15	0.23	0.06	0.08																															
Be	0.09	0.43	0.17	0.05	0.32	-0.02																														
Bi	0.61	0.09	0.32	0.28	0.02	0.03	0.01																													
Ca	-0.48	-0.20	-0.43	-0.49	-0.18	-0.01	-0.28	-0.27																												
Cd	0.81	0.14	0.52	0.53	0.18	0.12	0.05	0.62	-0.36																											
Co	0.30	0.51	0.38	0.18	0.35	0.08	0.33	0.31	-0.33	0.36																										
Cr	0.27	0.45	0.31	0.15	0.28	0.19	0.18	0.27	-0.18	0.33	0.51																									
Cu	0.71	0.01	0.40	0.49	0.03	-0.18	0.11	0.61	-0.42	0.69	0.36	0.25																								
Fe	0.60	0.42	0.53	0.42	0.25	-0.03	0.31	0.56	-0.57	0.56	0.60	0.43	0.67																							
Ga	0.43	-0.03	0.36	0.51	0.03	-0.01	0.10	0.16	-0.66	0.33	0.04	0.01	0.37	0.32																						
Hg	0.38	-0.05	0.32	0.38	0.01	0.02	-0.01	0.18	-0.43	0.27	0.05	0.03	0.27	0.22	0.54																					
K	0.25	0.35	0.45	0.25	0.16	0.43	0.16	0.10	-0.33	0.20	0.19	0.25	-0.01	0.23	0.18	0.11																				
La	0.23	0.17	0.10	0.12	0.05	0.03	0.22	0.21	-0.16	0.21	0.11	0.27	0.27	0.24	0.04	-0.03	0.09																			
Mg	-0.06	0.05	0.06	0.00	-0.09	0.04	0.06	-0.04	0.01	0.01	-0.09	-0.09	0.03	-0.01	-0.06	-0.11	0.29	0.07																		
Mn	0.56	-0.17	0.40	0.40	0.04	0.12	0.14	0.34	-0.33	0.52	0.15	0.08	0.67	0.45	0.28	0.21	-0.03	0.24	0.13																	
Mo	0.01	0.13	-0.01	0.01	-0.15	0.07	0.01	0.21	0.09	0.06	0.04	0.28	0.11	0.07	-0.09	-0.07	0.02	0.21	-0.06	-0.01																
Na	-0.09	0.42	0.14	-0.02	0.16	0.06	0.26	-0.19	-0.13	-0.06	0.25	-0.03	-0.21	0.16	-0.03	-0.13	0.27	-0.09	0.08	-0.26	-0.15															
Ni	0.22	0.52	0.38	0.16	0.35	0.14	0.22	0.27	-0.21	0.33	0.67	0.63	0.23	0.47	0.01	0.00	0.18	0.17	-0.13	0.02	0.33	0.22														
P	0.26	0.64	0.28	0.11	0.36	0.06	0.33	-0.24	0.36	0.54	0.53	0.27	0.52	-0.02	-0.03	0.17	0.38	-0.08	0.11	0.18	0.22	0.63														
Pb	0.85	0.18	0.65	0.57	0.22	0.26	0.12	0.49	-0.44	0.76	0.29	0.32	0.51	0.51	0.41	0.38	0.38	0.11	-0.08	0.46	0.03	-0.03	0.27	0.28												
S	0.49	0.41	0.39	0.31	0.21	0.04	0.19	0.50	-0.34	0.51	0.46	0.35	0.50	0.73	0.21	0.12	0.20	0.16	-0.06	0.24	0.05	0.15	0.40	0.45	0.43											
Sb	0.78	0.00	0.67	0.56	0.13	0.17	0.05	0.56	-0.40	0.67	0.25	0.28	0.66	0.52	0.41	0.32	0.28	0.25	-0.06	0.56	0.11	-0.15	0.22	0.19	0.78	0.43										
Sc	0.26	0.51	0.43	0.19	0.28	0.19	0.38	0.23	-0.34	0.23	0.57	0.58	0.24	0.53	0.03	-0.03	0.35	0.32	0.01	0.21	0.20	0.20	0.55	0.54	0.32	0.38	0.35									
Sr	-0.51	0.03	-0.31	-0.44	-0.05	0.21	-0.14	-0.38	0.72	-0.38	-0.20	-0.07	-0.62	-0.54	-0.48	-0.33	-0.14	-0.26	-0.09	-0.57	0.08	0.14	0.00	-0.13	-0.36	-0.27	-0.44	-0.20								
Th	-0.09	-0.17	-0.19	0.00	-0.11	-0.31	0.05	-0.22	-0.04	0.00	-0.05	-0.23	0.17	0.01	-0.02	-0.08	-0.23	0.05	0.28	0.21	-0.24	0.07	-0.19	0.00	-0.26	-0.08	-0.27	-0.15	-0.20							
Ti	0.20	0.83	0.24	0.13	0.46	0.16	0.37	0.13	-0.30	0.26	0.60	0.55	0.08	0.48	0.01	-0.01	0.33	0.16	-0.06	-0.12	0.02	0.42	0.62	0.69	0.27	0.44	0.05	0.53	-0.01	-0.11						
Tl	0.23	-0.07	0.18	0.20	-0.02	0.06	-0.02	0.06	-0.11	0.21	0.01	-0.01	0.13	0.11	0.12	0.06	-0.01	0.03	0.00	0.00	0.00	-0.03	-0.02	0.26	0.10	0.23	0.02	-0.07	-0.07	-0.02						
U	-0.10	-0.24	-0.14	-0.05	-0.18	-0.07	-0.13	-0.17	0.16	-0.16	-0.36	-0.27	-0.11	-0.24	-0.03	0.14	-0.12	-0.16	0.04	-0.05	-0.02	-0.16	-0.29	-0.30	-0.13	-0.19	-0.09	-0.27	0.08	0.00	-0.28	0.09				
V	0.22	0.35	0.34	0.21	0.14	0.17	0.13	0.28	-0.13	0.33	0.39	0.63	0.27	0.39	0.02	-0.07	0.26	0.28	0.01	0.12	0.52	0.10	0.70	0.51	0.26	0.31	0.31	0.55	-0.01	-0.20	0.39	0.07	-0.21			
W	0.44	0.09	0.25	0.30	-0.02	0.03	-0.01	0.44	-0.32	0.38	0.19	0.18	0.40	0.46	0.27	0.20	0.20	0.17	-0.01	0.21	0.00	-0.04	0.11	0.14	0.35	0.31	0.39	0.16	-0.39	-0.03	0.16	0.09	-0.05	0.17		
Zn	0.83	0.04	0.51	0.53	0.13	0.04	0.04	0.67	-0.42	0.94	0.30	0.29	0.78	0.59	0.40	0.34	0.14	0.22	-0.02	0.65	0.06	-0.21	0.25	0.28	0.76	0.49	0.73	0.20	-0.50	-0.04	0.15	0.21	-0.14	0.26	0.41	

Color Coding (signficance 0.950)

- very strong
- strong
- moderate
- weak
- very weak
- null

Table 5.7. Correlation matrix for the recrystallization halo.

Summary of geochemistry associations for the recrystallization halo											
Very strong	**Strong**			**Moderate**							
Ag-Pb	Ag-Cd	Cd-Cu	Fe-S	Ag-As	Al-Co	Au-Ca	Bi-Cu	Cd-Mn	Cr-Ti	Fe-Sr	Ni-Sc	Sc-V
Ag-Zn	Ag-Cu	Cd-Pb	Mn-Zn	Ag-Au	Al-Cr	Au-Cd	Bi-Fe	Cd-S	Cu-Pb	Fe-Ti	P-S	Sr-Zn
Al-Ti	Ag-Sb	Cd-Sb	Ni-P	Ag-Bi	Al-Ni	Au-Cu	Bi-Pb	Co-Cr	Cu-S	Fe-W	P-Sc	
Cd-Zn	Al-P	Co-Ni	Ni-Ti	Ag-Ca	Al-Sc	Au-Ga	Bi-S	Co-Fe	Cu-Sr	Fe-Zn	P-V	
	As-Pb	Cr-Ni	Ni-V	Ag-Fe	As-Au	Au-Pb	Bi-Sb	Co-S	Fe-Mn	Ga-Hg	Pb-S	
	As-Sb	Cr-V	P-Ti	Ag-Mn	As-Ca	Au-Sb	Bi-W	Co-Sc	Fe-Ni	Ga-Sr	S-Sb	
	Bi-Cd	Cu-Fe	Pb-Sb	Ag-S	As-Cd	Au-Sr	Ca-Fe	Co-Ti	Fe-P	Mn-Pb	S-Ti	
	Bi-Zn	Cu-Mn	Pb-Zn	Ag-Sr	As-Fe	Au-Zn	Ca-Hg	Cr-Fe	Fe-Pb	Mn-Sb	S-Zn	
	Ca-Ga	Cu-Sb	Sb-Zn	Ag-W	As-K	B-Ti	Ca-Pb	Cr-P	Fe-Sb	Mn-Sr	Sb-Sr	
	Ca-Sr	Cu-Zn		Al-Be	As-Zn	Ba-K	Cd-Fe	Cr-Sc	Fe-Sc	Mo-V	Sc-Ti	

Correlation Matrix for the Weak Phyllic Alteration

The correlation matrix for the weak phyllic alteration (Table 5.8) revealed that gold is most moderately correlated with silver (0.42), copper (0.45), lead (0.48), antimony (0.47), cadmium (0.45), and zinc (0.47). Silver is most strongly correlated with lead (0.75), antimony (0.65), and cadmium (0.62). Lead is most strongly correlated with zinc (0.77), cadmium (0.76), and antimony (0.71). Zinc is most strongly correlated with cadmium (0.91), antimony (0.83). Aluminum is most strongly correlated with magnesium (0.65), vanadium (0.65). Strontium is strongly correlated with calcium (0.67). Arsenic is most strongly correlated with manganese (0.66) and antimony (0.71). Cadmium is strongly correlated with antimony (0.64).

These correlations may suggest that this hydrothermal alteration halo included sulfosalts and fewer primary sulfides; however, gold and silver appear to be associated with sulfosalts.

	Ag	Al	As	Au	B	Ba	Be	Bi	Ca	Cd	Co	Cr	Cu	Fe	Ga	Hg	K	La	Mg	Mn	Mo	Na	Ni	P	Pb	S	Sb	Sc	Sr	Th	Ti	Tl	U	V	W	Zn
Ag																																				
Al	-0.39																																			
As	0.57	-0.54																																		
Au	0.42	-0.33	0.39																																	
B	-0.18	0.30	-0.22	-0.11																																
Ba	-0.15	0.05	-0.10	-0.03	0.20																															
Be	-0.01	0.33	0.06	-0.05	0.24	-0.09																														
Bi	0.27	-0.20	0.22	0.37	-0.10	-0.04	-0.05																													
Ca	-0.26	0.07	-0.26	-0.33	0.00	0.02	-0.10	-0.30																												
Cd	0.62	-0.48	0.53	0.45	-0.23	0.02	-0.15	0.29	-0.20																											
Co	-0.04	0.23	0.03	0.01	0.05	0.01	0.25	0.02	-0.17	-0.09																										
Cr	-0.14	0.65	-0.31	-0.19	0.27	0.01	0.14	-0.13	-0.06	-0.22	0.11																									
Cu	0.44	-0.17	0.31	0.45	-0.12	0.04	-0.01	0.51	-0.33	0.52	0.16	-0.05																								
Fe	0.14	0.27	0.14	0.21	0.16	-0.06	0.41	0.18	-0.48	0.07	0.46	0.19	0.29																							
Ga	-0.07	0.27	-0.12	-0.04	0.14	-0.05	0.18	-0.05	-0.03	-0.08	0.06	0.27	-0.03	0.11																						
Hg	0.16	-0.13	0.15	0.25	-0.01	-0.02	-0.01	0.21	-0.16	0.17	0.00	-0.01	0.23	0.14	-0.02																					
K	0.05	0.25	0.05	0.02	0.35	0.14	0.45	-0.05	-0.18	-0.10	0.19	0.16	-0.01	0.46	0.05	-0.01																				
La	0.02	0.04	0.11	0.03	0.14	0.11	0.17	-0.01	-0.15	0.03	0.13	0.00	0.04	0.19	0.02	-0.01	0.24																			
Mg	-0.27	0.65	-0.40	-0.29	0.19	-0.12	0.24	-0.23	0.23	-0.39	0.09	0.45	-0.27	0.23	0.17	-0.08	0.20	-0.05																		
Mn	0.50	-0.50	0.66	0.36	-0.01	0.11	0.06	0.18	-0.10	0.44	0.14	-0.39	0.21	0.25	-0.12	0.13	0.08	0.19	-0.28																	
Mo	0.12	-0.29	0.16	-0.07	-0.07	0.12	-0.11	0.07	0.02	0.30	-0.19	-0.16	0.18	-0.28	-0.04	-0.01	-0.20	-0.08	-0.34	-0.04																
Na	-0.13	0.17	-0.05	-0.09	-0.18	-0.13	0.06	-0.04	0.09	-0.09	-0.01	-0.04	-0.13	-0.12	0.18	-0.06	-0.25	-0.12	0.04	-0.10	0.09															
Ni	0.03	0.19	0.03	-0.02	0.08	-0.05	0.34	-0.04	0.08	0.03	0.42	0.17	0.18	0.23	0.13	0.04	0.11	0.02	0.14	-0.05	0.26	0.05														
P	-0.01	0.24	0.02	-0.07	0.17	-0.04	0.29	-0.10	-0.13	-0.04	0.21	0.25	0.03	0.36	0.07	-0.02	0.28	0.15	0.16	-0.03	-0.02	-0.01	0.32													
Pb	0.75	-0.41	0.60	0.48	-0.15	-0.13	0.02	0.30	-0.34	0.76	0.01	-0.17	0.50	0.29	-0.06	0.17	0.13	0.08	-0.28	0.55	0.11	-0.20	0.01	0.03												
S	0.14	-0.06	0.00	0.04	0.00	-0.34	0.04	-0.04	0.14	-0.01	-0.05	0.07	-0.08	0.06	0.02	0.06	0.05	-0.28	0.33	-0.06	-0.10	-0.07	0.12	0.03	0.13											
SB	0.65	-0.54	0.71	0.47	-0.18	-0.07	0.00	0.31	-0.27	0.64	-0.03	-0.26	0.50	0.13	-0.11	0.22	0.02	0.08	-0.42	0.58	0.22	-0.20	0.02	-0.02	0.71	0.04										
Sc	-0.47	0.54	-0.46	-0.27	0.29	0.15	0.29	-0.23	0.16	-0.51	0.27	0.31	-0.23	0.26	0.14	-0.12	0.30	0.14	0.38	-0.24	-0.27	0.08	0.17	0.21	-0.48	-0.13	-0.50									
Sr	-0.50	0.24	-0.55	-0.35	0.07	0.10	-0.11	-0.27	0.67	-0.45	-0.13	0.03	-0.36	-0.42	-0.05	-0.15	-0.13	-0.19	0.21	-0.52	-0.03	0.12	0.07	-0.12	-0.60	-0.03	-0.53	0.37								
Th	-0.10	-0.06	0.04	-0.03	-0.32	-0.13	0.00	0.02	0.06	-0.03	0.03	-0.25	-0.11	-0.09	0.01	-0.06	-0.20	-0.01	-0.10	0.07	0.06	0.59	-0.03	-0.07	-0.15	-0.14	-0.12	0.01	0.04							
Ti	-0.05	0.22	-0.15	-0.08	0.13	0.10	0.14	-0.04	0.08	-0.04	0.03	0.27	-0.02	-0.06	0.36	-0.05	-0.10	-0.18	0.11	-0.22	0.17	0.25	0.23	0.03	-0.05	0.12	-0.06	0.01	0.03	0.07						
Tl	0.11	-0.09	0.11	0.17	-0.01	0.04	-0.03	0.11	-0.08	0.13	0.06	-0.05	0.14	0.09	0.00	0.18	0.02	0.01	-0.09	0.17	0.03	-0.06	0.06	-0.05	0.14	0.00	0.17	-0.06	-0.07	-0.02	-0.05					
U	-0.02	-0.05	-0.04	0.03	-0.01	0.02	-0.05	0.02	0.07	0.03	-0.05	0.01	0.00	0.00	-0.08	-0.03	-0.03	-0.09	-0.07	-0.04	-0.04	0.07	-0.03	0.02	-0.04	-0.02	0.03	0.00	-0.03	0.07	-0.05	-0.02	0.02			
V	-0.31	0.65	-0.39	-0.25	0.21	0.13	0.17	-0.15	0.18	-0.23	0.03	0.57	-0.06	-0.10	0.32	-0.13	-0.04	-0.04	0.34	-0.52	0.20	0.29	0.31	0.20	-0.38	-0.10	-0.35	0.34	0.24	0.06	0.43	-0.05	0.01			
W	0.17	-0.08	0.09	0.13	-0.06	-0.04	0.00	0.12	-0.06	0.15	0.02	-0.03	0.27	0.10	0.01	0.10	-0.01	-0.02	-0.04	0.09	0.02	0.00	0.10	-0.03	0.15	0.03	0.16	-0.09	-0.10	0.01	-0.02	0.10	0.00	-0.06		
Zn	0.60	-0.42	0.53	0.47	-0.22	0.04	-0.09	0.30	-0.25	0.91	0.00	-0.21	0.55	0.19	-0.06	0.18	-0.02	0.07	-0.36	0.48	0.20	-0.10	0.03	-0.03	0.77	-0.07	0.63	-0.43	-0.48	-0.03	-0.06	0.15	0.01	-0.27	0.14	

Color Coding (signficance 0.950)
- very strong
- strong
- moderate
- weak
- very weak
- null

Table 5.8. Correlation matrix for the weak phyllic alteration.

Summary of geochemistry associations for the weak phyllic alteration							
Very strong	**Strong**		**Moderate**				
Cd-Zn	Ag-Cd	As-Sb	Ag-As	Al-Sb	Au-Sb	Co-Ni	Mn-Sr
	Ag-Pb	Ca-Sr	Ag-Au	Al-Sc	Au-Zn	Cr-Mg	Mn-V
	Ag -Sb	Cd-Pb	Ag-Cu	Al-Zn	Be-K	Cr-V	Mn-Zn
	Al-Sr	Cd-Sb	Ag-Mn	As-Sd	Bi-Cu	Cu-Pb	Na-Th
	Al-Mg	Pb-Sb	Ag-Sc	As-Pb	Ca-Fe	Cu-Sb	Pb-Sc
	Al-V	Pb-Zn	Ag-Sr	As-Sc	Cd-Cu	Cu-Zn	Pb-Sr
	As-Mn	Sb-Zn	Ag-Zn	As-Sr	Cd-Mn	Fe-K	Sb-Sc
			Al-As	As-Zn	Cd-Sc	Fe-Sr	Sb-Sr
			Al-Cd	Au-Cu	Cd-Sr	Mg-Sb	Sc-Zn
			Al-Mn	Au-Pb	Co-Fe	Mn-Pb	Sr-Zn
						Mn-Sb	Ti-V

Correlation Matrix for the Moderate-Pervasive Phyllic Alteration

The correlation matrix for the moderate-pervasive phyllic alteration (Table 5.9) showed that gold is most moderately correlated with silver (0.47), cadmium (0.42), lead (0.55), antimony (0.43), and zinc (0.44). Silver is most strongly correlated with lead (0.80), antimony (0.70), zinc (0.76), and cadmium (0.75). Lead is most strongly correlated with zinc (0.82), cadmium (0.82), and antimony (0.62). In addition, zinc is most strongly correlated with cadmium (0.94) and antimony (0.64). Aluminum is most strongly correlated with barium (0.63) and chromium (0.63). Copper is most strongly correlated with bismuth (0.71). Vanadium is most strongly correlated with scandium (0.61) and titanium (0.63), and chromium (0.64). Strontium is strongly correlated with calcium (0.65). Cobalt is most strongly correlated with nickel (0.64). Sodium is strongly correlated with titanium (0.68).

These correlations may suggest that the hydrothermal alteration halo included sulfosalts and fewer primary sulfides; however, gold and silver may be associated with sulfosalts, and some high temperature minerals may be present, suggesting direct magmatic fluids.

	Ag	Al	As	Au	B	Ba	Be	Bi	Ca	Cd	Co	Cr	Cu	Fe	Ga	Hg	K	La	Mg	Mn	Mo	Na	Ni	P	Pb	S	Sb	Sc	Sr	Th	Ti	Tl	U	V	W
Ag																																			
Al	-0.34																																		
As	0.48	-0.35																																	
Au	0.47	-0.31	0.37																																
B	-0.14	0.18	0.05	-0.11																															
Ba	0.01	-0.21	0.13	0.02	-0.01																														
Be	-0.27	0.63	-0.21	-0.21	0.11	-0.17																													
Bi	0.44	-0.18	0.03	0.30	-0.23	-0.18	-0.19																												
Ca	-0.27	-0.03	-0.04	-0.20	0.10	0.08	0.11	-0.48																											
Cd	0.75	-0.34	0.49	0.42	-0.10	0.06	-0.24	0.31	-0.08																										
Co	0.03	0.38	-0.01	-0.02	-0.03	-0.20	0.17	0.16	-0.21	-0.02																									
Cr	-0.01	0.63	-0.16	-0.09	0.08	-0.36	0.33	0.19	-0.29	-0.06	0.42																								
Cu	0.46	-0.09	0.05	0.25	-0.27	-0.06	-0.14	0.71	-0.53	0.33	0.23	0.21																							
Fe	0.35	0.27	0.20	0.24	-0.06	-0.10	0.05	0.42	-0.55	0.19	0.58	0.43	0.47																						
Ga	-0.16	0.54	-0.21	-0.13	0.17	-0.34	0.43	-0.06	-0.03	-0.16	0.13	0.39	-0.08	0.05																					
Hg	0.14	-0.12	0.10	0.14	-0.05	0.06	-0.11	0.06	-0.08	0.11	-0.08	-0.07	0.10	0.05	-0.05																				
K	0.22	-0.05	0.26	0.11	-0.08	0.47	-0.13	0.08	-0.19	0.14	0.19	0.00	0.19	0.40	-0.35	0.03																			
La	0.21	-0.13	0.21	0.13	-0.12	0.10	-0.02	0.17	-0.12	0.18	0.10	0.08	0.19	0.20	-0.17	-0.03	0.29																		
Mg	-0.30	0.54	-0.20	-0.22	0.13	-0.28	0.42	-0.20	0.28	-0.25	0.24	0.41	-0.29	0.02	0.33	-0.16	-0.11	-0.04																	
Mn	0.35	-0.22	0.48	0.25	0.09	0.06	0.00	-0.06	0.25	0.42	0.12	-0.11	-0.10	0.16	-0.13	0.03	0.16	0.25	0.11																
Mo	0.10	-0.10	-0.13	0.02	-0.10	0.00	-0.04	0.20	-0.18	0.07	-0.04	0.04	0.30	-0.08	-0.02	0.03	-0.05	-0.03	-0.26	-0.21															
Na	-0.26	0.56	-0.31	-0.18	0.09	-0.36	0.39	-0.10	0.03	-0.24	0.12	0.26	-0.09	-0.01	0.52	-0.05	-0.48	-0.34	0.25	-0.26	0.05														
Ni	0.04	0.44	0.03	-0.04	0.05	-0.26	0.23	0.18	0.14	0.03	0.74	0.50	0.22	0.55	0.17	-0.07	0.15	0.10	0.31	0.12	0.01	0.17													
P	0.04	0.47	0.03	-0.04	0.09	-0.13	0.24	0.08	-0.14	0.03	0.44	0.45	0.10	0.43	0.10	-0.10	0.24	0.21	0.31	0.31	0.14	0.57													
Pb	0.80	-0.25	0.55	0.40	-0.04	0.07	-0.21	0.23	-0.16	0.82	0.06	-0.02	0.27	0.36	-0.15	0.12	0.26	0.21	-0.22	0.51	-0.03	-0.27	0.07	0.12											
S	0.23	0.10	0.01	0.16	-0.15	-0.42	-0.06	0.37	-0.23	0.11	0.41	0.33	0.32	0.55	0.04	0.03	0.07	-0.01	0.16	0.06	-0.02	0.12	0.45	0.27	0.18										
Sb	0.70	-0.43	0.48	0.43	-0.22	0.07	-0.29	0.51	-0.30	0.59	0.02	-0.09	0.61	0.34	-0.26	0.19	0.26	0.25	-0.42	0.30	0.18	-0.33	0.01	-0.05	0.62	0.20									
Sc	-0.15	0.48	-0.02	-0.08	0.12	-0.28	0.44	-0.01	0.05	-0.12	0.35	0.52	-0.10	0.23	0.29	-0.11	-0.01	0.26	0.55	0.21	-0.18	0.17	0.46	0.50	-0.18	0.16	-0.21								
Sr	-0.45	0.22	-0.28	-0.30	0.12	0.28	0.26	-0.54	0.65	-0.35	-0.34	-0.29	-0.54	-0.54	0.08	-0.02	-0.18	-0.23	0.12	-0.17	-0.09	0.21	-0.33	-0.23	-0.37	-0.41	-0.47	-0.05							
Th	-0.19	-0.16	-0.02	0.02	-0.10	-0.03	0.04	-0.14	0.19	-0.14	-0.21	-0.35	-0.18	-0.32	0.00	-0.04	-0.31	-0.11	0.04	-0.03	-0.05	0.18	-0.23	-0.20	-0.20	-0.17	-0.15	-0.09	0.20						
Ti	-0.14	0.52	-0.31	-0.08	0.16	-0.54	0.41	0.10	-0.12	-0.14	0.19	0.53	0.04	0.04	0.55	-0.07	-0.49	-0.30	0.34	-0.22	0.11	0.68	0.27	0.21	-0.18	0.22	-0.24	0.37	-0.47	-0.02					
Tl	0.06	-0.06	0.11	0.12	-0.01	0.00	-0.03	0.05	0.00	0.06	0.02	-0.01	0.01	0.08	-0.02	0.10	0.05	0.03	0.00	0.11	0.00	0.00	0.05	0.00	0.06	0.04	0.12	0.01	-0.04	-0.07	-0.04				
U	-0.06	-0.21	-0.08	0.00	-0.05	0.08	-0.16	-0.06	0.22	0.00	-0.27	-0.23	-0.09	-0.36	-0.07	0.06	-0.18	-0.13	-0.14	-0.12	0.16	-0.01	-0.22	-0.25	-0.12	-0.13	-0.02	-0.23	0.23	0.06	-0.05	0.00			
V	-0.20	0.60	-0.16	-0.14	0.17	-0.40	0.44	-0.01	-0.04	-0.17	0.18	0.64	-0.08	0.02	0.52	-0.11	-0.31	-0.05	0.53	-0.15	0.12	0.42	0.35	0.37	-0.19	0.04	-0.30	0.61	-0.04	-0.05	0.66	-0.03	-0.05		
W	0.17	-0.10	0.12	0.19	-0.04	-0.07	-0.01	0.22	-0.05	0.16	0.01	0.00	0.15	0.10	-0.01	0.01	-0.02	0.08	-0.05	0.07	0.09	-0.05	0.00	-0.02	0.14	0.06	0.17	0.03	-0.14	0.04	0.07	0.03	-0.01	0.03	
Zn	0.76	-0.30	0.48	0.44	-0.14	0.05	-0.23	0.40	-0.19	0.94	0.07	0.00	0.42	0.32	0.26	0.18	0.12	0.22	-0.23	0.04	0.04	-0.26	0.12	0.10	0.82	0.18	0.64	-0.06	-0.19	-0.15	0.07	-0.07	-0.16	0.15	

Color Coding (signficance 0.950)
- very strong
- strong
- moderate
- weak
- very weak
- null

Table 5.9. Correlation matrix for the moderate-pervasive phyllic alteration.

Summary of geochemistry associations for the moderated-pervasive phyllic alteration										
Very strong	Strong		Moderate							
Cd-Pb	Ag-Cd	Co-Ni	Ag-As	Al-Sb	Au-Sb	Bi-Fe	Cr-Fe	Fe-P	Mg-V	Mg-V
Cd-Zn	Ag-Pb	Cr-V	Ag-Au	Al-Sc	Au-Zn	Bi-Sb	Cr-Ni	Fe-S	Mn-Pb	Mn-Pb
Pb-Zn	Ag-Sb	Na-Ti	Ag-Bi	Al-Ti	Ba-K	Bi-Sr	Cr-P	Fe-Sr	Mn-Zn	Mn-Zn
	Ag-Zn	Pb-Sb	Ag-Cu	Al-V	Ba-S	Ca-Cu	Cr-Sc	Ga-Na	Na-V	Na-V
	Al-Be	Sb-Zn	Ag-Sr	As-Cd	Ba-Ti	Ca-Fe	Cr-Ti	Ga-Ti	Ni-P	Ni-P
	Al-Cr	Sc-V	Al-Ga	As-Mn	Be-Ga	Cd-Mn	Cu-Fe	Ga-V	Ni-S	Ni-S
	Bi-Cu	Ti-V	Al-Mg	As-Pb	Be-Mg	Co-Cr	Cu-Sb	K-Na	Ni-Sc	Ni-Sc
	Ca-Sr		Al-Na	As-Sb	Be-Sc	Co-Fe	Cu-Sr	K-Ti	P-Sc	P-Sc
			Al-Ni	As-Zn	Be-V	Co-Cr	Cu-Zn	Mg-Sb	Sb-Sr	Sb-Sr
			Al-P	Au-Cd	Bi-Ca	Co-P	Fe-Ni	Mg-Sc	Sr-Zn	Sr-Zn

Correlation Matrix for the Peñasco Breccia

The correlation matrix for the Peñasco Breccia (Table 5.10) showed that gold is most strongly correlated with silver (0.66) and moderately correlated with bismuth (0.49), cadmium (0.55), copper (0.56), lead (0.55), antimony (0.60), and zinc (0.58). Silver is most strongly correlated with lead (0.87), antimony (0.83), zinc (0.81), cadmium (0.79), and copper (0.69). Lead is most strongly correlated with zinc (0.87), and antimony (0.77). Zinc is most strongly correlated with cadmium (0.94), antimony (0.77). Copper is most strongly correlated with antimony (0.78) and bismuth (0.69).

These correlations may suggest that the bulk of the economic mineralogy included sulfosalts and primary sulfides, whereas, gold and silver may be associated with sulfosalts.

	Ag	Al	As	Au	B	Ba	Be	Bi	Ca	Cd	Co	Cr	Cu	Fe	Ga	Hg	K	La	Mg	Mn	Mo	Na	Ni	P	Pb	S	Sb	Sc	Sr	Th	Ti	Tl	U	V	W	Zn
Ag																																				
Al	-0.43																																			
As	0.24	-0.07																																		
Au	0.66	-0.31	0.13																																	
B	-0.41	0.31	0.14	-0.31																																
Ba	0.17	0.06	0.19	0.05	0.04																															
Be	-0.28	0.36	0.11	-0.20	0.41	0.07																														
Bi	0.53	-0.12	0.00	0.49	-0.25	0.02	-0.09																													
Ca	-0.43	0.05	-0.18	-0.30	0.22	-0.33	0.10	-0.29																												
Cd	0.79	-0.46	0.21	0.55	-0.33	0.19	-0.22	0.38	-0.30																											
Co	-0.01	0.00	0.03	0.05	-0.02	-0.07	-0.02	-0.03	0.06	0.11																										
Cr	0.08	0.10	-0.03	0.09	0.01	0.02	0.08	0.09	0.03	0.07	0.08																									
Cu	0.69	-0.19	0.19	0.56	-0.28	0.12	-0.18	0.69	-0.40	0.54	-0.07	0.12																								
Fe	0.40	0.01	0.39	0.38	-0.12	0.10	-0.01	0.41	-0.39	0.28	0.29	0.10	0.40																							
Ga	0.15	0.08	0.15	0.10	0.14	0.07	0.38	0.14	-0.05	0.14	-0.11	0.10	0.13	0.15																						
Hg	0.23	0.01	0.12	0.21	-0.02	0.14	0.21	0.22	-0.12	0.21	-0.03	0.26	0.20	0.19	0.31																					
K	0.20	0.34	0.03	0.16	0.07	0.30	0.05	0.27	-0.30	0.10	-0.03	0.03	0.17	0.27	0.16	0.03																				
La	0.20	-0.12	0.01	0.12	-0.05	0.18	-0.03	0.02	-0.11	0.25	0.02	0.10	0.06	-0.04	0.01	0.03	0.09																			
Mg	-0.22	0.12	-0.38	-0.06	-0.02	-0.26	-0.01	-0.09	0.58	-0.20	0.18	0.13	-0.25	-0.21	-0.03	-0.05	-0.07	-0.04																		
Mn	0.07	-0.24	0.14	0.01	0.07	0.04	0.08	-0.18	0.39	0.28	0.20	-0.07	-0.18	-0.15	0.07	0.06	-0.14	0.14	0.16																	
Mo	0.03	-0.01	0.17	-0.04	0.06	0.19	0.13	0.07	-0.13	0.01	-0.12	0.14	0.14	0.05	0.00	0.15	-0.05	0.10	-0.30	-0.03																
Na	-0.31	0.28	-0.06	-0.23	0.22	-0.09	0.31	-0.12	0.30	-0.25	-0.07	-0.12	-0.26	-0.17	0.19	-0.03	-0.08	-0.09	0.15	0.06	-0.01															
Ni	-0.01	-0.02	0.13	0.08	0.04	-0.11	0.01	0.02	0.32	0.10	0.46	0.39	0.12	0.12	-0.03	0.16	-0.18	0.04	0.19	0.15	0.10	-0.08														
P	-0.09	0.15	-0.04	-0.10	0.05	-0.04	0.05	-0.08	0.22	-0.03	-0.03	-0.03	-0.19	0.02	-0.07	-0.12	0.03	0.10	0.26	0.20	-0.04	0.14	0.05													
Pb	0.87	-0.46	0.22	0.55	-0.37	0.21	-0.28	0.37	-0.40	0.86	0.00	0.06	0.55	0.32	0.14	0.19	0.16	0.26	-0.23	0.21	0.02	-0.31	-0.03	-0.07												
S	0.21	-0.27	-0.19	0.25	-0.34	-0.33	-0.48	0.19	0.15	0.10	0.15	-0.04	0.11	0.11	-0.26	-0.13	0.01	-0.17	0.29	-0.03	-0.27	-0.19	0.06	0.07	0.16											
Sb	0.83	-0.39	0.31	0.60	-0.32	0.19	-0.19	0.58	-0.42	0.74	-0.02	0.05	0.78	0.40	0.15	0.20	0.20	0.18	-0.30	0.08	0.08	-0.27	0.02	-0.11	0.77	0.10										
Sc	0.12	-0.05	-0.22	0.15	-0.14	-0.01	0.00	0.12	0.26	0.17	0.16	0.27	0.03	-0.05	0.00	0.13	0.05	0.26	0.47	0.16	-0.08	0.05	0.31	0.17	0.12	0.05	0.11									
Sr	-0.58	0.44	0.13	-0.51	0.42	0.11	0.35	-0.49	0.38	-0.53	-0.10	0.03	-0.47	-0.28	-0.04	-0.05	-0.14	-0.03	0.08	0.09	0.12	0.32	0.08	0.09	-0.52	-0.33	-0.54	-0.03								
Th	-0.10	0.05	-0.04	-0.10	0.03	-0.07	-0.03	-0.03	0.08	-0.08	-0.13	-0.49	-0.04	-0.13	-0.03	-0.03	-0.35	0.07	-0.09	-0.04	0.05	-0.04	0.18	-0.27	0.09	-0.06	0.08	-0.07	-0.13	-0.02						
Ti	0.06	0.10	-0.36	0.16	-0.16	-0.16	-0.01	0.28	0.10	0.02	-0.04	0.13	0.14	-0.03	0.03	-0.01	0.06	0.09	0.23	-0.13	-0.04	0.19	0.02	0.11	-0.01	0.14	0.09	0.43	-0.14	0.10						
Tl	0.07	0.00	0.08	0.07	0.02	0.05	0.18	0.23	-0.05	0.08	0.00	-0.04	0.03	0.05	0.02	0.39	-0.01	0.00	-0.06	0.09	0.13	0.09	-0.02	-0.02	0.06	-0.02	0.07	0.22	-0.02	-0.02	-0.01					
U	0.04	0.01	-0.02	0.03	-0.01	0.03	0.09	0.17	0.01	0.04	-0.02	-0.05	0.03	0.01	-0.03	0.34	-0.03	-0.02	0.03	0.02	0.09	0.06	-0.06	-0.03	0.02	0.03	0.02	0.18	-0.07	-0.01	0.00	0.73				
V	0.08	0.22	-0.31	0.18	-0.13	0.03	0.06	0.18	0.15	0.07	0.10	0.39	0.13	0.03	0.07	0.09	0.15	0.23	0.51	-0.08	-0.01	0.09	0.29	0.19	0.04	0.03	0.05	0.73	-0.01	-0.15	0.54	-0.02	-0.01			
W	0.24	0.01	0.08	0.22	-0.07	0.03	0.16	0.37	-0.05	0.21	-0.02	0.05	0.22	0.21	0.18	0.28	0.14	0.07	-0.02	0.03	0.06	0.03	0.01	-0.03	0.19	0.04	0.26	0.21	-0.14	-0.02	0.17	0.48	0.37	0.13		
Zn	0.81	-0.44	0.21	0.58	-0.34	0.19	-0.23	0.43	-0.33	0.94	0.12	0.06	0.58	0.31	0.16	0.22	0.13	0.26	-0.17	0.28	0.00	-0.27	0.12	-0.02	0.87	0.12	0.77	0.18	-0.56	-0.07	0.04	0.07	0.02	0.10	0.21	

Color Coding (signficance 0.950)

- very strong
- strong
- moderate
- weak
- very weak
- null

Table 5.10. Correlation matrix for the Peñasco Breccia.

Summary of geochemistry associations for the Peñasco Breccia					
Very strong	Strong	Moderate			
Ag-Pb	Ag-Au	Ag-Al	Au-Cu	Ca-Mg	Cu-Zn
Ag-Sb	Ag-Cd	Ag-Bi	Au-Sb	Ca-Sb	Mg-Sc
Ag-Zn	Ag-Cu	Ag-Cu	Au-Sr	Cd-Cu	Mg-V
Cd-Pb	Bi-Cu	Ag-Ca	Au-Zn	Ca-Sb	Pb-Sr
Cd-Zn	Cd-Sb	Ag-Sr	B-Sr	Cd-Cu	Sb-Sr
Pb-Zn	Cu-Sb	Al-Cd	Be-S	Cd-Sr	Sc-Ti
	Pb-Sb	Al-Pb	Bi-Fe	Co-Ni	Sr-Zn
	Sb-Zn	Al-Sr	Bi-Sb	Cr-Th	Ti-V
	Sc-V	Al-Zn	Bi-Sr	Cu-Pb	Tl-W
	Tl-Cu	Au-Bi	Bi-Zn	Cu-Sr	
		Au-Cd			

Correlation Matrix for the Azul Breccia

The correlation matrix for the Azul Breccia (Table 5.11) showed that gold is most moderately correlated with silver (0.52) bismuth (0.42), cadmium (0.42), lead (0.47), antimony (0.42), and zinc (0.42). Silver is most strongly correlated with lead (0.78), antimony (0.76), zinc (0.69), cadmium (0.68), and copper (0.72). Zinc is most strongly correlated with cadmium (0.95), and lead (0.83). Copper is most strongly correlates with antimony (0.93). These chemical correlations may suggest that the bulk of the economic mineralogy was formed by sulfosalts and minor primary sulfides, whereas, gold and silver may be associated with sulfosalts.

Cobalt is most strongly correlated with nickel (0.66), suggesting a mineralization of magmatic iron that could have been integrated as small fragments during the brecciation stage. The Azul Breccia, however, exhibited less strong element correlations than the Peñasco Breccia, which may indicate a reduced amount of the metallic mineralization.

	Ag	Al	As	Au	B	Ba	Be	Bi	Ca	Cd	Co	Cr	Cu	Fe	Ga	Hg	K	La	Mg	Mn	Mo	Na	Ni	P	Pb	S	Sb	Sc	Sr	Th	Ti	Tl	U	V	W	Zn
Ag																																				
Al	-0.34																																			
As	0.17	0.21																																		
Au	0.52	-0.15	0.18																																	
B	-0.35	0.43	0.12	-0.14																																
Ba	-0.22	0.39	0.28	-0.08	0.26																															
Be	-0.28	0.40	0.16	-0.09	0.66	0.36																														
Bi	0.72	-0.28	0.16	0.42	-0.32	-0.29	-0.26																													
Ca	-0.24	-0.04	-0.07	-0.19	0.13	-0.18	0.09	-0.13																												
Cd	0.68	-0.24	0.11	0.42	-0.27	-0.07	-0.16	0.51	-0.30																											
Co	0.09	0.04	0.01	0.10	-0.11	-0.11	-0.16	0.16	0.02	0.10																										
Cr	0.23	0.07	-0.06	0.16	-0.04	-0.13	-0.09	0.20	-0.19	0.17	0.15																									
Cu	0.72	-0.04	0.50	0.40	-0.14	-0.04	-0.10	0.60	-0.15	0.54	0.04	0.15																								
Fe	0.34	0.13	0.55	0.31	-0.03	0.04	0.01	0.39	-0.26	0.24	0.35	0.15	0.40																							
Ga	0.12	0.15	0.09	0.13	0.30	0.08	0.51	0.17	-0.08	0.20	-0.10	0.11	0.14	0.15																						
Hg	0.12	0.09	0.12	0.14	0.21	0.14	0.42	0.10	-0.10	0.17	-0.11	0.05	0.15	0.12	0.56																					
K	-0.21	0.76	0.06	-0.10	0.30	0.25	0.25	-0.19	-0.24	-0.16	0.04	0.22	-0.10	0.10	0.15	0.11																				
La	0.06	-0.19	-0.30	-0.01	-0.11	-0.03	-0.09	-0.03	-0.08	0.01	0.02	0.02	-0.16	-0.19	-0.15	-0.09	-0.05																			
Mg	0.22	-0.29	-0.33	0.03	-0.25	-0.57	-0.31	0.27	0.43	0.02	0.15	0.14	0.02	-0.16	-0.06	-0.12	-0.16	0.07																		
Mn	0.03	-0.21	0.01	-0.01	-0.12	-0.01	-0.07	0.02	0.22	0.10	0.15	-0.06	-0.05	-0.14	-0.06	0.00	-0.13	0.17	0.27																	
Mo	0.13	-0.02	-0.22	0.03	-0.09	0.03	-0.07	0.07	-0.08	0.03	0.16	0.08	0.04	-0.03	0.03	0.03	0.00	0.18	0.05	0.03																
Na	0.02	0.07	0.03	0.02	0.13	0.11	0.25	0.08	0.00	0.08	-0.14	-0.09	0.01	0.08	0.31	0.30	0.10	0.00	-0.03	0.06	-0.01															
Ni	0.17	0.05	0.26	0.13	-0.06	-0.12	-0.08	0.25	0.23	0.10	0.66	0.16	0.25	0.40	-0.01	-0.02	-0.01	-0.07	0.23	0.20	0.06	-0.08														
P	0.21	-0.06	-0.20	0.07	-0.24	-0.26	0.19	0.02	0.10	0.34	0.18	0.03	0.02	-0.11	-0.07	0.09	0.28	0.31	0.31	0.08	0.31	-0.04	0.40													
Pb	0.78	-0.35	-0.01	0.47	-0.32	-0.18	-0.24	0.55	-0.36	0.82	0.05	0.21	0.45	0.24	0.12	0.11	-0.15	0.13	0.13	0.09	0.04	0.07	0.01	0.16												
S	0.33	-0.29	-0.18	0.13	-0.48	-0.59	-0.59	0.33	0.15	0.12	0.19	0.08	0.12	0.10	-0.30	-0.23	-0.13	-0.05	0.60	0.01	-0.03	-0.12	0.13	0.20	0.24											
Sb	0.76	-0.16	0.47	0.42	-0.22	-0.03	-0.12	0.59	-0.18	0.58	-0.03	0.12	0.93	0.35	0.11	0.14	-0.17	-0.07	0.02	0.04	0.04	0.01	0.18	0.03	0.55	0.11										
Sc	0.26	-0.27	-0.08	0.07	-0.32	-0.28	-0.29	0.31	0.21	0.12	0.18	0.15	0.08	-0.06	-0.10	-0.09	-0.14	0.27	0.47	0.42	0.13	0.02	0.38	0.42	0.19	0.22	0.14									
Sr	-0.35	0.40	0.38	-0.17	0.32	0.57	0.38	-0.36	0.21	-0.26	-0.20	-0.31	-0.08	-0.01	0.04	0.07	0.16	-0.22	-0.42	0.08	-0.08	0.15	-0.04	-0.34	-0.39	-0.39	-0.11	-0.16								
Th	-0.04	-0.05	-0.04	-0.05	-0.05	-0.05	-0.07	0.02	0.04	-0.07	0.01	-0.20	-0.05	0.01	-0.07	-0.05	-0.09	-0.04	0.01	-0.14	0.02	0.09	-0.03	0.05	-0.07	0.09	-0.05	-0.05	-0.05							
Ti	0.17	0.04	-0.12	0.15	-0.15	-0.11	-0.12	0.16	-0.09	0.15	0.10	0.19	0.06	0.15	0.10	-0.02	0.05	0.14	0.07	-0.03	0.11	0.04	0.07	0.18	0.22	0.14	0.06	0.21	-0.17	0.02						
Tl	0.03	0.06	0.08	0.04	0.32	0.14	0.52	0.14	-0.03	0.08	-0.07	0.06	0.06	0.07	0.55	0.48	-0.06	-0.07	0.03	0.02	0.29	0.02	-0.07	0.04	-0.35	0.05	-0.03	0.05	-0.05	-0.04						
U	-0.06	0.02	0.01	-0.02	0.01	0.01	0.02	-0.06	0.06	-0.02	-0.04	-0.04	-0.03	-0.04	0.00	0.25	0.00	-0.03	-0.04	0.08	-0.01	0.09	-0.02	-0.04	-0.06	0.00	-0.02	-0.02	0.06	-0.04	-0.03	0.00				
V	0.32	-0.01	0.02	0.19	-0.23	0.03	-0.20	0.34	-0.08	0.26	0.11	0.23	0.23	0.13	0.06	0.05	0.05	0.19	0.24	0.14	0.21	0.10	0.28	0.40	0.29	-0.03	0.27	0.58	-0.12	-0.06	0.25	0.02	-0.03			
W	0.09	-0.03	0.09	0.11	0.10	0.09	0.36	0.10	0.01	0.15	-0.16	-0.05	0.09	0.09	0.30	0.23	-0.17	-0.06	-0.11	-0.02	0.02	0.21	-0.06	-0.12	0.10	-0.21	0.15	0.00	0.09	0.00	0.11	0.26	-0.01	0.03		
Zn	0.69	-0.24	0.09	0.43	-0.29	-0.10	-0.20	0.51	-0.33	0.95	0.13	0.20	0.53	0.26	0.20	0.15	-0.15	0.00	0.06	0.11	0.04	0.06	0.15	0.15	0.83	0.15	0.57	0.15	-0.31	-0.08	0.17	0.05	-0.03	0.29	0.14	

Color Coding (signficance 0.950)
- very strong
- strong
- moderate
- weak
- very weak
- null

Table 5.11. Correlation matrix for the Azul Breccia.

Summary of geochemistry associations for the Azul Breccia					
Very strong	Strong	Moderate			
Cd-Pb	Ag-Bi	Ag-Au	B-S	Bi-Pb	Hg-Tl
Cd-Zn	Ag-Cd	Al-B	Ba-Mg	Bi-Sb	Mg-S
Cu-Sb	Ag-Cu	As-Cu	Ba-S	Bi-Zn	Mg-Sc
Pb-Zn	Ag-Pb	As-Fe	Ba-Sr	Ca-Mg	Mg-Sr
	Ag-Sb	As-Sb	Be-Ga	Cd-Cu	Mn-Sc
	Ag-Zn	Au-Bi	Be-Hg	Cd-Sb	P-Sc
	Al-K	Au-Cd	Be-S	Cu-Pb	Pb-Sb
	B-Be	Au-Pb	Be-Tl	Cu-Zn	Sb-Zn
	Co-Ni	Au-Sb	Bi-Cd	Ga-Hg	Sc-V
		Au-Zn	Bi-Cu	Ga-Tl	

Correlation Matrix for the Skarn System

The correlation Matrix for the skarn system (Table 5.12) showed that silver is most strongly correlated with cadmium (0.72), lead (0.79), antimony (0.74), and zinc (0.73). Lead is most strongly correlated with antimony (0.62), cadmium (0.69), and zinc (0.68). Zinc is most strongly correlated with cadmium (0.94), and antimony (0.63). Aluminum is most strongly correlated with beryllium (0.70) and titanium (0.63). Calcium is most strongly correlated with manganese (0.63) and strontium (0.75). Iron is most strongly correlated with sulfur (0.76). Chromium is most strongly correlated with scandium (0.62). Copper is moderately correlated with antimony (0.49).

These correlations may suggest that the bulk of the economic mineralogy included primary sulfides and fewer sulfosalts; however, silver may be associated with sulfosalts. High temperature minerals increased and calcium association may indicate calc-silicate minerals, whereas strontium association may indicate late magmatic fluids.

	Ag	Al	As	Au	B	Ba	Be	Bi	Ca	Cd	Co	Cr	Cu	Fe	Ga	Hg	K	La	Mg	Mn	Mo	Na	Ni	P	Pb	S	Sb	Sc	Sr	Th	Ti	Tl	U	V	W	Zn
Al	-0.34																																			
As	0.58	-0.44																																		
Au	0.41	-0.28	0.38																																	
B	0.13	-0.04	0.15	0.12																																
Ba	-0.02	-0.12	0.23	0.11	-0.04																															
Be	-0.37	0.70	-0.38	-0.26	-0.10	-0.08																														
Bi	0.53	-0.30	0.34	0.36	0.03	-0.11	-0.38																													
Ca	0.24	-0.17	0.00	-0.02	0.26	-0.34	-0.16	0.16																												
Cd	0.72	-0.33	0.39	0.35	0.22	-0.15	-0.38	0.51	0.49																											
Co	0.08	0.17	0.12	0.18	0.05	0.05	0.09	0.12	-0.32	-0.01																										
Cr	-0.08	0.32	-0.06	0.01	-0.15	0.05	0.18	0.03	-0.41	-0.23	0.34																									
Cu	0.35	0.06	0.17	0.19	-0.12	-0.10	0.04	0.38	0.04	0.21	0.27	0.14																								
Fe	0.01	0.13	0.16	0.12	-0.29	0.15	0.11	0.10	-0.63	-0.29	0.48	0.47	0.32																							
Ga	-0.05	0.40	-0.15	-0.02	-0.09	0.00	0.31	-0.09	-0.15	-0.12	0.04	0.22	0.10	0.20																						
Hg	0.16	-0.08	0.14	0.12	0.02	0.08	-0.01	0.09	0.11	0.15	-0.04	-0.09	0.15	-0.02	0.06																					
K	-0.12	0.12	0.20	0.08	-0.18	0.48	0.12	-0.17	-0.79	-0.38	0.30	0.39	-0.11	0.56	0.13	-0.04																				
La	-0.02	-0.06	0.15	0.06	-0.15	0.14	0.00	0.03	-0.30	-0.08	0.16	0.21	-0.04	0.22	0.01	-0.02	0.37																			
Mg	-0.29	0.46	-0.10	-0.12	-0.21	0.21	0.47	-0.24	-0.55	-0.41	0.20	0.38	-0.06	0.41	0.25	-0.06	0.56	0.21																		
Mn	0.44	-0.27	0.26	0.16	0.01	-0.24	-0.20	0.35	0.63	0.50	-0.07	-0.08	0.26	-0.12	-0.13	0.15	-0.41	-0.03	-0.26																	
Mo	0.02	0.05	-0.16	-0.08	0.02	-0.21	0.00	0.03	0.08	0.08	0.05	0.03	0.29	-0.20	-0.03	0.02	-0.36	-0.18	-0.27	0.28																
Na	-0.09	0.43	-0.15	-0.11	0.16	-0.04	0.31	-0.19	0.20	0.00	-0.04	-0.21	-0.16	-0.24	0.23	0.04	-0.19	-0.23	0.02	-0.15	0.00															
Ni	0.03	0.19	0.11	0.10	0.01	0.07	0.10	0.05	-0.22	-0.04	0.59	0.25	0.20	0.29	0.03	-0.04	0.20	0.11	0.19	-0.16	0.06	0.08														
P	-0.01	0.27	-0.04	-0.02	-0.01	-0.19	0.10	0.10	0.00	0.00	0.20	0.26	0.14	0.13	0.02	-0.09	-0.02	0.15	0.04	0.00	0.04	-0.01	0.26													
Pb	0.79	-0.34	0.57	0.36	0.17	0.07	-0.34	0.34	0.18	0.69	0.05	-0.12	0.07	-0.06	-0.05	0.15	0.03	0.05	-0.22	0.36	-0.08	-0.08	-0.01	-0.06												
S	0.08	0.12	0.14	0.12	-0.22	0.09	0.08	0.10	-0.55	-0.14	0.49	0.37	0.26	0.76	0.16	0.00	0.50	0.22	0.32	-0.18	-0.24	-0.12	0.37	0.18	0.04											
Sb	0.74	-0.30	0.61	0.41	0.05	0.05	-0.31	0.56	0.11	0.56	0.10	0.00	0.49	0.13	-0.03	0.19	0.01	0.09	-0.19	0.42	-0.02	-0.20	0.01	0.02	0.62	0.14										
Sc	-0.15	0.36	-0.02	-0.01	-0.21	0.07	0.34	-0.04	-0.42	-0.31	0.39	0.62	0.02	0.48	0.19	-0.04	0.51	0.34	0.51	-0.13	-0.10	0.26	0.19	-0.10	0.35	-0.01										
Sr	-0.02	0.09	-0.15	-0.14	0.29	-0.17	0.10	-0.15	0.75	0.23	-0.33	-0.46	-0.18	-0.70	0.02	0.09	-0.61	-0.32	-0.32	0.14	0.26	0.53	-0.07	-0.10	0.01	-0.51	-0.17	-0.44								
Th	-0.13	0.00	-0.01	-0.12	-0.08	0.04	0.06	-0.20	-0.08	-0.13	0.04	-0.11	0.05	0.08	-0.10	0.05	0.09	0.02	0.06	0.01	0.05	-0.16	0.07	0.00	-0.07	0.08	-0.13	0.00	-0.07							
Ti	-0.13	0.63	-0.39	-0.17	0.18	-0.29	0.45	-0.09	0.25	-0.01	0.03	0.17	-0.01	-0.20	0.26	-0.06	-0.25	-0.31	0.09	-0.01	0.19	0.48	0.02	0.14	-0.15	-0.17	-0.19	0.18	0.34	-0.15						
Tl	0.03	-0.03	0.09	0.04	0.01	0.01	-0.02	0.08	0.12	0.03	0.03	-0.07	0.10	-0.01	-0.04	0.11	-0.03	-0.01	-0.09	0.14	0.11	0.05	0.03	0.06	0.02	-0.04	0.11	0.02	0.06	-0.04	-0.02					
U	0.05	-0.11	-0.08	0.00	-0.02	-0.16	-0.12	0.11	0.34	0.20	-0.22	-0.19	0.02	-0.25	0.01	0.07	-0.34	-0.12	-0.23	0.16	0.26	-0.06	-0.06	0.00	-0.12	0.01	-0.27	0.32	0.00	0.04	0.01					
V	-0.09	0.43	-0.26	-0.12	-0.07	-0.26	0.21	0.07	0.17	-0.02	0.08	0.41	0.18	0.03	0.21	-0.04	-0.17	-0.05	0.20	0.19	0.40	0.11	0.28	0.32	-0.07	0.36	0.14	-0.07	0.54	0.07	0.13					
W	0.27	-0.11	0.16	0.21	-0.03	-0.08	-0.14	0.32	0.21	0.21	-0.03	-0.02	0.25	0.14	0.06	0.11	-0.15	-0.05	-0.18	0.27	0.20	-0.06	-0.08	0.01	0.19	0.03	0.24	-0.05	0.02	-0.06	0.02	0.06	0.18	0.13		
Zn	0.73	-0.36	0.42	0.36	0.16	-0.13	-0.42	0.59	0.44	0.94	0.01	-0.18	0.27	-0.20	-0.11	0.15	-0.33	-0.04	-0.38	0.55	0.06	-0.10	-0.04	0.02	0.68	-0.08	0.63	-0.25	0.12	-0.13	-0.06	0.05	0.18	0.00	0.25	

Color Coding (signficance 0.950)

- very strong
- strong
- moderate
- weak
- very weak
- null

Table 5.12. Correlation matrix for the skarn system.

Summary of geochemistry associations for the skarn system							
Very strong	Strong		Moderate				
Cd-Zn	Ag-Cd	Cd-Pb	Ag-As	Ba-K	Ti-V	Cu-Sb	S-Sr
	Ag-Pb	Cr-Sc	Ag-Bi	Be-Mg	Ca-S	Fe-K	Sc-Sr
	Ag-Sb	Fe-S	Ag-Mn	Be-Ti	Ca-Zn	Fe-Sc	
	Ag-Zn	Fe-Sr	Al-As	Be-Zn	Cd-Mn	K-Mg	
	Al-Be	K-Sr	Al-Mg	Bi-Cd	Cd-Sb	K-S	
	Al-Ti	Pb-Sb	Al-Na	Bi-Sb	Co-Fe	K-Sc	
	Ca-Fe	Pb-Zn	Al-V	Bi-Zn	Co-Ni	Mg-Sc	
	Ca-K	Sb-Zn	As-Pb	Ca-Cd	Co-S	Mn-Zn	
	Ca-Mn		As-Sb	Ca-Mg	Cr-Fe	Na-Sr	
	Ca-Sr		As-Zn	Ca-Mo	Cr-Sr	Na-Ti	

Correlation Matrix for the Porphyry Complex

The correlation matrix for the porphyry complex matrix (Table 5.13) showed that gold is most strongly correlated with silver (0.71), cadmium (0.62), lead (0.67), antimony (0.63), zinc (0.64), and arsenic (0.64), as well as moderately correlated with chrome (0.44), and iron (0.45). Silver is most strongly correlated with lead (0.86), arsenic (0.68), antimony (0.79), zinc (0.80), and cadmium (0.80). Lead is most strongly correlated with zinc (0.89), cadmium (0.88) arsenic (0.75), and antimony (0.74). Zinc is most strongly correlated with arsenic (0.72) cadmium (0.93) antimony (0.72). Molybdenum is most strongly correlated with thorium (0.68). Thallium is most strongly correlated with uranium (0.89) and mercury (0.64). Vanadium is most strongly correlated with aluminium (0.63), scandium (0.70), and titanium (0.64). Mercury is most strongly correlated with uranium (0.65). Cadmium is most strongly correlated with antimony (0.70).

These correlations may indicate that the bulk of the mineralogy is primary sulfides and fewer sulfosalts. The high temperature minerals increased and are locally associated with molybdenum and copper, whereas the gold may be associated with iron sulfides and sulfosalts.

	Ag	Al	As	Au	B	Ba	Be	Bi	Ca	Cd	Co	Cr	Cu	Fe	Ga	Hg	K	La	Mg	Mn	Mo	Na	Ni	P	Pb	S	Sb	Sc	Se	Sr	Th	Ti	Tl	U	V	W	Zn
Ag																																					
Al	-0.35																																				
As	0.68	-0.36																																			
Au	0.71	-0.34	0.64																																		
B	0.07	0.02	0.15	0.05																																	
Ba	0.12	-0.04	0.06	-0.03	0.12																																
Be	-0.05	0.43	-0.06	-0.10	0.33	0.09																															
Bi	0.30	-0.12	0.11	0.23	0.13	-0.02	0.07																														
Ca	-0.37	0.25	-0.40	-0.29	-0.06	-0.34	0.09	0.07																													
Cd	0.80	-0.34	0.70	0.62	0.09	0.08	-0.03	0.15	-0.35																												
Co	-0.02	0.08	0.05	0.07	-0.05	-0.08	0.02	0.07	0.12	-0.02																											
Cr	0.34	-0.12	0.49	0.44	0.26	-0.05	0.01	0.01	-0.26	0.41	0.01																										
Cu	0.13	0.13	-0.22	-0.03	-0.08	0.15	0.13	0.37	0.06	-0.11	0.21	-0.36																									
Fe	0.45	-0.02	0.42	0.45	0.09	0.03	0.06	0.33	-0.17	0.35	0.39	0.26	0.21																								
Ga	-0.09	0.31	-0.10	-0.07	0.33	0.00	0.35	0.14	0.11	-0.08	0.04	0.08	0.10	0.12																							
Hg	0.18	0.00	0.15	0.12	0.43	0.14	0.34	0.28	-0.06	0.16	-0.01	0.20	0.08	0.17	0.40																						
K	0.24	-0.08	0.17	0.15	0.14	0.51	0.01	0.06	-0.40	0.18	0.07	0.10	0.15	0.21	-0.01	0.15																					
La	-0.04	0.06	-0.07	-0.02	-0.49	-0.02	-0.41	-0.27	0.02	-0.06	-0.02	-0.18	-0.02	-0.12	-0.37	-0.44	-0.12																				
Mg	-0.37	0.42	-0.36	-0.24	-0.09	-0.24	0.04	-0.13	0.58	-0.32	0.19	-0.04	-0.14	-0.17	0.18	-0.09	-0.13	0.08																			
Mn	0.34	-0.12	0.33	0.26	0.06	-0.01	0.14	0.04	0.28	0.44	0.08	0.15	-0.13	0.19	0.07	0.11	-0.09	0.01	-0.09																		
Mo	-0.31	0.18	-0.50	-0.41	-0.08	0.14	0.16	0.14	0.16	-0.45	0.16	-0.52	0.59	-0.06	0.05	0.02	0.08	-0.01	-0.04	-0.26																	
Na	-0.46	0.43	-0.40	-0.40	0.08	-0.13	0.09	-0.09	0.32	-0.46	-0.04	-0.21	0.00	-0.23	0.21	-0.05	-0.25	-0.04	0.37	-0.17	0.16																
Ni	0.25	0.08	0.35	0.29	0.07	-0.16	0.15	0.14	0.02	0.29	0.41	0.40	0.02	0.37	0.07	0.05	-0.05	-0.04	0.00	0.20	-0.09	-0.17															
P	-0.05	0.37	0.05	0.00	-0.08	-0.09	0.08	-0.09	0.13	-0.03	0.23	0.11	-0.09	0.10	0.10	-0.04	-0.03	0.22	0.34	0.09	-0.09	0.11	0.23														
Pb	0.86	-0.41	0.75	0.67	0.10	0.12	-0.07	0.15	-0.40	0.88	-0.08	0.43	-0.14	0.35	-0.12	0.17	0.24	-0.04	-0.36	0.41	-0.45	-0.49	0.24	-0.05													
S	-0.02	-0.09	-0.14	0.05	-0.49	-0.31	-0.57	0.03	0.26	-0.10	0.21	-0.18	0.12	0.11	-0.30	-0.38	-0.15	0.41	0.18	-0.11	0.04	-0.01	0.02	0.05	-0.10												
Sb	0.79	-0.36	0.71	0.63	0.08	0.13	0.01	0.34	-0.33	0.70	0.03	0.29	0.24	0.41	-0.07	0.19	0.24	-0.08	-0.44	0.30	-0.21	-0.46	0.30	-0.08	0.74	-0.08											
Sc	-0.24	0.46	-0.22	-0.17	0.04	-0.12	0.24	-0.07	0.40	-0.21	0.11	0.05	-0.04	-0.07	0.20	0.12	-0.12	0.09	0.53	0.16	0.04	0.03	0.12	0.32	-0.25	-0.06	-0.25										
Se	0.17	-0.07	0.13	0.14	-0.15	0.00	0.04	-0.04	-0.10	0.18	-0.03	-0.01	0.00	0.08	-0.35	-0.15	0.04	0.03	-0.12	0.06	-0.04	-0.19	0.05	-0.07	0.17	0.03	0.15	-0.08									
Sr	-0.34	0.51	-0.38	-0.41	0.02	0.12	0.23	-0.16	0.33	-0.34	-0.17	-0.33	0.09	-0.22	0.10	-0.01	-0.20	0.16	0.20	0.01	0.19	0.40	-0.21	0.11	-0.37	-0.09	-0.36	0.37	-0.05								
Th	-0.49	0.26	-0.65	-0.54	-0.23	0.03	0.08	-0.02	0.36	-0.58	0.07	0.49	-0.77	0.49	-0.04	-0.23	-0.06	0.13	0.14	-0.22	0.68	0.33	-0.28	-0.09	-0.09	0.18	-0.40	0.10	0.06	0.38							
Ti	-0.38	0.43	-0.35	-0.23	0.00	-0.25	-0.06	-0.07	0.25	-0.37	0.06	0.02	-0.08	-0.19	0.21	-0.06	-0.28	-0.01	0.45	-0.02	0.22	-0.40	0.11	-0.40	0.45	-0.20	0.24	0.12									
Tl	-0.03	0.09	-0.03	-0.02	0.28	0.08	0.13	0.21	0.06	-0.06	0.06	0.05	0.06	0.07	0.41	0.64	0.05	-0.17	0.05	0.01	0.09	0.11	-0.03	0.09	-0.05	-0.14	-0.03	0.21	-0.53	0.10	-0.11	0.13					
U	-0.04	0.11	-0.03	-0.03	0.31	0.04	0.23	0.09	0.09	-0.05	0.06	0.08	0.06	0.08	0.41	0.65	0.03	-0.23	0.07	0.03	0.10	0.10	0.01	0.11	-0.06	-0.20	-0.07	0.24	-0.51	0.09	-0.09	0.11	0.89				
V	-0.30	0.63	-0.28	-0.19	0.00	-0.16	0.14	-0.15	0.31	-0.28	0.14	0.10	-0.01	-0.01	0.24	-0.06	-0.17	0.14	0.60	-0.01	-0.01	0.44	0.18	0.42	-0.34	0.00	-0.35	0.70	-0.12	0.38	0.11	0.64	0.08	0.10			
W	0.12	0.01	0.09	0.08	0.15	0.04	0.23	0.31	0.05	0.08	-0.01	0.04	0.07	0.18	0.17	0.45	-0.04	-0.15	0.10	0.07	-0.03	0.08	0.00	0.09	-0.17	0.17	0.10	-0.11	0.02	-0.07	0.02	0.47	0.48	-0.03			
Zn	0.80	-0.33	0.72	0.64	0.08	0.03	-0.03	0.20	-0.26	0.93	0.02	0.43	-0.12	0.37	-0.05	0.16	0.13	-0.05	-0.25	0.51	-0.47	-0.44	0.35	0.02	0.89	-0.08	0.72	-0.18	0.14	-0.37	-0.59	-0.34	-0.04	-0.04	-0.25	0.09	

Color Coding (signficance 0.950)
- very strong
- strong
- moderate
- weak
- very weak
- null

Table 5.13. Correlation matrix for the porphyry complex.

Summary of geochemistry associations for the porphyry complex									
Very strong	Strong			Moderate					
Ag-Pb	Ag-As	As-Zn	Pb-Sb	Ag-Fe	As-Fe	Be-S	Cu-Th	Na-Pb	Tl-W
Cd-Pb	Ag-Cd	Au-Cd	Pb-Th	Ag-Na	As-Mo	Ca-Mg	Hg-La	Na-Sb	U-W
Cd-Zn	Ag-Sb	Au-Pb	Sb-Zn	Ag-Th	Au-Cr	Cd-Mn	Hg-W	Na-Ti	
Pb-Zn	Ag-Zn	Au-Sb	Sc-V	Al-Be	Au-Fe	Cd-Mo	Mg-Sb	Na-V	
Tl-U	Al-V	Au-Zn	Ti -V	Al-Mg	Au-Mo	Cd-Na	Mg-Sc	Na-Zn	
	As-Au	Cd-Sb		Al-Na	Au-Th	Cd-Th	Mg-Ti	P-V	
	As-Cd	Cr-Th		Al-Sc	B-Hg	Cr-Mo	Mg-V	Sc-Ti	
	As-Pb	Hg-Tl		Al-Sr	B-La	Cr-Pb	Mn-Zn	Se-Tl	
	As-Sb	Hg-U		Al-Ti	B-S	Cr-Zn	Mo-Pb	Se-U	
	As-Th	Mo-Th		As-Cr	Ba-K	Cu-Mo	Mo-Zn	Th-Zn	

Geochemistry halos

Geochemical Halos on the Original Surface at Peñasquito

The soil geochemistry exhibited several broad anomalies. These anomalies presented two main linear trends: (1) On the north-south anomalous trend, Pb, Zn, Ag, Au, Cd, As, and Cu exhibited a similar distribution, and (2) on the west-east anomalous trend, Pb, Zn, Ag, Cu, W, Bi, Sb, and As were in strong agreement and formed longitudinal anomalies (Fig. 5.20).

Furthermore, these anomalies were in agreement with geophysical anomalies, such as low gravity and low resistivity. It is noteworthy that the north-south anomaly was correlated with the southwestern part of the Peñasco Breccia. The distribution of elements may occur due to mobility of metallic elements throughout time from diatreme breccias and stockwork zone. Therefore, it is believed that the anomalies suggested an economic buried mineralization that has been corroborated by the drilling campaigns.
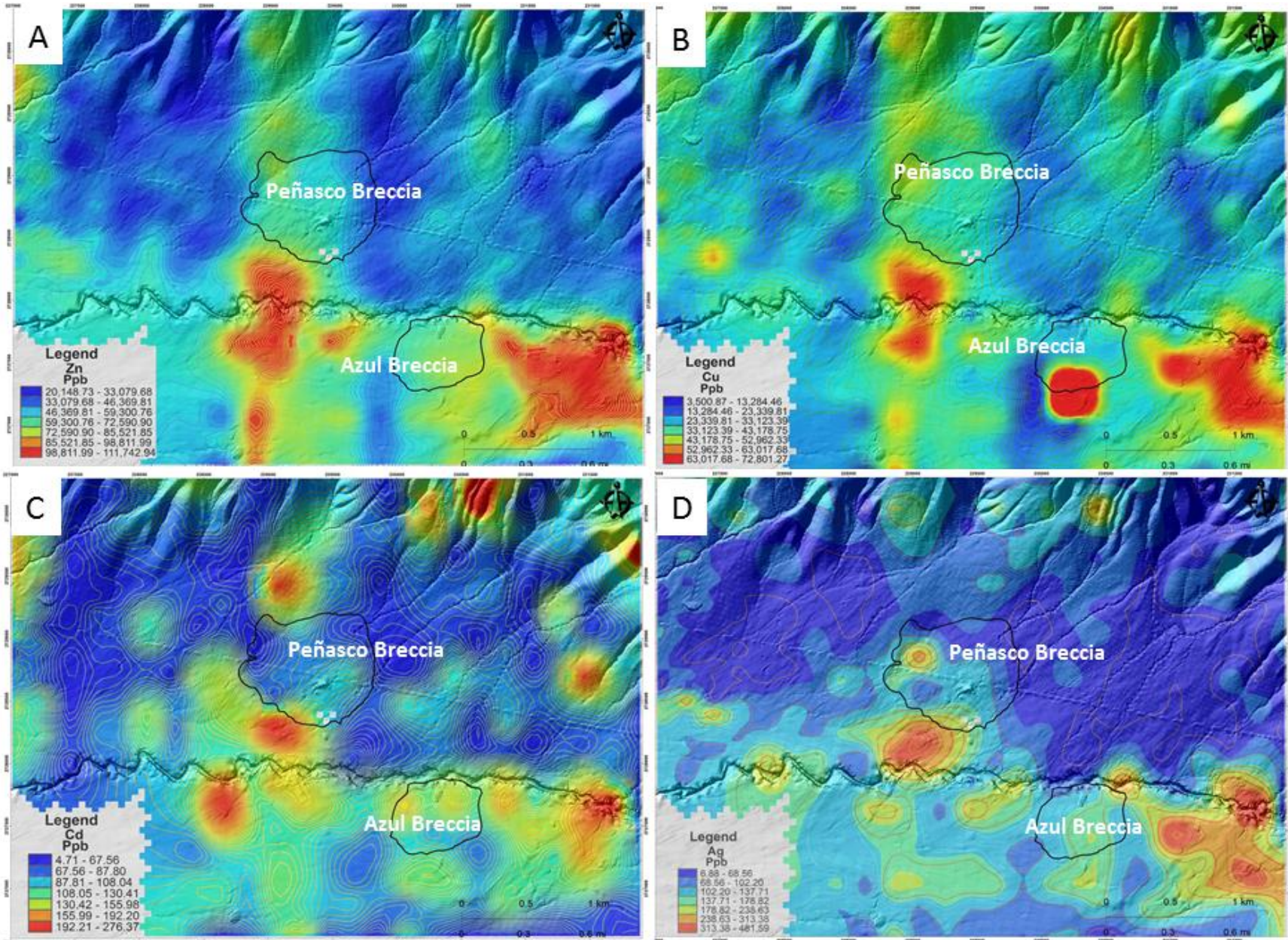
Fig. 5.20. Maps of soil geochemistry showing the distribution of zinc, copper, cadmium, and silver on the surface. Also shown are the diatreme breccia contours.

Geochemical Halos in the Peñasquito Ore Deposit

In the Peñasquito polymetallic deposit, the spatial distribution of chemical elements through the bedrock is evident, revealing spatial concentrations and chemical associations. This chemical distribution exhibits horizontal and vertical zonation of elements of economic importance. Gold and silver are distributed most frequently between 1,300 and 1,970 (m.a.s.l.) and show a strong correlation with arsenic and antimony. Zinc and lead are most frequently concentrated between 1,800 and 700 (m.a.s.l.). Copper and molybdenum are concentrated at deep levels (1,300 to 100 m.a.s.l.). These chemical distributions may suggest that the diatreme breccias functioned as vents and feeders during hydrothermal pulses from a plutonic complex, as well as mixed hydrothermal minerals during repeated breccia events.

The bulk of economic gold mineralization exhibits a horizontal distribution, forming a high-level zone with local protrusions to depth that extends from the surface to 1,300 m.a.s.l. The best values (1 to 536 ppm) are concentrated in the diatreme breccias. In general, the skarn system exhibits zones with gold values ranging from 2 to 0.5 ppm. Additionally, the plutonic complex locally exhibits concentrations of gold, which may be related to the copper mineralization and the potassic alteration shell (Fig. 5.21).

The bulk of economic silver mineralization is distributed in the diatreme breccias and stockwork zones. Silver formed a high-level zone that ranged from the surface to 1,300 m.a.s.l. The best silver values (up to 8280 ppm) are concentrated in both diatreme breccias. The silver exhibits moderate concentrations in the skarn system with minimum

concentrations in the porphyry system. The silver distribution is in strong agreement with

gold, arsenic, and antimony distribution (Fig. 5. 21).
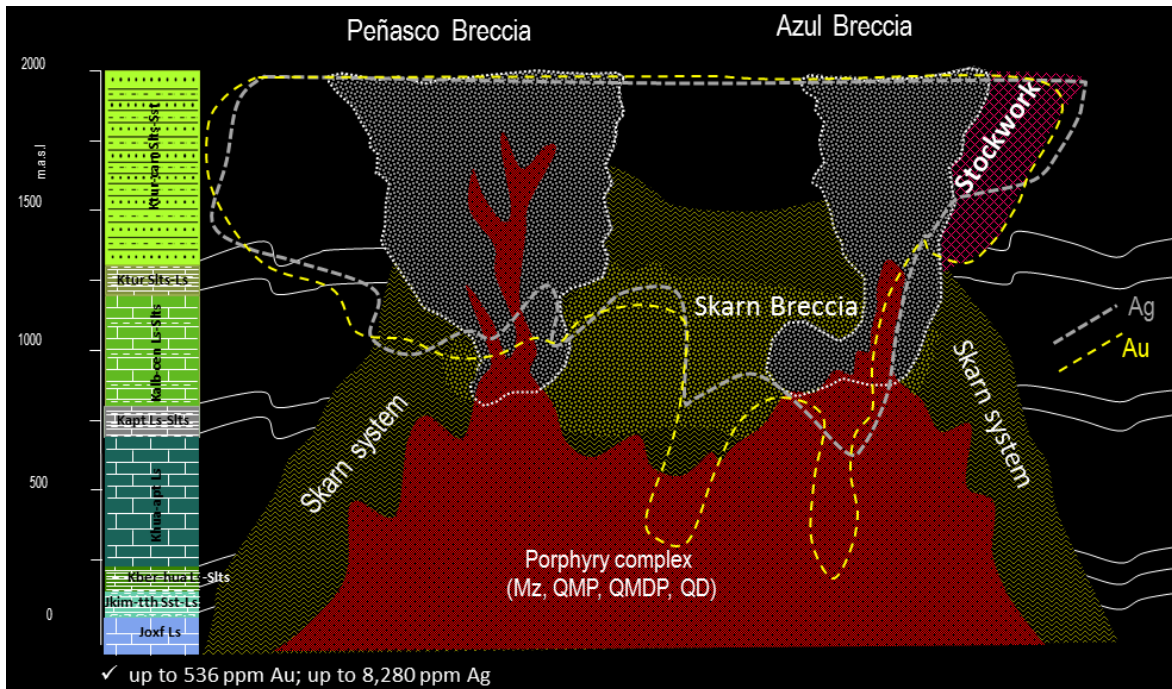
Fig. 5.21. Schematic cross section showing distribution of gold and silver through the Peñasquito polymetallic ore deposit. The cross section is oriented at 340° and looking to the northeast. The chemical data are projected in the cross section and the lithology column is displayed on left side followed by white lines. The cut-off values are 0.13 g/t Au, and 20 g/t Ag.

Arsenic shows a clear distribution in both diatreme breccias and stockwork zones.

This element is concentrated from the surface to 1,300 m.a.s.l. The arsenic exhibits values

up to 2,080 ppm, a strong spatial correlation with Au, Ag, Pb, and Zn, and is locally related

to the skarn system (Fig. 5.22).

Antimony concentrations are up to 1,850 ppm and distributed in the middle parts of

both diatreme breccias, stockwork zones (e.g. Chile Colorado), and in the upper portion of

the skarn system. The best values of arsenic occur between the 1,800 and 1,200 levels

(m.a.s.l.), which are in spatial correlation with high values of Au, Ag, Zn and Pb. The

antimony is locally related to the porphyry system and moderately related to the skarn system (Fig. 5.22).
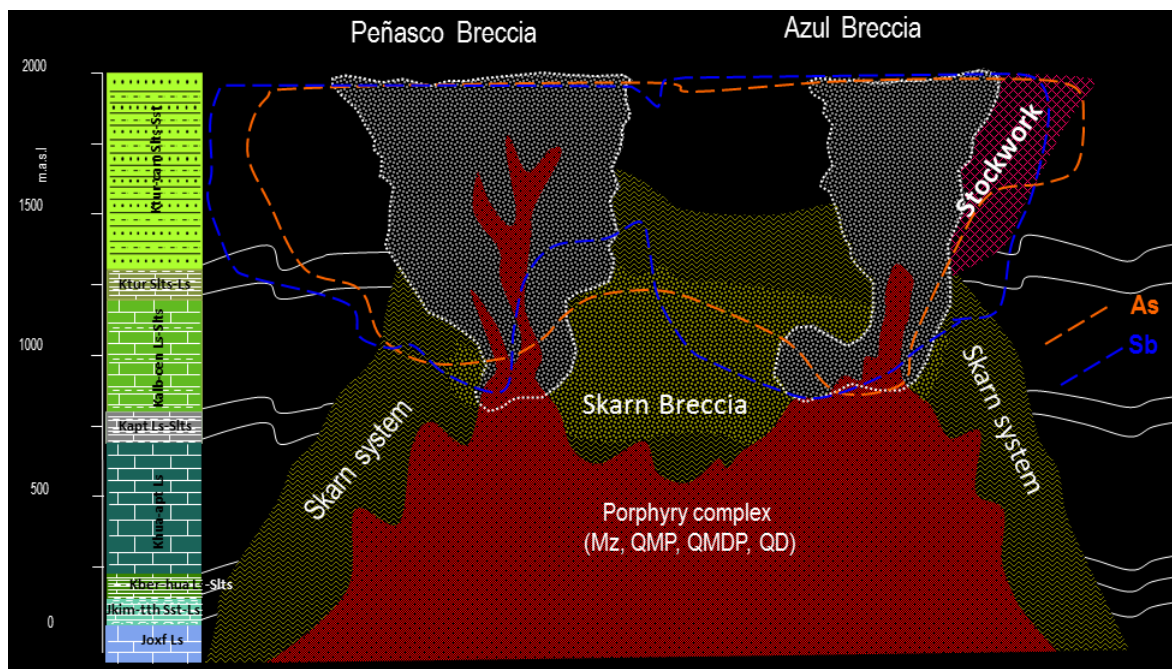
Fig. 5.22. Schematic cross section showing distribution of arsenic (As) and antimony (Sb) through the Peñasquito polymetallic ore deposit. The cross section is oriented at 340° and looking to the northeast. The chemical data are projected in the cross section and the lithology column is displayed on left side followed by white lines.

The economic mineralization of lead is concentrated in the diatreme breccias and forms a horizontal distribution between the surface and 1,300 m.a.s.l. The best values of lead (up to 496,000 ppm) are distributed in the middle part of the Peñasco Breccia as well as throughout the Azul Breccia and Chile Colorado stockwork. The skarn system revealed a moderate concentration of lead related to borders of the diatreme breccias (Fig. 5.23).

The economic concentration of zinc occurs from the surface to 600 m.a.s.l. The distribution is homogeneous throughout the area occupied by both diatreme breccias. The best values of zinc (up to 397,000 ppm) are most strongly concentrated in the Azul Brec-cia. The skarn system exhibits good concentrations of zinc while the porphyry system lo-

cally exhibits concentrations more than 2 % zinc. The zinc distribution is in strong agreement with gold distribution (Fig. 5.23).
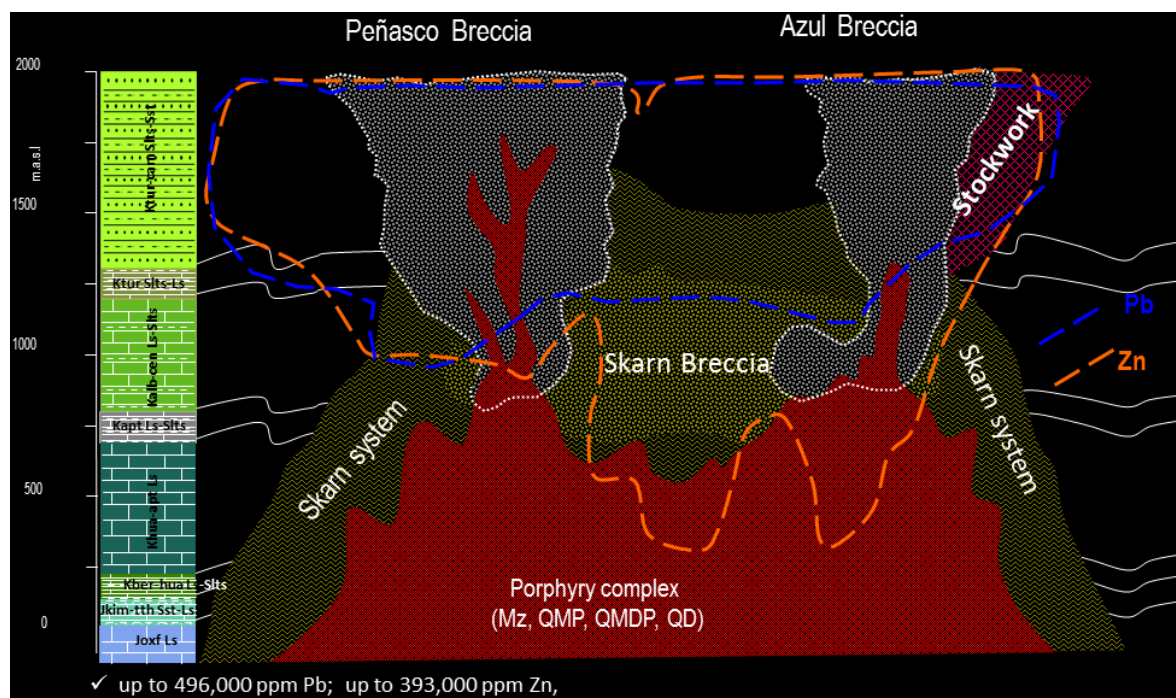
Fig. 5.23. Schematic cross section showing distribution of lead (Pb) and zinc (Zn) through the Peñasquito polymetallic ore deposit. The cross section is oriented at 340° and looking to the northeast. The chemical data are projected in the cross section and the lithology column is displayed on left side followed by white lines.

Copper presents a wide range of vertical distributions from the surface to 100 m.a.s.l. The best economic concentrations of copper (273,000 ppm) are concentrated between 1,300 and 100 m.a.s.l., which falls within the skarn system; however, lower copper concentrations are also present in the porphyry system. The copper shows moderate concentrations throughout both diatreme breccias and stockwork zones, forming an irregular halo (Fig. 5.24).

Molybdenum is concentrated below 1,300 m.a.s.l. The best values of molybdenum (4,880 ppm) are related to the porphyry system (Fig. 5.21). The skarn system exhibits a

constant range of molybdenum (i.e. 51 to 200 ppm) with erratic spatial distribution. The

Azul Breccia locally exhibits some low molybdenum concentrations (i.e. 50-200 ppm),

which developed in the middle and upper portions (Fig. 5.24).
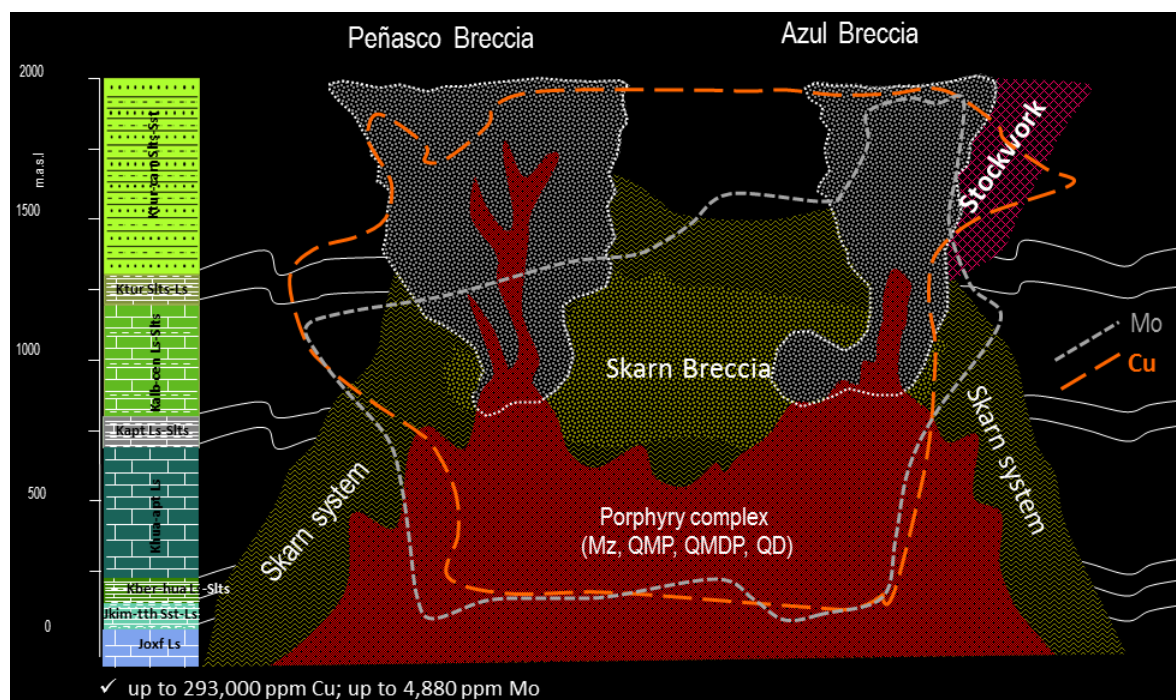
Fig. 5.24. Schematic cross section showing distribution of copper and molybdenum through the Peñasquito polymetallic ore deposit. The cross section is oriented at 340° and looking to the northeast. The chemical data are projected in the cross section and the lithology column is displayed on left side followed by white lines.

CHAPTER VI

GEOLOGICAL ANALYSIS OF GEOPHYSICAL DATA FOR THE PEÑASQUITO AREA

Introduction to Analysis of Geophysical Data

In the Peñasquito region, geophysical surveys have been conducted at different times and have shown a combination of magnetic, gravitational, electrical (resistivity and controlled source audio magnetotelluric) anomalies related to the ore deposits. The present study shows magnetic, gravitational, and electrical data that may be useful in helping to establish the local geological setting of the Peñasquito ore deposit. Due to extensive alluvial cover by Tertiary and Quaternary sediments in the region of Peñasquito, the geophysical surveys that were conducted by explorers suggested a buried pluton as well as low gravity and low resistivity anomalies related to the diatreme breccia system and stockwork.Geophysical analysis includes regional-scale aeromagnetic data that may be useful in determining the influence of buried magmatic bodies. It is believed that the plutonic system contributed to a large extent in the development of hydrothermal alteration and mineral deposition in the Peñasquito area. In addition, a local-scale gravity analysis is included in order to demonstrate the geophysical signature for the diatreme breccia system.

In 1997, the Mexican Geological Survey(i.e. Servicio Geológico Mexicano "SGM") conducted a regional-scale aeromagnetic survey. The local-scale gravity and electrical geophysical surveys, however, were conducted by private companies as well as the Mexican Geological Survey during various exploration episodes, and these results are part of Gold-

corp's unpublished in-house data. For that reason, in this analysis, some processed figures are presented to help interpret the geophysical anomalies related to the Peñasquito area.

Aeromagnetic Survey Data

Regional-scale aeromagnetic data contain two prominent magnetic highs with the Peñasquito ore deposit situated in the western magnetic anomaly. The western magnetic anomaly has two dipoles, elongated distribution in a north-south orientation, spatially associated with outcrops of intrusive rocks in the Noche Buena area (Fig. 6.1). At Peñasquito, the magnetic anomaly dimensions are: 40 km in longitude, 20 km in width, covering 63.053 ha, and extending between the Noche Buena area and the southern part of Peñasquito. This bipolar magnetic anomaly is characterized by a moderate intensity that ranges from -260 to +600 nanoteslas (nT). This anomaly may be interpreted as the response to a buried igneous rock complex that played an important role during the hydrothermal mineralization stages in the region.

Filtering techniques permit mapping of the igneous bodies associated with the Peñasquito region and allows the recognition of magnetic influence as well as the pathways that plutons followed through the upper crust. Some portions of the magnetic anomalies are spatially associated with outcrops of intrusive rocks that are equivalent in age to those found in the Peñasquito area. Merged regional aeromagnetic data are further processed utilizing the reduced-to-pole (RTP) transform method in order to better delimit magnetic anomalies, resulting in minimized anomaly asymmetry (Anderson et al., 2013). This map

(Fig. 6.2) was plotted withOasis MontajGeosoft 4.3 in order to obtain the real magnetic influence in space (Hernández-Perez et al., 1997).
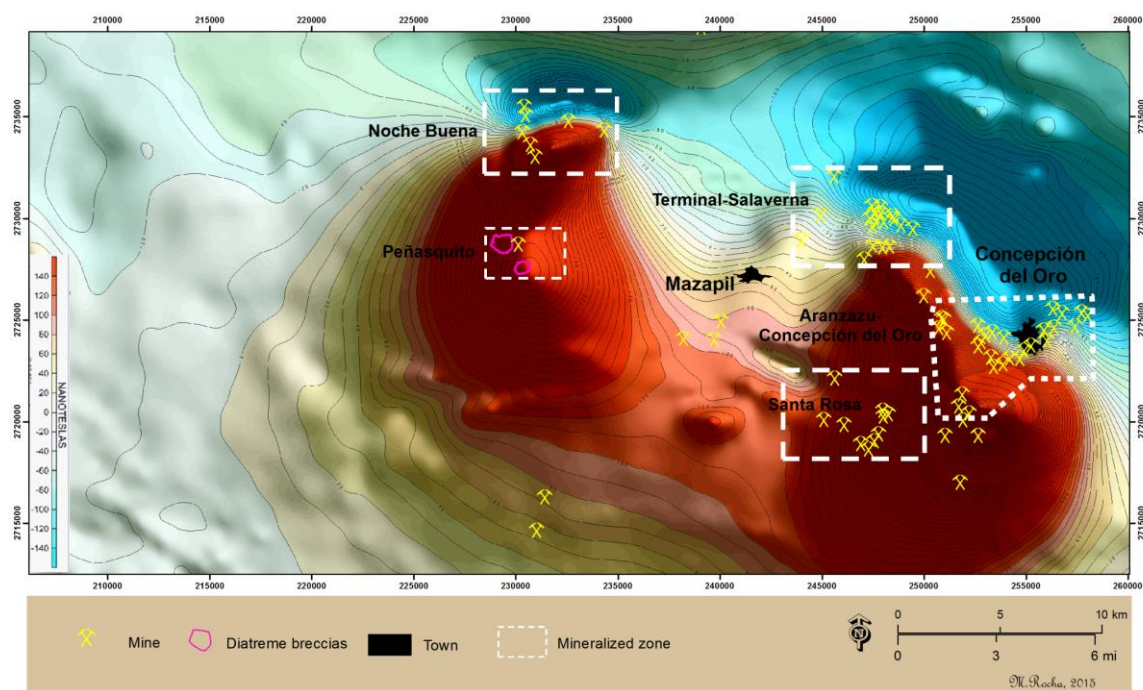
Fig. 6.1. Map showing aeromagnetic data (Total Field) and mineralized zones (modified from SGM, 2013).

The RTP transformation of the regional aeromagnetic data shows two contrasting magnetic anomalies with Peñasquito situated in the southwestern portion of the western RTP anomaly. The western anomaly exhibits a dominant magnetic trend in a north-south orientation, whereas, the eastern RTP anomaly is dominated by a magnetic trend in a northwest-southeast orientation, which corresponds to mineralized zones (i.e. Terminal-Salaverna and Aranzazu-Concepción Del Oro) and the presence of exposed igneous rocks (Fig. 6.2).The prominent magnetic anomalies have values greater than 1,000 nT, suggesting the real influence of buried igneous bodies and/or stocks partially exposed in the Sierra La Caja-Concepción del Oro anticline.
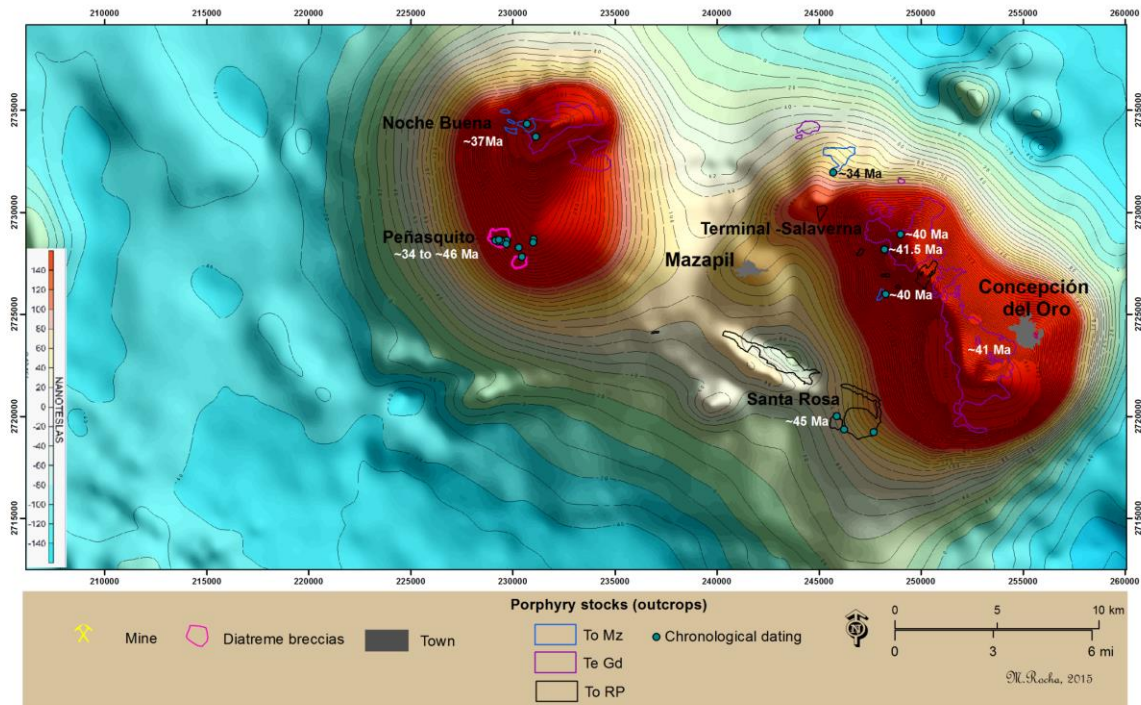
Fig. 6.2. Map showing RTP transformed aeromagnetic data (modified fromSGM, 2013), radiometric age dates (Valencia, 2010, Mújica-Mondragón et al., 1983; and by this author), and plutonic outcrops, such as Gd (Granodiorite), RP (Rhyolite porphyry), Mz (Monzonite) (modified from MSG database).

In addition, a map of the first vertical derivative(Fig. 6.3) (i.e. reduction of the total magnetic pole) was transformed from the regional aeromagnetic data using filtering techniques and a specialized software (i.e.Oasis MontajGeosoft 4.3). The objective was the delineation of shallow magnetic anomalies, such as magnetic bodies and shallow geological structures (i.e. 500 m depth below the current surface). The map shows two magmatic highs and revealsthat the Peñasquito breccia system is in the southwestern portion of a prominent magnetic high, suggesting that magmatic bodies may occur at a shallow depth. The picoTesla sensitivity is up to 100 values for both anomalies. In the Peñasquito area, the prominent magnetic high has a 4 km diameter, suggesting a shallow magmatic body between the Noche Buena and Peñasquito areas (Fig. 6.3).These magnetic anomalies have

been corroborated with drilling programs, which have intercepted the plutonic complex at hundreds of meters below the current surface at Peñasquito, as well as the sets of faults (i.e. Lluvia de Oro and Peñasco faults). Furthermore, in the western portion of Peñasquito, the map shows a linear magnetic low striking with northwest-southeast orientation and an intensity of 0 picoTelsas/meter, suggesting the influence of a geological structure that is in agreement with the San Tiburcio sinistral fault.
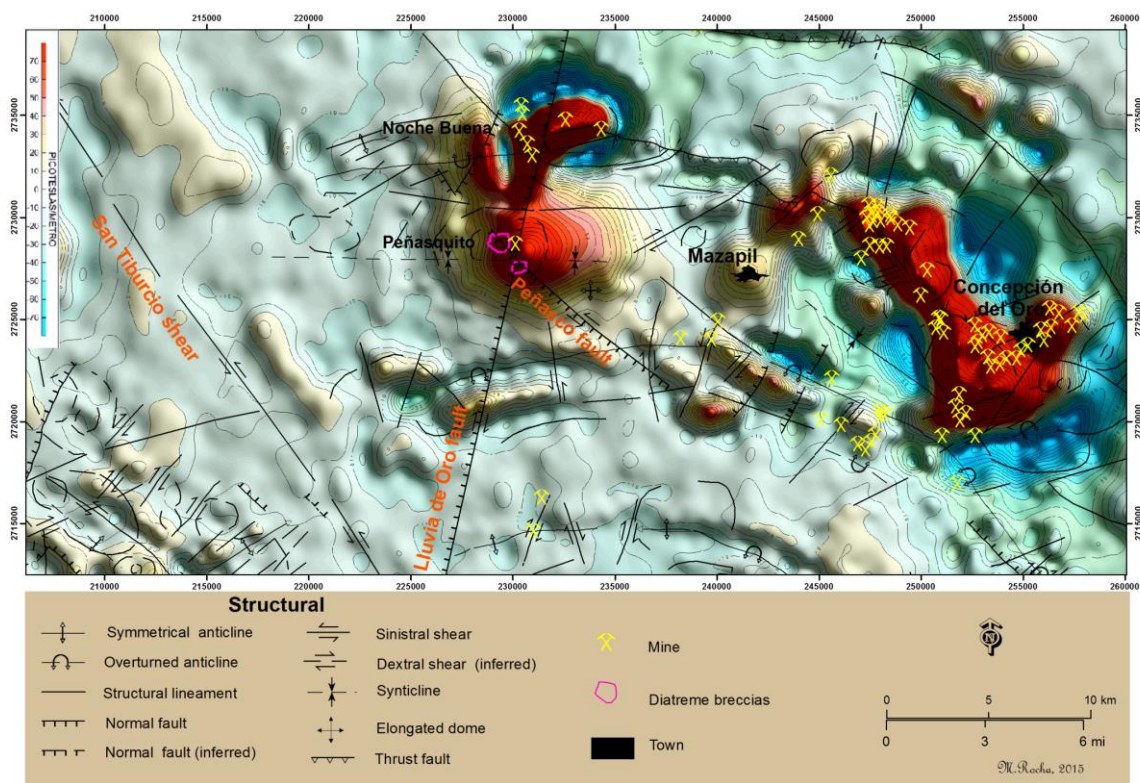
Fig. 6.3. Map showing the first vertical derivative of the magnetic field, structural control, fault, and mines (modified from SGM, 2013).

Finally, maps of downward continued data of the total field magnetic anomalies were constructed and reveal magnetic anomaly highs bound together, which correlate with known plutonic-style occurrences in the Peñasquito region. The aim was to look for continuity of magnetic bodies at depth. The magnetic data have been interpreted at a

depth of 2,000, 3,000, and 8,000 meters below the current surface. This analysis may eliminate the magnetic anomaly from surface magnetic bodies and integrated magnetic anomalies at depth. The results confirm shallow magnetic anomalies and suggest pathways that the igneous bodies followed through the crust. The map interpreted at a depth of 2,000m shows two linked broad magnetic highs and a magnetic influence that extends from the Peñasquito area to Concepción del Oro. The broad dominant magnetic trend occurs in a northwest-southeast orientation and exhibits an elongated influence, suggesting a deep large magmatic complex (Fig. 6.4).
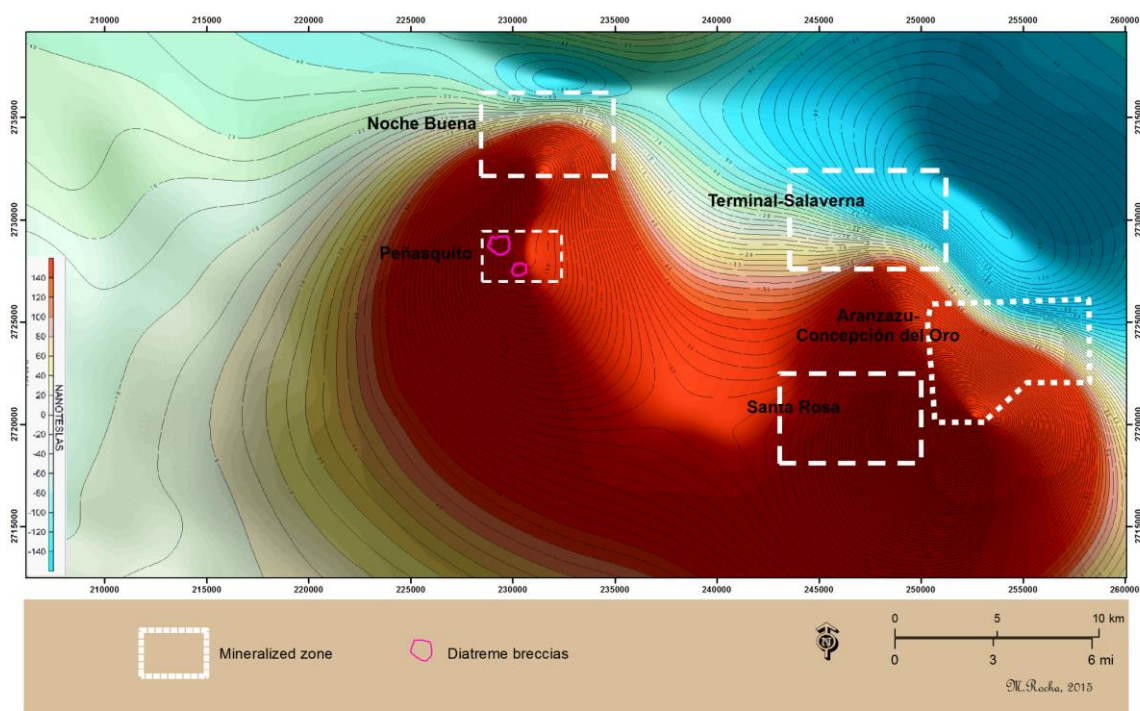
Fig. 6.4. Map showing aeromagnetic data downward continued to 2 km depth (modified from SGM, 2013). Also shown are mineralized zones.

Moreover, maps of downward continued data of the total magnetic field at a depth of 3,000 meters show two magnetic highs with an obvious partition (Fig. 6.5). It is believed that areas of weakness and the constitution of rocks in the crust played an

important role in the ascension of magmas which could have caused a separation of magmas at about 3,000 meters depth. However, at 8,000 meters depth (Fig. 6.6), the magnetic highs exhibit a similar behavior to the magnetic anomaly that is present at 2,000 meters depth. Furthermore, at depth, the influence of the bipolar magnetic anomalies gradually broadens southward, suggesting that the plutonic system was emplaced from the southern portion through the sedimentary sequence (Fig. 6.6). In addition, the correlation of magnetic highs at different depths suggests that magmas were emplaced along inclined pathways toward the south, that may possibly be anticline axes, and subsequent deformation may have occurred due to these magmatic intrusions.
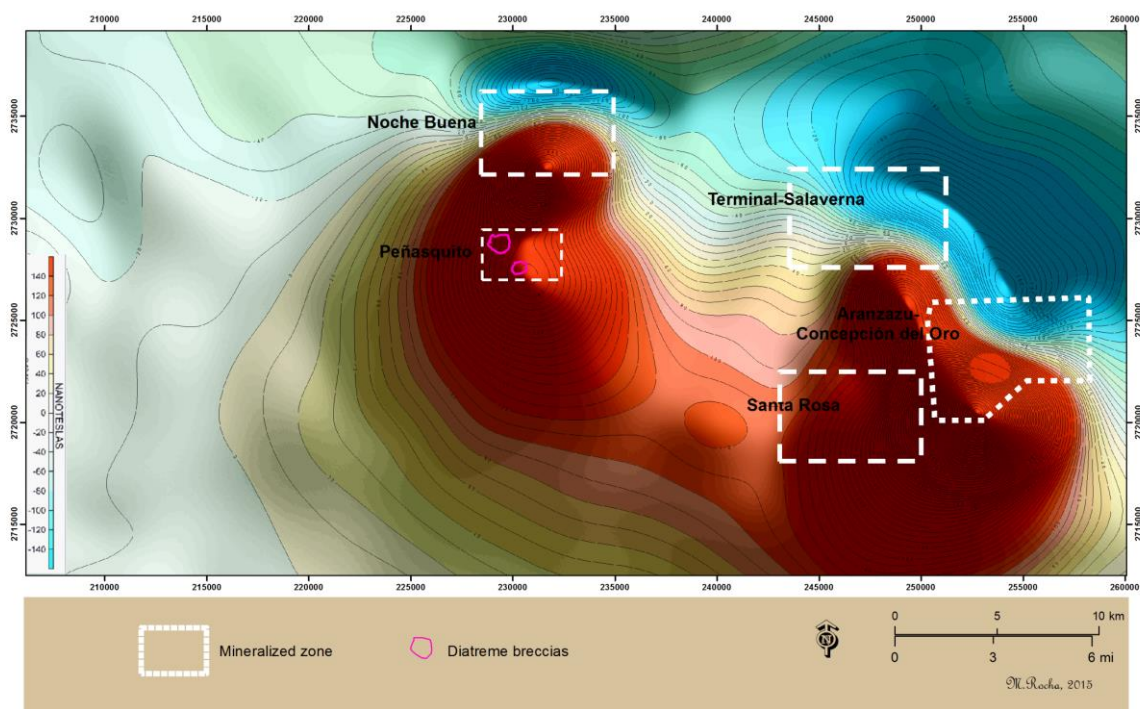
Fig. 6.5. Map showing aeromagnetic data downward continued to 3 km at depth (modified from SGM, 2013). Also shown are mineralized zones.

In short, the analysis of regional-scale aeromagnetic data suggests the presence of a largely concealed Tertiary magmatic plutonic complex in the Peñasquito region. There-

fore, the region is highly prospective for polymetallic replacement ore deposits and epi-thermal ore deposits, such as stockwork zones and pipes that may be linked to porphyry copper systems similar in age to the 46 to 33 Ma Peñasquito ore deposit-related magmatism.
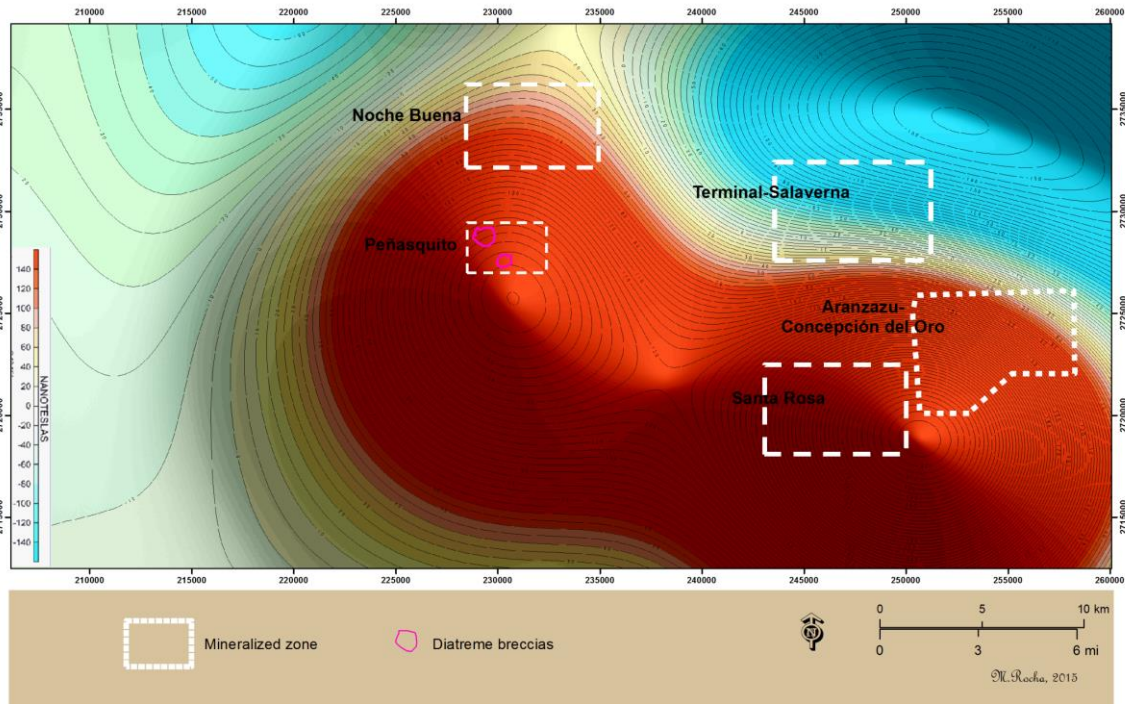
Fig. 6.6. Map showing aeromagnetic data downward continued to 8 km depth (modified from SGM, 2013). Also shown are mineralized zones.

Local Geophysical Signature

Although various geophysical methods, including gravitational, electrical, and radiometric surveys have been conducted in the Peñasquito area, only data from gravity, resistivity, and controlled source audio magnetotelluric (CSAMT) surveys have demonstrated singular anomalies in agreement with the ore body distributions, suggesting a combination of geophysical signatures to identify these polymetallic deposits. In the late 1990s and

in 2005, the local-scale geophysical surveys, including gravity and resistivity, were conducted by private companies and funded by Minera Kennecott and Western Silver. In 2008, however, the Mexican Geological Survey conducted a local-scale electrical geological survey throughout the Mazapil valley and this survey highlighted the geophysical results (CSAMT) for the Azul Breccia.
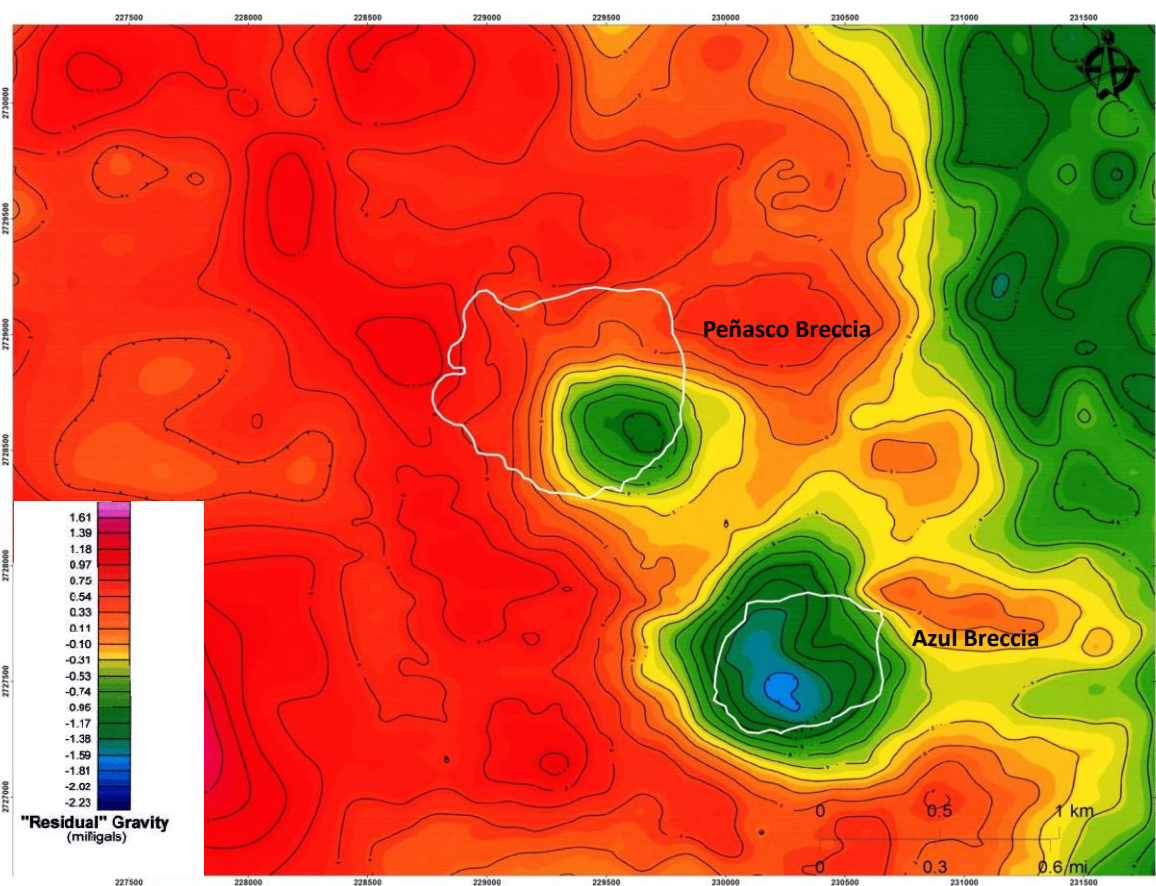
Fig. 6.7. Maps showing residual gravity and contours of the diatreme breccias (Modified from Geosciences Aplicadas, 2005).

The gravity data suggest two marked low anomaly zones within the Peñasquito area. Both low anomalies are linked and spatially associated with the diatreme breccia systems, which generally exhibit an elongated distribution in a northwest-southeast orientation. The anomalies are characterized by an intensity that ranges from -0.31 to -1.59 milligals.

The gravity's lower anomaly (southeastern zone) is, spatially, in agreement with the Azul Breccia, whereas that Peñasco Breccia is partially related to the second gravimetric low (Fig. 6.7) These gravity anomalies may be interpreted as a geophysical signature due to the physical constitution betweenof the bedrock and breccia system, indicating different compaction and low density in the diatreme breccias, which indicatesthe spatial influence of the diatreme breccia system.

Resistivity geophysical surveys measure variations in the electrical resistivity of the ground by applying small electric currents across arrays of electrodes. The survey data may indicate thickness as well as resistivity of subsurface electrical layers and may provide detailed information on the subsurface ground conditions (Wilds and MacIness, 1991). Resistivity data suggest marked low anomalies in the Peñasquito area. These resistivity anomalies generally exhibit an elongated distribution in northwest-southeast orientation and are spatially associated with the stockwork zones as well as veins and faults of high ore grade (Fig. 6.8).

The resistivity anomalies are characterized by intensities that range from 79 to 13 ohm-ms. The resistivity low anomaly, situated in the southwestern part from the Azul Breccia, is, spatially, in agreement the Chile Colorado zone, which is a large stockwork sulfide zone. The low resistivity anomaly situated between the Peñasco and Azul Breccias is partially related to mineralized faults and fractures. The low resistivity anomaly to the northeast is partially related to the Palma zone, which includes shallow veins of sulfides and the skarn system at depth (Fig. 6.8). These low resistivity anomalies may be interpreted as a geophysical signature due to the structural control and mineralogical

composition in the country rock, indicating the sulfides, and suggesting the influence of hydrothermal mineralization in fractures.
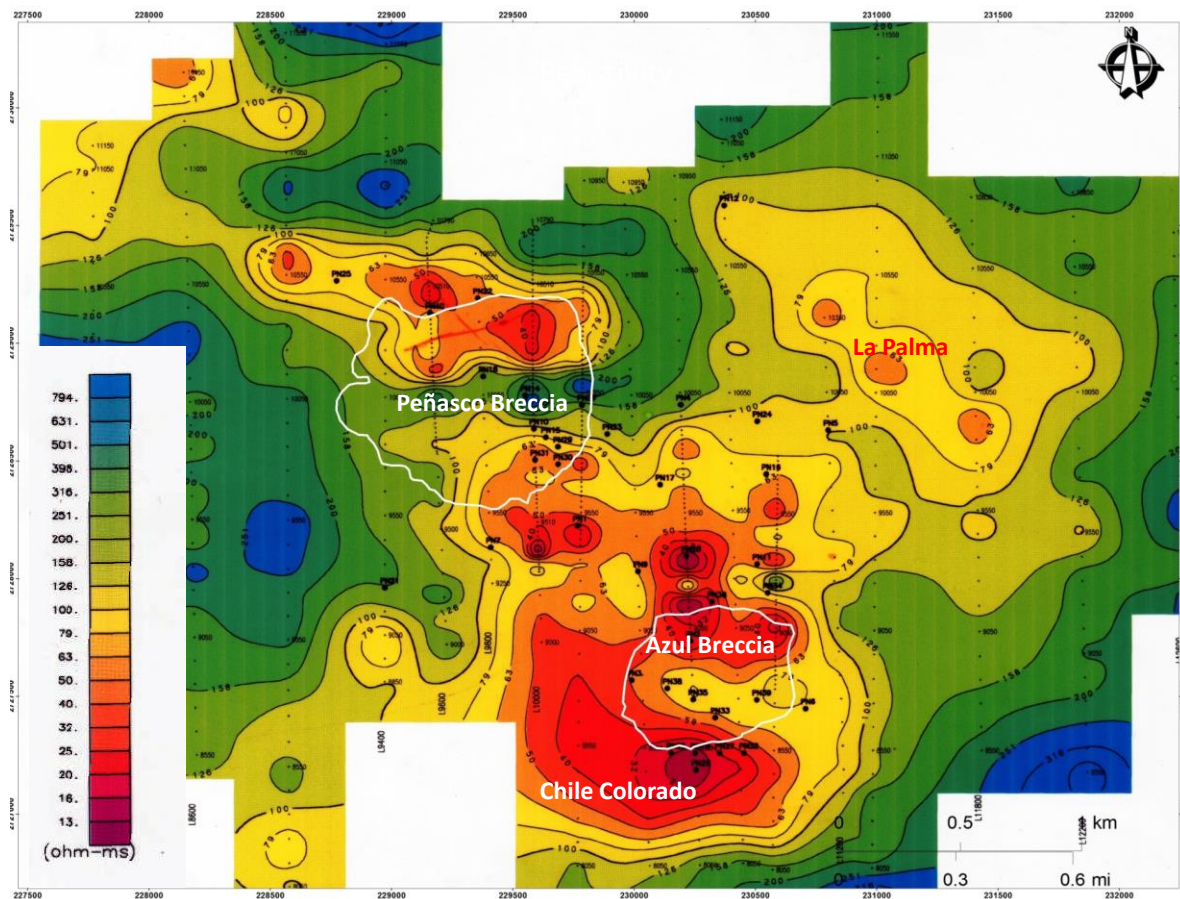
Fig. 6.8. Maps showing CSAMT and contours of the diatreme breccias (Modified from Minera Kennecott, 1996).

In addition, a CSAMT geophysical survey was conducted by Mexico Geological Survey and confirms a CSAMT low anomaly. The survey was conducted on the Azul Breccia through a section with west-east orientation. A total of 43 survey points (CSAMT) with a separation of 50 meters were completed on the test line, using an electromagnetic receiver V8 and transmitter T3 (Phoenix brand) (Hernández-Perez et al., 2008). The data were plotted in a cross section that showed a noticeable low resistivity anomaly. The

anomaly intensity ranges between 40 and 180 ohm-m (Fig. 6.9). This anomaly is in perfect agreement with the extent of the Azul Breccia but at depth, the anomaly extends horizontally. This resistivity low anomaly may be attributed to metallic mineralization. The low resistivity may be interpreted as the response caused by the fracturing and the content of metallic minerals. The horizontal extension of low anomaly (between 800 and 1000 m in depth) may indicate the presence of metallic mineralization in the skarn system.

The analysis of local-scale geophysical data suggests that the Peñasquito area is characterized by two main geophysical signatures, low gravity and low resistivity, and both anomalies may be useful in exploration. For example, a low gravity anomaly may be useful in the exploration of concealed breccias. In addition, a low resistivity anomaly may be useful in the identification of concealed mineralized fracturing and metallic mineralization at depth.
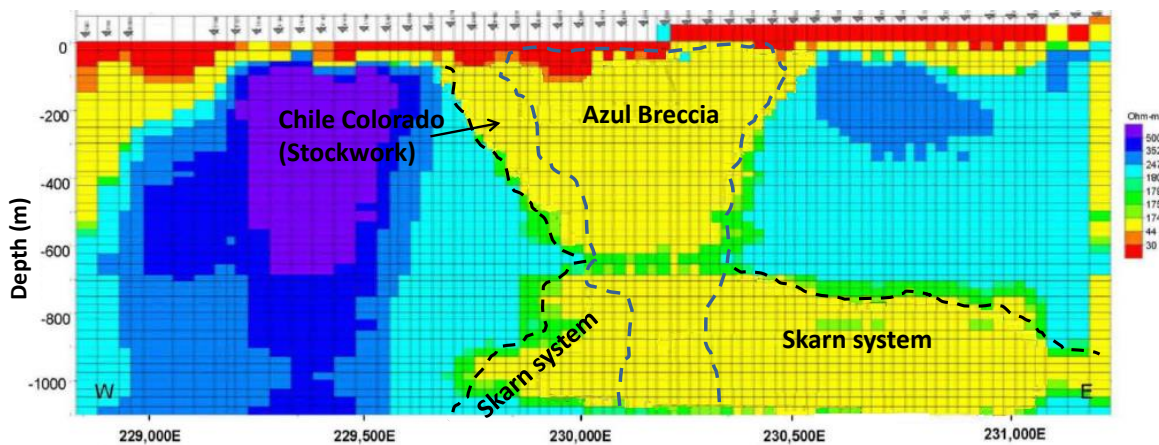
Fig. 6.9. Cross section showing CSAMT anomaly and contours of the Azul breccias, and skarn system looking to north (Modified from Hernández-Perez et al., 2008)

CHAPTER VII

NATURE OF THE HYDROTHERMAL FLUIDS, TEMPERATURES, SOURCE OF THE ORE FLUIDS

Fluid inclusions

Synopsis of Fluid Inclusions

The study of fluid inclusions allows deciphering of the physicochemical conditions that prevailed during the formation of each mineral. Certain parameters must be considered during the study of fluid inclusions in order to obtain accurate results. The advantages of studies, such as these, include knowledge of the original nature of the trapped fluid as the fluid inclusion has remained hermetically and chemically inert; furthermore, every fluid inclusion acts as an isolated thermodynamic system. The microthermometry reveals the relationship between the event of fluid entrapment and the geological record.

However, during the study of fluid inclusions, one must consider several phenomena that may occur in many fluid inclusions found in heterogeneous systems. For instance, (1) suspended particles may be present due to breaking of the host rock and these may appear in the interior of the fluid inclusions in varying quantities and sizes; and (2) simultaneously trapped phases may be present that could generate heterogeneous immiscible fluids (i.e. aqueous liquid as CO_2) (Roedder and Bodnar, 1997).

Terminology of Fluid Inclusions

The study of fluid inclusions implies a singular terminology and several terms must be defined in order to understand the meaning of each parameter given in this type of research. Therefore, the most common terms as well as a description of fluid inclusions and their implications are briefly described below. This research only includes results from primary fluid inclusions.

Fluid inclusions are filled with gas and/or liquid and, in some cases, minor amounts of one or more solid phases. Fluid inclusions result from defects in the crystals during their growth, which lead to the entrapment of fluid from the system. Therefore, there are three types of fluid inclusions: (1) primary fluid inclusions that are formed during the growth of the enclosing crystal, which tend to be solitary or isolated, and yield information on the conditions of the formation or crystallization of the host mineral; (2) secondary fluid inclusions occur along healed fractures that are trapped after crystal growth has been completed and may be recognized by their occurrence in trails or clusters that commonly cut across grain boundaries; and (3) pseudosecondary inclusions are formed during late fracturing in the crystallization of the host mineral and the fluid is trapped in inclusions along these fractures; thus they occur along trails that end abruptly against grain boundaries or one of the growth zones (Goldstein, 2003).

The temperature of homogenization (Th) is when all phases become one phase and are totally homogenized during the heating process. For example, this temperature is reached when a vapor bubble disappears in the liquid phase by heating the fluid inclusion.

This temperature of phase change represents the minimum temperature that occurred when fluid was trapped during the formation of a crystal (Goldstein, 2003).

The temperature of entrapment (Tt) is the temperature at which a fluid inclusion was formed. The temperature of entrapment corresponds to the temperature of homogenization with a correction due to pressure. However, if Tt is same as Th, no pressure correction is needed (Goldstein, 2003).

The temperature of decrepitation (Td) is when a fluid inclusion decrepitates due to excessive pressure, and fluids and gases are lost. The temperature of eutectic (Te) is when the first recognizable formation of liquid appears during the warming process of a completely crystalline and frozen inclusion. It is only an approximate value, as traces of other components will always modify first melting (Goldstein, 2003).

The temperature of melting (Tm) is usually considered when the last ice crystal melts; however, this also includes other parameters. For ordinary water-rich inclusions, this temperature may refer to the melting of ice. The specific solid phase that melts (or dissolves) should always be designated after Tm; for instance, when NaCl dissolves, it would be written as Tm_{NaCl}, Tm_{ice}, and Tm_{CO2}. This temperature is interpreted as the composition of the fluid and is equivalent to the dissolved salts in the system. Otherwise, Eq. wt % NaCl is the quantity of NaCl that would yield the same Tm_{ice} value (Goldstein, 2003).

Analytical Methodology

The fluid inclusions are the only direct samples of the fluids that have circulated and interacted with the host mineral. The fluid inclusions preserve the original signature of the physicochemical conditions that prevailed during the emplacement of the hydrothermal fluids. Analysis and interpretation must be made on fluid inclusions that have kept their volume and original composition since their entrapment (Roedder, 1984; González-Partida et al., 2008; Camprubí, 2010).

In this research, forty-five selected and representative samples were prepared and analyzed. The specimens were from the diatreme breccia system, the stockwork, the skarn system, and the porphyry complex. The purpose of the study was to learn about the thermometric conditions that prevailed during the development of the polymetallic ore deposits. The study of primary fluid inclusions was conducted from samples of hydrothermal quartz (veinlets), sphalerite, garnet, and fluorite. In addition, primary fluid inclusions in quartz phenocrysts, which correspond to the plutonic rocks, were analyzed.

The methodology in the study of fluid inclusions suggests a preliminary petrographic analysis (Goldstein and Reynolds, 1994). Therefore, doubly polished sections were initially prepared at a thickness of 90 microns on a glass slide made by the Spectrum Petrographics Laboratory. Subsequently, the petrography was completed with a traditional optical microscope, where the components of the samples and fluid inclusions were identified. Afterward, the samples were removed from the glass slide for the microthermometry analyses.

The microthermometric analyses were performed at the laboratory of Experimental Chihuahua Center of the Mexican Geological Survey, at the laboratory of Geosciences Center of National Autonomous University of Mexico (UNAM at Queretaro, Mex.), and at the CREG laboratory of the University of Nevada Reno (UNR). Specifically, the bulk of microthermometric analyses were completed on a petrographic microscope with transmitted light (Carl Zeiss AX10-IMAGER A2M) that included a heating and freezing microscope (Linkam scientific instrument MDSG 600). This Linkam microscope stage is motorized on X and Y axes and has a thermal capacity of -196°C to 600°C. In addition, a digital video capture option and a screen system are attached to the microscope.

Data obtained include the quantification of thermometric and physiochemical components. Specifically, these data include the homogenization temperature (Th), eutectic temperature (Te), and melting temperature (Tm). The salinity was estimated from the ice melting and /or solubilization of halite, for the H_2O-NaCl system (Bodnar, 1993). Finally, the data are plotted on tables and graphs in order to interpret the results.

Sampling of Microthermometric Analyses

Samples were obtained from drill cores where the geological context and paragenetic setting are well known due to detailed logging undertaken as part of the general geological description of the ore bodies and surrounding altered rocks. The fluid inclusion study focused on primary inclusions hosted by quartz from different epigenetic stages (i.e. pre-syn-post mineralization). The inclusions were investigated by conventional and electronic microscopy and subjected to microthermometric analyses.
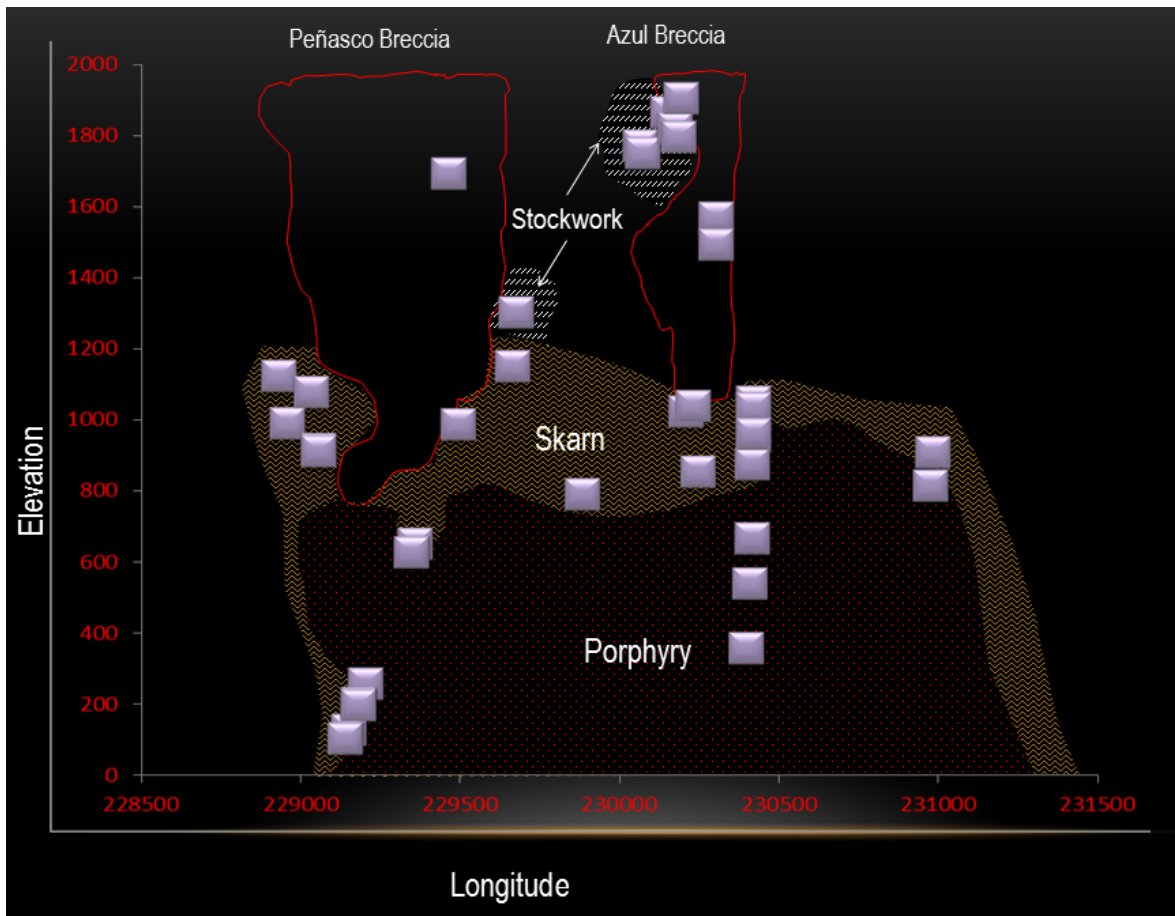
Fig. 7.1. Schematic cross section showing the distribution of fluid inclusions samples (looking to the northeast)

The sampling included the porphyry complex, the skarn system, stockwork, and the diatreme breccia system. The specimens were collected from 100 to 1,901 m in elevation (m.a.s.l.) and distributed through the Peñasquito hydrothermal system (Fig. 7.1). Specifically, eight samples from the porphyry complex were examined, including seven samples of quartz (i.e. D veinlets and quartz eyes) and a sample of a fluorite veinlet. In addition, nineteen samples from the skarn system were investigated, including eleven samples of quartz (i.e. quartz related to sericite and pyrite), five samples of sphalerite, two samples of fluorite, and a sample of garnet. Five samples from the diatreme breccia system were analyzed, including three samples of quartz veinlets (i.e. quartz related to sericite and pyrite)

and two samples of sphalerite. Finally, six samples from the stockwork system were analyzed, including five samples of sphalerite and a sample of fluorite related to primary sulfides.

Petrography of Fluid Inclusions

The samples for the fluid inclusion analyses were selected from different ore bodies that contain quartz, garnet, amphibole, fluorite, and/or sphalerite. Doubly polished sections were chosen, mapped, and examined petrographically in order to determinate the morphology and composition of fluid inclusions for the magmatic hydrothermal system from Peñasquito.

The quartz samples selected for microthermometry included quartz phenocrysts from the porphyries, as well as quartz in veinlets from porphyries, skarn system, stockwork, and diatreme breccia systems. The garnet and amphibole from the skarn system was brown-green and gray in color, respectively, euhedral in shape, and both were related to calc-silicate alteration, which presumably was developed by early hydrothermal fluids.

The fluorite occurs as veinlets in porphyries, purple in color, cutting quartz and biotite veinlets, and exhibited a spatial relationship to molybdenite. Fluorite from the diatreme breccias and the skarn system is fine-grained and purple in color; however the fluorite from the skarn system locally exhibited massive concentration and intercalation with andradite. The fluorite from the stockwork is medium-grained, purple in color, and intercalated with primary sulfides (i.e. pyrite and arsenopyrite). The selected sphalerite

exhibits a light-brown or blond color and is related to an early mineralization stage (Fig. 5.2. Chapter V.).

Fluid Inclusions in the Porphyry System

The quartz feldspar porphyry presents quartz eye and D-A veinlets (filled mainly by quartz) that include multiphase fluid inclusions (Fig. 7.2). These inclusions range in size and shape, and the composition of inclusions includes liquid, vapor, and several solids.
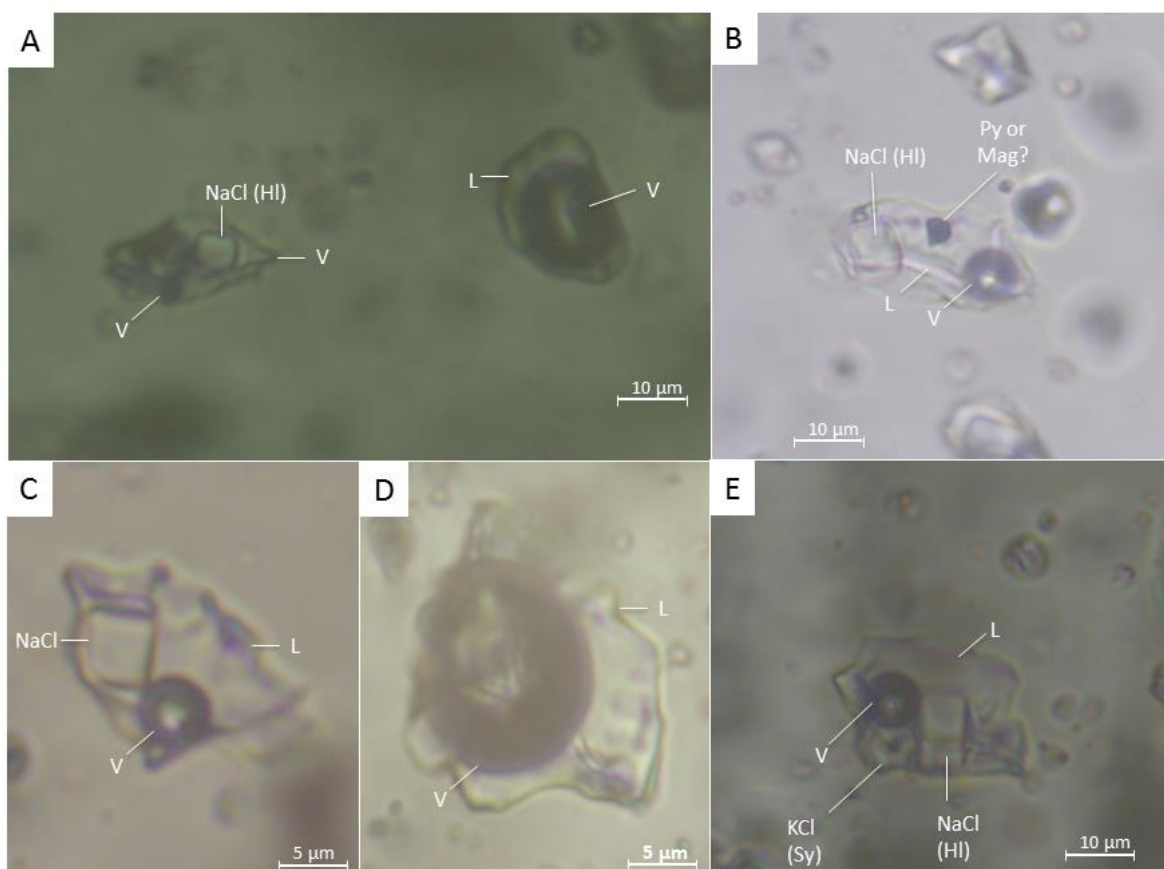
Fig. 7.2. Photomicrographs showing morphology and phases of fluid inclusions in the plutonic complex (GP621R12-1629). A. Three and two-phase fluid inclusions consist of liquid, water vapor (V), and halite (Hl). B. Multiphase fluid inclusions consist of liquid, water vapor (V), halite (Hl), and pyrite (Py) or magnetite (Mag). C. Three-phase fluid inclusion consists of liquid, water vapor (V), and halite (Hl). D. Two-phase fluid inclusion consists of liquid and water. E. Three-phase fluid inclusion consists of liquid, water vapor (V), halite (Hl), and sylvite (Sy).

The liquid phase generally occupied up to 60% in fluid inclusions. The vapor phase consisted of a spherical bubble of water vapor, which locally occupied up to 80% of the total volume, suggesting boiling effects. The porphyry contains fluid inclusions that included three solid phases; such as halite, sylvite, and opaque solids (presumably pyrite or magnetite), which occupied up to 30% of the total volume. These heterogeneity phases indicate saturation of chlorides and opaque in the plutonic system.

At Peñasquito it is believed that the porphyry complex provided the hydrothermal solutions and mineralization. The quartz-feldspar porphyry exhibits quartz veinlets (i.e. A and D type) and during the study of microthermometry, D veins and quartz eyes were analyzed in thin sections from this
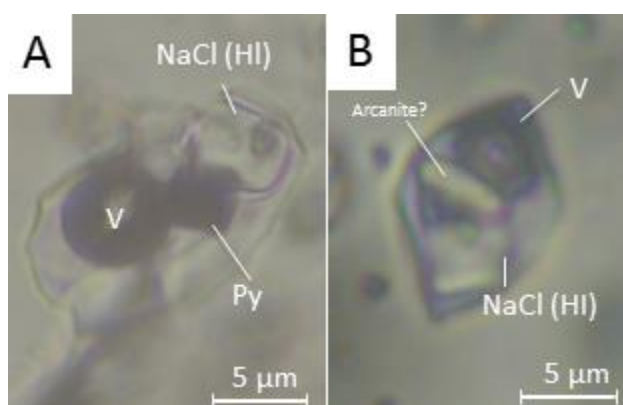
Fig. 7.3. Photomicrographs showing morphology, size, and daughter minerals of saturated fluid inclusions in quartz (sample GP621R12-1629) Note: Arcanite (K_2SO_4).

porphyry situated from 125 and 811 meters above mean sea level. These phenocrysts and quartz veinlets included both unsaturated fluid inclusions made up of liquid and water vapor (L + V) and saturated fluid inclusions made up of clear liquid, water vapor, and solids as halite, sylvite, and a prismatic translucent crystal (presumably arcanite) (Fig. 7.3B), and opaque solids (magnetite or pyrite) (Fig. 7.2B, Fig. 7.3A). These fluid inclusions are irregular in shape and ranged in size with best inclusions about 32 μm in length (Fig. 7.3). Generally, in the two-phase fluid inclusions from the plutonic complex, the liquid occupies up to ~60% of the volume, while, the vapor bubble (i.e. water vapor) may occupy up to 80% (Fig.

7.2D). In three-phase fluid inclusions, the liquid occupies up to ~50% of the volume, the vapor bubbles (i.e. water vapor) occupy up to 35% of volume, and the crystalline products, such as halite, sylvite, and local opaque minerals occupy up to 30% of the volume (Fig. 7.2, 3). The heterogeneity of daughter minerals (halite, sylvite, and possible sulfates) found in these inclusions may be interpreted as an obvious evidence of sodic and potassic brines; while, opaque minerals may be interpreted either physical entrapment or supersaturation with metal precipitation within the plutonic complex veinlets and/or quartz phenocrysts.
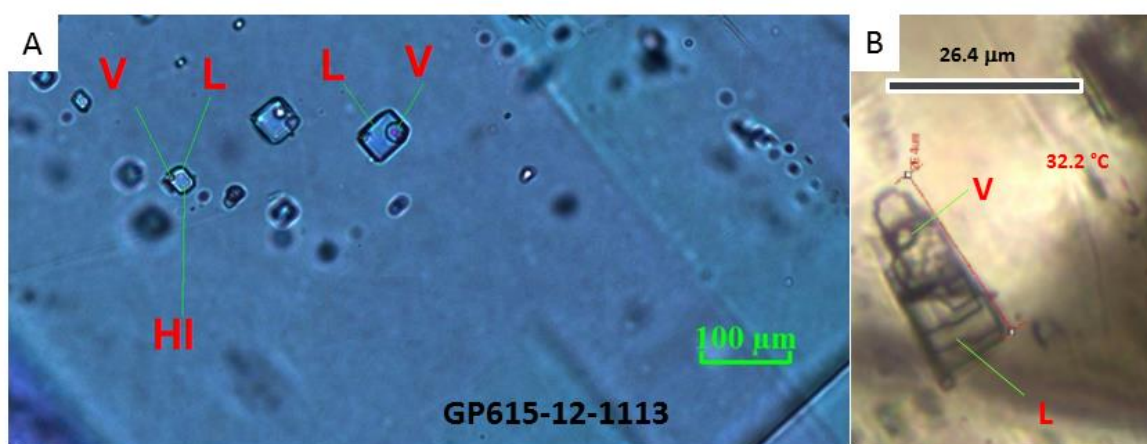
Fig. 7.4. Photomicrographs (polarized plane light and 50x) showing phases, morphology, and size of fluid inclusions in fluorite. A. Two and three phase fluid inclusions consist of liquid, halite, and water vapor. B. Two phase fluid inclusions consist of liquid and water vapor.

Fluid inclusions in fluorite from veins exhibited two-phase and three-phase compositions and usually a rectangular negative crystal shape. These specimens come from the porphyry complex (905 m.a.s.l.), which exhibited unsaturated fluid inclusions made up of vapor and liquid (L + V), as well as local supersaturated fluid inclusions made up of vapor, liquid, and solid (L+V+S). The size of the fluid inclusions ranged with the best fluid inclusions up ~26μm in length (Fig. 7.4B). Generally, in these two-phase inclusions, the fluid occupied up to 75% of the volume and vapor bubble (water vapor) occupied up to 25% of

the volume (Fig. 7.4A, B). In three-phase fluid inclusions, the liquid occupies ~45% of the volume, the vapor bubble (i.e. water vapor) occupies up to 10% of volume, and the solid (halite) occupies up to 35% of the volume (Fig. 7.4A). The daughter minerals (i.e. halite) found in these inclusions corroborates the evidence of sodic brines.

Fluid Inclusions in the Skarn System

The system skarn contains amphibole, garnet, fluorite, quartz, and sphalerite which included two-phase and three-phase fluid inclusions. These inclusions range in size and shape (irregular and rectangular), with a composition of liquid phase, vapor phase,
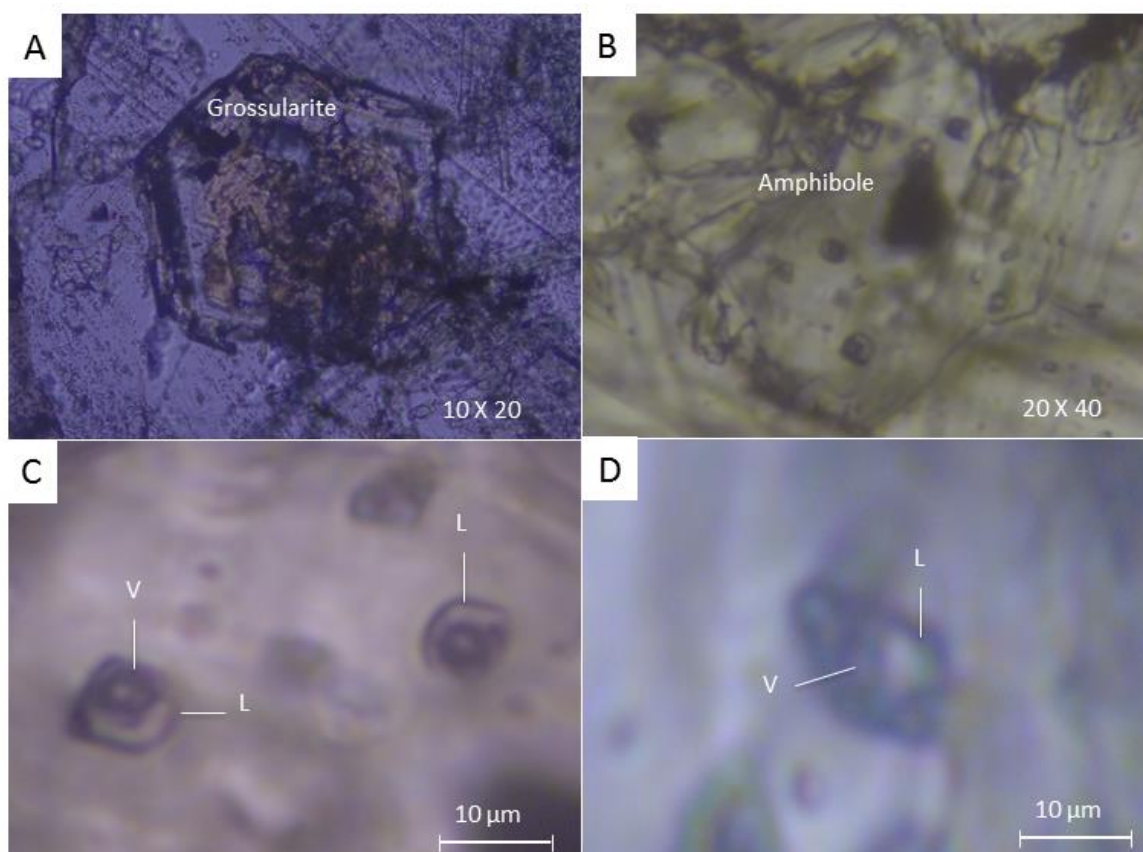
Fig. 7.5. Photomicrographs showing morphology and phases of fluid inclusions in the skarn. A. Grossularite garnet. B. Fluid inclusions in amphibole. C. D. Two-phase fluid inclusions consist of liquid and vapor water.

and solids. The liquid phase generally occupies up to 85% of volume of fluid inclusions. The vapor phase consists of spherical bubble of water vapor, and locally occupied up to 25% of the total volume in fluid inclusions. The composition of these fluid inclusions suggests unsaturated and local brines.

Fluid inclusions in amphibole exhibit two-phase compositions and rectangular shape. These specimens come from the skarn system (~200 m.a.s.l.), which exhibited unsaturated fluid inclusions made up of vapor and liquid (L + V). The size of the fluid inclusions ranged with the best fluid inclusions about ~12μm in length. Generally, in these two-phase inclusions, the fluid occupies up to 75% of the volume and vapor bubble (water vapor) occupies up to 25% of the volume (Fig. 7.5D).
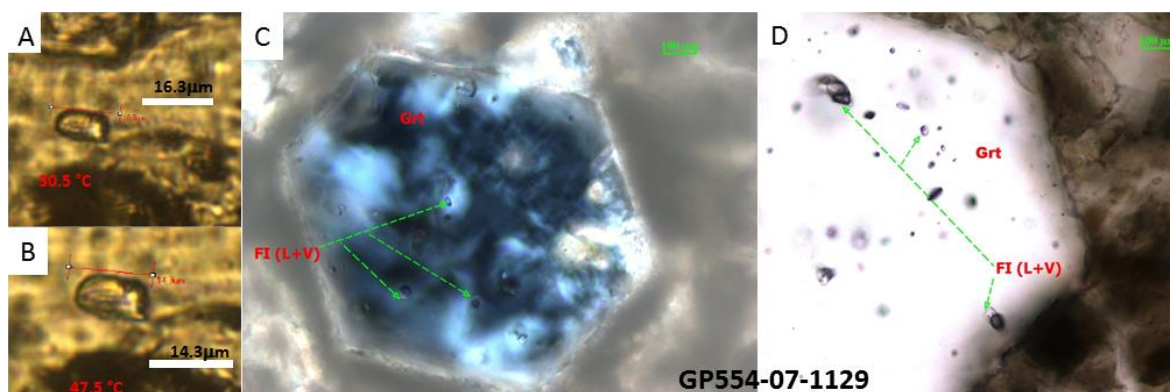
Fig. 7.6. Photomicrographs (polarized plane light and 50x) showing phases, morphology, and size of fluid inclusions in garnet. A-B. Two-phase fluid inclusions consist of liquid and water vapor. C.D. Two-phase fluid inclusions consist of liquid and vapor in garnet.

Fluid inclusions in garnet were examined and exhibit two-phase compositions. These skarn specimens are composed of grandite garnets (~787 m.a.s.l.) and exhibit unsaturated fluid inclusions made up of liquid and water vapor (L + V). The shape of the fluid inclusions is irregular. The size of the fluid inclusions ranged with the best inclusions about

~16μm in length. Generally, in these two-phase inclusions, the fluid occupies up to ~85% of the volume and vapor bubble (water vapor) occupies ~15% of the volume (Fig. 7.6).

Fluid inclusions in fluorite exhibit two-phase and three-phase compositions and rectangular shape. These specimens come from the skarn system (~ 200 m.a.s.l.), which exhibits unsaturated fluid inclusions made up of vapor and liquid (L + V). The size of the fluid inclusions ranges with the best fluid inclusions about ~20 μm in length. Generally, in these two-phase inclusions, the fluid occupies up to 75% of the volume and vapor bubble (water vapor) occupies up to 25% of the volume (Fig. 7.7). In three-phase fluid inclusions, the liquid occupies ~70% of the volume, the vapor bubble (i.e. water vapor) occupies up to 20% of volume, and the solid, such as halite and local euhedral opaque occupies up to 10% of the volume (Fig. 7.7)
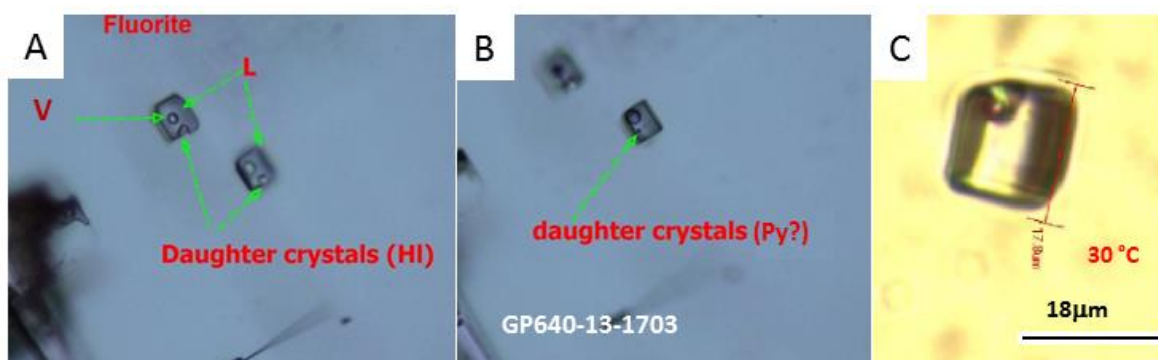
Fig. 7.7. Photomicrographs (polarized plane light and 50x) showing phases, morphology, and size of fluid inclusions in fluorite. A. Three-phase fluid inclusions consist of liquid, water vapor, and halite. B. Three-phase fluid inclusions consist of liquid, vapor (water vapor), and opaque (Py?). C. Two-phase fluid inclusions consist of liquid and water vapor.

In addition, quartz from the skarn system (647 to 1,120 m.a.s.l.) was petrograph-ically examined. The prismatic quartz is filling veins and exhibits a euhedral shape. The anhedral quartz is filling veins and usually associated with sericite and pyrite. The quartz

exhibits fluid inclusions with two and three-phase compositions, and solid inclusions (i.e. halite and opaque) are usually present (Fig. 7.8). The size of the fluid inclusions ranged with the best fluid inclusions about ~15µm in length. Generally, in two-phase in-clusions, the fluid occupied up to 50% of the volume and water vapor bubble occupied up to 75% of the volume (Fig. 7.8). In three-phase fluid inclusions, the liquid occupies ~60% of the volume, the water vapor bub-

Fig. 7.8. Photomicrographs (polarized plane light and 50x) showing phases, morphology, and size of fluid inclusions in quartz. Three-phase flu-id inclusions consist of liquid, vapor (water vapor), and solid (halite and magnetite). Two-phase fluid inclusions consist of liquid and water vapor.

ble occupies up to 20% of volume, and the solid (i.e. halite and local opaque presumably pyrite) occupies up to 15% of the volume (Fig. 7.8). Daughter minerals (i.e. halite and magnetite) found in these inclusions, suggests evi-dence of sodic brines within the skarn system.

Fluid inclusions in sphalerite exhibit two-phase compositions. These specimens came from the skarn system (between 852 to 987 m.a.s.l.). The fluid inclusions are two-phase and unsaturated,

Fig. 7.9. Photomicrograph (polarized plane light and 50x) showing fluid inclusions in sphalerite.

made up of vapor and liquid (L + V). The shape of the fluid inclusions is irregular and as negative crystals. The size of the fluid inclusions ranges with the best inclusions about ~12 µm in length. Generally, in these two-phase inclusions, the fluid occupies up to 70% of the volume and vapor bubble (water vapor) occupies up to 30% of the volume (Fig. 7.9). In addition, the sphalerite locally exhibited monophase inclusions with irregular shape, pre-sumably, the content of these inclusions may be water vapor, suggesting boiling effects.

Fluid Inclusions in the Stockwork

The stockwork quartz exhibits two-phase, three-phase, and monophase fluid inclu-sions. These inclusions range in size and shape (rounded and rectangular), and their com-positions include liquid, water vapor, and solids (Fig.7. 10B), as well as local only water vapor (Fig.7. 10A). The liquid phase generally occupies up to 70% of the total volume in fluid inclusions. The vapor phase consists of water vapor bubble that displays a spherical shape, which locally occupies up to 95% of volume, indicating boiling effects. In the stock-work, fluid inclusions included up to two solid phases (i.e. halite and sylvite), which occupy up to 30% of the volume.

The stockwork contains blonde sphalerite with local quartz that were analyzed during this microthermometric study, using doubly polished thin sections in order to identify and characterize the fluid inclusions.The samples come from between 1,862 and 1,748 meters above mean sea level. The quartz includes both unsaturated fluid inclusions made up of liquid and water vapor (L + V) and (V) (Fig. 7.10A), as well as saturated fluid inclusions made up of liquid, water vapor, and halite and, locally, sylvite (L + S + V) (Fig.

7.10B). The monophase fluid inclusions are irregular in shape and range in size with best

inclusions about ~12 μm in diameter with 100% of water vapor (Fig. 7.10A). Generally, in

the two-phase fluid inclusions from the stockwork, the liquid occupies up to ~70% of the

volume, while, the vapor bubble (i.e. water vapor) occupies up to 30%. In three-phase

fluid inclusions, the liquid occupies up to ~50% of the volume, the vapor bubble (i.e. water

vapor) occupy up to 20% of volume, and solids, such as halite and sylvite occupy up to

30% of the volume (Fig. 7.10B).The heterogeneity of daughter minerals in these fluid in-

clusions (Fig. 7.10B) suggests saturated brines with sodic and potassic compositions within

stockwork zones due to close relationship with the plutonic complex.
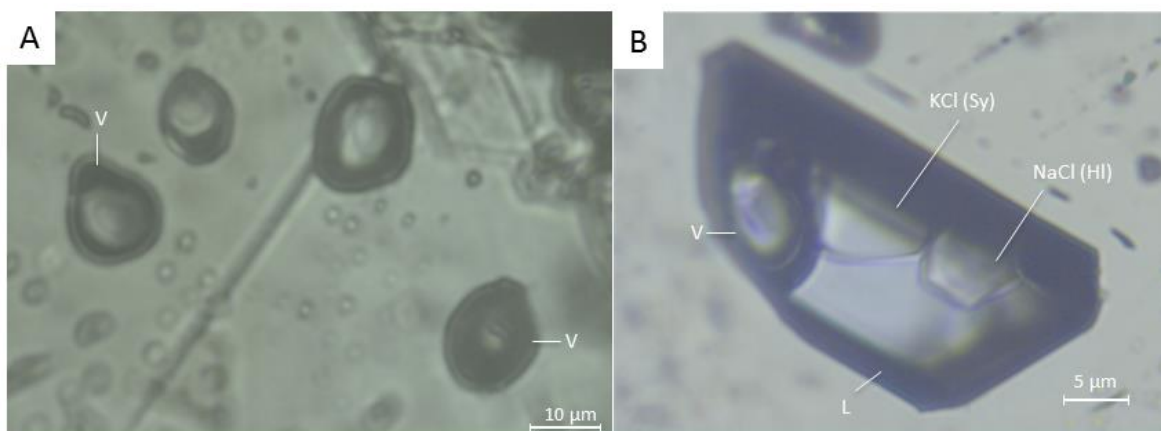
Fig. 7.10. Photomicrographs showing morphology and phases of fluid inclusions in the stockwork.
A. Monophase fluid inclusions consist of water vapor. B Three-phase fluid inclusion con-
sists of liquid, vapor water, halite (Hl), and sylvite (Sy).

Fluid inclusions in fluorite from stockwork exhibited two-phase composition with

irregular and rectangular shape. These specimens come from stockwork (1,300 m.a.s.l.).

The fluorite exhibited unsaturated fluid inclusions made up of vapor and liquid (L + V). The

size of the fluid inclusions ranged with the best fluid inclusions ~20 μm in length. Genera-

lly, in these two-phase inclusions, the fluid occupies up to 75% of the volume and bubble water vapor occupies up to 25% of the volume (Fig. 7.11).
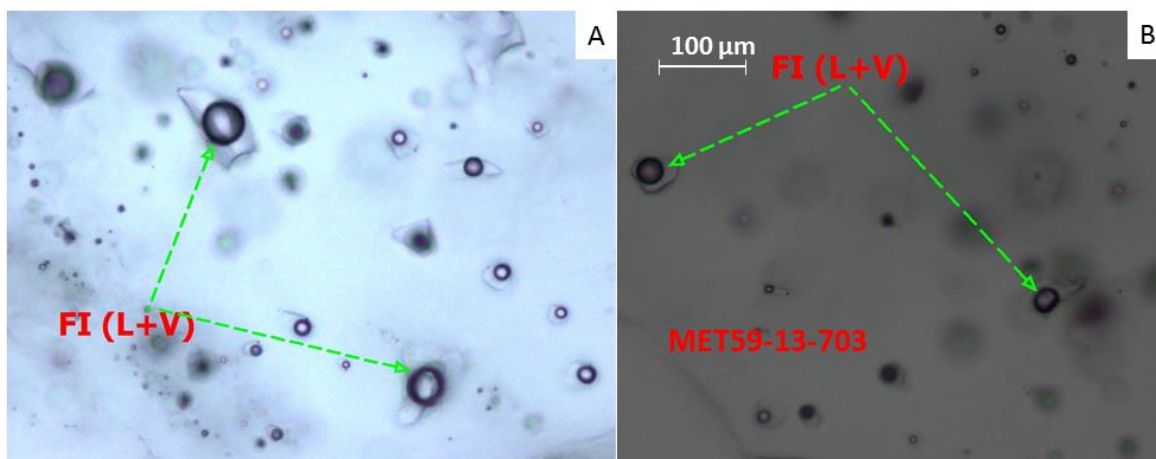
Fig. 7.11. Photomicrographs (polarized plane light and 50x) showing phases, morphology, and size of fluid inclusions on fluorite. A.B. Two-phase fluid inclusions consist of liquid and water vapor.

Fluid Inclusions in the Diatreme Breccia System

The diatreme breccia system includes quartz fragments and local veinlets filled by hydrothermal quartz with multiphase fluid inclusions (Fig. 7.12), as well as blond sphalerite with two-phase fluid inclusions. These inclusions range in size (~15 µm) and shape (irregular and elongate), but their compositions include liquid, vapor, and two salt types. In most fluid inclusions, the liquid phase generally occupies up to 50% of the volume. The vapor phase consists of spherical bubble of water vapor, which locally occupies up to 90% of volume, suggesting boiling effects. Some breccias contain fluid inclusions that include up to two solid phases (halite and sylvite) occupying up to 50% of the total volume in fluid inclusions. This heterogeneity of fluid inclusions suggests saturated inclusions due to the close relationship and connectivity to the plutonic complex.
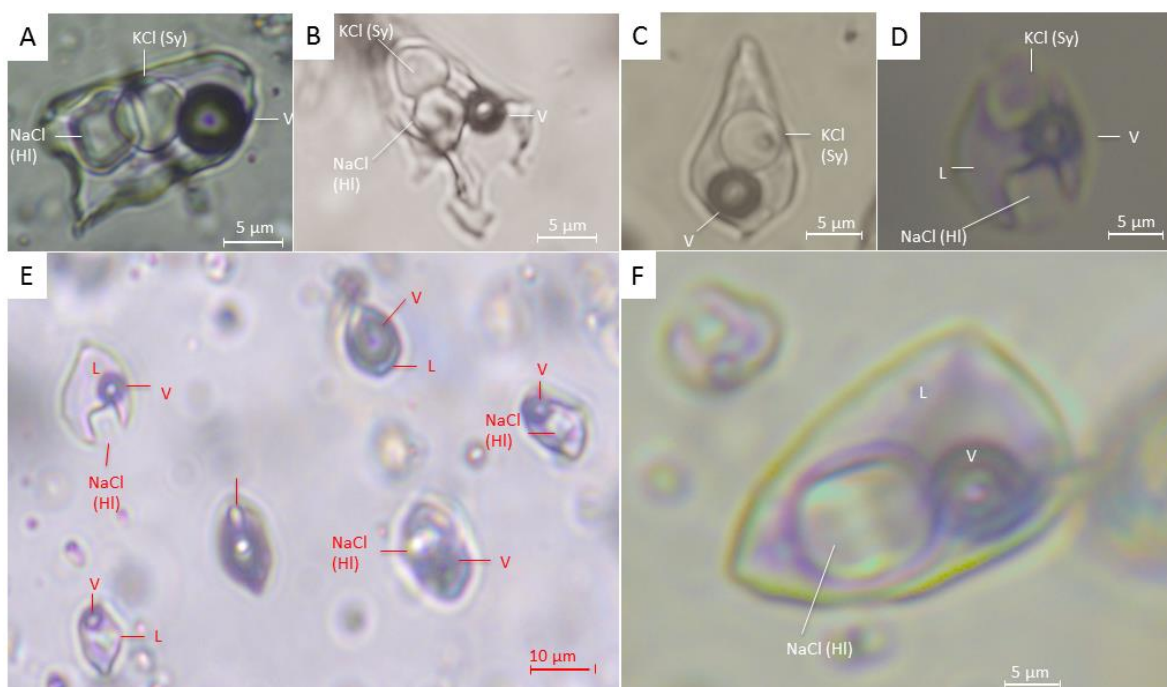
Fig. 7.12. Photomicrographs showing morphology and phases of fluid inclusions in the diatreme breccia system. A. B. C. D Three-phase fluid inclusions consist of liquid, water vapor (V), halite (Hl), and sylvite (Sy). E.F. Two-phase fluid inclusions consist of liquid, water vapor (V), and halite (Hl). E. Three-phase and two-phase fluid inclusion consists of liquid, water vapor (V), and halite (Hl).

Some quartz veinlets that cut up through the diatreme breccia system (between 1,149 to 1,901 m.a.s.l.) were analyzed. This quartz exhibits fluid inclusions with the same phases found in the porphyry complex (i.e. two and three-phase compositions). These inclusions display evident daughter minerals (i.e. halite and sylvite) (Figs. 7.12A, B,F). The size of the fluid inclusions ranges with the best inclusions about ~12 μm in length. The two-phase fluid inclusions from the diatreme breccia system contain liquids that occupy up to ~70% of the volume, while, the vapor bubble (i.e. water vapor) occupies up to 90% (Fig. 7.12E). In three-phase fluid inclusions, the liquid occupies up to ~50% of the volume, the vapor bubble (i.e. water vapor) occupies up to 25% of volume, and the solids, such as halite and sylvite occupy up to 40% of the volume (Fig. 7.12A, B). The daughter minerals

(e.g. halite and sylvite) corroborate supersaturated inclusions made by brines of sodium and potassium, due to connectivity to the plutonic complex.

Irregular shaped fluid inclusions in blonde sphalerite were analyzed and these specimens come from the di-atreme breccia system (between 983 to 1,564 m m.a.s.l.). The fluid inclusions are two-phase and unsaturated, made up of vapor and liquid (L + V). The shape of the fluid inclusions is irregular and as negative crystals with prismatic ends. In these two-phase inclusions, the fluid occupies up to 70% of the volume and
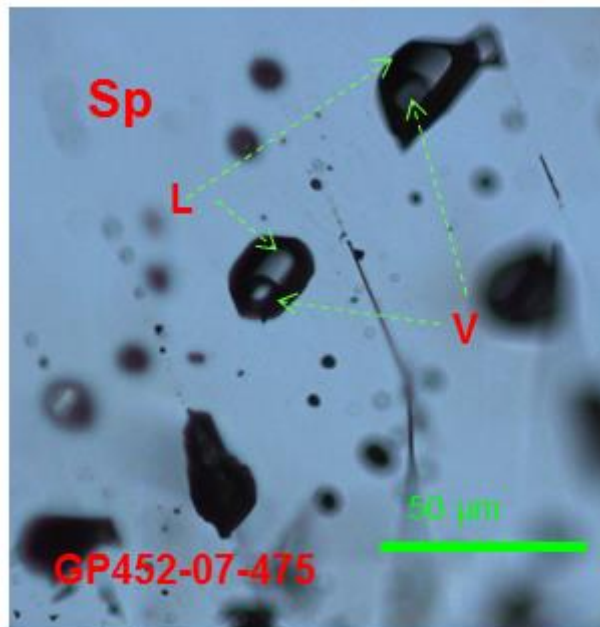
Fig. 7.13. Photomicrograph showing morphology, size, and homogenization temperature of fluid inclusions in sphalerite from the diatreme breccia system.

vapor bubble (water vapor) occupies up to 30% of the volume (Fig. 7.13). Generally, fluid inclusions in sphalerite are dark color due to the light refraction.

Microthermometry Results

A total of 383 fluid inclusions from 38 samples, consisting of monophase, two-phase and three-phase compositions, were analyzed. Most fluid inclusions homogenized to a liquid phase during the heating procedure.

Salinities of these unsaturated fluid inclusions were calculated using the Tm_{ice} results with the relation determined by Bodnar (1993). The salinity of saturated fluid inclusions was calculated using the Tm of halite and a graphic published by Sourirajan et al. (1962). This salinity was corroborated with formula: Equivalent weight% NaCl $=26.218+0.0072T_{mHI}+0.000106T_{mHI}\pm0.05$ suggested by Potter (1977). In addition, the salinity of saturated fluid inclusions was determinate using the Tm of sylvite graph of NaCl-KCl-H_2O phase diagram from by Hezarkhani et al. (1998). The microthermometric data are graphically illustrated in Figs. 7.14, 15 and summarized in Table 7.1.
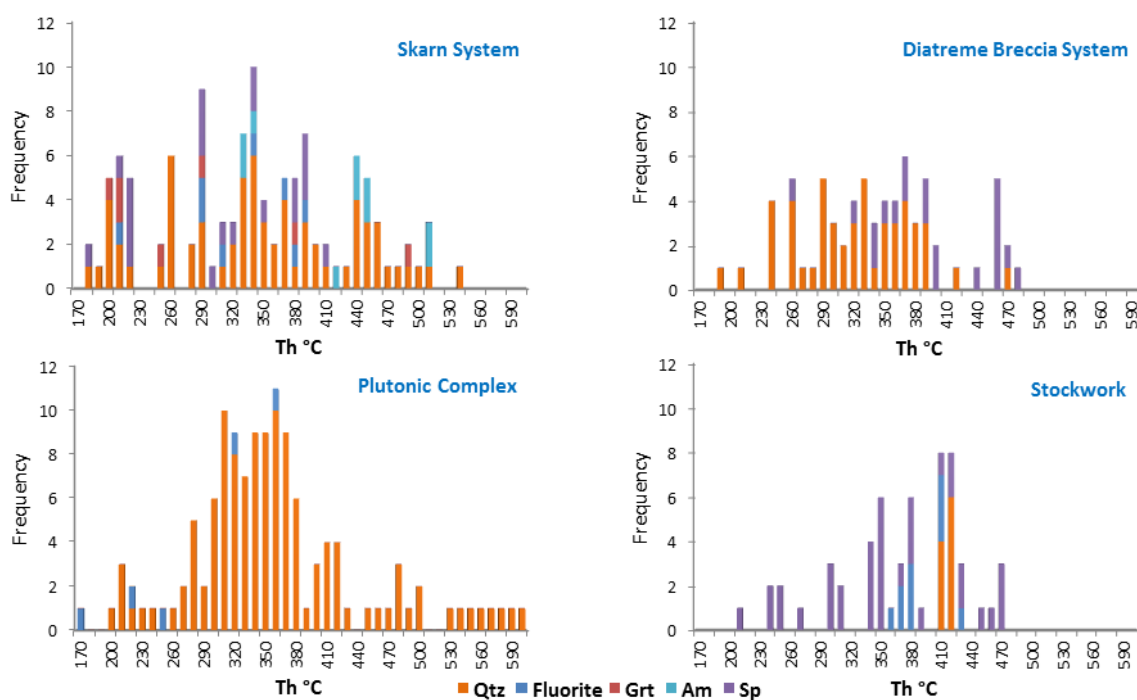
Fig. 7.14. Histograms of total homogenization temperatures vs frequency. Graphics are based on microthermometric data for fluid inclusions from different minerals and hydrothermal systems.

Analyzed fluid inclusions in quartz and fluorite from quartz-feldspar porphyries exhibit final homogenization temperatures that range from 177°C to 600°C, and a high frequency of Th ranged between 280°C to 420°C (Fig. 7.14). The salinity of these inclusions ranges from 11.11 to 44.39 equiv. wt. % NaCl and 21.12 to 22.03 equv. wt. % KCl. Plots of microthermometric data suggest effects of boiling for the plutonic complex (Fig. 7.15).
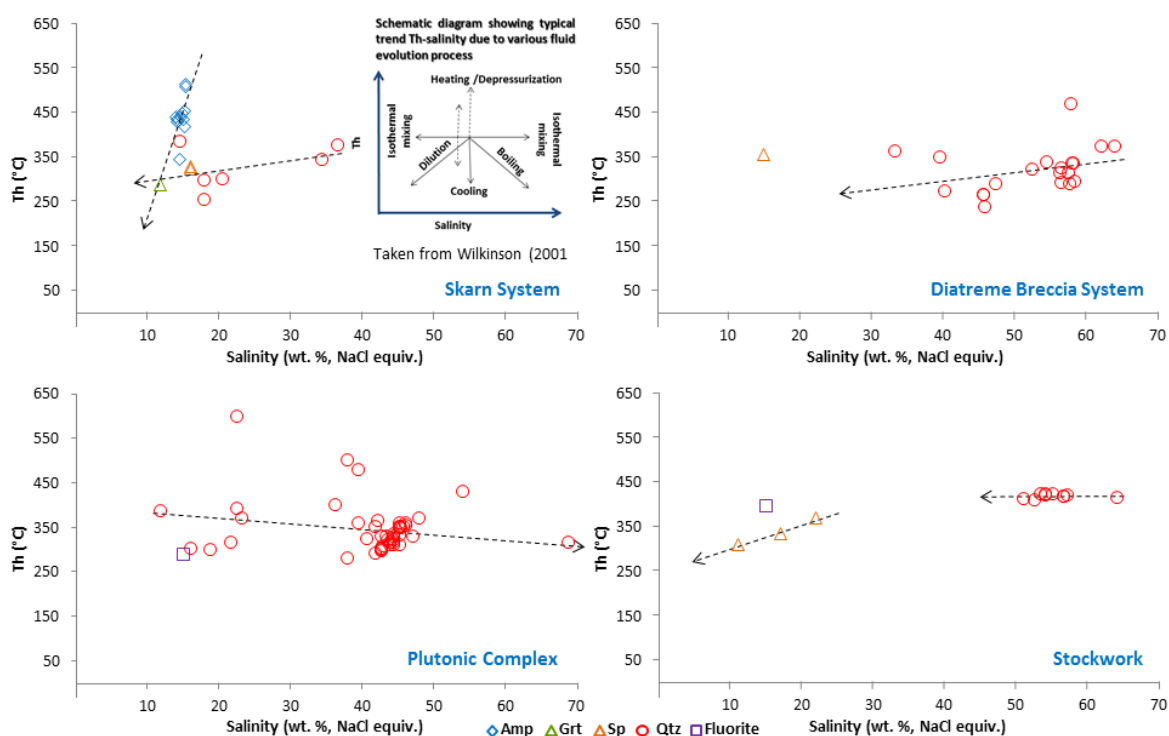
Fig. 7.15. Diagrams of homogenization temperature vs calculated salinities. Graphics are based on microthermometric data for fluid inclusions from different minerals. The evolution tendencies were taken from Wilkinson (2001).

Fluid inclusions in quartz, fluorite, garnet, and amphibole from the skarn system exhibited a range of final homogenization temperatures from 180°C to 540°C and a high frequency of Th ranges between 260°C to 390°C (Fig. 7.14). The salinity of these inclusions ranges from 11.71 to 36.57 equiv. wt. % NaCl. These microthermometric data suggest dilution of fluids for the minerals formed within the skarn system (Fig. 7.15).

Analyzed fluid inclusions in quartz, fluorite, and sphalerite from the stockwork system exhibit a range of final homogenization temperatures from 210°C to 470°C, and a high frequency of Th range between 340°C to 420°C (Fig. 7.14). The salinity of these inclusions ranges from 11.11 to 41 equiv. wt. % NaCl and from 20 to 23 equiv. wt. % KCl. These microthermometric data demonstrate dilution and isothermal mixing of fluids for the stockwork (Fig. 7.15).

Analyzed fluid inclusions in quartz and sphalerite from the diatreme breccia system show a range of final homogenization temperatures that range from 184°C to 480°C, and a higher frequency of Th range between 240°C to 450°C (Fig. 7.14). The salinity of these inclusions ranges from 12.8 to 58.32 equiv. wt. % NaCl and from 20 to 22.1 equiv. wt. % KCl. In general, these microthermometric data demonstrate dilution of fluids in the diatreme breccia system (Fig. 7.15), although a group of saturated inclusions in quartz suggests boiling effects for the diatreme breccia system (Fig. 7.15).

Table 7.1. Summary of microthermometric data obtained during the fluid inclusion analyses of different hydrothermal minerals at the Peñasquito deposit.

Sample	Longitude	Latitude	Elevation (m.o.s.l)	Rock	Mineral	Th °C	Th °C (average)	Tm$_{ice}$°C (average)	Equiv. wt. % NaCl (unsaturated FI)	Tm (Halite)	Equiv. wt. % NaCl (saturated FI)	Tm (Sylvite)	Equiv. wt. % KCl (saturated FI)	observations (n and phases)
GP615-12-1113	230986	2728536	906	Porphyry	Fluorite	177 to 360	290	-11	15.04	-	-	-	-	5
GP615-12-1208	230981	2728536	812	Porphyry	Qtz	276 to 370	307	-	-	-	-	-	-	11
WC112-04-330	229468	2728829	1690	Breccia	Qtz	190 to 360	261	-	-	-	-	-	-	5
GP621R-1034	230423	2727823	950	Skarn	Sp	180 to 410	313	-	-	-	-	-	-	11
GP621R-1111	230422	2727823	873	Skarn	Sp	210 to 380	329	-12	16.04	-	-	-	-	3
GP640-13-1785	229154	2728720	125	Porphyry	Qtz	215 to 405	304	-12	16.04	-	-	-	-	8
GP640-13-1810	229144	2728724	101	Skarn	Qtz	200 to 367	302	-17	20.43	-	-	-	-	9
GP624A12-1194	229886	2727967	787	Skarn	Grt	208 to 445	287	-8	11.71	-	-	-	-	7
GP501-07-910	228936	2728434	1121	Skarn	Qtz	327 to 505	375	-	-	-	-	-	-	4
GP501-07-1058	228963	2728492	988	Skarn	Sp	289 to 340	317	-	-	-	-	-	-	3
GP554-07-957	229039	2728499	1076	Skarn	Qtz	250 to 337	301	-14	17.92	-	-	-	-	3
GP554-07-1129	229060	2728554	914	Skarn	Qtz	267 to 453	387	-10.5	14.52	-	-	-	-	3
GP554-07-1135	229061	2728556	909	Skarn	Qtz	243 to 547	414	-	-	-	-	-	-	10
MET57-13-850	229668	2728918	1149	Breccia	Qtz	241 to 470	335	-12	16.04	380.8611	44.39	128.4	21.12	32, Sy, Op
MET59-13-703	229679	2729073	1300	Stockwork	Fluorite	360 to 435	396	-11	15.04	-	-	-	-	10
GP639-13-814	230213	2728195	1021	Skarn	Qtz	184 to 350	256	-14	17.92	-	-	-	-	5
GP621-12-937	230424	2727824	1047	Skarn	Qtz	201 to 370	279	-	-	-	-	-	-	6
GP582-08-1145	230234	2727860	1035	Skarn	Qtz	321 to 480	375	-	-	-	-	-	-	6
GP582-08-1370	230250	2727990	852	Skarn	Sp	298 to 342	324	-12	16.04	-	-	-	-	5
MET40-09-267	230068	2727062	1768	Stockwork	Sp	298 to 426	378	-13	17	340.27	33.40	108.68	22.034	16 Sy, Hl
GP621R12-954	230423	2727824	1030	Skarn	Qtz	296 to 473	379	-	-	280	36.59	-	-	9, Hl, Op
GP621R12-1028	230423	2727823	956	Skarn	Qtz	294 to 344	320	-	-	-	-	-	-	2
GP621R12-1320	230419	2727820	664	Porphyry	Qtz	228 to 363	318	-	-	-	-	-	-	8
GP621R12-1447	230411	2727818	538	Porphyry	Qtz	272 to 500	400	-7.5	11.11	273	36.13	-	-	16
GP621R12-1629	230400	2727817	356	Porphyry	Qtz	200 to 600	387	-19.1	21.624	375.7327	44.17	-	-	68
MHC02-277	230077	2727091	1748	Stockwork	Sp	258 to 439	369	-19	21.94	-	-	-	-	7
MHC04-129	230156	2727131	1862	Stockwork	Sp	271 to 432	345	-	-	-	-	-	-	5
MHC04-178	230179	2727130	1818	Stockwork	Sp	353 to 473	420	-	-	-	-	-	-	6
MHC04-205	230191	2727130	1794	Stockwork	Sp	212 to 383	310	-7.5	11.11	-	-	-	-	10
WC13-02-88	230196	2727231	1901	Breccia	Qtz	290 to 368	366	-9	12.8	225	33.25	-	-	12, Hl
GP452-07-475	230308	2727645	1565	Breccia	Sp	260 to 480	417	-	-	-	-	-	-	15
GP452-07-558	230308	2727683	1491	Breccia	Sp	320 to 391	356	-11	15.04	-	-	-	-	2
GP640-13-852	229500	2728600	983	Breccia	Sp	357 to 394	374	-	-	-	-	-	-	3
GP640-13-1218	229363	2728645	647	Skarn	Qtz	265 to 412	346	-10	13.99	245	34.39	-	-	9, Hl
GP640-13-1244	229353	2728649	623	Porphyry	Qtz	326 to 534	388	-8	11.71	-	-	-	-	10
GP640-13-1650	229206	2728701	256	Porphyry	Qtz	347 to 450	390	-	-	-	-	-	-	3
GP640-13-1703	229186	2728708	200	Skarn	Am & Grt	210 to 515	381	-11.381818	14.74545455	-	-	-	-	15
GP640-13-1708	229186	2728708	195	Skarn	Fluorite	298 to 379	336	-	-	-	-	-	-	4

Freezing Behavior of Fluid Inclusions

Although, it was difficult to observe melting temperatures due to the small size of fluid inclusions and color, most analyzed high-salinity inclusions have low initial ice-melting temperatures that ranged from -80°C to -50°C. In unsaturated fluid inclusions, the Te was observed ca. -23°C, indicative of KCl-NaCl-H_2O fluids. Final ice-melting temperatures for most inclusions yielded large ranges from -19°C to -7.5°C, corresponding to salinities from 21.64 to 11.11 equiv. wt. % NaCl, respectively.
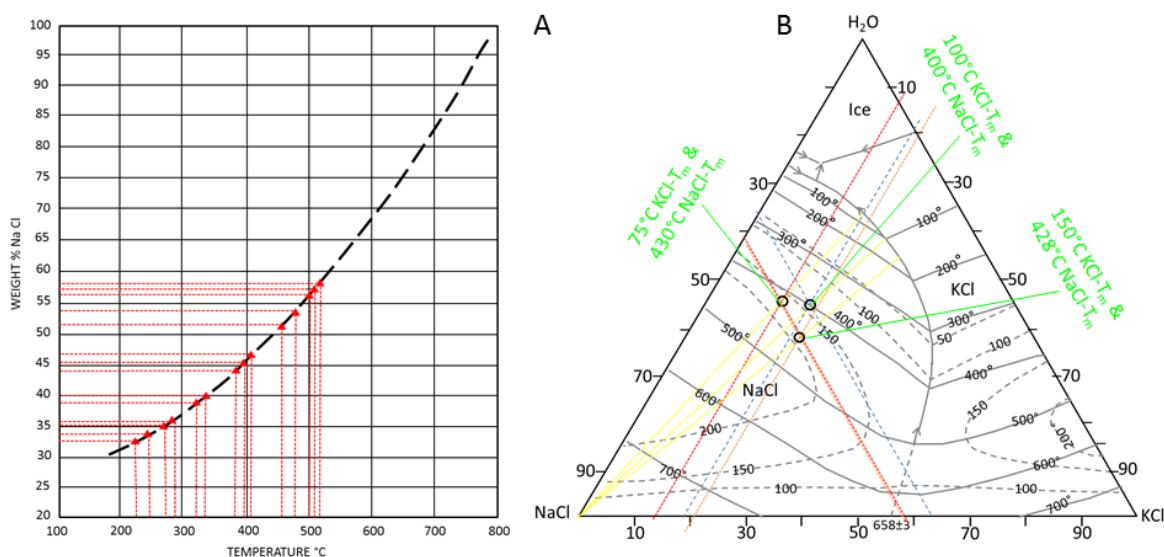
Fig. 7.16. Graphic showing the determination of salinity in fluid inclusions. A. The salinity of fluid inclusions using the T_{mHI} data (graph from by Sourirajan et al., 1962). B. Example for the salinity calculation of saturated fluid inclusions, using the T_{mHI} and T_{mSy} data (graphic suggested by Hezarkhani et al., 1998). Note: solid lines are equivalent wt. % NaCl; dashed contours are equivalent wt. % KCl; and O intersection to calculate salinities, using yellow, red and blue dashed lines.

Final melting temperatures for halite in saturated fluid inclusions ranged from 336°C to 517°C, corresponding to salinities from 33.25 to 58.33 equiv. wt. % NaCl (Fig. 7.16A). Final melting temperatures for sylvite in saturated fluid inclusions (halite-sylvite-bearing)

ranged from 100°C to 152°C, corresponding to salinities from 20 to 22.1 equiv. wt. % KCl (Fig. 7.16B).

Heating Behavior of Fluid Inclusions

In general, fluid inclusions exhibited vapor bubbles that gradually decreased in diameter until final homogenization ($Th_{(total)}$) to liquid at temperatures between 177°C to 598°C. The vapor bubbles were present in all inclusions, and exhibited irregular sizes; apparently, some exhibited a double meniscus with a black color due to light refraction (Fig. 7.17), suggesting the presence of CO_2.
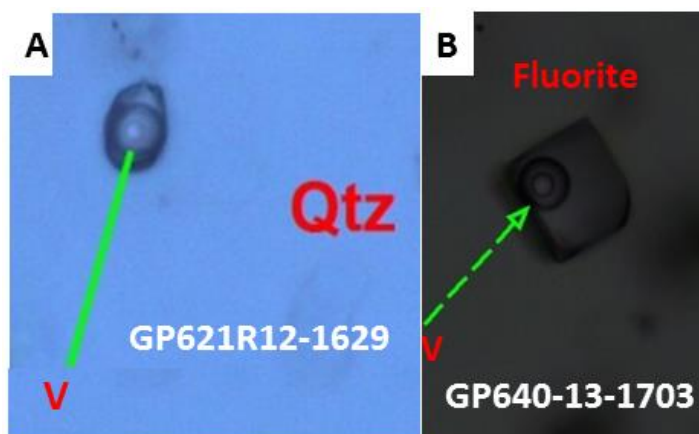
Fig. 7.17. Photomicrographs (polarized plane light and 50x) showing water vapor.

Inclusions in D quartz veinlets from the quartz-feldspar porphyry showed a wider range of final homogenization temperatures that range from 276°C to 598°C; whereas inclusions in quartz veinlets from the skarn system range from 184°C to 543°C; and inclusions in quartz veinlets from diatreme breccias exhibit a range from 190°C to 470°C. Inclusions in quartz phenocrysts from the quartz feldspar porphyry range from 326°C to 534°C.

Inclusions in sphalerite display a wide range from 180°C to 480°C. Specifically, inclusions in sphalerite from the skarn system range from 180°C to 410°C, whereas inclusions in sphalerite from the stockwork range from 212°C to 439°C, and inclusions in sphalerite from diatreme breccias exhibit a range from 260°C to 480°C.

Inclusions in garnet from the skarn system display a wide range from 208°C to 485°C; whereas, inclusions in amphibole from the skarn system display a wide range from 345°C to 515°C.

Inclusions in fluorite display a wide range from 177°C to 435°C. Specifically, inclusions in fluorite from the plutonic complex range from 177°C to 360°C, whereas inclusions in fluorite from the skarn system range from 210°C to 392°C, and inclusions in fluorite from the stockwork exhibit a range from 360°C to 435°C.

Interpretation and Discussion of Microthermometric Data

Microthermometric results showed that fluid inclusions in transparent minerals from the Peñasquito ore deposit have a wide range of the final homogenization temperatures. Histograms of homogenization temperatures (Fig. 7.14) demonstrate that the plutonic complex has the wider range of final homogenization temperature (from 177°C to ~600°C), followed by the skarn system (from ~180°C to ~540°C), the diatreme breccias system (from ~190°C to ~480°C), and the stockwork (from ~210°C to ~470°C). This wide range of final homogenization temperatures may suggest several or continuous hydrothermal pulses. In addition, these data suggest that the plutonic complex was the principal source of hydrothermal fluids that were cooled during their pathway throughout the Mesozoic sedimentary marine sequence and the diatreme breccia system.

On the graph of elevation versus temperature of homogenization it is possible to visualize the temperature behavior with respect to depth. In general, the homogenization temperatures gradually decrease toward upper levels within the plutonic complex, the

skarn system, stockwork, and the diatreme breccia system (Fig. 7.18A). The data suggest that hydrothermal fluids migrated from the plutonic complex, and were gradually cooled toward the surface. However, the diatreme breccia system presented varied temperatures of homogenization on different levels, demonstrating an indefinite pattern of temperatures regarding the elevation; presumably this effect is due to introduction of dikes through breccias (Fig. 7.18A) as well as the transport of minerals analyzed from areas of higher temperature regimes to areas where cooler ore fluids were present.
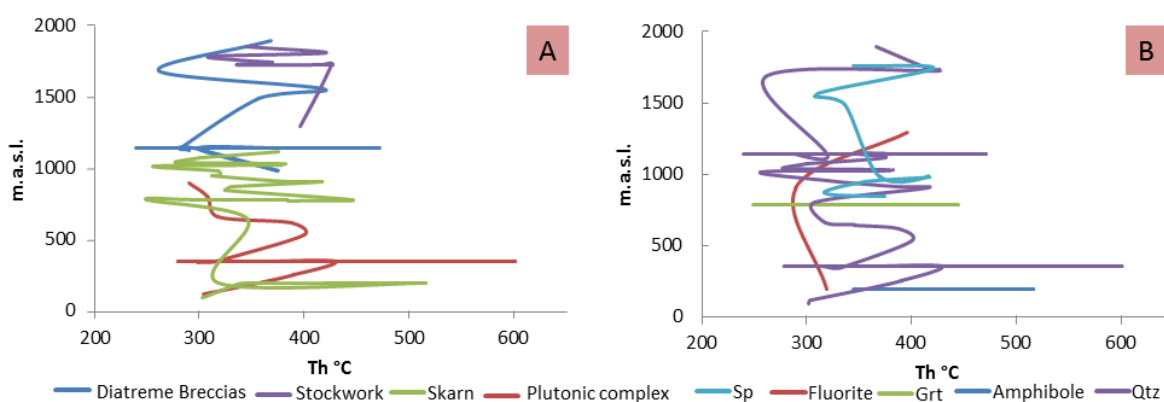
Fig. 7.18. Graphics showing the relation of elevation and temperature of homogenization of fluid inclusions. A. Elevation versus temperature of homogenization of fluid inclusions separated by ore deposit type and mineral. B. Elevation versus temperature of homogenization of fluid inclusions separated by minerals.

The quartz exhibits a large population and gradual decreasing temperatures toward the surface (Fig. 7.18B). Generally, the quartz from the skarn system and plutonic complex exhibit high and low temperatures, ranging between ~430°C and 256°C, and are hosted between 1,149 and 125 m.a.s.l. The quartz from diatreme breccia exhibits high and low temperatures, ranging between ~470°C and ~190°C, and are hosted between 1,901 and 1,149 m.a.s.l. These results corroborate that ore fluids have migrated from the plutonic

complex; presumably, the ore fluids were gradually cooling and diluting toward the surface.

The fluorite exhibits three populations with varied temperatures. The fluorite from the stockwork exhibits a high temperature (~395°C) at ~1,400 m.a.s.l. whereas fluorite from the skarn system exhibits medium temperatures (between ~319°C and ~336°C) at 200 m.a.s.l.; and fluorite in the porphyritic complex yielded a lower temperature (~290°C) at 200 m.a.s.l. (Fig. 7.18B). These results suggest a great range of migration in hydrothermal systems, indicating; 1) fluorite from the stockwork could be directly derived from late magmatic fluids that have mineralized the diatreme breccia system; 2) fluorite from the skarn system could have derived from diluted early magmatic fluids; and 3) fluorite from the porphyritic complex could be residual magmatic fluids with low temperature.

The sphalerite exhibits two populations with gradual decreasing temperature toward the surface. The sphalerite from the skarn system exhibits a decrease in temperatures toward the surface, ranging between ~346°C and ~319°C, and is hosted between 320 m.a.s.l. and 873 m.a.s.l. The sphalerite from diatreme breccias and stockwork exhibit high to medium temperatures, ranging between ~420°C and ~310°C, and is hosted between 983 m.a.s.l. and 1,862m.a.s.l. (Fig. 7.18B). The sphalerite data suggest a mixing at shallow levels, and sphalerite in skarn system was deposited from hydrothermal fluids with decreasing temperatures.

Finally, as is seen in the histogram of homogenization temperature versus salinity, analyzed microthermometry samples form an extensive field (Fig. 7.19). This field fits within the skarn and porphyry fields suggested by Wilkinson (2001). However, some temperature in quartz inclusions from the porphyry presented low to high homogenization temperatures as well as a low to high salinity in comparison to reported microthermometric results for porphyry systems. Therefore, it is believed that the hydrothermal fluids that formed the hydrothermal alteration and ore bodies in Peñasquito were from a productive magmatic source. These fluids were gradually diluted and cooled; however during the cooling process, boiling effects may have been present due to depressurization. Isothermal mixing was present due to multiple hydrothermal events and/or interaction of magmatic and meteoric fluids.
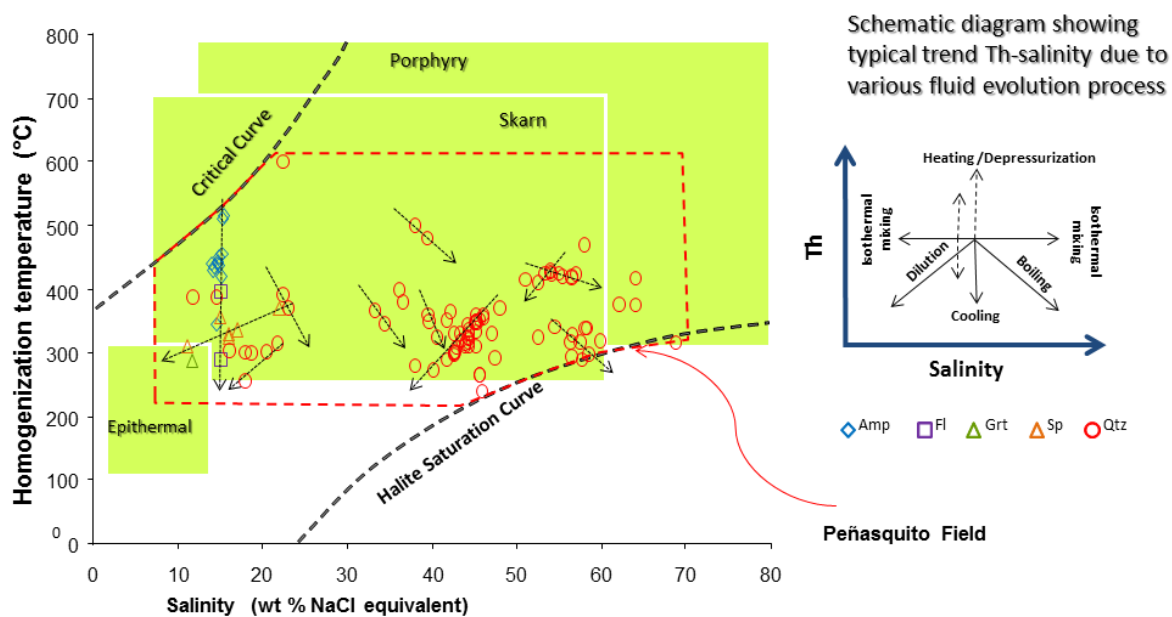
Fig. 7.19. Histograms of total homogenization temperature versus calculated salinities showing the comparative fields. The red outline corresponds to samples from Peñasquito. The light green fields and schematic typical trend Th-salinity were suggested by Wilkinson (2001).

Stable isotope analysis

Forty-nine samples from the Peñasquito ore deposit were analyzed for stable isotope compositions. The specimens are carbonates (calcite and rhodochrosite) and primary sulfides (pyrite, arsenopyrite, sphalerite, galena, and chalcopyrite), which represent the minerals from the diatreme breccia system, the stockwork zones, the skarn system, and the plutonic complex. Most minerals analyzed for their isotopic compositions were hand-picked from drill cores and one sample was handpicked from the surface of the Peñasco open pit. The purpose of this investigation was to determine the isotopic signature of carbonates and sulfides in mineralized zones and interpret the source of these elements.

Initially, minerals were separated better than 95 percent pure and after separation all minerals were finely crushed in order to obtain a homogeneous sample. The samples were then submitted to Dr. Simon Poulson at the Nevada Stable Isotope Laboratory at the University of Nevada, Reno campus. The analytical procedure consisted of using a Micromass Isoprime stable isotope ratio mass spectrometer on selective samples of sulfides and carbonates, and results were reported to the author.

On receiving the data, their ratios were plotted on diagrams. Specifically, the stable isotope results were compared to compilations by Ohmoto (1986) and Ohmoto and Rye (1979) in order to identify the possible precursor source. In addition, isotope equilibrium temperatures were calculated for the sphalerite-galena pair, the sphalerite-pyrite pair, and the pyrite-arsenopyrite pair.

Carbon and Oxygen Isotopes

Twelve specimens of carbonates were analyzed for stable isotope ratios of oxygen and carbon. The calcite exhibited a euhedral shape, was white in color, and occurred in parallel bands in veins. The rhodochrosite was located in veins that cut the Caracol Formation and the Peñasco Breccia. A sample of rhodochrosite was associated with the calcite and primary sulfides (pyrite, sphalerite, and galena). Both calcite and rhodochrosite are part of a post-ore stage. The data for carbon and oxygen isotopes from carbonate samples are listed in Table 7.2. Additionally, the results were plotted graphically and the sampling was plotted in Fig. 7.20, which represents the data projection on graphics (depth vs δ^{18}O and δ^{13}C).

Table 7.2. Summary data for stable isotope ratios for oxygen and carbon obtained from calcite and rhodochrosite.

Sample	Longitude	Latitude	Elevation (m.a.s.l)	Rock	Mineral	δ^{13}C ‰ (VPDB)	δ^{18}O ‰ (VPDB)	δ^{18}O ‰ (VSMOW)
GP640-13-852	229500	2728600	983	Diatreme breccia	Cal	-4.9	-13.2	17.4
WC112-04-744	229493	2729079	1361	Diatreme breccia	Rds	-5.6	-13.9	16.6
GP615-12-552	231011	2728527	1466	Caracol F. (Stockwork)	Cal	-5.4	-16.4	14.0
GP615-12-613	231009	2728528	1406	Caracol F. (Stockwork)	Rds	-6.1	-15.2	15.3
GP640-13-1650	229206	2728701	256	Porphyry	Cal	-1.8	-15.4	15.0
GP609-11-1062	230997	2728684	964	Porphyry	Cal	-1.6	-14.0	16.5
GP624A12-1194	229886	2727967	787	Skarn	Cal	-5.6	-12.1	18.4
GP501-07-1058	228963	2728492	988	Skarn	Cal	-3.4	-12.0	18.6
GP621-12-937	230424	2727824	1047	Skarn	Cal	-6.2	-17.8	12.5
GP621R12-938	230423	2727824	1046	Skarn	Cal	-6.9	-15.9	14.5
GP636-13-706	229832	2728155	1128	Skarn (Breccia)	Cal	-5.5	-11.6	19.0
GP582-08-1145	230234	2727860	1035	Skarn (Manto)	Cal	-4.5	-13.7	16.8

The background δ^{18}O levels appeared to be around -17 to -11 per mil (‰) VPDB. Specifically, the calcite has δ^{18}O (VPDB) values of -17.8 to -11.6‰; values for rhodochrosite are -15.2 to -13.9‰ (Fig. 7.20a). Carbon isotope samples average around 4.8 per mil (‰) VPDB for these background carbonates. Specifically, the calcite δ^{13}C values range from -6.9 to -1.6‰, whereas values for rhodochrosite are from -6.1 to -5.6‰ (Fig. 7.20b).
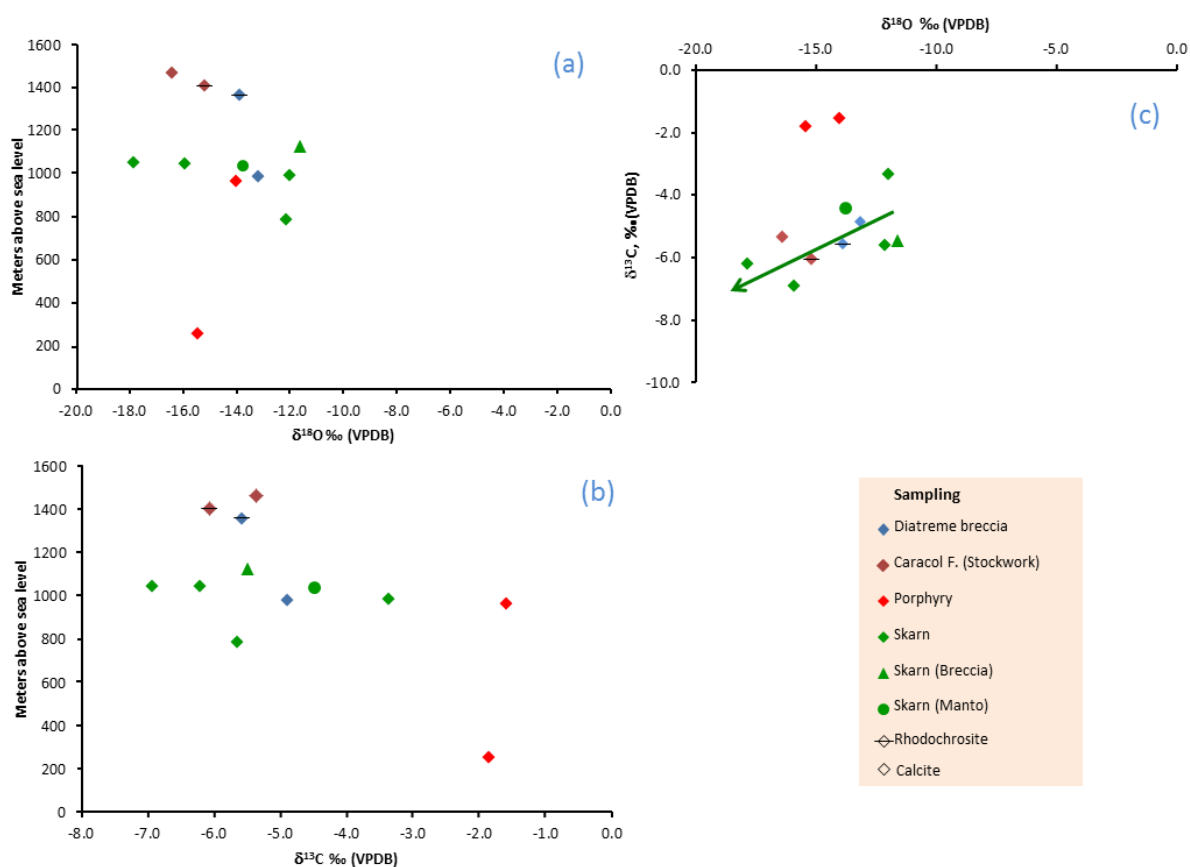
Fig. 7.20. Graphs exhibiting the range of the stable isotopes (δ^{18}O, δ^{13}C) for samples of calcite and rhodochrosite from Peñasquito. The green arrow represents depletion of oxygen and carbon in the skarn system.

The plot of δ^{13}C vs. δ^{18}O suggests that samples tend to skew towards depletion (Fig. 7.20c). In addition, the δ^{13}C and δ^{18}O isotopic values exhibited a significant pattern that would be useful for differentiating two populations within the data (Fig. 7.20c). For example, the carbonates in the diatreme breccia, stockwork zones, and skarn system were more depleted in ^{13}C than calcite in the porphyry complex (Fig. 7.20c).

Interpretation and Comparison of Carbon and Oxygen Isotopes

The patterns for carbon and oxygen isotopes in this study suggest that the bulk of the carbonate source may have been meteoric waters (Fig. 7.21a). In addition, the interaction of the meteoric water, limestones, and the hydrothermal process played an important role during the isotopic exchange process (Fig. 7.21b). Moreover, it is believed that the depletions took place during a late hydrothermal stage, which affected the hydrothermal system.
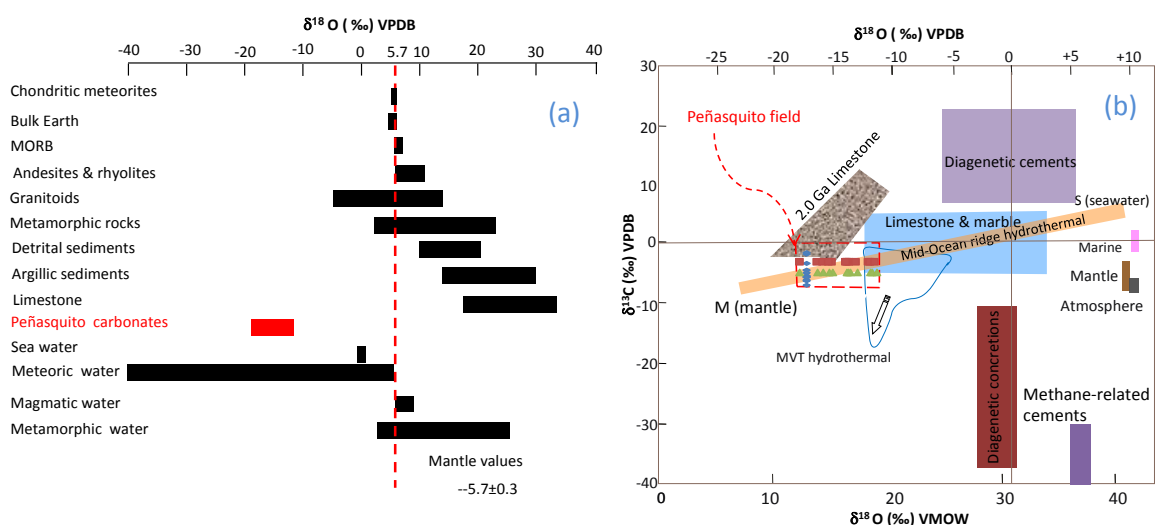
Fig. 7.21. Graphs showing carbonate isotopic fields in Peñasquito compared to data compiled by Rollinson (1993)

The minimum depletion in δ^{13}C for calcite from the porphyry complex suggests that depletion of the other carbonates was related to interaction of magmatic water with limestone. The evident depletion in δ^{13}C and δ^{18}O isotope values in the skarn system may be attributed to the increased intensity of fluid/limestone reactions taking place immediately adjacent to the plutonic complex and developed during a metasomatic reaction.

Sulfur Stable Isotope

Stable isotopes of sulfur were also analyzed from minerals that were collected in the primary mineralization. Initially, thirty-seven specimens of primary sulfides were selected, including primary pyrite, sphalerite, galena, chalcopyrite and arsenopyrite. The bulk of specimens are from drill cores but a sample was also taken from the Peñasco open pit, and the sampling ranged between 1,901 and 256 meters above sea level (Fig. 7.22).
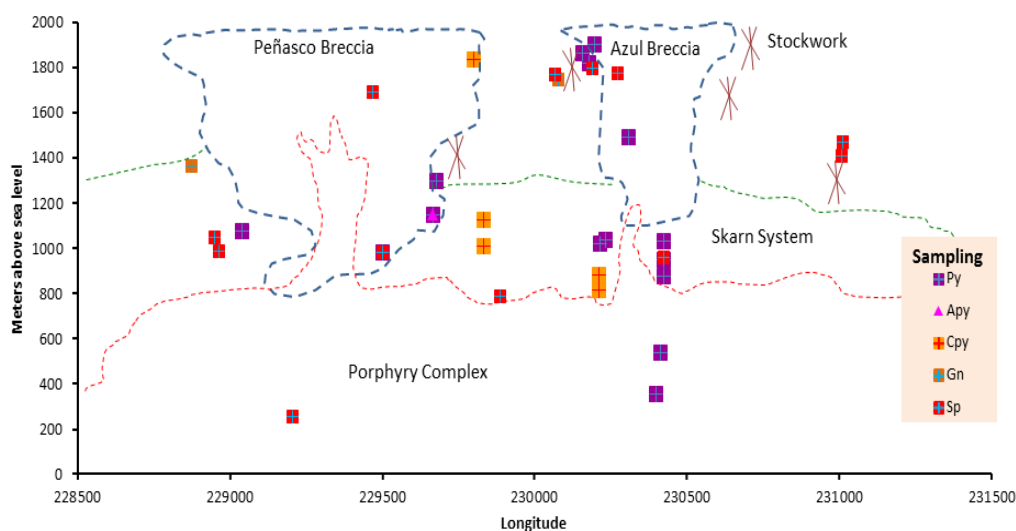
Fig. 7. 22. Schematic cross-section looking to the northeast and showing samples of sulfides for the stable isotope analysis.

These geothermometry data are calculated for a sphalerite and galena pair, sphalerite and pyrite pair, and pyrite-arsenopyrite pair using δ^{34}S values and the equations suggested by Ohmoto and Rye (1979).

Three equilibrium temperatures (Table 7.3) ranged from 250°C to 432°C; however, two equilibrium temperatures for the sphalerite-galena pair were calculated to be 742°C on average, indicating geochemical disequilibrium.

Table 7.3. Summary data for the stable isotope analyses of sulfur obtained from pyrite, sphalerite, galena, chalcopyrite, and arsenopyrite. Note: the analyzed pyrite corresponds to stage 1

Sample	Longitude	Latitude	Elevation (m.a.s.l)	Rock	Mineral	δ³⁴S ‰ (VCDT)	Temperature °C		
							(Sp-Gn pair)	(Sp-Py pair)	(Py-Apy pair)
MET57-13-850	229668	2728918	1149	Diatreme breccia	Apy	0.8	-	-	349
GP636-13-706	229832	2728155	1128	Skarn (Breccia)	Cpy	-1.4	-	-	-
GP639-13-956	230212	2728193	879	Skarn	Cpy	-0.9	-	-	-
GP636-13-824	229833	2728154	1011	Skarn	Cpy	-0.3	-	-	-
GP639-13-1018	230211	2728193	817	Skarn	Cpy	-2.1	-	-	-
Bank-1835	229800	2728565	1835	Diatreme breccia	Cpy	0.2	-	-	-
GP615-12-552	231011	2728527	1466	Caracol F. (Stockwork)	Gn	-0.1	365	-	-
MET40-09-267	230068	2727062	1768	Caracol F. (Stockwork)	Gn	-0.1	779	-	-
MHC02-277	230077	2727091	1748	Caracol F. (Stockwork)	Gn	-1.1	-	-	-
GP512-07-640	228873	2728367	1362	Skarn	Gn	-1.1	-	-	-
GP621R-1034	230423	2727823	950	Skarn (Manto)	Py	1.6	-	448	-
GP621R-1111	230422	2727823	873	Skarn	Py	1.8	-	-	-
GP554-07-957	229039	2728499	1076	Skarn (Hornfels)	Py	2.1	-	-	-
MET57-13-850	229668	2728918	1149	Diatreme breccia	Py	1.7	-	-	264
MET59-13-703	229679	2729073	1300	Indidure F. (Stockwork)	Py	1.2	-	-	-
GP639-13-814	230213	2728195	1021	Skarn	Py	0.3	-	-	-
GP582-08-1145	230234	2727860	1035	Skarn (Manto)	Py	1.3	-	-	-
GP621R12-954	230423	2727824	1030	Skarn	Py	0.4	-	-	-
GP621R12-1447	230411	2727818	538	Porphyry	Py	1.4	-	-	-
GP621R12-1629	230400	2727817	356	Porphyry	Py	0.9	-	-	-
MHC04-129	230156	2727131	1862	Caracol F. (Stockwork)	Py	1.9	-	-	-
MHC04-178	230179	2727130	1818	Caracol F. (Stockwork)	Py	2.3	-	-	-
WC13-02-88	230196	2727231	1901	Diatreme breccia	Py	1.1	-	-	-
GP452-07-558	230308	2727683	1491	Diatreme breccia	Py	0.3	-	-	-
GP640-13-852	229500	2728600	983	Diatreme breccia	Py	2.8	-	432	-
GP615-12-552	231011	2728527	1466	Caracol F. (Stockwork)	Sp	2.0	322	-	-
GP615-12-613	231009	2728528	1406	Caracol F. (Stockwork)	Sp	3.2	-	-	-
WC112-04-330	229468	2728829	1690	Diatreme breccia	Sp	0.8	-	-	-
GP624A12-1194	229886	2727967	787	Skarn	Sp	0.9	-	-	-
GP501-07-1058	228963	2728492	988	Skarn	Sp	1.7	-	-	-
MET40-09-267	230068	2727062	1768	Caracol F. (Stockwork)	Sp	0.8	707	-	-
GP621R12-1028	230423	2727823	956	Skarn (Manto)	Sp	1.1	-	561	-
MHC04-205	230191	2727130	1794	Caracol F. (Stockwork)	Sp	1.7	-	-	-
WC13-02-234	230271	2727227	1776	Diatreme breccia	Sp	0.7	-	-	-
GP640-13-852	229500	2728600	983	Diatreme breccia	Sp	2.1	-	336	-
GP640-13-1650	229206	2728701	256	Porphyry	Sp	-0.1	-	-	-
GP501-07-990	228950	2728465	1047	Skarn	Sp	0.3	-	-	-

The range of δ³⁴S values is 3.2 to -2.1 per mil (‰) VCDT. Specifically, the pyrite has δ³⁴S (VCDT) values from 2.8 to 0.3‰, while the values for sphalerite range from 3.2 to -1.1‰ (Fig. 7.23). A single arsenopyrite value is 0.3‰. Chalcopyrite and galena exhibit small depletions relative to pyrite, sphalerite and arsenopyrite. Specifically, the chalcopyrite ranges in δ³⁴S values from 0.2 to -2.1‰, whereas the values are from -0.1 to -1.1‰ for galena (Fig. 7.23).
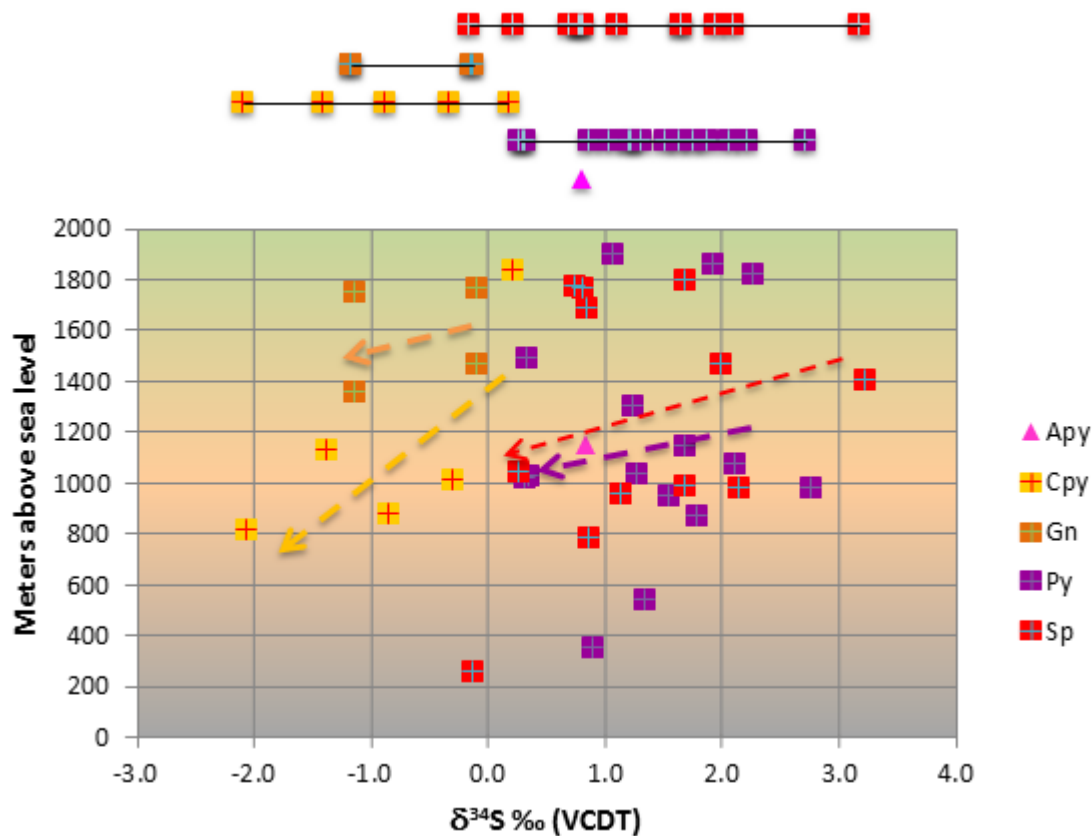
Fig. 7.23. Sulfur stable isotope (δ^{34}S) ratios versus elevation for samples of arsenopyrite, galena, pyrite, chalcopyrite, and sphalerite in the Peñasquito ore system.

The plot of δ^{34}S (VCDT) vs. altitude suggested that sulfides tend to skew towards depletion at lower elevations (Fig. 7.23). In addition, the δ^{34}S values exhibit a significant pattern, indicating a slight δ^{34}S fractionation. For example, the chalcopyrite and galena were more depleted than the pyrite, sphalerite, and arsenopyrite (Fig. 7.16).

Interpretation and Comparison of Sulfur Isotopes

The sulfur isotope ratios of five sulfide pairs were used to estimate the formation temperature of these ore minerals using fractionation factors determined by Ohmoto and Rye (1979). Specifically, a blond brown sphalerite-galena pair from the main ore stage in the Caracol Formation with δ^{34}S values of 2 and -0.1 ‰, respectively, yielded isotopic equilibration temperatures of 322° ± 20°C and 365° ± 25°C. A pyrite-brown sphalerite pair from the main ore stage in the Peñasco diatreme breccia with δ^{34}S values of 2.8 and 2.1 ‰, respectively, suggested isotopic equilibration temperatures of 336° ± 40 °C and 432° ± 55°C. A pyrite-brown sphalerite pair from the main ore stage in the skarn system with δ^{34}S values of 1.6 and 1.1 ‰, respectively, yielded isotopic equilibration temperatures of 448° ± 40°C and 561° ± 55°C. In addition, a pyrite-arsenopyrite pair from the main ore stage in the Peñasco diatreme breccia with δ^{34}S values of 1.7 and 0.8 ‰, respectively, yielded isotopic equilibration temperatures of 264° ± 40°C and 349° ± 55°C. The above results are in agreement with the homogenization temperatures of fluid inclusions in the sphalerite and quartz related to these samples. Furthermore, an estimated temperature for the sphalerite-galena pair from the main ore stage in the Caracol Formation ranged from 707° ± 20°C to 779° ± 25°C; however, these temperatures are much higher than most homogenization temperatures of fluid inclusions in the hydrothermal system, suggesting geochemical disequilibrium.
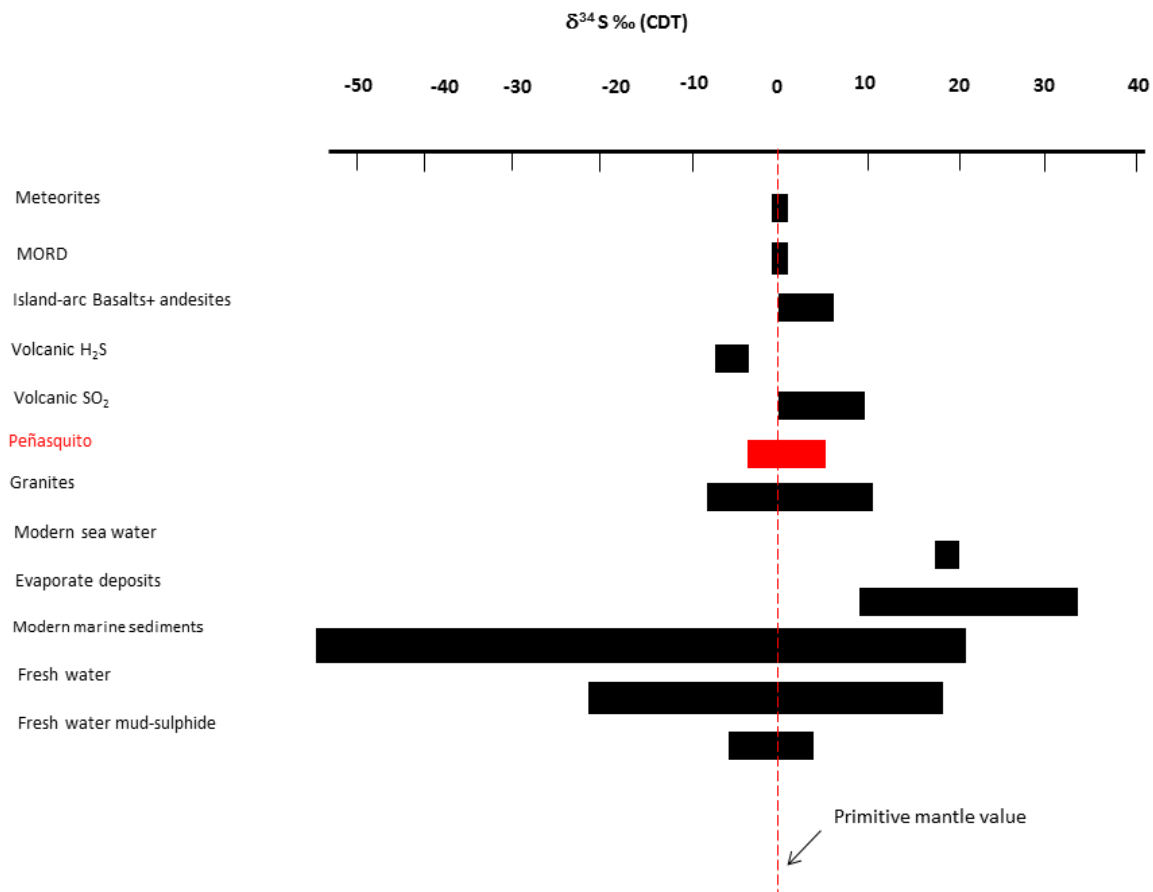
Fig. 7.24. The δ^{34}S values for Peñasquito ore deposits. Also shown are the δ^{34}S natural sulfur isotope reservoirs. Modified from Rollinson (1993).

The δ^{34}S (VCDT) values of the sulfide samples are relatively uniform with an arithmetic mean of 0.8 ‰. The pyrite, sphalerite, and arsenopyrite generally are more enriched in δ^{34}S than the chalcopyrite and galena; however, a sphalerite sample from porphyry showed a δ^{34}S value lower than those of the sphalerite from the skarn system, stockwork zones, and breccia system. The patterns for sulfur isotopes in this study suggest that the sulfide source was from the magmatic system (Fig. 7.24). In addition, the δ^{34}S values for Peñasquito are in agreement with compiled δ^{34}S values for porphyry-copper deposits and sedimentary rock massive sulfides all of which confirms a magmatic source (Fig. 7.25).
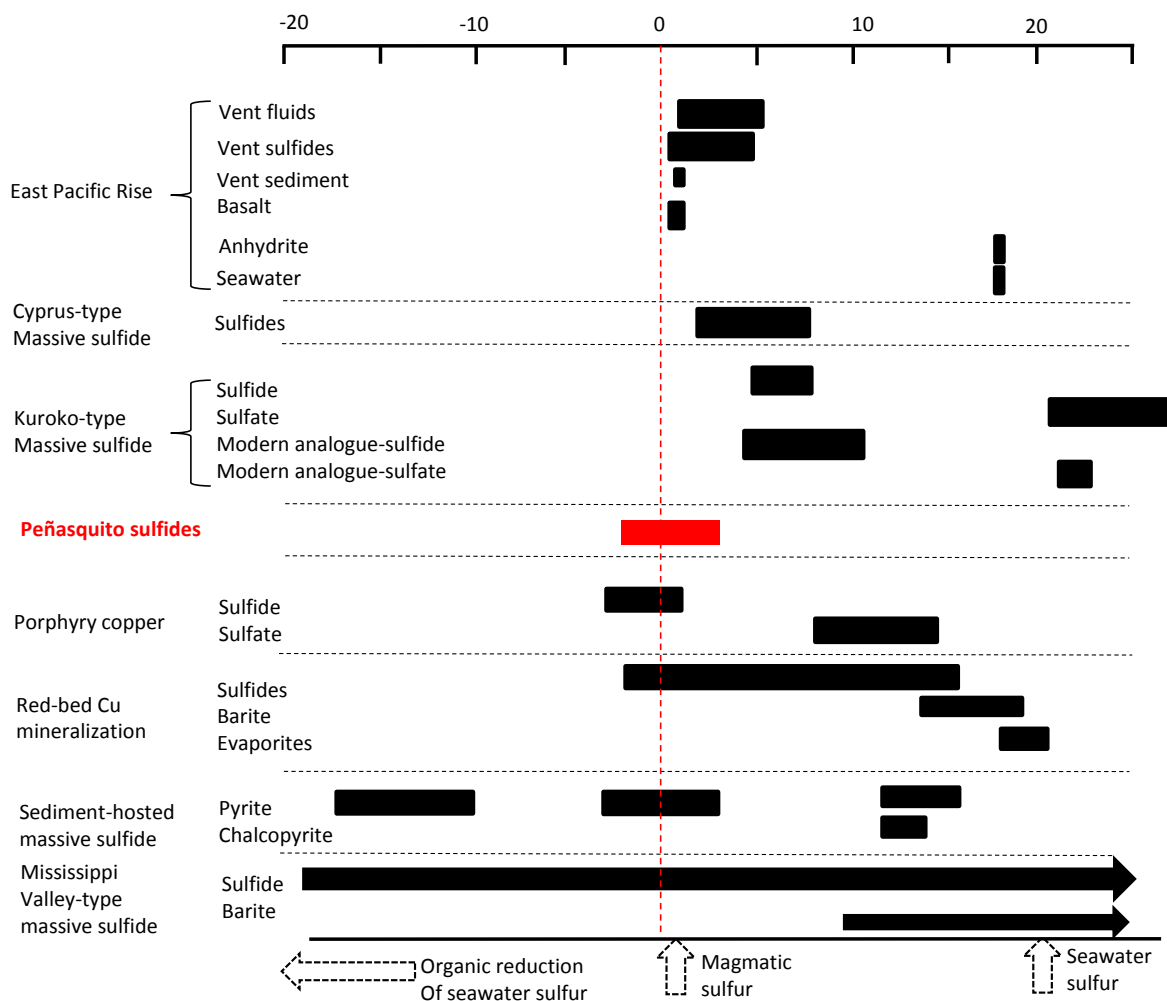
Fig. 7.25. The δ^{34}S values in Peñasquito and δ^{34}S values for sulfur-bearing minerals in hydrothermal deposits. Modified from Rollinson (1993).

CHAPTER VIII

AGES FOR THE CRYSTALLIZATION OF PLUTONIC SYSTEM AND THE MAGMATIC-HYDROTHERMAL SYSTEM IN PEÑASQUITO ORE DEPOSIT

This section presents results of the geochronological dating for the plutonic crystallization, the hydrothermal alteration and the mineralization at Peñasquito, as well as the relationship of the magmatism emplaced in anticlines and synclines of the Peñasquito region between ranges of La Caja-Concepcion del Oro and Santa Rosa. In the Mazapil syncline, the plutonic complex has been recognized between ~250 and ~2,000 m depth, emplaced throughout the Mesozoic marine sequence and the diatreme breccia system. The diatreme breccia system includes diverse porphyry fragments, and a large part of breccia matrix is composed of magmatic products due to connection with the plutonic complex. In the Mazapil syncline, the exploration program performed by Goldcorp has intercepted a large pluton localized below 1,000 m depth, and the dating suggests crystallization ages between Middle Eocene and Early Oligocene. Presumably, the major magmatic pulse (Early Oligocene) developed large halos of hydrothermal alteration, the formation of the diatreme breccia system, and deposition of the polymetallic mineralization. However, some geochronological data suggest the presence of two additional magmatic pulses during Middle Eocene that may be correlated with crystallization ages for stocks localized in anticlines of La Caja-Concepcion del Oro and Santa Rosa. Therefore, the detailed dating of magmatic-hydrothermal events is presented in order to understand the genetic evolution of the plutonic complex.

Age of magmatism

In 2010, geochronological research was performed by Valencia (2010) and funded by Goldcorp that determined the plutonic crystallization ages for the Peñasquito region. The dating research using the U-Pb-Th chronological method was done on zircons that were separated from dikes, porphyry, intrusive fragments, and magmatic products that formed the diatreme breccia system. The data summary is displayed in Fig. 8.1 and Table 8.1.
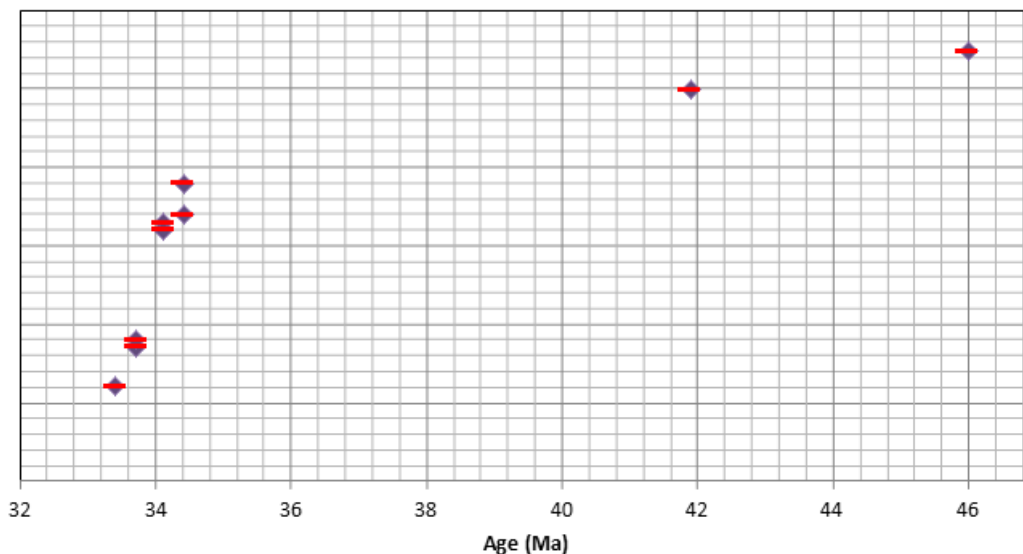
Sample	Coor-X	Coor-Y	Elevation (m.a.s.l)	Age (Ma)	Error (±)	Dated mineral	Method	Locality	Rock
342-1	229669	2728464		33.4	0.4	Zrn	U-Pb-Th	Azul	Green dike
GP595-08-1391	229669	2728464	~579	33.7	0.4	Zrn	U-Pb-Th	Peñasquito	QFP
GP568-08-670	229669	2728464	~1300	33.7	0.5	Zrn	U-Pb-Th	Peñasquito	QFP
282-1	229669	2728464		34.1	0.7	Zrn	U-Pb-Th	Peñasquito	QFP
WC300-511	229418	2728601	1513	34.1	0.6	Zrn	U-Pb-Th	Peñasquito	QFP
GP557-08-1140	229261	2728565	949	34.4	0.4	Zrn	U-Pb-Th	Peñasquito	QFP
WC360-525	229126	2728619	1494	34.4	0.01	Zrn	U-Pb-Th	Peñasquito	QFP
WC335-332	229674	2728623	1682	41.9	0.6	Zrn	U-Pb-Th	Azul	Fragment of porphyry in Felsite
342-1	229669	2728464		46.0	0.02	Zrn	U-Pb-Th	Azul	Felsite

Fig. 8.1. and Table 8.1. Summary of crystallization ages (U-Pb) of plutonic complex in the Mazapil syncline (data from Valencia, 2010). m.a.s.l.

According to Valencia (2010) the plutonic complex found in Peñasquito could have crystallized between Middle Eocene and Early Oligocene. Specifically, Valencia (2010) reported that zircons from tuffisite and zircons in porphyry fragments within the Azul diatreme ranged from 46±0.02 to 41.9 ±0.6 Ma (Fig. 8.2). Additionally, the radiogenic analyses on zircons from the Peñasquito plutonic complex ranged between 34.7 ±0.1 and 33.4±0.4 Ma.
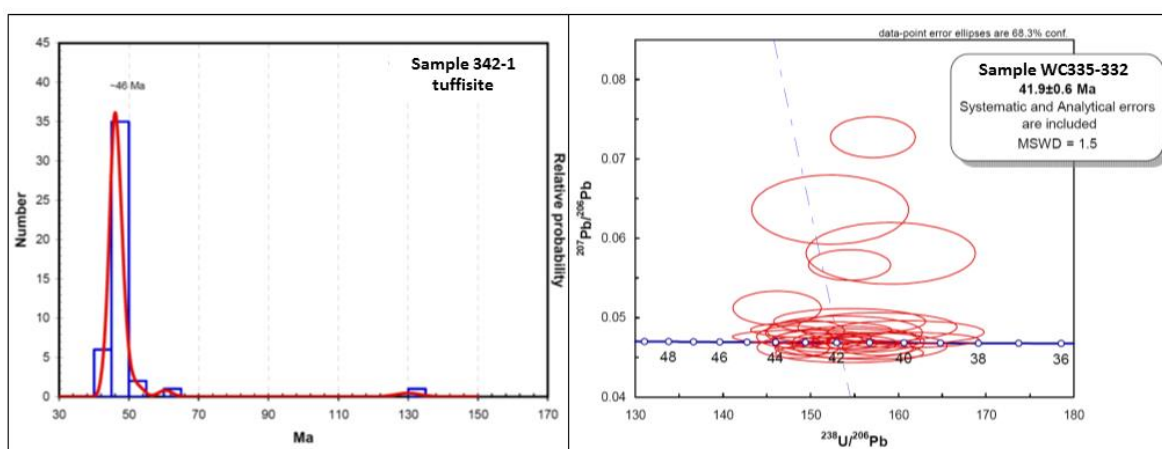
Fig. 8.2. The right diagram displays the relative probability for zircon dates of the sample 342-1 (tuffisite dike). The left diagram displays the concordia diagram for dating zircons of the sample WC335-332 (porphyry fragment). Diagrams were taken and modified from Valencia, 2010.

Valencia (2010) demonstrated that two zircons from a sample of tuffisite yielded a date of 45.95 ± 0.02 Ma (206/238 weighted average), and their inherited cores yielded a range of dates from Eocene (53 Ma) to Cretaceous (~ 130 Ma). Furthermore, Valencia (2010) claimed that twenty-six zircons from a fragment of porphyry found in the tuffisite yielded an age of 41.9 ± 0.6 Ma (intercepted age), but their inherited zircon cores yielded dates from Eocene (~ 44-47 Ma) to Cretaceous (~ 97 Ma). These geochronological results

suggest that the diatreme breccia system included fragments from several plutons that were emplaced during the Middle Eocene through the Mazapil syncline.
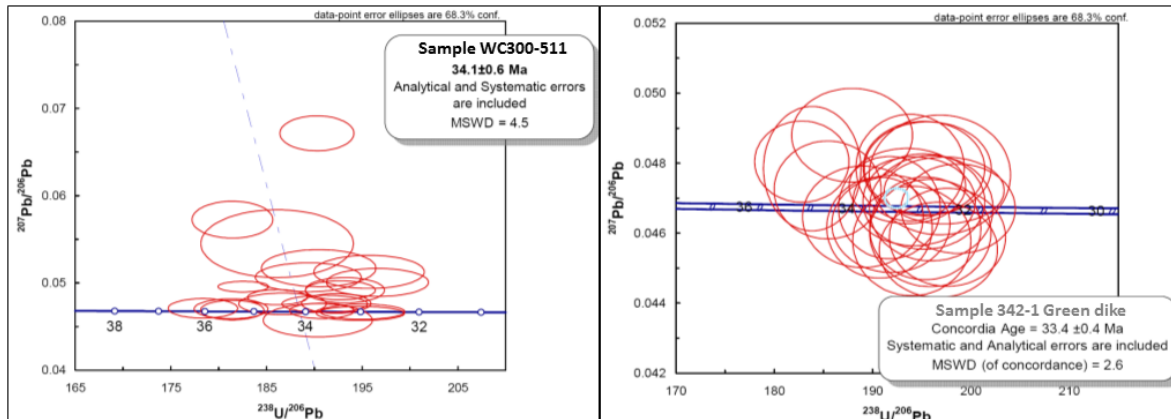
Fig. 8.3. The right diagram displays the concordia diagram for zircon dates of the sample WC300-511 (QFP). The left diagram displays the concordia diagram for zircon dates of the sample 342-1 (green dike-diorite). Diagrams were taken and modified from Valencia, 2010.

Valencia (2010) demonstrated that zircon dates in QFP ranged between Late Eocene (~34.4 Ma) and Early Oligocene (~33.7 Ma). For example, the zircons from a QFP (sample WC300-511) were 34.1 ±0.6 Ma (n=22, MSWD =4.5, 2 sigma) (Fig. 8.3.), and their inherited zircon cores ranged from Eocene (~37-41Ma) to Jurassic (~173 Ma) (Valencia, 2010). According to Valencia (2010), youngest zircons in the Peñasquito were from a green dike (diorite) with an intercepted age of crystallization from 33.4 ±0.4 Ma (n=24, MSWD =2.6, 2 sigma) (Fig. 8.3.), and their inherited zircon cores extended from Eocene (~ 39 Ma) to the Cretaceous and Jurassic (~79-144 Ma).These geochronological results suggest that the bulk of the plutonic complex in the Mazapil syncline began crystallization in the Late Eocene and ended in the Early Oligocene.

Interpretation and Comparison of Isotopic Dating of Zircons

The Peñasquito plutonic complex is chronologically correlated with the known stocks in the region (ranges of Sierra La Caja-Concepción del Oro and Sierra Santa Rosa). The Middle Eocene ages (46±0.02 and 41.9 ±0.6 Ma) are a good agreement with radio-genic ages documented by Valencia (2010) for the rhyolitic porphyry of Santa Rosa (~45 Ma) and the granodiorite of Salaverna-Concepción del Oro (~40 Ma) (Valencia, 2010; Ohmoto et al., 1966; Buseck, 1962; Mújica-Mondragón et al., 1983), suggesting that these plutons may be from the same magmatic source; presumably, these represent the oldest magmatic pulse in the Peñasquito area. The youngest ages (33.4 and 34.7 Ma) are a good agreement with a productive plutonic stock in Salaverna (33.6 ±0.6) at the Sierra La Caja-Concepción del Oro.

Age of mineralization and hydrothermal alteration

Isotopic Dating of Molybdenite

In this research, two molybdenite samples were selected from the plutonic com-plex in order determine the timing of hydrothermal mineralization in the Peñasquito sys-tem. The molybdenite veinlets were 2 to 4 mm in width, and disseminated molybdenite that occurred throughout the porphyry ranged from 1 to 4 mm in size. The study consisted of a Re-Os dating procedure and was performed by Dr. Jason Kirk at the University of Ari-zona. The Re-Os dating of molybdenite is the only direct method to routinely date a sul-fide mineral with a high internal precision (±0.2%) throughout the geologic time scale. Therefore, the dating represents the crystallization age of molybdenite.
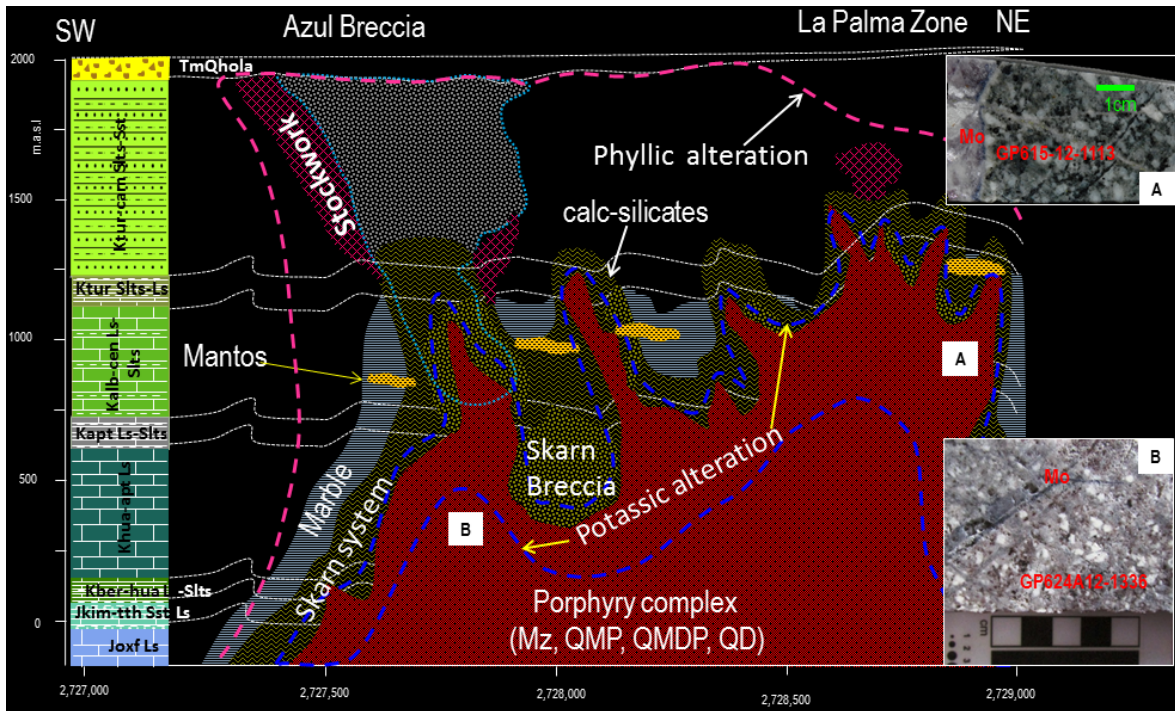
Fig. 8.4. Schematic cross-section showing location of samples for isotopic dating of molybdenite. The cross section is oriented at 40° and looking to the northwest. Note: Mo (molybdenite in veinlets).

Samples were handpicked from exploratory drillcores (i.e. GP615-12 and GP624A12). These specimens were intercepted between 906 and 648 meters above sea level (Fig. 8.4). The sample GP615-12-1113 exhibited a vein filled by pink (purple?) fluorite and molybdenite that cut through D veinlets (Fig. 8.5.). This specimen was from the Palma zone, which exhibits porphyritic texture, is grayish in color, and contains three stages of veinlets. This porphyry consists of plagioclase (~25%) phenocrysts, quartz eyes (7%), biotite (10%), and magnetite (5%), which are floating in a fine groundmass made up of fine hydrothermal orthoclase, quartz, sericite, and pyrite. The sample exhibited D veinlets filled by quartz and pyrite that cut through veinlets filled by hydrothermal biotite. The sample GP621R-12-1336 included fractures partially filled by molybdenite, pyrite and quartz as well as disseminated molybdenite, which is present in the groundmass. This

specimen is a porphyry consisting of phenocrysts (i.e. plagioclase and quartz eyes that occupy up to 30%), primary sulfides (i.e. pyrite, local sphalerite, and molybdenite), which are floating in a fine groundmass made up of quartz, opaque minerals, sericite, hydrothermal biotite, and lesser hydrothermal orthoclase. The specimen is cut by A veinlets of quartz, and D veinlets filled by
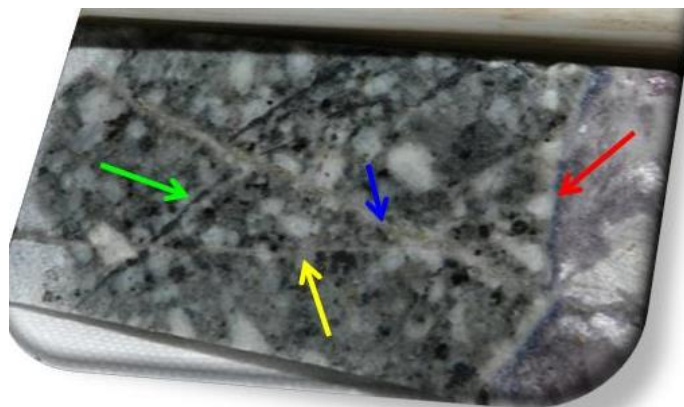
Fig. 8.5. Photography showing the core drill sample (GP615-12-1113) of quartz-monzonite with molybdenite. The chalcopyrite veinlet with orthoclase is flooding the groundmass (blue arrow) and cross-cuts a biotite veinlet (green arrow). The fine orthoclase veinlet which is flooding the groundmass (yellow arrow) also cuts the biotite veinlet (green veinlet). The molybdenite-fluorite-quartz vein (red arrow) is cutting the chalcopyrite and orthoclase veinlet.

quartz, sericite, and pyrite. This porphyry exhibits moderate to pervasive phyllic alteration made up of sericite, quartz, and pyrite (7%), which was overprinted by carbonates.

Results of Isotopic Dating of Molybdenite

The ^{187}Re and ^{187}Os concentrations in molybdenite were determined by isotope dilution mass spectrometry in the isotope facility in the Department of Geosciences at the University of Arizona, Tucson campus. According to Dr. Jason Kirk (verbal communication), approximately 20 to 50 mg of molybdenite were dissolved and homogenized using the Carius tube technique (Shirey and Walker, 1998). Osmium was separated using CCl_4 solvent extraction and Re was separated through standard anion exchange columns (Cohen and Waters 1996; Morgan and Walker 1989). Molybdenite samples were analyzed by

NTIMS (Negative Thermal Ionization Mass Spectrometry) using a VG Sector 54 in negative mode at the University of Arizona, Tucson with procedures similar to Creaser et al. (1991). The ages were calculated using the equation $[^{187}Os]$today = [187Re]today $(e\lambda t-1)$ with a decay constant (λ) of 1.666 x 10-11 yr -1 (Smoliar et al., 1996).

Table 8.2. Summary data of isotopic dating of molybdenite.

Sample	Longitude	latitude	Elevation (m.a.s.l)	Rock	Mineral	Total Re (ppm)	^{187}Re (ppm)	^{187}Os (ppb)	Age (Ma)	Error (±0.5%)
GP615-12-1113	230986	2728536	906	Porpyry	Molybdenite	188.69	118.63	69.73	35.27	0.18
GP621R12-1336	230418	2727820	648	Porpyry	Molybdenite	219.80	138.18	80.70	35.04	0.18
						255.87	160.86	93.74	34.97	0.17

Total rhenium concentration ranged from 188.69 to 255.87 ppm, whereas, the ^{187}Os concentration ranged from 69.97-93.74 ppb. The sample GP615-12-1113 yielded an age of 35.27 ± 0.18 Ma (~0.5% error) and the sample GP624R-12-1336 yielded two similar ages that averaged 35.1 ± 0.18 Ma (~0.5% error) (Table 8.2).

Interpretation and Comparison of Isotopic Dating of Molybdenite

The Re-Os ages reported here are somewhat older than the average of U-Pb-Th zircon ages (~34 Ma) that were calculated by Valencia (2010) for the porphyry complex. The data may support a conclusion of molybdenite mineralization age, suggesting that productive hydrothermal fluids from the plutonic complex started about 35 Ma. In general, both Re-Os molybdenite dates and U-Pb-Th zircon ages may be in agreement if the age error is considered. Therefore, the ages in this study and previous ages suggest that the Peñasquito molybdenite mineralization was the result of an early hydrothermal mineralization that started at ~35 Ma.

Isotopic Dating of Biotite and K-feldspar (orthoclase)

Four samples were selected for ^{40}Ar/^{39}Ar dating in the present study from the plutonic complex at Peñasquito area. This study was performed on hydrothermal products located between 295 (1,695 m.a.s.l.) and 1,500 (470 m.a.s.l.) meters beneath the original surface. This research focused on understanding the relationship of pluton complex coeval magmatic and hydrothermal polymetallic mineralization in the Peñasquito polymetallic ore deposit. Samples were handpicked from drill cores from quartz-monzonite porphyries (Fig. 8.6) with pervasive hydrothermal K-feldspar and biotite, which appear to be in a cupula of a stock emplaced through the Mesozoic sedimentary sequence, and related to mineralization. The rock selected for isotope analyses had obvious hydrothermal altered domains (i.e. black-brown fine biotite and fine K-feldspar detected in prior stained samples using sodium cobaltinitrite).
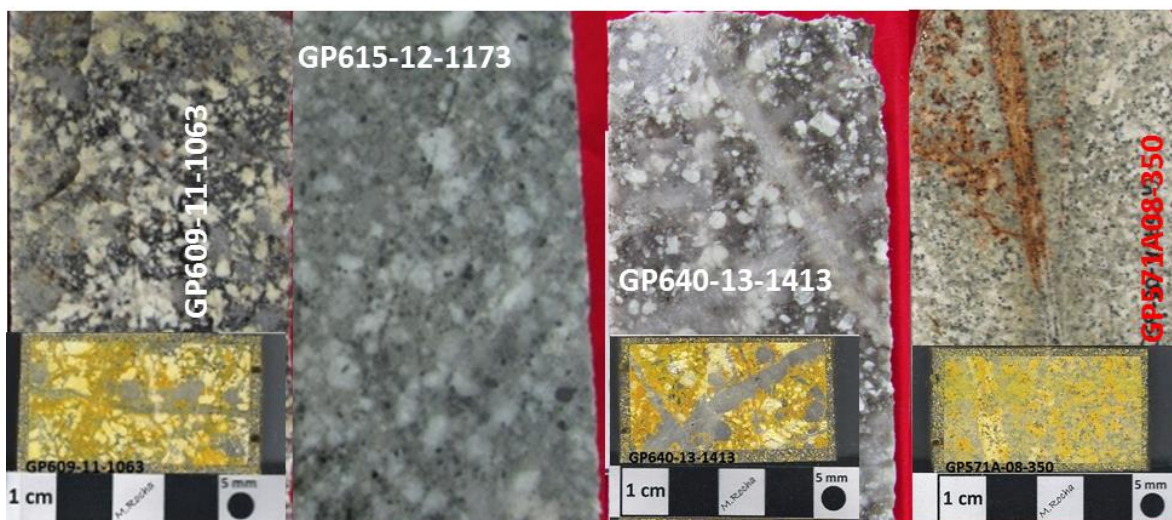
Fig. 8.6. Hand samples and billets of quartz-monzonite porphyry granite used for the ^{40}Ar/^{39}Ar dating. Billets showing staining of K-feldspar (Kfs) with sodium cobaltinitrite in yellow color.

Samples GP609-11-1062 and GP615-12-1173 were used for isotopic dating of hydro-thermal biotite (Fig. 8.6) that correspond to depths about 1,006 (964 m.a.s.l.) and 1,122 m (848 m.a.s.l.), respectively. Samples GP640-13-1413 and GP571A-08-350 were used for isotopic dating of hydrothermal orthoclase (Fig. 8.6) that correspond to depths about 295 (1,695 m.a.s.l.) and 1,500 (470 m.a.s.l.), respectively.

Samples selected for $^{40}Ar/^{39}Ar$ geochronology were analyzed in the Auburn Univer-sity Noble Isotope Mass Analysis Laboratory by Dr. Willis E. Hames. According to Dr. Hames, the $^{40}Ar/^{39}Ar$ radiometric analyses were performed using a spectrometer with an ultra-high vacuum, 90-degree sector, and 10 cm radius spectrometer. The spectrometer employs second-order focusing and is fitted with a high sensitivity electron-impact source and a single ETP electron multiplier. Analyses comprise 8 cycles of measurement over the range of masses and half-masses from m/e=40 to m/e=35.5 with baseline corrected values extrapolated to the time of inlet. Analysis of samples and blanks is fully automated under computer control. Pumping of residual and sample reactive gases is accomplished through use of SAES AP-10 non-evaporable getters. The extraction line is fitted with a 50W Synrad CO_2 IR laser for heating and fusing silicate minerals and glasses. The sample chamber uses a Cu planchet, KBr cover slips, and low-blank UHV ZnS window that is suitable for incremental heating and fusion analysis of single crystals and multigrain samples. Finally, initial data reduction is accomplished through an in-house Excel spreadsheet, with final reduction using Isoplot (Ludwig, 2003).

Results of Isotopic Dating of ^{40}Ar/^{39}Ar for Biotite

Twenty four analyzes were performed on the sample GP609-11-1063 (biotite). Ages ranged between 34.22 ±0.11and 26.57 ±4.27 Ma; however the bulk of ages obtained from single crystals averaged ~33.58 Ma. The best average age considered for this sample is 33.952 ± 0.085 Ma with 95% of confidence. On the sample GP615-12-1173 (biotite), twenty two analyzes were performed. The bulk of ages obtained from single crystals were consistently about ~33.30, but ages ranged between 38.66 ±3.14 and 26.57 ±4.27 Ma. The
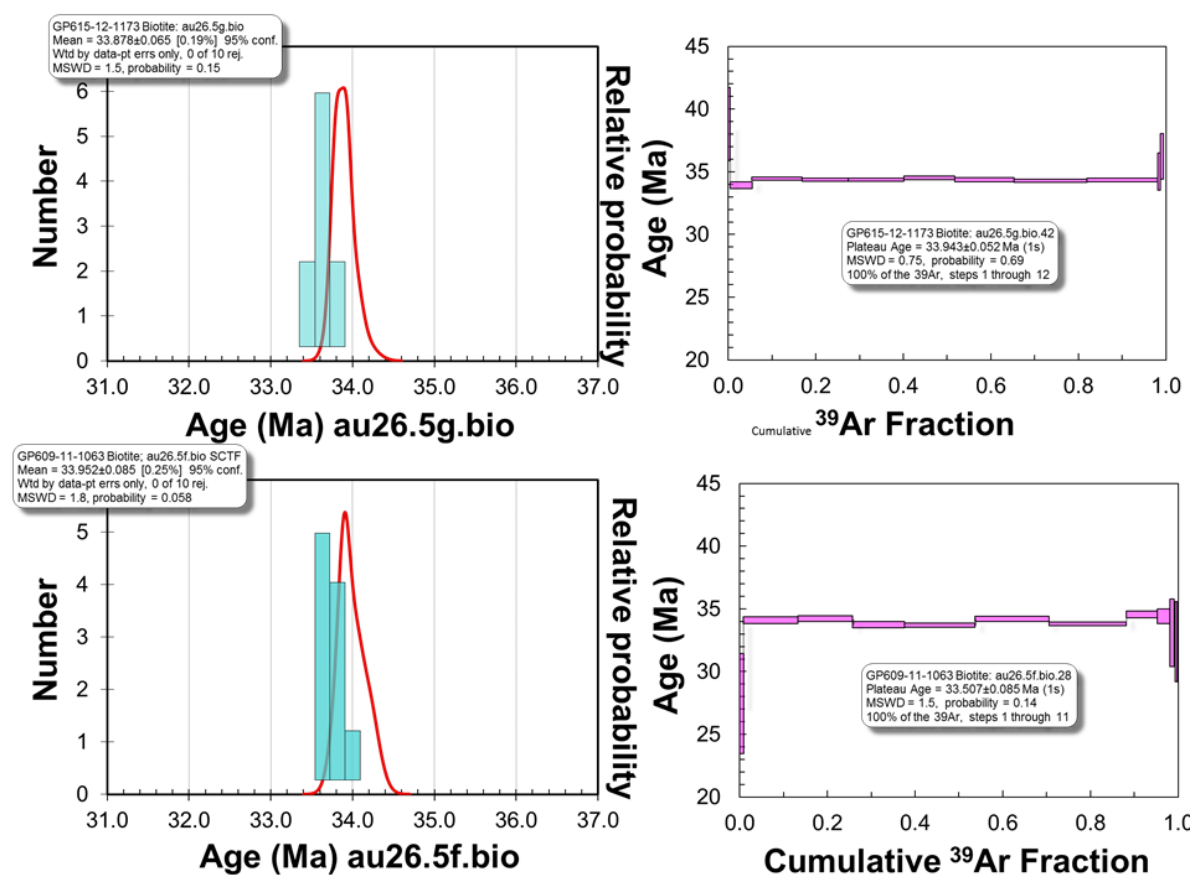
Fig. 8.7.The probability plots of laser-fusion of single-grain (left) and diagrams of average age (right) for the dating of biotite. The mean ages, MSWD values, and standards are shown (right). Analysis represented in pink are considered in the calculation of age (right). The errors are 1 σ. Detailed analytical data are given on Table 8.3.

best average age considered for this sample is 33.878 ±0.065Ma with 95% of confidence.

All biotite ages are reported in Fig. 8.7 and Table 8.3.

Table 8.3.Summary data of isotopic dating of biotite (Bi) and K-feldspar (Kfs).

Sample-Field	Coor-X	Coor-Y	Elevation (m.o.s.l)	Age (Ma)	Error (±)	Dated mineral	Method	Locality	Rock
GP640-13-1413	229292	2728670	470	32.82	0.12	Kfs	Ar-Ar	Peñasco Breccia	QFP
GP571A-08-350	230273	2728280	1675	33.32	0.16	Kfs	Ar-Ar	Azul Breccia	QFP
GP609-11-1063	230997	2728684	964	33.95	0.09	Bi	Ar-Ar	La Palma	QFP
GP615-12-1173	230983	2728536	848	33.88	0.07	Bi	Ar-Ar	La Palma	QFP

Results of Isotopic Dating of $^{40}Ar/^{39}Ar$ for K-feldspar (orthoclase)

Sixteen analyzes were performed on the sample GP640-13-1413 (K-feldspar). Ages

ranged between 32.77 ±0.11 and 28.46 ±13.83 Ma, however the bulk of ages obtained

from single crystals averaged ~32.77 Ma. The best average age considered for this sample

is 33.878 ±0.065 Ma. On the sample GP-571A-08-350 (K-feldspar), eighteen analyzes were

performed. Ages ranged between 45.98 ±1.4 and 32.99 ±0.13 Ma; however, the bulk of

ages obtained from single crystals overaged ~33.25 Ma. The best average age considered

for this sample is 33.32±0.16 Ma with 95% of confidence. All orthoclase ages are reported

in the Fig. 8.8 and Table 8.3. All biotite and orthoclase data are reported in Appendix B.

Interpretation and Comparison of Isotopic Dating of Biotite and K-Feldspar

The $^{39}Ar/^{40}Ar$ dates suggest ~33 Ma for the potassic alteration that may be consi-

dered the early polymetallic mineralization age at Peñasquito. The $^{40}Ar/^{39}Ar$ dating results

of biotite (~33.9) and K-feldspar (~33.07) indicate that the biotite alteration was slightly

older than the K- feldspar alteration (Fig. 8.9). Generally, the $^{40}Ar/^{39}Ar$ dates are in good

agreement with U-Pb crystallization dating at ~34 Ma for the quartz feldspar porphyry and

green dike (Valencia, 2010). Definitely, ^{40}Ar/^{39}Ar dating of hydrothermal biotite (~33.9) and K- feldspar (~33.07) are somewhat slightly younger than the average of U-Pb-Th zircon ages (~34) that were calculated by Valencia (2010), suggesting that the temperature of closure of each mineral may have caused the different ages (Chiaradia et al., 2013).
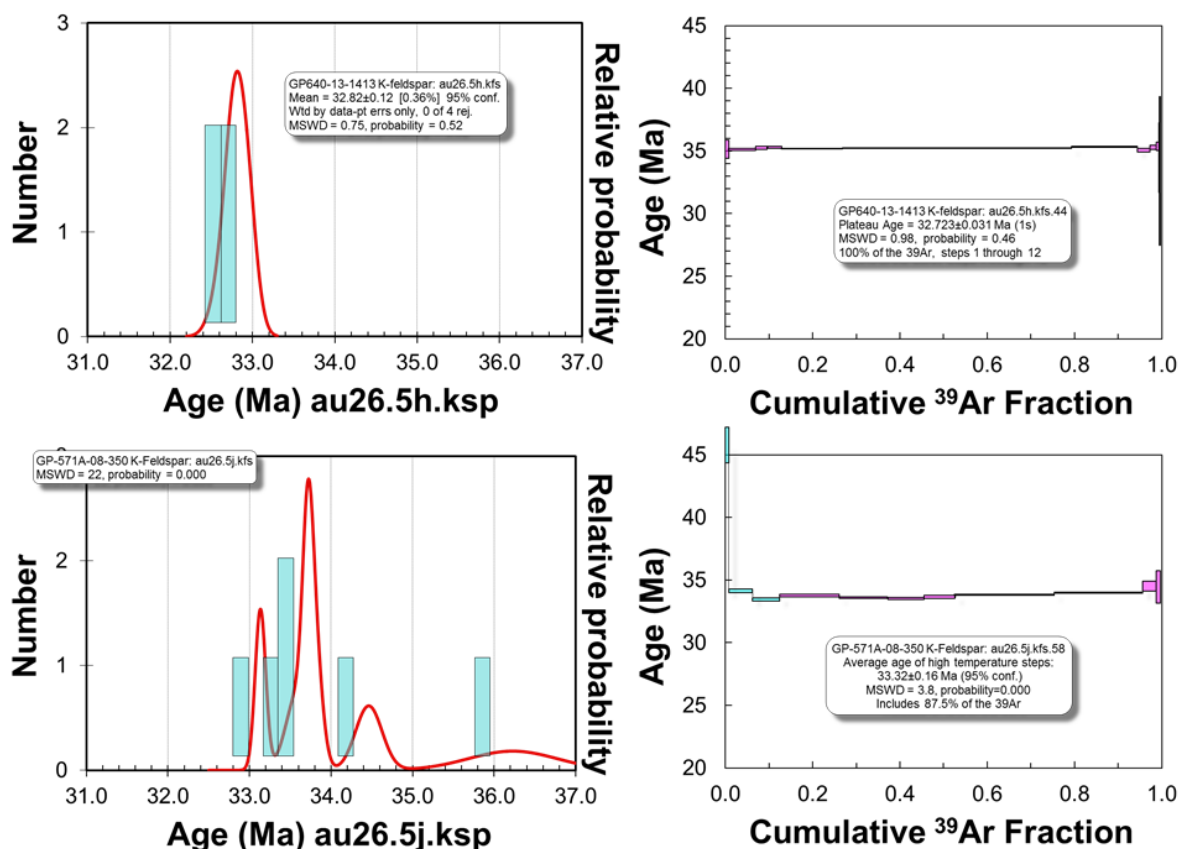
Fig. 8.8. The probability plots of laser-fusion of single-grain results (left) and diagrams showing the average age (right) for dating of K-feldspar. The mean ages, MSWD values, and standards are shown (right). Analysis represented in pink are considered in the calculation of age (right). The errors are 1 σ.

Finally, the ages in this study and previous ages (^{40}Ar/^{39}Ar, U-Pb-Th, and Re-Os) suggest that the Peñasquito polymetallic mineralization was the result of a continuous magmatic-hydrothermal system that started at ~35.2 Ma and ended at ~32.8 Ma with duration of about ~2.4 Ma during Early Eocene and Late Oligocene (Fig. 8.9). In addition, some U-

Pb-Th zircon ages reported by Valencia (2010) suggest that the Peñasquito area was emplaced and prepared by magmatic pulses during ~46 and ~41.9 Ma (Fig. 8.9).Therefore, the radiometric ages and geological data suggest that the Mazapil syncline was intruded by several magmatic pulses that ranged from Early Eocene to Early Oligocene, but during Priabonian and Rupelian epochs, a magmatic productive episode developed the potassic and phyllic alteration halos, as well as the bulk of polymetallic mineralization (Fig. 8.9).
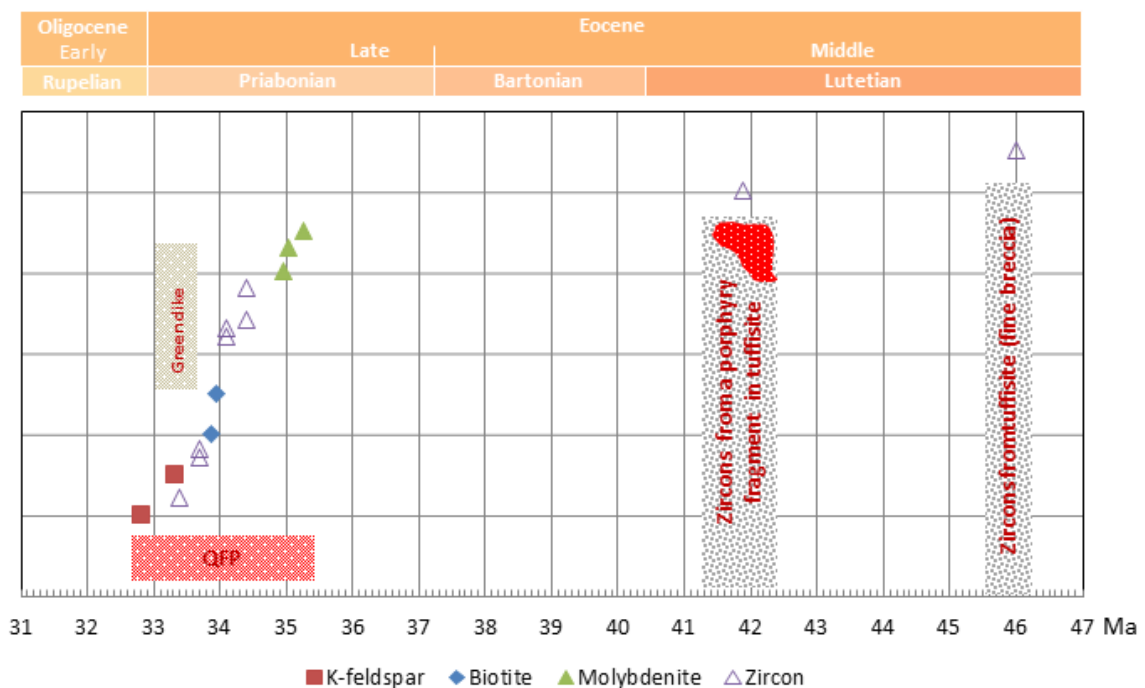
Fig. 8.9. Graphic showing the radiometric dating and schematic sources of dated minerals for the Peñasquito area. The K-feldspar and biotite data correspond to the ^{40}Ar/^{39}Ar dating obtained by this author. The molybdenite was dated using the Re-Os method during this research. Zircon data correspond to U-Pb-Th dating by Valencia (2010). Note: Quartz-feldspar porphyry (QFP).

CHAPTER IX

DISCUSSION, SUMMARY, AND CONCLUSIONS

The Peñasquito magmatic hydrothermal ore deposit appears to represent part of the continental, calc-alkaline province of widespread magmatic activity during the mid-Tertiary, which influenced the central-northeastern portion of Mexico and formed large polymetallic concentrations, such as replacement ore bodies, epithermal veins, and local diatreme breccia pipes through a Jurassic and Cretaceous sedimentary sequence. Specifically, Peñasquito is an example of productive calc-alkaline magmatism where the plutons traversed a great thickness of continental crust and were emplaced in a syncline, that developed hydrothermal alteration (i.e. potassic, phyllic, calc-silicates, carbonate, and marble halos) in the porphyry complex and the Mesozoic marine sedimentary sequence, as well as a large skarn system, mantos, two large diatreme breccias, stockwork zones, and epithermal veins with concentrations of polymetallic mineralization through 2,000 vertical meters.

The magmatism in the Peñasquito area was developed by a regionally extensive episode that took place during the Eocene-Oligocene, forming a plutonic complex during several magmatic pulses that were emplaced throughout the Late Jurassic and Early Cretaceous sedimentary marine sequences and the diatreme breccia system. This magmatism was emplaced as stocks and dikes along the Mazapil syncline and where three set of faults converged. The petrological and petrographic results have demonstrated a mineralogical and textural differentiation of the plutonic complex, exhibiting a noticeable textural

differentiation arrangement; for example, the plagioclase microlites form stock boundaries and the tops of cupulas, followed by porphyries made up of phenocrysts of plagioclase and resorbed quartz eyes, as well as local orthoclase, amphibole and pyroxene with fine-medium-grained texture; whereas below the cupula, phenocrysts of orthoclase and plagioclase (up to 3 cm), biotite, and quartz eyes form a porphyritic zone with medium-grained texture; and beneath the biotite hydrothermal alteration zone, the orthoclase phenocrysts are abundant and up to 5 cm in diameter. The petrographic modal classification (QAP diagram) suggests a mineralogical and textural differentiation in the plutonic complex (i.e. quartz-monzonite, quartz-monzodiorite, and quartz-microdiorite), indicating a magmatic differentiation by moderate diapiric mobilization (Fig. 9.1). The quartz eyes exhibit noticeable resorption texture, and veinlet types A and D are developed in the plutonic complex. The plutonic complex exhibits pervasive (at top) to weak (at depth) hydrothermal potassic alteration, moderate phyllic alteration, and both are overprinted by carbonate (Fig. 9.1). The auriferous and polymetallic systems are primarily associated with quartz-monzonite and quartz-monzodiorite porphyries. The molybdenum mineralization is associated with quartz-monzonite porphyry as veinlets and disseminations that have been found beneath 1,100 m (870 m.a.s.l.)

The major oxides and trace elements obtained from samples of plutonic products suggest that this magmatism could have been related to subduction-related uplift with arc magmatism that interacted with crustal rocks that generated partial melting. The Harker diagrams demonstrate that the bulk of the plutonic complex exhibited intermediate and high SiO_2 and K_2O contents due to hydrothermal alteration and low contents of Na_2O, CaO,

MnO, and MgO. The chemical classification diagrams (Le Maitre et al., 1989; Cox et al., 1979) demonstrated that the bulk of the plutonic complex exhibited an intermediate and sub-alkaline composition. According to Irvine and Baragar (1971) diagrams, porphyries were influenced by sub-alkaline and calc-alkaline magma sources, indicating that these magmas were generated in the continental crust.
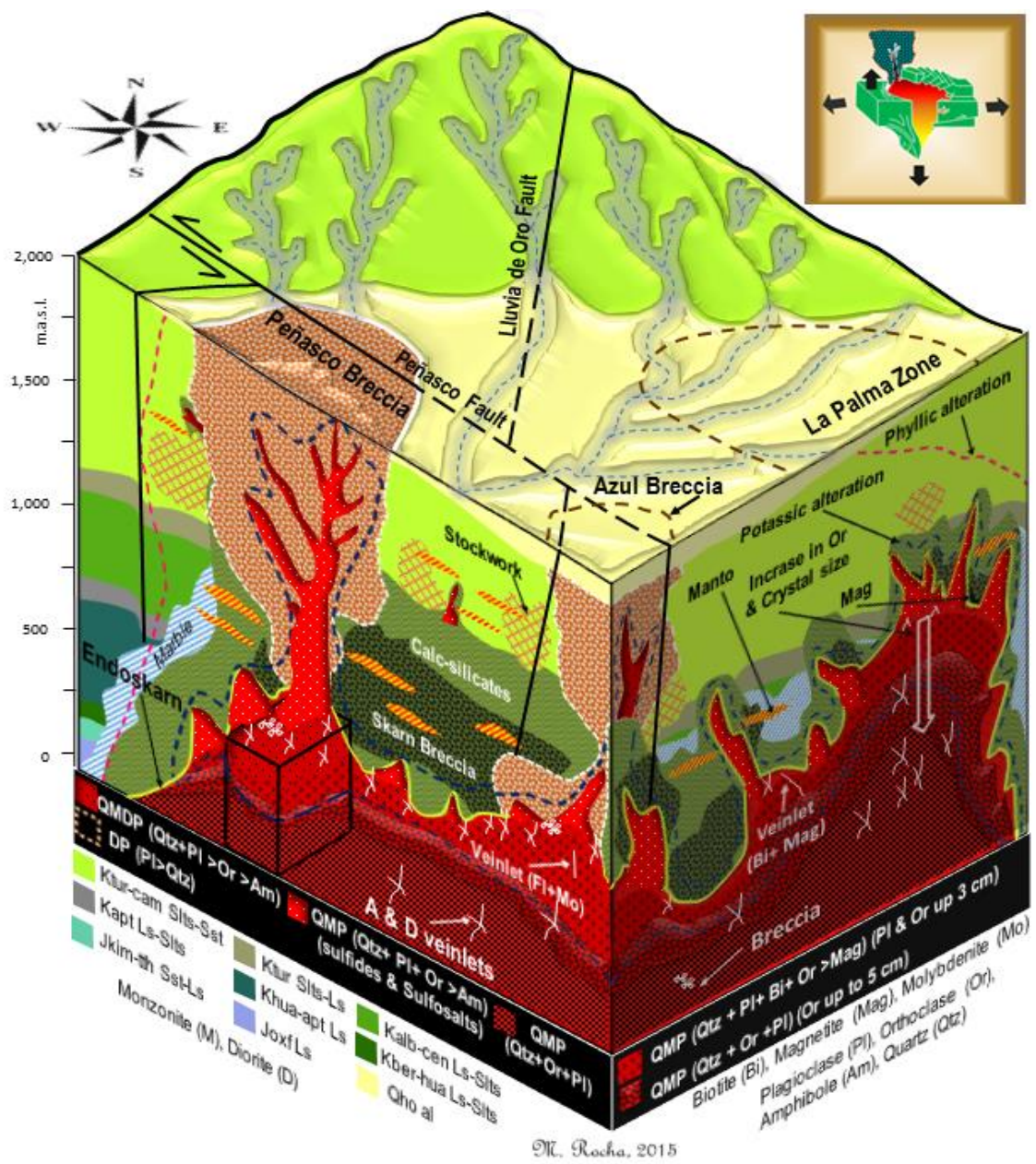
Fig. 9.1. 3D block and schematic mechanism of magmatic emplacement (top right) for the plutonic complex and the diatreme breccia system at the Peñasquito ore deposit.

At the Mazapil syncline, the early emplacement of the magmatic stock complex caused metasomatism in the marine sedimentary sequence forming a large skarn system. The skarn system is found within the Late Jurassic and Early Cretaceous sedimentary marine sequence, which include mantos, disseminated mineralization, and local stockwork and mineralized breccias. This skarn system exhibits mineralogical and textural zonation, forming aureoles of endoskarn, exoskarn, skarnoid, and hornfels, which are in contact and locally intercalated with a marble shell (Fig. 9.1). The skarn system consists of grandite (andradite and grossularite), pyroxene, amphibole, wollastonite, primary sulfides and oxides (magnetite) and lesser amounts of sulfosalts, gold, chlorite, epidote, fine orthoclase, sericite-quartz, carbonate, and secondary oxides. The bulk of skarn has been intercepted between 700 and 1,300 meters below the surface. The skarn system exhibits local potassic alteration, phyllic alteration, and both are overprinted by aphanitic carbonate (i.e. calcite>>dolomite).

At the Mazapil valley, two diatremes owe their formation to energy released by magmas ascending including vapor produced by the contact of magma with groundwater (presumably Indidura Formation KturSlst-Ls). The diatreme breccias are hosted mainly in the Late Cretaceous marine sequence, related to the plutonic complex and the skarn system, and range from surface (1,920 m.a.s.l.) to 750 (m.a.s.l.) at depth (Fig. 9.1). These mineralized diatremes are aligned in a northwest-southeast direction (Peñasco and Azul Breccias), exhibit a conical shape which tapers downward, and at their bases, both breccias take on a sub-horizontal shape and are connected to a porphyry complex (i.e. quartz-monzodiorite and quartz-monzonite). These diatreme pipes (including the horizon-

tal cross-section and depth of emplacement) have no direct correlation with the composition of some infilling rocks (i.e. sedimentary rock and skarn). However, these diatremes include greater volumes of intermediate composition igneous fragments from depths that reached shallow levels, as well dikes, indicating a close relationship to the plutonic complex. Among products filling the Peñasco and Azul diatremes are magmatic fragments of various textures and compositions (i.e. intermediate to felsic) intermixed with varieties of sedimentary rocks, fewer fragments of skarn, varieties of tuffisite breccia, sulfides, which are cemented by a breccia matrix and cut by dikes of tuffisite and altered igneous dikes (i.e. quartz-monzonite and local quartz-monzodiorite), indicating duration of hydrothermal activity from porphyry-skarn-veins with subsequent brecciation (i.e. the formation of diatremes), followed by hydrothermal activity that caused the late mineralization and hydrothermal alteration (i.e. local potassic alteration, phyllic alteration, and both are overprinted by carbonate). According to Milashev (1984), the duration of eruptive events associated with the formation of simple diatremes is several days to many weeks or months. Therefore, it is concluded that in Peñasquito, the driving mechanism of the process may have been the emission of highly compressed and heated gases that were generated between the Caracol Formation and the plutonic complex due to the interaction of hydrothermal fluids and ground water. Hence, this interaction led to thermomechanical abrasion of intruded strata and gradual transformation of two fissured channels into cone-shaped breccia bodies. The diatreme breccia system occurred in the weakened zones of the Late Cretaceous sedimentary sequence (i.e. Caracol Formation), which is characterized by high permeability due to its lithological constitution (i.e.

intercalation of sandstone and siltstone), but affected by a convergence of sets of faults. Therefore, these geological structures served as paths for the ascent of deep-seated material to the surface. The Peñasquito area mainly consists of sedimentary rocks with dense fissure systems, and the diatreme breccias occur at the intersections of several fissures. Both diatremes form a linear group, are more or less cone shaped, though different in size, with a more or less regular pattern in distribution, internal structure, and morphology. In the Peñasquito area, eruptive products related to the diatreme breccias have not been identified, suggesting that both diatremes may be classified as eroded and exposed feeders. The presence of high-level sedimentary fragments suggests that no volcanic activity occurred as the sedimentary fragments would have been erupted away from the diatreme pipes. Subsequent erosion occurred due to the position of the diatreme breccias along an ancient valley and the path of an ancient stream, which are along the axis of the Mazapil syncline.

In addition, stockwork zones are found surrounding the diatreme breccia system and within the Caracol Formation (Fig. 9.1). Stockwork zones owe their formation to stress and pressure generated by magmas ascending. The stockwork is composed of mineralized fractures, faults, and veinlets with diverse lengths and thicknesses. The mineralogy includes primary sulfides, sulfosalts, and subordinate carbonates, but secondary oxides are also locally present.

Gangue minerals and sphalerite exhibit unsaturated fluid inclusions made up of liquid and vapor (i.e. water vapor), as well as saturated fluid inclusions made up of clear liquid, vapor (i.e. water vapor), and solids (i.e., halite and sylvite, as well as presumably,

pyrite and/or magnetite). Microthermometric studies of fluid inclusions revealed homogenization temperatures (Th) in a range from 177°C to 598°C. Specifically, the fluid inclusions in quartz have a wider range of final homogenization temperature that range from 184°C to 598°C. The fluid inclusions in sphalerite have a wide range of final homogenization temperatures from 180°C to 480°C. The fluid inclusions in fluorite yield high final homogenization temperatures from 390°C to 440°C; and the garnet inclusions were formed from 210°C to 440°C. The determined eutectic temperature (Te) was around -23°C, suggesting sodium-potassium-chloride brine. The ice melting temperatures (Tm) of the unsaturated fluid inclusions ranged between -7.5°C and -19°C, which corresponds to 11.1 to 21.94 equivalent weight percent NaCl, but saturated fluid inclusions averaged between 33.25 to 44.39 equivalent weight percent NaCl and some fluid inclusions averaged between 21.12 to 22 equivalent weight percent KCl. The fluid inclusion results are in agreement with the historical signature of the skarn and porphyry fields suggested by Wilkinson (2001), suggesting that the hydrothermal fluids in the Peñasquito ore deposit were from a magmatic source. These fluids were gradually diluted and cooled, with local boiling effects due to depressurization, and isothermal mixing caused by multiple hydro-thermal events.

The sulfur isotope compositions of five sulfide pairs yielded isotopic equilibration temperatures between 561° ± 55°C and 264° ± 40°C. Specifically, blond brown sphalerite-galena pair from stockwork demonstrated equilibration temperatures of 322° ± 20°C to 365° ± 25°C. A pyrite-brown sphalerite pair from the Peñasco diatreme breccia yielded isotopic equilibration temperatures of 336° ± 40°C and 432° ± 55°C. A pyrite-brown spha-

lerite pair from the skarn system yielded isotopic equilibration temperatures of 448° ± 40°C and 561° ± 55°C. A pyrite-arsenopyrite pair from the Peñasco diatreme breccia yielded isotopic equilibration temperatures of 264° ± 40°C and 349° ± 55°C. The above results are in agreement with the homogenization temperatures of fluid inclusions in the sphalerite and quartz related to these samples.

At the Peñasquito ore deposit, the presence of sulfides, sulfosalts, orthoclase, fluorite, epithermal quartz, garnets, and other minerals suggest that hydrothermal fluids were enriched by chemical components derived from magmatic volatiles and liquids, whereas the presence of some carbonates and secondary oxides suggest an interaction with limestone and meteoric fluids. The δ^{34}S (VCDT) values of sulfides from Peñasquito are relatively uniform with an arithmetic mean of 0.8 ‰. Specifically, the range of δ^{34}S values is 3.2 to -2.1 per mil (‰) VCDT. These isotopic ranges suggest that the sulfur source was from magmas, and these results are in a good agreement with compiled δ^{34}S values for porphyry-copper sulfides. The background δ^{18}O levels of carbonates from Peñasquito appear to be around -17 to -11 per mil (‰) VPDB, and carbon isotope ratios averaged around 4.8 per mil (‰) VPDB. Specifically, the calcite δ^{13}C values ranged from -6.9 to -1.6‰, whereas the values for rhodochrosite were from -6.1 to -5.6‰. These isotopic patterns suggest that the bulk of the carbonate source may have been influenced by meteoric interaction with limestone but the interaction of the meteoric and magmatic waters played an important role during the isotopic exchange process.

In the Peñasquito ore deposit, the mineralization was produced by hydrothermal fluids and influenced by late meteoric fluids that deposited metallic ions in several stages through the porphyry gold-copper-molybdenum system, skarn system, stockwork and veins, and diatreme breccia system. Specifically, the early mineralization, related to the potassic and calc-silicate shells, was largely produced by magmatic fluids and deposited in zones of the plutonic complex (i.e. quartz-monzonite and local quartz-monzodiorite porphyries) and the skarn system (i.e. as disseminated mineralization and massive mantos). However, the bulk of shallow mineralization tended to be a late stage event, produced largely by the fluid mixing (i.e. hydrothermal-magmatic and meteoric fluids) through open spaces (e.g. porosity, fractures, faults, and vents), which deposited metallic ions in stockwork zones, veins, local brecciated zones, and in the diatreme breccia system. The deposition of epithermal mineralization was well controlled by permeability, such as faults, fractures, and open spaces. This mineralization was developed in the vicinity of the diatreme breccia system (i.e. stockwork zones and veins), in local brecciated zones developed in the vicinity and at the base of the diatreme system (i.e. hydrothermal breccias in the Caracol Formation and collapse breccias in the exoskarn shell) and especially in a variety of poorly lithified breccias (i.e. internal structure of the diatreme system) and/or accompanied in the generation of permeability caused by phreatic brecciation. Finally, it is believed that the erosion surface of the diatreme system was partially coincident in time with the oxidation of hypogene minerals (i.e. primary sulfides and sulfosalts throughout the shallow levels and local deep levels). Finally, oxidation of hypogene minerals by a supergene cycle related to meteoric water took place, which consisted of oxidation,

leaching, and possible enrichment up to 90 meter downward from the current surface, developed in the Caracol Formation and the diatreme system, as well as local oxidation at deeper levels related to some open fractures where meteoric water infiltrated and locally affected the mantos and collapse breccias in the exoskarn system. In general, the mineral processes began anew and produced another cycle of mineral enrichment in which a young supergene ore body is superimposed on the first. Hence, an important effect of the leaching process is the release of gold and silver from primary sulfides and sulfosalts.

Based on the chemical data and mineralogical distribution of the whole Peñasquito ore system, it is concluded that the magmatic fluids were responsible for the hydrothermal activity at deeper levels (i.e. the system of gold-copper-molybdenum porphyry and skarn), which developed concentric and cylindrical shells in the porphyry complex and the Late Jurassic and Early Cretaceous marine sedimentary sequence. These hydrothermal aureoles include mineralogical assemblages, suggesting different hydrothermal alterations, such as, potassic, calc-silicates, phyllic, and local propylitic alterations as well as deposition of mineralization. Subsequently, collapse of the system took place, composed mainly of meteoric external fluids that had access to magmatic-hydrothermal residual ore emplaced through the vents and/or fractures along dikes. This stage could have instigated a retrograde hydrothermal effect on the calc-silicates shell, phreatomagmatic activity in the diatreme breccia system, and possible remobilization of mineralization from deeper levels, as well as the development of a large halo of phyllic alteration in the Caracol Formation, especially in the vicinity of diatreme system. The later

hydrothermal fluids deposited carbonates through the whole hydrothermal system, which overprinted all the above hydrothermal alterations as well as the mineralization.

In the Peñasquito ore deposit, the bulk of economic gold and silver mineralization occurred as electrum, native minerals and in sulfosalts (the most common of which are tetrahedrite, tennantite, and acanthite). Sulfosalts are present as intergrowths up to a centimeter across, replacing stage 1 pyrite, galena, and sphalerite, and locally replaced by chalcopyrite, native gold and silver, electrum, bismuth, and secondary oxides. These mineralogical assemblages indicate a depressurization of the hydrothermal system and a relative decrease of temperature and pressure (Pough, 1988) during the metallic deposition time. It is believed that at depth, the physical and thermodynamic conditions could have changed during the diatreme breccia formation (i.e. from a closed hydrothermal system), causing a release of fluids and a subsequent formation of large amounts of sulfosalts deposited at shallow levels.

In the Peñasquito ore deposit, the shallow polymetallic mineralization (i.e. between 1,970 and 1,300 m.a.s.l.) principally occurred as primary sulfides, sulfosalts, free gold and silver, and secondary oxides, which are hosted in the diatreme breccia system, stockwork zones, and lesser amount of high-grade veins (i.e. through the Late Cretaceous sedimentary marine sequence). This polymetallic mineralization occurs in fracture fillings, swarms of narrow veins and lesser amounts of disseminations. Polymetallic mineralization (i.e. between 1,300 and 100 m.a.s.l.) predominantly occurs as primary sulfides, sulfosalts, free gold, and secondary and primary oxides, which are hosted in the skarn and porphyry systems as well as the base of the diatreme breccia system and local veins. This mineraliza-

tion occurred in mantos (i.e. massive mineralization), open spaces in the breccias, narrow veins and, in lesser amounts, disseminations. The spatial distribution of chemical elements through the bedrock is obvious, revealing spatial concentrations and chemical associations. Specifically, there is a chemical distribution in the horizontal and vertical zonation of economic elements; for instance, gold and silver are usually concentrated between 1,300 and 1,970 (m.a.s.l.), whereas zinc and lead exhibit a greater concentration between 1,800 and 700 (m.a.s.l.), and copper and molybdenum are concentrated at deep levels (1,300 to 100 m.a.s.l.).

According to Valencia (2010), the magmatic crystallization of the bulk of the plutonic complex could have lasted about 1 Ma (from ~33.4 to ~34.4 Ma). However, the radiometric older ages (46±0.02 and 41.9 ±0.6 Ma) on zircons confirm heterogeneity of magmatic products in the tuffisite dikes and/or heterolithic breccia, indicating the first magmatic pulses in the Mazapil syncline. Re-Os ages from two molybdenite samples are about 35 Ma, however these ages are little bit older than U-Pb zircon ages reported by Valencia (2010) from samples of these porphyries (i.e. ~34 Ma), and the ^{40}Ar/^{39}Ar dating for biotite and K- feldspar (~33 Ma). Therefore, it is concluded that mineralization in the Mazapil syncline was the result of a continuous magmatic activity during ~2 Ma that ranged from ~35 to ~33 Ma, but the best productive magmatic activity was during Priabonian and Rupelian epochs, which developed the potassic and phyllic alteration halos and deposition of polymetallic mineralization, and the age differences may be interpreted as the result of different temperatures of closure for each mineral.

BIBLIOGRAPHY

Aguilar-Casillas D, E., 2013, Porphyry Cu-Au Review, Geocronologia U-Pb En Zircon De Intrusivos Del Distrito Concepcion Del Oro-Penasquito, and Noche Buena. Mazapil, Zacatecas: Peñasquito Goldcorp. 09 Jan. 2013. Speech

Anderson, E.D., Hitzman, M.W., Monecke, T., Bedrosian,P.A., Shah, A. K., and Kelley, K. D., 2013, Geological Analysis of Aeromagnetic Data from Southwestern Alaska: Implications for Exploration in the Area of the Pebble Porphyry Cu-Au-Mo Deposit. Economic Geology, p. 421-436.

Anderson, H. T., and Schmidt, A. V., 1983, The evolution of Middle America and the Gulf of Mexico-Caribbean sea region during Mesozoic time: Geological Society American Bulletin, v. 94, p. 941-966.

Aranda-Gómez, J.J., Luhr J.F., Housh,T. B., Valdez-Moreno, G., and Chávez-Cabello, G., 2005, El volcanismo tipo intraplaca del Cenozoico tardío en el centro y norte de México: Sociedad Geológica Mexicana, Tomo LVII, 3, p. 187-225.

Bakewell, P.J., 1971, Silver Mining and Society in Colonial Mexico 1545-1700: Cambridge University Press, p. 4-221

Barboza-Gudiño, J. R., Orozco-Esquivel, M. T., Gomez-Anguiano M., and Zavala-Monsiváis A., 2008, The Early Mesozoic volcanic arc of western North America in northeastern Mexico: Journal of South American Earth Sciences v. 25, p. 49-63.

Barboza-Gudiño, J. R., Zavala-Monsiváis, A., Venegas-Rodríguez, G., and Barajas-Nigoche, L. D., 2010, Late Triassic stratigraphy and facies from northeastern Mexico: Tectonic setting and provenance: Geosphere, v. 6 (5), p. 621-640.

Barboza-Gudiño, J.R., Hoppe, M., Gómez-Anguiano, M., and Martínez-Macías, P.R., 2004, Aportaciones para la interpretación estratigráfica y estructural de la porción noroccidental de la Sierra de Catorce, San Luis Potosí, México: Revista Mexicana de Ciencias Geológicas, v. 21(3), p. 299-319.

Barboza-Gudiño, J.R., Ramírez-Fernández, J.A., Torres-Sánchez, S.A., and Valencia, V.A., 2011, Geocronología de circones detríticos de diferentes localidades del Esquisto Granjeno en el noreste de México: Sociedad Geológica Mexicana, 63 (2), p. 201-216.

Barboza-Gudiño, J.R., Tristán-González, M., and Torres-Hemández, J.R., 1999, Tectonic setting of pre-Oxfordian units from central and northeastern Mexico: A review, in Bartollini, C., Wilson, J.L., and Lawton, T.F., (eds.) Mesozoic Sedimentary and Tectonic History of North-Central Mexico: Boulder, Colorado, Geological Society of America Special Paper 340, p. 197-210.

Bartolini, C., Lang, H., and Spell, T., 2003, Geochronology, Geochemistry, and Tectonic setting of the Mesozoic Nazas Arc in North-Central Mexico, and its Continuation to Northern South America: American Association of Petroleum Geologists, v.79, p. 427-461.

Bassett, K.N., and Busby, C.J., 2005, Tectonic setting of the Glance Conglomerate along the Sawmill Canyon fault zone, southern Arizona: A sequence analysis of an intra-arc strike-slip basin: Geological Society of America, Special Paper 393, p. 377-400.

Belanger, M., and Pareja, G. 2014, Peñasquito Polymetallic Operation Zacatecas State Mexico, NI 43-101, Technical Report: Goldcorp Inc. Vancouver, Canada.

Belanger, M., Pareja, G., and Nahan, P., 2010, Peñasquito Polymetallic Operation Zacate-cas State Mexico NI 43-101 Technical Report: Goldcorp Inc. Vancouver, Canada.

Bodnar, R.J., 1993, Revised equation and table for determining the freezing point depres-sion of H_2O-NaCl solutions: Geochimica et Cosmochimica Acta, 57, p. 683-684.

Burckhardt, C., 1906a, La Faune jurassiquc de Mazapil avec un appendice sur les fossiles du Cretacique inferieur: Inst. geol. Mexico, Bol. 23, 2v.

Burckhardt, C., 1930, Etude synthétique sur le Mesozoïque Mexicain: Soc. Paléont. Suisse Mém., 49-50, p. 280.

Buseck P.R., 1962, Contact metasomatism and ore deposition: Concepcion del Oro, Mé-xico: Economic Geology, v. 6, p. 97-136

Campa M.F., and Coney P.J.1983, Tectonostratigraphic terranes and mineral resource dis-tributions in Mexico: Canadian Journal of Earth Sciences, v. 20, p. 1040–1051.

Camprubí, A., 2010, Criterios para la exploración minera mediante microtermometría de inclusiones fluidas: Boletín de la Sociedad Geológica Mexicana, 62, p. 25-42.

Carrillo-Bravo, J., 1961, Geología del Anticlinorio Huizachal-Peregrina al noroeste de Ciu-dad Victoria, Tamaulipas: Boletín de la Asociación Mexicana de Geólogos Petrole-ros, 13(1-2), p. 1-98.

Centeno-García, E., 2005, Review of Upper Paleozoic and Lower Mesozoic stratigraphy and depositional environments of central and west Mexico: Geological Society of America, Special Paper 393, p. 377-358.

Chiaradia, M., Schaltegger, U., Spikings R, Wotzlaw, J. F., and Ovtcharova, M., 2013, How Accurately Can We Date the Duration of Magmatic-Hydrothermal Events in

Porphyry Systems-An Invited Paper: Society of Economic Geologists, v.108, p. 255-583.

Cohen, A. S., and Waters, F. G., 1996, Separation of osmium from geological materials by solvent extraction for analysis by thermal ionisation mass spectrometry. Anal. Chim. Acta 332, p. 269-275.

Cordoba, D., 1964. Resumen de la Geología de la Hoja Apizolaya, Estados de Zacatecas y Durango, Hoja Apizolaya 13R-I (9). Carta Geológica de México, Serie 1:100,000, Instituto Geología, Universidad Nacional Autónoma de México.

Cox, K. G., Bell, J. D., and Pankhurst, R. J., 1979, The Interpretation of Igneous Rocks: Springer-Science Business Media, B.V, p. 1-418

Damon, P. E., Shafiqullah, M., and Clark, K. F., 1981, Evolución de los arcos magmáticos en México y su relación con la metalogénesis: Universidad Nacional Autónoma de México, Journal v. 5 - 2, p. 223-238.

Damon, P.E., Shafiqullah, M., and Clark, K.F., 1981, Age trends of igneous activity in relation to metallogenesis in the southern Cordillera: in Relations of tectonics to ore deposits in the southern Cordillera: Arizona Geol. Soc. Digest, v. 14, p. 137-153.

De Cserna, Z., 1956, Tectónica de la Sierra Madre Oriental de México, entre Torreón y Monterrey: XX Congreso Geológico Internacional: Contribución del Instituto Nacional para la Investigación de Recursos Minerales de México.

Dickinson, W.R., and Coney, P.J., 1980, Plate tectonic constraints on the origin of the Gulf of México and the early opening of the central north Atlantic: Baton Rouge, Louisiana State University, p. 27-36.

Dickinson, W.R., and Lawton, T.F., 2001, Carboniferous to Cretaceous assembly and fragmentation of Mexico: Geological Society of America Bulletin 113, p.1142–1160.

Goldcorp 2011, Technical Presentation: Regional localization stratigraphic, and Peñasquito exploration history: Peñasquito Goldcorp records 2013, unpublished document.

Goldcorp Inc., 2012, Annual Information Form for The Financial Year Ended December 31, 2011. Peñasquito Mine, Mexico (2012): 46-57. Web. 10 Jan. 2013. <http://www.goldcorp.com/files/FINAL%20_%20Goldcorp%20AIF%20SEDAR_v001_m4a6xy.PDF>.

Goldcorp Inc., 2013, Fact Sheet. Http://www.goldcorp.com. Web. 10 Jan. 2013. <http://www.goldcorp.com/files/Corporate%20Fact%20Sheet%20-%20Jan%202013.pdf>.

Goldcorp, 2014, Annual information form for the financial year ended December 31, 2013, Vancouver, Canada.

Goldcorp, 2015, Annual information form for the financial year ended December 31, 2014. Vancouver, Canada.

Goldcorp, 2016, Annual information form for the financial year ended December 31, 2015. Vancouver, Canada.

Goldhammer, R.K., 1999, Mesozoic sequence stratigraphy and paleogeographic evolution of northeast Mexico: Geological Society of America, Special Paper 340, p. 1-58.

Goldstein, R.H. 2003, Petrographic analysis of fluid inclusions. In Samson, I., Anderson, A., Marshall, D. eds. Fluid Inclusions: Analysis and Interpretation, Mineralogical Association of Canada, Short Course Ser. 32, p. 9-53.

Goldstein, R.H., and Reynolds T.J. 1994, Systematics of fluid inclusions in diagenetic minerals: Society for Sedimentary Geology Short Course 31, p. 199

González-Partida, E., Camprubí, A., Canet, C., and González-Sánchez, F., 2008, Termodinámica e inmiscibilidad de fluidos aplicada en las inclusiones fluidas para entender las condiciones PVTX en la evolución de salmueras e hidrocarburos en cuencas petroleras y en yacimientos estratoligados. Parte I: temperatura, presión y composición de inclusiones fluidas: Boletín de la Sociedad Geológica Mexicana, 60, p. 11-22.

González-Sánchez, F., Puente-Solís, R., González-Partida, E., and Camprubi, A., 2007, Estratigrafía del noreste de México y su relación con los yacimientos estratoligados de fluorita, barita, celestina y Zn-Pb: Boletín de la Sociedad Geológica Mexicana, v. 59, p. 43-62.

Grajales-Nishimura, J.M., Terrell, D., and Damon, P., 1992, Evidencias de la prolongación del arco volcánico cordillerano del Triásico tardío-Jurásico en Chihuahua, Durango y Coahuila: Asociación Mexicana de Geólogos Petroleros 42, p. 1–18.

Gursky, H.J., and Michalzik, D., 1989, Lower Permian turbidites in the northern Sierra Madre Oriental, Mexico: Zentralblatt für Geologie und Paläontologie, TeilI (5-6) p. 821-838.

Harker, A., 1909, The natural history of igneous rocks. Methuen, London.

Hernández-Pérez, I., 2008, Pruebas con métodos geofísicos sobre las estructuras mineralizadas, Brecha Peñasco y Brecha Azul, en la mina el Peñasquito municipio de Mazapil, Zac., Servicio Geológico Mexicano.

Hernández-Pérez, I., Vélez-López, J., and Pascacio-Toledo, R., 1997, Texto guía Carta Magnética "Concepción del Oro" G14-10 escala 1:250,000: Consejo de Recursos Minerales, Secretaría de Economía, Coordinación General de Minería.

Hezarkhani, A., and Williams-Jones, A.E., 1998, Controls of Alteration and Mineralization in the Sungun Porphyry Copper Deposit, Iran: Evidence from Fluid Inclusions and Stable Isotopes: Economic Geology, v.93, p. 651-670

http://www.alsglobal.com/Our-Services/Minerals/Geochemistry/Service-Schedule, Nov. 2014.

Imlay, R. W., 1936, Geology of the western part of the Sierra de Parras: Geol. Soc. America Bull., v. 47, p. 1091-1152.

Imlay, R. W., 1937, Geology of the middle part of the Sierra de Parras, Coahuila, Mexico: Geological Society of America Bulletin, v. 48, p. 567-630.

Imlay, R. W., 1938, Studies of the Mexican Geosyncline: Geological Society of America Bulletin, 49, p. 1651-1694.

Imlay, R.W., 1953, Las formaciones Jurásicas de México: Boletín de la Sociedad Geológica Mexicana, v. 16, p. 1-64.

Instituto Nacional de Estadística, Geografía e Informática (INEGI), 2012, Mapa Digital De México. inegi.org.mx. Web. 27 Jan. 2013. <http://www.infomex.inegi.org.mx/>.

Irvine, T.N., and Baragar, W.R.A., 1971, A guide to the chemical classification of the common volcanic rocks: Canadian Journal of Earth Sciences, v. 8, p. 523-548.

Jones, N.W., McKee, J.W., Anderson, T.H., and Silver, L. T., 1995, Jurassic volcanic rocks in northeastern Mexico: A possible remnant of a Cordilleran magmatic arc: Geological Society of America Special Paper, v. 301, p. 179-190.

Kelly W. A., 1936, Geology of the Mountains bordering the valleys of Acatita and Las Delicias: Geol. Soc. of America, Bull. v. 47, p. 1039-1063.

Keppie, J., D. and Ortega-Gutiérrez, F, 2010, 1.3–0.9 Ga Oaxaquia (Mexico): Remnant of an arc/back arc on the northern margin of Amazonia: Journal of South American Earth Sciences, v.29 p. 21–27.

Le Bas, M.J., 1989. Nephelinitic and basanitic rocks: Journal of Petrology 30 (5), p.1299-1312.

Le Bas, M.J., 2000, IUGS reclassification of the high-Mg and picritic volcanic rocks: Journal of Petrology 41 (10), p.1467-1470.

Le Bass, M.J., Le Maitre, R.W., Streckeisen, A., and Zanettin, B., 1986, A chemical classification of volcanic rocks based on the total alkali-silica diagram: Journal of Petrology, 27, p. 745-750.

Le Maitre, R. W., 1989, A Classification of Igneous Rocks and Glossary of Terms. Recommendations of the IUGS Commission on the Systematics of Igneous Rocks. Oxford: Blackwell.

Le Maitre, R. W., Bateman, P., Dudek, A., Keller, J., Lameyre, J., Le Bas, M. J., Sabine, P. A., Schmid, R., Sorensen, H., Streckeisen, A., Woolley, A. R., and Zanettin, B., 1989, A Classification of Igneous Rocks and Glossary of Terms: Recommendations of the In-

ternational Union of Geological Sciences Subcommission on the Systematics of Igneous Rocks. Oxford: Blackwell Scientific.

López-Doncel, R., and Navarro-Moctezuma, A., 2007, Estudio estratigráfico-microfacial de los depósitos del Aptiano-Albiano inferior en la porción occidental de San Luis Potosí, centro-oriente de México y su relación con la incipiente plataforma Valles - San Luis Potosí: GEOS, v. 27, p. 108.

Ludwig, K.R., 2003, User's manual for Isoplot, v. 3.0, a geochronological toolkit for Microsoft Excel: Berkeley Geochronological Center, Special Publication no. 4.

M3 Engineering & Technology, 2006, Peñasquito Feasibility Study. Goldcorp.com. GLAMIS GOLD LTD., 31 July 2006. Web. 22 Jan. 2013. <http://www.goldcorp.com/files/Doc_news/jul31-06_3.pdf>.

Malishev, V.A., 1984, Explosion Pipes, Springer Verlag.

Maniar, P. D. and Piccoli, P. M., 1989, Tectonic discrimination of granitoids: Geological Society of America Bulletin 101, 635–643.

Mapes- Vázquez, E., Zamora-Montero, S., and Gerónimo-Godoy, J., 1964, Geología y Yacimientos minerales del distrito de Concepción del Oro y Avalos, Zacatecas. Consejo de Recursos No Renovables.

Martínez-Esparza., G, 2008, Geoquímica del Volcanismo Básico-Intermedio desde El Eoceno al Reciente: Su Importancia en la Evolución del Campo Volcánico de San Luis Potosí: Unpublished Universidad Autónoma de San Luis Potosí (Master's Thesis).

MC Mexico, 2001, Proyecto peñasquito exploraciones 2000, Zac. Mexico, unpublished technical inform, collection in Goldcorp Mexico.

Meschede, M., 1986, A method of discriminating between different types of mid-ocean ridge basalts and continental tholeiites with the Nb-Zr-Y diagram: Chemical Geology, v. 56, p. 207-218.

Middlemost E.A.K., 1989, Iron oxidation ratios, norms and the classification of volcanic rocks: Chem. Geol., 77, 19-26.

Mitre-Salazar L., M., 1989, La Megafalla Laramídica de San Tiburcio, Estado De Zacatecas: Universidad Nacional Autónoma de México, Inst. Geología, v. 8, p. 47-51.

Mixon, R. B., Murray, G. E., and Díaz, T., 1959, Age and correlation of Huizachal Group (Mesozoic), state of Tamaulipas, Mexico: American Association of Petroleum Geologists Bulletin, v. 43, p. 757-771.

Miyashiro, A., 1974, Volcanic rock series in island arcs and active continental margins: American Journal of Science 274, p. 321-355.

Montañés-Castro, A., and Torres-Duran, 2003, Informe de la Carta Geológico-Minera-Concepción del Oro, G14-C62, escala 1:50,000: Consejo de Recursos Minerales.

Montañés-Castro, A., Ramírez-Gutiérrez, G., Luevano-Pineda, A., and Escalante-Martínez, J. C., 2000, Informe Geológico-Minero y Geoquímico de la Carta Concepción del Oro, G14-10, escala 1:250,000 Estado de Zacatecas: Consejo de Recursos Minerales.

Morgan J.W., and Walker, R.J., 1989, Isotopic determinations of rhenium and osmium in meteorites by using fusion, distillation and ion-exchange separations. Anal. Chim. Acta 222: p. 291-300

Mújica-Mondragón, R., and Jacobo-Albarrán, J., 1983, Estudio petrogenético de las rocas ígneas y metamórficas del Altiplano Mexicano: Instituto Mexicano del Petróleo, Subdirección Técnica deExploración, Proyecto C-1156, technical report.

Mullen, E. D., 1983, MnO/TiO$_2$/P$_2$O$_5$: a minor element discriminant for basaltic rocks of oceanic environments and its implications for petrogenesis: Earth and Planetary Science Letters 62, p. 53-62.

Ocampo-Díaz, Y.Z.E., 2011, Implicaciones tectonosedimentarias de las intercalaciones clásticas en el límite Jurásico-Cretácico del Noreste de México (Fosa de Monterrey y Cuenca de Sabinas): Linares, N. L., Facultad de Ciencias de la Tierra, Universidad Autónoma de Nuevo León, disertación, p. 275

Ocejo-Paredes, T., and Bustos-Gutiérrez, L. A., 2003, Informe de la Carta Geológica-Minera Cedros G14-C61, escala 1:50,000 estado de zacatecas: Consejo de Recursos Minerales.

Ohmoto H., 1986, Stables isotope geochemistry of ore deposit: Reviews in Mineralogy and Geochemistry, v. 16, p. 491-559, in Rollinson, H. R. ed., 1993, Using geochemical data: Evaluation, Presentation, Interpretation. Book, p. 229-315.

Ohmoto, H. and Rye, R.O., 1979, Isotopes of sulfur and carbon, in Rollinson, H. R., 1993, Using geochemical data: Evaluation, Presentation, Interpretation. Book, p. 229-315.

Ohmoto, H., Hart, S. R. and Holland, H. D., 1966, Studies in the Providencia area, Mexico: Part 2, K-Ar and Rb-Sr ages of intrusive rocks and hydrothermal minerals.

Ortega-Gutiérrez, F., Mitre-Salazar, L. M., Roldán-Quintana J., Aranda-Gómez, J. J., Morán-Zenteno, D., Alaniz-Álvarez, S. A, and Nieto-Samaniego, Á. F., 1992, Texto explicativo de la quinta edición de la carta geológica de la República Mexicana escala 1:2'000,000: Universidad Nacional Autónoma de México, Instituto de Geología y SEMIP Consejo de Recursos Minerales.

Ortega-Gutiérrez, F., Ruiz, J., and Centeno-García, E., 1995, Oaxaquia, a Proterozoic microcontinent accreted to North America during the Paleozoic: Geology, 23, p. 1127-1130.

Padilla y Sánchez, R.J., 1982, Geologic evolution of the Sierra Madre Oriental between Linares, Concepción del Oro, Saltillo and Monterrey, Mexico: Texas, U.S.A., University of Texas at Austin, Doctoral dissertation, p. 217

Pantoja-Alor, J., 1972, Datos Geológicos-Estratigráficos de la Formación Nazas (abs.). Memoria, II Convención Nacional, Sociedad Geológica Mexicana, p. 25-31 and 194-196.

Peacock, M. A., 1931, Classification of igneous rock series: Journal of geology, v.39, p. 54-67.

Pearce, J. A., 1996, A User's Guide to Basalt Discrimination Diagrams, in Wyman, D. A., ed., Trace Element Geochemistry of Volcanic Rocks: Applications for Massive Sulfide Exploration, Geological Association of Canada, Short Course Notes, v. 12, p. 79-113.

Pearce, J.A. and Cann, J.R., 1973, Tectonic setting of basic volcanic rocks determined using trace element analysis: Earth and Planetary Science Letters, v. 19, p. 290-300.

Pearce, J.A., 1983, The role of sub-continental Lithosphere in magma genesis at destructional plate boundaries, in Hawkesworth, C.J., and Norry, M. J. (eds.), Continental Basalts and Mantle Xenoliths, Shiva, Nantwich, p. 230-249.

Pearce, J.A., Harris, N.B.W., and Tindle, A.G., 1984, Trace element discrimination diagrams for the tectonic interpretation of granitic rocks: Journal of Petrology v.25, p. 956-983.

Pearce, T.H., Gorman, B.E., and Birkett, T.C., 1977, The relationship between major element chemistry and tectonic environment of basic and intermediate volcanic rocks: Earth and Planetary Science Letters, v. 36, p. 121-132.

Pindell, J.L., and Dewey, J.F., 1982, Permo-Triassic reconstruction of western Pangea and the evolution of the Gulf of Mexico/Caribbean region: Tectonics, v. 1, p. 179-212.

Pindell, J.L., Barrett, S.F., 1990, Geological evolution of the Caribbean region, in Dengo, G., Case, J.E. (Eds.), The Caribbean Region: Boulder, Colorado, Geological Society of America, Geology of North America H, p. 405-432.

Pinzón-Sotelo, M., 2012, Análisis Sedimentológico y Petrográfico de la Formación Caracol (Cretácico Tardío), Sierra Madre Oriental, NE, Zacatecas. Master Thesis: Universidad Autónoma de Nuevo León, Facultad De Ciencias De La Tierra.

Potter R. W. 11, Clynne M. A., and Brown D. L., 1978, Freezing point depression of aqueous sodium chloride solutions.Econ. Geol. 73, p. 284-285.

Potter. R.W., 1977, Pressure correction for fluid inclusions homogenization temperatures based on the volumetric properties of the system $NaCl-H_2O$. U.S. Geological Survey Journ. Res. 5, p. 603-607.

Pough, F. H., 1988, A Field Guide to Rocks and Minerals. Boston: Houghton Mifflin, Fifth Edition, p. 108, 132.

Rivera-Zamora, H, R., 2014, Presentation and Tour through the heap leaching procedure.

Roedder, E., 1984, Fluid inclusions: Reviews in Mineralogy, 12, 644 pp.

Roedder, E., and Bodnar, R.J., 1997, Fluid inclusion studies of hydrothermal ore deposits, in Samson, I., Anderson, A., and Marshall, D. (eds.) Fluid Inclusions: Analysis and Interpretation. Mineralogical Association of Canada, Short Course Ser. 32, p.81-100.

Rogers, C. L., De Cserna, Z., Talaver, E., and Ulloa, S., 1956, Geology and Phosphate Deposits of Concepcion del Oro District, Zacatecas, Mexico: Geological survey Bulletin 1037-A.

Rogers, C. L., De Cserna, Z., Vloten, R., Tavera-Amezcua, E., and Ojeda-Rivera, J., 1961, Reconocimiento geológico y depósitos de fosfatos del norte de Zacatecas y áreas adyacentes en Coahuila, Nuevo León y San Luis Potosí: Cons. Recursos Nat. No Renovables (México), Boletin 56, p. 322

Rogers, C.L., De Cserna, Z., Tavera-Amezcua, E., and Ulloa, S., 1957, Geología general y depósitos de fosfatos del Distrito de Concepción del Oro, Estado de Zacatecas: Instituto Nacional para la Investigación de Recursos Minerales, Boletín 38, 129 p.

Rollinson, H. R., 1993, Using geochemical data: Evaluation, Presentation, Interpretation. Book, p. 229-315.

Rubio-Cisneros, I. l., and Lawton, T. F., 2011, Detrital zircon U-Pb ages of sandstones in Continental red beds at Valle de Huizachal, Tamaulipas, NE Mexico: Record of

Early-Middle Jurassic arc volcanism and transition to crustal extension: Geosphere, v. 7, p. 112

Ruiz, J., Patchett, P.J., and Ortega-Gutierrez, F., 1988, Proterozoic and Phanerozoic basement terranes of Mexico from Nd isotopic studies: Geological Society of America Bulletin, v. 100, p. 274-281.

Salvador, A., 1987, Late Triassic-Jurassic paleogeography and origin of Gulf of Mexico Basin: American Association of Petroleum Geologists Bulletin, 71, p. 419-451.

Servicio Geológico Mexicano (SGM) (Mexican Geological Survey –MGS-), 2013, Interactive database of Carta Geológico-Minera Concepción del Oro, G14-C62, scale 1:50,000; Carta Geológica-Minera Cedros, G14-C61, scale 1:50,000; aeromagnetic data of Concepción del Oro region, scala 1:250,000; and mines.

Servicio Geológico Mexicano (SGM), 2000, Carta Geológico-Minera Concepción Del Oro, Escala 1:250,000 G14-10, Zac, N.L. Coah, S.L.P. Http://www.sgm.gob.mx. Web. 15 Jan. 2013.

http://mapserver.sgm.gob.mx/cartas_impresas/productos/cartas/cartas250/geologia/pdf/73_G14-10_GM.pdf>.

Servicio Geológico Mexicano (SGM), 2004, Carta Geológico-Minera Concepción del Oro, Escala 1:50,000 G14-C62, Zac.-Coah. Http://www.sgm.gob.mx. Web. 15 Jan. 2013. <http://mapserver.sgm.gob.mx/cartas_impresas/productos/cartas/cartas50/geologia50/pdf/1352_G14-C62_GM.pdf>.

Shirey, S.B., and Walker, R. J., 1998, The Re-Os Isotope system in cosmochemistry and high-temperature geochemistry: Annu. Rev. Earth Planet. Sci. v. 26, p .423-500.

Silva-Romo, G., Arellano-Gil, J., Mendoza-Rosales, C., and Nieto-Obregon, J., 2000, A submarine fan in the Mesa Central, Mexico: Journal of South American Earth Sciences. p. 429-442.

Smoliar M.I., Walker R.J., Morgan, J.W., 1996. Re-Os ages of Group IIA, IIIA, IVA, and IVB iron meteorites: Science 271, p. 1099-102.

Soto-Araiza, R, G., and García-Ortiz, M., 2012, Texto explicativo, Carta Geológico-Minera y Geoquímica San Tiburcio G14-C82, escala 1:50,000, Estado de Zacatecas: Servicio Geológico Mexicano.

Sourirajan, S., and Kennedy, G.C., 1962, The system H_2O-NaCl at elevated temperatures and pressures: American Journal of Science, v. 260, p. 115-141.

Stewart, J.H., Blodgett, R.B., Boucot, A.J., Carter, J.L., and López, R., 1999, Exotic Paleozoic strata of Gondwanan provenance near Ciudad Victoria, Tamaulipas, México. Geological Society of America Special Paper, v. 336, p. 227-252.

Streckeisen, A. L., 1974. Classification and Nomenclature of Plutonic Rocks. Recommendations of the IUGS Subcommission on the Systematics of Igneous Rocks: Geologische Rundschau. Internationale Zeitschrift für Geologie. Stuttgart. v.63, p. 773-785.

Streckeisen, A. L., 1978. IUGS Subcommission on the Systematics of Igneous Rocks. Classification and Nomenclature of Volcanic Rocks, Lamprophyres, Carbonatites and Melilite Rocks. Recommendations and Suggestions: Neues Jahrbuch für Mineralogie, Abhandlungen, v. 141, p. 1-14.

Tardy, M., Blanchet, R., and Zimmermann, M., 1989, Les linéaments du Texas et Caltam entre Cordilléres Américanes et Sierras Madre Mexicanes: Nature, Origine et Évo-

lution structurale: Bulletin des Centre de Recherches Exploration-Production Elf-Aquitaine, 13 (2), p. 219-227.

Valencia, V. A., 2010; Reporte de los resultados analíticos del estudio realizado en el Distrito Peñasquito: private report for Goldcorp.

Verma, S.P., Sotelo-Rodríguez Z.T., and Torres-Alvarado I.S., 2002, SINCLAS: Standard Igneous Norm and Volcanic Rock Classification System: Computers and Geosciences, v. 28, p. 711-715.

Wilds, S, R., and MacIness, S., 19901, High Resolution CSAMT Aplication in Gold Exploration- A case History: Geological Society of Nevada, v.II, p. 1231-1251

Wilkinson, J. J., 2001, Fluid inclusions in hydrothermal ore deposits: Lithos 55, p. 229-272.

Winchester, J.A. and Floyd, P.A. 1977, Geochemical discrimination of different magma series and their differentiation products using immobile elements: Chemical Geology, v.20, issue 4, p. 325-343.

Wood, D.A., 1980. The application of a Th-Hf-Ta diagram to problems of tectonomagmatic classification and to establishing the nature of crustal contamination of basaltic lavas of the British Tertiary volcanic province: Earth and Planetary Science Letters v. 50, p. 11-30.

Wood, D.A., Joron, J.L., and Treuil, M., 1979b, A re-appraisal of the use trace elements to classify and discriminate between magma series erupted in different tectonic setting: Earth Planet Science Letters 45: p. 326-336.

Wood, D.A., Joron, J.L., Treuil, M., Norry, M., and Tarney, J., 1979a, Elemental and Sr iso-

tope variations in basic lavas from the Iceland and the surronding ocean floor: Con-

trib Mineral Petrol 70: p. 319-339.

APPENDIX A.

List of Abbreviations and Chemical Formulas

Element or mineral

Al-Aluminum

Ar-Argon

Au-Gold

Ba-Barium

Bi-Bismuth

Ca-Calcium

Cd-Cadmium

Cr-Chromium

Cu-Copper

Fe-Iron

Ga-Gallium

Hf-Hafnium

La-lanthanum

Na-Sodium

Nb- Neodymium

O-Oxygen

Pb-Lead

Sb-Antimony

Sm-Samarium

Th- Thorium

Ti- Titanium

V-Vanadium

Y- Yttrium

Yb-Ytterbium

Zn Zinc

Zrn-Zircon

Mineral

Adr-Andradite ($Ca_3Fe_2(SiO_4)_3$)

Ag-Silver

Altaite (PbTe)

Am-Amphibole

Ap-Apatite ($Ca_5(PO_4)_3(F,Cl,OH)$)

Apy-Arsenopyrite (FeAsS)

Bn-Bornite (Cu_5FeS_4)

Bournonite ($PbCuSbS_3$)

Cal-Calcite ($CaCO_3$)

Cb-Carbonate

Chlorargyrite (AgCl)

Cpy-Chalcopyrite ($CuFeS_2$)

Cv-Covellite (CuS)

Dol-Dolomite ($CaMg(CO_3)_2$)

Ele-Electrum (AuAg)

Enr- Enargite (Cu_3AsS_4)

Fl-Fluorite (CaF_2)

Gn-Galena (PbS)

Goethite ($Fe^{3+}O(OH)$)

Grt-Garnet ($X_3Y_2(SiO_4)_3$)

Jarosite ($KFe^{3+}_3(OH)_6(SO_4)_2$)

K-Fto-K-feldspar

Mo-Molybdenite (MoS_2)

Mrc-Marcasite (FeS_2)

Ox-Oxide

Py-Pyrite (FeS_2)

Qtz-Quartz (SiO_2)

Rdn-Rhodonite (($Mn^{2+},Fe^{2+},Mg,Ca)SiO_3$)

Rds-Rhodochrosite ($MnCO_3$)

Sp- Sphalerite (($Zn,Fe)S$)

Syl-Sylvanite (($Au,Ag)_2Te_4$)

Tellurobismuthite (Bi_2Te_3)

Wo-Wollastonite ($CaSiO_3$)

Ser-Sericite

Si-Siliceous (SiO_2)

Hem-Hematite (Fe_2O_3)

Mag-Magnetite ($Fe^{2+}Fe^{3+}2O_4$)

Dg-Digenite (Cu_9S_5)

Di-Diopside ($MgCaSi_2O_6$)

Px-Pyroxene (XYZ_2O_6,)

Ep-Epidote (${Ca_2}{Al_2Fe^{3+}}(Si_2O_7)(SiO_4)O(OH)$)

Pl-Plagioclase ($NaAlSi_3O_8 - CaAl2Si_2O_8$)

Adl-Adularia ($KAlSi_3O_8$)

Fto-Feldspar (orthoclase) ($KAlSi_3O_8$)

Or-Orthoclase ($KAlSi_3O_8$)

Sa-Sanidine ($KAlSi_3O_8$)

Bi-Biotite ($K (Mg,Fe)_3(AlSi_3O_{10})(F,OH)_2)$)

Mnt-Montmorillonite

$((Na,Ca)0,_3(Al,Mg)_2Si_4O_{10}(OH)^{2*n}(H_2O))$

Freibergite ($(Ag,Cu,Fe)_{12}(Sb,As)_4S_{13}$)

Tenn- Tennantite $(Cu,Fe)12As_4S_{13}$)

Tetra-Tetrahedrite $(Cu,Fe)12Sb_4S_{13}$)

Hessite (Ag_2Te)

Ac-Acanthite (Ag_2S)

Cc-Chalcocite (Cu_2S)

Cpr-Cuprite (Cu_2O)

Po-Pyrrhotite ($Fe_{1-x}S$ (x = 0 to 0.2))

Rock

Br-Breccia

Br-Marble (mineralized breccia of marble)

Br-Sk (mineralized breccia of skarn)

Dr (Diorite)

Hn-Horfels

Ls -limestone

Mz (monzonite)

Ox-manto (Oxides in manto)

QD (Quartz diorite Porphyry)

QMDP (Quartz monzodiorite Porphyry)

QMP (Quartz monzodiorite Porphyry)

Sdt (Sandstone)

Sk (Skarn)

Slts (Siltstone)

S-Skarn (massive sulfide in skarn)

Tuff (tuffisite)

Miscellaneous

μm-Microns

> more than

°C-Centigrade grade

cm- centimeter

dtm- Dry Metric Tonnes

E-East

g/t-Gram per Tonnes

ha- hectares

Klb-Thousand pounds

Km-kilometer

Lb-Pounds

L-Liquid

m.a.s.l.-meter above sea level

Ma-Million years

Mg-Magnesium

Mic-QD (quartz micromonzodiorite)

Mlbs-Million pounds

mm- Millimeter

m-meter

Moz-Million onces

Mtrx-Matrix

N-North

Oz ounces

PDB- Pee Dee Belemnite

ppm- parts per million

QAP-Quartz-Alkaline-feldspar-Plagioclase

RC-Reverse circulation

Re-Os Rhenium-Osmium

S-South

t/d-Tonnes per day

VCDt- Vienna Canyon Diablo Troilite

VCDT-Vienna Canyon Diablo Troilite),

VMOW -Vienna Standard Mean Ocean Water

Vs-Versus

V-Vapor

W -West

APPENDIX B.

Summary of data (chemical, petrography, mineragraphy, and isotopic dates)

Data of trace element for magmatic products from Peñasquito. Note: results are shown in ppb

Sample	Ba	Rb	Sr	Y	Zr	Nb	Th	Pb	Ga	Zn	Cu	Ni	V	Cr	Hf	Cs	Sc	Ta	Co	Li	U	W	Sn	Mo	La	Ce	Pr	Nd	Sm	Eu	Gd	Tb	Dy	Ho	Er	Tm	Yb	Lu
GP622-12-1059	542	115	150	15.6	196	13.2	9.63	3	17.8	48	158	5	68	10	5.6	2.59	4	1	7	50	2.78	36	1	296	30.9	59.7	7.07	27.8	5.11	1.17	4.05	0.56	3.09	0.56	1.6	0.2	1.31	0.19
GP621R-1792-5	291	195	71.5	17.7	162	11.2	8.84	7	8.3	22	17	9	72	10	4.4	1.77	5	0.8	15	10	1.9	38	5	3600	30.9	66.9	8.8	36.1	6.44	1.03	4.55	0.6	3.42	0.67	1.67	0.29	1.6	0.23
GP621R-1794-2	791	309	166	16.1	180	13.3	9.54	48	14.6	102	63	6	66	10	5.1	2.67	5	1	2	10	2.06	57	2	570	18.2	41.7	5.59	24.1	4.86	0.94	3.73	0.54	2.79	0.54	1.48	0.25	1.56	0.2
GP621R-1794-8	222	183	32.5	13.3	142	9.8	5.58	30	6.4	80	36	5	70	10	3.7	1.82	4	0.7	7	10	1.42	76	4	2200	19.9	42.1	5.56	22.2	4.14	0.74	3.41	0.45	2.5	0.46	1.33	0.16	1.22	0.17
GP621R-1798-4	481	238	98	12.3	133	7.8	6.87	19	10.9	40	107	11	62	40	3.6	2.81	5	0.6	3	10	1.6	23	2	3570	22.2	45.2	5.65	23.3	4.06	0.73	3.11	0.42	2.35	0.43	1.13	0.15	1.07	0.14
GP621R-1786-7	68.6	131	59.5	31.2	157	10.3	5.12	4	11.7	23	730	7	59	10	4.3	2.93	5	0.7	5	10	4.29	45	6	5970	36.4	72.6	9.58	40	8.18	1.5	7.3	1.02	6.04	1.15	2.91	0.41	2.63	0.35
GP621R-1800-3	600	255	141	17.9	140	10.1	9.81	19	12.1	66	172	2	44	10	4	2.38	3	0.8	0.9	10	1.6	20	1	852	27.8	56.3	7.34	30.3	5.42	1.07	4.15	0.59	3.06	0.62	1.7	0.22	1.42	0.2
GP622-12-1067	918	283	115	10.1	197	11.1	10.1	71	19.8	168	10	5	39	10	5.6	5.77	3	0.8	4	10	3.63	3	1	2	39.1	72.7	8.31	31.4	4.83	1.17	3.11	0.44	2.05	0.35	0.98	0.14	0.87	0.11
GP557-08-1140	152	86.9	490	19	173	12.9	11.4	15	17.1	77	30	5	51	10	5.2	4.57	3	1	1	20	5.02	2	1	16	20	42.4	5.54	23.5	4.7	0.96	3.83	0.6	3.3	0.64	1.75	0.27	1.84	0.27
WC300-05-511	796	249	188	16.5	166	12.4	9.56	26	18.8	153	6	7	73	10	4.6	3.05	6	0.9	6	10	3.51	2	2	3	34	68.5	8.32	32.7	5.46	1.28	4.05	0.54	3.16	0.58	1.53	0.26	1.46	0.25
MR-12	985	204	364	16.6	177	11.3	8.87	10	18.7	26	2	5	81	20	5	4.87	6	0.8	8	20	3.54	2	1	1	27.8	55.5	6.79	27	4.48	1.12	3.51	0.55	3.02	0.57	1.53	0.21	1.6	0.23
WC218-385	636	168	344	15.4	148	14	8.7	19	18	40	9.9	19.9	70	19.9	4.2	4.6	0	1.01	5	0	10.4	2.1	1	1.9	33.1	63.8	7.43	27.4	4.86	1.25	3.96	0.54	2.82	0.51	1.42	0.21	1.43	0.23
WC335-05-332	1050	432	156	23.6	169	9.2	11.5	41	17	182	26	9	101	20	5.2	3.59	11	0.7	3	40	3.1	8	2	0.9	33	64.6	7.76	28.8	5.73	0.88	4.64	0.71	4.29	0.82	2.51	0.36	2.19	0.31
GP640-13-825	1125	346	99.6	12.8	153	11.6	10.4	32	15.2	222	60	3	49	10	4.5	2.62	4	0.9	5	9	4.92	7	3	11	7.4	22.1	3.47	15.6	3.48	0.45	2.82	0.39	2.34	0.45	1.14	0.2	1.26	0.18
GP652-13-501	1215	465	150	13.8	160	12.3	11.5	165	17.5	124	7	7	51	10	4.5	3.8	4	1	4	10	6.13	22	1	3	32	63	7.29	27.3	4.6	0.89	3.13	0.45	2.59	0.45	1.35	0.21	1.36	0.18
WC36-661	669	568	108	12.7	178	12.6	9.59	466	16	50	9.9	19.9	57	19.9	4.8	4.6	0	0.92	3	0	7.69	22.4	1	4	25.2	57.4	7.18	27.4	5.04	1.15	3.85	0.5	2.41	0.42	1.17	0.17	1.09	0.18
GP640-13-1813	475	126	175	19.5	306	15.6	4.21	13	19.8	95	35	69	193	140	7.9	45.2	19	0.8	27	40	1.26	12	2	1	39.9	84.5	10.4	41.3	6.82	1.5	5.09	0.7	3.97	0.72	2.03	0.29	1.8	0.26
WC334-05-571	749	205	332	18.3	173	12	9.12	26	18.5	175	2	6	84	20	5.1	5.98	8	0.9	7	20	4.03	3	1	2	31.5	59.6	7.12	28.6	5.05	1.23	4.49	0.61	3.15	0.63	1.79	0.27	1.81	0.26
WC296-05-356	709	233	398	18.5	193	12	6.49	100	21.3	71	1	8	123	10	5.4	9.49	8	0.8	14	20	2.52	3	1	2	39.9	76.2	9.19	37.9	7.01	1.81	5.09	0.74	3.84	0.64	1.65	0.27	1.59	0.19
GPI14-13-102	557	150	409	17.7	175	11.7	6.76	11	20	32	1	6	119	10	4.8	3.46	8	0.8	5	0	2.31	1	1	1	34.1	68.2	8.62	34.8	6.61	1.36	4.91	0.7	3.58	0.65	1.69	0.22	1.47	0.18
WC296-343	1106	253	229	14.3	176	13	8.9	125	19	130	9.9	19.9	75	19.9	4.7	5.2	0	1.02	6	0	12.3	8.9	2	1.9	25	51.4	6.1	22.7	4.18	1	3.33	0.5	2.59	0.47	1.34	0.21	1.45	0.24
GP640-13-1334	799	128	516	17.6	182	13.1	10.3	6	17.1	27	67	10	67	10	5.3	1.96	5	1	5	10	2.99	4	2	5	40.7	77.8	9.31	36.5	6.35	1.23	4.5	0.6	3.34	0.64	1.63	0.27	1.53	0.23
GP640-13-1410	581	119	487	16.8	160	13.2	8.97	1.9	18	28	32	6	71	10	4.5	4.91	6	0.9	1	20	3.36	0.9	1	4	28.1	59.3	7.57	30.3	5.43	1.18	4.24	0.59	3.11	0.56	1.55	0.23	1.64	0.24
GP615-12-1172	576	100	498	15.2	152	12.3	10	14	17.8	45	41	7	61	10	4.4	1.74	5	1	5	10	3.84	1	1	4	29.8	57.7	6.95	26.4	4.5	1.1	3.48	0.51	2.91	0.53	1.41	0.21	1.43	0.2
1-1865	455	243	56.7	13.9	155	11.4	10.1	65	17.2	61	4	9	50	30	4.4	11.7	5	0.9	4	10	4.31	7	1	1	25.8	50.2	6.03	23.2	4.13	1.03	3.09	0.42	2.47	0.46	1.35	0.19	1.44	0.19
2-1865	189	226	20	25.4	140	8.1	6.48	1140	23.5	2070	605	18	141	40	3.9	12.9	10	0.7	9	20	2.46	3	2	5	16.9	32.4	3.84	14.8	3.1	0.6	3.51	0.6	3.99	0.85	2.47	0.38	2.37	0.33
3-1865	806	274	91.2	13	141	11	9.11	83	18.2	325	5	7	72	20	4.2	9.01	6	0.9	6	20	3.55	2	1	1	29.5	55.4	6.75	25.7	4.32	1.14	3.4	0.45	2.49	0.45	1.31	0.18	1.32	0.2
3-1865A	211	293	34.1	18.2	153	9.1	7.25	644	19	1060	12	10	88	30	4.4	7.75	8	0.8	10	10	2.39	3	1	1	23	45.1	5.4	20.8	3.79	0.82	3.39	0.49	3.02	0.69	2.03	0.27	1.75	0.24
6-1865	583	212	141	16.3	141	10.4	8.46	17	17.6	375	7	7	70	20	4.1	10.1	5	0.8	5	10	3.62	1	1	1	26.6	51.5	6.22	24.6	4.73	1.19	3.85	0.52	2.75	0.54	1.5	0.22	1.44	0.2
7-1865	1010	292	96	14.9	161	10.6	8.47	37	17.4	114	7	11	73	20	4.7	10.9	6	0.8	6	9	3.31	2	1	2	30.4	56.8	6.74	25.5	4.48	1.08	3.33	0.49	2.67	0.52	1.44	0.2	1.52	0.21
WC360-06-526	611	145	488	16.2	176	12.2	8.81	18	19.1	57	2	5	73	10	5	3.89	6	0.9	6	10	3.7	1	1	1	30.5	60.3	7.22	29.5	5.15	1.38	3.99	0.57	3.08	0.57	1.53	0.21	1.49	0.21
WC224-05-730	621	347	152	14.2	162	12.5	10.2	62	18.2	100	2	7	53	10	4.5	5.69	5	1	5	10	4.05	2	1	2	29.3	54.5	6.44	24.3	4.51	0.9	3.34	0.46	2.63	0.48	1.34	0.21	1.44	0.21
GP609-11-999	723	228	244	9.3	192	11.3	10.9	22	20.1	150	3	5	39	10	5.6	7.72	3	0.8	4	10	3.73	3	1	1	38.5	72.4	8.24	30.3	4.89	1.01	3.11	0.35	1.8	0.32	0.87	0.12	0.72	0.1
GP622-12-1042 F	7.1	4.6	264	4.4	4	0.5	2.86	2	0.6	12	11	5	4.9	10	0.19	0.23	1	0.09	9	10	1.06	2630	0.9	10	7.5	15.2	1.95	8	1.52	0.32	1.32	0.2	0.98	0.15	0.43	0.05	0.31	0.05
WC218-404	714	201	133	14	174	15	8.96	32	19	250	9.9	19.9	83	19.9	4.6	8.2	0	1.1	5	0	8.79	37.8	1	1.9	37.2	69.4	8.11	30	5.25	1.6	3.87	0.52	2.54	0.45	1.29	0.19	1.32	0.23
WC296-322	883	247	115	17.8	180	13.1	8.62	281	18	550	9.9	19.9	81	19.9	4.8	8.2	0	0.95	7	0	8.42	3.9	1	1.9	35	68.9	8.05	29.3	5.17	1.31	4.05	0.58	3.11	0.58	1.65	0.24	1.55	0.26
13-1865	321	263	72.4	19.5	137	8.5	7.92	100	16.8	182	24	35	189	70	3.9	7.72	12	0.6	5	10	2.65	2	2	2	24.2	48.5	5.58	21.5	3.78	0.88	3.34	0.53	3.24	0.71	2.06	0.36	2.1	0.31
GP452-07-381	814	465	158	25.6	258	14.8	7.42	107	18.8	273	23	13	121	10	6.9	3.77	9	0.9	14	10	12.2	10	2	3	48.7	99.9	12.7	51.3	9.11	2.09	6.99	0.92	4.87	0.94	2.6	0.38	2.29	0.31

Summary of petrography, mineralogy, and grade of hydrothermal alteration for porphyries from Peñasquito (1 of 2). Note: abbreviations in Appendix A.

Sample	Sample Lab	Longitude	Latitude	Altitude (m.o.s.l.)	Py	Sp	Gn	Cpy	Tetra-Tenn	Ac	Cal	Qtz	Or_Pheno	Bi	Ser	Chl	Mag	Fl	Hem	Pl	Cb	Hy-Or	Wo	Ep	Mo	Sphene	Zrn	Am	Ap	Total %	Potassic Alteration Grade	Phyllic Alteration Grade
GP615-12-1113	5PS003	230986	2728536	906	3	-	-	2	2	-	-	10	18	10	7	3	5	10	2	20	-	7	-	-	-	-	-	-	-	99	Moderate	Moderate
GP615-12-1208	5PS004	230981	2728536	812	2	-	-	1	1	-	-	5	7	3	5	-	2	55	-	8	3	7	-	-	-	-	-	-	-	99	Moderate	Weak
GP640-13-1785	5PS009	229154	2728720	125	2	-	-	1	-	-	-	5	25	7	7	-	1	15	-	15	5	15	-	-	-	-	-	-	-	98	Pervasive	Moderate
GP621R12-1320	5PS027	230419	2727820	664	5	3	-	1	-	-	-	15	25	-	10	-	-	-	-	35	-	-	-	-	1	-	-	-	-	95	No	Pervasive
GP621R12-1345	5PS028	230417	2727820	640	5	-	-	1	-	-	-	20	18	3	10	-	-	-	-	30	10	-	-	-	2	-	-	-	-	99	No	Pervasive
GP621R12-1447	5PS029	230411	2727818	538	7	-	-	1	-	-	-	35	15	3	5	-	-	-	-	30	-	-	-	-	2	-	-	-	-	98	No	Weak
GP621R12-1629	5PS030	230400	2727817	356	5	2	-	1	-	-	-	40	10	-	10	-	-	-	-	25	5	-	-	-	1	-	-	-	-	99	No	Pervasive
GP640-13-1244	5PS042	229353	2728649	623	3	-	-	-	-	-	-	15	5	-	10	-	-	10	-	10	7	35	-	-	-	-	3	-	-	98	Pervasive	Pervasive
GP640-13-1650	5PS043	229206	2728701	256	5	65	7	3	5	2	5	3	-	-	1	-	-	-	-	-	-	-	-	-	-	-	-	-	-	96	-	Weak
GP628-12-1065	5ME009	230023	2727824	908	15	5	2	1	35	-	-	15	10	-	7	-	-	-	-	-	5	3	-	-	-	-	-	-	1	99	Weak	Moderate
WC229-05-235	5ME058	229513	2728580	1765	10	5	5	-	-	-	-	15	30	5	15	-	-	-	-	5	-	3	-	-	-	-	-	-	2	95	Weak	Pervasive
GP621R12-1282	6KS043	230420	2727821	702	15	3	-	2	5	-	2	15	25	-	15	-	-	-	-	15	-	-	-	1	-	-	-	-	-	98	No	Pervasive
GP621R12-1401	6KS044	230414	2727819	584	10	3	-	2	2	-	3	15	20	10	10	-	-	-	-	15	-	5	-	-	3	-	-	-	-	98	Weak	Pervasive
GP621R12-1902	6KS045	230382	2727822	84	5	-	-	-	-	-	7	15	25	3	15	-	-	-	-	20	-	1	-	-	3	-	-	-	-	94	No	Pervasive
WC229-05-284	6KS074	229512	2728604	1723	7	2	1	-	1	1	2	7	35	-	3	-	-	-	-	25	-	7	-	-	-	1	-	-	2	94	Moderate	Weak
GP622-12-1059	6KS080	230867	2728568	961	3	2	-	-	-	-	-	15	25	3	5	-	-	-	-	25	7	10	-	-	-	1	-	-	-	96	Pervasive	Weak
GP622-12-1067	6KS081	230866	2728568	953	5	2	1	1	2	-	5	7	20	7	7	-	-	-	-	25	-	15	-	-	-	-	-	-	-	97	Pervasive	Moderate
WC300-05-511	6KS082	229418	2728601	1513	7	3	-	-	-	-	5	7	20	2	7	-	-	-	-	30	-	15	-	-	-	1	-	-	-	97	Pervasive	Moderate
WC360-06-526	6KS083	229126	2728619	1494	3	1	-	-	-	-	-	7	25	-	1	-	-	-	-	35	2	15	-	-	-	1	-	7	-	97	Pervasive	Weak
GP557-08-1140	6KS085	229261	2728565	949	2	-	-	-	-	-	-	10	20	-	10	-	1	-	-	40	5	3	-	-	-	1	-	7	-	99	Weak	Pervasive
WC296-05-356	6KS086	229617	2728579	1654	7	2	-	-	-	-	-	7	20	-	5	-	-	-	-	45	-	5	-	-	-	1	-	7	-	99	Weak	Weak
WC224-05-730	6KS087	229393	2728698	1372	5	3	-	-	-	-	5	10	20	-	7	-	-	-	-	30		15	-	-	-	1	-	1	-	97	Pervasive	Moderate
GP640-13-1334	6KS088	229320	2728660	540	3	3	-	1	-	-	-	10	20	5	3	-	-	-	-	35	2	15	-	-	-	-	-	2	-	99	Pervasive	Weak
GP615-12-1172	6KS089	230983	2728536	847	5	1	-	2	-	-	-	10	20	5	7	2	-	-	-	30	5	7				-	1	3	1	99	Moderate	Moderate
MR-09	5MD004	229399	2728885	1800	5	2	-	-	-	-	-	15	20	5	10	3	-	-	-	20	7	10	-	-	-	1	1	-	-	99	Pervasive	Pervasive
MR-10	5MD005	229399	2728885	1800	5	3	-	-	-	-	-	15	15	5	7	7	-	-	-	25	7	5	-	-	-	2	1	-	-	97	Weak	Weak
MR-11	5MD006	229399	2728885	1800	10	3	-	-	-	-	-	10	10	7	15	3	-	-	-	20	10	7	-	-	-	2	2	-	-	99	Moderate	Pervasive
MR-12	5MD007	229399	2728885	1800	7	2	-	-	-	-	10	10	15	5	10	3	-	-	-	25	-	7	-	-	-	1	1	-	-	96	Moderate	Pervasive

Summary of petrography, mineralogy, and grade of hydrothermal alteration for porphyries from Peñasquito (2 of 2). Note: abbreviations in Appendix A.

Sample	Sample Lab	Longitude	Latitude	Altitude (m.o.s.l.)	Py	Sp	Gn	Cpy	Tetra-Tenn	Ac	Cal	Qtz	Or_Pheno	Bi	Ser	Chl	Mag	Fl	Hem	Pl	Cb	Hy-Or	Wo	Ep	Mo	Sphene	Zrn	Am	Ap	Total %	Potassic Alteration Grade	Phyllic Alteration Grade
GP615-12-826	5MD009	231000	2728534	1193	5	-	-	-	-	-	3	10	30	5	10	-	-	-	-	5	5	20	-	-	-	-	-	-	-	93	Pervasive	Pervasive
GP615-12-951	5MD010	230994	2728536	1068	7	-	-	-	-	-	-	10	15	5	3	3	-	-	-	35	7	10	-	5	-	-	-	-	-	100	Pervasive	Weak
GP615-12-993	5MD011	230992	2728536	1026	5	2	-	-	-	-	-	7	15	10	10	3	-	-	-	30	7	5	-	-	-	-	2	3	-	99	Weak	Pervasive
GP615-12-1099	5MD012	230986	2728536	920	7	-	-	-	-	-	-	15	15	10	5	3	-	-	-	30	5	10	-	-	-	-	-	-	-	100	Pervasive	Moderate
GP640-13-1411	5MD017	229292	2728670	470	7	-	-	-	-	-	-	15	15	15	3	3	-	-	-	25	5	10	-	-	-	-	-	-	-	98	Pervasive	Weak
GP640-13-1413	5MD018	229291	2728670	468	1	-	-	-	-	-	-	20	35	7	7	-	-	-	-	5	7	15	-	-	-	-	-	-	-	97	Pervasive	Moderate
GP640-13-1610	5MD019	229218	2728697	286	5	-	-	-	-	-	-	15	40	7	5	-	-	-	-	5	5	10	-	-	-	-	-	2	-	94	Pervasive	Weak
GP479-07-974	5MD021	229179	2728456	1064	7	-	-	-	-	-	-	10	10	7	3	-	-	-	-	40	5	15	-	-	-	-	-	2	-	99	Pervasive	Weak
GP628-12-1028	5MD022	230022	2727824	945	5	-	-	-	-	-	-	20	30	10	10	-	-	-	-	20	3	1	-	-	-	-	-	-	-	99	Weak	Pervasive
WC224-05-735	5MD023	229394	2728701	1368	5	-	-	-	-	-	5	15	15	3	10	-	-	-	1	35	-	10	-	-	-	-	1	-	-	100	Pervasive	Pervasive
WC296-05-314	5MD024	229617	2728560	1692	5	-	-	-	-	-	2	10	15	3	15	-	-	-	-	30	-	15	-	-	-	-	-	-	2	97	Pervasive	Pervasive
WC246-05-359	5MD025	228682	2729258	1648	5	-	-	-	-	-	-	7	10	10	7	-	-	-	-	30	10	15	3	-	-	1	-	-	-	98	Pervasive	Moderate
WC246-05-367	5MD026	228683	2729262	1641	5	-	-	-	-	-	-	10	35	-	3	-	-	-	-	20	5	15	2	-	-	-	-	-	2	97	Pervasive	Weak
GP624A12-1644	5MD028	229916	2728018	341	5	-	-	-	-	-	-	10	30	7	10	-	-	-	-	20	5	5	-	-	-	-	2	3	-	97	Weak	Pervasive
GP538-08-1340	5MD036	230248	2727973	877	5	-	-	-	-	-	-	15	25	10	10	-	-	-	-	10	10	10	-	-	1	-	1	-	2	99	Pervasive	Pervasive
GP621R12-1336	5MD038	230418	2727820	648	5	-	-	-	-	-	-	25	25	5	15	-	-	-	-	10	3	3	-	-	1	-	1	-	-	93	Weak	Pervasive
GP643-13-1555	5MD044	230259	2727390	695	3	-	-	-	-	-	-	10	25	-	7	-	-	-	-	35	5	10	-	-	-	1	1	-	-	97	Pervasive	Moderate
GP452-07-381	5MD049	230309	2727601	1648	3	-	-	-	-	-	-	7	5	2	5	15	-	-	-	35	5	20	-	-	-	-	-	1	-	98	Pervasive	Weak
GP452-07-411	5MD050	230309	2727615	1621	10	-	-	-	-	-	-	7	20	10	5	5	-	-	2	20	7	10	-	-	-	2	2	-	-	100	Pervasive	Weak
GPI014-13-103	5MD052	229773	2728556	1691	10	-	-	-	-	-	-	10	10	-	5	2	-	-	-	45	7	3	-	5	-	-	1	-	-	98	Weak	Weak
GPI014-13-175	5MD053	229730	2728591	1643	10	-	-	-	-	-	-	10	15	5	7	1	-	-	-	35	5	7	-	-	-	3	1	-	-	99	Moderate	Moderate
WC271-05-670	5MD059	229629	2728665	1387	7	-	-	-	-	-	-	10	15	3	5	-	-	-	-	35	5	15	-	-	-	-	2	2	-	99	Pervasive	Weak
WC334-05-565	5MD061	229365	2728539	1490	10	-	-	-	-	-	-	7	20	7	3	-	-	-	-	30	5	10	-	-	-	3	-	-	-	95	Pervasive	Weak
GP640-13-1191	5MD066	229373	2728642	672	3	-	-	-	-	-	-	20	15	7	3	-	-	-	-	35	3	5	-	-	-	3	-	2	-	96	Weak	Weak
GP571A-08-350	5MD068	230273	2728280	1675	10	-	-	-	-	-	-	20	35	-	7	-	-	-	3	4	10	10	-	-	-	-	-	-	1	100	Pervasive	Moderate
WC229-05-338	5MD069	229511	2728631	1676	10	-	-	-	-	-	-	10	15	1	7	-	-	-	3	25	7	20	-	-	-	-	2	-	-	100	Pervasive	Moderate
WC246-05-354	5MD070	228682	2729256	1652	7	-	-	-	-	-	-	10	15	-	5	-	-	-	2	30	7	20	-	-	-	2	1	-	1	100	Pervasive	Weak
WC246-05-355	5MD071	228682	2729258	1648	5	-	-	-	-	-	-	7	15	5	3	-	-	-	2	40	5	10	-	-	-	2	-	-	-	94	Pervasive	Weak
GP609-11-1003	5MD072	230999	2728686	1027	5	-	-	-	-	-	-	10	20	5	15	-	-	-	2	15	15	7	-	-	-	1	2	-	-	97	Moderate	Pervasive
GP609-11-1063	5MD073	230997	2728684	964	5	-	-	-	-	-	-	10	35	15	7	-	-	-	2	3	5	10	-	-	-	2	2	-	-	96	Pervasive	Moderate
GP621R12-1811	5MD039	230389	2727820	174	10	-	-	-	-	-	-	10	10	10	10	7	-	-	-	35	7	-	-	-	-	-	1	-	-	100	No	Pervasive
GP640-13-1813	5MD020	229143	2728724	100	5	-	-	-	-	-	-	7	3	5	3	-	-	-	-	65	7	5	-	-	-	-	-	-	-	100	Weak	Weak

Summary of petrography and mineragraphy for the skarn system (1 of 2). Note: abbreviations in Appendix A.

Percentage of minerals (columns Py through Hessite)

Sample	Longitude	Latitude	Altitude (m.o.s.l.)	Rock	Py	Sp	Gn	Cpy	Tetra-Tenn	Ac	Au	Cal	Qtz	Or	Ser	Chl	Mag	Fl	Hem	Cb	Cv	Mrc	Grt	Ox	Wo	Bn	Ep	Px	Ground mass	Apy	Dol	Am	Adr	Cpr	Dg	Po	Enr	Cc	Adl	Hessite
GP621R-1034	230423	2727823	950	S-Manto	3	35	-	3	-	-	-	-	65	-	-	-	-	-	-	-	1	-	-	-	-	-	-	-	-	-	-	-	-	-	-	-	-	-	-	-
GP621R-1111	230422	2727823	873	Sk	5	85	2	5	-	-	-	2	-	-	-	-	-	-	-	-	1	-	-	-	-	-	-	-	-	-	-	-	-	-	-	-	-	-	-	-
GP640-13-1727	229175	2728712	178	Sk	3	-	-	1	1	-	-	2	-	-	-	1	40	-	-	-	-	-	50	-	-	-	-	-	-	-	-	-	-	-	-	-	-	-	-	-
GP640-13-1810	229144	2728724	101	Sk	3	-	-	1	-	-	-	-	7	-	-	-	3	-	-	-	-	-	85	-	-	-	-	-	-	-	-	-	-	-	-	-	-	-	-	-
GP624A12-1194	229886	2727967	787	Sk	3	35	-	3	2	-	1	-	-	-	2	-	-	-	-	3	-	-	50	-	-	-	-	-	-	-	-	-	-	-	-	-	-	-	-	-
GP501-07-910	228936	2728434	1121	Sk	3	75	3	1	1	-	-	-	10	-	3	-	-	-	-	3	-	-	-	-	-	-	-	-	-	-	-	-	-	-	-	-	-	-	-	-
GP501-07-1058	228963	2728492	988	S-Sk	5	85	10	3	3	1	-	-	-	-	-	-	-	-	-	-	-	-	-	-	-	1	-	-	-	-	-	-	-	-	-	-	-	-	-
GP554-07-957	229039	2728499	1076	Hn	2	2	-	1	-	-	-	-	70	-	-	-	-	-	-	5	-	-	-	-	-	-	-	-	-	-	-	-	-	-	-	-	-	-	-	-
GP554-07-1129	229060	2728554	914	Sk	1	-	-	1	-	-	-	-	40	-	10	-	-	-	-	5	-	-	40	-	-	-	-	-	-	-	-	-	-	-	-	-	-	-	-	-
GP554-07-1135	229061	2728556	909	Sk	1	1	-	1	-	-	-	-	90	-	3	-	-	-	-	3	-	-	-	-	-	-	-	-	-	-	-	-	-	-	-	-	-	-	-	-
GP639-13-814	230213	2728195	1021	Sk	10	35	-	7	2	-	-	-	35	-	5	1	-	-	-	-	-	-	-	1	-	1	-	-	-	-	-	-	-	-	-	-	-	-	-	-
GP621-12-937	230424	2727824	1047	Sk	0.5	-	-	-	-	-	-	40	60	-	-	-	-	-	-	-	0.5	-	-	-	-	-	-	-	-	-	-	-	-	-	-	-	-	-	-	-
GP582-08-1145	230234	2727860	1035	Ox-manto	7	3	3	2	2	-	-	-	80	-	-	-	-	-	1	-	1	-	-	-	-	-	-	1	-	-	-	-	-	-	-	-	-	-	-	-
GP538-08-1370	230250	2727990	852	Sk	10	3	5	2	-	-	-	-	7	15	-	5	-	-	-	-	10	1	30	-	-	-	-	7	-	-	-	-	-	-	-	-	-	-	-	-
GP621R12-938	230423	2727824	1046	Sk	2	3	-	5	-	-	-	5	5	-	5	-	-	-	-	-	-	-	75	-	-	-	-	-	-	-	-	-	-	-	-	-	-	-	-	-
GP621R12-954	230423	2727824	1030	Sk	15	-	-	1	-	-	-	-	80	-	3	-	-	-	-	-	-	-	-	-	-	-	-	-	-	-	-	-	-	-	-	-	-	-	-	-
GP621R12-1028	230423	2727823	956	Sk	7	85	-	7	-	-	-	-	-	-	-	-	-	-	-	-	1	-	-	-	-	-	-	-	-	-	-	-	-	-	-	-	-	-	-	-
GP640-13-1003	229443	2728618	845	Sk	3	3	-	3	2	-	-	5	70	-	7	-	-	-	-	5	-	1	1	-	-	-	-	-	-	-	-	-	-	-	-	-	-	-	-	-
GP640-13-1218	229363	2728645	647	Hn	3	-	-	1	-	-	-	-	7	-	-	-	3	-	-	-	-	-	85	-	-	-	-	-	-	-	-	-	-	-	-	-	-	-	-	-
GP640-13-1703	229186	2728708	200	Sk	3	-	-	1	-	-	-	-	7	-	-	-	3	-	-	-	-	-	85	-	-	-	-	-	-	-	-	-	-	-	-	-	-	-	-	-
GP640-13-1708	229186	2728708	195	Sk	3	-	-	1	-	-	-	-	7	-	-	-	3	-	-	-	-	-	85	-	-	-	-	-	-	-	-	-	-	-	-	-	-	-	-	-
GP621R-1015	230423	2727823	969	Sk	3	5	1	5	2	-	-	-	5	-	2	-	-	-	-	3	2	1	65	-	-	1	-	2	-	-	-	-	-	-	-	-	-	-	-	-
GP621R-1034	230423	2727823	950	S-Manto	3	85	-	5	-	-	-	-	3	2	1	-	-	-	-	-	1	-	-	-	-	-	-	-	-	-	-	-	-	-	-	-	-	-	-	-
GP621R-1111	230422	2727823	873	Sk	7	85	-	2	2	-	1	-	1	-	-	-	-	-	-	1	-	-	-	-	-	-	-	-	-	-	-	-	-	-	-	-	-	-	-	-
GP624A12-1160	229884	2727963	822	S-Sk	65	2	-	3	-	-	-	3	2	-	2	-	20	-	-	3	-	-	-	-	-	-	-	-	-	-	-	-	-	-	-	-	-	-	-	-
GP501-07-910	228936	2728434	1121	Sk	10	55	15	1	5	-	-	-	3	-	3	-	-	-	-	-	1	-	-	-	-	-	-	-	-	-	-	-	-	-	-	-	-	-	-	-
GP501-07-990	228950	2728465	1047	Sk	5	60	5	15	2	1	-	-	1	-	1	-	-	-	-	-	1	-	-	-	-	-	-	-	-	-	-	-	-	-	5	-	-	-	1
GP501-07-1055	228963	2728491	990	S-Sk	10	60	7	7	5	3	-	-	3	-	1	-	-	-	-	3	-	-	-	-	-	-	-	-	-	-	-	-	-	-	-	-	-	-	-
GP512-07-640	228873	2728367	1362	Sk	10	20	60	2	-	2	-	1	1	-	1	-	-	-	-	1	-	-	-	-	-	-	-	-	-	-	-	-	-	-	-	-	-	-	-
GP554-07-503	229020	2728334	1498	S-Manto	40	7	15	-	5	3	-	-	10	5	10	-	-	-	-	5	-	-	-	-	-	-	-	-	-	-	-	-	-	-	-	-	-	-	-
GP639-13-956	230212	2728193	879	Br-Sk	15	3	1	10	1	-	-	1	3	-	3	-	-	-	-	-	1	1	55	-	-	-	1	-	-	-	-	-	-	-	-	-	-	-	-
GP639-13-1018	230211	2728193	817	Sk	3	3	2	80	-	1	-	1	3	-	3	-	3	-	-	-	1	-	-	-	-	-	-	-	-	-	-	-	-	-	-	-	-	-	-
GP636-13-793	229833	2728154	1042	Br-Sk	15	-	-	5	-	-	-	-	7	-	5	-	2	-	-	20	-	-	10	-	-	-	35	-	-	-	-	-	-	-	-	-	-	-	-	-
GP636-13-824	229833	2728154	1011	Sk	20	7	-	15	3	2	-	5	7	5	-	2	3	-	-	10	-	-	10	-	-	2	3	-	-	2	-	-	-	-	-	-	-	-	-	1
GP636-13-943	229832	2728151	891	Sk	20	7	-	15	-	-	-	15	-	-	-	-	3	-	-	10	-	1	10	-	-	1	3	-	-	-	-	-	-	-	-	-	-	-	-	-
GP636-13-1144	229827	2728150	691	Sk	85	-	-	3	1	1	-	-	2	-	-	-	5	-	1	2	-	-	-	-	-	-	-	-	-	-	-	-	-	-	-	-	-	-	-	-
GP636-13-1419	229825	2728151	416	Sk	10	-	-	3	-	-	-	-	2	-	-	-	30	-	-	-	-	-	-	-	1	-	15	-	-	-	-	35	-	-	-	-	-	-	-	-
GP633-12-1736	229758	2728012	262	S-Manto	80	-	-	3	-	-	-	-	10	-	2	-	1	-	-	-	-	-	-	1	-	-	-	-	-	-	2	-	-	-	-	-	-	-	-	-
GP621-12-808	230423	2727827	1176	Sk	10	20	25	5	2	-	-	2	25	-	2	-	-	-	-	-	7	-	-	-	-	-	-	-	-	-	-	-	-	1	-	-	-	-	-
GP621-12-810	230423	2727826	1174	Br-marble	30	7	25	1	-	1	-	-	10	5	-	-	-	-	-	20	-	-	-	-	-	-	-	-	-	-	-	-	-	-	-	-	-	-	-	-
GP621R12-853	230423	2727825	1131	Sk	15	50	3	5	3	-	-	-	7	-	5	-	-	-	-	-	7	1	-	-	-	-	-	-	-	-	-	-	-	-	-	-	-	-	-	-
GP621R12-1779	230391	2727819	206	EnSk	10	-	-	3	2	-	-	-	55	7	3	5	10	-	-	5	-	-	-	-	-	-	-	-	-	-	-	-	-	-	-	-	-	-	-	-
GP647-13-1068	229034	2728994	807	Marble	20	45	15	1	-	-	-	-	-	-	-	-	-	-	-	15	-	1	-	-	-	-	-	-	-	-	-	-	-	-	-	-	-	-	-	-

Summary of petrography and mineragraphy for the skarn system (2 of 2). Note: abbreviations in Appendix A.

Sample	Longitude	Latitude	Altitude (m.o.s.l.)	Rock	Py	Sp	Gn	Cpy	Tetra-Tenn	Ac	Au	Cal	Qtz	Or	Ser	Chl	Mag	Fl	Hem	Cb	Cv	Mrc	Grt	Ox	Wo	Bn	Ep	Px	Ground mass	Apy	Dol	Am	Adr	Cpr	Dg	Po	Enr	Cc	Adl	Hessite
GP514-07-606	230387	2728888	1465	Hn	7	-	-	-	-	-	-	-	-	-	5	-	-	-	-	3	-	-	-	-	-	-	5	-	80	-	-	-	-	-	-	-	-	-	-	-
WC63-03-233	230619	2728584	1791	Hn	10	15	7	-	20	15	-	-	10	12	7	-	-	-	3	5	1	1	-	-	-	-	-	-	-	-	-	-	-	-	-	-	-	-	-	-
GP640-13-1003	229443	2728618	845	Sk	7	60	3	7	-	-	-	1	15	-	2	-	-	-	-	2	-	2	-	-	-	1	-	-	-	-	-	-	-	-	-	-	-	-	-	-
GP571A08-402	230273	2728304	1629	Hn	10	5	-	-	-	-	-	-	35	15	25	-	-	-	-	10	-	-	-	-	-	-	-	-	-	-	-	-	-	-	-	-	-	-	-	-
GP640-13-1579	229230	2728693	315	S-Sk	70	-	-	3	-	-	-	14	-	1	-	-	10	-	-	1	-	-	-	-	-	-	1	-	-	-	-	-	-	-	-	-	-	-	-	-
GP624A12-1144	229883	2727962	838	S-Sk	30	-	-	3	-	-	-	7	1	-	-	-	3	-	-	-	-	-	-	-	-	-	-	-	-	-	-	-	50	-	2	-	-	-	-	-
GP624A12-1272	229891	2727976	711	S-Sk	70	7	-	3	-	-	-	7	-	1	1	-	7	-	-	-	-	-	-	-	-	-	3	-	-	-	-	-	-	-	-	-	-	-	-	-
GP624A12-1293	229893	2727978	689	S-Sk	35	-	1	7	-	-	-	45	5	-	19	-	-	-	-	-	-	-	1	-	-	-	5	-	-	-	-	-	-	-	-	-	-	-	-	-
GP624A12-1307	229894	2727980	675	S-Sk	30	5	-	35	-	-	-	15	-	-	-	-	10	-	-	-	-	-	-	-	-	-	5	-	-	-	-	-	-	-	-	-	-	-	-	-
GP624A12-1404	229900	2727991	579	Br-Marble	30	-	-	5	-	-	-	-	-	-	-	-	7	-	-	-	-	-	40	-	10	-	5	-	-	-	-	-	-	-	-	-	-	-	-	-
GP624A12-1452	229903	2727996	532	S-Sk	15	-	-	5	-	-	-	3	-	-	-	-	60	-	-	-	-	-	-	-	-	-	5	-	-	-	-	-	-	-	-	-	-	-	-	-
GP624A12-1546	229909	2728007	439	S-Sk	75	-	-	3	-	-	-	3	2	1	-	-	7	-	-	-	-	-	-	-	-	-	5	-	-	-	-	-	-	-	-	-	-	-	-	-
GP624A12-1588	229912	2728012	398	S-Sk	40	5	-	2	1	-	-	5	-	-	2	-	3	-	-	-	-	-	-	-	40	-	2	-	-	-	-	-	-	-	-	-	-	-	-
GP501-07-817	228923	2728400	1206	Hn	15	5	-	3	-	-	-	-	5	40	15	-	-	-	1	10	1	-	-	-	-	-	3	-	-	-	-	-	-	-	-	-	-	-	-	-
GP643-13-1328	230260	2727389	651	S-Sk	80	-	-	3	-	-	-	5	1	1	-	-	5	-	-	-	-	-	-	-	-	-	-	-	-	-	-	-	-	-	-	-	-	5	-	-
GP639-13-780	230213	2728195	1055	Sk	20	2	1	5	2	1	-	-	55	-	-	-	-	-	-	-	-	-	-	-	-	-	-	1	-	-	-	-	-	-	-	-	-	-	-	-
GP639-13-912	230212	2728194	923	Sk	35	2	-	5	1	-	-	-	-	1	-	-	20	-	1	35	-	-	-	-	-	-	-	-	-	-	-	-	-	-	-	-	-	-	-	-
GP639-13-950	230212	2728193	885	Br-Sk	25	-	-	5	-	-	-	20	-	-	-	-	7	-	-	30	-	-	-	-	-	-	10	-	-	-	-	-	-	-	-	-	-	-	-	-
GP636-13-562	229830	2728155	1273	Sk	15	3	-	3	2	1	-	15	-	-	-	-	-	-	1	10	-	-	-	-	-	-	45	-	-	-	-	-	-	-	-	-	-	-	-	-
GP636-13-743	229833	2728154	1092	Sk	7	2	-	2	2	-	-	5	-	-	-	-	-	-	1	60	-	-	-	-	-	-	5	-	-	-	-	-	-	-	7	2	-	-	-	-
GP636-13-1077	229829	2728150	757	Sk	35	-	-	7	-	-	-	5	-	-	-	-	10	-	-	25	-	-	-	-	-	-	5	-	-	-	-	-	-	-	10	-	-	-	-	-
GP636-13-1112	229828	2728150	723	Sk	35	1	-	5	-	-	-	5	-	-	-	-	1	-	1	30	-	-	-	-	-	-	5	-	-	-	-	-	-	-	-	-	-	-	-	-
GP636-13-1273	229825	2728152	562	Br-marble	25	3	-	5	-	-	-	65	-	-	-	-	-	-	-	-	-	-	-	-	-	-	-	-	-	-	-	-	-	-	-	-	-	-	-	-
GP633-12-1643	229749	2727999	354	Sk	65	-	-	2	1	-	-	-	-	3	-	-	3	-	1	25	-	-	-	-	-	-	-	-	-	-	-	-	-	-	-	-	-	-	-	-
GP633-12-1661	229751	2728001	336	Sk	5	-	-	2	-	-	-	25	-	-	-	-	-	-	1	5	-	-	-	-	-	-	1	-	-	-	-	-	-	-	60	-	-	-	-	-
GP633-12-1807	229766	2728022	193	S-Sk	35	2	1	5	1	-	-	40	5	3	-	-	1	-	-	-	-	1	-	-	-	-	2	-	-	-	-	-	-	-	-	-	-	-	-	-
GP621-12-820	230423	2727826	1164	Sk	25	15	5	3	3	-	-	-	10	25	2	-	-	-	-	7	-	-	-	-	-	-	-	-	-	-	-	-	-	-	-	-	-	-	-	-
GP621-12-833	230423	2727826	1151	Sk	-	-	-	-	-	-	-	-	-	-	-	-	-	-	-	-	-	-	-	-	-	-	-	-	-	-	-	-	-	-	-	-	-	-	-	-
GP621-12-872	230423	2727825	1112	Sk	-	-	-	-	-	-	-	-	-	-	-	-	-	-	-	-	-	-	-	-	-	-	-	-	-	-	-	-	-	-	-	-	-	-	-	-
GP621-12-915	230424	2727824	1069	Sk	-	-	-	-	-	-	-	-	-	-	-	-	-	-	-	-	-	-	-	-	-	-	-	-	-	-	-	-	-	-	-	-	-	-	-	-
MET40-09-318	230068	2727094	1729	Hn	20	5	5	-	2	1	-	15	35	5	-	-	-	-	-	7	1	-	-	-	-	-	-	-	-	-	-	-	-	-	-	-	-	-	-	-
GP621R12-867	230423	2727825	1117	Sk	10	3	-	35	1	-	-	10	3	-	-	-	-	-	-	35	1	-	-	-	-	-	2	-	-	-	-	-	-	-	-	-	-	-	-	-
GP621R12-982	230423	2727824	1002	Sk	35	15	2	3	2	1	-	35	3	-	2	-	-	-	-	-	-	-	2	-	-	-	-	-	-	-	-	-	-	-	-	-	-	-	-	-
GP621R12-1104	230422	2727823	880	Sk	7	55	3	5	-	-	-	20	-	-	-	-	-	-	-	-	-	-	-	-	-	-	-	-	-	-	-	-	-	-	-	-	-	-	-	-
GP621R12-1222	230421	2727821	762	Sk	20	-	1	2	-	-	-	35	10	7	-	-	-	-	-	-	-	-	-	-	-	5	10	-	-	-	-	-	-	-	10	-	-	-	-	-
GP643-13-765	230241	2727393	1214	Sk	7	2	1	-	1	-	-	45	1	35	-	-	-	-	-	-	-	-	-	-	-	-	5	-	-	-	-	-	-	-	3	-	-	-	-	-
GP643-13-1283	230259	2727390	696	Sk	5	25	-	5	-	-	-	25	1	7	1	-	-	-	-	1	-	-	-	-	-	-	1	-	-	-	-	-	25	-	1	-	-	1	2	-
GP514-07-467	230375	2728828	1589	Hn	20	3	-	-	2	-	-	-	-	40	20	-	-	-	1	10	1	-	-	-	-	-	3	-	-	-	-	-	-	-	-	-	-	-	-	-
WC63-03-349	230623	2728527	1691	Sk	75	-	-	2	-	-	-	7	3	-	-	2	-	-	-	-	1	-	-	-	-	-	5	-	-	-	-	-	-	-	1	-	1	-	-	-
GP640-13-973	229454	2728615	872	Sk	35	2	-	1	1	-	-	20	15	5	5	-	-	-	-	-	-	-	-	-	10	-	1	-	-	-	-	-	-	-	-	-	-	-	-	-
GP640-13-1546	229242	2728688	345	Sk	45	-	-	5	-	-	-	3	1	5	-	-	3	-	3	25	1	-	-	-	-	2	5	-	-	-	-	-	-	-	-	-	-	1	-	-
GP640-13-1614	229217	2728697	283	Sk	64	-	-	5	-	-	-	7	7	-	-	-	8	-	5	-	-	-	-	-	-	2	1	-	-	-	-	-	-	-	-	-	-	1	-	-

Summary of petrography and mineragraphy for the stockwork. Note: abbreviations in Appendix A.

Sample	Longitude	Latitude	Altitude (m.o.s.l.)	Percentage of minerals and components																			
				Py	Sp	Gn	Cpy	Tetra-Tenn	Ac	Au	Cal	Rds	Qtz	Ser	Fl	Hem	Cb	Cv	Or	Sdt	Groundmass	Slts	Tellurobismuthite
GP615-12-552	231011	2728527	1466	5	70	7	2	3	2	1	5	-	-	-	-	-	-	-	-	-	-	-	-
GP615-12-613	231009	2728528	1406	3	50	5	3	3	1	7	-	25	-	-	-	-	-	-	-	-	-	-	-
MET59-13-703	229679	2729073	1300	94	1	1	1	-	-	-	-	-	-	3	-	-	-	-	-	-	-	-	-
MET40-09-267	230068	2727062	1768	5	70	7	2	2	-	-	-	-	-	-	-	1	-	-	-	10	-	-	-
MHC02-277	230077	2727091	1748	3	75	10	-	-	-	-	-	10	-	-	-	-	-	-	-	-	-	-	-
MHC04-178	230179	2727130	1818	40	30	5	-	10	-	-	3	5	-	-	-	5	-	-	-	-	-	-	-
MHC04-205	230191	2727130	1794	7	70	5	1	10	-	-	2	2	-	-	-	3	-	-	-	-	-	-	-
GP615-12-552	231011	2728527	1466	7	70	3	1	5	-	-	7	-	2	2	-	-	3	-	-	-	-	-	-
GP615-12-613	231009	2728528	1406	10	30	10	3	5	2	-	-	25	2	2	-	-	10	-	-	-	-	-	-
GP554-07-513	229020	2728338	1489	10	3	2	1	2	-	-	3	-	3	3	-	-	-	1	1	-	70	-	-
GP636-13-512	229829	2728155	1323	15	3	2	1	3	-	-	-	-	5	5	-	-	5	-	-	-	-	60	-
GP636-13-582	229830	2728155	1252	20	10	-	1	25	-	-	-	-	5	5	-	-	1	1	-	-	30	-	-
MET40-09-210	230068	2727025	1811	20	40	10	-	-	15	-	-	-	-	-	-	-	-	-	-	-	10	-	-
MET40-09-375	230068	2727131	1685	10	3	1	1	-	-	-	-	-	2	7	-	-	-	-	-	-	75	-	-
MHC04-205	230191	2727130	1794	25	30	3	1	30	3	3	-	-	-	-	-	-	2	3	-	-	-	-	-
WC15-02-347	230053	2727041	1663	45	2	-	1	25	2	1	-	-	10	7	-	-	7	-	-	-	-	-	1
WC268-06-227	229277	2728317	1755	20	25	20	5	-	-	-	-	-	15	7	-	-	7	-	-	-	-	-	-
GP512-07-638	228873	2728366	1363	10	15	7	3	7	1	-	-	-	20	-	-	-	35	-	-	-	-	-	-
GP621-12-755	230423	2727828	1229	7	7	5	3	7	-	-	-	-	15	-	-	-	5	-	50	-	-	-	-
MHC02-310	230096	2727092	1722	20	5	3	-	3	-	-	-	-	10	2	-	-	5	-	50	-	-	-	-
PN28-260	230013	2727065	1729	10	60	5	1	3	2	1	-	-	3	5	-	1	3	1	2	-	-	-	-
WC63-03-281	230621	2728560	1750	7	20	7	-	-	-	-	-	-	3	25	-	-	5	-	30	-	-	-	-

Summary of petrography and mineragraphy for the diatreme breccia system (1 of 2). Note: abbreviations in Appendix A.

Sample	Longitude	Latitude	Altitude (m.o.s.l.)	Rock	Py	Sp	Gn	Cpy	Tetra-Tenn	Ac	Syl	Au	Cal	Rds	Qtz	Or	Bi	Ser	Hem	Mag	Pl	Cb	Cv	Mrc	Hy-Or	Ep	Breccia Matrix	Zrn	Ele	Fragments	Cal-Dol	Sphene
MET57-13-850	229668	2728918	1149	Br	7	5	5	1	5	-	-	-	-	-	35	30	-	5	-	-	-	5	1	-	-	-	-	-	-	-	-	-
WC13-02-88	230196	2727231	1901	Br	7	3	-	1	2	-	-	-	-	-	85	-	-	1	-	-	-	-	-	-	-	-	-	-	-	-	-	-
WC13-02-234	230271	2727227	1776	Br	5	60	5	-	25	-	-	1	-	-	3	-	-	1	-	-	-	-	-	-	-	-	-	-	-	-	-	-
GP452-07-475	230308	2727645	1565	Br	3	85	5	1	-	-	-	-	-	-	-	-	-	3	-	-	-	-	-	-	-	-	-	-	-	-	-	-
GP452-07-558	230308	2727683	1491	Br	25	30	2	1	3	-	-	-	-	-	-	-	-	3	3	-	-	-	1	-	-	-	30	-	-	-	-	-
GP640-13-852	229500	2728600	983	Br	20	70	3	1	3	-	-	-	-	-	-	-	-	2	-	-	-	-	-	-	-	-	-	-	-	-	-	-
WC112-04-470	229474	2728912	1569	Br	10	3	2	1	2	-	-	-	-	-	15	30	-	5	-	-	-	2	-	-	-	-	-	-	-	-	30	-
WC112-04-619	229483	2728997	1454	Br	10	15	10	-	10	3	-	-	-	-	10	10	-	10	3	-	-	3	-	-	-	-	-	-	-	-	10	-
WC112-04-744	229493	2729079	1361	Br	25	10	10	1	7	-	-	-	-	7	10	-	-	15	-	-	-	7	-	-	-	-	-	-	-	-	-	-
GP501-07-912	228936	2728435	1119	Br	10	10	2	2	5	-	-	-	-	-	45	15	-	3	-	-	-	5	-	-	-	-	-	-	-	-	-	-
GP512-07-642	228873	2728367	1360	Br	10	45	10	2	-	-	-	-	2	-	15	7	-	5	-	-	-	3	-	-	-	-	-	-	-	-	-	-
MET40-09-361	230068	2727122	1696	Br	20	30	3	-	-	-	-	-	-	-	15	-	-	-	-	-	-	-	-	-	-	-	-	-	-	-	30	-
OC26-13-113	229616	2727997	1723	Br	10	-	-	7	60	20	-	1	-	-	-	-	-	-	-	-	-	-	1	-	-	-	-	-	-	-	-	-
WC13-02-207	230257	2727228	1799	Br	25	30	5	1	35	-	-	-	-	-	2	-	-	-	-	-	-	-	1	1	-	-	-	-	-	-	-	-
WC24-02-283	230603	2727733	1743	Br	15	20	10	-	10	-	-	-	-	-	10	7	-	5	-	-	-	5	-	-	-	-	-	-	-	15	-	1
WC24-02-615	230434	2727760	1459	Br	15	7	5	1	1	-	-	1	-	-	10	15	-	5	-	-	-	3	-	-	10	-	-	1	-	20	-	3
PN28-228	230013	2727075	1759	Br	55	-	-	-	35	-	-	-	-	-	-	-	-	-	-	-	-	10	-	-	-	-	-	-	-	-	-	-
GP452-07-475	230308	2727645	1565	Br	15	7	5	1	3	-	-	-	-	-	20	25	-	3	-	-	-	5	-	-	5	-	-	1	-	7	-	2
GP452-07-558	230308	2727683	1491	Br	45	5	2	1	3	-	-	-	-	-	7	15	-	5	-	-	-	5	-	-	-	-	-	-	-	7	-	5
WC271-05-375	229628	2728795	1651	Br	15	7	5	-	-	-	-	-	-	-	15	20	-	15	3	-	5	5	-	-	7	-	-	-	-	-	-	3
WC271-05-473	229632	2728754	1563	Br	15	3	3	-	-	-	-	-	-	-	20	30	-	15	1	-	-	5	-	-	3	-	-	1	-	-	-	2
WC350A06-722	229301	2728513	1301	Br	20	7	5	1	3	-	-	1	-	-	15	35	-	5	-	-	-	3	-	-	2	-	-	-	-	-	-	3
WC268-06-665	229308	2728489	1354	Br	10	-	-	2	25	-	-	1	-	-	25	15	-	10	5	-	-	1	1	-	2	-	-	-	-	-	-	-
GP640-13-810	229517	2728595	1024	Br	7	3	3	5	5	1	-	-	-	-	45	10	-	7	-	-	-	5	-	-	2	-	-	1	-	-	-	3
GP640-13-852	229500	2728600	983	Br	40	35	10	3	5	-	-	-	-	-	3	-	-	1	-	-	-	2	-	-	-	-	-	-	-	-	-	-
WC303-05-568	229708	2729035	1486	Br	25	10	3	2	15	2	-	1	-	-	15	-	-	10	5	-	-	10	1	1	-	-	-	-	-	-	-	-
WC229-05-530	229518	2728740	1518	Br	10	5	3	-	7	2	-	1	1	-	40	15	-	3	2	-	-	5	1	-	2	-	-	-	1	-	-	3

Summary of petrography and mineragraphy for the diatreme breccia system (2 of 2). Note: abbreviations in Appendix A.

Sample	Longitude	Latitude	Altitude (m.o.s.l.)	Rock	Py	Sp	Gn	Cpy	Tetra-Tenn	Ac	Syl	Au	Cal	Rds	Qtz	Or	Bi	Ser	Hem	Mag	Pl	Cb	Cv	Mrc	Hy-Or	Ep	Breccia Matrix	Zrn	Ele	Fragments	Cal-Dol	Sphene
WC229-05-821	229569	2728909	1287	Br	15	5	3	1	7	-	-	-	-	-	20	30	-	3	2	-	-	3	-	-	5	-	-	-	-	-	-	3
MR-05	229767	2728756	1750	Br	10	3	1	1	-	-	-	-	-	-	20	10	-	10		-	-	7	-	-	30	3	-	-	-	-	-	-
MR-07	229660	2728892	1750	Br	10	7	-	1	-	-	-	-	-	-	10	3	-	15	1	-	-	10	-	1	5	-	-	-	-	35	-	-
MR-08	228907	2728624	1750	Br	30	5	-	1	-	-	-	-	-	-	25	5	-	15	1	-	-	10	-	1	5	-	-	-	-	-	-	-
GP512-07-785	228881	2728414	1225	Br	7	5	3	1	-	-	-	-	-	-	3	-	-	3	-	-	-	5	-	-	20	-	-	-	-	50	-	-
GP512-07-800	228882	2728419	1211	Br	7	3	2	2	-	-	-	-	-	-	1	-	-	3	-	-	-	10	-	-			-	-	-	70	-	-
MHC02-414	230157	2727095	1637	Br	7	5	3	2	-	-	-	-	-	-	5	-	-	5	-	-	-	10	-	-	60	-	-	-	-	-	-	-
WC13-02-141	230223	2727230	1856	Br	20	25	10	1	-	-	-	-	-	-	1	-	-	3	-	-	-	5	-	-	30	-	-	-	-	-	-	-
WC24-02-601	230442	2727758	1471	Br	10	7	7	2	5	-	-	-	-	-	20	-	-	3	3	-	1	5	2	-	30	-	-	-	-	-	-	-
PN28-191	230013	2727088	1794	Br	10	25	10	2	5	2	-	-	-	-	10	-	-	3	1	1	-	5	1	-	20	-	-	-	-	-	-	-
PN28-337	230013	2727038	1656	Br	20	30	7	3	5	2	-	1	-	-	-	-	-	3	1	-	-	5	-	-	20	-	-	-	-	-	-	-
GP452-07-121	230315	2727476	1875	Br	15	3	-	-	2	-	-	-	-	-	15	-	-	3	-	-	-	15	-	-	10	-	35	-	-	-	-	-
GP452-07-517	230308	2727664	1528	Br	15	7	7	3	5	2	-	1	-	-	7	15	-	5	2	1	1	1	3	2	15	3	10	-	-	-	-	-
WC271-05-241	229625	2728853	1773	Br	15	3	-	-	3	-	-	-	-	-	10	-	-	15	1	-	-	2	-	-	5	-	35	-	-	-	-	-
WC271-05-341	229628	2728809	1682	Br	15	3	2	-	2	-	-	-	-	-	10	-	-	10	1	-	-	3	1	-	35	-	15	1	-	-	-	-
WC271-05-634	229631	2728682	1419	Br	15	3	1	1	2	1	-	-	-	-	10	-	-	5	-	-	-	7	-	-	50	-	-	-	1	-	-	-
WC350A-06-277	229322	2728346	1713	Br	15	2	-	-	3	1	-	-	-	-	20	-	-	15	-	-	-	-	-	-	5	-	30	1	-	-	-	-
WC350A-06-441	229314	2728411	1563	Br	20	3	-	-	2		-	-	-	-	15	-	-	35	-	-	-	3	-	-	3	-	15	-	-	-	-	-
WC350A-06-571	229307	2728459	1442	Br	15	3	3	-	2	1	-	-	-	-	10	-	-	-	-	-	-	-	-	-	35	-	15	1	-	-	-	-
WC334-05-422	229369	2728460	1617	Br	15	3	-	-	7	3	-	-	-	-	10	-	-	15	-	-	-	3	-	-	10	-	25	-	-	-	-	-
WC334-05-614	229365	2728561	1453	Br	10	3	-	-	3	2	-	1	-	-	10	5	-	7	2	-	-	5	1	-	30	-	20	-	-	-	-	-
WC268-06-317	229279	2728354	1673	Br	10	3	2	2	3	1	-	-	-	-	10	5	-	5	-	-	-	5	-	-	30	-	20	-	-	-	-	-
WC268-06-530	229292	2728438	1478	Br	10	5	-	-	3	2	-	1	-	-	10	5	-	7	1	-	-	3	1	-	30	-	20	-	-	-	-	-
WC303-05-408	229707	2728958	1626	Br	10	5	2	-	-	-	-	-	-	-	7	7	-	3	-	-	-	7	-	-	30	-	25	-	-	-	-	-
WC229-05-414	229512	2728673	1613	Br	15	7	2	-	-	-	-	-	-	-	3	7	1	7	-	-	-	7	-	-	30	-	20	-	-	-	-	-
WC229-05-572	229523	2728765	1484	Br	10	7	7	-	-	-	-	-	-	-	3	7	-	1	-	-	-	3	-	-	35	-	25	-	-	-	-	-
WC112-04-139	229467	2728733	1854	Felsite	15	5	3	-	-	-	-	-	-	-	7	10	-	2	-	-	-	15	-	2	40	-	-	-	-	-	-	-
WC229-05-340	229511	2728631	1676	Felsite	7	5	5	-	-	-	-	-	-	-	7	15	-	3	-	-	-	7	-	-	50	-	-	-	-	-	-	-
WC335-05-332	229674	2728623	1682	Felsite	10	5	-	-	-	-	-	-	-	-	7	15	-	3	-	-	-	3	-	-	55	-	-	-	-	-	-	-
MET57-13-828	229668	2728918	1149	Felsite	7	5	2	1	2	1	-	-	-	-	-		-	7	-	-	-	7	-	1	67	-	-	-	-	-	-	-

Results of radiometric dating (^{39}Ar/^{40}Ar) for hydrothermal biotite and K-feldspar (orthoclase) from the Peñasquito plutonic complex (1 of 4).

Monitor	P	t	40	39	38	37	36	Moles 40Ar*	% Rad	R	J-value	% -sd
au25.5a.bio.117a.txt	1.8	10	2.28502 ± 0.002174	0.29776 ± 0.000441	0.02453 ± 0.000224	0.00044 ± 0.000067	0.000222 ± 0.000007	1.76E-14	97.13%	7.45356	0.00755161 ± 0.000016	0.21%
au25.5a.bio.118a.txt	1.8	10	2.68568 ± 0.001721	0.33891 ± 0.000663	0.02950 ± 0.000187	0.00649 ± 0.000157	0.000495 ± 0.000008	2.06E-14	94.55%	7.49310	0.00751176 ± 0.000018	0.24%
au26.5a.bio.4a.txt	1.8	10	0.99647 ± 0.001312	0.13127 ± 0.000610	0.01104 ± 0.000067	0.00013 ± 0.000061	0.000068 ± 0.000006	7.65E-15	97.97%	7.43725	0.00756817 ± 0.000040	0.52%
au26.5a.bio.3a.txt	1.8	10	1.65645 ± 0.001280	0.18881 ± 0.000771	0.01603 ± 0.000134	0.00010 ± 0.000061	0.000788 ± 0.000012	1.27E-14	85.95%	7.54007	0.00746496 ± 0.000041	0.55%
au26.5a.bio.5a.txt	1.8	10	0.97225 ± 0.001307	0.12751 ± 0.000393	0.01060 ± 0.000150	0.00024 ± 0.000059	0.000064 ± 0.000009	7.47E-15	98.07%	7.47754	0.00752739 ± 0.000033	0.44%
au26.5e.bio.6a.txt	1.8	10	1.41094 ± 0.001890	0.18608 ± 0.000534	0.01527 ± 0.000156	0.00158 ± 0.000076	0.000066 ± 0.000012	1.08E-14	98.62%	7.47796	0.00752697 ± 0.000031	0.41%
au26.5e.bio.7a.txt	1.8	10	1.96344 ± 0.001756	0.25016 ± 0.000682	0.02122 ± 0.000172	0.00031 ± 0.000062	0.000304 ± 0.000011	1.51E-14	95.42%	7.48924	0.00751563 ± 0.000026	0.35%
au26.5e.bio.8a.txt	1.8	10	1.51488 ± 0.001920	0.19479 ± 0.000438	0.01631 ± 0.000156	0.00046 ± 0.000061	0.000220 ± 0.000011	1.16E-14	95.72%	7.44420	0.00756110 ± 0.000026	0.35%
au26.5e.bio.11a.txt	1.8	10	0.70948 ± 0.001331	0.07405 ± 0.000269	0.00606 ± 0.000088	0.00021 ± 0.000050	0.000534 ± 0.000011	5.45E-15	77.76%	7.45086	0.00755434 ± 0.000060	0.79%
au26.5e.bio.12a.txt	1.8	10	1.60536 ± 0.000916	0.19588 ± 0.000823	0.01648 ± 0.000118	0.00073 ± 0.000044	0.000466 ± 0.000010	1.23E-14	91.43%	7.49320	0.00751165 ± 0.000038	0.51%
au26.5i.bio.13a.txt	1.8	10	3.57012 ± 0.002956	0.47065 ± 0.000473	0.03983 ± 0.000139	0.00030 ± 0.000035	0.000187 ± 0.000008	2.74E-14	98.45%	7.46816	0.00753684 ± 0.000011	0.15%
au26.5i.bio.14a.txt	1.8	10	10.07863 ± 0.006919	1.31938 ± 0.001096	0.11518 ± 0.000295	0.11344 ± 0.001102	0.000705 ± 0.000011	7.74E-14	97.93%	7.48248	0.00752242 ± 0.000009	0.11%
au26.5i.bio.15a.txt	1.8	10	3.05489 ± 0.002708	0.38801 ± 0.000816	0.03281 ± 0.000069	0.00055 ± 0.000067	0.000498 ± 0.000009	2.35E-14	95.18%	7.49412	0.00751074 ± 0.000019	0.26%
au26.5i.bio.16a.txt	1.8	10	5.63895 ± 0.003826	0.74542 ± 0.001110	0.06251 ± 0.000222	0.00495 ± 0.000140	0.000171 ± 0.000008	4.33E-14	99.11%	7.49730	0.00750754 ± 0.000013	0.17%
au26.5i.bio.17a.txt	1.8	10	4.56223 ± 0.003127	0.60290 ± 0.000911	0.05238 ± 0.000303	0.00220 ± 0.000147	0.000132 ± 0.000007	3.50E-14	99.15%	7.50255	0.00750229 ± 0.000013	0.17%
											Layer 5 Radial Monitors: Mean = 0.0075227±0.0000089 [0.12%] 2σ Wtd by data-pt errs only, 0 of 15 rej. MSWD = 1.11, probability = 0.34	
au25.5s.bio.110a.txt	1.8	10	2.26266 ± 0.002158	0.29040 ± 0.000610	0.02559 ± 0.000160	0.00195 ± 0.000117	0.000280 ± 0.000008	1.74E-14	96.34%	7.50669	0.00749816 ± 0.000020	0.26%
au25.5s.bio.113a.txt	1.8	10	1.13936 ± 0.000884	0.14031 ± 0.000520	0.01213 ± 0.000084	0.00035 ± 0.000054	0.000317 ± 0.000008	8.75E-15	91.78%	7.45236	0.00755282 ± 0.000035	0.47%
au25.5s.bio.114a.txt	1.8	10	1.71400 ± 0.001609	0.19389 ± 0.000580	0.01635 ± 0.000163	0.00201 ± 0.000096	0.000872 ± 0.000011	1.32E-14	84.97%	7.51135	0.00749350 ± 0.000032	0.43%
au25.5s.bio.115a.txt	1.8	10	3.38846 ± 0.002327	0.44876 ± 0.000806	0.03919 ± 0.000228	0.00107 ± 0.000100	0.000080 ± 0.000006	2.60E-14	99.30%	7.49833	0.00750652 ± 0.000015	0.20%
au25.5s.bio.116a.txt	1.8	10	1.45247 ± 0.001917	0.18239 ± 0.000494	0.01588 ± 0.000165	0.00123 ± 0.000077	0.000288 ± 0.000008	1.12E-14	94.14%	7.49698	0.00750787 ± 0.000027	0.36%
au26.5s.san.100a.txt	1.8	10	13.23881 ± 0.005083	6.32422 ± 0.004932	0.08108 ± 0.000261	0.04121 ± 0.000357	0.000111 ± 0.000018	1.02E-13	99.75%	2.08829	0.00749548 ± 0.000007	0.10%
au26.5s.san.106a.txt	1.8	10	10.75389 ± 0.005360	5.11944 ± 0.003019	0.07275 ± 0.000296	0.03383 ± 0.000271	0.000287 ± 0.000024	8.26E-14	99.21%	2.08413	0.00751042 ± 0.000008	0.10%
au26.5s.san.107a.txt	1.8	10	15.08666 ± 0.006904	7.20658 ± 0.005457	0.09352 ± 0.000395	0.04422 ± 0.000265	0.000157 ± 0.000024	1.16E-13	99.69%	2.08712	0.00749966 ± 0.000008	0.10%
au26.5s.san.108a.txt	1.8	10	10.90986 ± 0.007835	5.19539 ± 0.005051	0.06767 ± 0.000512	0.03566 ± 0.000413	0.000212 ± 0.000024	8.38E-14	99.43%	2.08800	0.00749653 ± 0.000010	0.14%
au26.5s.san.109a.txt	1.8	10	9.66243 ± 0.007773	4.58858 ± 0.006533	0.05907 ± 0.000312	0.02801 ± 0.000454	0.000300 ± 0.000011	7.42E-14	99.08%	2.08654	0.00750175 ± 0.000013	0.17%
											Layer 5 Central Monitors: Mean = 0.0075016±0.0000071 [0.095%] 2σ Wtd by data-pt errs only, 0 of 10 rej. MSWD = 0.52, probability = 0.86	
GP609-11-1063 Biotite, 18-40 mesh size; Single crystal total fusion analyses.												
au26.5f.bio.18a.txt	1.8	10	0.66223 ± 0.000777	0.25081 ± 0.000661	0.01240 ± 0.000069	0.00276 ± 0.000066	0.000091 ± 0.000008	5.09E-15	96.0%	2.5338	34.06 ± 0.16	0.48%
au26.5f.bio.19a.txt	1.8	10	0.84835 ± 0.001251	0.31281 ± 0.000810	0.01539 ± 0.000160	0.00487 ± 0.000096	0.000180 ± 0.000007	6.52E-15	93.7%	2.5421	34.17 ± 0.14	0.42%
au26.5f.bio.20a.txt	1.8	10	0.89971 ± 0.001062	0.34595 ± 0.001035	0.01590 ± 0.000136	0.00542 ± 0.000143	0.000095 ± 0.000006	6.91E-15	96.9%	2.5196	33.88 ± 0.13	0.39%
au26.5f.bio.21a.txt	1.8	10	1.05964 ± 0.001713	0.40338 ± 0.000684	0.02020 ± 0.000212	0.01560 ± 0.000375	0.000127 ± 0.000008	8.14E-15	96.5%	2.5344	34.07 ± 0.11	0.33%
au26.5f.bio.22a.txt	1.8	10	0.94960 ± 0.001000	0.36190 ± 0.000746	0.01915 ± 0.000142	0.00289 ± 0.000109	0.000096 ± 0.000007	7.29E-15	97.0%	2.5457	34.22 ± 0.11	0.32%
au26.5f.bio.23a.txt	1.8	10	1.73748 ± 0.002331	0.64822 ± 0.000776	0.03016 ± 0.000265	0.00980 ± 0.000147	0.000328 ± 0.000006	1.33E-14	94.4%	2.5311	34.03 ± 0.08	0.22%
au26.5f.bio.24a.txt	1.8	10	2.78932 ± 0.001680	1.03916 ± 0.001273	0.04892 ± 0.000234	0.01124 ± 0.000112	0.000566 ± 0.000010	2.14E-14	94.0%	2.5236	33.93 ± 0.06	0.18%
au26.5f.bio.25a.txt	1.8	10	2.16479 ± 0.001937	0.82687 ± 0.001626	0.04132 ± 0.000243	0.01163 ± 0.000176	0.000276 ± 0.000007	1.66E-14	96.2%	2.5197	33.88 ± 0.08	0.25%
au26.5f.bio.26a.txt	1.8	10	4.03198 ± 0.003327	1.56792 ± 0.001345	0.07161 ± 0.000357	0.06453 ± 0.000396	0.000276 ± 0.000017	3.10E-14	98.0%	2.5202	33.88 ± 0.06	0.18%
au26.5f.bio.27a.txt	1.8	10	2.95467 ± 0.003557	1.14986 ± 0.001810	0.05117 ± 0.000238	0.01935 ± 0.000228	0.000215 ± 0.000015	2.27E-14	97.8%	2.5146	33.81 ± 0.09	0.26%
											GP609-11-1063 Biotite; au26.5f.bio SCTF Mean = 33.952±0.085 [0.25%] 95% conf. Wtd by data-pt errs only, 0 of 10 rej. MSWD = 1.8, probability = 0.058	

Results of radiometric dating (^{39}Ar/^{40}Ar) for hydrothermal biotite and K-feldspar (orthoclase) from the Peñasquito plutonic complex (2 of 4).

Monitor	P	t	40	39	38	37	36	Moles 40Ar*	% Rad	R	J-value	% -sd
GP615-12-1173 Biotite, 18-40 Mesh Size; Single crystal total fusion analyses.												
au26.5g.bio.31a.txt	1.8	10	2.81593 ± 0.001715	1.07094 ± 0.001168	0.05562 ± 0.000331	0.08256 ± 0.000869	0.000430 ± 0.000010	2.16E-14	95.5%	2.5119	33.77 ± 0.06	0.17%
au26.5g.bio.32a.txt	1.8	10	2.40902 ± 0.001547	0.92069 ± 0.000853	0.04468 ± 0.000237	0.04404 ± 0.000352	0.000318 ± 0.000011	1.85E-14	96.1%	2.5153	33.82 ± 0.06	0.18%
au26.5g.bio.33a.txt	1.8	10	0.67089 ± 0.001137	0.25346 ± 0.000504	0.01266 ± 0.000084	0.00334 ± 0.000074	0.000095 ± 0.000008	5.15E-15	95.8%	2.5364	34.10 ± 0.15	0.45%
au26.5g.bio.34a.txt	1.8	10	0.85511 ± 0.000875	0.31289 ± 0.000363	0.01650 ± 0.000226	0.01041 ± 0.000159	0.000223 ± 0.000007	6.57E-15	92.3%	2.5230	33.92 ± 0.10	0.30%
au26.5g.bio.35a.txt	1.8	10	2.90710 ± 0.002013	1.10135 ± 0.000994	0.05612 ± 0.000267	0.05709 ± 0.000651	0.000434 ± 0.000008	2.23E-14	95.6%	2.5239	33.93 ± 0.05	0.14%
au26.5g.bio.36a.txt	1.8	10	1.90647 ± 0.001755	0.70492 ± 0.000978	0.03547 ± 0.000227	0.00927 ± 0.000167	0.000434 ± 0.000008	1.46E-14	93.3%	2.5226	33.91 ± 0.08	0.22%
au26.5g.bio.37a.txt	1.8	10	2.24661 ± 0.001681	0.83799 ± 0.001327	0.04143 ± 0.000239	0.03583 ± 0.000203	0.000463 ± 0.000009	1.73E-14	93.9%	2.5185	33.86 ± 0.08	0.22%
au26.5g.bio.38a.txt	1.8	10	1.55341 ± 0.000933	0.57551 ± 0.000824	0.02912 ± 0.000147	0.01055 ± 0.000132	0.000326 ± 0.000009	1.19E-14	93.8%	2.5321	34.04 ± 0.08	0.24%
au26.5g.bio.39a.txt	1.8	10	2.33943 ± 0.002187	0.87244 ± 0.000973	0.04485 ± 0.000250	0.03950 ± 0.000344	0.000499 ± 0.000020	1.80E-14	93.7%	2.5132	33.79 ± 0.10	0.31%
au26.5g.bio.40a.txt	1.8	10	2.38276 ± 0.001968	0.89985 ± 0.001202	0.04479 ± 0.000256	0.02196 ± 0.000242	0.000407 ± 0.000019	1.83E-14	94.9%	2.5146	33.81 ± 0.10	0.30%

GP615-12-1173 Biotite: au26.5g.bio
Mean = 33.878±0.065 [0.19%] 95% conf.
Wtd by data-pt errs only, 0 of 10 rej.
MSWD = 1.5, probability = 0.15

Monitor	P	t	40	39	38	37	36	Moles 40Ar*	% Rad	R	J-value	% -sd
GP640-13-1413 K-feldspar, 18-40 Mesh; Single crystal total fusion analyses.												
au26.5h.kfs.45a.txt	1.8	10	2.02319 ± 0.002249	0.76966 ± 0.001592	0.01196 ± 0.000088	0.00435 ± 0.000130	0.000483 ± 0.000020	1.55E-14	92.9%	2.4433	32.86 ± 0.13	0.40%
au26.5h.kfs.46a.txt	1.8	10	1.76447 ± 0.001568	0.66697 ± 0.000797	0.00960 ± 0.000060	0.00365 ± 0.000094	0.000444 ± 0.000017	1.36E-14	92.6%	2.4489	32.93 ± 0.11	0.35%
au26.5h.kfs.47a.txt	1.8	10	1.53591 ± 0.001299	0.57594 ± 0.000553	0.00815 ± 0.000060	0.00646 ± 0.000117	0.000462 ± 0.000020	1.18E-14	91.1%	2.4298	32.68 ± 0.14	0.44%
au26.5h.kfs.48a.txt	1.8	10	1.98969 ± 0.001596	0.76992 ± 0.000716	0.01069 ± 0.000078	0.00458 ± 0.000082	0.000385 ± 0.000019	1.53E-14	94.3%	2.4367	32.77 ± 0.11	0.32%

GP640-13-1413 K-feldspar: au26.5h.kfs
Mean = 32.82±0.12 [0.36%] 95% conf.
Wtd by data-pt errs only, 0 of 4 rej.
MSWD = 0.75, probability = 0.52

Monitor	P	t	40	39	38	37	36	Moles 40Ar*	% Rad	R	J-value	% -sd
GP-571A-08-350 K-Feldspar, 20-40 Mesh; Single crystal total fusion analyses.												
au26.5j.kfs.52a.txt	1.8	10	2.82665 ± 0.001797	1.00012 ± 0.000765	0.02061 ± 0.000205	0.07054 ± 0.000610	0.001083 ± 0.000013	2.17E-14	88.7%	2.5075	33.71 ± 0.06	0.19%
au26.5j.kfs.53a.txt	1.8	10	0.75495 ± 0.001198	0.28313 ± 0.000543	0.00539 ± 0.000096	0.01175 ± 0.000188	0.000162 ± 0.000008	5.80E-15	93.7%	2.4978	33.58 ± 0.14	0.42%
au26.5j.kfs.54a.txt	1.8	10	0.24718 ± 0.000222	0.06639 ± 0.000382	0.00462 ± 0.000059	0.01826 ± 0.000166	0.000232 ± 0.000008	1.90E-15	72.3%	2.6964	36.23 ± 0.55	1.51%
au26.5j.kfs.55a.txt	1.8	10	0.80052 ± 0.001380	0.27894 ± 0.000733	0.00950 ± 0.000059	0.04802 ± 0.000357	0.000292 ± 0.000008	6.15E-15	89.2%	2.5637	34.46 ± 0.16	0.47%
au26.5j.kfs.56a.txt	1.8	10	2.75588 ± 0.001760	0.97401 ± 0.001758	0.02033 ± 0.000216	0.07459 ± 0.000802	0.001045 ± 0.000013	2.12E-14	88.8%	2.5136	33.79 ± 0.09	0.27%
au26.5j.kfs.57a.txt	1.8	10	6.42494 ± 0.005254	2.22999 ± 0.002393	0.04047 ± 0.000180	0.95026 ± 0.002632	0.003200 ± 0.000021	4.94E-14	85.3%	2.4640	33.13 ± 0.07	0.20%

GP-571A-08-350 K-Feldspar: au26.5j.kfs
MSWD = 22, probability = 0.000

Results of radiometric dating (^{39}Ar/^{40}Ar) for hydrothermal biotite and K-feldspar (orthoclase) from the Peñasquito plutonic complex (3 of 4).

Monitor	P	t	40	39	38	37	36	Moles 40Ar*	% Rad	R	J-value	% -sd
GP-571A-08-350 K-Feldspar, 20-40 Mesh; Incremental heating analyses of a single crystal.												
au26.5j.kfs.58a.txt	0.5	10	0.24038 ± 0.000369	0.03039 ± 0.000206	0.00394 ± 0.000044	0.00558 ± 0.000147	0.000462 ± 0.000009	1.85E-15	43.2%	3.4319	45.98 ± 1.40	3.05%
au26.5j.kfs.58b.txt	0.6	20	0.70914 ± 0.000975	0.25256 ± 0.000522	0.00437 ± 0.000060	0.14502 ± 0.001255	0.000303 ± 0.000007	5.45E-15	87.4%	2.5067	33.70 ± 0.15	0.43%
au26.5j.kfs.58c.txt	0.65	20	0.72420 ± 0.000820	0.28262 ± 0.000633	0.00370 ± 0.000029	0.17739 ± 0.001244	0.000161 ± 0.000007	5.56E-15	93.4%	2.4528	32.99 ± 0.13	0.40%
au26.5j.kfs.58d.txt	0.7	20	1.62044 ± 0.001626	**0.62679 ± 0.000973**	0.00824 ± 0.000071	0.11662 ± 0.000653	0.000266 ± 0.000008	1.24E-14	95.2%	2.4773	**33.31 ± 0.08**	0.25%
au26.5j.kfs.58e.txt	0.72	20	1.26168 ± 0.000720	**0.49794 ± 0.000914**	0.00678 ± 0.000033	0.00567 ± 0.000112	0.000120 ± 0.000007	9.69E-15	97.2%	2.4636	**33.13 ± 0.09**	0.26%
au26.5j.kfs.58f.txt	0.76	20	0.95748 ± 0.001044	**0.37261 ± 0.000641**	0.00593 ± 0.000080	0.00303 ± 0.000124	0.000137 ± 0.000006	7.35E-15	95.8%	2.4614	**33.10 ± 0.10**	0.29%
au26.5j.kfs.58g.txt	0.82	20	0.84392 ± 0.000992	**0.32428 ± 0.000682**	0.00545 ± 0.000038	0.00252 ± 0.000091	0.000150 ± 0.000008	6.48E-15	94.8%	2.4669	**33.17 ± 0.13**	0.40%
au26.5j.kfs.58h.txt	0.9	20	2.75111 ± 0.000844	**1.03395 ± 0.001191**	0.01844 ± 0.000145	0.00918 ± 0.000098	0.000621 ± 0.000013	2.11E-14	93.3%	2.4841	**33.40 ± 0.06**	0.19%
au26.5j.kfs.58i.txt	1	20	2.50929 ± 0.001468	**0.92598 ± 0.001266**	0.01603 ± 0.000108	0.01429 ± 0.000196	0.000675 ± 0.000013	1.93E-14	92.1%	2.4960	**33.56 ± 0.08**	0.23%
au26.5j.kfs.58j.txt	1.15	20	0.39659 ± 0.000746	**0.14535 ± 0.000490**	0.00254 ± 0.000044	0.00518 ± 0.000110	0.000096 ± 0.000014	3.05E-15	92.8%	2.5367	**34.10 ± 0.41**	1.19%
au26.5j.kfs.58k.txt	1.3	20	0.09292 ± 0.000489	**0.03460 ± 0.000266**	0.00063 ± 0.000023	0.00065 ± 0.000081	0.000018 ± 0.000012	7.14E-16	94.2%	2.5325	**34.05 ± 1.38**	4.06%
au26.5j.kfs.58l.txt	1.4	10	0.00869 ± 0.000292	**0.00326 ± 0.000099**	0.00005 ± 0.000014	-0.00010 ± 0.000037	-0.000001 ± 0.000011	6.68E-17	105.1%	2.6667	**35.83 ± 13.49**	37.65%
GP640-13-1413 K-feldspar, 18-40 Mesh; Incremental heating analyses of a single crystal.												
au26.5h.kfs.44a.txt	0.5	20	0.34160 ± 0.000565	0.03688 ± 0.000187	0.00363 ± 0.000049	0.00289 ± 0.000073	0.000856 ± 0.000014	2.62E-15	26.0%	2.4145	32.47 ± 1.72	5.30%
au26.5h.kfs.44b.txt	0.6	20	0.83542 ± 0.000485	0.31831 ± 0.000988	0.00438 ± 0.000051	0.00817 ± 0.000147	0.000230 ± 0.000011	6.42E-15	91.9%	2.4134	32.46 ± 0.18	0.55%
au26.5h.kfs.44c.txt	0.63	20	0.33987 ± 0.000959	0.13604 ± 0.000386	0.00184 ± 0.000056	0.00127 ± 0.000096	0.000030 ± 0.000012	2.61E-15	97.4%	2.4346	32.74 ± 0.37	1.12%
au26.5h.kfs.44d.txt	0.66	20	0.42632 ± 0.000392	0.17130 ± 0.000572	0.00221 ± 0.000048	0.00102 ± 0.000082	0.000026 ± 0.000006	3.27E-15	98.2%	2.4436	32.86 ± 0.18	0.56%
au26.5h.kfs.44e.txt	0.7	20	1.81085 ± 0.001088	0.71953 ± 0.001457	0.00963 ± 0.000079	0.00311 ± 0.000074	0.000228 ± 0.000011	1.39E-14	96.3%	2.4236	32.60 ± 0.09	0.29%
au26.5h.kfs.44f.txt	0.75	20	6.74558 ± 0.005194	2.67562 ± 0.001155	0.03702 ± 0.000188	0.00778 ± 0.000084	0.000797 ± 0.000014	5.18E-14	96.5%	2.4334	32.73 ± 0.04	0.11%
au26.5h.kfs.44g.txt	0.8	20	1.95529 ± 0.001331	0.77181 ± 0.001111	0.01087 ± 0.000088	0.00188 ± 0.000069	0.000221 ± 0.000017	1.50E-14	96.7%	2.4490	32.93 ± 0.10	0.32%
au26.5h.kfs.44h.txt	0.9	20	0.36801 ± 0.000460	0.14601 ± 0.000563	0.00200 ± 0.000032	0.00024 ± 0.000087	0.000059 ± 0.000011	2.83E-15	95.2%	2.4007	32.29 ± 0.33	1.01%
au26.5h.kfs.44i.txt	1	20	0.17951 ± 0.000472	0.07178 ± 0.000303	0.00098 ± 0.000012	0.00020 ± 0.000025	0.000015 ± 0.000007	1.38E-15	97.6%	2.4398	32.81 ± 0.40	1.23%
au26.5h.kfs.44j.txt	1.15	20	0.08917 ± 0.000443	0.03532 ± 0.000162	0.00041 ± 0.000034	-0.00001 ± 0.000080	0.000008 ± 0.000007	6.85E-16	97.2%	2.4545	33.01 ± 0.78	2.38%
au26.5h.kfs.44k.txt	1.3	20	0.01815 ± 0.000302	0.00788 ± 0.000153	0.00009 ± 0.000010	-0.00020 ± 0.000060	-0.000010 ± 0.000013	1.39E-16	115.8%	2.2988	30.93 ± 6.44	20.83%
au26.5h.kfs.44l.txt	1.4	10	0.00753 ± 0.000282	0.00355 ± 0.000113	0.00003 ± 0.000015	-0.00018 ± 0.000077	-0.000011 ± 0.000012	5.78E-17	142.6%	2.1140	28.46 ± 13.83	48.58%

GP-571A-08-350 K-Feldspar: au26.5j.kfs.58
Average age of high temperature steps:
33.32±0.16 Ma (95% conf.)
MSWD = 3.8, probability=0.000
Includes 87.5% of the 39Ar

GP640-13-1413 K-feldspar: au26.5h.kfs.44
Plateau Age = 32.723±0.031 Ma (1s)
MSWD = 0.98, probability = 0.46
100% of the 39Ar, steps 1 through 12

Results of radiometric dating ($^{39}Ar/^{40}Ar$) for hydrothermal biotite and K-feldspar (orthoclase) from the Peñasquito plutonic complex (4 of 4).

Monitor	P	t	40	39	38	37	36	Moles 40Ar*	% Rad	R	J-value	% -sd
GP609-11-1063 Biotite, 18-40 mesh size; Incremental heating analyses of a single crystal.												
au26.5f.bio.28a.txt	0.5	20	0.04140 ± 0.000314	0.01161 ± 0.000069	0.00038 ± 0.000016	0.01405 ± 0.000248	0.000067 ± 0.000012	3.18E-16	52.2%	1.9724	26.57 ± 4.27	16.05%
au26.5f.bio.28b.txt	0.6	20	0.48704 ± 0.000828	0.18126 ± 0.000219	0.00742 ± 0.000038	0.01363 ± 0.000129	0.000118 ± 0.000014	3.74E-15	92.8%	2.5016	33.63 ± 0.31	0.92%
au26.5f.bio.28c.txt	0.65	20	0.46230 ± 0.000615	0.18118 ± 0.000477	0.00767 ± 0.000108	0.00166 ± 0.000050	0.000025 ± 0.000011	3.55E-15	98.4%	2.5112	33.76 ± 0.25	0.75%
au26.5f.bio.28d.txt	0.7	20	0.43428 ± 0.000901	0.17069 ± 0.000470	0.00696 ± 0.000056	0.00165 ± 0.000085	0.000041 ± 0.000009	3.34E-15	97.2%	2.4736	33.26 ± 0.25	0.75%
au26.5f.bio.28e.txt	0.75	20	0.58360 ± 0.001176	0.22909 ± 0.000631	0.01012 ± 0.000175	0.00229 ± 0.000091	0.000060 ± 0.000009	4.48E-15	97.0%	2.4712	33.23 ± 0.20	0.59%
au26.5f.bio.28f.txt	0.8	20	0.62392 ± 0.001306	0.24517 ± 0.000926	0.01094 ± 0.000075	0.00281 ± 0.000105	0.000030 ± 0.000012	4.79E-15	98.6%	2.5099	33.75 ± 0.24	0.71%
au26.5f.bio.28g.txt	0.85	20	0.65332 ± 0.000730	0.25420 ± 0.000760	0.01168 ± 0.000109	0.00439 ± 0.000095	0.000080 ± 0.000008	5.02E-15	96.4%	2.4783	33.32 ± 0.16	0.50%
au26.5f.bio.28h.txt	0.9	20	0.25606 ± 0.000272	0.10096 ± 0.000234	0.00456 ± 0.000057	0.00723 ± 0.000135	0.000001 ± 0.000007	1.97E-15	99.9%	2.5394	34.14 ± 0.29	0.84%
au26.5f.bio.28i.txt	1	20	0.10675 ± 0.000475	0.04175 ± 0.000181	0.00146 ± 0.000034	0.00653 ± 0.000265	0.000006 ± 0.000006	8.20E-16	98.3%	2.5289	34.00 ± 0.63	1.86%
au26.5f.bio.28j.txt	1.1	20	0.03031 ± 0.000252	0.01251 ± 0.000085	0.00030 ± 0.000018	0.00009 ± 0.000066	-0.000016 ± 0.000009	2.33E-16	115.5%	2.4239	32.60 ± 2.87	8.81%
au26.5f.bio.28k.txt	1.2	20	0.01874 ± 0.000247	0.00793 ± 0.000095	0.00018 ± 0.000014	0.00005 ± 0.000051	-0.000014 ± 0.000007	1.44E-16	122.0%	2.3647	31.81 ± 3.38	10.63%
au26.5f.bio.28l.txt	1.3	10	0.00309 ± 0.000195	0.00123 ± 0.000066	0.00002 ± 0.000013	0.00001 ± 0.000049	0.000035 ± 0.000008	2.37E-17	-233.0%	-5.8604	-81.34 -± 27.00	33.19%
GP615-12-1173 Biotite, 18-40 Mesh Size; Incremental heating analyses of a single crystal.												
au26.5g.bio.42a.txt	0.5	20	0.06943 ± 0.000559	0.00904 ± 0.000067	0.00035 ± 0.000021	0.00230 ± 0.000104	0.000148 ± 0.000007	5.33E-16	37.2%	2.8792	38.66 ± 3.14	8.12%
au26.5g.bio.42b.txt	0.6	20	0.34031 ± 0.000602	0.11200 ± 0.000358	0.00539 ± 0.000083	0.00324 ± 0.000185	0.000209 ± 0.000007	2.61E-15	81.9%	2.4897	33.48 ± 0.29	0.86%
au26.5g.bio.42c.txt	0.65	20	0.70743 ± 0.001314	0.26046 ± 0.000462	0.01288 ± 0.000125	0.00146 ± 0.000064	0.000163 ± 0.000007	5.43E-15	93.2%	2.5319	34.04 ± 0.14	0.41%
au26.5g.bio.42d.txt	0.7	20	0.59953 ± 0.000785	0.23328 ± 0.000528	0.01146 ± 0.000139	0.00123 ± 0.000059	0.000035 ± 0.000006	4.61E-15	98.3%	2.5259	33.96 ± 0.13	0.40%
au26.5g.bio.42e.txt	0.75	20	0.72564 ± 0.000934	0.28346 ± 0.000866	0.01382 ± 0.000151	0.00180 ± 0.000096	0.000034 ± 0.000006	5.57E-15	98.6%	2.5247	33.94 ± 0.14	0.41%
au26.5g.bio.42f.txt	0.8	20	0.66097 ± 0.001116	0.25890 ± 0.000461	0.01261 ± 0.000128	0.00255 ± 0.000072	0.000017 ± 0.000007	5.08E-15	99.2%	2.5346	34.07 ± 0.14	0.41%
au26.5g.bio.42g.txt	0.85	20	0.77710 ± 0.001070	0.30467 ± 0.000903	0.01508 ± 0.000137	0.00594 ± 0.000232	0.000029 ± 0.000011	5.97E-15	98.9%	2.5244	33.94 ± 0.18	0.54%
au26.5g.bio.42h.txt	0.9	20	0.94956 ± 0.001335	0.37163 ± 0.000585	0.01895 ± 0.000146	0.01218 ± 0.000103	0.000053 ± 0.000010	7.29E-15	98.4%	2.5164	33.83 ± 0.13	0.38%
au26.5g.bio.42i.txt	1	20	0.93554 ± 0.001180	0.36132 ± 0.000715	0.01968 ± 0.000219	0.03737 ± 0.000299	0.000093 ± 0.000010	7.19E-15	97.1%	2.5230	33.92 ± 0.14	0.41%
au26.5g.bio.42j.txt	1.1	20	0.03725 ± 0.000211	0.01452 ± 0.000089	0.00090 ± 0.000013	0.00789 ± 0.000233	0.000002 ± 0.000006	2.86E-16	98.3%	2.5735	34.59 ± 1.56	4.51%
au26.5g.bio.42k.txt	1.2	20	0.03818 ± 0.000208	0.01440 ± 0.000072	0.00078 ± 0.000021	0.00439 ± 0.000119	0.000000 ± 0.000007	2.93E-16	99.7%	2.6732	35.92 ± 1.93	5.37%
au26.5g.bio.42l.txt	1.3	10	0.01041 ± 0.000210	0.00387 ± 0.000080	0.00023 ± 0.000009	0.00220 ± 0.000120	0.000002 ± 0.000012	8.00E-17	95.2%	2.6136	35.13 ± 11.90	33.88%

GP609-11-1063 Biotite: au26.5f.bio.28
Plateau Age = 33.507±0.085 Ma (1s)
MSWD = 1.5, probability = 0.14
100% of the 39Ar, steps 1 through 11

GP615-12-1173 Biotite: au26.5g.bio.42
Plateau Age = 33.943±0.052 Ma (1s)
MSWD = 0.75, probability = 0.69
100% of the 39Ar, steps 1 through 12